KfK 2830
Juli 1979

"What Do We Know about the Radial Shape of Nuclei in the Ca-Region?"

Proceedings of the Karlsruhe International Discussion Meeting, held at Kernforschungszentrum Karlsruhe, May 2-4, 1979

Edited by: H. Rebel, H. J. Gils, G. Schatz
Institut für Angewandte Kernphysik

Kernforschungszentrum Karlsruhe

KERNFORSCHUNGSZENTRUM KARLSRUHE

Institut für Angewandte Kernphysik

KfK 2830

"WHAT DO WE KNOW ABOUT THE RADIAL SHAPE OF NUCLEI IN THE Ca-REGION?"

Proceedings of the Karlsruhe International Discussion Meeting, held at Kernforschungszentrum Karlsruhe May 2-4, 1979

Edited by H. Rebel, H.J. Gils, and G. Schatz

Kernforschungszentrum Karlsruhe GmbH, Karlsruhe

Kernforschungszentrum Karlsruhe GmbH
ISSN 0303-4003

PREFACE

The Discussion Meeting "What Do We Know about the Radial Shape of Nuclei in the Ca-Region?", held in the Kernforschungszentrum Karlsruhe, May 2-4, 1979 was arranged on an international level in order to discuss the present status of our knowledge about shapes of nuclei in the Ca-region. For this, in a series of introductory lectures and short contributions following topics have been covered:

- Electron scattering
- Muonic atoms
- Intermediate and high energy α-particle and proton scattering
- $\pi^{\pm}$-scattering
- Total cross sections
- Pionic atoms
- Optical isotope shifts
- Coulomb displacement energies
- Subcoulomb scattering
- Magnetic electron scattering and transfer reactions.

The nuclei of the Ca-region served as representative examples for which the information from various kinds of experiments could be critically compared and the concepts could be illustrated. It was in the spirit of the meeting that the discussions took often more time than the lectures themselves. Therefore we may regret that these proceedings do not include many valuable and clarifying comments. In fact, the main success of the meeting has been the lively and stimulating discussion between nuclear physicists coming from quite different methods and experimental tools, but attacking the same problems.

On this occasion we would like to thank Mrs. E. Maaß and Mr. P. Emmerich for their help in organizing the discussion meeting. The meeting has been supported by the Kernforschungszentrum Karlsruhe.

Kernforschungszentrum Karlsruhe, May 1979

H. Rebel

Table of Contents

Page

Page

PARTICIPANTS

Barrett, R.C.	University of Surrey, Guildford, England
Boschitz, E.	University of Karlsruhe, Federal Republic of Germany
Brissaud, I.	Institute of Nuclear Physics, Orsay, France
Brix, P.	MPI Heidelberg, Federal Republic of Germany
Budzanowski, A.	Institute of Nuclear Physics, Cracow, Poland / KFA Jülich
Campi, X.	Institute of Nuclear Physics, Orsay, France
Chiang, H.C.	University of Peking, China/ MPI Heidelberg, Federal Republic of Germany
De Jager, C.W.	IKO Amsterdam, The Netherlands
Duggan, F.	Institute of Nuclear Physics, Orsay, France
Durell, J.	University of Manchester, England
Egger, J.-P.	University of Neuchâtel, Switzerland
Fernandez, B.	CEN Saclay, France
Fricke, G.	University of Mainz, Federal Republic of Germany
Friedman, E.	The Hebrew University, Jerusalem, Israel
Friedrich, J.	University of Mainz, Federal Republic of Germany
Frois, B.	CEN Saclay, France
Gils, H.J.	KfK Karlsruhe, Federal Republic of Germany
Grange, P.	MPI Heidelberg, Federal Republic of Germany
Grotowski, K.	Institute of Nuclear Physics, Cracow, Poland
Gubler, H.	University of Basel, Switzerland

Heilig, K.	University of Hannover, Federal Republic of Germany
Hüfner, J.	University of Heidelberg, Federal Republic of Germany
Jackson, D.F.	University of Surrey, Guildford, England
Klewe-Nebenius, H.	KfK Karlsruhe, Federal Republic of Germany
Klose, W.	KfK Karlsruhe, Federal Republic of Germany
Kluge, H.J.	University of Mainz, Federal Republic of Germany
Kowalski, J.	University of Heidelberg, Federal Republic of Germany
Lejeune, A.	University of Liège, Belgium
Mahaux, C.	University of Liège, Belgium
Majka, Z.	Institute of Nuclear Physics, Cracow, Poland
Meyer, H.O.	Indiana University, Bloomington, U.S.A.
Michel, F.	University of Mons, Belgium
Miska, H.	University of Mainz, Federal Republic of Germany
Moalem, A.	Ben Gurion University, Beer Sheva, Israel
Nowicki, G.	KfK Karlsruhe, Federal Republic of Germany
Palmer, C.	University of Oxford, England
zu Putlitz, G.	GSI Darmstadt, Federal Republic of Germany
Rebel, H.	KfK Karlsruhe, Federal Republic of Germany
Schaeffer, R.	CEN Saclay, France
Schatz, G.	KfK Karlsruhe, Federal Republic of Germany
Schellenberg, L.	University of Fribourg, Switzerland
Shlomo, S.	CEN Saclay, France
Sick, I.	University of Basel, Switzerland
Steudel, A.	University of Hannover, Federal Republic of Germany
Träger, F.	University of Heidelberg, Federal Republic of Germany
Wagner, G.	MPI Heidelberg, Federal Republic of Germany

Wiegemann, H. — University of Heidelberg, Federal Republic of Germany

Wohlfahrt, H.D. — Los Alamos, U.S.A.

NUCLEAR RADII

Daphne F. Jackson
University of Surrey,
Guildford, England

NUCLEAR RADII

Daphne F. Jackson

Department of Physics
University of Surrey, Guildford, UK

1. Introduction

In a summary of proton and neutron radii presented at the EPS conference in 1976, I concluded that [1] ... "It is evident that the problem of determining the proton and charge distributions is well understood and that some moments of these distributions are quite well determined. In contrast, the situation for neutron distributions is rather confused. There are too many methods and each one suffers from deficiencies; for proton and α-particle scattering the effective interaction is not precisely known while for pion and kaon interactions the experimental uncertainties are often large and the resonant nature of the meson-nucleon interaction complicates the theory". At about the same time, R.C. Barrett and I used the quotation [2]... "Fact is theory and fiction is experiment" to introduce a review of the nuclear matter distribution [3].

The work carried out in many groups during the past 2-3 years has very largely resolved the confusion over the matter and neutron distributions, particularly in the region of the Periodic Table to be discussed at this conference, and has probably reversed the relationship between theory and experiment. I anticipate that many of the following papers will indicate a new sense of confidence in our understanding of nuclear radii and distributions. In this talk, I will indicate where some of the remaining points of weakness or uncertainty may lie, in the hope that other speakers may be able to deal with them. I have selected a few topics to illustrate these points but will leave detailed discussion of new results to later speakers.

2. Special Features of the Calcium Region

Calcium itself provides the first long sequence of stable isotopes, conveniently stretching between the magic numbers at N=20 and N=28, while the stable isotopes of potassium, argon, titanium provide useful comparisons.

Thus we expect to be able to study the following basic nuclear properties - (i) the effects of shell closure at Z=20, N=20 and N=28, (ii) the change in the distribution of a fixed number of protons as the neutron number increases, and (iii) the change in the neutron and the matter distributions as the neutron number increases. The emphasis is very definitely on changes in distributions and hence we are particularly interested in those phenomena which depend on differences between these quantities. Experiments which measure directly differences or ratios will be especially useful.

The stability and abundance of most of the relevant nuclides means that a wide variety of measurements are possible and hence we have the possibility of comparison of methods and conclusions. Further, the availability of a nucleus with Z=N, i.e. ^{40}Ca, makes it possible to perform calibration measurements and to determine parameters of a theory.

3. Definitions

If the ground state of a nucleus with Z protons and N=A-Z neutrons is represented by $|0\rangle$, the one-particle proton and neutron distributions are given by

$$Z\rho_p(\underset{\sim}{r}) = \langle 0 | \sum_{i=1}^{Z} \delta(\underset{\sim}{r}-\underset{\sim}{r}_i) | 0 \rangle \tag{1}$$

$$N\rho_n(\underset{\sim}{r}) = \langle 0 | \sum_{i=1}^{N} \delta(\underset{\sim}{r}-\underset{\sim}{r}_i) | 0 \rangle \tag{2}$$

where each sum runs over like particles only and the normalization is

$$\int \rho_n(\underset{\sim}{r}) d^3r = \int \rho_p(\underset{\sim}{r}) d^3r = 1. \tag{3}$$

The matter distribution is

$$A\rho_m(\underset{\sim}{r}) = Z\rho_p(\underset{\sim}{r}) + N\,\rho_n(\underset{\sim}{r}). \tag{4}$$

These are all distributions of point nucleons in the nucleus. The two-particle density distribution is defined as

$$A(A-1)\rho(\underset{\sim}{r},\underset{\sim}{r}') = \langle 0 | \sum_{i\neq j} \delta(\underset{\sim}{r}-\underset{\sim}{r}_i)\delta(\underset{\sim}{r}-\underset{\sim}{r}_j) | 0 \rangle \tag{5}$$

and in a single-particle model is given by

$$A(A-1)\rho(\underset{\sim}{r},\underset{\sim}{r}') = A^2\,\rho(\underset{\sim}{r})\rho(\underset{\sim}{r}') - A\,\rho_{ex}(\underset{\sim}{r},\underset{\sim}{r}') \tag{6}$$

$$A\,\rho_{ex}(\underset{\sim}{r},\underset{\sim}{r}') = \sum_{\mu}\sum_{\nu}\phi_{\mu}^{*}(\underset{\sim}{r}')\,\phi_{\nu}^{*}(\underset{\sim}{r})\,\phi_{\nu}(\underset{\sim}{r}')\,\phi_{\mu}(\underset{\sim}{r}) \tag{7}$$

$$A\,\rho(\underset{\sim}{r}) = \sum_{\mu}|\phi_{\mu}(\underset{\sim}{r})|^{2} \tag{8}$$

This model includes only Pauli correlations and excludes short-range dynamical correlations and medium range correlations arising from configuration mixing and deformations.

It is possible to define various distribution differences, such as the neutron excess distribution

$$\rho_{ne}(\underset{\sim}{r}) = N\,\rho_{n}(\underset{\sim}{r}) - Z\,\rho_{nc}(\underset{\sim}{r}) \tag{9}$$

where ρ_{nc} is the distribution of a core of Z neutrons. The difference between two proton distributions may be written as

$$\Delta\rho_{p}(\underset{\sim}{r}) = Z_{1}\,\rho_{1}(\underset{\sim}{r}) - Z_{2}\,\rho_{2}(\underset{\sim}{r}), \tag{10}$$

and so on.

For a distribution of the form

$$\rho(\underset{\sim}{r}) = \rho_{0}\,f(\underset{\sim}{r}) \tag{11}$$

where $f(0) = 1$ and $f(\infty) = 0$, Süssmann [4] has defined the volume moments

$$F_{\nu} = \int_{0}^{\infty} f(r)\,r^{\nu}dr \tag{12}$$

and the radius parameters -

$$\text{central radius } C = F_{0} \tag{13}$$

$$\text{uniform radius } U = (3F_{2})^{1/3} \tag{14}$$

$$\text{quadratic radius } Q = (5F_{4}/3F_{2})^{\frac{1}{2}}. \tag{15}$$

The volume integral is given by

$$J = 4\pi\,\rho_{0}\,F_{2} = \frac{4\pi}{3}\,\rho_{0}\,U^{3} \tag{16}$$

and hence U has the physical significance of the radius of the uniform sphere which contains the same amount of matter as the real distribution. Thus U

may be expected to depend on $A^{1/3}$, at least along the line of maximum β-stability, but C and Q have more complicated dependence on A[4,5]. The disadvantage of this approach is that it implies a precise knowledge of ρ_0, but the matter distribution is not well-determined at r=0 and the uncertainty in the proton distribution at this point is still quite large. Also, if the distribution is not approximately monotonic, ρ_0 must be defined as some average value in the interior of the nucleus. For these reasons, the moments defined by Friedrich and Lenz [6]

$$M(k) = \langle r^k \rangle^{1/k} \tag{17}$$

or the moments defined by Ford and Wills [7]

$$R_k = \left[\frac{1}{3}(k+3)\langle r^k \rangle\right]^{1/k} = \left[\frac{1}{3}(k+3)\right]^{1/k} M(k) \tag{18}$$

have been widely used. For studies of muonic atoms, the generalized moments defined by Ford and Rinker [8] as

$$\langle u(r) r^k \rangle = \int_0^\infty \rho(r)\ u(r)\ r^{k+2}\ dr \tag{19}$$

are used, where r^k times the weighting function $u(r)$ is frequently taken to be related to the function $a + b\ r^k e^{-\alpha r}$ introduced by Barrett [9] to describe the spherically averaged potential due to the muon cloud.

The charge distribution of a closed-shell nucleus is given by the folding integral

$$Z\,\rho_{ch}(\underset{\sim}{r}) = Z\int \rho_p(\underset{\sim}{r}')\ g_p(|\underset{\sim}{r}-\underset{\sim}{r}'|)d^3r' + N\int \rho_n(\underset{\sim}{r}')\ g_n(|\underset{\sim}{r}-\underset{\sim}{r}'|)d^3r' \tag{20}$$

where g_p, g_n are, respectively the internal charge distribution of the proton and of the neutron. It is necessary to remember that for other nuclei there may also be a contribution [10] arising from the spin-orbit interaction of the lepton with valence nucleons and hence the rms charge radius is given by

$$\langle r^2 \rangle_{ch} = \langle r^2 \rangle_p + \langle r^2 \rangle_{proton} + \frac{N}{Z}\langle r^2 \rangle_{neutron} + \langle r^2 \rangle_{\ell s}. \tag{21}$$

The change in the r.m.s. charge radius of ^{48}Ca due to the neutron charge form factor has been calculated to be -0.007 fm and that due to the neutron spin-orbit term to be -0.014 fm[10].

4. High Energy Proton Scattering

The very good quality of the proton scattering data now available in the energy region 600 MeV - 1 GeV makes the analysis of these data a popular method for the study of nuclear radii. This choice of energy has much to commend it; in particular, it seems very reasonable to use the impulse approximation and relate the scattering to the amplitudes for free nucleon-nucleon scattering. In this approximation, the first-order nuclear optical potential is given by

$$U_{pA}(r) \propto \int [Z\ F_p(q)\ f_{pp}(q) + N\ F_n(q)\ f_{pn}(q)]\ e^{-i\underset{\sim}{q}.\underset{\sim}{r}}\, d^3q \qquad (22)$$

where q is the momentum transfer, F_p and F_n are the nuclear form factors, i.e.

$$F_p(q) = \int e^{i\underset{\sim}{q}.\underset{\sim}{r}}\, \rho_p(\underset{\sim}{r})\, d^3r, \quad F_n(q) = \int e^{i\underset{\sim}{q}.\underset{\sim}{r}}\, \rho_n(\underset{\sim}{r})\, d^3r, \qquad (23)$$

and f_{pp}, f_{pn} are the amplitudes for p-p and p-n scattering. The latter may be approximated as [11,12]

$$f_{pp}(q) = A_{pp}(q) + C_{pp}(q)\ \hat{\underset{\sim}{\sigma}}.\hat{\underset{\sim}{n}} \qquad (24)$$

$$A_{pp}(q) = \frac{ik}{4\pi}\, \sigma_{pp}[1-i\ \alpha_{pp}(q)]\ \exp(-\beta^2_{pp} q^2/2) \qquad (25)$$

$$\alpha_{pp}(q) = \alpha_0 + \alpha_1\ q^2 \qquad (26)$$

$$C_{pp}(q) = \frac{ik}{4\pi}\, \sigma_{pp}\ \ \frac{q\ D_s}{2M}\ [1-i\alpha_s]\ \exp(-\beta_s^2\ q^2/2) \qquad (27)$$

and similarly for f_{pn}.

The total cross-sections σ for pp and pn scattering may be related to the cross-sections in the pure isospin T=1 and T=0 states, i.e.

$$\sigma_{pp} = \sigma(T=1) \quad , \quad \sigma_{pn} = \tfrac{1}{2}[\sigma(T=1) + \sigma(T=0]. \qquad (28)$$

Examination of the behaviour of these total cross-sections, shown in Figure 1, indicates that σ_{pp} goes through a maximum at 1 GeV. This means that the absorption of protons on protons steadily increases from about 250 MeV up to a maximum at 1 GeV and hence the penetration of the proton into the interior of the nucleus steadily falls. The absorption of protons on neutrons rises steeply below 300 MeV, but is $\sim$ 25% below that on protons at 1 GeV. The

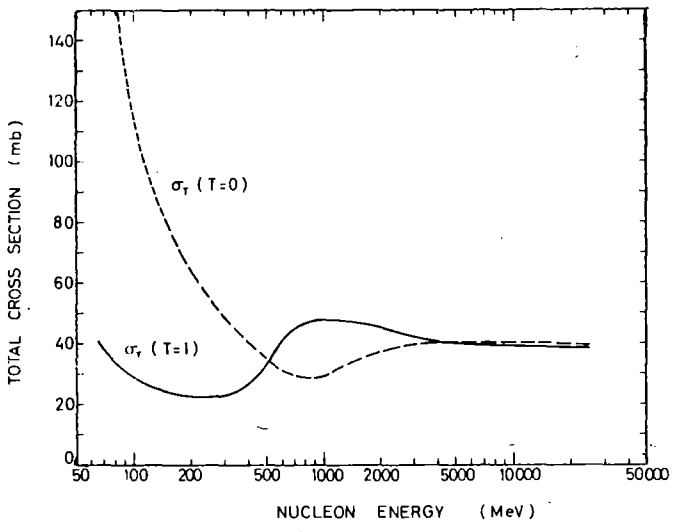

Figure 1: The total cross-sections for the nucleon-nucleon interaction in the pure isospin states T=0 and T=1 [13]

discrimination between neutrons and protons is not large and therefore proton scattering may be expected to be sensitive to the behaviour of the matter distribution in the surface of the nucleus.

The nuclear scattering may be calculated using the first-order potential in a Schrödinger equation with relativistic kinematics or using the Glauber formalism. In the optical limit, the scattering amplitude can be written in the form

$$f_{pA}(q) = \frac{ik}{2\pi}\int e^{i\underset{\sim}{q}.\underset{\sim}{b}}\{1-\exp[-Z\int\Gamma_p^c(\underset{\sim}{b}-\underset{\sim}{s})\rho_p(\underset{\sim}{r})d^3r - N\int\Gamma_n(\underset{\sim}{b}-\underset{\sim}{s})\rho_n(\underset{\sim}{r})d^3r]\}d^2b \quad (29)$$

$$\Gamma_p^c(\underset{\sim}{b}) = [1-e^{i\chi_c(\underset{\sim}{b})}] + e^{i\chi_c(\underset{\sim}{b})}\Gamma_p(\underset{\sim}{b}) \quad (30)$$

$$\Gamma_p(\underset{\sim}{b}) = \frac{1}{2\pi ik}\int e^{-i\underset{\sim}{q}.\underset{\sim}{b}} f_{pp}(q)d^3q, \qquad \Gamma_n(\underset{\sim}{b}) = \frac{1}{2\pi ik}\int e^{-i\underset{\sim}{q}.\underset{\sim}{b}} f_{pn}(q)d^3q \quad (31)$$

where χ_c is the phase shift function for the Coulomb interaction. Slightly different formulations are possible and all seem to yield quite good agreement with the data provided that Coulomb and spin-orbit effects are taken into account, at least approximately. Figure 2 shows the effect of neglecting these parts of the interaction for 1 GeV proton scattering on ^{40}Ca and ^{48}Ca[14]. The parameters of the spin-orbit terms can be checked by fitting polarization data [11] and it is therefore very welcome to see good measurements of analysing powers at 800 MeV[15]. Data for calcium isotopes are shown in

figure 3.

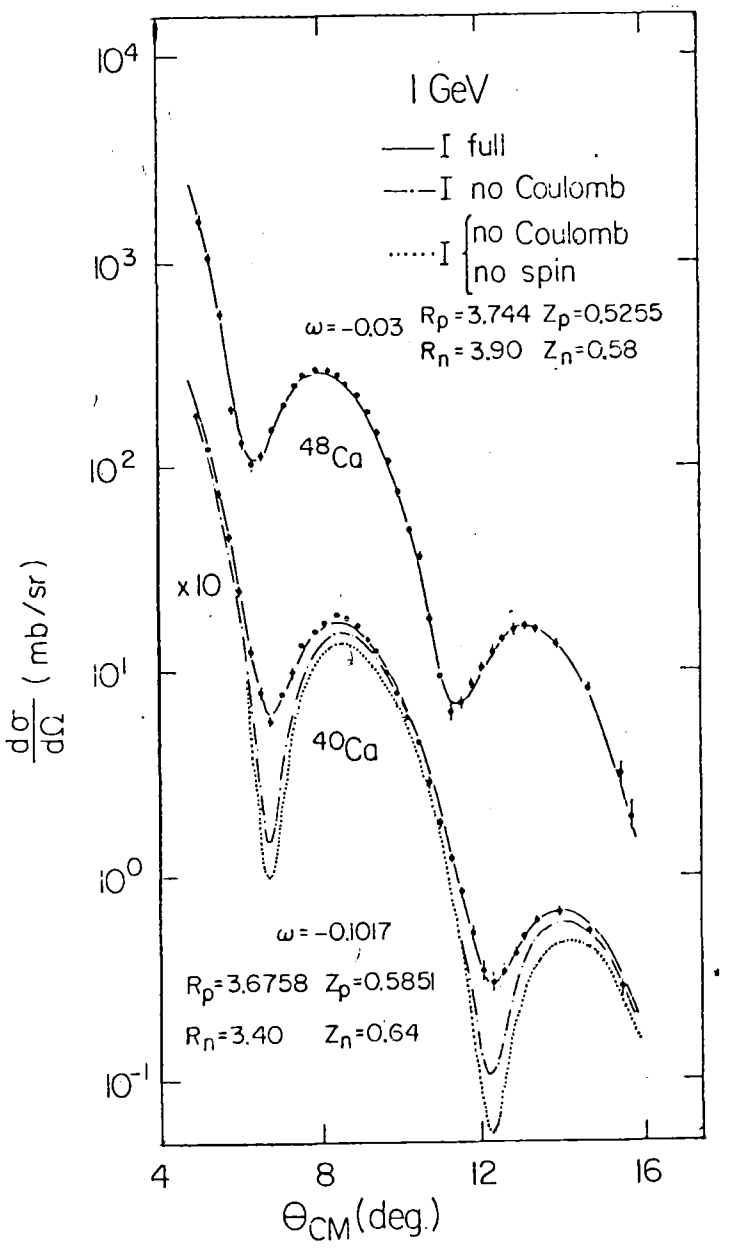

Figure 2. Elastic scattering of 1 GeV protons from ^{40}C and ^{48}Ca [14]

Equation (27) describes single scattering only. Double and higher multiple scattering can be included and are quite important for light nuclei[16]. Harrington and Varma [17] have given an estimate of the effect of Pauli correlations in an oscillator model and find that they are more important than corrections to the Glauber formalism. For ^{40}Ca, the cross-section is increased by $\sim$ 10%, 13% and 20% at the second, third and fourth maxima, respectively. Some authors [11,12,18] also include a centre of mass correction

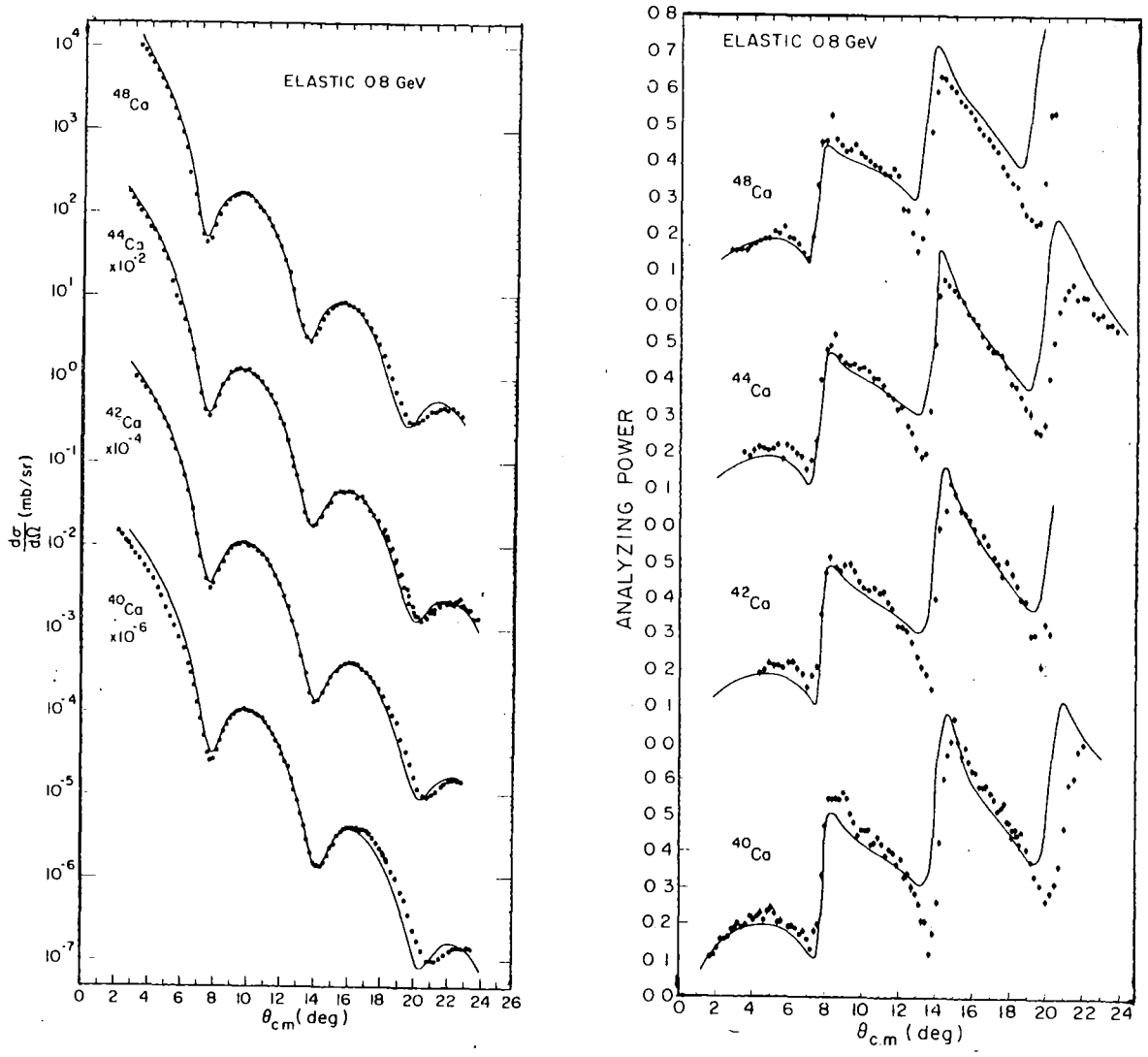

Figure 3. Angular distributions and analysing powers for elastic scattering of 800 MeV polarized protons from calcium isotopes. The curves are calculated from the first order optical potential [15].

factor derived from oscillator functions, but it seems rather doubtful whether this factor should be included if comparison is to be made with realistic forms for ρ_p and ρ_n which have been fitted directly to experiment.

The introduction of model-independent representations of the density distributions appearing in equations (22) or (27) have confirmed [11,18] that the central region of the matter distribution is not well-determined, although some moments of the distribution are quite well-defined. Figures 4 and 5 show the results of one of the earliest studies of ^{40}Ca, but more recent work does not seem to change this general conclusion. Thus it is reasonable to

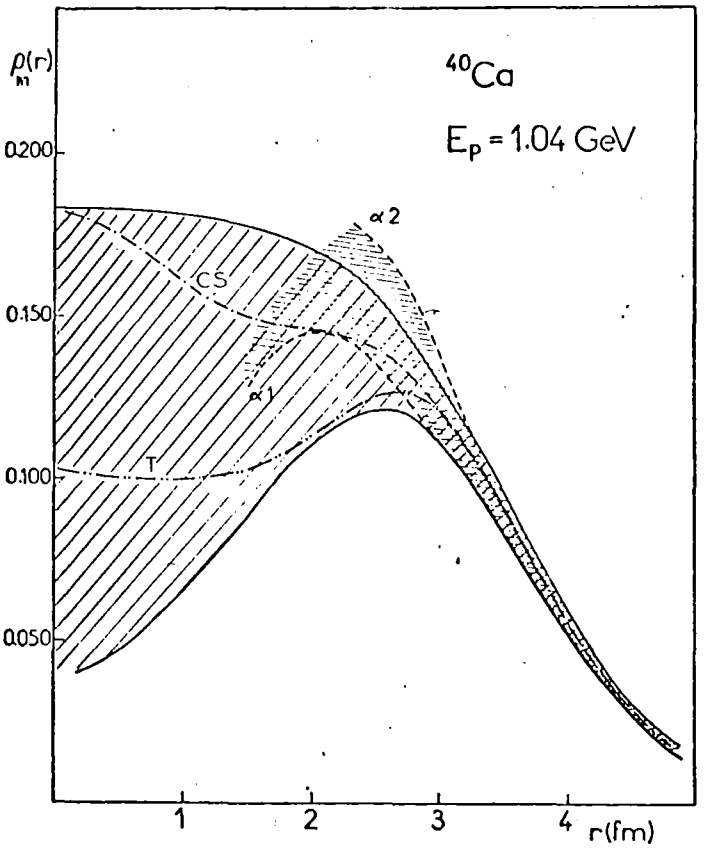

Figure 4 . Envelope of trial matter distributions for ^{40}Ca which give agreement with the 1 GeV proton scattering data. The region α1-α2 gives the envelope of distributions which fit 166 MeV α-particle scattering

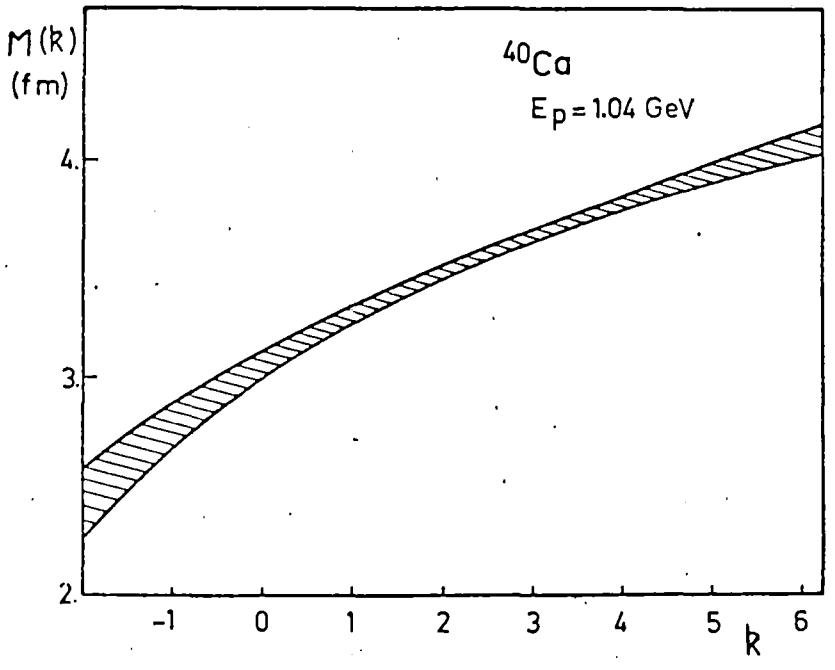

Figure 5. Envelope of moments M(k) of the trial distributions shown in Figure 4

express the results of these analyses in terms of differences of moments of the matter distributions and particularly in terms of r.m.s. radii. When conclusions are drawn about the neutron radii it must always be remembered that they depend critically on the results for the proton radii derived from electron scattering or other electromagnetic data.

I do not know of any model-independent method of calculating the multiple-scattering correction to the Glauber scattering formalism or the second-order optical potential, although it is possible to construct Pauli correlation functions from realistic single-particle wavefunctions [19] and to make a realistic single-particle estimate of the second-order potential [20]. It is also important to estimate the effect of medium-range correlations.

5. Pion-nucleus Interactions

It has long been hoped that differences between the πp and the πn interactions could be used to obtain direct information about the neutron distribution. From charge symmetry, the total cross-sections are related in the following manner

$$\sigma(\pi^+ p) = \sigma(\pi^- n) = \sigma(T={}^3/_2). \tag{32}$$

$$\sigma(\pi^- p) = \sigma(\pi^+ n) = \frac{2}{3}\sigma(T=\tfrac{1}{2}) + \frac{1}{3}\sigma(T={}^3/_2). \tag{33}$$

where the $\sigma(T)$ are the cross-sections in the state with pure isospin $T = {}^3/_2$ and $T = \frac{1}{2}$ which are plotted in Figure 6. Although averaging over the fermi

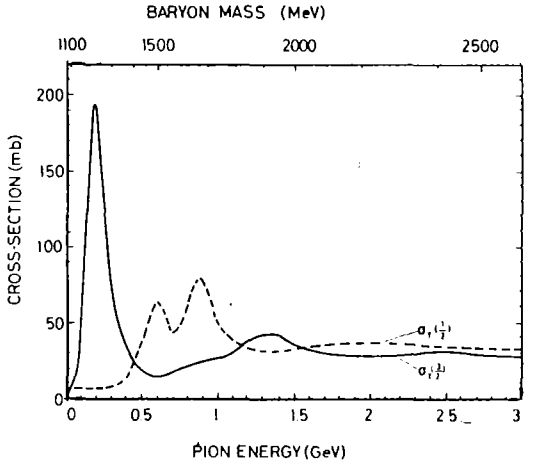

Figure 6. The total cross-section for the pion-nucleon interaction in the pure isospin states $T = {}^3/_2$ and $T = \frac{1}{2}$ [13]

momentum of the nucleons in the nucleus suppresses the resonance structure in the $T = \frac{1}{2}$ cross-section in the energy region 0.5-1.0 GeV [21], the $\pi^- p$ cross-section still exceeds the $\pi^+ p$ cross-section by a factor of ~ 2 in this region. In contrast, in the region of the (3, 3) resonance $\sigma(T=\frac{1}{2})$ is negligible and hence $\sigma(\pi^+ p) \sim 3\ \sigma(\pi^- p)$. Hence, in the upper energy region, the penetration of pions into the nucleus is comparable with that for 1 GeV protons but at the (3, 3) resonance the nucleus is very black for pions.

The earliest attempts to exploit these differences involved measurements of ratios of π^+ and π^- reaction cross-sections on various nuclei [21,22]. The data can be analysed using an optical potential constructed in a similar manner to the proton optical potential defined in equation (22), which in a forward scattering approximation yields the imaginary part

$$\text{Im } U^{\pm}(\underset{\sim}{r}) \propto \tfrac{1}{2}\{\sigma(\pi^+ p) + \sigma(\pi^- p)\} A\ \rho_m(\underset{\sim}{r})$$

$$\pm \tfrac{1}{2}\{\sigma(\pi^- p) - \sigma(\pi^+ p)\}[N\ \rho_n(\underset{\sim}{r}) - Z\ \rho_p(\underset{\sim}{r})]. \qquad (34)$$

It is essential to include the Coulomb interaction accurately because this affects the π^+ and π^- scattering differently, but use of ratios of cross-sections reduces the importance of other corrections. Differences of total cross-sections for isotopes such as $^{16,18}O$ and $^{40,48}Ca$ have been measured[23] for both π^+ and π^- in the region of the (3,3) resonance where the results are rather insensitive to the details of the optical potential.

Differential cross-sections for pion scattering have been studied at 1 GeV [24] and in the energy range 50-300 MeV [25]. It is found that the depths and separation of the minima are sensitive to changes in the nuclear distribution but these features are also sensitive to the magnitude and sign of the real part of the pion-nucleon amplitude. Sternheim and Yoo [26] have studied differential cross-sections for π^+ and π^- scattering from ^{48}Ca at 130 MeV and have shown that a fit to a single angular distribution does not determine the neutron radius uniquely unless the potential parameters are known, because changes in the neutron distribution can be compensated by changes in the coefficient of the p-wave isovector term in the potential. In order to avoid some of these difficulties Rost et al [27] have proposed that the ratios of angular distributions of π^- scattering from neighbouring nuclei should be studied at low energy. This method exploits the large s-wave isovector part of the πN interaction. They use a potential based on that derived from studies of pionic atoms with the form

$$U(r) = U_0 + U_p + U_{SA} + U_{Coul} \tag{35}$$

where U_0 is the Ericson potential [28] without the Lorentz-Lorenz effect and with the parameters taken from free πN scattering, U_p is a Pauli blocking term of the form

$$U_p \propto \langle \frac{1}{r} \rangle \rho_m(r) \tag{36}$$

where $\langle \frac{1}{r} \rangle$ is the Pauli correlation length, and U_{SA} is an s-wave annihilation term

$$U_{SA} \propto B_0 [\rho_m(R)]^2 \tag{37}$$

which represents the effect of annihilation of pions by absorption on two nucleons. Figure 7 shows the sensitivity of ratios of cross-sections of 29 MeV pion scattering from ^{18}O and ^{16}O; in the latter case it is assumed that the proton and neutron distributions are identical.

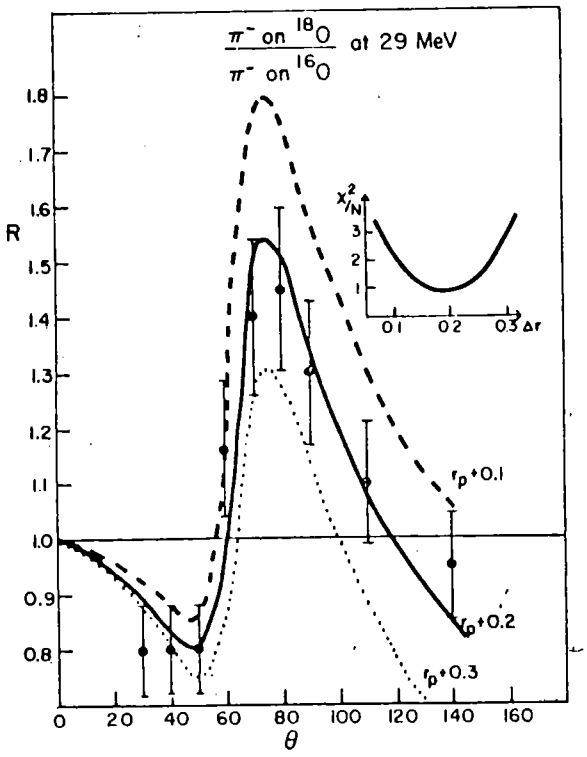

Figure 7. The ratio R of differential cross-sections of 29 MeV negative pions scattered from ^{18}O and ^{16}O. The curves show the effect of variations of the neutron rms radius. The inset shows the behaviour of χ^2/N as a function of the difference between the neutron and proton rms radii.

An alternative approach is to obtain the parameters of the potential by fitting data on pionic atoms. This has recently been done by Batty et al [29] using the Ericson potential with the Lorentz-Lorenz correction. They take a complex annihilation term in both s-wave and p-wave and write the density dependence of this term to be 4 $\rho_p(r)\rho_n(r)$, instead of the customary $[\rho_m(r)]^2$, on the grounds that the absorption of pions occurs preferentially on n-p pairs.

Their analysis of 2p shifts and widths in a range of nuclei showed a strong link between the coefficient of the s-wave isovector term and the values of $\langle r_n^2 \rangle^{\frac{1}{2}} - \langle r_p^2 \rangle^{\frac{1}{2}}$. The same group has studied the 2p states in pionic ^{40,44}Ca and obtain [30] a value for the difference in the neutron rms radii which disagrees sharply with the much larger values obtained [31] using less accurate data and different parameters in the potential. They obtain good results for 1s states, except in ^{4}He and ^{7}Li, and for 3d and 4f states in heavier elements. Nevertheless, it is not possible to give a unique set of parameters for an effective pion-nucleus potential valid throughout the Periodic Table.

A number of questions are prompted by these studies. (i) Are as many as 9 parameters really necessary? (ii) Should any of the parameters be tied to the free πN values and, if so, which ones? (iii) Should the Lorentz-Lorenz correction influence the absorptive term? (iv) Is there any theory to define the form of the absorptive term?

6. Radii of Valence Nucleons

There are three methods which have been widely used for the study of the radii of the distributions of valence nucleons. One of these is the comparison of elastic electron scattering on neighbouring nuclei [32, 33, 34]. The now familiar model-independent analyses of electron scattering data make it possible to present the error band for the density difference, as shown in Figure 8. It is attractive to associate the density difference between

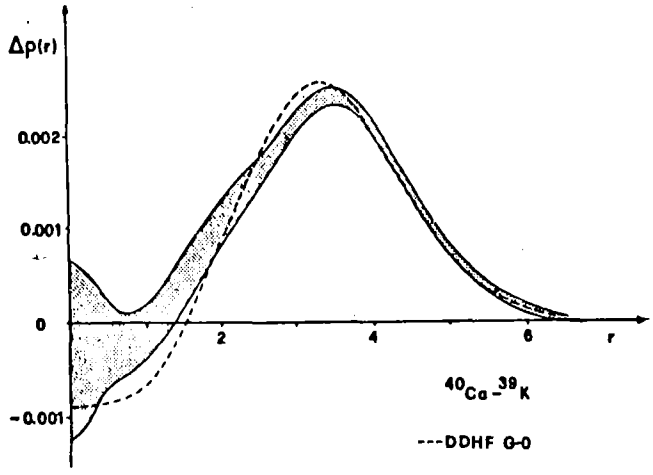

Figure 8. Charge density difference for ^{40}Ca-^{39}K derived from elastic electron scattering and muonic atom data. The dashed curve is the contribution from the $d_{3/2}$ proton plus core polarization [32].

^{40}Ca-^{39}K, and similar pairs, with the density distribution of the added protons, but there is strong evidence for core polarization which may give rise to an increase in size of the core and a change in its deformation parameters. These effects are also very important for comparison of isotones, where another very interesting effect is seen, namely evidence for a change in the occupation numbers of the valence protons.

Another method which may be used for nuclei of non-zero spin is the study of the transverse magnetic component of elastic electron scattering which is dominant at large angles [35]. In this method, the model-independent technique of analysis is not used; instead the magnetic operator is represented as a sum of single-particle operators and the nuclear wavefunction is expanded in a single-particle basis. Thus both the occupation probabilities of the single-particle states and the radial forms of the single-particle wavefunctions are needed. The sensitivity of the data to the radial function is shown in Figure 9. In the calculations with the Saxon-Woods wavefunctions the

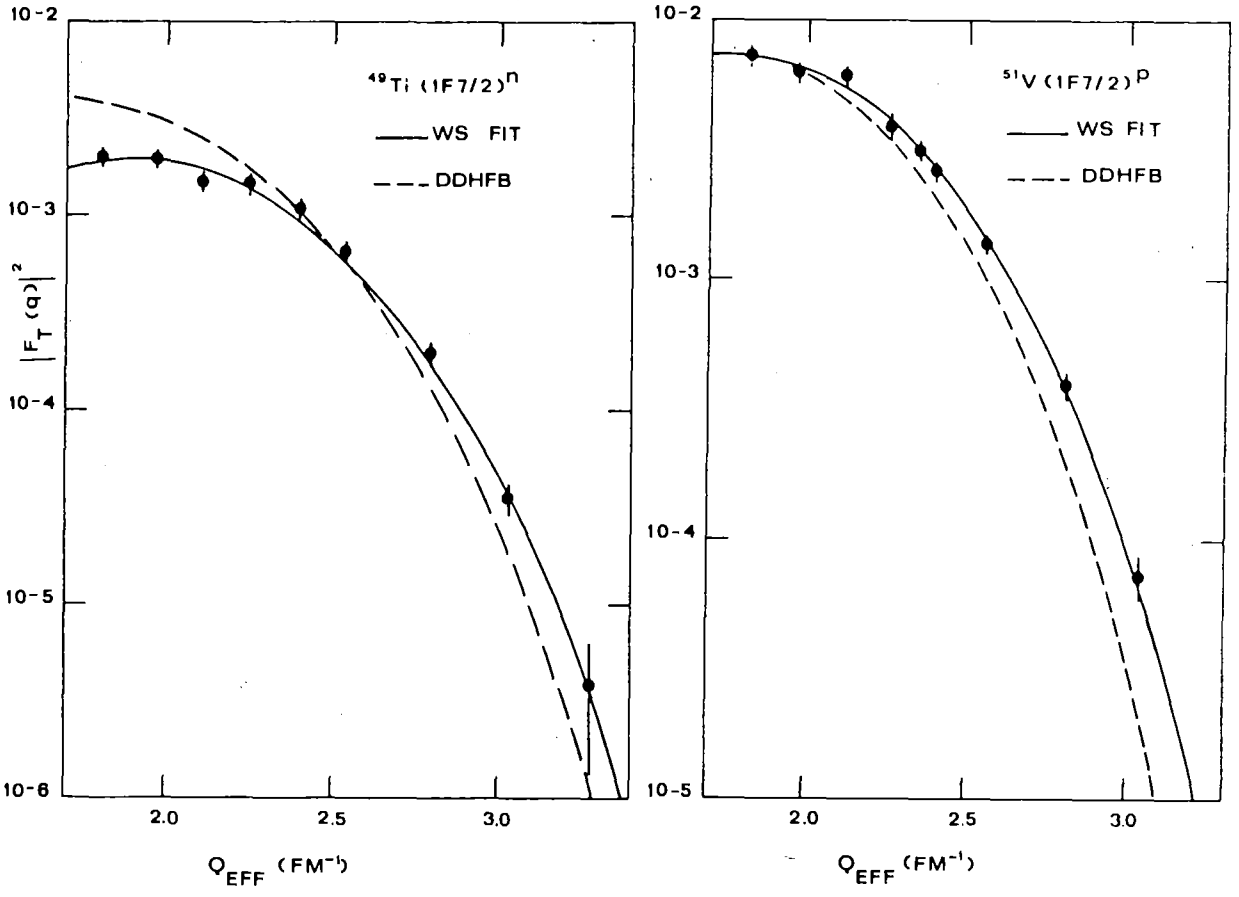

Figure 9. Magnetic form factors of ^{49}Ti and ^{51}V [35].

separation energies of the single-particle states are also needed. In this method, core polarization produces a very large change in the magnitude of the cross-section, but does not significantly change the shape of the contribution to the form factor from the maximum magnetic multipole, as can be seen from Figure 10. The change in the rms radius of the $1g_{9/2}$ neutron is <0.3%. An

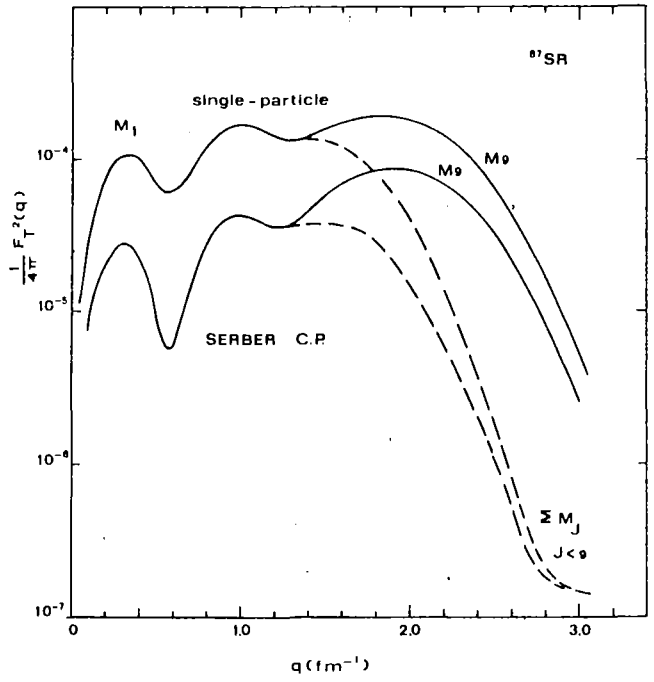

Figure 10. M9 form factor and sum of lower multipole form factors in the single-particle model and including core polarization [35].

apparently more significant correction is that due to meson exchange currents. Calculations in an oscillator basis, discussed by Rothaas [33], suggest a change of $\sim$ 2.5% in the radius of a single neutron outside a closed shell and of $\sim$ 1.5% for an extra-core proton are necessary to allow for the effects of meson exchange currents.

The third method is the study of sub-Coulomb single-nucleon transfer reactions with light [36] and heavy ions [37,38]. This method depends on the assumption that the reaction is localized in the extreme surface of the nucleus where the radial shape of the wavefunction is determined by the separation energy and that the spectroscopic factors and normalization factors can be determined by calibration experiments. Recent studies [38] with Carbon and Oxygen ions have given the values for the radii of neutron states in ^{208,209}Pb shown in Figure 11.

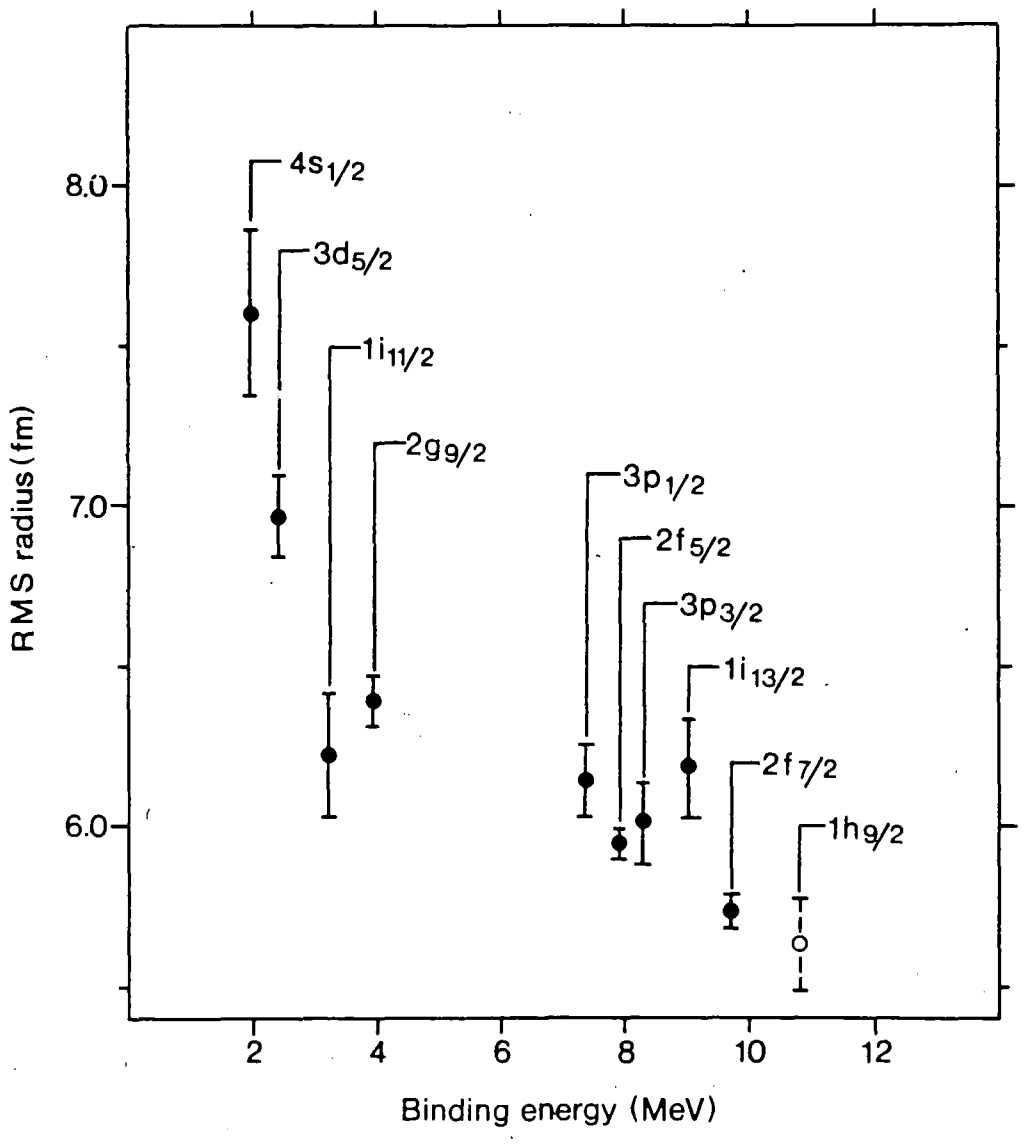

Figure 11. Rms radii of neutron states in ^{208,209}Pb [38].

Information on occupation probabilities and separation energies also comes from single-nucleon transfer and knock-out reactions. The essential feature of the DWBA analysis is the assumption that the overlap of the wavefunctions of the initial nucleus A in state J_A and the final nucleus B in state J_B can be written as

$$\mathcal{O}^{j}_{J_A J_B}(\underset{\sim}{r}) = \sum_{jm} (J_B M_B jm | J_A M_A) \mathcal{J}_{J_A J_B}(j)\ \psi^{m}_{j}(\underset{\sim}{r}) \tag{38}$$

where the ψ^{m}_{j} is a normalized single-particle wavefunction with separation energy

$$\varepsilon_j = -[E_A^{J_A} - E_B^{J_B}] \tag{39}$$

and $\mathcal{J}(j)$ is the fractional parentage coefficient which is related to the spectroscopic factor by

$$S_{J_A J_B}(j) = N_j |\mathcal{J}_{J_A J_B}(j)|^2 . \tag{40}$$

where N_j is the number of nucleons in the shell j. Using sum rules for the spectroscopic factors for pick-up and stripping [39] it is possible to derive the occupation probabilities of shells and sub-shells.

It is well known [40,41] that the procedure of generating the radial part of ψ_j in a spherically symmetric Saxon-Woods potential with separation energy ε_j is unlikely to give the correct interior behaviour unless some additional conditions are imposed. In many cases [42,43], agreement with experimentally-determined charge distributions or radii is required. The relation between the proton distribution and the overlap integral is given by [40,42]

$$A\, \rho_p(\underset{\sim}{r}) = \sum_{i=1}^{Z} \sum_{J_B} |\sigma^{j}_{J_A J_B}(\underset{\sim i}{r'})|^2 \tag{41}$$

$$\underset{\sim}{r} = \frac{A-1}{A}\, \underset{\sim}{r'} \tag{42}$$

$$\varepsilon_j^c = -[E_A^{J_A} - \sum_{J_B} \mathcal{J}^2_{J_A J_B}(j)\, E_B^{J_B}] \tag{43}$$

where the sum is over all the possible states J_B in the parent nucleus. The correct separation energy is now the centroid energy which can be determined only if the location and strength of the components of the single-particle state are known.

Some of the difficulties arising in the comparison of these three methods are now evident. (i) The single-particle wavefunctions used in the DWBA formalism are not quite the same quantities as the single-particle contributions to the density distribution; the change in the radial coordinate is probably not important but the difference in the separation energies is significant. (ii) It is not clear whether experiments with low energy projectiles determine fully the fragmentation of the single-particle strength, particularly for deep hole states, and higher energy experiments may not yet have achieved the required resolution. (iii) If occupation probabilities are taken from, or compared with, shell model calculations there is uncertainty due to the use in

the calculations of oscillator basis states and of a truncated space.

7. Conclusions

Despite the substantial progress made in the past 2-3 years there are still some problems needing further attention. A number of corrections need to be estimated although their effects may prove to be small. The connection between Hartree-Fock mean field calculations, shell model calculations and the nuclear structure component of direct reaction theories needs further exploration.

* * * *

I am indebted to many colleagues who have kept me informed about their work.

References

1. D.F. Jackson, Proc. EPS Conference on Radial Shapes of Nuclei, Krakow (1976) 141
2. L. Wilets, Gordon Conf. on Nuclear Chemistry (1972)
3. R.C. Barrett and D.F. Jackson, Nuclear Sizes and Structure, Oxford, Clarendon Press, (1977), Chapter 2
4. G. Süssmann, UCRL Report 19960 (1970); LBL Report 1615 (1972)
5. W.D. Myers, Nucl. Phys. A204 (1973) 465
6. J. Friedrich and F. Lenz, Nucl. Phys. A183 (1972) 523
7. K.W. Ford and J.G. Wills, Phys. Rev. 185 (1969) 1429
8. K.W. Ford and G.A. Rinker, Phys. Rev. C7 (1973) 1206
9. R.C. Barrett, Phys. Lett.33B (1970) 388
10. W. Bertozzi, J. Friar, J. Heisenberg and J.W. Negele, Phys. Lett. 41B (1972) 408
11. J.P. Auger and R.J. Lombard, Ann. Phys. 115 (1978) 442
12. I. Brissaud and X-Campi, IPNO/TH 79-11 (1979)
13. W.O. Lock and D.F. Measday, Intermediate Energy Nuclear Physics, Methuen (1970)
14. G.K. Varma and L. Zamick, Phys. Rev. C16 (1977) 308
15. G. Igo et al, Phys. Lett.81B (1979) 151
16. R.H. Bassel and C. Wilkin, Phys. Rev. 174 (1968) 1179
17. D.R. Harrington and G.K. Varma, preprint
18. I. Brissaud and M.K. Brussel, Phys. Rev. C15 (1977) 452

19. D.F. Jackson and S. Murugesu, Nucl. Phys. A149 (1970) 261
20. R.C. Johnson and D.R. Martin, Nucl. Phys. A192 (1972) 496
21. B.W. Allardyce et al, Nucl. Phys. A209 (1973) 1
22. A. Abashian, R. Cool and J.W. Cronin, Phys. Rev. 104 (1956) 855
23. M.D. Cooper, Meson-Nuclear Physics - 1976, AIP Conf. Proceedings No.33 (1976) 237
24. V.K. Kembhavi, Ph.D. Thesis, University of Surrey (1971)
25. L.S. Kisslinger, R.L. Burman, J.H. Koch and M.M. Sternheim, Phys. Rev. C6 (1972) 469
26. M.M. Sternheim and K-B Yoo, Phys. Rev. Lett.41 (1978) 1781
27. E. Rost, R.R. Johnson, T. Marks and B. Gyles, University of Colorado Annual Report (1978) 181
28. M. Ericson and T.E.O. Ericson, Ann. Phys. 36 (1966) 323
29. C.J. Batty et al, Phys. Rev. Lett.40 (1978) 931; Nucl. Phys. to be published
30 C.J. Batty et al, Phys. Lett. 81B (1979) 165
31 R. Kunselman and G.A. Grin, Phys. Rev. Lett.24 (1970) 838
L. Tauscher and S. Wycech, Phys. Lett.62B (1976) 413
32. P. Brix, Proc. EPS Conference on Radial Shapes of Nuclei, Krakow (1976) 1
33. H. Rothaas, Proc. Conference on Modern Trends in Elastic Electron Scattering, Amsterdam, (1978), 135
34. H. Euteneuer, J. Friedrich and N. Voegler, preprint
35. P.K.A. de Witt Huberts, Proc. Conference on Modern Trends in Elastic Electron Scattering, Amsterdam (1976) 21
36. H.J. Korner and J.P. Schiffer, Phys. Rev. Lett.27 (1971) 1457
J.P. Schiffer and H.J. Korner, Phys. Rev. C8 (1973) 841
37. G.D. Jones, J.L. Durrell, J.S. Lilley and W.R. Phillips, Nucl. Phys. A230 (1974) 173
J.L. Durrell, P.J.A. Buttle, L.J.B. Goldfarb, W.R. Phillips, G.D. Jones, D.W. Hooton and M. Ivanovitch, Nucl. Phys. A269 (1976) 443
38. M.A. Franey, J.S. Lilley and W.R. Phillips, preprint DL/NSF/p89
39. M.H. Macfarlane and J.B. French, Rev. Mod. Phys. 32 (1960) 567
40. T. Berggren, Nucl. Phys. 72 (1965) 337
41. W.T. Pinkston and G.R. Satchler, Nucl. Phys. 72 (1965) 641
42. L.R.B. Elton and A. Swift, Nucl. Phys. A94 (1967) 52
43. C.J. Batty and G.W. Greenlees, Nucl. Phys. A133 (1969) 673
M.M. Giannini and G. Riccio, Ann. Phys. 102 (1976) 458

43. F. Malaguti, A. Uguzzoni, E. Verondini and P.E. Hodgson, Nucl. Phys. A297 (1978) 287

THE CHARGE DISTRIBUTION OF THE Ca-ISOTOPES FROM ELASTIC ELECTRON-SCATTERING

J. Friedrich
University of Mainz,
Federal Republic of Germany

THE CHARGE DISTRIBUTION OF THE CA-ISOTOPES FROM ELASTIC ELECTRON-SCATTERING

J. Friedrich
Institut für Kernphysik der Johannes Gutenberg-Universität, Mainz

Among all experimentalists present at this meeting I am one of the very few who never did an experiment on the Ca-isotopes. Perhaps this was just the reason for the organisers of this workshop to invite me for this talk on the results from electron scattering, hoping that in this way they might get an independent description of the particular field which they themselves are not so familiar with. - I had to choose whether to to give a report on what has already been published or to look into the data again myself. Since the methods of data analysis have improved substantially since most of the publications about electron scattering from the Ca-isotopes, I have chosen the second way. Thus I spent much more time for analysing the available data than for rewiewing all other information and presenting it here too - I must apologise for that in advance.

The field will be covered in three sections. In the first I'll give a brief survey on the method of data analysis in electron scattering; it is meant particularly for those who are not so familiar with this field. In the second section I'll deal with the charge distribution of a single nucleus, namely that of ^{40}Ca. The third section is devoted to charge distribution differences, mainly to that between ^{48}Ca and ^{40}Ca.

I. The determination of the nuclear charge density distribution from electron scattering cross sections

An electron incident on a nucleus experiences the electromagnetic interaction. In this talk I restrict myself to charge scattering only, for

which the cross section for scattering from spin zero nuclei is given by

$$(1) \qquad \left(\frac{d\sigma}{d\Omega}\right) = \left(\frac{d\sigma}{d\Omega}\right)_{Mott} \cdot F^2(q)$$

where $(d\sigma/d\Omega)_{Mott}$ is the cross section for scattering of spin-1/2-particles from a point-nucleus, and the formfactor $F(q)$ contains all information about the structure of the nucleus. If the process were correctly described by the Born approximation, then $F(q)$ is related to the charge distribution according to

$$(2) \qquad F(q) = \int \rho_{if}(r)\, e^{i\vec{q}\cdot\vec{r}}\, d\vec{r} \,,$$

this means: in an electron scattering experiment we measure the Fourier-transform of the structure function $\rho_{if}(r) = \psi_f^*(r)\, \psi_i(r)$, that contains the nuclear wave function in the initial and in the final state. I'll restrict myself further to elastic scattering only, thus $\rho_{if} = \rho(r)$, that means: we measure the static ground state charge distribution, or I better say: that is the quantity which we want to deduce from the measured data.

Although the Born approximation does not describe the cross section correctly the principle problem in determining $\rho(r)$ can be recognised best - and correctly! - in this approximation: we find $\rho(r)$ by the Fourier-transform of $F(q)$ given by

$$(3) \qquad \rho(r) = \frac{1}{2\pi^2} \int F(q)\, j_0(qr)\, q^2\, dq \,.$$

Well, nobody knows the quantity $F(q)$ from a measurement with mathematical accuracy, there are errors, and the range of the argument for which the form factor is measured is limited to a certain q_{max}.

The story that has been written on this problem is known as "model-independent analysis of electron scattering cross sections". The first chapter - or better: the introduction has been written in the fifties and sixties: particular functional forms had been chosen for $\rho(r)$, possibly with some free parameters in it, which then were fitted to the measured cross sections. A particular form that seemed to be well suited to describe heavier nuclei was the Fermi-distribution eq. (4 a)

$$(4)\quad \begin{matrix}(a)\\(b)\\(c)\end{matrix}\ \rho(r) = \frac{\rho_o}{1+\exp(\frac{r-c}{z})} \begin{cases} * & 1 \\ * & (1+wr^2/c^2) \\ * & (1+wr^2/c^2) + \end{cases}$$

$$+\ Aj_0(\bar{q}r)\exp(-\bar{p}^2 r^2/4)$$

with the half density radius c and the skin thickness t = 4.4 z. When more data became available, more parameters had to be added in order to make the model-distribution flexibel enough, e.g. a parabolic modification with a parameter w (eq. (4 b)). - Later it became necessary to add some more flexibility to allow for oscillations on $\rho(r)$ (eq. (4 c)).

I'll not tell the whole story of model-independent analysis here, but the current status should be reported briefly, since representatives of the two existing methods are present and results achieved with both of them will certainly be presented.

Method one is a direct further development of Lenz' proposal to represent the charge distribution by a sum of δ-functions [1].

They give the same cross section as a model distribution where actually data have been taken, but beyond q_{max} everything can happen to the Fourier-transform of ρ^{δ} (fig. 1). Nobody felt really happy with this caricature of a nucleus, from which only integral quantities could be deduced reasonably. In order to get back to reasonable charge distributions one had to introduce some means to cut down the unreasonable Fourier transform of ρ^{δ} at high q. This could be done either in r-space or in q-space. The first possibility was chosen by Sick [2] who smeared out the δ-functions to Gaussians, thus bringing his SOG-model into being:

$$(5) \qquad \rho^{SOG}(r) = A \sum_{i=1}^{N} \frac{p_i}{1 + 2\, R_i^2/\gamma^2} * \left[\exp\left(-\left(\frac{r-R_i}{\gamma}\right)^2\right) + \exp\left(-\left(\frac{r+R_i}{\gamma}\right)^2\right) \right]$$

The damping of the unphysically large high Fourier components from the δ-functions is achieved by an appropriate choice of the width γ, which is chosen with regard to the extension of the proton or to structures expected from shell model calculations.

The second method has been developped at several places independently, one of these having been Mainz [3]. Therefore I have a certain tendency of favorizing this one. The basic idea is to cling as close as possible to eq.(3). The very weak assumption, that $\rho(r) = 0$ for r beyond some cut-off radius R allows to convert the integral into a series which we can look at as the Fourier-Bessel expansion of $\rho(r)$:

$$(6) \qquad \varrho(r) = \begin{cases} \frac{2}{R} \sum q_\nu^2\, F(q_\nu)\, j_0(q_\nu r) & \text{for } r \leq R \\ 0 & \text{for } r > R \end{cases}$$

$$= \sum a_\nu\, j_0(q_\nu r)$$

The great advantage of this expansion as compared to other ones lies in the fact that here the expansion coefficients are given very directly by the measured quantity itself, namely the formfactor at certain values q_ν of the momentum transfer :

$$a_\nu = \frac{1}{2\pi} \frac{q_\nu^2}{R} F(q_\nu), \tag{7}$$

$$q_\nu = \frac{\pi\nu}{R} . \tag{8}$$

And this is one of the advantages of this model-independent model: one can see very directly which laboratory contributes with its data to the determination of which of the coefficients. The dominant contributions are those at low q - whether they are also the important ones, that depends on what we are looking for.

From the measurement alone only part of the series is determined, the remainder must be estimated by some reasonable assumption :

$$\rho(r) = \underbrace{\sum_{\nu=1}^{N} a_\nu j_0(q_\nu r)}_{\text{from measurement}} + \underbrace{\sum_{\nu=N+1} a_\nu j_0(q_\nu r)}_{\text{from estimate in q-space}} . \tag{9}$$

For large q the Fourier-transform of the distribution of pointlike particles must decrease at least as q^{-4}, the extension of the protons gives an additional decreasing factor $F_p(q)$:

$$|F(q)|_{\text{high-q}} \leq C\, q^{-4}\, F_p(q) \tag{10}$$

(the constant c is matched to the last measured maximum of F(q)).

The coefficients a_ν are determined by a fit to the measured data. This fit is not done in Born approximation but with a correct phase-shift calculation. This makes only correct the whole procedure - it does not change basically what we have learned from looking at the Born approximation, namely that we measure a certain part of the Fourier-expansion of the charge distribution - and that we have to estimate the other part.

The measured data give information on $\rho(r)$ with a certain uncertainty, which we call the statistical error of $\rho(r)$; the estimate yields another contribution to $\Delta\rho(r)$ which we formerly called model error, other people have invented another name, which might better describe where it comes from: copleteness error.

If only very little information is available from the measurement, then the completeness error prevails - may be to such an extent that the whole procedure is no longer meaningful. Once the measurement is extended to large q than this source of error might be negligeable.

II. The charge distribution of ^{40}Ca determined from elastic electron scattering cross sections

I have reanalysed the existing data for ^{40}Ca, more precisely: the published data [4,5,6]. The latest news from this field will be presented in the contribution by Bernard Frois, who has actually done new measurements at Scalay [7], and that allways means: better data at higher momentum transfers. -

Somewhat artificially I have omitted the information about the Ca-nuclei from the other electromagnetic probe, namely from the transition energies of muonic atoms, which yield extremely precise values of the Barrett moments [8]. The results of these measurements will be presented in the next talk by Dieter Wohlfahrt.

I have restricted myself to analysing the cross sections from the papers given in table 1. I need not mention the laboratories since only one was involved, namely Stanford, although people from many places took part. The older the data the more difficult it is to incorporate them into an analysis - I'll point out what I mean by that in a minute with respect to the Frosch-data. At any rate, I have omitted older data from the Stanford group.-In the same table are given the uncertainties of the different data sets. Where no numbers are given it is assumed, that the older data are not measured more accurately than the more recent ones.

The charge distribution of ^{40}Ca is well known from the Frosch paper [6] (in Mainz we are used to call it the Nöldeke-measurement), it looks like curve (1) in figure 2, a very clean description of the nuclear charge distribution. However, looking into the paper by Heisenberg et al. [9] we find a set of different parameters for the same type of distribution (curve (2)). In the paper by Sinha et al. [4] more data are collected, they also give the values for the older Bellicard-measurement which cover the highest q-region - and it is just this part of the data that requires some modification of an oscillating character, which cannot be extracted uniquely from the data as is demonstrated by curves (3) and (4) (this problem has been investigated in some detail by Sick [10]). - We are already left

with four different distributions and we must ask ourselves: how does the nucleus really looks like.

In the meantime, the methods of analysing electron scattering cross sections have been improved considerably, I talked about it in some detail. I have reanalysed the data with the Fourier-Bessel-expansion, which is flexible enough to allow for all possible density fluctuations.

In a first step one must chose an appropriate value for the cut-off radius R. As one recognises from fig. 3 the data cannot be fitted under the restriction that the charge density be zero already beyond 6.0 fm or even 6.5 fm. But there appears a saturation in χ^2 from 7.0 fm on. - In order bo be sure that there is enough flexibility for the charge distribution I have chosen a cut-off radius of 8 fm.

Entering all data into the fitting program gives the dashed uncertainty band in figure 2. The qualitative agreement with the model distribution (3) is not so bad in particular the smooth oscillation appears in this analysis too. The error band I have plotted here corresponds just to one standard deviation, this means: whenever the density is shifted from the center to this limit at one point r, one can find a curve within this band for which the increase in χ^2 is just unity. The error band originates from a pure statistical treatment of the data. There are, however, other sources of error such as normalisation of the data as a whole or energy calibration etc. We must look at these uncertainties too (in particular I must envisage the fact that the better determination of $\rho(r)$ due to the new Saclay data does not reproduce the curve with the bump in the centre

of the nucleus but that with lower $\rho(r = 0)$ corresponding to a change in the sign of F(q) at $q \simeq 3.1$ fm^{-1} [10]).

Fig. 4 shows a plot of the best fit cross section curve calculated for 750 MeV, the measured data are normalised to the same energy. The fit to the data is excellent - at least at the level of accuracy which such a logarithmic scale can provide; we get a better feeling for the quality of the data - or the fit - when looking at the percentage deviation of the data from the fit.

Fig. 5 a shows the older Stanford data by Frosch et al., which deviate systematically from the fit, which is dominated by the majority of the later measurement with smaller error bars. A possible source for this discrepancy might be recognised by comparing the deviation from the fit with the variation of the cross section due to a systematic error in the scattering angle Θ (or the energy). The curve in fig. 5 a corresponds to $\Delta\sigma(\Delta\Theta = + 0.1^{\circ})$ at 750 MeV. - An uncertainty of 0.1 degree and of 0.5 % in E has been estimated by the authors. When Θ is changed by - 0.1° and E by - 0.5 %, the deviation from the common fit is reduced considerably. Although the data might be interpreted correctly by such a measure, I have preferred to omit them in the further analysis, and henceforth I am only talking about the data from refs. 4) and 5) (set 1-7 in table 1). However, here too there exist obvious s y s t e m a t i c deviations from the fit (fig. 5 b). By adding 3 % to the statistical errors (cf. table 2) one gets reasonable values for χ^2, but this measure has also some influence on the best-fit distribution itself, and one must doubt, whether or not the obvious systematic uncertainties are taken into account appropriately in this way.

According to the different sources of uncertainty the data have been analysed

a) just as they are published;
b) after shifting the absolute normalisation (cf. table 1);
c) the same for the energy;
d) the same for the scattering angle;
e) fitting the normalisation of each set separately;
e')same as e) but including the additional error of 3 %.

In order to check the assumptions of the "model-independent" model :

f) same as e') but with different cut-off radii;
g) same as e') but taking the data only up to a certain momentum transfer.

A selection of resulting numbers are compiled in table 2, the fit, that should be taken as the most reasonable one, being that in column 3. - Some interpreting remarks may be valuable:

1. The quality of the different evaluations may be recognised from the value of χ^2. The great break-down in χ^2 occurs when one allows the different sets of data to float independently and when one adds the additional uncertainty of 3 % to the statistical errors.

2. In general the normalisation comes out within the margin given by the experimentalists, although it may not be justified to shift the different sets individually. The normalisation of the old

750 MeV-data is quite undetermined and the individual deviations from the fit scatter to such an extent that there is an urgent need for better data.

Those who are not so familiar with electron scattering might ask the question: how can it be that measured data normalise themselves. This can be understood most readily by looking at the form factor at q=0 :

$$(11) \qquad F(q=0) = \begin{cases} \frac{4\pi}{Z} \int \rho(r)\, r^2\, dr = 1 \\ \\ 2 \sum (-1)^{\nu+1} F(q_\nu) \end{cases}$$

which must be unity on the one hand side - that is just what normalisation means; on the other hand, inserting the expansion for $\rho(r)$, one finds something like a sum rule for the coefficients a_ν or - what is the same - for the formfactors at the positions q_ν. Therefore, if the relative strength of these Fourier-components is determined, the absolute value is fixed by eq.(11). The problem with electron scattering generally is that the information for the first coefficient (corresponding to very low momentum transfer) is poor. It is exactly at this point where the data from muonic atom data help.

Column 10 again demonstrates the incompatibility of the data with too small a cut-off radius: for R = 6.5 fm the χ^2 is too large and also the normalisation of the data acquires unreasonable values.

3. The quantity that is certainly discussed most in the literature for the Ca-isotopes is the rms-radius, which was found to deviate substantially from an $A^{-1/3}$-increase when going from ^{40}Ca to ^{48}Ca. This quantity is determined from electron scattering in a completely model-independent way by measurements at sufficiently low momentum transfer, a requirement which is very difficult to meet with sufficient accuracy. The problem in determining this quantity in a general

experiment may be recognised by looking at it in terms of the Fourier-Bessel coefficients [3]

$$(12) \quad \langle r^2 \rangle^{1/2} = 2 R^2 \Sigma (-1)^{\nu+1} \left(1 - \frac{6}{(\pi\nu)^2}\right) F(q_\nu).$$

Due to the additional factor ν^{-2} and to the generally decreasing behavior of F(q) only the first few formfactor values contribute, in particular the first one at $q_1 = 0.39$ fm^{-1} (R = 8 fm), which is only determined indirectly via the normalisation; correspondingly it is subject to the uncertainty in the normalisation, which therefore contributes most to the error.

Table 3 summarises the results for the rms-radius. It is clearly seen that the determination of the rms-radius is the domain of muonic atoms. - Although the value from this analysis is compatible with that from Sinha et al., the difference between the two values should be taken serious, since both values result from essentially the same set of data. Fig. 6 b shows the values of $\langle r^2 \rangle^{1/2}$ determined from the data taken up to different q_{max}. Up to 2 fm^{-1} this model-independent analysis gives the same value as that from Sinha et al.: therefore the final difference must originate from a different description of the high-q data. At the level of this talk one should just state the situation as it is - it will be clearified by taking into account the Barrett-moment from muonic atoms [8] and the new high-q data from Saclay [7].

4. A striking feature of the charge distribution is the bump in the centre of the nucleus, which comes out in several evaluations of the data and which would fit nicely into a shell-model picture, where it is due to the

two 2s-protons. However, the latest results from Saclay sustain the solutions without bump, they lead to a density distribution which is essentially flat in the inner part of the nucleus.

In order to understand the problem with the determination of $\rho(r=0)$ let us look at the inverse of eq. (11) which gives a corresponding sum rule (11), now for the charge density at the centre of the nucleus

$$(13) \qquad \rho(r = 0) = \frac{1}{2\pi^2} \int F(q)\, q^2\, dq.$$

This relation is most convenient for discussing how accurate the charge density is determined at the centre. Let us assume that the measurement spans the q-range up to a certain q_{max}, then the corresponding part of the integral (or the series expansion) is determined by the data. The integral is plotted as a function of its upper limit q_{max} in fig. 6 a. - In order to dermine $\rho(r = 0)$ with good accuracy one must do three things :

a) good absolute normalisation;
b) good data f o r a l l q in order to determine the integral with the correct integrand;
c) measuring up to momentum transfers such that contributions from possible further oscillations are negligeable.

After these preliminaries let's look on the accuracy with which $\rho(r = 0)$ is determined from the measured data. In fig. 6 b the values found for this quantity in different fits is plotted as a function of the maximum momentum transfer up to which the data have been incorporated into the

analysis. The inner error bars indicate the statistical error, the outer bars (dashed) also take into account the completeness error, which is getting smaller and smaller when data to higher q are taken into account; finally it is getting negligeable as compared to the other contributions. One should doubt however about this result here since the quality of the 750 MeV-data is poor. - Contributions to the error from the systematic uncertainties may be recognised from fig. 7 b.

Finally let us look at $\rho(r)$ again. Fig. 7 a shows the best-fit curve to the data sets 1-7 (fit 3, table 2) together with several theoretical descriptions and the Saclay result 7). The statistical uncertainty is plotted in fig. 7 b, the systematics in fig. 7 c. The error from normalisation and from the variation of the cut-off radius dominate the uncertainty. It is shown in fig. 6 b that the latter is related to the problem with the sign of $F(q)$ at 3.5 fm^{-1}, which is settled now by the new Saclay data. Therefore, the charge density can be given with much better accuracy now, taking together all information, as is demonstrated in the contribution to this conference by B. Frois. - One has certainly reached a level of accuracy, that effects which are omitted so far, must be considered before the measured formfactor can be interpreted as the Fourier transform of the proton distribution (dispersion corrections 11), 12), contributions from neutrons 13) and meson exchange currents 14)).

III. The charge-distribution-differences of the Ca-isotopes

In the third and last part of my talk I am going to discuss the differences in the charge density of the Ca-isotopes as registered in the electron

scattering experiment by Frosch et al. for $^{40,42,44,48}Ca$. There have also been taken data for $^{40,42,44}Ca$ by Heisenberg et al.[9] in a measurement dedicated to inelastic scattering in particular on Ca- and Ti-isotopes. Since these data are not published explicitly I restrict the analysis to the Frosch-data. These data had revealed the striking fact that - when looking at the rms-radius - ^{48}Ca is not larger than ^{40}Ca though it contains 8 nucleons more. This phenomenon has attracted much attention in the past decade as well from the theoretical point of view [15-21] as from additional experimental efforts based on other methods (cf. the proceedings of this conference).

Frosch et al. have analysed the cross sections in terms of 3-parameter-Fermi-distributions. The resulting charge density differences are shown in fig. 8. The obvious surprise is that the 8 additional neutrons in ^{48}Ca do not only pull charge outwards by just expanding the nucleus - but they also pull charge from the tail of the ^{40}Ca-nucleus to the inner region. This phenomenon is expressed most simply by saying that the skin thickness decreases due to the additional neutrons. Actually the parameter t is smaller for ^{48}Ca than for ^{40}Ca.

In figure 9 the contributions from Δc, Δt and Δw are plotted separately. The big change in Δw compensates partly that from Δt, therefore the change in the skin-thickness is not directly given by Δt. - One thus sees that it is difficult to attribute specific features of $\Delta\rho(r)$ to a change in a particular parameter. Beyond this, one must ask again, whether or not $\Delta\rho(r)$ is appropriately parametrised by c, t and w, since we know that this is not the case for the individual nuclei. It is certainly necessary to analyse the data with more general functional forms for $\rho(r)$.

The analysis of a relative measurement is done as follows (emphasis is put on $^{48}Ca/^{40}Ca$) :

1. fit to the ^{40}Ca cross sections;
2. calculate "measured" cross sections for ^{48}Ca from the best-fit charge density for ^{40}Ca and from the cross section ratios, which are measured with an accuracy of up to 2 % (compared to 6 %-errors for the individual data);
3. analyse these ^{48}Ca cross sections with the small error bars with the Fourier-Bessel-expansion;
4. the difference between the resulting best-fit distribution and the reference distribution of ^{40}Ca gives $\varrho(^{48}Ca) - \varrho(^{40}Ca)$ with errors, that only contain the small statistical errors from the measurement of the ratio; all systematic errors essentially cancel.

Here again the data have been handled in a variety of ways (cf. table 4). In particular, reference is made to three different evaluations of the ^{40}Ca charge distribution.

Although the resulting rms-radius depends strongly on how the data are handled, the difference in the values for $^{40}Ca/^{48}Ca$ is always the same; taking fits 2, 5 and 10 as reasonable ones we find

$$\Delta\langle r^2\rangle^{1/2}_{48/40} = -0.004(9)\ \text{fm}$$

in excellent agreement with the value given by Frosch et al.[6] and also with the muonic result [8].

In figure 10 I have plotted the envelope of the charge distribution difference (fits 1 to10 in table 4, fits 2 and 10 with error bars). The result from the 3-parameter-Fermi distribution lies well within the band, although the region with the negative difference between 5 and 6 fm does not come out so clean in the model-independent analysis.

There have been different attempts to explain the shrinking (or unexpected slow increase) of the charge distribution in the Ca-isotopes, in particular a change in deformation and in zero-point-oscillations have been considered to be responsible for the drastic change in the skin-thickness between ^{40}Ca and ^{48}Ca. Rothhaas has developed a method of analysing electron-scattering data along these lines [22]. In a first step the cross sections from nucleus A1 are fitted with the Fourier-Bessel expansion for $\rho(A1)$, in a next step one tries to fit the cross sections for nucleus A2 by a certain modification of the same charge density, namely an extension and a change in the surface thickness; this is achieved by parametrising $\rho(A2)$ in the form

$$(14) \qquad \rho_{A2}(r) = \sum_{\nu} \int d\Omega \; a_{\nu}(A1) j_0(q_{\nu} r') d\Omega$$

with

$$(15) \qquad r' = r \cdot (1 + \alpha + \beta \; Y_{20}(\Theta))^{-1} .$$

α describes the expansion of nucleus A2 as compared to nucleus A1, β describes the change in skin thickness (which is parametrised as if it originates from a change in deformation). The difference between two isotopes is given by

$$(16) \qquad \Delta\rho(\alpha,\beta) = \rho(a_{\nu}; \alpha,\beta) - \rho(a_{\nu}).$$

Table 5 summarises the resulting values for the three isotope pairs $^{42,44,48}Ca/^{40}Ca$.

The cross section difference for $^{42}Ca/^{40}Ca$ can be described within this model, there is even no need for a change in the skin thickness. $\Delta\langle r^2\rangle^{1/2}$ comes out in excellent agreement with the Frosch analysis and also with the muonic result.

The $^{44}Ca/^{40}Ca$ difference demands for a change in skin thickness ($\beta > 0$ means: ^{40}Ca is more "deformed", it has a larger skin-thickness than ^{44}Ca). However χ^2 is quite large due to a big contribution from one data point in the first diffraction minimum; one must therefore be careful in accepting this result. Here, the value for $\Delta\langle r^2\rangle^{1/2}$ does not agree with that from muonic atoms. This might be due to an inadequacy of the model or to some problem with the data. I do not persue this problem here.

The $^{48}Ca/^{40}Ca$ data, which span a larger q-range (in particular they contain one more diffraction pattern), are clearly incompatible with the present model. Therefore in a next step we add a further physically motivated modification to the charge density difference, as first introduced into the analysis by Rothhaas [22] for the Zr-isotopes: the neutrons added in a shell outside a closed core might weaken that core and cause protons to move into another shell, in particular into that where the neutrons have gone. The interaction of these neutrons should be particularly large with those protons with which there exists an important overlap. Up to now, in the present analysis I have only tried a change from 2s to $_1$f, corresponding to a charge distribution difference

$$(17) \qquad \Delta\rho_p = \gamma\,(R^2_{1f}(r) - R^2_{2s}(r)).$$

For R(r) I take harmonic oscillator wave functions with oscillator parameters taken from Negele [23] (b_{2s} = 2.050 fm, b_{1f} = 1.953 fm).

The result for the $^{48}Ca/^{40}Ca$ difference is the following:

α	β	γ	χ^2
- 0.0158(4)	0.316(2)	0.0	874
- 0.0188(4)	0.317(3)	- 0.24(1)	126

One observes a substantil decrease in χ^2 when a change in the "proton occupation number" is taken into account according to the value of γ.

However three things remain to be ciscussed :

1. $\gamma < 0$ means, that in ^{48}Ca there are less protons in the 2s shell and more in the 1f-shell than in ^{40}Ca. From stripping and pick-up reactions one knows [24] that this is very unlikely. Therefore one should be careful in interpreting eq. (17) as a change in proton occupation numbers. In electron scattering one basically measures the momentum components of the protons and the following may be a reasonable interpretation of eq. (17) :

   The added neutrons bring in momentum components corresponding to their probability distribution in r-space. These components are compensated partly among the added neutrons themselves, partly by the nucleons of the core. In this way the protons take over a certain amount of momentum components corresponding to the 1f-distribution. Because of normalisation

other components must disappear, here (somewhat arbitrarily) these have been taken only from the 2s-shell.

2. The fraction of momentum transferred from the neutrons to the protons certainly depends on the wave functions used, and - for harmonic oscillator functions - on the oscillator parameter b.

3. If one wants to interprete the charge-distribution difference, one must also take into account the effective charge of the neutrons [13] which contribute via two effects :

   a) The neutron formfactor

$$\rho_{eff}(r) = \mathcal{F}(\mathcal{F}(\rho^{n}_{point}) \cdot F_n(q)) \tag{18}$$

   Here, $\mathcal{F}$ denotes the Fourier-transform, ρ^{n}_{point} the distribution of the (pointlike) neutrons and $F_n(q)$ the formfactor of the neutron. This effect contributes via the change of the neutron-distribution in the core (I have omitted this one here) and through the added 1f-neutrons.

   b) The spin-orbit-contribution

$$\rho_{s.o.}(r) = - N \frac{\mu_n}{2m_n^2} \frac{\ell}{r^2} \frac{d}{dr} (r\, \rho_\ell(r)). \tag{19}$$

   N is the number neutrons in the unsaturated shell, μ_n the magnetic moment, m_n the mass and ℓ the angular momentum.

Figure 11 shows the different contributions to $\Delta\rho(r)$ and it is seen that the contribution from the neutrons is not negligeable. Since this analysis

has only been performed straightforward up to now without carefully rechecking it, I quote the result only qualitatively: χ^2 decreases considerably when the neutrons are taken into account and the values of the model-parameters are also influenced (cf. caption of figure 11).

I have outlined here, how the information available from electromagnetic probes can be interpreted. The results must not yet be looked at as being definite, since a l l existing data should be taken into account simultaneously, i.e. the Barrett-moment from muonic atoms and the hig-q datafrom electron scattering. In addition there are still to be done some checks of consitstency between the model-independent and the model analysis.

Many helpful discussions and advice in using their computer programs with Drs. H. Rothhaas and K. Merle are gratefully acknowledged.

References

1) F.Lenz, Z.Physik 222 (1969) 491

2) I.Sick, Nucl.Phys. A 218 (1974) 509

3) B.Dreher et al., Nucl.Phys. A 235 (1974) 219 and references therein in particular to (i) U.Meyer-Berkhout, (ii) J.Borysowicz and J.H.Hetherington, (iii) J.L.Friar and J.W.Negele

4) B.B.P.Sinha et al., Phys.Rev. C 7 (1973) 1930

5) J.B.Bellicard et al., Phys.Rev.Lett. 19 (1967) 527
J.B.Bellicard et al., Phys.Rev. C 16 (1977) 1262

6) R.F.Frosch et al., Phys.Rev. 174 (1968) 1380

7) B.Frois, in Proceedings of the Conference "Modern Trends in Elastic Electron Scattering", Amsterdam, 1978

8) H.D.Wohlfahrt et al., Phys.Lett. 73 B (1978) 131

9) J.Heisenberg et al., Nucl.Phys. A 164 (1971) 353

10) I.Sick, Phys.Lett. 53 B (1974) 15

11) Wing-Fai Lin, Nucl.Phys. A 119 (1973) 14

12) R.L.Mercer, Phys.Rev. C 15 (1977) 1786

13) W.Bertozzi et al., Phys.Lett. 60 B (1976) 409

14) Il-Tong Cheon, Phys.Lett. 60 B (1976) 409

15) F.G.Perey and J.P.Schiffer, Phys.Rev.Lett. 17 (1966) 174

16) A.Swift and L.R.B.Elton, Phys.Rev.Lett. 17 (1966) 484

17) L.R.B.Elton, Phys.Rev. 158 (1967) 970

18) B.F.Gibson and K.J.van Oostrum, Nucl.Phys.A 90 (1967) 159

19) R.B.Raphael and N.Rosen, Phys.Rev. C 2 (1970) 1040

20) A.Faessler et al., Z.Physik A 276 (1976) 91

21) P.G.Reinhard and D.Drechsel, Z.Physik A 290 (1979) 85

22) H. Rothhaas, Thesis, Mainz, 1976, and Proceedings Amsterdam, cf. [7]

23) J.W.Negele, Phys.Rev. C1(1970)1260

24) P.Doll et al., Nucl.Phys. A263(1976)210

data set	date	energy MeV	effective momentum transfer fm^{-1}	authors ref.	uncertainties in the data					
					systematic				statistic	
					normalisation		energy	angle	add. stat.error	stat.error
					target thickness	reference cross sect.				
1	1973	249.3	0.90-1.89	Sinha et al.[4]	2%	3%	0.1%	0.05°	3%	≥ 1.1%
2	<1973	"	0.55-1.86	Heisenberg et al. 4)						2.8%
3	"	"	0.59-2.01	"						1.4%
4	1973	496.8	1.50-2.90	Sinha et al.[4]						1.5%
5	<1973	"	0.90-2.56	Heisenberg et al. 4)						2.8%
6	1967	757.5	1.02-2.91	Bellicard et al. 5)						7.0%
7	"	"	2.97-3.40	"						26.0%
8	1968	249.5	0.73-2.33	Frosch et al.[6]			0.5%	0.10°		7.0%
9	"	499.5	1.42-2.02	"						7.1%
10	"	"	2.02-2.69	"						8.6%

Table 1: Sets of e^- scattering cross sections which are available from the literature and which have been taken into account in this analysis.

	1	2	3	4	5	6	7	8	9	10	11	12	13
R fm	8.0	8.0	8.0	8.0	8.0	8.0	9.0	7.5	7.0	6.5	8.0	8.0	8.0
normal.	1.000	1.000	free	1.000	1.000	0.950	free	free	free	free	free	free	free
energy	E_o	E_o	E_o	$E_o \cdot 1.001$	E_o	E_o	E_o	E_o	E_o	E_o	E_o	E_o	E_o
angle	θ_o	θ_o	θ_o	θ_o	$\theta_o + 0.05^o$	θ_o	θ_o	θ_o	θ_o	θ_o	θ_o	θ_o	θ_o
add. error %	0.	3.	3.	0.	0.	0.	3.	3.	3.	3.	3.	3.	3.
q_{max}	all	all	all	all	all	all	all	all	all	all	3.0	2.5	2.0
χ^2/point	2.98	1.19	0.70	2.84	3.24	3.10	0.72	0.71	0.71	1.21	0.74	0.74	0.70
$\varrho(r=0)$	893(10)	901(11)	902(12)	897(10)	898(10)	886(10)	868(10)	869(9)	907(12)	938(10)	886(16)	881(23)	790(46)
$\langle r^2 \rangle^{1/2}$	3.471(3)	3.463(5)	3.448(11)	3.463(2)	3.463(2)	3.505(3)	3.445(10)	3.446(10)	3.426(6)	3.368(3)	3.451(18)	3.458(19)	3.480(21)
n o r m a l i s a t i o n s													
set 1	fixed	fixed	1.029(23)	fixed	fixed	fixed	1.040(23)	1.035(22)	1.066(18)	1.187(16)	1.027(29)	1.019(31)	.993(31)
2	"	"	.997(20)	"	"	"	1.006(19)	1.002(18)	1.029(15)	1.137(12)	.995(25)	.988(26)	.964(27)
3	"	"	1.056(21)	"	"	"	1.066(20)	1.061(19)	1.092(15)	1.207(13)	1.054(27)	1.046(28)	1.022(29)
4	"	"	.990(29)	"	"	"	1.002(29)	.999(28)	1.025(26)	1.158(27)	.991(32)	.977(33)	.972(37)
5	"	"	.982(21)	"	"	"	.992(21)	.987(20)	1.016(16)	1.126(15)	.979(27)	.972(29)	.952(30)
6	"	"	.927(28)	"	"	"	.936(28)	.932(26)	.959(25)	1.068(25)	.929(31)	.924(32)	.894(34)
7	"	"	.834(273)	"	"	"	fixed	fixed	fixed	fixed	fixed	fixed	fixed

Table 2: Typical numbers resulting from different evaluations of the data
(χ^2/point, $\varrho(r=0) \cdot 10^4$ e fm^{-3}, $\langle r^2 \rangle^{1/2}$ fm, and the normalisation of the different sets)

	$\langle r^2 \rangle^{1/2}$ fm	$\Delta \langle r^2 \rangle^{1/2}$ fm
this analysis	3.448	0.011 statisctical 0.034 normalisation (5%) 0.017 additional statistical error 0.002 ΔR = 0.5 fm
Sinha et al. [4]	3.482	0.025
Frosch et al. [6]	3.487	
u - atoms [8]	3.480	$5 \cdot 10^{-4}$ (assumed same accuracy as for Barrett-moment, statistics only)

Table 3: rms - radius of ^{40}Ca deduced with different methods from electron scattering cross sections and also from muonic atoms

^{40}Ca reference charge density from fits A, B, C:

	e^--data sets	Barrett-moment 8)	energy	angle	normalisation	cut-off radius	$\langle r^2 \rangle^{1/2}$
A	1-10	yes	E_0	θ_0	free	8.0 fm	3.4793(2) fm
B	8-10	no	E_0-.5%	θ_0-.1°	free	8.0 fm	3.4172(641) fm
C	8-10	no	E_0-.5%	θ_0-.1°	free	7.5 fm	3.4605(104) fm

Evaluation of ^{48}Ca - data:

^{40}Ca ref.	N° of fit	energy	angle	cut-off radius fm	normalisation 250 MeV	500 MeV	$\Delta\Omega$ correction applied	χ^2/point	$\langle r^2 \rangle^{1/2}$ fm	$\Delta\langle r^2 \rangle^{1/2}$ (^{48}Ca - ^{40}Ca) fm
A	1	E_0	θ_0	8.0	1.000	1.000	no	2.90	3.481(3)	0.002(3)
"	2	"	"	"	1.013(21)	1.043(26)	"	2.79	3.473(13)	-0.006(13)
"	3	E_0-0.5%	θ_0-0.1°	"	1.071(18)	1.124(25)	"	2.76	3.474(9)	-0.005(9)
B	4	"	"	"	1.000	1.000	"	1.50	3.417(3)	0.000(3)
"	5	"	"	"	1.005(17)	1.054(24)	"	1.23	3.414(9)	-0.003(9)
"	6	"	θ_0	"	0.982(18)	1.010(24)	"	1.08	3.414(10)	-0.003(10)
"	7	"	θ_0+0.1°	"	0.959(19)	0.968(24)	"	0.99	3.414(11)	-0.003(11)
"	8	"	θ_0-0.1°	"	1.002(17)	1.049(24)	yes	1.29	3.414(9)	-0.003(9)
C	9	"	"	7.5	1.000	1.000	"	1.23	3.447(3)	-0.014(3)
"	10	"	"	"	0.982(21)	1.011(26)	"	1.07	3.459(14)	-0.002(14)

Table 4: Different evaluations of the cross section ratios for $^{48}Ca/\ ^{40}Ca$

	Isotope	α	β	χ^2/point	$\langle r^2 \rangle^{1/2}$ fm	q-range fm^{-1}
1.	^{40}Ca	-	-	0.08	3.483(8)	0.73-1.76
2.	^{42}Ca	0.0103(8)	-0.006(224)	0.74	3.519	"
1.	^{44}Ca	-	-	1.57	3.528(6)	0.73-1.86
2.	^{40}Ca	-0.0171(6)	0.191(7)	2.73	3.503	"
1.	^{48}Ca	-	-	2.90	3.483(5)	0.73-2.58
2.	^{40}Ca	-0.0158(4)	0.316(2)	15.00	3.528	"

Table 5: Parameter values from fitting the measured cross section ratios for the pairs of Ca-isotopes with the model given by eqs. (14) and (15).

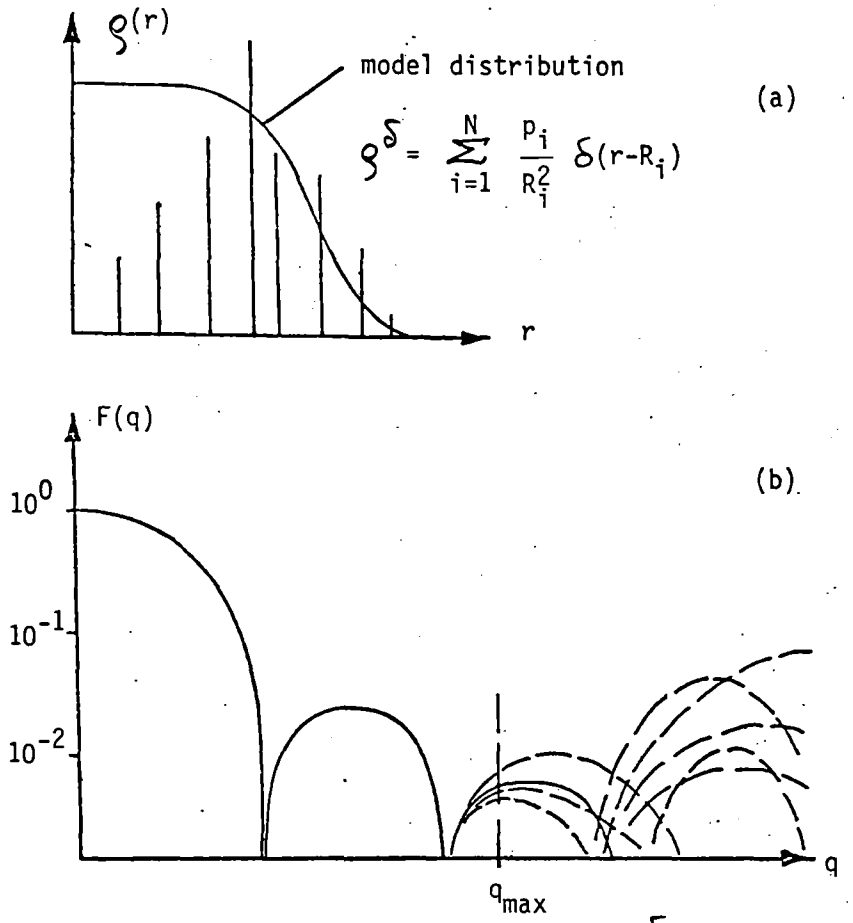

Figure 1: (a) Model distribution and Lenz' ϱ^{δ}
(b) Fourier transform of the two distributions of (a)

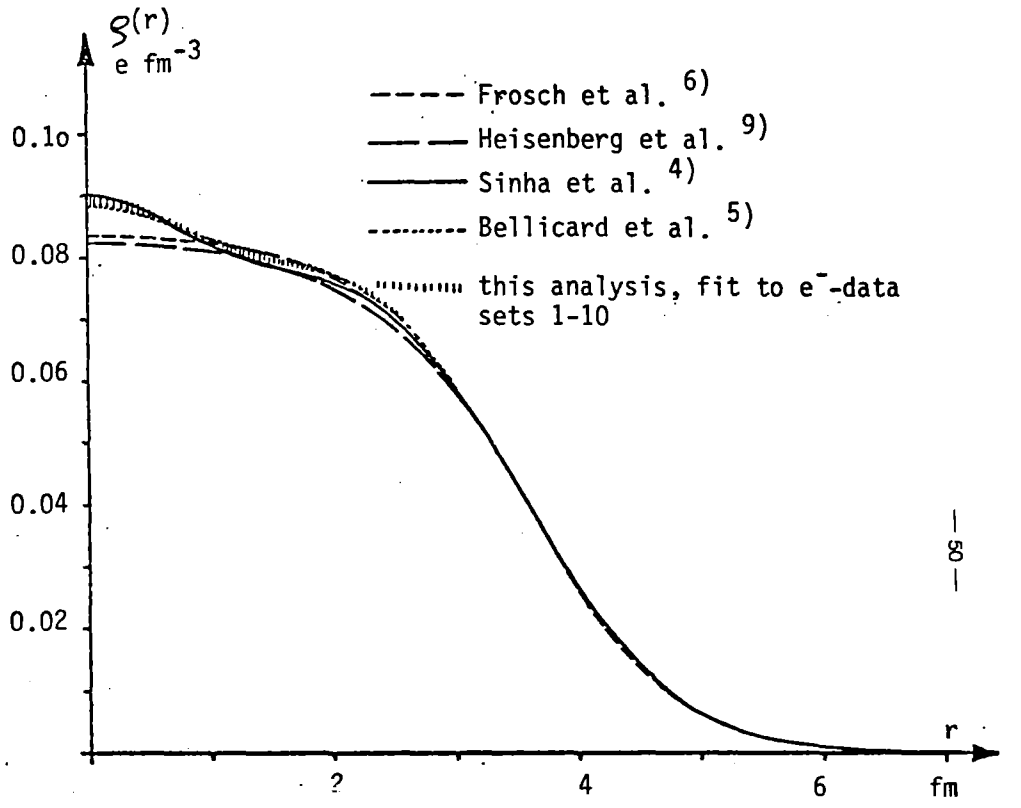

Figure 2: Charge distribution of ^{40}Ca deduced by different authors from different sets of e$^-$ scattering cross sections with different parametrisations for $\varrho(r)$

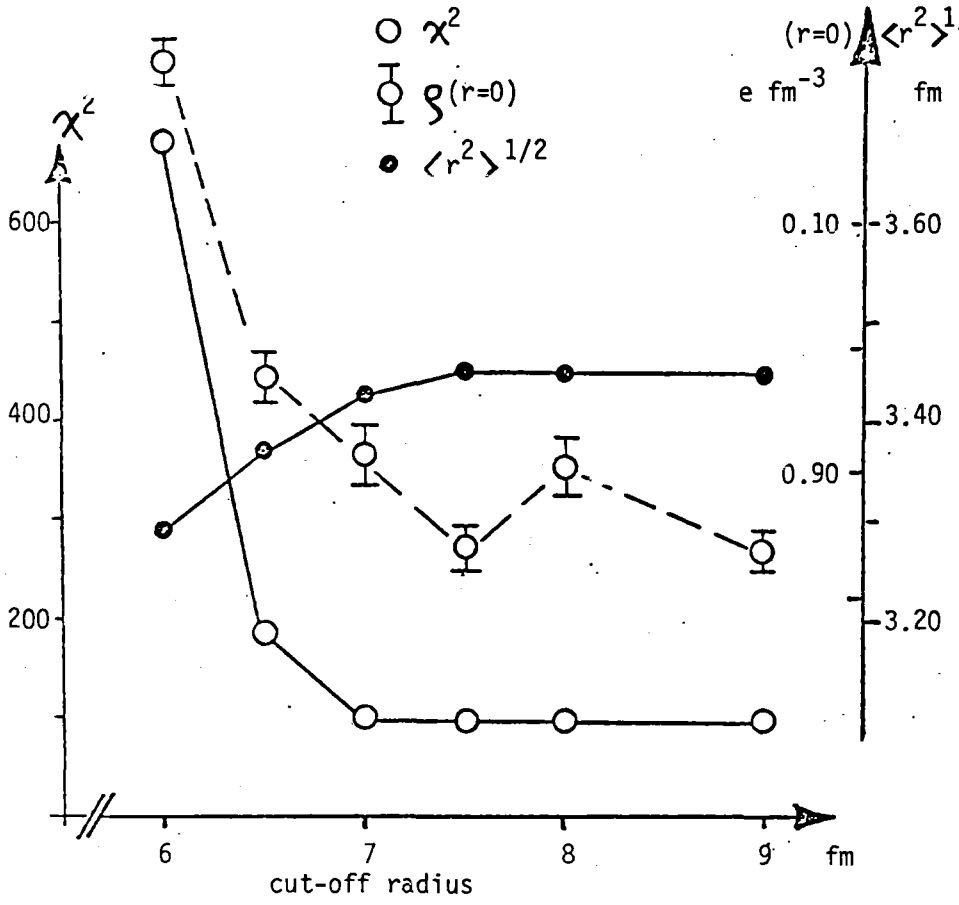

Figure 3: The goodness of the fit as a function of the cut-off radius.
Resulting rms-radius and $\varrho(r=0)$ for different cut-off radii.

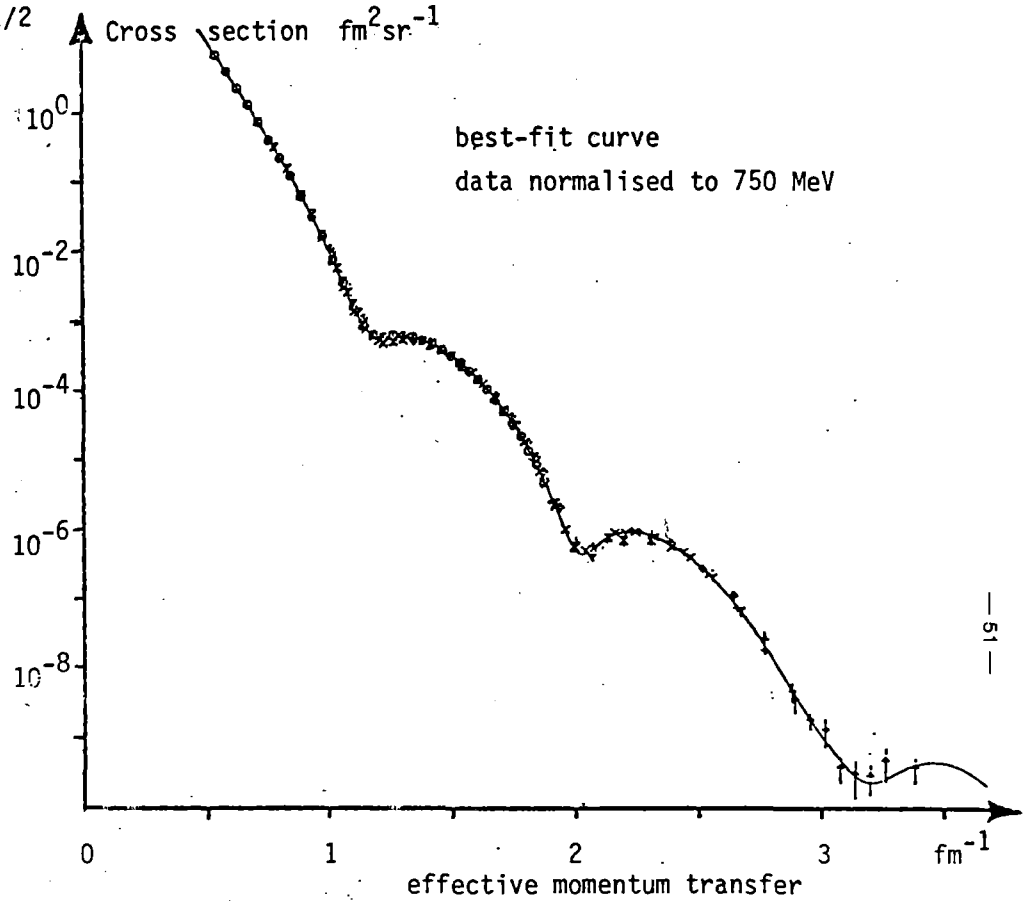

Figure 4: Fit to electron scattering cross sections sets 1 - 10
The fit curve is calculated for 750 MeV, the data are normalised to the same energy

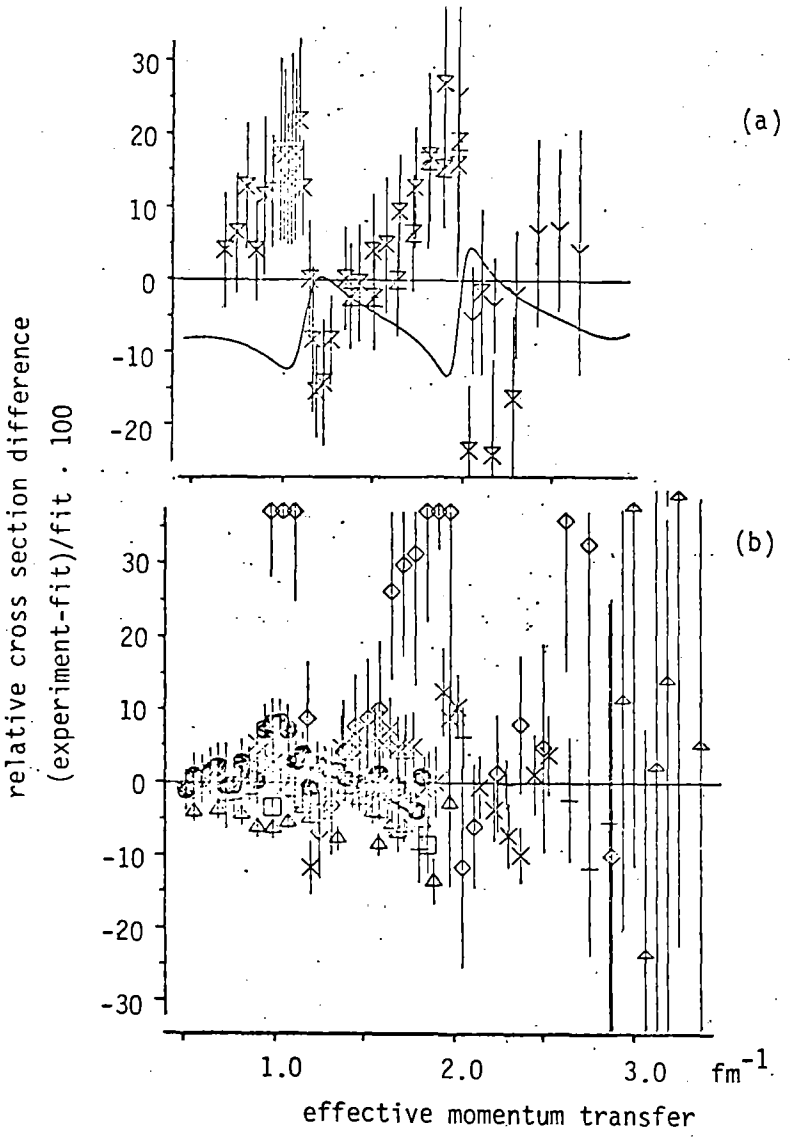

Figure 5: Percentage deviation of the measured cross sections from the fit to the data
(a) Deviation of data 8-10 from a fit to sets 1-10
(b) Deviation of sets 1-7 from a fit to sets 1-7

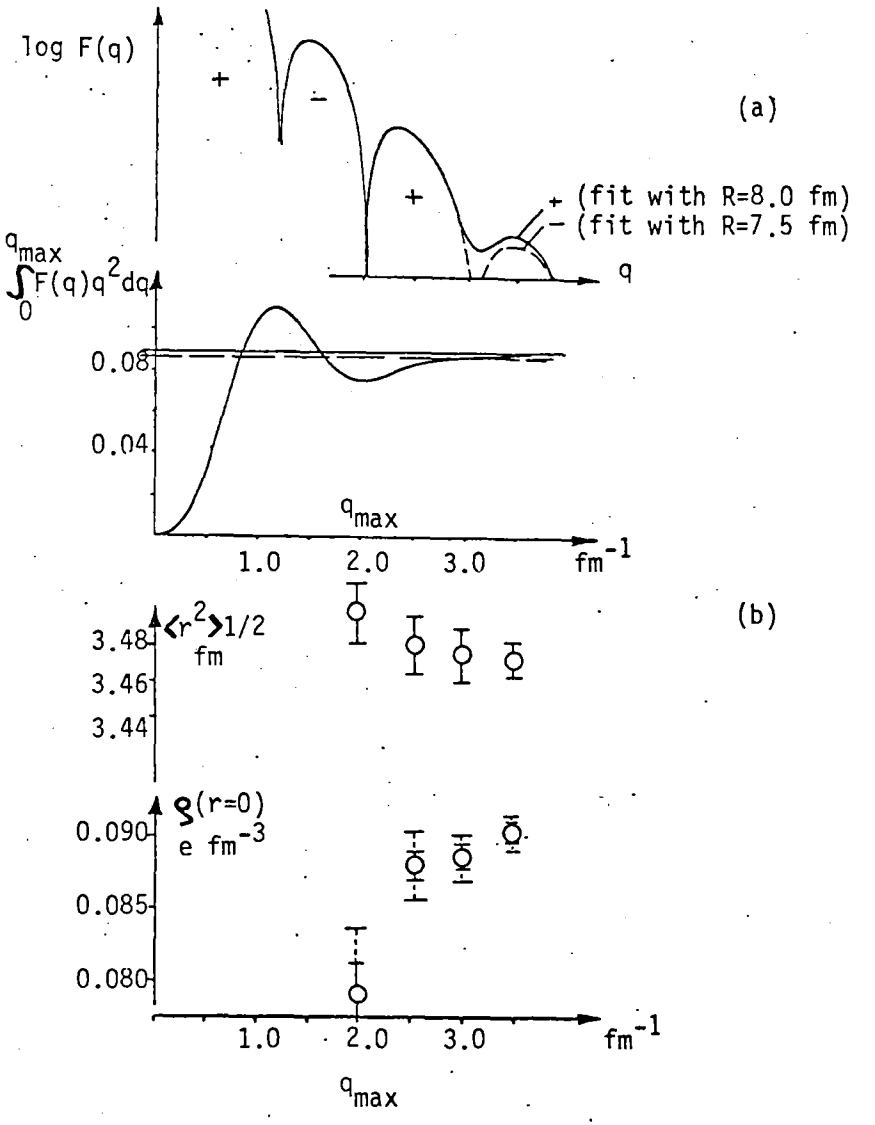

Figure 6: (a) Illustration of the determination of $\varrho(r=0)$ from data covering different q-ranges. The splitting into the two solutions due to the different sign in F(q) is demonstrated.
(b) Resulting values for $\langle r^2\rangle^{1/2}$ and $\varrho(r=0)$

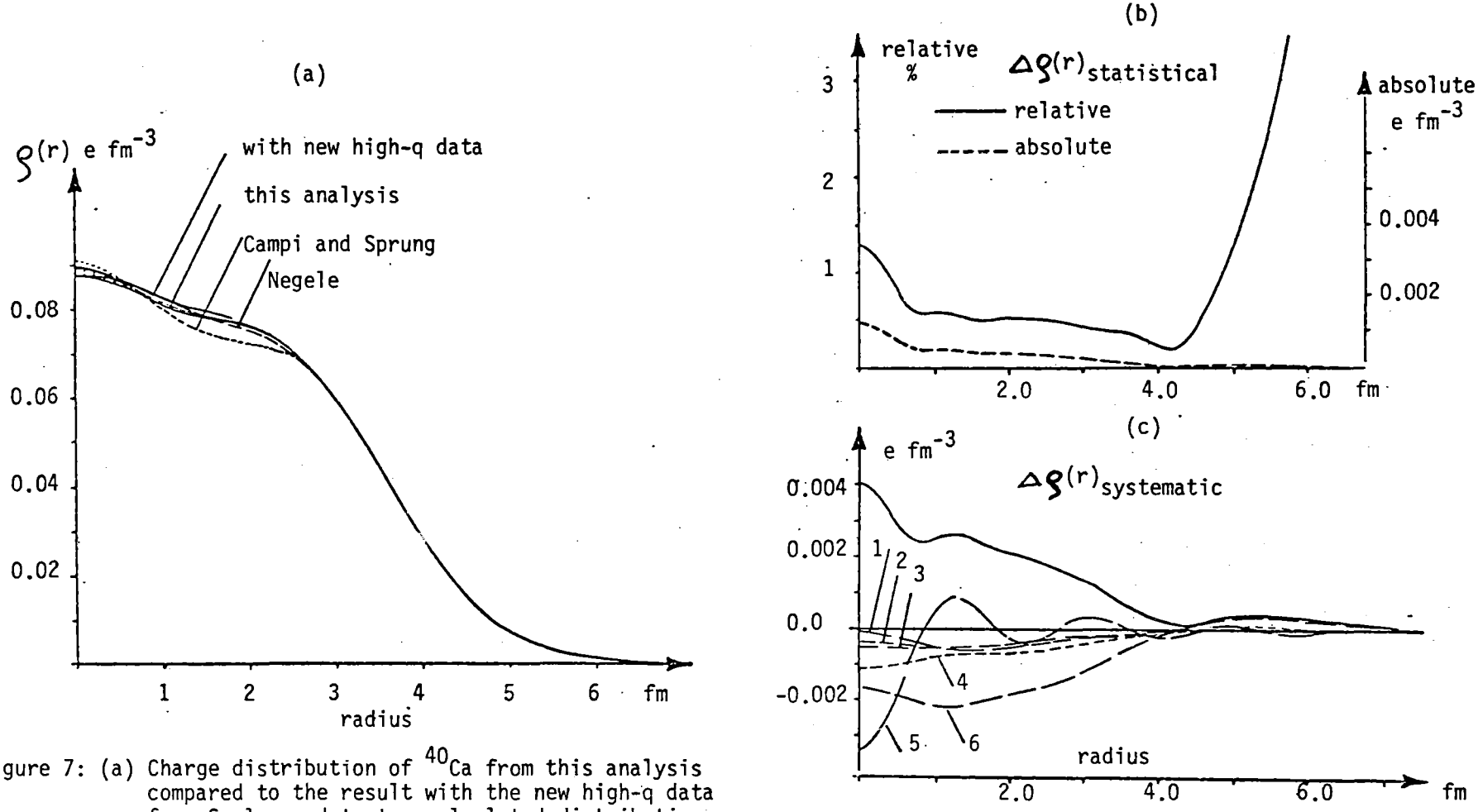

Figure 7: (a) Charge distribution of ^{40}Ca from this analysis compared to the result with the new high-q data from Saclay and to two calculated distributions (all from B. Frois 7)).

(b) Uncertainty in $\varrho(r)$ from the measured data (relative and absolute scale)

(c) Uncertainty in $\varrho(r)$ from systematic errors ((1) normalisation = 1.00, fixed , (2) θ_0+0.05^o, (3) E_o·1.001, (4) without additional stat. error, (5) R from 8.0 to 7.5 am, (6) normalisation = 0.95, fixed)

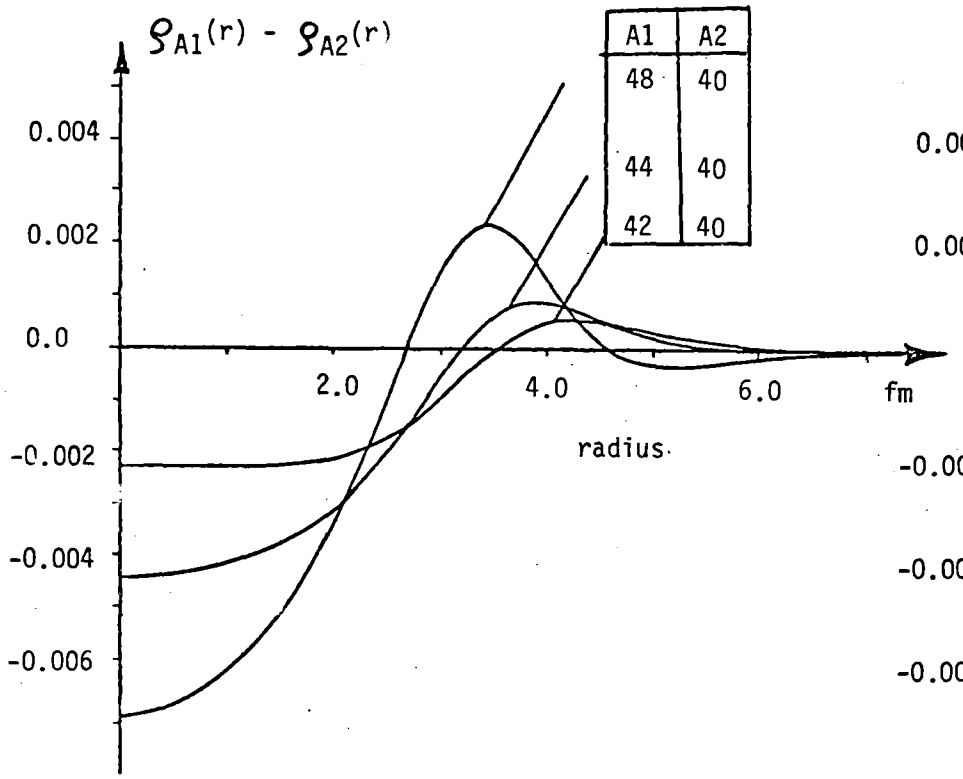

Figure 8: Charge distribution difrerences as measured and determined by Frosch et al [7] for the indicated Ca-isotopes from electron scattering cross sections

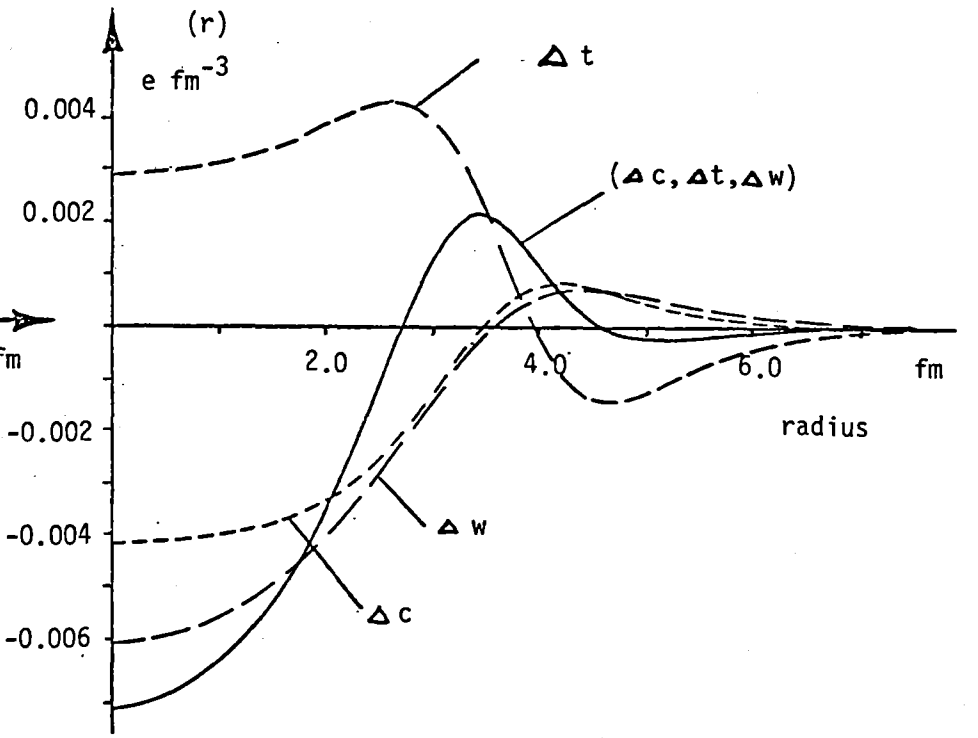

Figure 9: Contributions to the charge distribution difference between ^{48}Ca and ^{40}Ca resulting from the difference in the single parameters

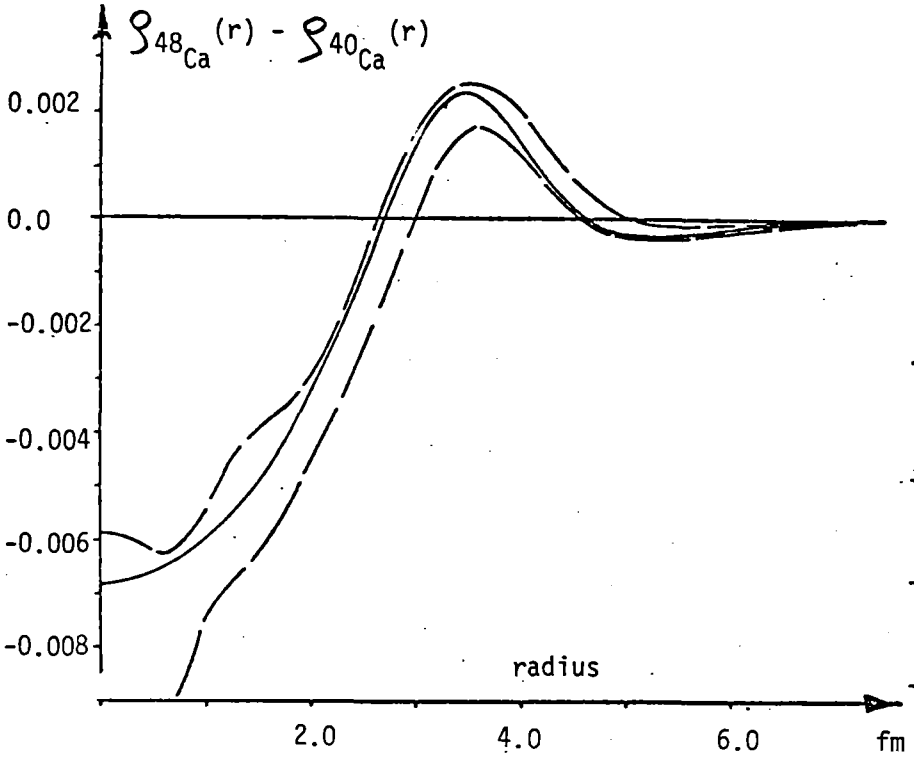

Figure 10: Envelope of the different charge distribution differences (fits 1 to 10, table 4) (region between dashed lines) and the result from Frosch et al. with a 3-parameter Fermi distribution (continuous line)

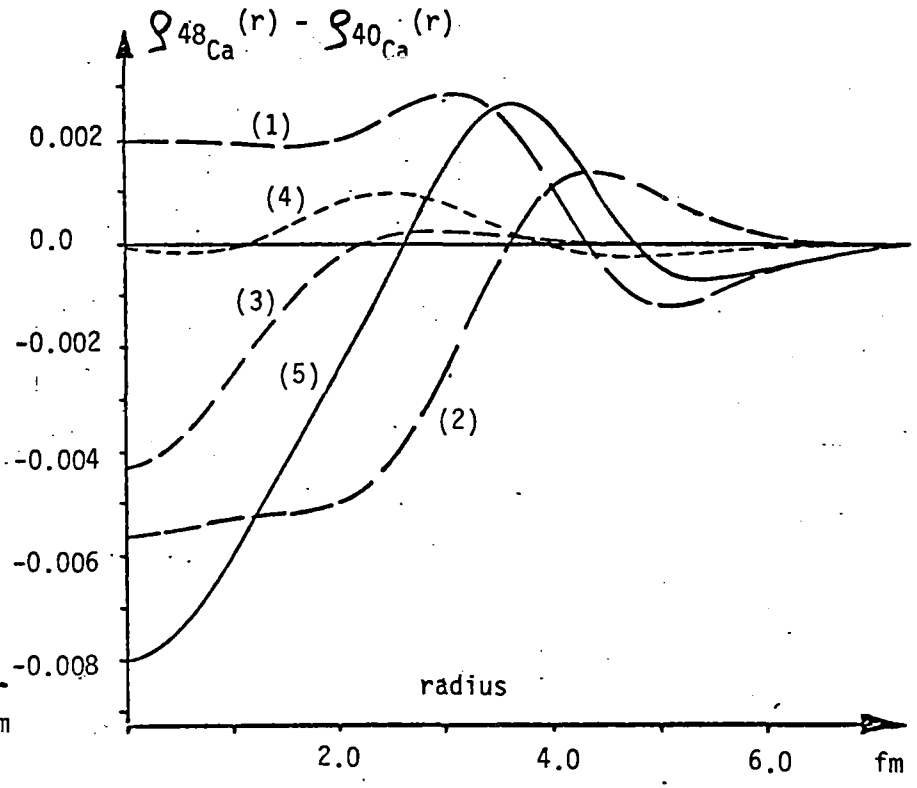

Figure 11: Different contributions to the charge distribution difference for ^{48}Ca / ^{40}Ca within the model eqs. (14-19) ((1) β=0.313, (2) α=-0.021, (3) γ=-0.175, (4) from neutrons eqs. (18,19), (5) sum of (1) - (4)).

NUCLEAR CHARGE RADII OF THE $1f_{7/2}$ SHELL NUCLEI FROM MUONIC ATOMS

H.D. Wohlfahrt
Los Alamos Scientific Laboratory,
U.S.A.

NUCLEAR CHARGE RADII OF THE $1F_{7/2}$ SHELL NUCLEI FROM MUONIC ATOMS

H. D. Wohlfahrt
Los Alamos Scientific Laboratory
Los Alamos, New Mexico 87545

I. Introduction

The experimental accuracy obtained in recent measurements of charge radii shows clearly that the usual empirical mass-radius formulae [e.g. 1,2] are only approximate. The variations of actual charge radii are strongly modified by nuclear shell structure and deformation effects [3,4]. The deviations of the measured charge radii from the mass-radius formulae seem to follow regular trends as indicated by Fig. 1.

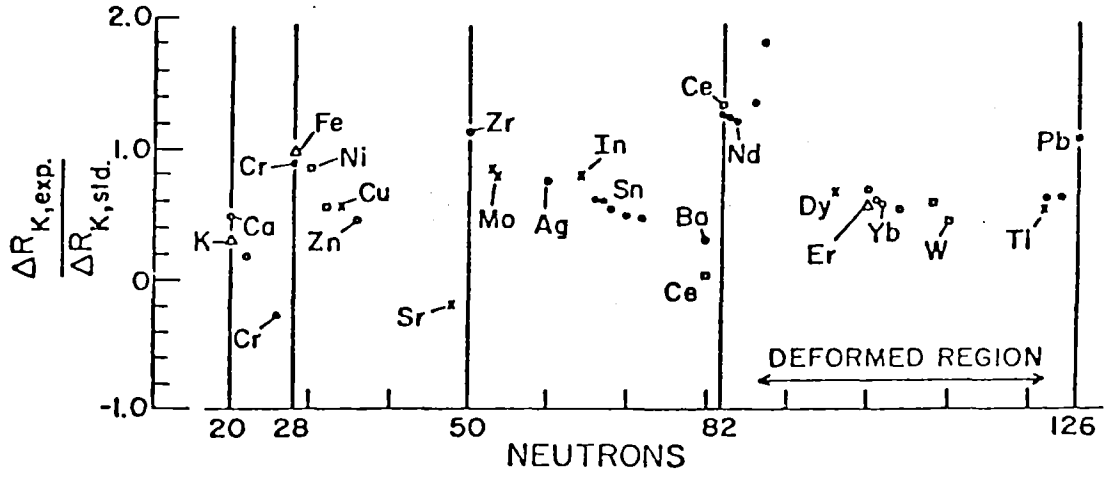

Fig. 1. $\Delta N = 2$ isotope shifts from muonic x-ray measurements prior to 1974.

The figure represents a compilation of muonic isotope shift data [5] taken prior to 1974. It shows $\Delta N = 2$ charge radii differences for even nuclei

as a function of the neutron number. To emphasize the departure of the data from the mass-radius formulae, the experimental shift values have been divided by "standard" shift values, calculated with a mass-radius formula. The data available in 1974 [5] indicate that the isotope shifts are largest at the beginning of a neutron shell and become quite small just before the major shell closures N = 28, 50, 82 and 126. This trend is especially pronounced in the $1f_{7/2}$ shell ($20 < N \leqslant 28$), where large negative isotope shifts occur at the end of the shell.

To investigate these trends in detail, muonic x-ray studies of medium-weight nuclei have been performed in recent years by the Los Alamos muonic x-ray group, using the high intensity muon beam available at the LAMPF 800 MeV proton accelerator. Fig. 2 shows the $1f_{7/2}$ shell nuclei investigated [3,6,7]. These studies, which together include all stable $1f_{7/2}$ neutron shell nuclei, provide information about the proton core polarization due to the successive addition of neutrons for the proton cores Z = 20(Ca), 22(Ti), 24(Cr), 26(Fe) and 28(Ni). In addition, these studies, which represent the first systematic investigations of isotone shifts, provide the opportunity to compare the core polarization caused by protons with core polarization caused by neutrons in the same ($1f_{7/2}$) shell.

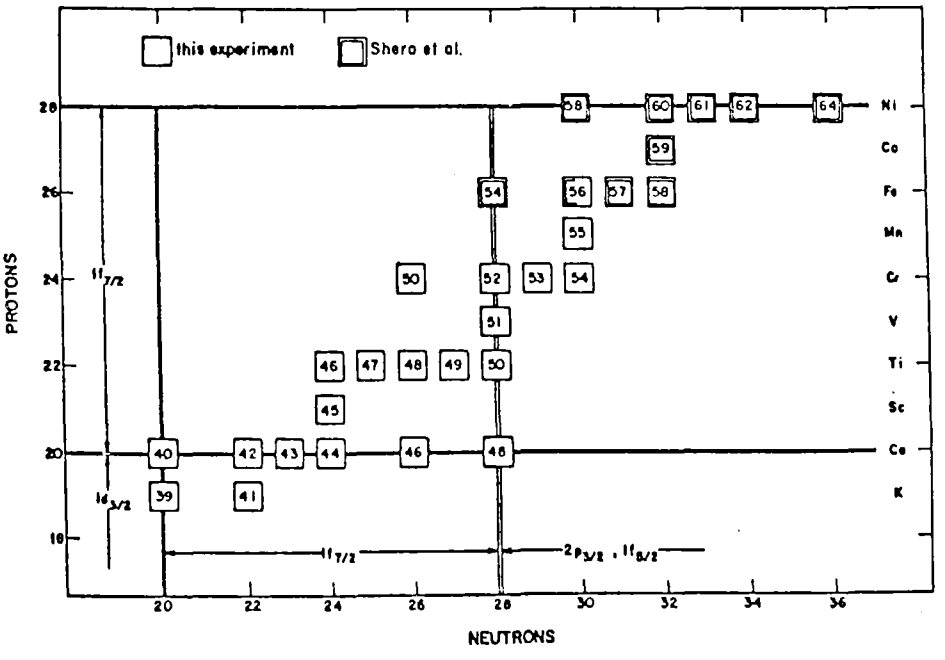

Fig. 2
Investigated nuclei and associated shell model configuration.

II. Nuclear Charge Distribution Parameters from Muonic Atoms

Fig. 3 illustrates 2p and 1s muonic energy levels for ^{40}Ca. The muon which has lost nearly all of its kinetic energy is captured in a high orbital and forms a muonic atom. The excited muonic atom decays mainly via electric dipole transitions and may reach states, where the overlap between the muon wave function and the nuclear charge distribution causes a measureable energy shift ΔE^{FS} of the binding energy from the binding energy calculated for a point nucleus E_B^{PN}. In the $1f_{7/2}$ shell nuclei, only in the 1s state is the

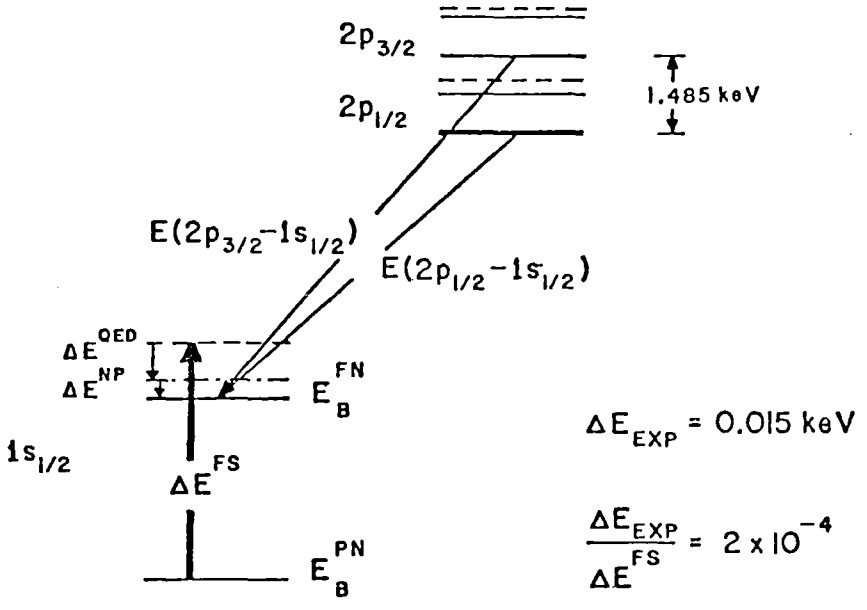

Fig. 3. Muonic (2p-1s) transitions. For exact scaling (^{40}Ca) see Table I.

finite size effect ΔE^{FS} large compared with the experimental error for determining muonic binding energies (15 eV). Table 1 lists ΔE^{FS} and E_B^{PN} for the 1s and 2p states. Note that the finite size effect in the 1s state (69.117 keV) is very large compared with the experimental error (15 eV), so the finite

State	E_B^{PN}/keV	ΔE^{FS}/keV	ΔE^{QED}/keV	ΔE^{NP}/keV
$1s_{1/2}$	1128.157	-69.117	6.810(20)	0.170(50)
$2p_{1/2}$	282.418	-0.087	0.929	0.001
$2p_{3/2}$	280.904	-0.033	0.904	0.001

Table I. Point nucleus binding energy E_B^{PN}, finite size effect ΔE^{FS}, quantum electrodynamical corrections ΔE^{QED} and nuclear plozarization correction ΔE^{NP} for the muonic ^{40}Ca atom in(keV).

size effect can be determined with a relative accuracy of about 2×10^{-4}. In the 2p states, which are separated by about 1.5 keV due to the fine-structure splitting, the finite size effect is about 3 orders of magnitude smaller than in the 1s state and ΔE^{FS}_{2p} is comparable to the experimental error. Therefore the experimentally observed 2p-1s transitions contain only information about the finite size effect in the 1s state. To deduce the finite size effect from the measured transition energies, theoretical corrections have to be included. The quantum electrodynamical corrections ΔE^{QED} (mainly vacuum polarization and Lamb-shift) of about 7 keV in the 1s state of ^{40}Ca are known with an accuracy of about 20 eV [8]. Nuclear polarization corrections ΔE^{NP}, which consider the polarizibility of the nucleus in the presence of the muon, are known much less accurately. An uncertainty of 30% is commonly attributed to these corrections, which results in an uncertainty of about 50 eV (see Table I). The uncertainty of the derived nuclear charge distribution parameters is therefore mainly determined by the uncertainty of the theoretical corrections, which is about 5 times larger than the experimental errors in the case of the $1f_{7/2}$ shell nuclei. However in the differences of the nuclear charge distribution parameters for neighboring isotopes, these uncertainties cancel to a high degree.

First order perturbation theory can tell us what information we may obtain from a muonic atom. In this context the finite size energy shift in a muonic transition is given by:

$$\Delta E^{FS}_{i,f} = \int_0^\infty \rho(r)\left[V^i_\mu(r) - V^f_\mu(r)\right] 4\pi r^2 dr - Z\left[V^i_\mu(0) - V^f_\mu(0)\right] \quad , \tag{1}$$

where V^i_μ and V^f_μ are the potentials produced by the bound muon in the initial and final states. As Barrett [9] has shown, these differences in the potentials can be approximated by an analytical expression of the form $A + Br^k e^{-\alpha r}$ In principal all 4 parameters A, B, k and α depend on $\rho(r)$, Z, n and l. The measured quantity in a muonic atom experiment can therefore be written as

$$\langle r^k e^{-\alpha r} \rangle = \frac{4\pi}{Z} \int_0^\infty \rho(r) r^k e^{-\alpha r} r^2 dr \quad , \tag{2}$$

the Barrett moment of the charge distribution.

In the actual analysis of the muonic data we adjust the parameters of a Fermi charge distribution

$$\rho_F(r) = \rho_0 \, (1 + \exp(r - c)/a)^{-1} \tag{3}$$

to the measured transition energies by solving the Dirac equation including all higher order corrections. In the case of the $1f_{7/2}$ shell nuclei only the half density radius c was adusted; the parameter a was fixed at 0.55 fm, which corresponds to a surface thickness parameter t = 2.42 fm. From the muon wave function, determined by solving the Dirac equation, the potential produced by the bound muon $V_\mu(r)$ can be deduced and the potential parameters A, B, k and α can be adjusted to fit the difference $V_\mu^i - V_\mu^f$. For the $1f_{7/2}$ shell nuclei ($20 \leq Z \leq 28$) we obtain a range of values of $2.114 \leq k \leq 2.121$ and $0.064 \text{fm}^{-1} \leq \alpha \leq 0.074 \text{ fm}^{-1}$ for the 2p-1s transitions. With these values of k and α, we can calculate the appropriate Barrett moments using equation 2.

These Barrett moments deduced using Fermi charge distributions are model-independent (at least to the level of accuracy set by the experimental errors). That is, a realistic charge distribution (for example, from electron scattering) with the same Barrett moment $\langle r^k e^{-\alpha r} \rangle$ as the adjusted Fermi charge distribution gives a transition energy equal to the observed transition energy within the experimental error. From the Barrett moments one can obtain model-independent equivalent radii R_k defined by:

$$3R_k^{-3} \int_0^{R_k} r^k e^{-\alpha r} r^2 dr = \frac{4\pi}{Z} \int_0^{\infty} \rho_F(r) r^k e^{-\alpha r} r^2 dr \tag{4}$$

For the comparison of the results from muonic x-ray experiments with those of other experiments and with theory, it is very convenient to have rms-radii $\langle r^2 \rangle^{1/2}$ instead of equivalent radii R_k. From muonic data alone rms-radii cannot be determined model-independently, since the radial shape of the charge distribution is not known. This fact can be easily shown by

changing the surface thickness parameter of the Fermi charge distribution by 10% and readjusting the half density radius to maintain the same transition energy. The resulting R_k changes by only 0.1×10^{-3}fm, whereas, the rms-radius changes by 5×10^{-3}fm. This change is large compared with the experimental error of 0.4×10^{-3}fm.

To obtain model-independent rms-radii we performed a combined analysis of our muonic data and electron scattering data from Stanford [10] (Ca and Ti) and Mainz [11] (Fe and Ni). The analysis used was based on the Fourier-Bessel expansion [12] of the charge distribution. With the radial shape of the charge distribution obtained from electron scattering, an extrapolation from the precise muonic Barrett moments to the rms-radii can be performed in this combined analysis without substantial loss of accuracy. In the following, I will present the results of such combined analyses.

III. Experimental Arrangement and Measurements

Before I present the experimental results, let me briefly discuss the experimental arrangement and the analysis of the measured spectra. At the time of the $1f_{7/2}$ shell experiment, LAMPF was running at a proton beam current of 150μA; the muon rates used in our measurements were about 10^5/sec. Fig. 4 shows our experimental target arrangement. The scintillators S_1, S_2 and S_3^i

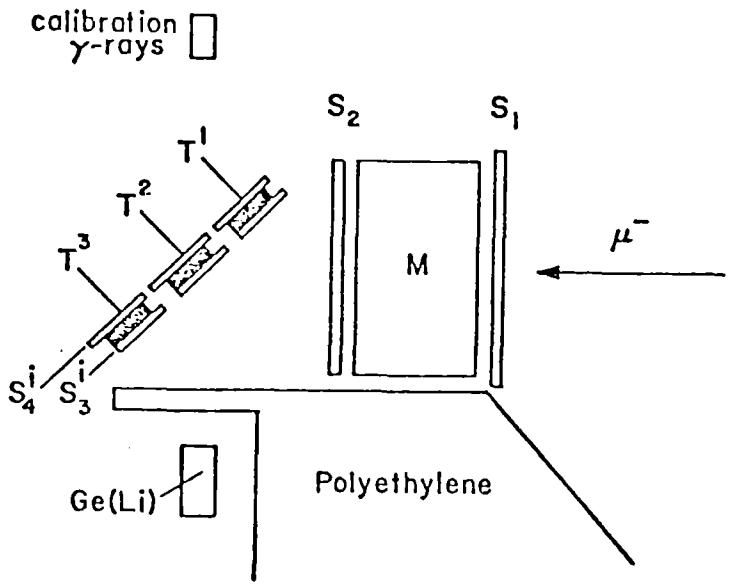

Fig. 4. Arrangement of scintillation counter telescope (S_i), muon moderator (M), targets (T^i), and Ge(Li) detector.

in anti-coincidence to S_4^i signal a stopped muon in one of the three simultaneously measured targets T^i. An x-ray event in the Ge(Li) in coincidence with $S_1\ S_2\ S_3^i\ \bar{S}_4^i$ is identified as a muonic x-ray. Simultaneously with the x-rays, we measure γ-rays from various calibration sources, using a beam gating technique to insure that the calibration spectra are stored at an average rate which is proportional to the intensity of the muonic x-rays. A sophisticated interface in connection with an on-line computer insures that the different events are stored in their respective spectra, and that ambiguous events are discarded. Eleven calibration lines, known with an individual accuracy of 5 eV, covered the energy region of interest (650-1600 keV) for the experiment. These lines provided both the energy calibration for the muonic x-ray lines and spectral line shape parameters used in the fitting of the muonic lines.

Fig. 5 shows the muonic 2p-1s x-ray doublets for Ti and Cr isotopes. The isotope shifts of the x-ray energies have opposite signs for ^{50}Ti-^{48}Ti and ^{54}Cr-^{52}Cr. The curves are "best fits" to the measured spectra considering the known isotopic impurities.

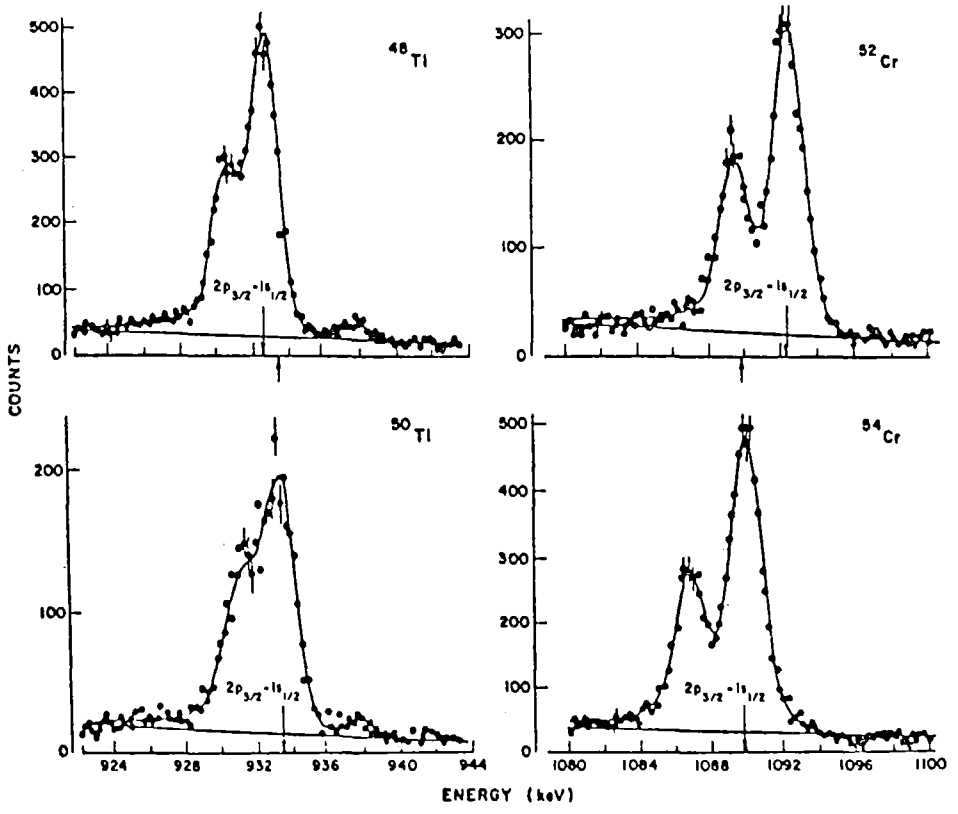

Fig. 5. Muonic x-ray spectra for Ti and Cr isotopes.

IV. Experimental Results and Interpretation

A. Discussion of the observed systematics

A graphical summary of our results for the $1f_{7/2}$ shell nuclei is shown in Fig. 6. The display shows rms-charge radii obtained from the combined analysis of the muonic data [3,6,7] and elastic electron scattering data [10,11], as a function of the neutron and proton number respectively. The Ca isotopes, which cover the whole $1f_{7/2}$ neutron shell, show increasing radii in the first half of the shell from ^{40}Ca to ^{44}Ca and decreasing radii in the second half of the shell from ^{44}Ca to ^{48}Ca. The increase in the first half of

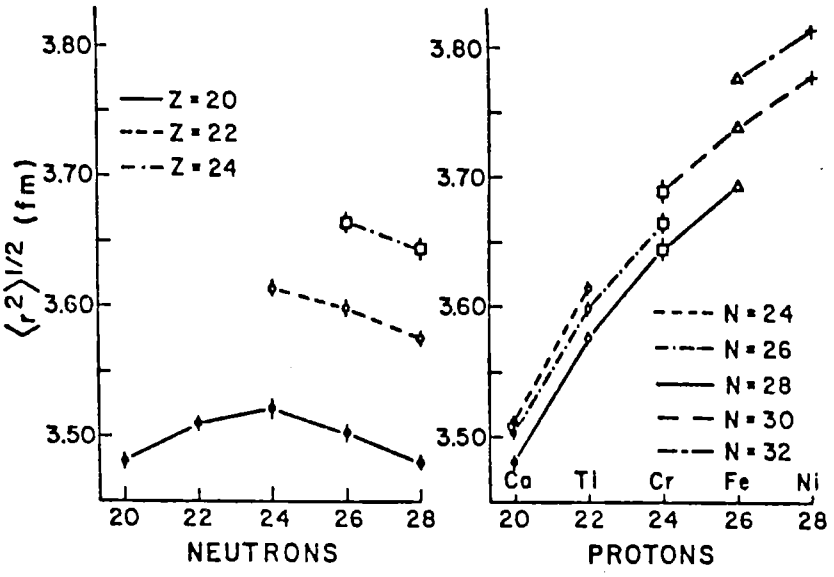

Fig. 6. Rms-charge radii for the $1f_{7/2}$ shell nuclei from a combined analysis of the muonic data and (e,e) data.

the shell is totally compensated by the decrease in the second half of the shell resulting in a net rms-charge radius change of zero for ^{40}Ca-^{48}Ca (within the experimental error of about 1×10^{-3}fm). The Ti and Cr isotopes, which are situated in the second half of the shell, show decreasing radii with increasing neutron number like the heavier Ca's. In the right part of Fig. 6 isotone shifts for the different isotone sequences involving the neutron numbers $24 \leqslant N \leqslant 32$ are displayed. Two features are apparent: 1. The curves for the various isotones are parallel. 2. A saturation effect exists; the magnitude of the increase in the rms-radii becomes smaller with increasing proton number.

To emphasize the observed effects, Fig. 7 displays the changes in the rms-radii between even neighboring isotones and isotopes. Both the isotone

and isotope $\delta\langle r^2\rangle^{1/2}$ shifts show an almost linear decrease in the radii differences with increasing proton and neutron number, respectively. Both the isotone and isotope shifts are independent of the neutron or proton configuration of the particular nuclei. That is, the Z = 20 proton core of the Ca isotopes shows the same polarizibility as the Z = 22 and Z = 24 proton cores of the Ti and Cr isotopes. Similar results had been obtained earlier from our studies of nuclei in the Ni region [3]. Thus, the Z = 28 proton core of the Ni isotopes shows the same polarizibility as the Z = 26 and Z = 30 proton cores of the Fe and Zn isotopes. These experimental results suggest that the added neutrons interact with the whole proton core rather then with the valence protons. The dashed lines in the figures above indicate that the slopes of the isotone and isotope shifts are almost the same. Both sets of data show a strong shell structure effect when crossing the shell closure at Z or N equal 28.

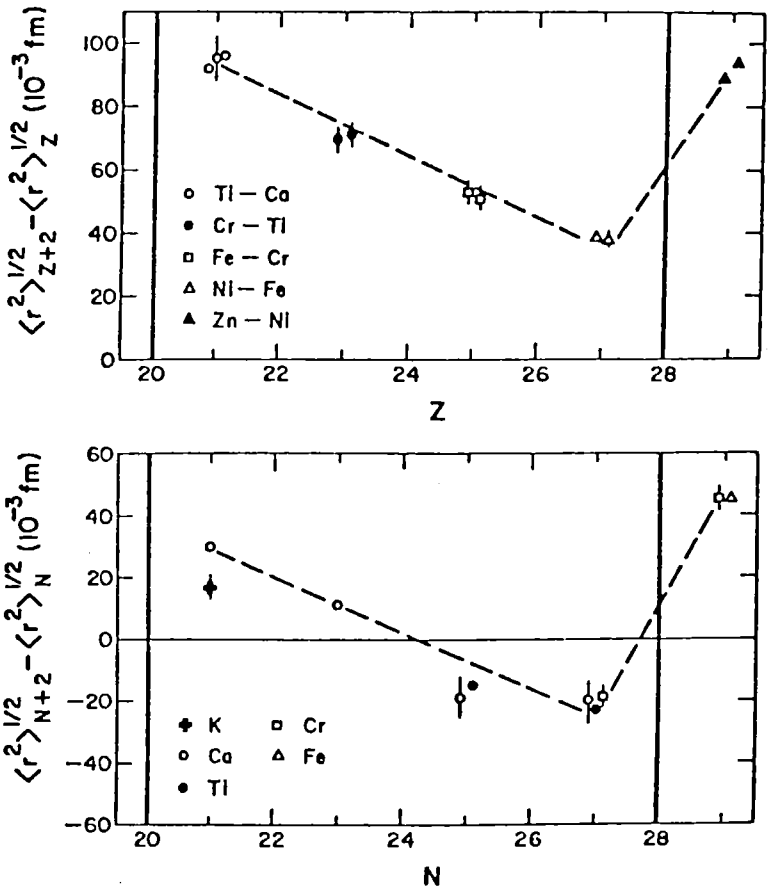

Fig. 7. ΔA=2 isotonic and isotopic rms-charge radii differences.

B. Interpretation and comparison with theory

In the following, I will try to compare the polarization of the charge distribution due to the added protons, which is reflected in the measured isotone shifts, with the polarization of the charge distribution due to the added neutrons, which we observe in the measured isotope shifts directly. The charge distribution densities of two nuclei that differ by two neutrons

(neglecting the neutron form factor) are related by:

$$\rho_{N+2} = \rho_N + \delta\rho_N^{core} \tag{5}$$

Here $\delta\rho_N^{core}$ describes the change of ρ_N due to the interaction with the 2 added neutrons. This change of ρ_N is directly measured as mean-square radius difference $\delta\langle r^2\rangle_N^{core}$. The charge distribution densities of two nuclei that differ by two protons are related by:

$$\rho_{Z+2} = \rho_Z + 2\rho_p + \delta\rho_Z^{core} \quad , \tag{6}$$

where ρ_p is the spatial distribution of the added protons and $\delta\rho_Z^{core}$ describes the polarization of the ρ_Z core due to the added protons. Including the normalization we obtain the change of $\langle r^2\rangle_Z$ that is caused by the interaction with the two added valence protons:

$$\delta\langle r^2\rangle_Z^{core} = \frac{Z+2}{Z}\left[\langle r^2\rangle_{Z+2} - \langle r^2\rangle_Z\right] + \frac{2}{Z}\left[\langle r^2\rangle_Z - \langle r^2\rangle_p\right] . \tag{7}$$

$\delta\langle r^2\rangle_Z^{core}$ can be deduced from the experimentally determined values $\langle r^2\rangle_{Z+2}$ and $\langle r^2\rangle_Z$ by making a model assumption for $\langle r^2\rangle_p$, the spatial distribution of the two added valence protons. We determined $\langle r^2\rangle_p$ by a shell model calculation, using $1f_{7/2}$ harmonic oscillator wave functions for the two added valence protons. The lower shadowed band of Fig. 8

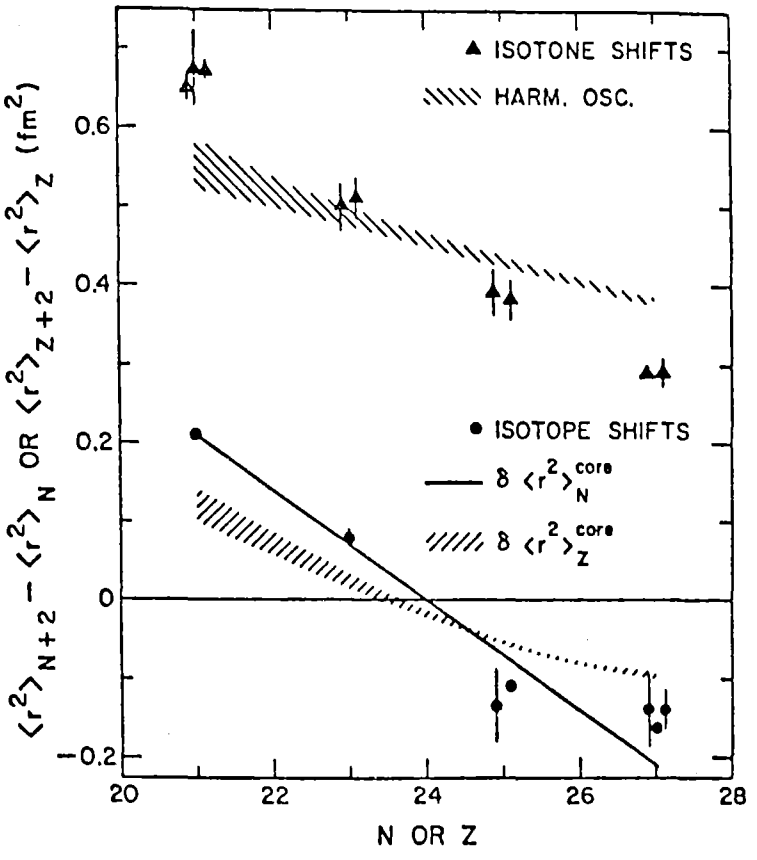

Fig. 8.
Proton core polarization due to protons $\delta\langle r^2\rangle_Z^{core}$ and neutrons $\delta\langle r^2\rangle_N^{core}$.

shows the core polarization due to the added protons $\delta\langle r^2\rangle_Z^{core}$ calculated with formula (7). The upper shadowed curve shows the result of the shell model calculation. The comparison of the shell model calculation and the measured isotone shifts indicates the presence of polarization. $\delta\langle r^2\rangle_Z^{core}$ is positive in the first half of the shell and negative in the second half of the shell, showing the same trend as the directly measured core polarization due to the added neutrons $\delta\langle r^2\rangle_N^{core}$, also displayed in Fig. 8. It is interesting to note that the core polarization due to the added protons, obtained in this way, is about 50% smaller than the core polarization due to added neutrons.

Note that the isotone core polarization effect shows the same feature we observed for isotopes in the Ca nuclei, namely increase of the rms-radii in the first half of the shell and decrease of the rms-radii in the second half of the shell. Again increase and decrease cancel almost totally over the whole shell. Quadrupole deformation parameters β_2 deduced from measured B(E2)-values [13], displayed in Fig. 9, show a systematic behavior that is reminiscent of that observed in the isotope shifts and in the core polarization due to the protons. The deformation for both the isotopes and isotones increases in the first half of the $1f_{7/2}$ shell and decreases in the second half of the $1f_{7/2}$ shell. The increase and decrease cancel almost totally

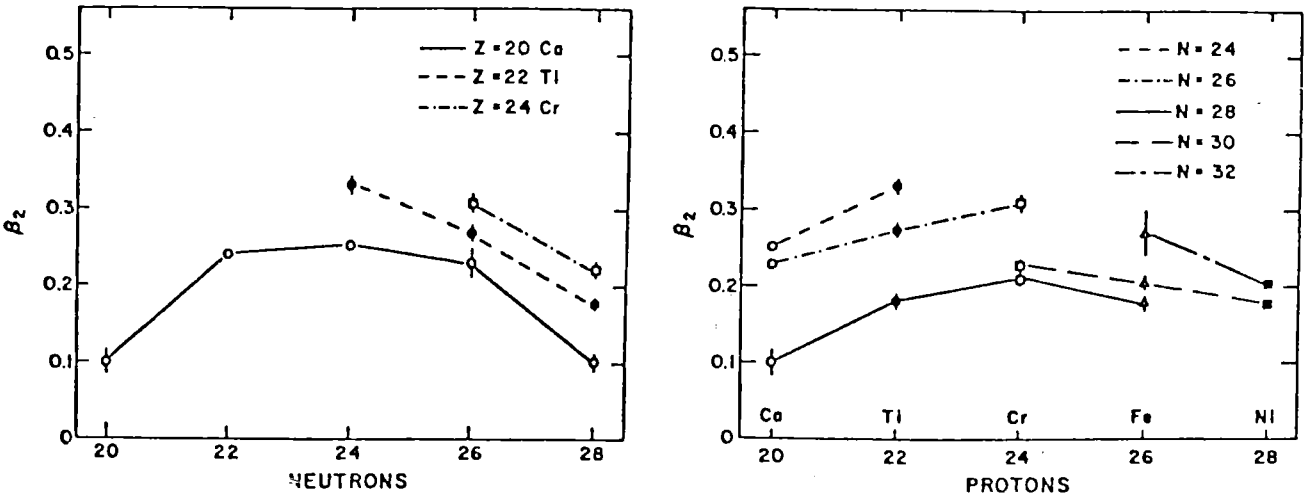

Fig. 9. Quadrupole deformation parameters β_2 for the $1f_{7/2}$ shell nuclei, deduced from measured B(E2)-values.

over the whole shell. The curves for the different elements and isotones are almost parallel. Qualitatively this is in agreement with the observed behavior of the rms-charge radii, suggesting that the observed increase in the rms-radii in the first half of the shell is due to an increase in deformation and the observed decrease in the second half of the shell is caused by a decrease in deformation. At the end of my talk I will come back to this, investigating this point quantitatively.

Fig. 10 displays some of our results for charge distribution differences from our combined analyses of the present muonic data and electron scattering data from Stanford [10]. These figures illustrate the results for the changes in the rms-charge radii differences. The charge distribution difference $^{44}Ca - ^{40}Ca$ shows that by adding the first four neutrons in the $1f_{7/2}$ shell, the Z=20 proton core is polarized in such a way that charge from the inner part of the nucleus is transferred to the outer part of the nucleus. The opposite effect is observed when the last four neutrons are added into the $1f_{7/2}$ orbital, as can be seen in the examples of $^{48}Ca - ^{44}Ca$ and $^{50}Ti - ^{46}Ti$. The charge distribution difference $^{48}Ca - ^{40}Ca$ illustrates that the observed $\delta\langle r^2\rangle^{1/2} = 0$ is the result of a rather complicated polarization effect. By adding 8 neutrons to ^{40}Ca to form ^{48}Ca, charge from both the inner and the outer part of the Z = 20 proton core is transferred into the surface region of ^{48}Ca.

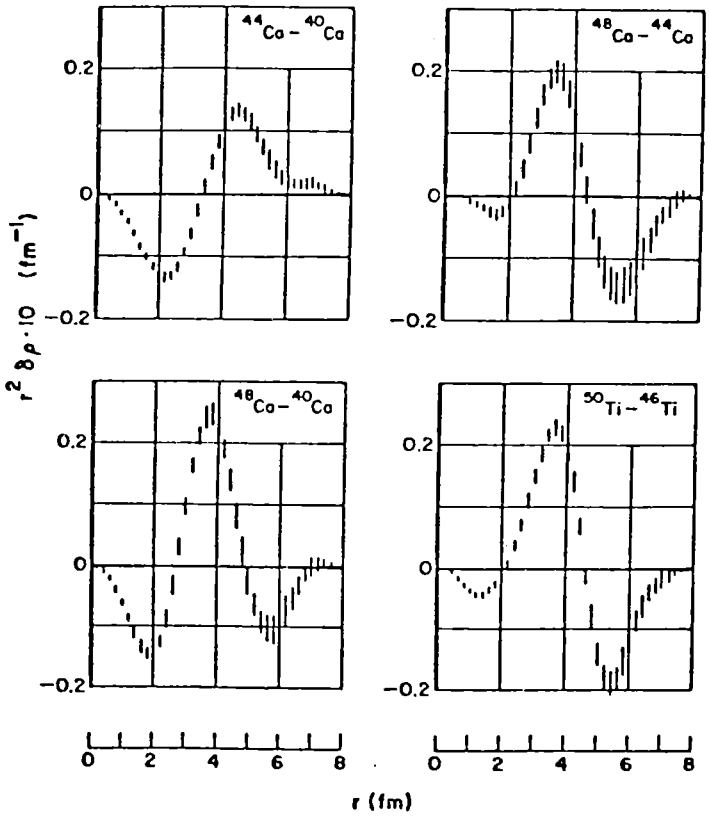

Fig. 10. Charge distribution differences from the combined analyses of the muonic data and (e,e) data.

Fig. 11 shows results of density dependent Hartree-Fock (DDHF) calculations of Negele [14] for the ^{40}Ca charge distribution and for the charge

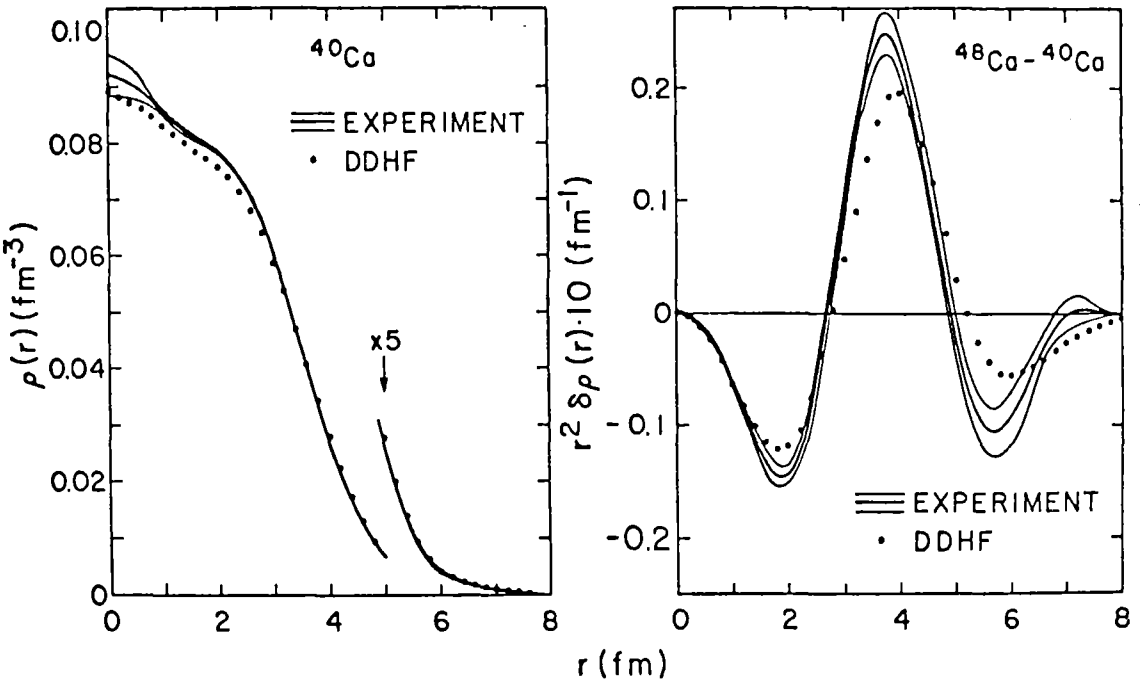

Fig. 11. Comparison of experiment ((e,e) + muonic atom) and theory.

distribution difference ^{48}Ca - ^{40}Ca. Also shown in Fig. 11 are the results of the combined analysis of the present muonic data and electron scattering data. The calculations are in satisfactory agreement with the experiment. The rms-radii and their differences are also in good agreement.

$$^{40}\text{Ca} \quad : \quad \langle r^2 \rangle^{1/2}_{EXP} = 3.481 \pm 0.005 \text{ fm} \qquad \langle r^2 \rangle^{1/2}_{TH} = 3.502 \text{ fm}$$

$$^{48}\text{Ca} - {}^{40}\text{Ca}: \; \delta\langle r^2 \rangle^{1/2}_{EXP} = (-0.7 \pm 0.9) \times 10^{-3} \text{ fm} \qquad \delta\langle r^2 \rangle^{1/2}_{TH} = -3 \times 10^{-3} \text{ fm}$$

The success of these calculations in the double closed shell nuclei ^{40}Ca and ^{48}Ca, however, does not necessarily imply that the other $1f_{7/2}$ shell nuclei can be equally well described by DDHF. This is illustrated in Fig. 12, where our $\Delta N=2$ experimental isotope shifts for the Ca nuclei are compared with spherical Hartree-Fock calculations [15]. The calculation does not reproduce the observed almost linear decrease in the shifts for the Ca nuclei. Even Hartree-Fock calculations including nuclear deformation [15] are not in satisfactory agreement with experiment.

Reinhard and Drechsel [15] have shown recently that ground state correlations, neglected in H. F. calculations, are important in isotope shifts. In their calculations the bulk properties of nuclei, varying smoothly and slowly with the nucleon number A, are obtained from spherical Hartree-Fock calculations. In addition they consider not only the influence of static deformations but also the contribution due to zero-point oscillations of the nuclear excitation modes. These contributions come mainly from the isoscalar 2^+ giant resonance, which varies slowly with A, and from the low lying collective 2^+ states, which vary characteristically over the $1f_{7/2}$ shell (see Fig. 9). Both the contribution of the zero point oscillations and the influence of the static deformation are related to experimental B(E2)-values. Including the experimental B(E2)-values [13, see Fig. 9] in their calculations, Reinhard and Drechsel calculated ΔN=2 isotope shifts for the Ca isotopes which are in satisfactory agreement with experiment (see Fig. 12 (H.F+G.S.C.)). This indicates that changes in deformation and zero-point oscillations are important in the Ca isotope shifts. Calculations for other $1f_{7/2}$ shell nuclei have not yet been performed. From the systematics of the β_2 quadrupole deformation parameters shown in Fig. 9, it seems very probable that this kind of calculations, which were very successfull for the Fe, Ni and Zn isotope shifts also, can give satisfactory agreement with experiment for the other $1f_{7/2}$ shell nuclei.

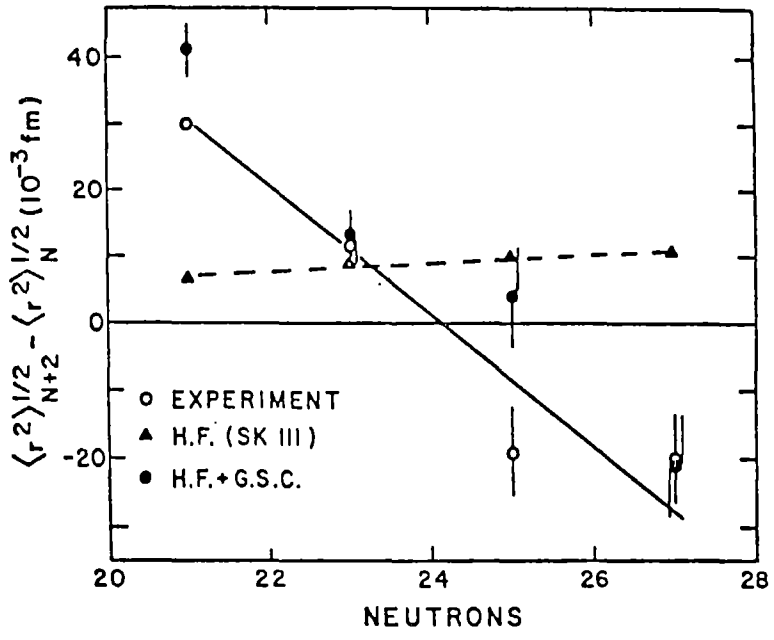

Fig. 12. Experimental and calculated ΔN=2 isotope shifts for the Ca isotopes.

Acknowledgment

The author wishes to thank M. V. Hoehn and E. B. Shera for helpful discussions.

References

1. H. R. Collard, L. R. B. Elton and R. Hofstadter, Nuclear Radii in Landolt-Börnstein I,2, 1 (Springer Verlag Berlin 1967).

2. W. D. Myers, Nucl. Phys. A204, 465 (1973).

3. E. B. Shera, E. T. Ritter, R. B. Perkins, G. A. Rinker, L. K. Wagner, H. D. Wohlfahrt, G. Fricke, and R. M. Steffen, Phys. Rev. C14, 731 (1976).

4. I. Angeli and M. Csatlos, Nucl. Phys. A288, 480 (1977).

5. R. Engfer, H. Schneuwly, J. L. Veuilleumier, H. K. Walter and A. Zehnder, At. Data Nucl. Data Tables 14, 509 (1974).

6. H. D. Wohlfahrt, E. B. Shera, M. V. Hoehn, Y. Yamazaki, G. Fricke, and R. M. Steffen, Phys. Lett. 73B, 131 (1978).

7. H. D. Wohlfahrt, E. B. Shera, M. V. Hoehn, Y. Yamazaki, and R. M. Steffen, to be published.

8. G. A. Rinker and R. M. Steffen, At. Data Nucl. Data Tables 20, 143 (1977).

9. R. C. Barrett, Phys. Lett. 33B, 388 (1970).

10. R. F. Frosch, R. Hofstadter, J. S. McCarthy, G. D. Nöldeke, K. J. Van Oostrum, M. R. Yearian, B. C. Clark, R. Herman, and D. G. Ravenhall, Phys. Rev. 174, 1380 (1968), and J. Heisenberg, R. Hofstadter, J. S. McCarthy, R. Herman, B. C. Clark and D. G. Ravenhall, Phys. Rev. C6, 381 (1972).

11. H. D. Wohlfahrt, O. Schwentker, G. Fricke, H. G. Andresen, and E. B. Shera, to be published.

12. B. Dreher, J. Friedrich, K. Merle, H. Rothhaas, and G. LÜhrs, Nucl. Phys. A235, 219 (1974).

13. P. H. Stelson and L. Grodzins, Nucl. Data Sheets A1, 21 (1965); A. Christy and O. Hansen, Nucl. Data Tables 11, 281 (1972).

14. J. W. Negele, Invited Talk at the 2nd Nucl. Phys. Div. Conf. of the Eur. Phys. Soc., Crakow (1976); and J. W. Negele, private communication (1978).

15. P. G. Reinhard and D. Drechsel, Z. Phys. A290, 85 (1979).

OPTICAL SPECTROSCOPY OF CALCIUM ATOMS

F. Träger
University of Heidelberg,
Federal Republic of Germany

OPTICAL SPECTROSCOPY OF CALCIUM ATOMS

F. Träger

Physikalisches Institut der Universität Heidelberg
Federal Republic of Germany

The Ca-nuclei, which are the topic of this conference, have attracted the interest of many experimentalists and theorists for more than twenty years. The main reason for that is, that Ca has two doubly magic nuclei, $^{40}_{20}Ca_{20}$ and $^{48}_{20}Ca_{28}$, and peculiar things occur for the nuclei in between, for example with the charge radii. Incorporation of neutrons or neutron pairs to ^{40}Ca into the $f_{7/2}$ shell up to the closed configuration of doubly magic ^{48}Ca opens the way for a study of changes in the radii if the mass number is changed by 20% and the neutron number by as much as 40%. In this respect, the long chain of Ca-isotopes can be regarded as a unique testing ground for a study of the distribution of nuclear matter, in particular for light nuclei.

Among all the methods to determine nuclear charge radii, optical isotope shifts have long been a valuable tool for precise and detailed investigations. During the last few years however, a rather rapid further development of more and more refined experimental techniques has taken place. So the advent of narrow-band tunable dye-lasers has opened new dimensions for the measurement of optical isotope shifts. The application of lasers instead of hollow-cathode lamps, as available in former experiments, and the possibility of using Doppler-free techniques like saturation or two-photon-spectroscopy has made possible an unprecedented high resolution. At the same time the lasers as intense light-sources have lead to a very high sensitivity, which is necessary in many cases for the study of very rare abundant, e.g. short-lived isotopes.

Optical spectra and nuclear charge distribution

The shift in an optical line "a" between two isotopes of the same element with mass numbers A_i and A_{i-1} is a very tiny effect. For $\Delta A=A_i-A_{i-1}=2$, for example, it is typically of the order of 10^8 Hz. Compared to the optical transition frequency of $\sim 5.10^{14}$ Hz the isotope shift only amounts to some 10^{-7}. Nevertheless, due to high resolution techniques, it provides accurate information on the nuclear charge distribution.

The isotope shift in an optical line is composed of two parts due to different effects: the so-called mass shift and the field shift.

The mass shift originates from the fact that the nucleus is not at rest as assumed in a very simplified model of the atom, but that it carries out a motion which may be caused by

1) the motion of the valence electron around the nucleus. This makes them both move around their common center of gravity, which leads to the "normal mass shift"
2) correlations in the movement of the core electrons, an effect called "specific mass shift".

The normal mass shift $\Delta\nu_{NMS}$ can be easily calculated

$$\Delta\nu_{NMS} = \frac{m_e}{m_p} \frac{A_i-A_{i-1}}{A_i \cdot A_{i-1}} \cdot \nu$$

where m_e, m_p stand for the electron and proton mass, respectively, and ν for the optical transition frequency.

Unfortunately an exact calculation of the specific mass shift

$$\Delta\nu_{SMS} = \frac{1}{M} \sum_{\substack{i=1 \\ k<i}}^{N} P_i P_k$$

with P_i, P_k momenta of the core electrons
M mass of the nucleus

N total number of core electrons

is not possible at present because the wavefunctions of all core electrons are generally not known and Hartree-Fock calculations only lead to rather unsatisfactory results. However, the normal as well as the specific mass shift depend in the same way on the massnumbers A_i and A_{i-1} of the isotopes under study. So $\Delta\nu_{NMS}$ and $\Delta\nu_{SMS}$ can be summarized as follows:

$$\Delta\nu_{NMS} + \Delta\nu_{SMS} = \frac{A_i - A_{i-1}}{A_i \cdot A_{i-1}} \cdot S = m_i S$$

This relation can be used to calculate the total mass shift for any pair of isotopes if it is known for one pair of the element under study.

The field shift $\Delta\nu_F$ is the contribution which has to be measured in order to determine nuclear charge radii. $\Delta\nu_F$ is the result of an overlap between the nuclear charge distribution and the charge distribution of the electrons. The overlap changes, if the nuclear charge radius increases or decreases. Thus $\Delta\nu_F$ reflects variations in the mean square charge radii $\delta \langle r^2 \rangle$. On the other hand the field shift also depends on the electron density at the nucleus. Therefore $\Delta\nu_F$ can be described as the product of two factors C_i and E_a

$$\Delta\nu_F = C_i E_a$$

C_i is a function of nuclear properties only, predominantly of $\delta \langle r^2 \rangle$ between the isotopes with mass numbers A_i and A_{i-1}. E_a only depends on electronic properties of the line a, namely on $\Delta |\psi(o)|^2$, which is the change of the total electron-charge density at the nucleus in the transition a.

The total isotope shift can then be written as the sum of the normal and the specific mass shift as well as of the field shift:

$$\Delta\nu_{IS} = \Delta\nu_{NMS} + \Delta\nu_{SMS} + \Delta\nu_F$$

Because $\Delta\nu_{MS}$ cannot be calculated with reasonable precision, the evaluation of the field shift and consequently of $\delta\langle r^2\rangle$ from the measured value of $\Delta\nu_{IS}$ is not straightforward. In many cases this seriously affects the interpretation of optical isotope shifts in terms of nuclear physics. For heavy nuclei the problem is not too aggravating because $\Delta\nu_F$ exceeds the total mass shift considerably. Therefore the specific mass shift is only a small correction and can be neglected. In light elements, however, like calcium for example, it is just the other way round: the field shift is only of the order of <10% of the total shift. This makes two things indispensable, when investigating optical isotope shifts of light elements in order to determine changes of nuclear charge radii:

1) The field shift must be exactly separated from the mass shift, in other words, the specific mass shift must be determined.

2) The experimental accuracy of $\Delta\nu_{IS}$ has to be very high in order to obtain the small value of $\Delta\nu_F$ and hence $\delta\langle r^2\rangle$ with reasonable precision.

The separation of mass and field shift in an optical line is possible by means of a so-called King-plot, if measurements in muonic atoms of the same element for at least two pairs of isotopes have been made. Fortunately this is the case for calcium, so that a relatively precise determination of the different contributions to $\Delta\nu_{IS}$ can be accomplished. This procedure, however, which is described in detail below,makes the results on the radii obtained from optical isotope shifts partly dependant on those from muonic atoms. The precise measurement of $\Delta\nu_{IS}$, as required and mentioned in 2), is possible by high resolution spectroscopic techniques.

Detailed discussions of optical isotope shifts have been given in [1-3].

Experimental situation

The stable Ca-isotopes (see Table 1) have been investigated by optical isotope shift measurements since 1953. Although six stable isotopes are present in the natural mixture, the experiments have proved to be rather complicated because the isotopes - apart from

^{40}Ca with ~97% - have a very small natural abundancy, so that enriched samples had to be used.

39	Ca 40	Ca 41	Ca 42	Ca 43	Ca 44	Ca 45	Ca 46	Ca 47	Ca 48	Ca
	96,94	$1{,}3 \cdot 10^5$ a	0,65	0,14	2,08	163 d	0,003	4,54 d	0,19	8.7
	$\sigma_{n,\alpha}$ 0,0025 σ 0,40	ε no γ	σ 0,65	σ 6,2	σ 1,0	β 0,3 γ e⁻	σ 0,7	γ 0.7 γ 1247 489	σ 1,1	

Table 1 Calcium isotopes with mass number A = 40-48. The stable isotopes are marked in black.

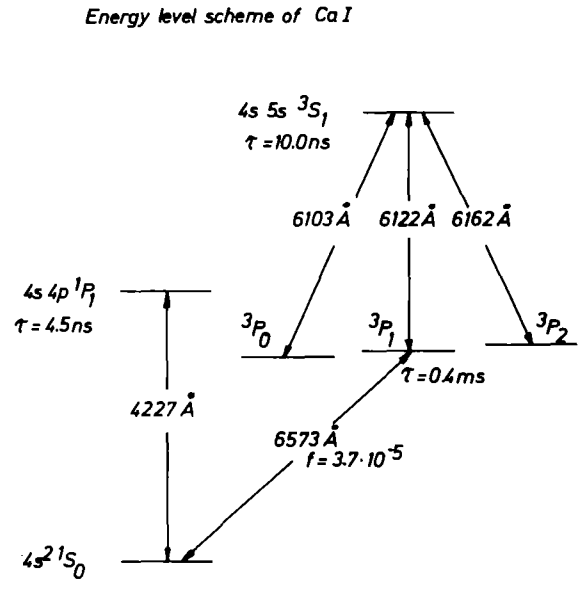

Fig. 1 Energy level scheme of calcium

Fig. 1 shows the CaI-spectrum with the most important lines. The strong transitions with λ = 6103 Å, 6122Å, 6162Å and 4227Å have been used for isotope shift measurements, the blue resonance line with λ = 4227 Å even repeatedly. In the experiments, which are summarized in Table 2, a hollow-cathode lamp combined with a Fabry-Perot-Interferometer for the investigation of the spectral distribution of the emitted light was used. In the recently published investigation [9] a collimated atomic beam of enriched isotopes served for improving the resolution by reducing the Doppler-width (see Fig. 2). In this experiment results for the charge radii of all stable Ca-isotopes could be obtained. It should be mentioned, that it was not until 1968, when muonic isotope shifts

Authors	year of publication	isotopes studied		lines examined
Anne Pery	1954 [4]	40,48	Ca	4227 Å $4s^2\ {}^1S_0$-$4s4p\ {}^1P_1$ 6103 Å $4s4p\ {}^3P_0$-$4s5s\ {}^3S_1$ 6122 Å $4s4p\ {}^3P_1$-$4s5s\ {}^3S_1$ 6162 Å $4s4p\ {}^3P_2$-$4s5s\ {}^3S_1$
			Ca^+	3934 Å $4s\ {}^2S_{1/2}$-$4p\ {}^2P_{3/2}$ 3968 Å $4s\ {}^2S_{1/2}$-$4p\ {}^2P_{1/2}$
K. Heilig	1968 [5]	40,42		4227 Å $4s^2\ {}^1S_0$-$4s4p\ {}^1P_1$
Bruch et al.	1969 [6]	44,48		3934 Å $4s\ {}^2S_{1/2}$-$4p\ {}^2P_{3/2}$
Epstein,Davis	1971 [7]	40,42 44,48		4227 Å $4s^2\ {}^1S_0$-$4s4p\ {}^1P_1$
Brandt et al.	1977 [8] 1978 [9]	40,42,43 44,46,48		4227 Å $4s^2\ {}^1S_0$-$4s4p\ {}^1P_1$

Table 2 Compilation of optical isotope shift measurements in calcium by "conventional" spectroscopy

were available, that the mass- and field shift could be separated and first results for the Ca-charge radii were derived from optical spectroscopy. However, disadvantages of all these measurements are that the resolution is seriously limited by Doppler-broadening and, even if a collimated atomic beam is used, by the large natural width of the investigated lines. Moreover, the sensitivity is not as high as it would be desirable. So rare isotopes can only be studied with difficulties and if enriched samples are accessible.

Isotope shifts in Ca by laser spectroscopy

In 1976 first investigation for all the stable Ca-isotopes were carried out [10]. In these experiments isotope shifts in the extremely weak intercombination line $4s^2\ {}^1S_0$-$4s4p\ {}^3P_1$ have been measured. At a first glance the intercombination transition seems to be a bad choice for spectroscopic studies, because - due to

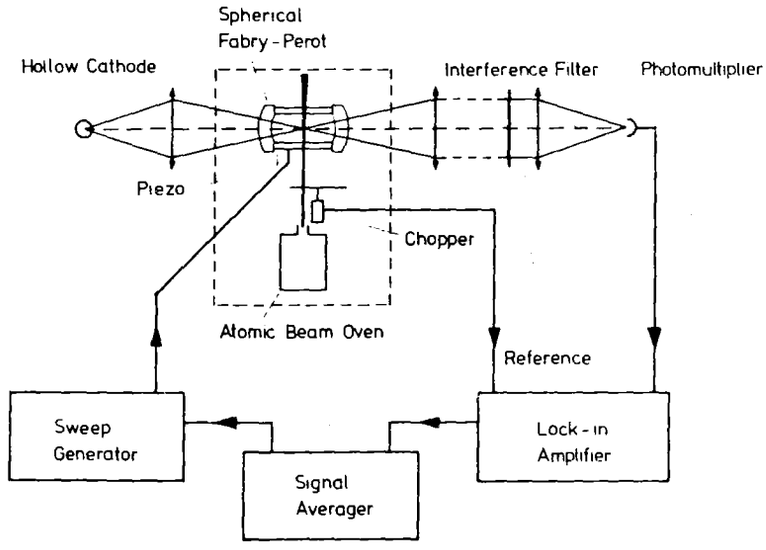

Fig. 2 Set-up for "conventional" isotope shift measurements using hollow-cathode lamps and Fabry-Perot-interferometers. (from Ref.9)

nearly pure Russell-Saunders-coupling in Ca - its oscillator-strength is exceedingly small and only amounts to $f = 3.7 \cdot 10^{-5}$. However, by using a narrow-band tunable dye laser it has proved possible to perform spectroscopy even in this line, which has considerable advantages compared to the transitions studied before [4-9] :

1.) The natural linewidth of the intercombination transition is rather small, it amounts to 410 Hz. Therefore this line in connection with Doppler-free experimental techniques, like saturation spectroscopy, opens the possibility to produce ultra-narrow signals and to obtain a very high resolution. In this respect the intercombination line is particularly well suited compared to all other transitions studied before, which have natural linewidths of the order of $\Delta\nu_{nat} \approx 30$ MHz.

2.) The experimental technique is extremely sensitive, so that very small quantities (several µg) of the isotope under study are sufficient for measurements. This even holds, if large

amounts of other isotopes are present, i.e. one can combine a low concentration with a small quantity of the isotope under study.

3.) Apart from the charge radii as obtained from optical isotope shifts, it is possible to get additional information on the nuclear charge distribution of odd isotopes by measuring the hyperfine structure splittting (hfs) of the excited $4s4p\ ^3P_1$ state. It can be used to calculate the nuclear quadrupole moment from the B-factor of the hfs. It should be mentioned that these parameters cannot be extracted from other states like the $4s4p\ ^1P_1$ level because their hfs is too small compared to the natural widths of the respective lines.

The experimental technique applied here [11,12] (see Fig. 3) makes use of a collimated atomic beam and a stabilized dye laser. Without going into details, it is sufficient to regard the laser as a coherent lightsource having the following properties:

linewidth:	$\Delta\nu_L$ = 500 kHz $\approx 10^{-5}$ Å
power:	I = 50 mW
beam divergence:	< 2 mrad
tunability:	range max. 70 GHz $\approx$ 1 Å

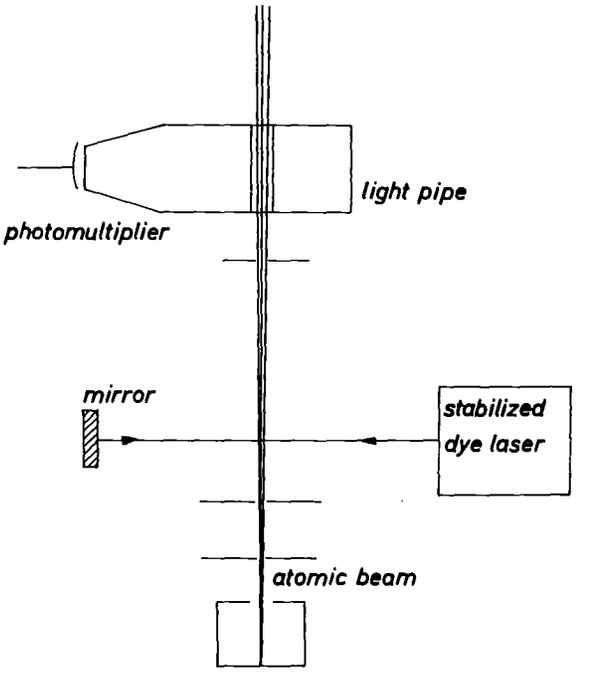

Fig. 3: Scheme of the experimental set-up for laser spectroscopy in the Ca-intercombination line.

The laser beam intersects the collimated atomic beam of natural calcium at right angles. The isotope shift in the intercombination transition being of the order of a few hundred MHz, which is large compared to the reduced Doppler-width of the beam as well as compared to the width of the laser line, the different Ca-isotopes can be excited selectively by tuning the laser. Due to the very long lifetime (τ = 0.4 ms) of the excited $4s4p\ ^3P_1$ level this makes the whole beam emit resonance fluorescence radiation along the path of flight of the atoms. The fluorescence is monitored about 12 cm downstream by a photomultiplier. Inserting appropriately shaped diaphragms any disturbing laser light or other background can be virtually eliminated, so that a high sensitivity is achieved. A curve measured with the set-up (Fig. 4)

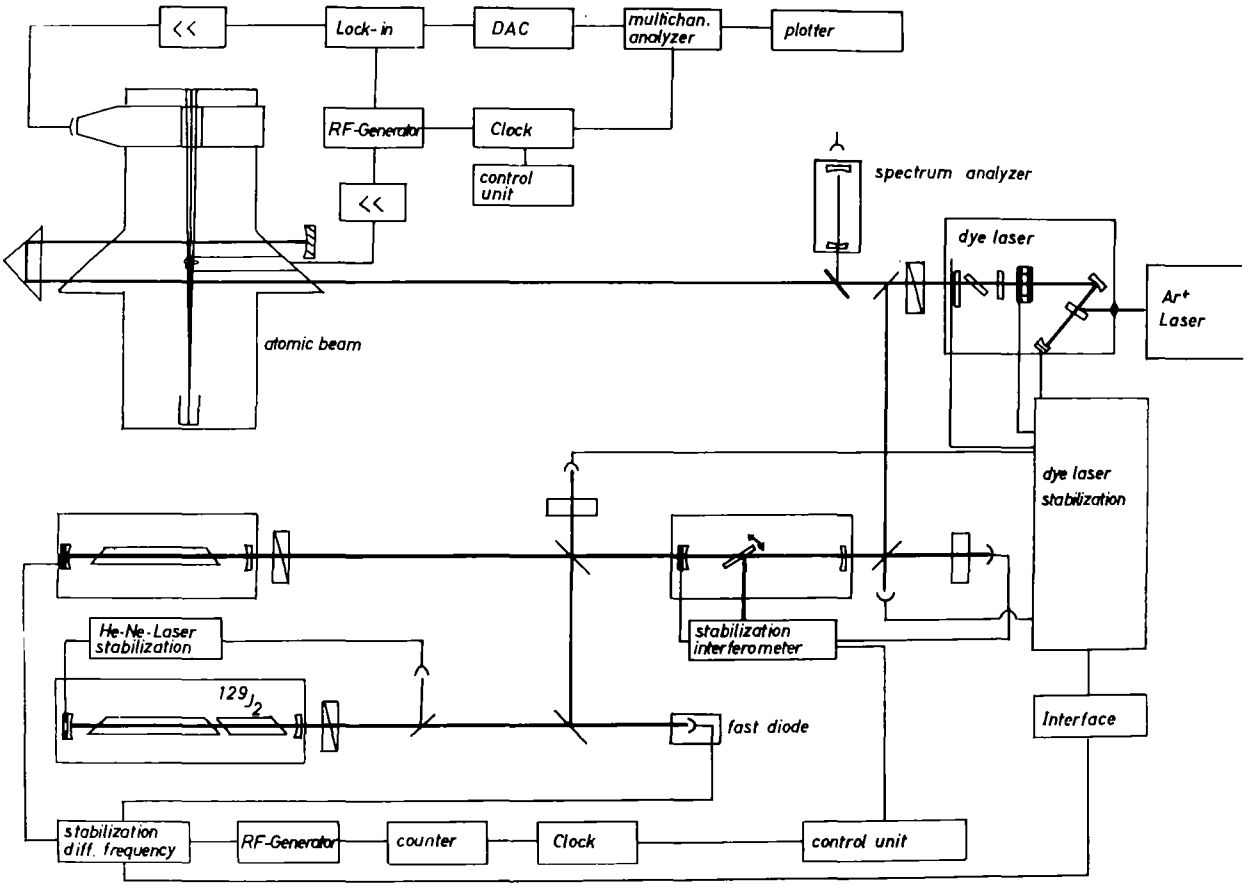

Fig. 4 Experimental set-up for laser spectroscopy in the Ca-intercombination line.

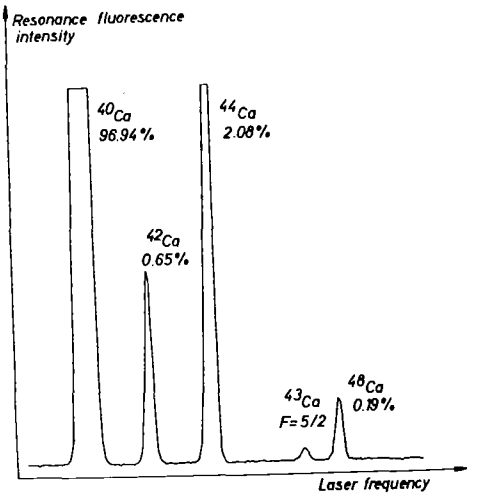

Fig. 5 Recording with signals of stable Ca-isotopes

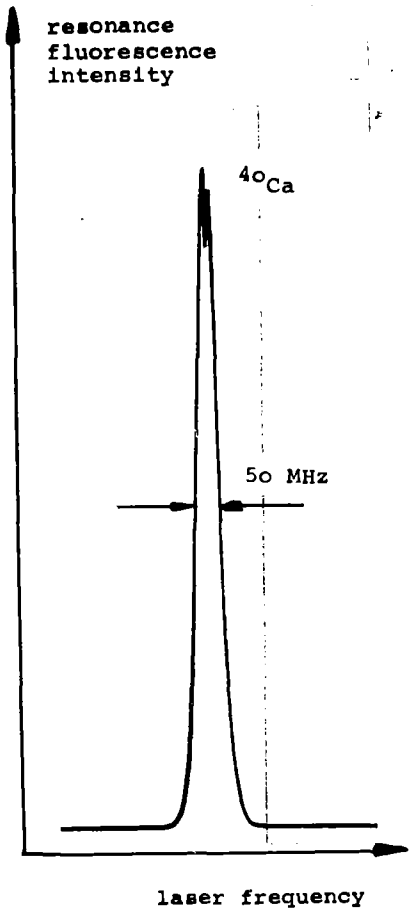

Fig. 6 Lamb-dip in the Doppler-profile of ^{40}Ca.

which follows the principle described above (Fig.3) is shown in Fig. 5. It was recorded with a very low vapour density in the atomic beam, the time for the total scan was only about one minute. Nevertheless, the recording exhibits well separated signals of five Ca-isotopes present in the natural mixture. However, curves of this type still permit only a rather limited resolution. This is due to the residual Doppler-broadening in the atomic beam. Much narrower signals can be produced by simply reflecting the laser beam back onto itself (see Fig.3). In this case, so called Lamb dips (see Fig.6), which are free of Doppler-broadening, can be observed in the Doppler profile at center frequency, provided that the optical transition is saturated. This technique is called saturation spectroscopy [13]. Dips as narrow as 900 kHz have been observed in the present experiment. Their width is determined by the following effects:

1.) Transit-time broadening. The atoms cross the laser beam within about 1μs. Due to the uncertainty-relation this corresponds to a homogeneous width of ~500 kHz.

2.) The width of the laser-line of also ~500 kHz.

3.) The natural width of the line. Because $\Delta\nu_{nat}$ of the regarded transition is only 410 Hz this contribution to the width of the Doppler-free dip is completely negligible here.

Fig. 7 shows a scan with signals originating from ^{48}Ca, the F=5/2 hfs-component of ^{43}Ca and ^{46}Ca. It demonstrates that the experimental technique is sufficiently sensitive to observe good signals (including Lamb-dips) even of the very rare isotope ^{46}Ca. The abundancy of ^{46}Ca in the natural mixture as used for the beam is only $3 \cdot 10^{-5}$. So the experimental technique leads to a very high resolution. At the same time it permits measurements of extremely rare abundant isotopes.

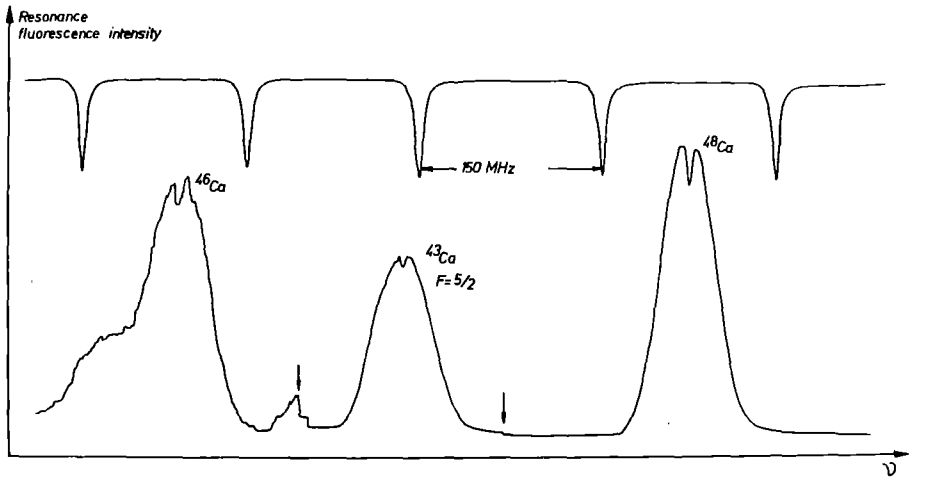

Fig. 7 Scan with signals of ^{48}Ca, ^{43}Ca and ^{46}Ca. The arrows indicate, where a reduction of the amplification of the recording system has been made.

A second method carries the resolution in hfs measurements even further: it is saturation-combined rf-spectroscopy, which is similar to the well-known classical double resonance method [14]. Fig. 8 shows the hfs-splitting of ^{41}Ca and ^{43}Ca which allows the determination of the nuclear quadrupole moment Q.An accurate measurement of Q can be performed by inducing radiofrequency

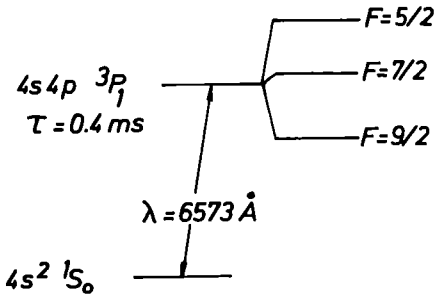

Fig. 8: Hyperfine structure splitting of the 4s4p $^3P_1$ state in ^{41}Ca and ^{43}Ca. The nuclear spin of the isotopes is I = 7/2.

transitions between the different hfs levels. Fig. 9 shows a scheme of the experimental arrangement applied for this purpose. The

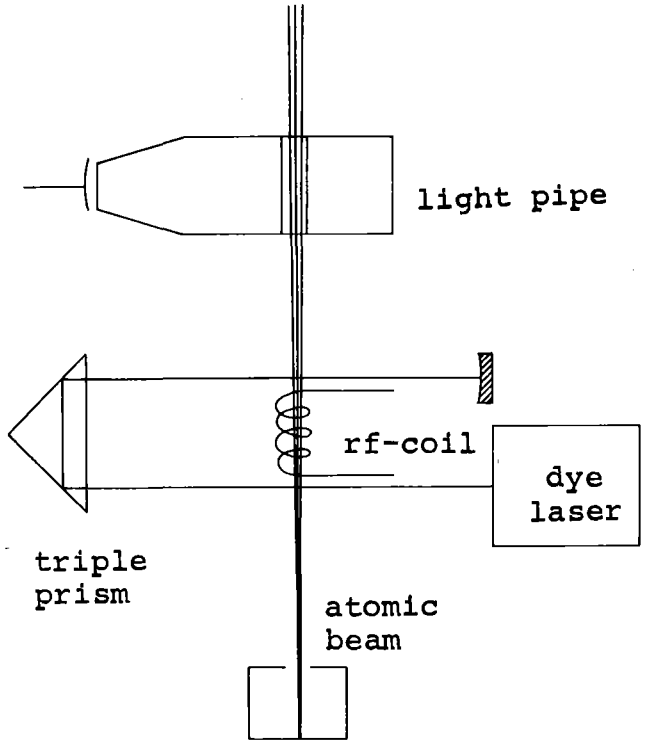

Fig. 9: Scheme of experimental set-up as used to detect rf-transitions by saturated absorption of the Ca-intercombination line.

atoms travel across the laser beam 1, which saturates the optical transition from the ground state to e.g. the F = 5/2 hfs

level. In the rf-coil the population of the F = 5/2 and 7/2 hfs levels is equalized, so that the F = 5/2 state can be refilled from the ground state when the atoms cross the laser beam 2, resulting in an increase of absorption or emitted resonance fluorescence radiation, respectively. This method which is in some sense similar to experiments recently performed in atomic ground states [15,16] has been tried out for one hfs transition in ^{43}Ca using the natural isotopic mixture with an abundancy of 0.14% of this isotope.

A curve is shown in Fig. 10. The intensity of the resonance fluorescence was observed as a function of the frequency of the rf-field. The width of the signal of 200 kHz is determined by

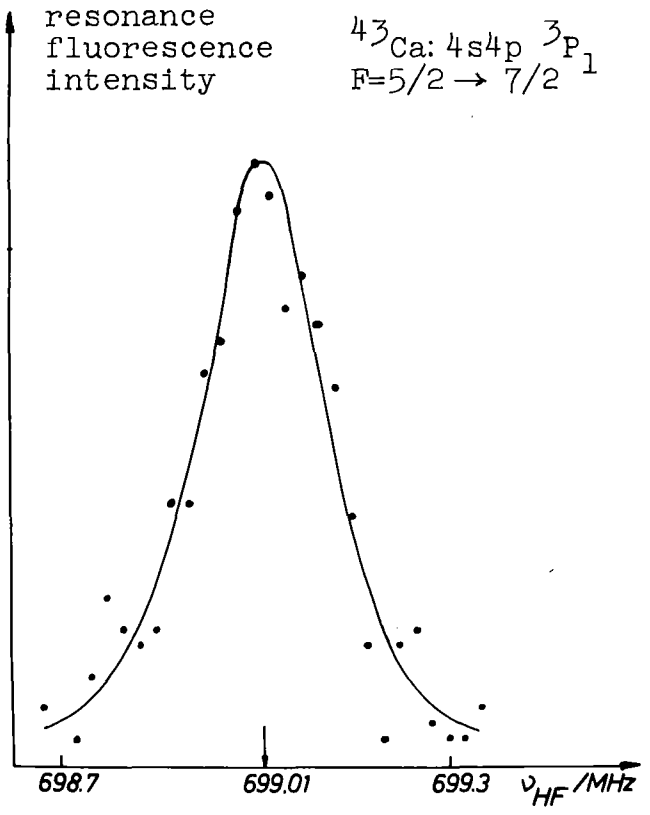

Fig. 10: Signal obtained when inducing an rf-transition between hfs-levels in ^{43}Ca. The averaging time was about 4 minutes.

transit-time broadening (~50 kHz) and the Zeeman-splitting of the hfs states, caused by the residual earth magnetic field of < 50 mGauss.

Results and Discussion

Table 3 compromises the experimental results obtained in the Ca-intercombination line.

	40-42	40-43	40-44	40-46	40-48	
$\Delta\nu_{IS}$	499(5)	782(4)	988(6)	1448(18)	1917(9)	MHz

^{43}Ca: A= -198.5(1.1) MHz B= 2(9) MHz Q= -0.09(16) b

Table 3 Results of experiments [10,17] in the Ca-intercombination line for all stable isotopes.

These values of $\Delta\nu_{IS}$ must be separated for mass and field shift, to get information on the changes of the mean square nuclear charge radii. This can be accomplished by means of a King-plot [18] which works as follows: The isotope shift in two lines, a and b can be described by the relations (see above):

$$\Delta\nu_{ia} = C_i E_a + m_i S_a$$

$$\Delta\nu_{ib} = C_i E_b + m_i S_b$$

where i stands for the pair of isotopes considered. Dividing by m_i and introducing the new variables $\Delta\tilde{\sigma}_{ia}$ and $\Delta\tilde{\sigma}_{ib}$ one obtains:

$$\Delta\nu_{ia}/m_i = \Delta\tilde{\sigma}_{ia} = \frac{C_i}{m_i} E_a + S_a$$

$$\Delta\nu_{ib}/m_i = \Delta\tilde{\sigma}_{ib} = \frac{C_i}{m_i} E_b + S_b$$

After eliminating C_i/m_i, it is possible to write $\Delta\tilde{\sigma}_{ia}$ as a function $\Delta\tilde{\sigma}_{ib}$:

$$\Delta\tilde{\sigma}_{ia} = \Delta\tilde{\sigma}_{ib} \frac{E_a}{E_b} + S_a + S_b \frac{E_a}{E_b}$$

Therefore a King-plot of $\Delta\tilde{\sigma}_{ia}$ against $\Delta\tilde{\sigma}_{ib}$ should give a straight line. This can be used for two purposes:

1.) As a check if the measurements in the two lines in question are consistent. Otherwise no straight line is obtained.

2.) For the separation of the mass from the field effect. $(S_a + S_b \frac{E_a}{E_b})$ and $\frac{E_a}{E_b}$ can be taken from the plot. Therefore S_a can be calculated provided S_b is known.

In other words, the principle of the separation is: if the mass shift in one line for some isotopes is known, it can be calculated for all other lines by means of a King-diagram. So, if an optical line is under study and the mass effect has to be determined, another line has to be found for which the mass shift is already known or easy to calculate. This is possible for the K_α -line of muonic atoms because the specific mass shift, which usually hampers exact calculations of $\Delta\nu_{MS}$, is completely negligible here due to the large mass of the muon. Fortunately measurements in muonic Ca-atoms have been made so that a King-plot can be drawn. An example is shown in Fig. 11 with the muonic data against the values in the intercombination line. The straight line obtained indicates that the measurements are consistent. For comparison the Fig. 12 shows a

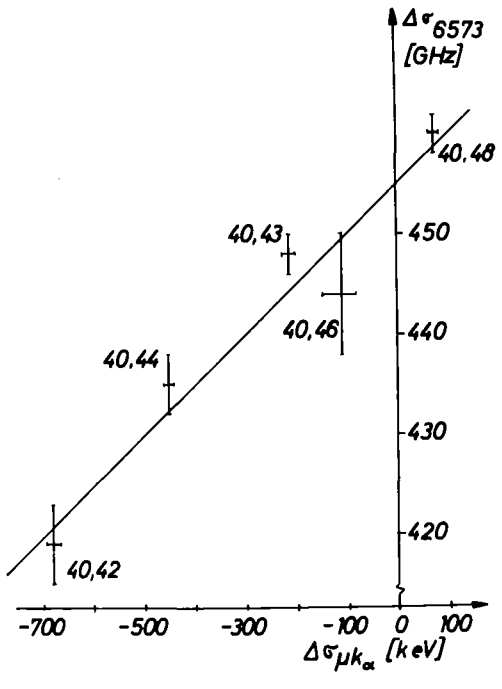

Fig. 11: King-plot of the muonic data [19] against the values measured in the Ca-intercombination line

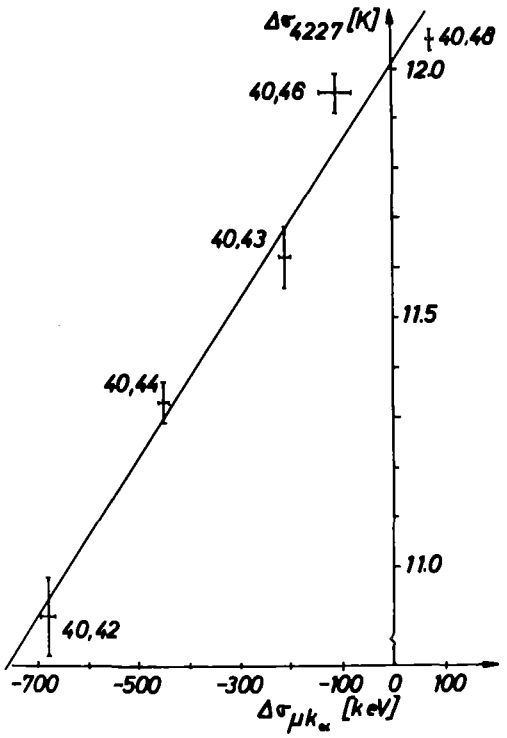

Fig. 12: King-plot of the muonic data against the values from the Ca-resonance line

King-plot of the muonic data against those from the blue resonance line [9]. It should be mentioned that for a more detailed interpretation of optical isotope shifts somewhat more refined King-plots must be used [2,3], which are for instance not directly based on the values in the K_α-line of muonic atoms but on the mean square charge radii extracted from these measurements.

Table 4 contains the field shifts of the intercombination transition derived from a King-plot and the specific mass shift for the

	40-42	40-43	40-44	40-46	40-48	
$\Delta\nu_F$	-48(8)	-20(13)	-56(8)	-50(19)	+3(15)	MHz

$^{40-42}\Delta\nu_{SMS}$ = 251 MHz from experiment [10]

$^{40-42}\Delta\nu_{SMS}$ = 60 MHz from theory, Hartree-Fock calculations [20]

Table 4 Field shifts and the specific mass shift for ^{40}Ca-^{42}Ca in the Ca-intercombination transition.

isotope pair 40,42. The experimental value is 251 MHz compared to 60 MHz as obtained from Hartree-Fock calculations [20]. This again demonstrates that the specific mass shift is at present inaccessible to a theoretical treatment. The values for the field shifts

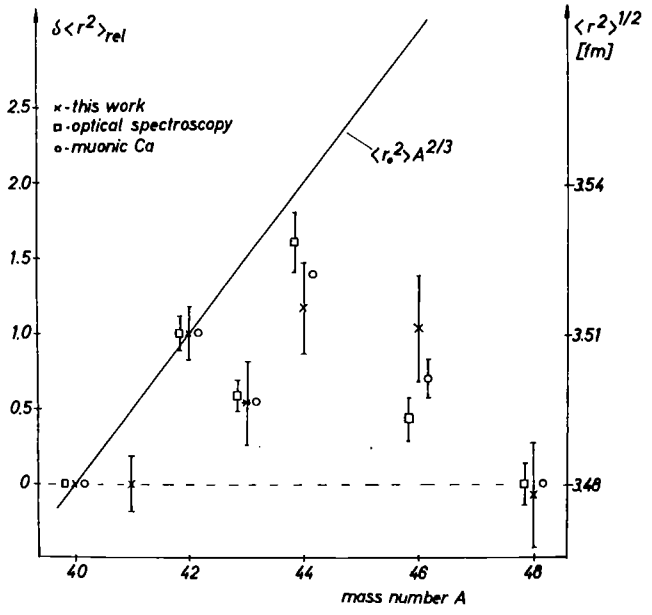

Fig. 13: Changes of mean square nuclear charge radii for the stable Ca-isotopes obtained from the intercombination line [10,17], from the resonance line [9] and from muonic Ca-atoms [19].

directly lead to changes of mean square nuclear charge radii for the stable Ca-isotopes. Fig. 13 shows the radii as a function of the mass number relative to ^{40}Ca and for $^{40,42}\delta\langle r^2\rangle = 1$. The mean square charge radius increases from 40 to 42, stays about constant to 46 and rapidly falls off at 48, which has the same charge radius as ^{40}Ca. The agreement of the different measurements is quite satisfactory, also some deviations for ^{46}Ca exist, which are also partly reflected in the King-plots (see Fig. 11,12) and which should be reexamined.

Usually only statistical errors enter the result of the experimental isotope shift. In the uncertainty of the charge radii the errors of the muonic data must also be taken into account. The laser spectroscopic results with the high resolution of the experimental technique make it necessary to consider very carefully systematic errors too. The errors in the isotope shifts of the intercombination line are mainly due to uncertainties in measuring how far the dye laser has been tuned from one signal to the next one. Nonlinearities in the scans also contribute to the final error. Therefore the experimental uncertainty of several MHz as given in the Tables 3 and 4 does not reflect the ultimate resolution which can be achieved by the methods described above. In principle the intercombination line and the $^3P_1$ state permit a much higher accuracy. Therefore new improved measurements by means of a so-called frequency offset-locking spectrometer have been started. This system makes it possible to tune the dye laser with an rf-synthesizer, which shortly will lead to results which are improved in accuracy by a factor of more than 10.These results can also be used for a test if the King-plot of our measurements against the muonic data is indeed a straight line. It is also interesting to measure another optical line with higher resolution than achieved so far. Moreover it would be a great improvement for the understanding of optical isotope shifts if the specific mass shift could be calculated. Therefore it is worth stimulating theorists, to try more accurate calculations than available at present. This problem is also of great interest for atomic physics.

Nuclear charge distribution of ^{41}Ca [21]

Althougt the stable Ca-nuclei have been studied rather extensively by using optical isotope shifts and many other methods, no information on the nuclear charge distribution of the radioactive Ca-isotopes was available so far. Therefore ^{41}Ca was investigated recently in this laboratory by the laser spectroscopic technique described above. ^{41}Ca is of special interest because it offers a chance to study the influence of a single neutron on the doubly magic, closed shell ^{40}Ca core. Moreover this isotope together with its mirror nucleus ^{41}Sc plays an important role in Coulomb displacement energy calculations.

^{41}Ca has been produced by neutron capture of ^{40}Ca. It decays with a half life of $\tau = 1.3 \cdot 10^{5}$y. The cross section for neutron capture ($\sigma = 0.4$b) being rather small, a ^{41}Ca concentration of only one part in a thousand could be obtained after a year of irradiation. As described above, the experimental technique makes use of a frequency controlled cw dye laser and a collimated atomic beam. The resonance fluorescence is again monitored by a photomultiplier installed 12 cm downstream along the beam.

In the preparation of an atomic beam which contains ^{41}Ca two difficulties arise: ^{41}Ca is available in small quantities only, and in addition in the chemical form of $CaCO_3$. Therefore a sample of 100 mg $CaCO_3$ containing $1 \cdot 10^{-3}$ ^{41}Ca was reduced forming a deposit of about 20 mg metallic Ca on a disk of tantalum. This disk served as the ^{41}Ca source in the atomic beam. So not more than about 20μg ^{41}Ca for the atomic beam were available.

Fig. 14 shows the experimental set-up with the apparatus for reducing the sample, the atomic beam containing ^{41}Ca and the dye laser. A second beam of natural Ca served for adjusting the laser to the intercombination line and for an easy identification of the recorded signals.

Fig. 15 shows a curve with signals of ^{41}Ca. For the production of ^{41}Ca isotopically enriched ^{40}Ca had been used. Therefore no signals originating from the isotopes in the natural mixture appear,

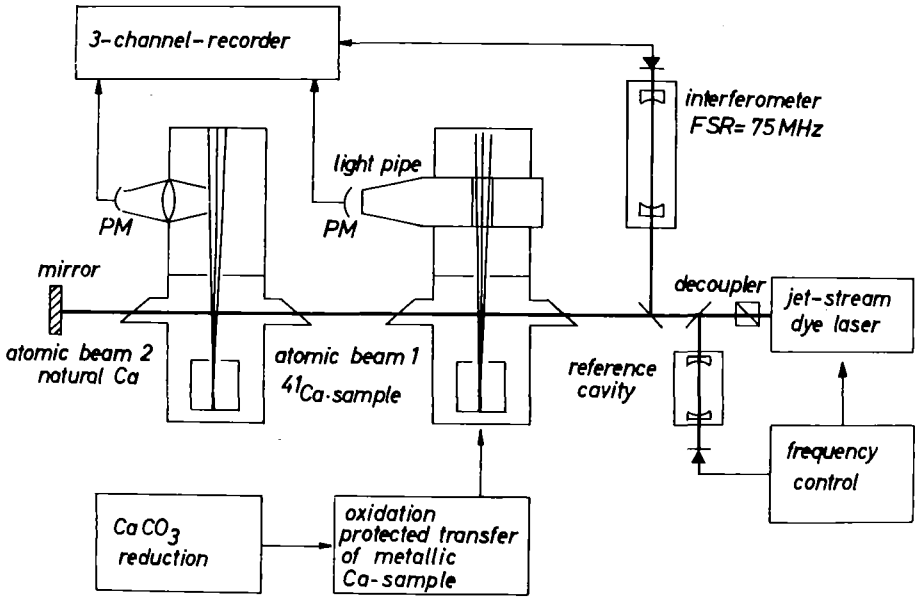

Fig. 14: Scheme of experimental set-up for laser spectroscopy in ^{41}Ca.

except for ^{40}Ca and a small ^{44}Ca-impurity. 20μg in the beam were sufficient to produce signals of ^{41}Ca with a signal-to-noise ratio as shown in Fig. 15 for about one hour. The curves yield the isotope shift in the intercombination line as well as the hyperfine

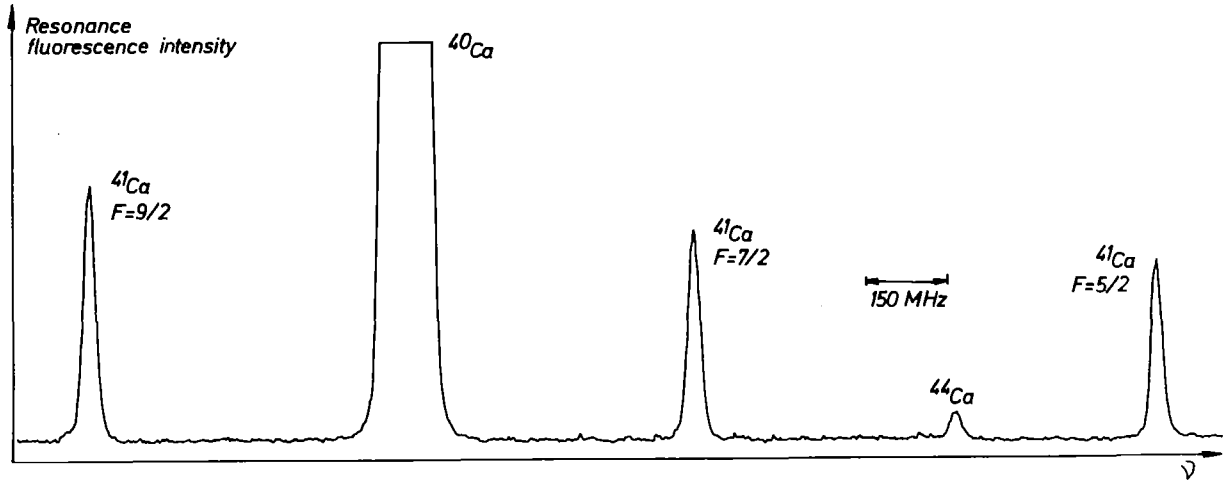

Fig. 15: Recording with signals of ^{41}Ca, ^{40}Ca and a small ^{44}Ca-impurity. The curve was recorded within two minutes, no signal-to-noise improving techniques have been applied.

structure splitting of the excited $^3P_1$ state [21].

From $B(^3P_1)$ = 5(7) MHz
Q = -0.09(13) b is obtained.

The isotope shift

$$\Delta\nu_{IS} = 280(8) \text{ MHz}$$

is the distance of the ^{40}Ca signal and the center of gravity of the three hfs components. Taking the mass shift from the King-plot one finds

$$\Delta\nu_{MS} = 280(4) \text{ MHz}$$

Therefore the field shift is consistent with zero:

$$\Delta\nu_F = 0(9) \text{ MHz}$$

This indicates that the mean square nuclear charge radii of ^{41}Ca and ^{40}Ca are equal. If the absolute radii of ^{40}Ca and ^{42}Ca are used for calibration, the absolute error of the ^{41}Ca radius can be computed from the error in the field shift:

$$^{41}\langle r^2\rangle^{1/2} = {}^{40}\langle r^2\rangle^{1/2} \pm 0.006 \text{ fm}.$$

Obviously the additional $f_{7/2}$-neutron in ^{41}Ca outside the closed proton- and neutron shells does not lead to a larger charge radius (see Fig. 16) compared to ^{40}Ca, whereas two paired neutrons in ^{42}Ca cause a marked increase of about 1%. Simply speaking, the additional $f_{7/2}$ neutron does not penetrate very much into the

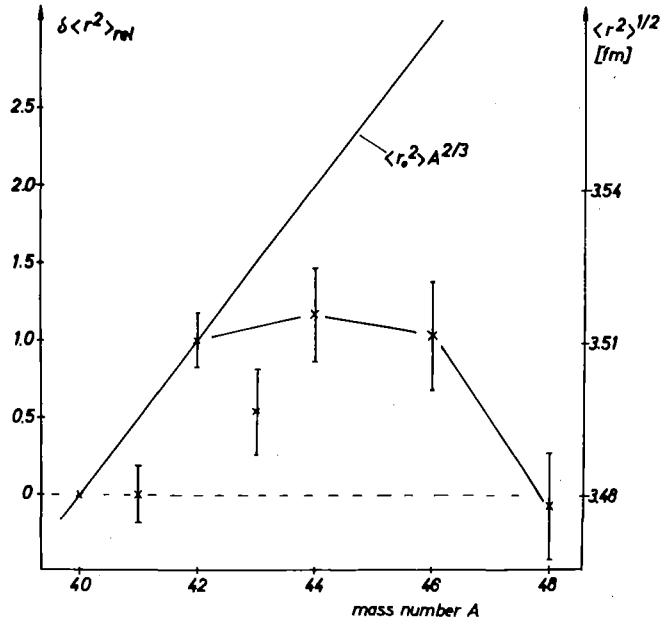

Fig. 16: Ca nuclear charge radii obtained from optical isotope shifts in the intercombination line

^{40}Ca core and does not polarize the core significantly either.

It is also interesting to know the neutron radius $\langle r^2 \rangle_n^{1/2}$ of ^{41}Ca too. Unfortunately, because of the very small quantities of isotopically pure ^{41}Ca available, there is not much hope that scattering experiments can be performed in the immediate future to measure $\langle r^2 \rangle_n^{1/2}$. However, Coulomb displacement energies can be used to get information on the neutron radius. Nolen and Schiffer have calculated the neutron excess radius of ^{41}Ca about 10 years ago [22,23], making the assumption of equal charge radii in ^{40}Ca and ^{41}Ca which is indeed confirmed by this experiment. They find for the neutron excess radius:

$$^{41}\langle r^2 \rangle_{exc}^{1/2} = 3.60 \text{ fm.}$$

A measurement of this quantity results in 4 fm [24], which is in agreement with a recently performed calculation [25]. These values indicate that in ^{41}Ca the root mean square (rms) neutron radius extends beyond the rms proton radius if the assumption of equal neutron and proton radii in ^{40}Ca is made.

The very peculiar behaviour of the nuclear charge radii (see Fig. 16) of the odd and even Ca-isotopes challenge a study of the shorter lived isotope ^{45}Ca. An experiment on ^{45}Ca is now under preparation in this laboratory.

Acknowledgements:

The author wants to thank very much Professor zu Putlitz and Dr. Kowalski for helpful discussions and advice.

This work was sponsored by the Deutsche Forschungsgemeinschaft.

References:

1 J. Bauche, R.-J. Champeau: Advances in Atomic and Molecular Physics Vol. 12, D.R. Bates, B. Bederson ed. (1976)

2 K. Heilig, A. Steudel: Atomic Data and Nuclear Data Tables 14, 613 (1974)

3 D.N. Stacy: Rep. Prog. Phys. XXIX, 171 (1966)

4 A. Pery: Proc. Phys. Soc. A57, 181 (1954)

5 K. Heilig: Habilitationsschrift, Hannover (1968)

6 R. Bruch, K. Heilig, D. Kaletta, A. Steudel, D. Wendlandt: J. Phys. (Paris) 30 suppl. C1-51 (1969)

7 G.L. Epstein, S.P. Davis: Phys. Rev. A4, 464 (1971)

8 H.-W. Brandt, K. Heilig, H. Knöckel, A. Steudel: Phys. Lett. 64A, 29 (1977)

9 H.-W. Brandt, K. Heilig, H. Knöckel, A. Steudel: Z. Physik A288, 241 (1978)

10 R. Neumann, F. Träger, J. Kowalski, G. zu Putlitz: Z. Physik A279, 249 (1976)

11 F. Träger, R. Neumann, J. Kowalski, G. zu Putlitz: Appl. Phys. 12, 19 (1977)

12 U. Klingbeil, J. Kowalski, F. Träger, H.-B. Wiegemann, G. zu Putlitz: Appl. Phys. 17, 199 (1978)

13 T.W. Hänsch, I.S. Shahin, A.L. Schawlow: Nature 253, 63 (1972)

14 J. Brossel, F. Bitter: Phys. Rev. 86, 308 (1952)

15 S.D. Rosner, R.A. Holt, T.D. Gaily: Phys. Rev. Lett. 35, 785 (1975)

16 W. Ertmer, B. Hofer: Z. Physik, A276, 9 (1976)

17 U. Klingbeil, J. Kowalski, F. Träger, H.-B. Wiegemann, G. zu Putlitz: Z. Physik, A290, 143 (1979)

18 W.H. King: J. Opt. Soc. Am.,53, 638 (1963)

19 H. Wohlfahrt, E. Shera, M. Hoehn, Y. Yamazaki, G. Fricke, R. Steffen: Phys. Lett. 73B, 131 (1978)

20 J. Bauche: J. de Phys. 35, 19 (1974)

21 J.Kowalski, F. Träger, S. Weißhaar, H.-B. Wiegemann, G. zu Putlitz: Z. Physik A290, 345 (1979)

22 J.A. Nolen, J. P. Schiffer: Ann. Rev. Nucl. Sci. 19, 471 (1969)

23 J.P. Schiffer, J.A. Nolen, N. Williams: Phys. Lett. 29B, 399 (1969)

24 J. Durell: Proceedings of this meeting

25 S. Shlomo: Rep. Prog. Phys.: 41, 957 (1978)

ELECTRON SCATTERING FROM ^{40}Ca

I. Sick, J. Bellicard, J.M. Cavedon,
B. Frois, M. Huet, P. Leconte, P.X. Ho,
and S. Platchkov
University of Basel, Switzerland

ELECTRON SCATTERING FROM ^{40}Ca

I.Sick, Department of Physics, University of Basel, Basel,
J.B.Bellicard, J.M.Cavedon, B.Frois. M.Huet, P.Leconte, P.X.Ho,
S.Platchkov, CEN Saclay, Gif-sur-Yvette, France

While the average charge density of the Ca-nuclei as determined by electron scattering[1] agrees quite well with theoretical predictions, this is not the case for the detailed structure of $\rho(r)$. The experimental density shows less shell structure (a less pronounced central peak) than predicted by Hartree-Fock calculations. A number of attempts[2] to explain this discrepancy have been published, but a conclusive answer is still lacking; this is mainly due to a discrete ambiguity discovered[3] in the experimental ^{40}Ca density.

In order to resolve these problems, a high-q experiment has been carried out at the Saclay linear accelerator. Data have been extended to $3.6 fm^{-1}$, hereby reducing the periously too large completeness error to <1%. The cross sections (fig.1) have been analyzed using the SOG-method[4]. The resulting density is shown in fig.2, where we also display a number of DDHF-densities. (X.Campi dash-dot, J.Negele dashed, M.Pearson dotted). They show too strong an oscillatory structure of $\rho(r)$; this is reduced only upon introducing RPA-correlations as done by D.Gogny (solid curve).

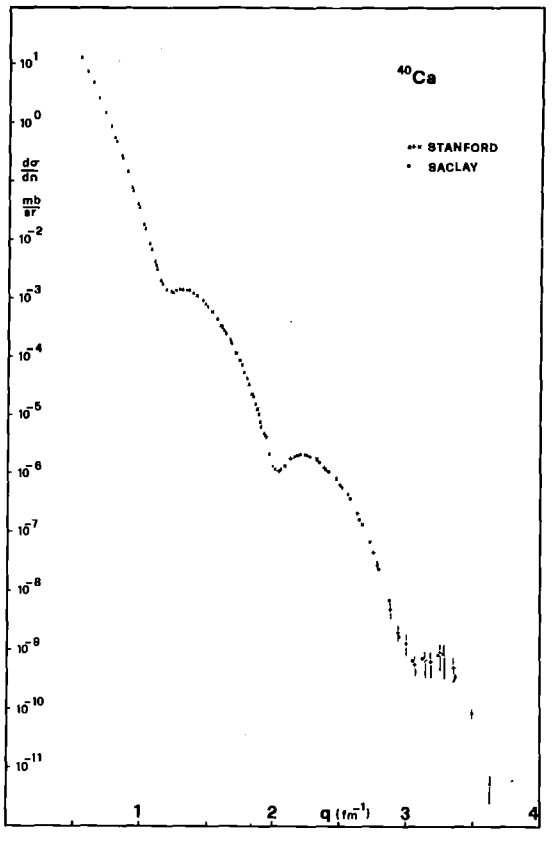

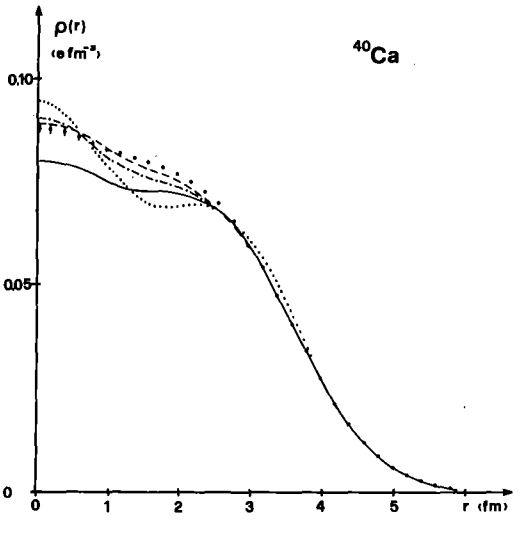

1) R.F.Frosch et al, PR174, 509 (74), J.B.Bellicard et al, PRL19, 527 B.B.Sinha et al, PRC7, 1930 (73).
2) L.R.B.Elton et al, PRL24, 145(70), F.C.Khanna PRL16, 871 (68), R.B. Raphael et al, PRC2, 1040 (70)
3) I.Sick PL52B, 15 (74)
4) I.Sick NP218, 509 (74)

PROTON SCATTERING AT 1 GeV AND NEUTRON DISTRIBUTION IN NUCLEI

Richard SCHAEFFER
Service de Physique Theoretique
C.F.A., CEN Saclay, B.P. no. 2
F-91190 Gif-sur-Yvette, France

The interest in neutron densities has not faded out for many years. One of the salient features of this subject is that it is highly controversial mainly because of the disagreement between neutron radii as obtained from Coulomb energy differences[1] and the Hartree-Fock predictions[2-4]. Moreover other means of getting the same information such as low energy proton and alpha particle scattering agree sometimes with the Coulomb energy result[5], and sometimes with the Hartree-Fock results[6,7], which indicates their degree of accuracy may not be as high as hoped - and claimed - by the authors. Indeed all the probes for measuring neutron densities use the strong interaction, and this makes very accurate calculations difficult. This is of course also the case for high energy protons, but the reaction mechanism is much better known[8-9] at these energies and the calculation of the optical potential that mediates the scattering much easier : *i)* it can be written as a term proportional to the ground-state density, plus a hierarchy of corrective terms that can be written explicitely and calculated, and *ii)* with a few additional approximations that can be checked experimentally, the coefficient of proportionnality is the free nucleon-nucleon scattering amplitude which can be measured independently. This was one of the strougest motivations to undertake experiments in the GeV region at Gatchina[10], Saclay[11] and Los Alamos[12].

Let us thus examine in some detail the approximations made for describing high energy proton scattering. We plan especially to discuss how these approximations can be checked. When possible we shall emphasize the difference with low energy proton or, alpha particle and also pion scattering. The elastic scattering amplitude for a proton of energy E can be obtained[8] by solving the Schrödinger equation including the proper[14] relativistic corrections with the potential

$$U(q) = t(q)\ \rho(q) + \text{corr.} \qquad (1)$$

written in momentum space, q being the momentum transfer. The factorisation of the scattering amplitude t and the ground state density ρ can be obtained by assuming t is a function of momentum transfer only, and in particular independent of the energy in an interval E $\pm$ 50 MeV. Provided E is large enough (E >> 200 MeV), t can be taken as the free nucleon-nucleon scattering amplitude. It can then be checked that in the 700 MeV-1.5 GeV region, the total cross-section is nearly constant as a function of energy, (fig.1) and

that the differential cross-section is a function of q only (fig.2), which justifies the factorization in (1). The same scaling properties are displayed by the polarization, as well as by the proton-neutron amplitude. The correction terms in (1) can be written[8] as an expansion involving the two-body, the three-body, etc... correlation function, the successive terms being expected to be smaller and smaller since nucleons are not strongly correlated in nuclei. Indeed, the effect of the two-body correlations is sizeable (fig. 3,4) but sufficiently small as compared to the first term so that higher order corrections are expected to be negligible. The last approximation to be checked is the replacement of the effective nucleon-nucleon interaction in the nuclear medium by the free interaction t. At high energies (E >> 200 MeV) the error can be shown to be proportional to the two-body correlation correction, with a reduction factor of 1/A where A is the target mass. The correlation correction is seen to be small enough in figs. 3,4 so one can neglect a term which is A times smaller. These three features - factorization, use of free interaction, smallness of corrective terms - are sufficient in order to assess the validity of (1). High energy protons are rather unique in this respect since all these approximations can be explicitely checked the factorization is valid only for interactions that are constant in a 100 MeV range. This is not the case neither for low energy hadrons nor for the pions. Moreover for nucleons because of exchange effects[15], t is not a function of q and E only : it depends also on the momentum of the incoming nucleon. At low energies, one cannot relate t to the free interaction, with calculable but vanishing corrections. One has to use a rather involved theory[15,16], with all the uncertainties this implies, in order to get the effective interaction t. Also, the higher order effects are much more difficult to calculate. There is no simple expansion to contrast with the high energy case where the correlation length is the naturally small expansion parameter. A low energy, these corrections depend explicitely on the excited states wave function since the closure approximation cannot be used below a few hundred MeV. Moreover, the standard low energy technique to include dispersive corrections (long range correlations) which is the coupled channel technique leads to a severe overcounting[13] when the same effective interaction as for the first order term is used and a large number of intermediate channels included. So, high energy protons provide a much cleaner probe, provided the calculation includes a well known, rather standard now, set of corrections[8,17,13].

Several other approximations are sometimes used, mainly for convenience,

although they are not really necessary. Often, one uses the Glauber approximation[9] which can be derived from the KMT[8] theory with the additional assumption of eikonal propagation in the intermediate states (as discussed in ref.13). Also, in some cases, the spin-orbit interaction is neglected. These two approximations, which are of a quite different nature, are associated here since they compensate each other to some extent, which makes the simplest theory (Glauber approximation without spin-orbit) quite attractive. This can be seen in fig.5 where the difference between the full and dashed curves gives the spin-orbit contribution to the cross-section. The difference in fig.5 is somewhat emphazied since the spin-orbit interaction is slightly too strong, (by about 30 %) in this case. When it is reduced by this amount, the KMT calculation with spin-orbit (full curve) and the Glauber calculation without spin-orbit (dash-dotted curve) are nearly identical. Correlations also have often been neglected. Although small, their effect is however not negligible (fig.3). Long range correlations are omitted in the latter calculation. They have been considered in detail in ref.18 and are important for deformed nuclei. For spherical nuclei they are negligible (fig.4) for small momentum transfer q but cannot be omitted for $q > 2$ fm^{-1}. Finally, in order to obtain the neutron densities from high energy proton scattering which merely determines matter densities, the proton density has to be obtained from esewhere. Usually, it is deduced from the charge density measured by electron scattering and the proper proton and neutron form factors[19] have to be used. More recent fits[20] of the proton form factor give larger values for the proton radius, but have recently been revised[21] and agree now with those of ref.19. All these corrections have to be made carefully. They can, however, be made with little uncertainty for high energy protons. This explains why errors are rather small for these probes, as can be seen from fig.6 which presents the results when neutron densities are fitted to the data, in terms of the difference $\Delta = \langle r^2 \rangle_n^{1/2} - \langle r^2 \rangle_p^{1/2}$. The errors are considerably smaller for the high energy protons.

Before presenting the fits of the neutron densities to the data that have been done by various people, let us discuss what can actually by measured by high energy proton scattering. The absorption is rather strong in the interior of the nucleus. The mean free path of the proton is nevertheless large enough so as to allow some flux to cross the entire nucleus (fig.7). Even for masses up to 60, the inner part contributes by about 10 %. So, one

is sensitive to the nuclear interior. Let us argue that one can also measure rather high momentum components of the nuclear density. Electron scattering cross-section, are directly proportional to the proton density (squared) to be measured. So, high momentum measurements lead to the high momentum components of the density. This is not the case for proton scattering. It would be only true if the Born approximation (single scattering term) could be used. But there is of course multiple scattering, the n^{th} scattering term leading[13] to a contribution proportional to $\rho^n(\frac{q}{n})$ (as compared to $\rho(q)$ for the single scattering term). For Gaussian densities (i.e. nuclei like ^{12}C), one has $\rho^n(\frac{q}{n}) \sim e^{-\frac{\lambda^2 q^2}{n}} >> \rho(q) \sim e^{-\lambda^2 q^2}$ at large transferts, so the multiple scattering terms hide the high momentum tail of the density. For medium weight nuclei, on the other hand, the density behaves as e^{-aq} at large q, and so $\rho^n(\frac{q}{n}) \approx \rho(q)$ even at high momentum, and the density tail is *not hidden* by the multiple scattering terms. This is illustrated in fig.8 where the proton cross-section is compared to its Born approximation. Note first the exponential slope of the Born approximation, which indeed shows $\rho(q)$ behaves like e^{-aq}. Note then that the slope of the full calculation is the same: all the multiple scattering terms behave like e^{-aq}. For this reason, the Born term is non-negligible even at 3 fm^{-1} momentum transfer. Momenta up to q = 2 fm^{-1} are already sufficient so as to get the most relevant information on the neutron density shape.

Let us now discuss the results. The procedure used by the various authors is nearly the same : the proton density is obtained from electron scattering, and then the 1 GeV proton scattering cross-section is calculated using some parametrized neutron density, the parameters of the latter being fitted to the data. The first generation calculations[11-13] use a three parameter Fermi form for the neutron density, do not include the correlations and do not worry about the neutron contributions when deducing the proton density from the charge form factor. A typical fit obtained with these (model dependent) analysis is shown in fig.9. This fit was done at low momentum ($q < 2.5$ fm^{-1}, that is $\theta < 16°$) only, and the χ^2 is nearly 1 per point which means the calculated curve goes nearly through every data point. The results for the neutron radii obtained this way are given in Table 1 and are all consistent. The second generation calculations[13,22,23] include correlations (which increases $r_n - r_p$ by an amount of 0.02 to 0.03 fm, constant for all isotopes)

and also extract the proton density from the charge density more accurately[22-24] (this decreases $r_n - r_p$, the effect being more pronounced for nuclei with a large neutron excess). The net effect of both corrections is to leave $r_n - r_p$ invariant for ^{40}Ca, but to decrease it by a rather large amount (0.07 fm) for ^{48}Ca. The final result[22] is given in fig.6 and in the last column of Table 1. Within the 3 parameter Fermi model for the neutron density, this last result represents the more involved calculation that can be done, including all known corrections. The difference between the neutron and proton radii is seen to be rather small even for ^{48}Ca (0.09 ± 0.05 fm). It is barely consistent (Table 2) with the Hartree-Fock (Bogoliubov) calculation of Gogny[4], and agrees with the neutron radii obtained from Coulomb energy differences[1]. It disagrees with the earlier Hartree-Fock calculations of Negele[2] or Vautherin and Brink[3].

Finally, let us present some results for the neutron density, using the 3 parameter Fermi form[13]. Proton and neutron densities are nearly identical for ^{40}Ca (fig.10). When two neutrons are added, they merely increase the bulk density, but at the surface, the densities are nearly the same. A neutron skin appears gradually at the surface when 4, but especially 8 neutrons are added to ^{40}Ca.

A third generation set of calculations is under way[23,25] which use the so called model independent fittering procedure. Without any doubt, they will one day overseed the model dependent results. Let us however point out that the available calculations may still be refined. The analysis[23] of the 800 MeV data (fig.10) contains practically all needed corrections, except for the long range correlations that cannot be neglected at $q > 2$ fm^{-1} (the third maximum, at the end of the measured angular distribution). Forcing the calculation to agree with the data in this region - which is possible in a model independent analysis - may be one of the reason for the large values of r_n obtained in this work[23]. The other reason is of course the bad fit obtained at forward angles. This is rather surprising for a model independent analysis which should in principle be able to reproduce any measured shape. To this extend, the analysis of the Saclay data done in ref.25) is much better since the χ^2 is near one per point (Incidentally, the model dependent fits[10-13] reach similar values for χ^2). Correlations have however been neglected in this work. Also, the authors rely on the Glauber approximation which is not totally equivalent to the KMT approach

because of the eikonal approximation. So, the results obtained in ref.25) may still be subject to some improvements in the near future. Let us however note that their larger value of $r_n - r_p$ for ^{48}Ca is due to a depletion in the interior of the neutron density. Such a feature may still (or may not) be present in a more complete calculation, and will decide whether $r_n - r_p$ is compatible (or not) the presently available Hartree-Fock results ($r_n - r_p \sim 0.14$-0.23). As a brief conclusion, let us simply say that high energy proton scattering seems to be quite an accurate tool for determining neutron densities. The differences between the various analyses are rather small, and a careful examination of the theory can decide among the latter which one is the most accurate. At low momentum transfer ($q < 2$ fm^{-1}), the only approximation that has not been thoroughfully checked are the relativistic corrections of ref.14). It would be worth to solve the Dirac equation exactly and to compare to the recipe used by all authors working with the KMT approach (the same assumption is also made in the Glauber approach, since the straight line trajectory assumption implies it). A large momentum transfer ($q > 2$ fm), almost nothing is known : the correlation calculation has to be refined, dispersive corrections carefully included ; the results may also be quite sensitive to the explicit form assumed for the t matrix which is usually taken as a gaussian. These problems should be considered, especially since high momentum transfer experiments are currently done, or planned in the near future. Whereas such experiments are quite stimulating and may lead to new informations on neutron densities, one should however not forget that the accuracy of the presently available information is severely limited by the quality of the data at low transfer. The measurements at various angles are sometimes not sufficiently consistent with each other and do not lead to smooth enough curves. Also, the angle measurement itself has to be extremely precise (less than 1 %) so as to permit to reach the desired 1 % accuracy on the neutron r.m.s. radii.

1) - J.A.Nolen and J.P.Schiffer, Ann.Rev.of Nucl.Sci. 19 (1969) 475.

2) - J.W.Negele, Phys.Rev. C1 (1970) 1260.

3) - D.Vautherin and D.Brink, Phys.Rev. C5 (1972) 626.

4) - D.Gogny et al., Phys.Lett. B55 (1975) 361.

5) - G.M.Lerner et al.,Phys.Rev. C12 (1975) 778.

6) - I.Brissaud et al., Phys.Lett. B48 (1974) 319.

7) - J.C.Lombardi et al., Nucl.Phys. A188 (1972) 103.

8) - A.K.Kerman, H.Mc Manus and R.M.Thaler, Ann.Phys.(N.Y) 8 (1959) 551.

9) - R.J.Glauber "Lectures in Theoretical Physics" Interscience, New-York 1959.

10) - G.D.Alkhazov et al., Phys.Lett. B42 (1972) 121 ; JETP Lett. 18 (1973) 119; Phys.Rep. 42 (1978) 90.

11) - R.Bertini et al., Phys.Rev.Lett. B45 (1973) 119 ; G.D.Alkhazov et al., Nucl.Phys. A274 (1976) 443 ; Phys.Lett. B67 (1977) 402 ; A compilation of the Saclay data was made by G.Bruge, J.Phys.(Paris) to appear.

12) - G.S.Blanpied et al., Phys.Rev.Lett. 39 (1977) 1447 ; G.W.Hoffman et al. Phys.Rev.Lett. 40 (1978) 1256 ; G.Igo et al., Phys.Lett. 81B (1979) 151.

13) - A.Chaumeaux, V.Layly and R.Schaeffer, Ann.Phys. 116 (1978) 247.

14) - M.L.Goldberger and K.M.Watson, "Collision Theory" Wiley, NY 1959.

15) - D.Slanina and H.Mc Manus, Nucl.Phys. A116 (1968) 271 ; J.Atkinson and V.A.Madsen, Phys.Rev.Lett. 21 (1968) 295 ; D.Agassi and R.Schaeffer, Phys.Lett. B26 (1968) 703.

16) - F.A.Brieva and J.R.Rook, Nucl.Phys. A291 (1977) 317.

17) - H.Feschbach, A.Gal and J.Hufner, Ann.Phys.(N.Y) 66 (1971) 20 ; E.Boridy and H.Feschbach, Ann.Phys. (N.Y) 109 (1977) 468.

18) - Y.Abgrall et al., Nucl.Phys. A271 (1976) 477 and Journées d'Etude Saturne II, Aussois 1977.

19) - W.Bertozzi et al., Phys.Lett. B41 (1972) 408.
C.W.De Jager, H.De Vries and C.Devries, At.Data and Nuc.Data Tables 14 (1974) 479.

20) - F.Borkovski et al., Nucl.Phys. B93 (1975) 461.

21) - B.Frois, Private Communication.

22) - A.Chaumeaux et al., to be published.

23) - L.Ray, to be published.

24) - S.Shlomo and R.Schaeffer, to be published.

25) - I.Brissaud and X.Campi, to be published ;
I.Brissaud and M.K.Brussel, Phys.Rev.C15 (1977) 452.

26) - G.Alkhazov et al., Nucl.Phys. A280 (1977) 365.

27) - L.Tauscher and S.Wyceck, Phys.Lett. B62 (1976) 413.

28) - R.Kumselman and G.A.Grin, Phys.Rev.Lett. 24 (1970) 838.

Table 1

$\Delta = r_n - r_p$ $\pm$ 0.05 fm	CLS [a] 1 GeV	Alk. [b] 1 GeV	Igo [c] 800 MeV	CLS [d] 1 GeV, revised
40	-0.03	-0.02	0.01	-0.04
42	0.04	0.03	0.08	0.03
44	0.06	0.06	0.10	0.02
48	0.16	0.15	0.19	0.09

a) Ref.13 b) Ref.11 c) Ref.12 d) Ref.22

Values of the difference $\Delta = r_n - r_p$ of the r.m.s. radii obtained by various authors. The first three analysis make nearly the same assumptions, but do not use the best proton and neutron form factors (see discussion in the text) and omit correlations. The last column includes all these corrections.

Table 2

$\Delta = r_n - r_p$	CLS [a] 1 GeV ± 0.05	Coul. [b]	G [c]	N [d]	VB [e]
40	-0.04		-0.04	-0.04	-0.05
42	0.03	0.01			
44	0.02	0.015			
48	0.09	0.06	0.14	0.23	0.18

a) Ref.22 b) Ref.1 c) Ref.4 d) Ref.2 e) Ref.3

Values of the difference $\Delta = r_n - r_p$ of the r.m.s. radii obtained from 1 GeV proton scattering (col.1), compared to the same quantity extracted from Coulomb energy differences (col.2). The last three columns give the Hartree-Fock results of Gogny, Negele and Vautherin-Brink.

Table 3

$\Delta = r_n - r_p$	a) 800 MeV ± 0.05 fm	b) 1 CeV-600 MeV ± 0.04 fm
40	0.10	-0.02
48	0.23	0.17

a) Ref. 23 b) Ref. 25

Values of the difference $\Delta = r_n - r_p$ of the r.m.s. radii obtained from various model independent analyses.

FIGURES

1 - From ref.13. Total proton-proton cross-section versus incident (kinetic) energy. For energies between 0.7 and 1.5 GeV it is nearly constant and close to 46 mb.

2 - From ref.13. Proton-proton differential cross-section from 650 MeV to 1732 MeV as a function of the momentum transfer q. Above 700 MeV, the cross-section appears practically independent of energy but for 650 MeV an important decrease of the differential cross-section for all transfered momenta is observed. The curve corresponds to the parametrization used in ref.13.

3 - From ref.13. Effect of correlations on ^{40}Ca. In the first calculation correlations are ignored (dashed line), in the second one (solid line) short range and center of mass correlations are introduced. Long range correlations are omitted. Their effect is show in fig.4.

4 - From ref.18. Effect of long range correlations (or dispersive corrections). Virtual excitation of the low lying 3^- (3.74 MeV) and 5^- (4.49 MeV) collective states, as well as the giant quadrupole state (18 MeV) are included. They are important for angles largen than 15° ($q > 2.3$ fm^{-1}), but negligible at small momentum transfer.

5 - From ref.13. Influence of the spin-orbit amplitude given by a comparison of two KMT calculations performed with (solid curve) and without (dotted curve) spin-orbit term. A difference of 20 % is obtained at the second maximum. The influence of the eikonal approximation is shown by a comparison of a KMT (dotted curve) and a Glauber (dash-dotted curve) calculation performed both with exactly the same nucleon-nucleon amplitude and the same form factors.

6 - From ref.13. Values of Δ, difference of proton and neutron r.m.s. radii obtained by various authors

a) KMT calculation[13] for 1 GeV proton scattering (upper values) and revised results[22] including correlations and the correct proton and neutron form factors (lower values).

b) KMT calculation[12] for 800 MeV proton scattering done with the same approximation as the upper values of (a).

c) Glauber calculation[11] without spin-orbit interaction, with the same approximation as the upper values of (a).

d) 16 MeV proton scattering[7].

e) Intermediate energy (1.37 GeV) alpha scattering[26], same approximation as the upper values of (a).

f) 166 MeV α particle scattering[6].

g) 79 MeV α particle scattering[5].

h) Neutron radii obtained from Coulomb energy shifts[1].

i) Pionic atoms[27].

j) Pionic atoms[28].

7 - From ref.13. Damping coefficient $\eta_\ell = |e^{2i\delta_\ell}|$ due to the absorption as a function of $x = \ell/kR$, with $R = 1.2\ A^{1/3}$. The values $x < 1$ correspond to the nuclear interior.

8 - From ref.13. Comparison of the Born term (dashed line) to a complete calculation (solid line) for 1 GeV elastic scattering on ^{58}Ni. Even at low transfered momentum, the difference is large since multiple scattering terms are important. But the Born term is never negligible. The dot-dashed curve is the full calculation when the last bump near 3 fm^{-1} of the form factor has been suppressed.

9 - From ref.13. Cross-sections for the four Ca isotopes obtained by a least-square fit of the neutron density. Tree parameter Fermi type densities are used for protons and neutrons. Only the neutron density parameters c (radius) and a (surface thickness) are adjusted to the data. Experimental points corresponding to angles above 16° ($q > 2.3\ fm^{-1}$) are not included in the fit. A model dependent analysis of the 800 MeV data[11] leads to fits of the same quality as those shown here.

10 - From ref.13. Three parameter Fermi densities for the protons (solid line) and the neutrons (dashed line) obtained by fitting the latter to the 1 GeV proton data.

11 - From ref.23. Model independent fits to the Ca isotope data at 800 MeV.

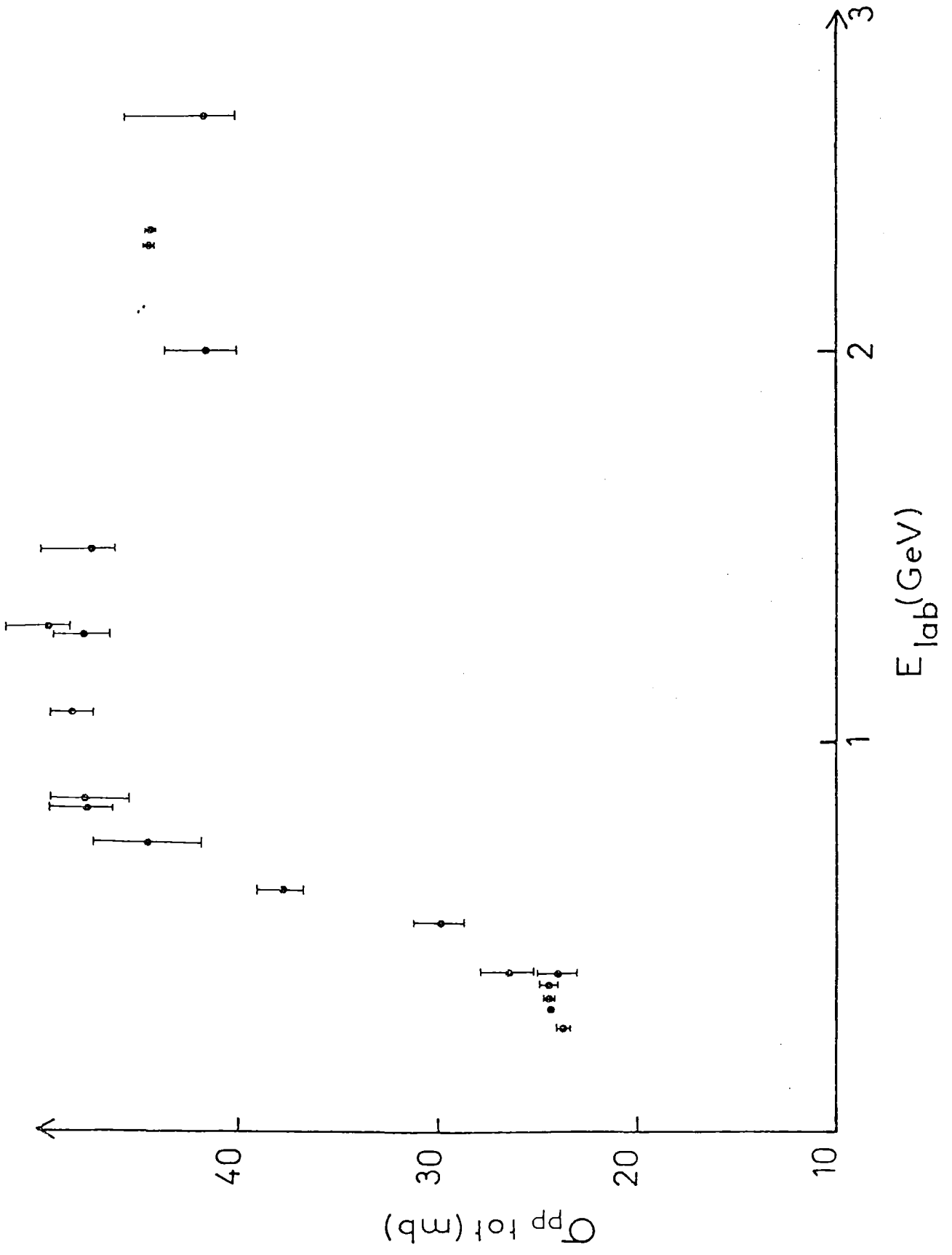

FIG.1

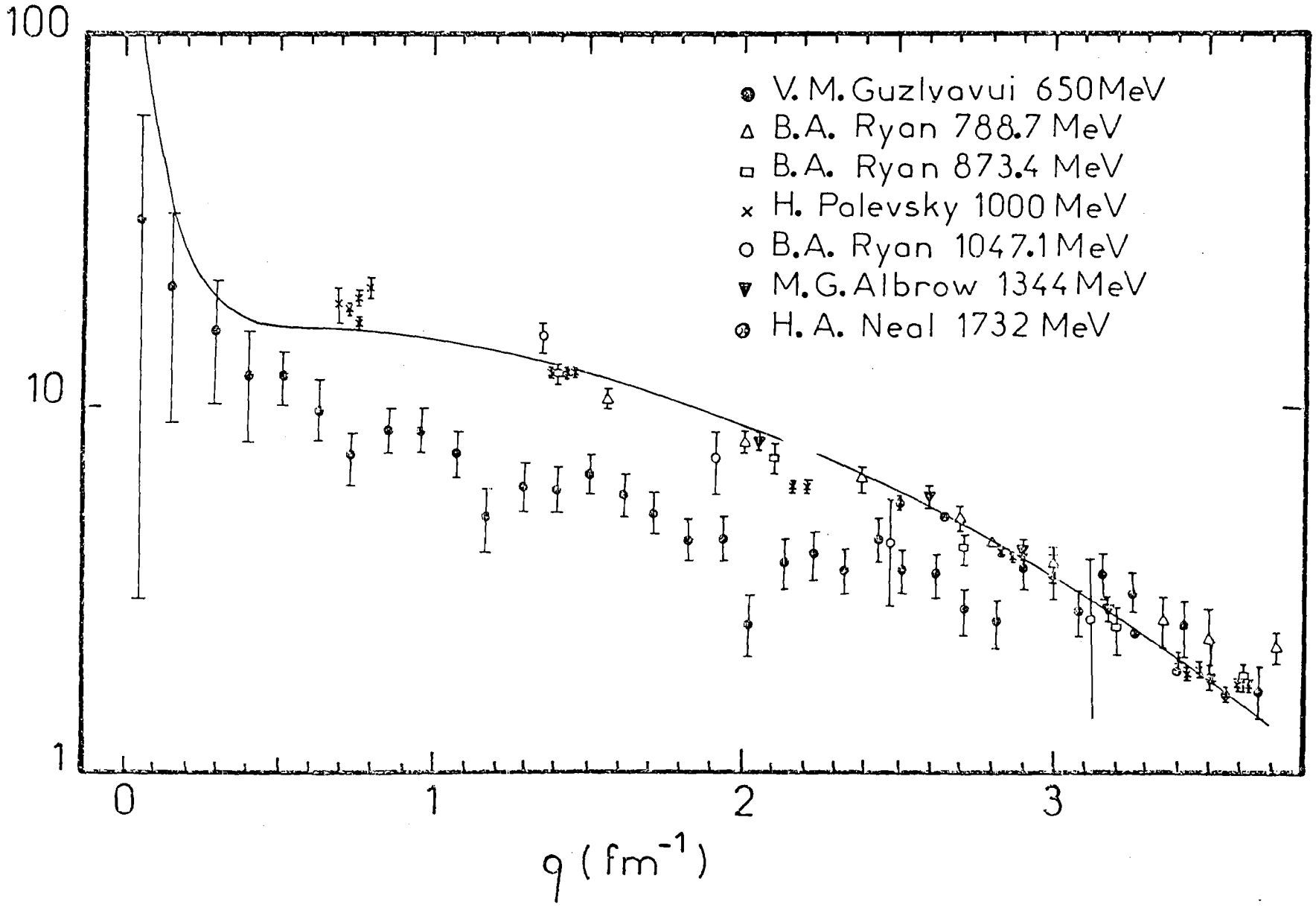
100
10
1
0
1
2
3
q (fm⁻¹)
(dσ/dΩ)pp cm (mb/sr)
V. M. Guzlyavui 650 MeV
B. A. Ryan 788.7 MeV
B. A. Ryan 873.4 MeV
H. Polevsky 1000 MeV
B. A. Ryan 1047.1 MeV
M. G. Albrow 1344 MeV
H. A. Neal 1732 MeV

FIG. 2

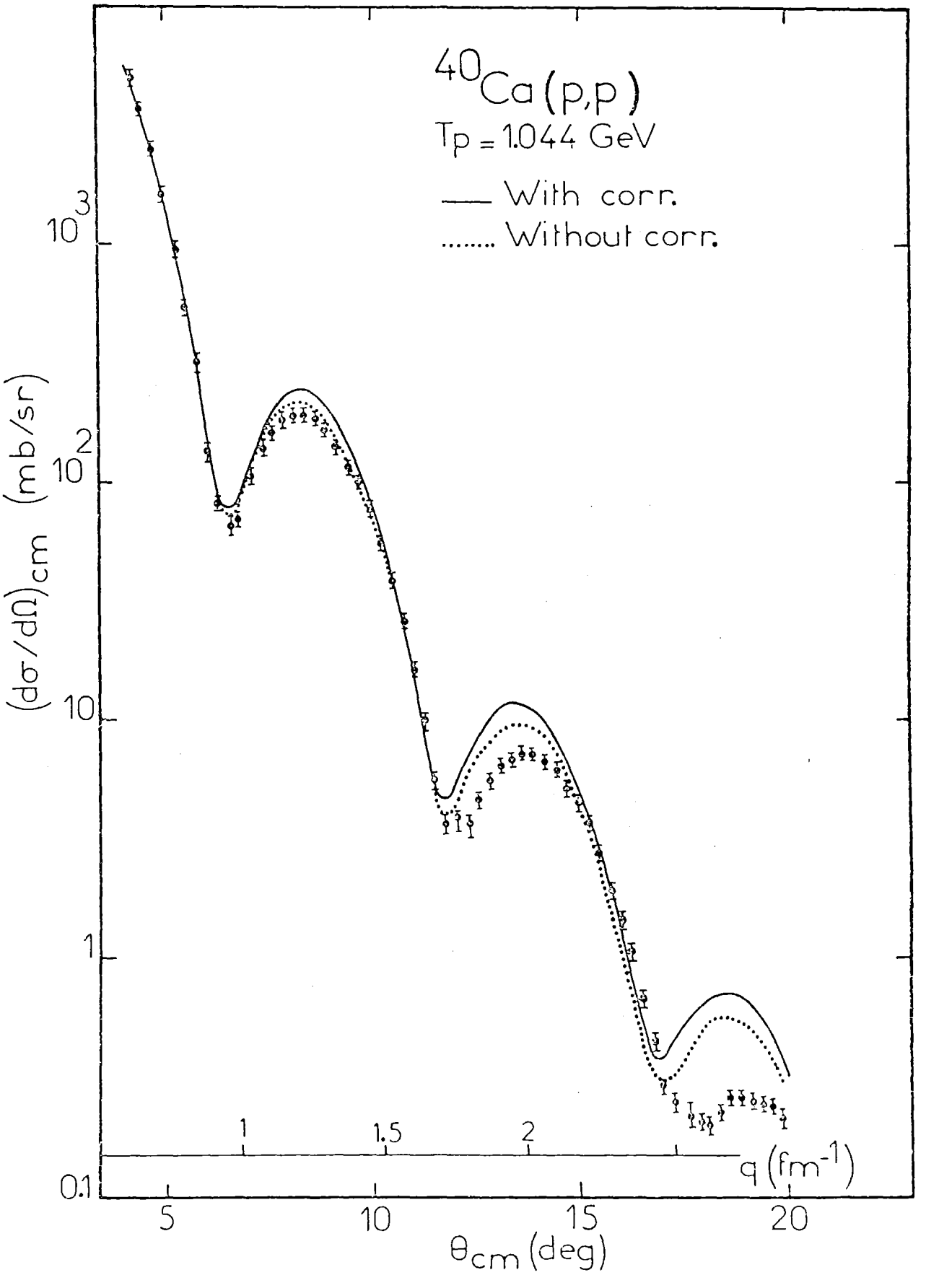
$^{40}Ca(p,p)$
Tp = 1.044 GeV
—— With corr.
..... Without corr.
$(d\sigma/d\Omega)_{cm}$ (mb/sr)
10^3
10^2
10
1
0.1
1
1.5
2
q (fm^{-1})
5
10
15
20
θ_{cm} (deg)

FIG.3

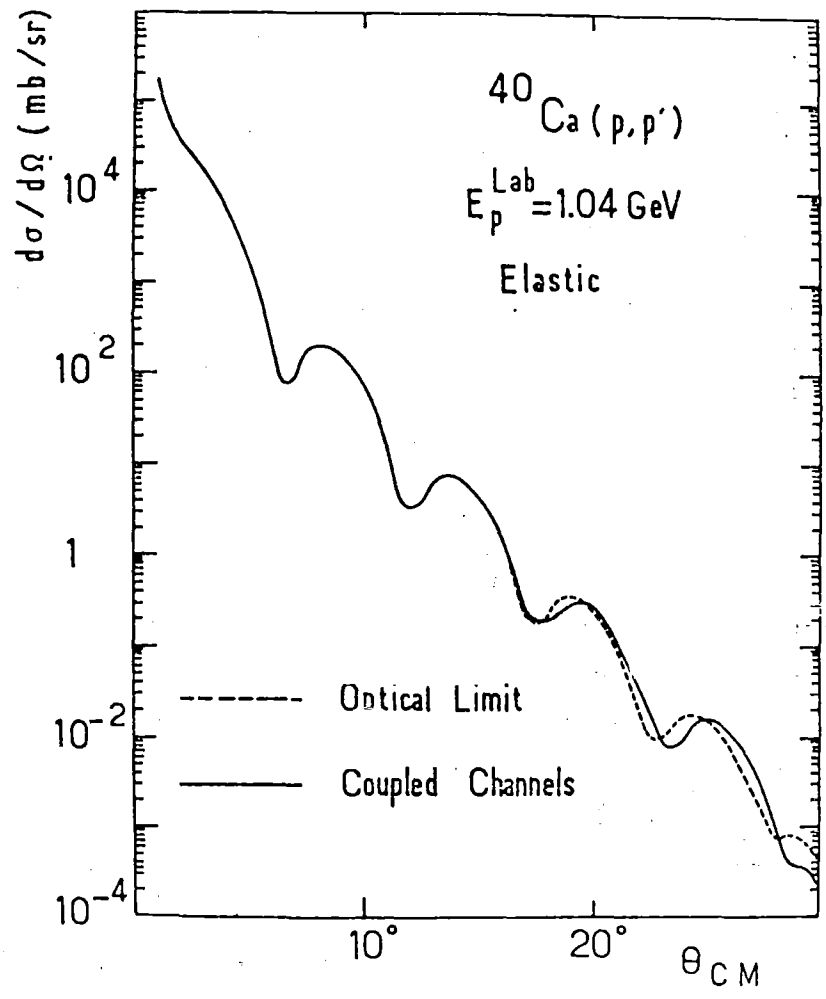
dσ/dΩ (mb/sr)
10^4
10^2
1
10^-2
10^-4
40Ca (p,p')
E_p^Lab = 1.04 GeV
Elastic
Optical Limit
Coupled Channels
10°
20°
θ C M

FIG.4

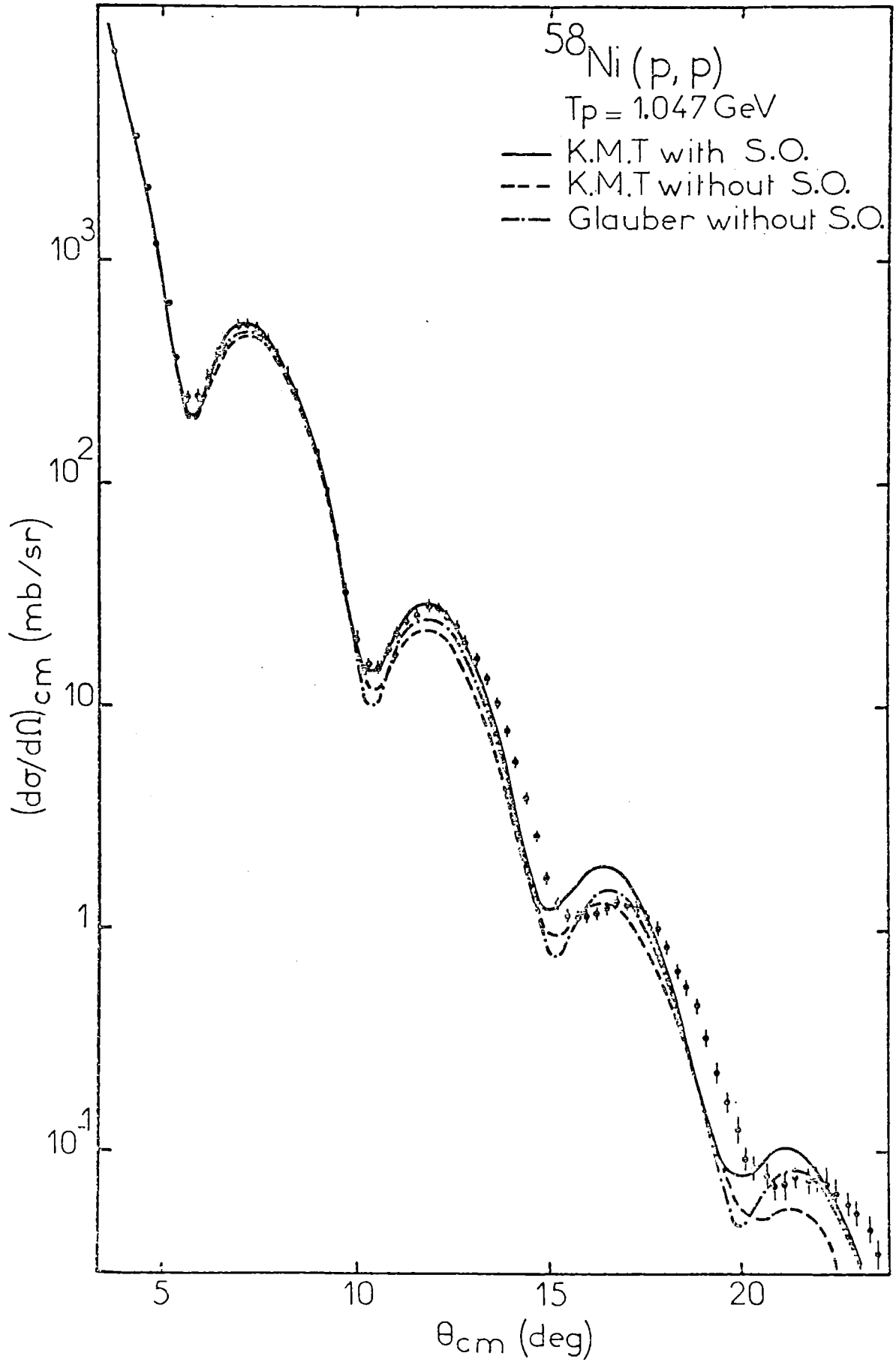
^{58}Ni (p, p)
Tp = 1.047 GeV
K.M.T with S.O.
K.M.T without S.O.
Glauber without S.O.
10^3
10^2
10
1
10^{-1}
$(d\sigma/d\Omega)_{cm}$ (mb/sr)
5
10
15
20
θ_{cm} (deg)

FIG.5

Δ = rn − rp (fm)
1
0.5
0
-0.5
40Ca
42Ca
44Ca
48Ca
a
b
p 1 GeV
c
d p 16 MeV
e α 137 GeV
f α 166 MeV
h Coul. Sh.
a
b
p 1 GeV
c
d p 16 MeV
e α 137 GeV
f α 166 MeV
h Coul. Sh.
i
Monte Carlo
j
a
b
p 1 GeV
c
d p 16 MeV
e α 137 GeV
f α 166 MeV
g α 79 MeV
h Coul. Sh.

FIG. 6

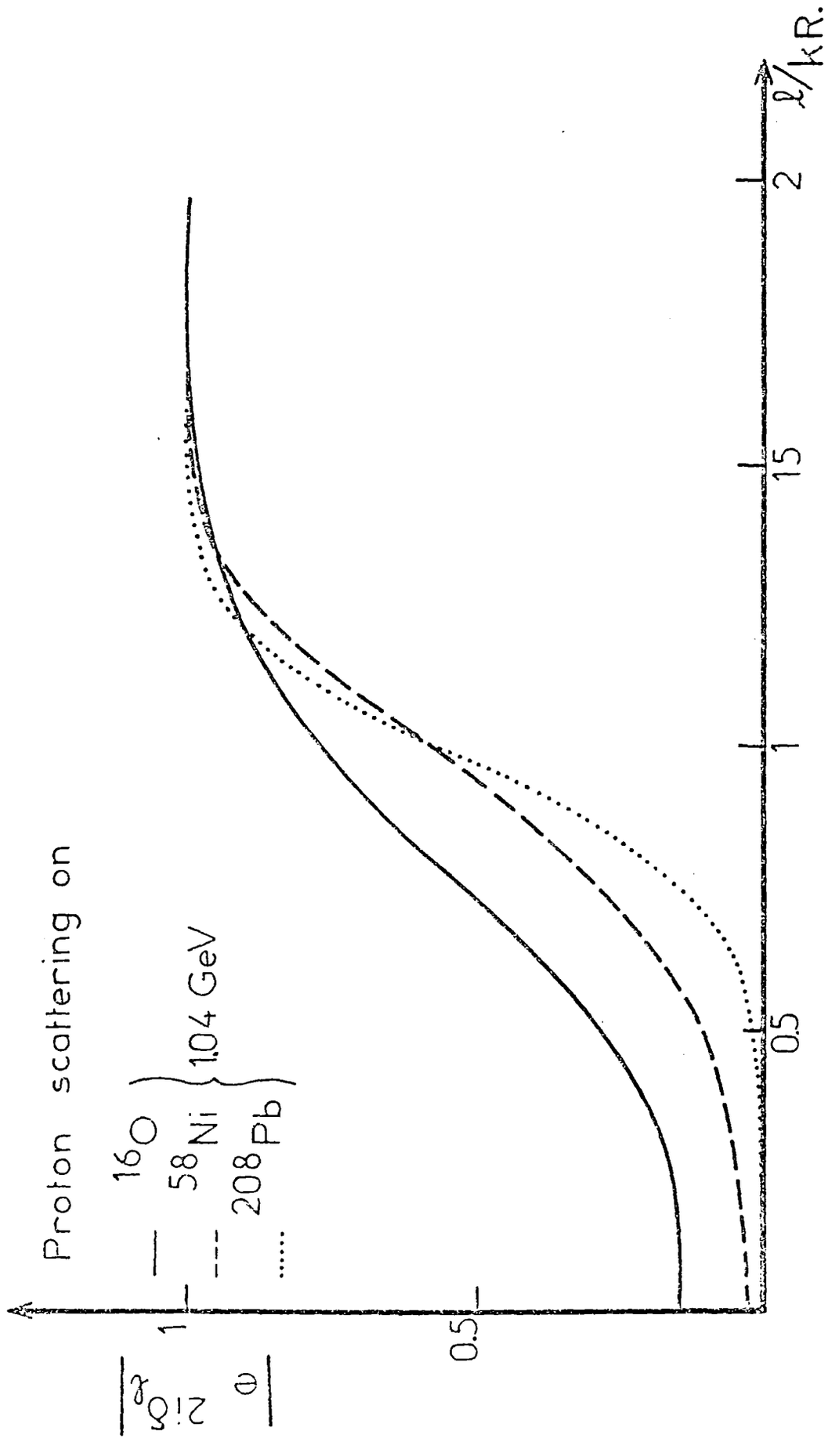
Proton scattering on
16O
58Ni
208Pb
1.04 GeV
1
0.5
0.5
1
1.5
2
ℓ/kR.
dσ/dσ_Ω

FIG.7

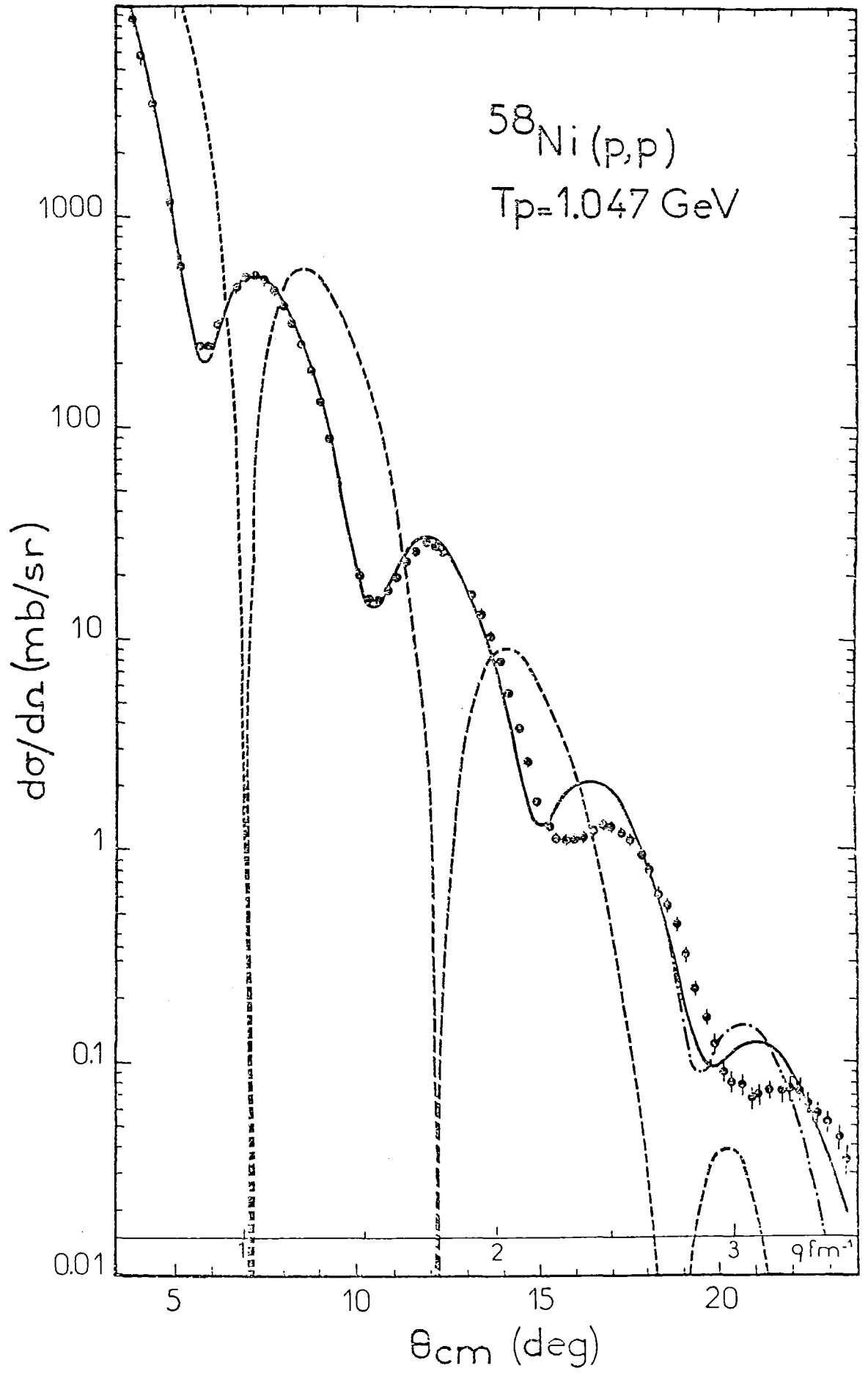
58Ni (p,p)
Tp=1.047 GeV
1000
100
10
1
0.1
0.01
dσ/dΩ (mb/sr)
5
10
15
20
θcm (deg)
1
2
3
q fm⁻¹

FIG.8

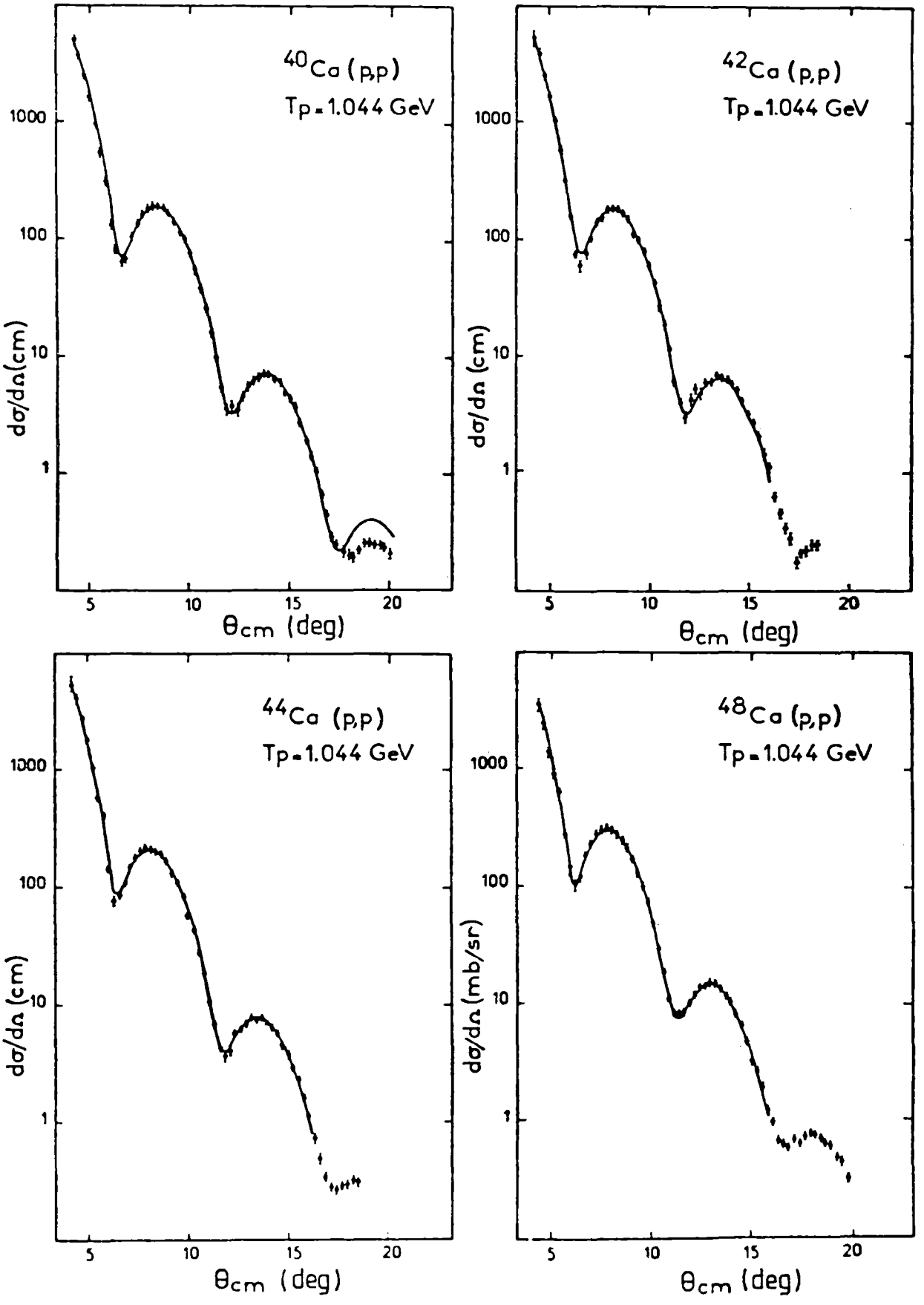
^{40}Ca (p,p)
Tp = 1.044 GeV
^{42}Ca (p,p)
Tp = 1.044 GeV
^{44}Ca (p,p)
Tp = 1.044 GeV
^{48}Ca (p,p)
Tp = 1.044 GeV
dσ/dΩ (cm)
dσ/dΩ (mb/sr)
θcm (deg)
1000
100
10
1
5
10
15
20

FIG. 9

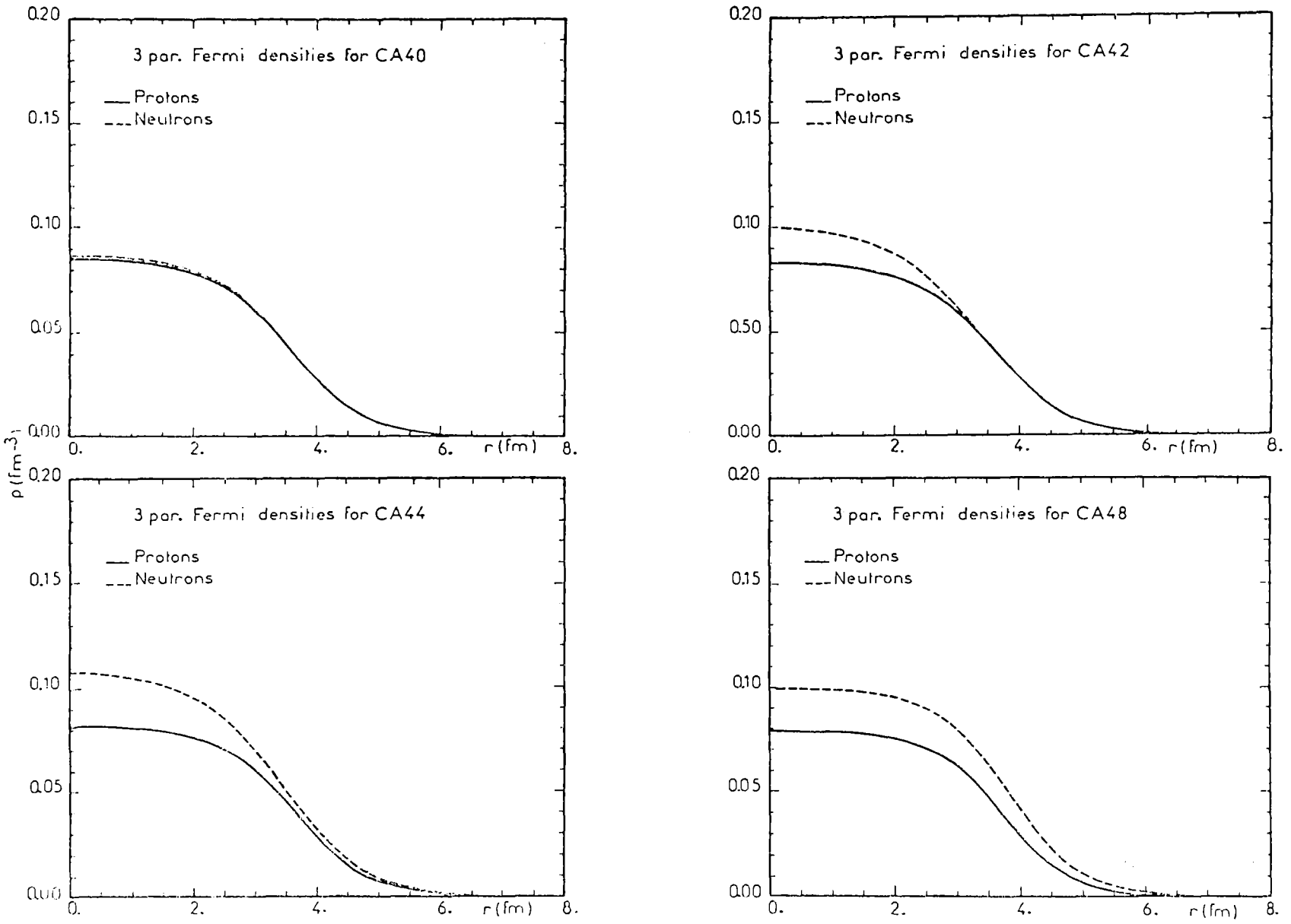
3 par. Fermi densities for CA40
Protons
Neutrons
3 par. Fermi densities for CA42
Protons
Neutrons
3 par. Fermi densities for CA44
Protons
Neutrons
3 par. Fermi densities for CA48
Protons
Neutrons
ρ (fm⁻³)
r (fm)
0.20
0.15
0.10
0.05
0.00
0.50
0.
2.
4.
6.
8.

FIG.10

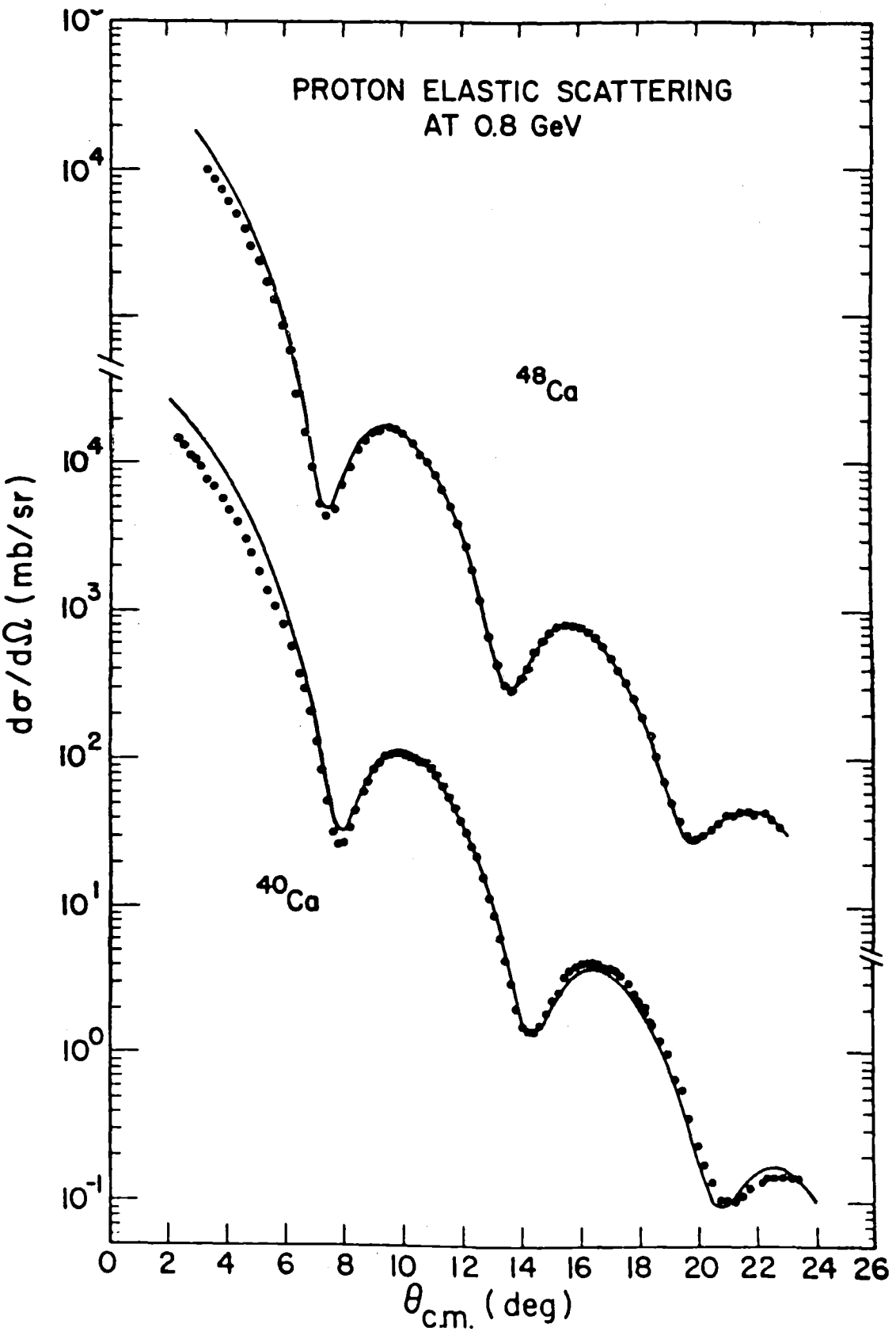
PROTON ELASTIC SCATTERING
AT 0.8 GeV
48Ca
40Ca
dσ/dΩ (mb/sr)
θc.m. (deg)
10~
10⁴
10⁴
10³
10²
10¹
10⁰
10⁻¹
0 2 4 6 8 10 12 14 16 18 20 22 24 26

FIG.11

ALPHA-PARTICLE SCATTERING FROM Ca-NUCLEI

H.J. Gils
Kernforschungszentrum Karlsruhe GmbH,
Federal Republic of Germany

Alpha-Particle Scattering from Ca-Nuclei*

H.J. Gils
Kernforschungszentrum Karlsruhe GmbH
Institut für Angewandte Kernphysik
P.O.B. 3640, D-7500 Karlsruhe
Federal Republic of Germany

Abstract

The possibilities, advantages, and difficulties of determining nuclear matter densities by elastic scattering of alpha-particles are generally discussed. On the basis of particular experimental data - 104 MeV alpha-particle scattering from ^{40,42,44,48}Ca - a refined folded potential is introduced using a density-dependent alpha-nucleon-interaction and target nucleus densities described by Fourier-Bessel-series. Thereby, the total nucleon densities of these isotopes were determined with little model dependence. The resulting root-mean-square radii and density differences are compared with other experimental results obtained by different methods.

---

*Talk presented at the International Discussion Meeting: "What do we Know about the Radial Shape of Nuclei in the Ca-Region?"
May 2-4, 1979, Karlsruhe, Germany

1. INTRODUCTION

Besides the proton scattering discussed in the previous talk elastic scattering of other strongly interacting projectiles - among them in particular alpha-particles - has been suggested as experimental source of informations about the neutron or total matter densities of nuclei[1]. For any hadronic projectile the general difficulties to interpret the experimental results in terms of the target nucleus density have, of course, the same reason, namely the incomplete knowledge of the projectile-target nucleon interaction which leads to simplified model assumptions of the reaction mechanism. However, for particular projectiles having special features one can imagine some problems to be reduced or better understood, or even completely to vanish even though other difficulties mayarise. In addition, it is near at hand that different projectiles at different energies probe different moments or radial regions of the nuclear matter densities. Thus one can hope to get a more complete picture of the whole slope of the nucleon distributions when comparing and combining the results of the *different* methods.

The strong absorption of alpha-particles at the nuclear surface known since a long time has been the most conspicuous hint that alpha-particle scattering should be a sensitive probe determining nuclear radii. Additionally, alpha-particle scattering analyses are distinctly simplified since the alpha-particle has vanishing spin and isospin $S = T = 0$. Finally, the great amount of available experimental data enabled many systematic and methodic studies helping better to understand the alpha-particle-nucleus interaction.

These general considerations favouring alpha-particle scattering, however, do not tell us which quantity of the target nucleus we can most reliably extract from elastic alpha-particle scattering cross sections and which experimental prerequisites have to be fulfilled. Thus, in the first part of the present talk some features of alpha-particle scattering

at low and medium energy important for the determination of nuclear radii will be specified, in order to get an insight into the advantages and limits of this experimental tool. High energy alpha-particle scattering in the GeV region will not be treated in detail here, since the dominant experimental features and the methods of analysis are quite similar as for GeV-proton scattering discussed in the previous talk. In the following ,refined phenomenological and microscopic procedures for the analyses of medium energy alpha-particle scattering will be introduced mainly basing on one particular experiment, namely the elastic scattering of 104 MeV alpha-particles from ^{40,42,44,48}Ca performed at the Karlsruhe Isochronous Cyclotron. By means of this experimental data and procedures the nuclear matter radii of the Ca-isotopes have been determined with little model dependence. The results will be compared with other methods and further efforts improving the analyses will be suggested finally.

2. DIFFRACTION AND RAINBOW SCATTERING

In order to get a clear understanding what happens in alpha-particle scattering we first look at some experimental gross features. The strong absorption of alpha-particles at the nuclear surface already mentioned leads to a pronounced diffraction pattern of the angular distributions of elastic scattering cross sections as demonstrated in Fig. 1. For the following considerations we focus our attention only to the scattering into the forward hemisphere since the backangle behavior - though also a very interesting field of investigations - is not strongly related to the size of the target nucleus. In analogy to the Fraunhofer diffraction known from classical optics one calculates for the angular difference $\Delta\Theta$ between the diffraction maxima:

$$\Delta\Theta \sim \frac{\pi}{k \cdot R} \qquad (2.1)$$

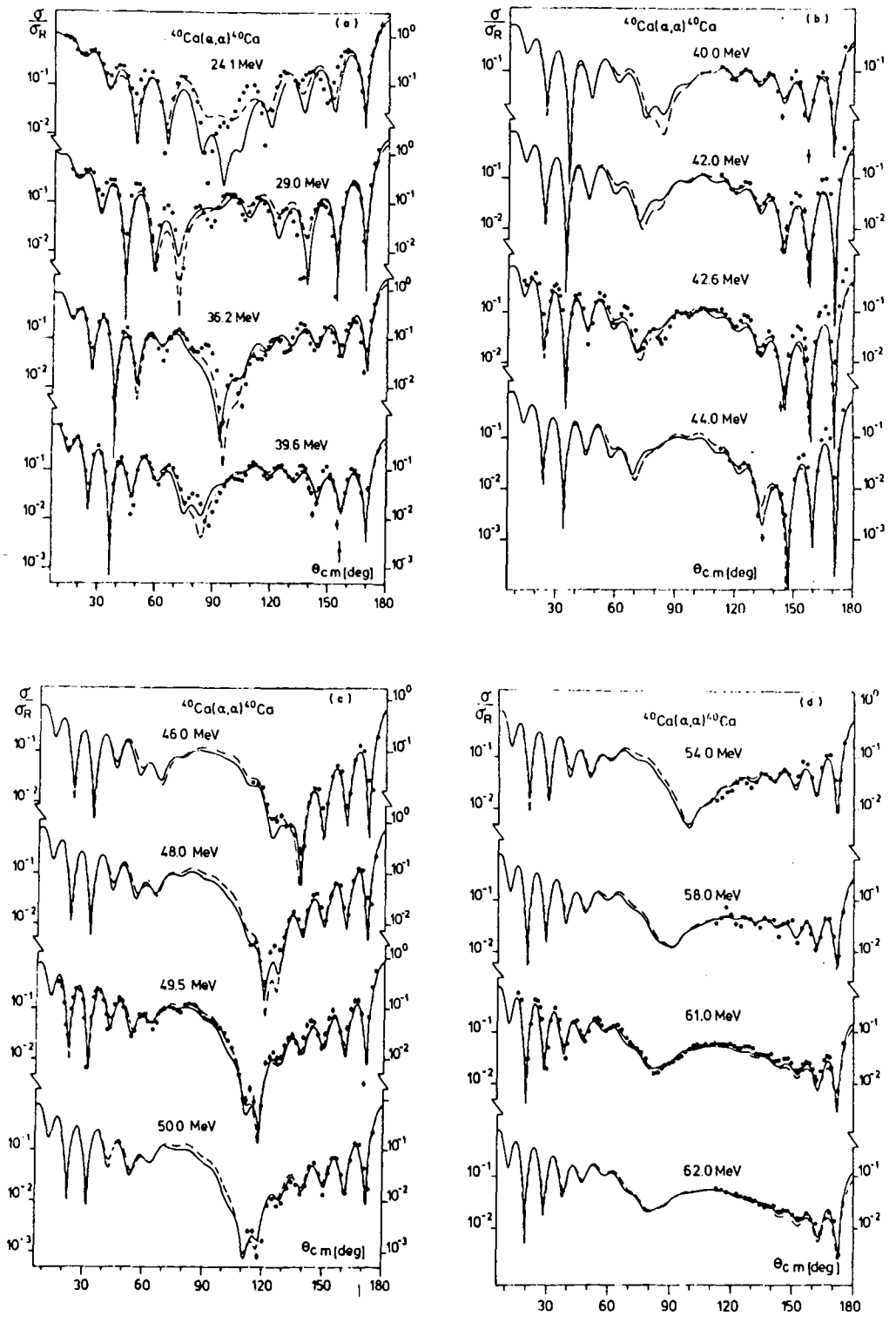

Fig. 1a: Differential cross sections of elastic alpha-particle scattering from ^{40}Ca (normalized to the Rutherford cross sections) at different projectile energies. The theoretical curves correspond to optical model descriptions (from Th. Delbar et al.; Ref. 2).

Herein $k = \lambda\!\!\!^{-}^{-1}$ is the wave number of the incoming particle and R is called the "diffraction radius", which can be looked at as a measure for the size of the target nucleus. In fact, the first investigations of nuclear radii by alpha-particle scattering[3,4] basically have compared diffraction radii.

With increasing alpha-particle energy $\Delta\theta$ becomes distinctly smaller as expected from eq. (2.1) due to the increase of k. For energies higher than about 50 MeV we observe a new phenomenon: the diffraction pattern is strongly damped at larger angles ($\geq 60°$) and after a maximum value the cross sections fall off exponentially. This behavior becoming more dominant at still higher energies (see Fig. 1b) can be understood by semiclassical considerations concerning the trajectory and deflection function $\theta(b)$ of a particle in a central potential as defined in Fig. 2.

The fundamental ideas of this treatment were at first elaborated by Ford and Wheeler[5] for scattering from a pure real potential. Lateron, it has been extended to complex potentials using some ad hoc assumptions or elaborating a more or less theoretically exact foundation, respectively[6,7]. The semiclassical treatment is physically based on the fact that at higher energies where a sufficient number of partial waves contribute to the scattering process, the angular momentum can be regarded as a continuous variable. Quantum mechanical quantities thus are identified by their classical analoga. For a realistic nuclear potential which consists of the Coulomb (C) and of the nuclear (N) part some characteristic trajectories and the deflection function $\theta(b)$ are shown in Fig. 3. The deflection function has extreme values $d\theta/db = 0$ at two particular angles θ_R (C,N) due to the different parts of the potential.

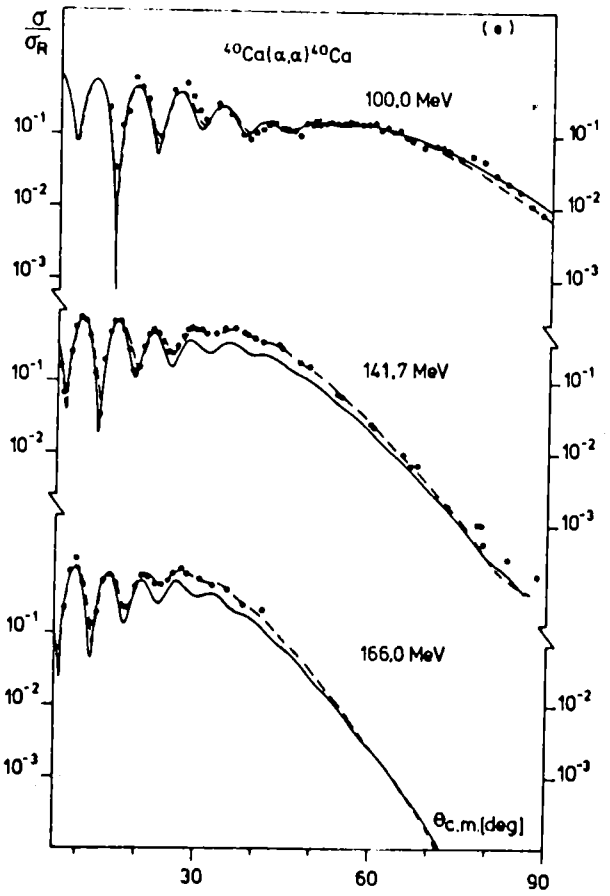

Fig. 1b continued

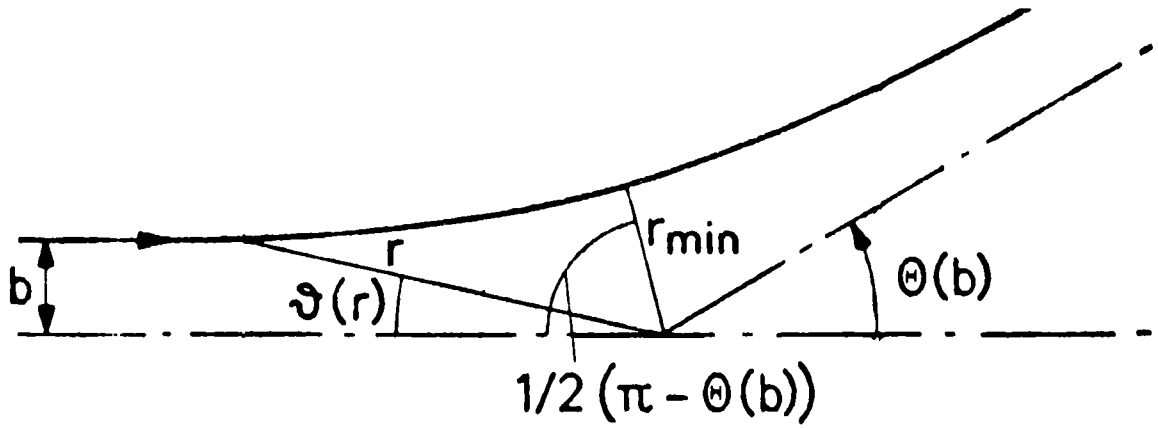

Fig. 2: Trajectory of a particle in a central potential.

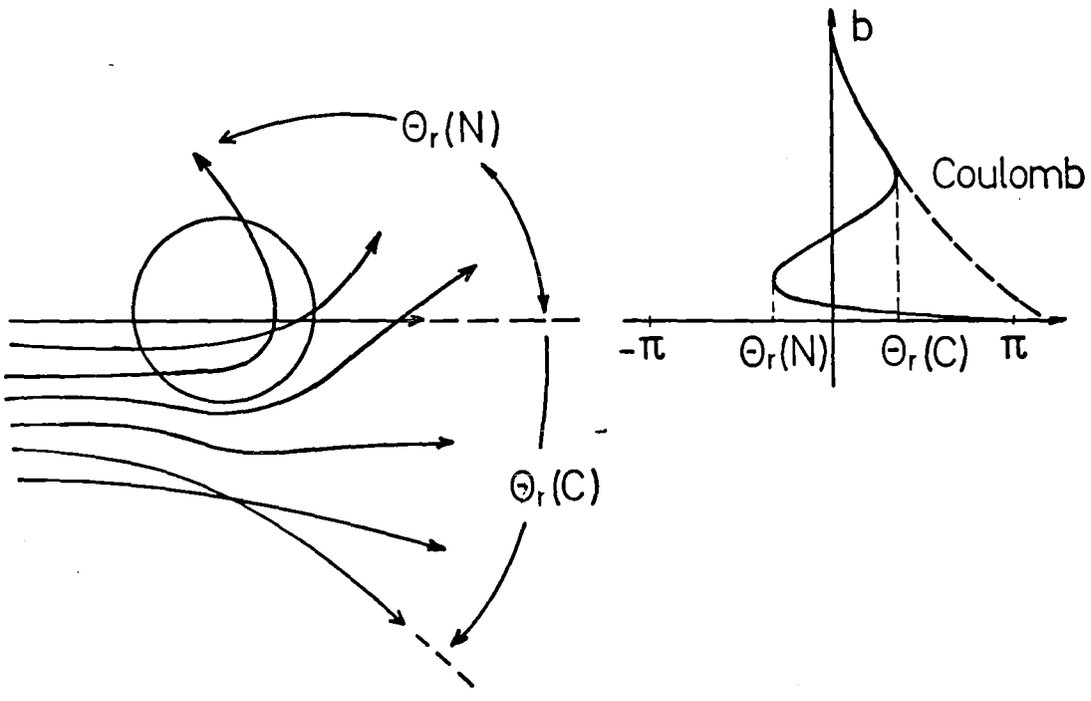

Fig. 3: Characteristic trajectories and deflection function for a Coulomb plus nuclear potential (schematically).

In the classical limit the scattering cross section grows towards infinity when approaching Θ_R from smaller angles and is zero beyond Θ_R as shown in Fig. 4. We call Θ_R the "rainbow angle" since the considered phenomenon is in formal analogy to refraction of light in rain droplets generating the natural rainbow at a certain "scattering" angle.

In the semiclassical description of scattering the interference of different trajectories is included, that means the amplitudes corresponding to the different impact parameters b are coherently added. Thereby the classical rainbow scat-

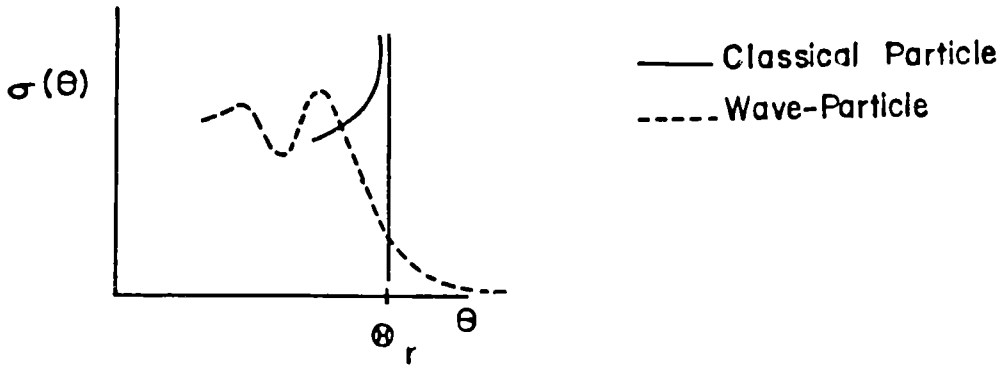

Fig. 4: Scattering cross sections at the "rainbow angle" θ_R (schematically).

tering is, of course, distinctly modified. The pole at θ_R is smeared out and the cross section reaches a finite maximum value at the rainbow angle θ_R and decreases exponentially beyond it as indicated by a dashed curve in Fig. 4. This behavior is expected at both the Coulomb and the nuclear rainbow angle. The Coulomb rainbow scattering has been demonstrated very nicely by heavy ion scattering whereas alpha-particle scattering above 50 MeV considered here is dominated by nuclear rainbow scattering as displayed in Fig. 5 for different target nuclei. The nuclear rainbow scattering has very intensively been studied by Goldberg and Smith[8] resulting in the so-called "nuclear rainbow criterion" for alpha-particle scattering which says: *"If the cross section measurements are extended to scattering angles in the refraction region far beyond the nuclear rainbow angle then the real optical potential can unambiguously be determined even in the interior of the nucleus."*

Therefore, from the semiclassical treatment of alpha-particle scattering the following gross features can qualitatively be concluded:

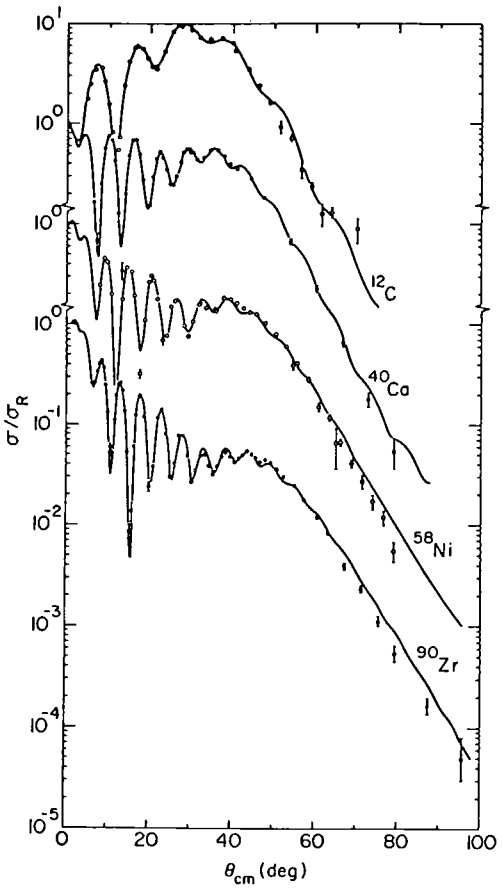

Fig. 5: Elastic scattering of 140 MeV alpha-particles from different target nuclei demonstrating nuclear rainbow scattering (from Goldberg and Smith, Ref. 8).

1. *The diffractive alpha-particle scattering sensitively probes the nuclear surface expressed in diffraction radii.*

2. *The refractive alpha-particle scattering beyond the nuclear rainbow angle should be able to answer questions about the optical potential at innermore parts of the nucleus under investigation.*

3. OPTICAL POTENTIALS

3.1 Phenomenological Potentials

The optical model is of central importance for interaction processes of nuclear particles and for many years now it has been a standard procedure to interpret scattering experiments in terms of an average complex potential

$$V(r) = - V_{real}(r) - iW_{imaginary}(r) + V_{Coulomb}(r) \qquad (3.1)$$

The shape of V_{real} is assumed to be of the same general form as that of the nuclear density because of the short range of the nuclear forces. Since also in more microscopic interpretations as e.g. folding models, the optical potential is the quantity which is primarily determined from the scattering cross sections we have to discuss some important features of the alpha-particle scattering potential in order to be able to judge the validity of the microscopic methods presented later.

Numerous analyses have established the gross features of the phenomenological forms of the potentials specified by empirical sets of parameters describing the strength and radial size. Most frequently the Saxon-Woods (SW) form has been used as parametrization of the potential

$$V^{SW}(r) = V_o \cdot f_V(r)$$

$$W^{SW}(r) = W_o \cdot f_W(r) \qquad (3.2a)$$

with

$$f^{SW}_{V,W} = \left[1 + \exp \frac{r - r_{V,W}}{a_{V,W}}\right]^{-1}$$

Since alpha-particle scattering requires different radial shapes of the real and imaginary part, not only the strengths V_o, W_o but also the half-way radii $r_{V,W}$ and skin thicknesses $a_{V,W}$ (diffuseness), respectively, have been treated as independent

parameters. At lower energies covering only the diffraction region sometimes a surface term has been added to the imaginary potential or used instead of the volume term (eq. 3.2a).

$$W_S^{SW} = W_S^{\circ}\, a_S \frac{d}{dr} \left[1 + \exp \frac{r-r_S}{a_S}\right]^{-1} \qquad (3.2b)$$

The improvement of the theoretical cross sections by using this term, however, is not observed at higher energies (≧ 100 MeV).

Because of some deficiencies of the Saxon-Woods form other parametrizations of the optical potential have recently been studied by different groups [2),9)] with the additional aspect of an energy dependence of V_o, W_o using global form factors $f_{V,W}$. Among others the Saxon-Woods form-factor squared (SW^2)

$$f_{V,W}^{SW^2} = \left[1 + \exp \frac{r-r_{V,W}}{a_{V,W}}\right]^{-2} \qquad (3.3)$$

has been found to describe the experimental cross sections over a wide energy range much better than the SW-form. Thereby, it is most important to introduce the squared form (3.3) in the <u>real</u> part of the potential whereas the squared form included in the imaginary part does not distinctly improve the reproduction of experimental cross sections (even if the surface term squared is added)[10)]. In fact, microscopic treatments[11)] of the optical potential for alpha-particle scattering reveal the real part to be close to the $(SW)^2$ form and the imaginary part to be close to the SW form.

However, the Saxon-Woods form and the Saxon-Woods form to some power and most of the other parametrizations studied

imply a coupling between the surface region and the interior part of the potential. This could introduce undesirable constraints in the analysis and lead to a strong dependence of the results on the model used. In order to remove these constraints and to reduce the model dependence we present a more flexible description of the real optical potential suggested by Friedman and Batty[12].

Following descriptions of nuclear charge distributions[13] a Fourier-Bessel (FB) expansion is chosen, namely

$$V_{real}(r) = V_o(r) + \sum_{n=1}^{N} b_n \, j_o \left(\frac{n\pi r}{R_c}\right) \qquad (3.4)$$

where $j_o(\frac{n\pi r}{R_c})$ are spherical Bessel functions and R_c is a suitably chosen cut-off radius beyond which the series vanishes. The Fourier-Bessel-coefficients b_n are varied parameters. The term $V_o(r)$ called "first guess" potential has a fixed form during the analyses which already reproduces the experimental cross sections under investigation rather well. This "first guess" term is <u>not necessary</u> for the FB-method, but it is used in addition to the FB series in order to prevent that the total potential vanishes beyond R_c. Additionally it leads to a rapid convergence of the FB fit procedure. Each commonly used parametrization (SW, SW^2 or others) can be chosen as first guess potential. The necessity of a flexible and less model dependent form for elastic alpha-particle scattering analyses is demonstrated by the χ^2-values per degree of freedom which are reduced by factors of 2-3 when introducing the FB-method as shown in Fig. 6.

Another very important advantage of the FB-method is the ability to determine realistic errors of the potential at each radial point as well as of integral quantities like rms-radius and volume integral. Thereby, also the error correlations between the different parameters are respected[12]. These correlations dominantly contribute to the total error and are not respected in error considerations connected with commonly parametrized potentials.

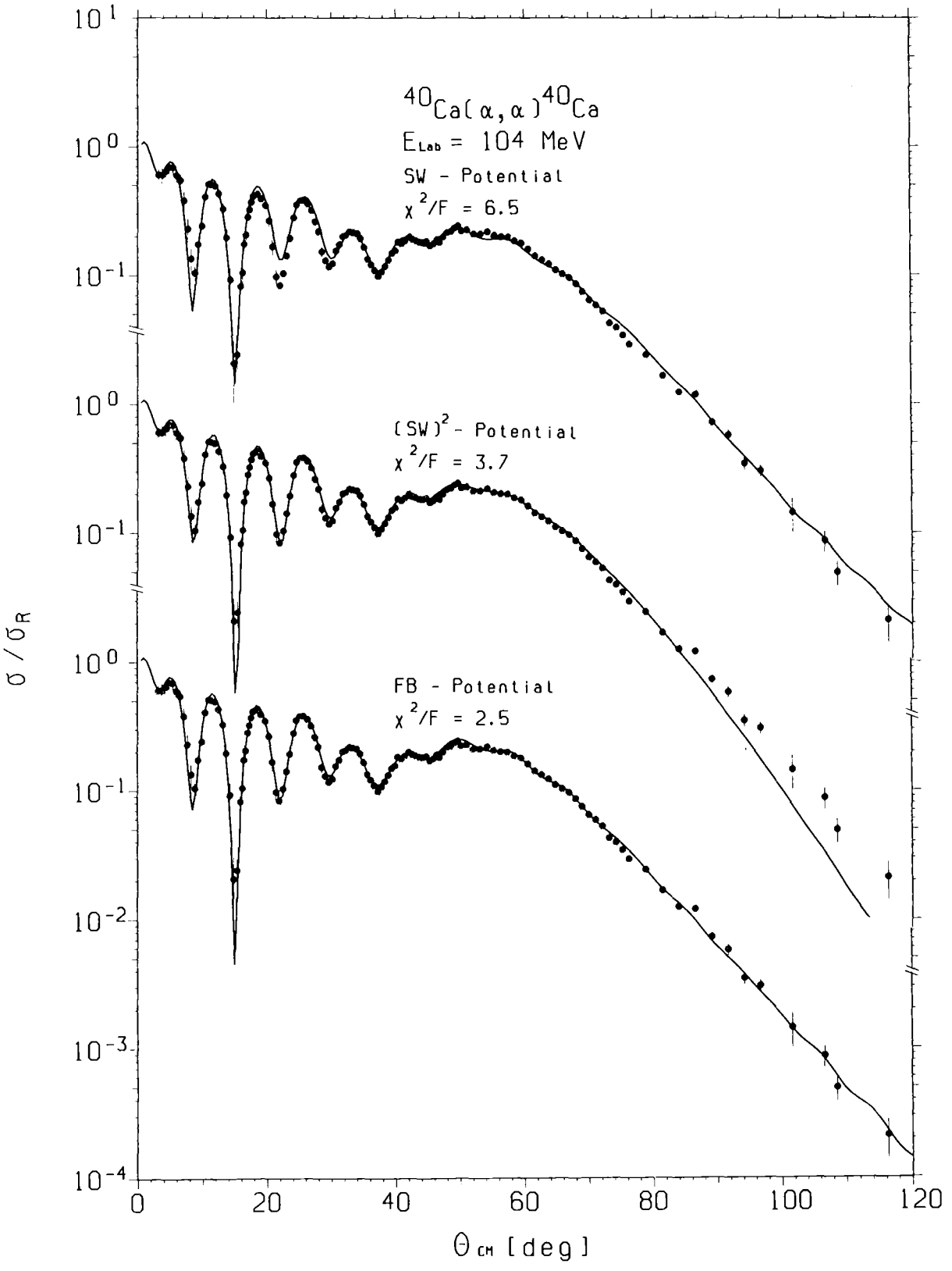

Fig. 6: Elastic scattering of 104 MeV alpha-particles from ^{40}Ca (normalized to the Rutherford cross sections) and different optical model descriptions: SW=Saxon-Woods, FB=Fourier-Bessel series.

In Fig. 7 the FB-potentials of 104 MeV alpha-particle scattering from ^{40}Ca and ^{48}Ca are displayed together with the respective error bands. These potentials result from analyses of data ranging from Θ_{CM} = 3° to Θ_{CM} = 110° which is far beyond the nuclear rainbow angle at about Θ_{CM} = 55°. One recognizes significant differences between the potentials particularly at the slope between r ∿ 3 fm and r ∿ 5 fm.

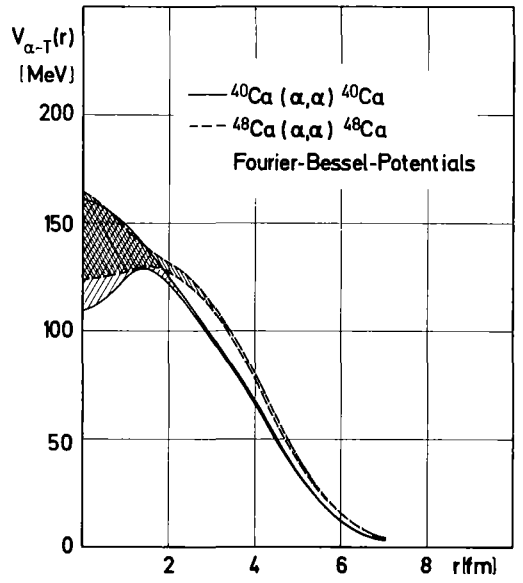

Fig. 7: Real optical potentials for elastic 104 MeV alpha-particle scattering from $^{40,48}Ca$ determined by the FB-method. The hatched areas are the error bands.

As an example the relative errors of the potential for a particular set of R_c and N are displayed in Fig. 8 as full line for the case of ^{48}Ca indicating that the optical potential is best determined in the radial region between 2 and 7 fm, respectively, where the errors are smaller than 2 %. When excluding the data points beyond the nuclear rainbow angle one still obtains small errors at r ∿ 7 fm which is the strong absorption radius as indicated by the dashed lines in the upper part of Fig. 8. The errors in the innermore part of the potential especially at the slope, however, are drastically increased and consequently also the errors of the rms-radii

(see inset in Fig. 8). On the other hand, when excluding the very forward angle data from the analyses the error band at larger radii remarkably increases (Fig. 8, lower part) underlining the importance of the forward angle data for a precise determination of the outer tail of the potential. The error band is also increased at larger radii ($r \gtrsim 3$ fm) by a factor of about two when taking larger angular steps of the data points (1.5° instead of 0.5°)[10].

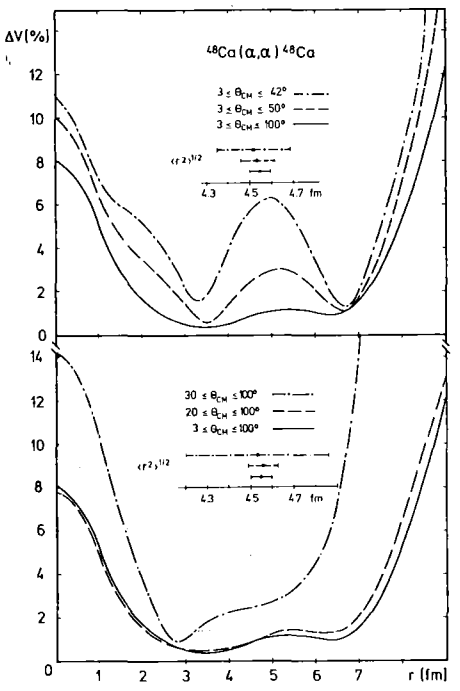

Fig. 8: Relative errors of the optical potential for alpha-particle scattering from ^{48}Ca at E_α = 104 MeV. The different curves correspond to different restricted ranges of the data points used for the analyses.

The remaining model dependence of the optical potential when using the FB-method can be characterized as follows: Even when starting from remarkably different "first guess" potentials as e.g. SW and SW^2 which deviate by 25 MeV at r = 0 fm the final FB-potentials agree within the error bands up to about

r = 8-9 fm. Hence, this radial region is determined rather model independently. At larger radii, however, where the errors exceed 100 % the potentials are dominantly determined by the "first guess" form. Therefore the rms-radii still depend on the "first guess" model when integrating up to large radii (12-14 fm). For the volume integral the model dependence is strongly reduced because of its weaker r-weighting. The resulting integral quantities as well as the detailed shape of the potential, however, do not depend on the form-factor of the imaginary part when using the FB-method[10]. This is in contrast to each common parametrization where one observes a remarkable coupling between the real and imaginary part of the potential which obviously is due to the deficiencies of these common parametrizations.

Besides the FB-method other flexible parametrizations have been used as e.g. Laguerre polynomials or spline functions. Though they have not been so intensively studied, they seem to give similar results as the FB-method.

We can now quantitatively conclude that the optical potential is well determined in a wide radial range by scattering of alpha-particles in the 100 MeV region if

- *the diffraction region is measured in sufficiently small angular steps*
- *the cross sections have been measured up to scattering angles far beyond the nuclear rainbow angle*
- *a flexible ("model independent") potential form is used.*

Furthermore, with these preconditions the model dependence of the deduced potential is strongly reduced.

3.2 Microscopic Potentials

After having discussed how reliably the primary quantity - the optical potential - can be determined by elastic alpha-

particle scattering and which experimental preconditions have to be fulfilled one would like to relate the potential in a more fundamental treatment to the proton and neutron densities of the interacting particles via an effective nucleon-nucleon - interaction between each pair of target and projectile nucleons. The final aim of such a procedure should be the possibility directly to deduce the target nucleon densities from the scattering cross sections using a well-founded interaction and a known projectile density. Important steps in this direction have been attempted by folding models, an approximation essentially based on the first term of a multiple scattering expansion of the (real part of the) optical potential[14-18]. Most of the calculations have been carried out by folding into the target nucleus density distribution ρ_T an effective alpha-particle-bound-nucleon interaction $V_{P-N_T}(\vec{R}_P)$:

$$U_{PT}^{(P)}(r) = \int d\vec{Z}_T \; \rho_T(\vec{Z}_T) \; V_{P-N_T}(\vec{R}_P) \qquad (3.5).$$

The interaction $V_{P-N_T}(\vec{R}_P)$ is either taken from phenomenological analyses of nucleon-α-particle scattering at low energy[19] or itself generated by folding a nucleon-nucleon interaction into the α-particle density distribution ρ_p[20]. The latter method is equivalent to a double folding procedure[16] calculating the leading (simple direct) term of the real part of the optical potential by

$$U_{PT}^{(S)}(r) = \int d\vec{Z}_P \; \rho_P(\vec{Z}_P) \int d\vec{Z}_T \; \rho_T(\vec{Z}_T) \; t(\vec{r}_{NN}) \qquad (3.6)$$

where the coordinates used are defined in Fig. 9. The quantities ρ_P and ρ_T are point matter density distributions of the projectile and the target nucleus, respectively, $t(\vec{r}_{NN})$ is an

effective nucleon-nucleon interaction assumed to be density independent in simple calculations. Eq. (3.6) neglects noncentral terms and isospin dependence in the nucleon-nucleon potential. Moreover, exchange and antisymmetrization effects due to the Pauli principle are omitted. On the other hand, single folding procedures using phenomenological projectile-nucleon potentials[19] or phenomenologically adjusted effective interactions[21)22)], sometimes supplemented by an energy-dependent pseudo-potential accounting for exchange effects[23)24)] implicitely absorb a great part of the neglected effects. This

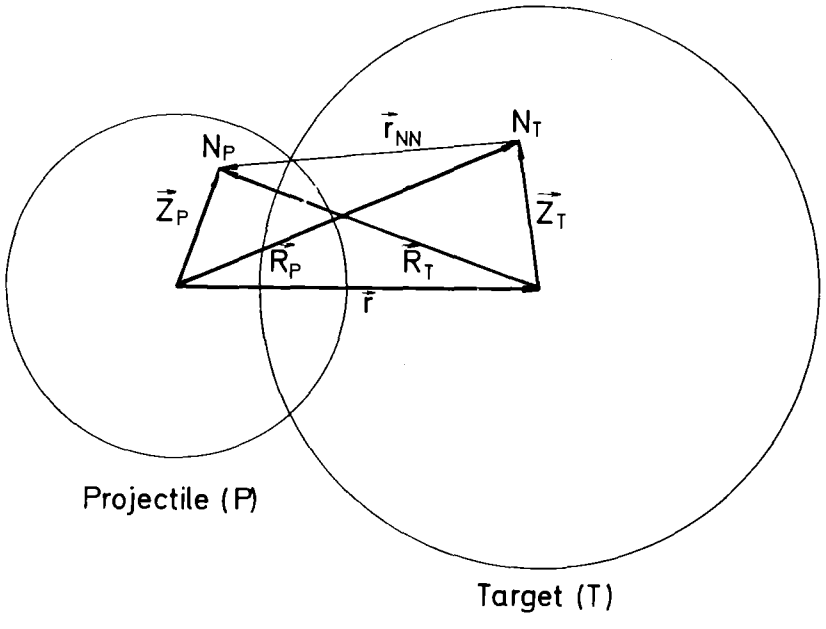

Fig. 9: Coordinates of the Projectil-Target-System

may explain why actually single folding models have proved to be more successful in describing experimental data when compared to the simple double folding procedure of the type of eq. (3.6).

As example for the single folding models we regard the most widely used Gaussian alpha-particle-nucleon-interaction

$$V_{P-N_T}(R_P) = \lambda_R \, V_o \, \exp(-|\vec{R}_P|^2/a^2) \qquad (3.7)$$

where the strength $V_o \sim 40$ MeV and range $a \sim 2$ fm have been determined by folding a nucleon-nucleon interaction into the

alpha-particle density[20]. The normalization parameter λ_R is energy-dependent and is empirically adjusted. For calibration purposes ^{40}Ca has been taken using a point-proton distribution $\rho_p(r)$ derived from experimental charge distribution $\rho_{ch}(r)$ by unfolding the charge form factor of the proton $\rho_{p-ch}(r)$ via

$$\rho_{ch}(\vec{r}) = \int d\vec{r}' \; \rho_p(|\vec{r} - \vec{r}'|) \; \rho_{p-ch}(\vec{r}') \qquad (3.8)$$

The neutron distribution in most cases has been assumed to be identical to the proton distribution, i.e.

$$\frac{A}{N} \rho_n(r) \equiv \frac{A}{Z} \rho_p(r) \equiv \rho_m(r)$$

In Fig. 10 angular distributions of $^{40}Ca(\alpha,\alpha)$-scattering at several energies are displayed with the corresponding folding model descriptions using the Gaussian interaction. In each case only the normalization factor λ_R and the imaginary part of the potential have been adjusted to the measured cross sections[25]. It turns out that this simple folding model yields a good reproduction of the diffraction cross sections in particular at higher energies ($\sim$100 MeV). The deficiencies at lower energies are dominantly due to the neglection of antisymmetrization effects which are less important at higher energies because of the shorter interaction time. Two other examples using the Gaussian folding model at alpha-energies of 79 and 166 MeV are shown in Fig. 11. These data are well reproduced by the theoretical descriptions which aimed at a determination of the radius differences between ^{40}Ca and ^{48}Ca and we shall discuss the results later (sect. 5). The Gaussian folding model has very successfully been used also for inelastic alpha-particle scattering cross sections to extract isoscalar transition probabilities which are - in contrast to more conventional methods - in excellent agreement with corresponding completely model independent spectroscopic investigations [26,27] corroborating the usefulness of this approach.

With a few exceptions, however, the Gaussian folding model has been restricted to the diffraction region of the angular distributions since in these cases only the outermost region of the target nucleus contributes to the scattering process where the density is expected to be low enough to neglect saturation effects originating from the density dependence of the N-N-interaction. In order to extend the single folding model to the very important refraction region recently an additional term has been introduced[29] accounting for the saturation effects:

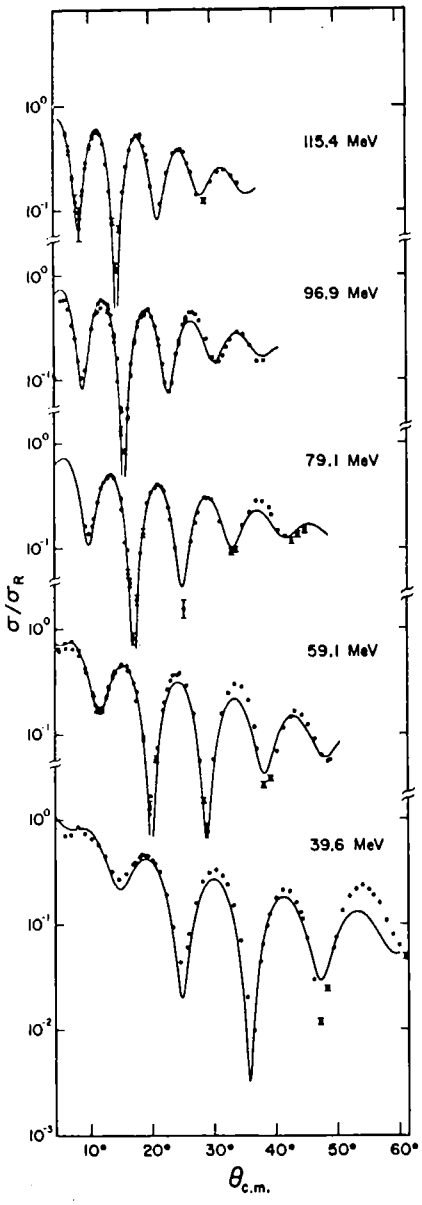

Fig. 10: Elastic alpha-particle scattering from ^{40}Ca at different energies. The theoretical curves correspond to folding model descriptions adjusting the strength of the effective Gaussian interaction to the experimental data (from Lerner et al. Ref. 25).

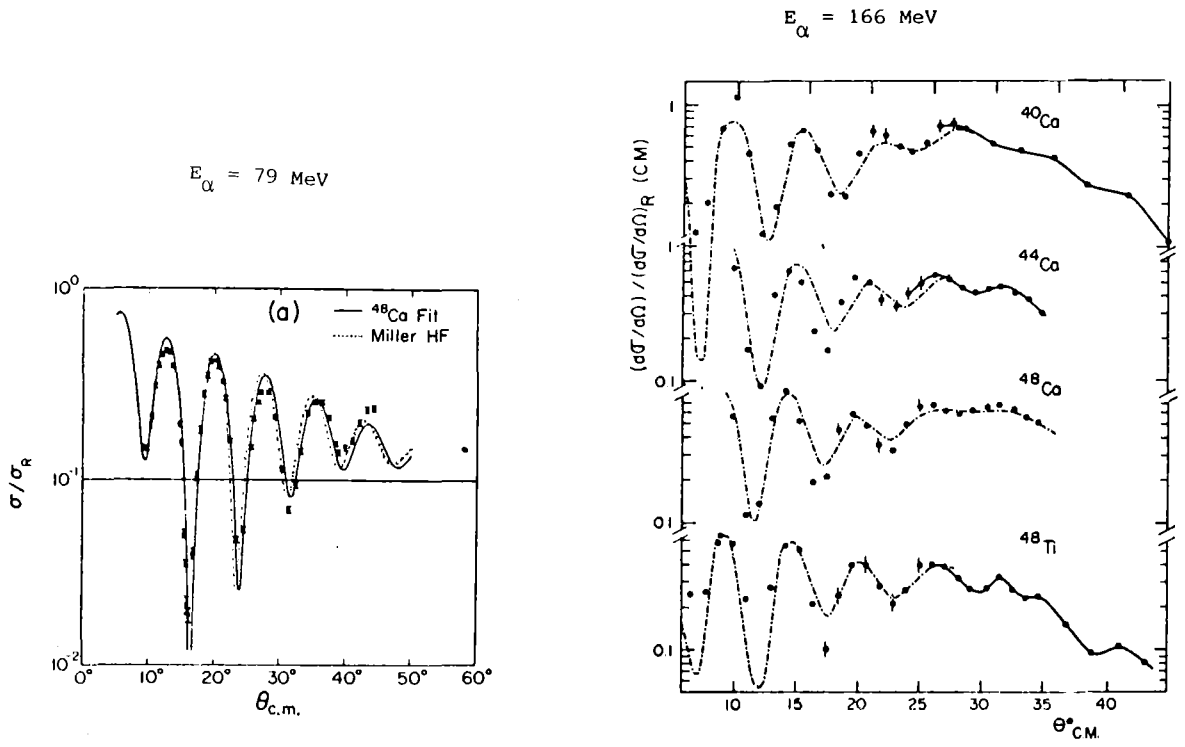

Fig. 11: Folding model fits to elastic alpha-particle scattering cross sections at E_α = 79 MeV and E_α = 166 MeV (from Refs. 24,28).

$$V_{\alpha\text{-}N_T}(\vec{R}_P) = V_o \exp(-|\vec{R}_P|^2/a^2)\,(1 - \gamma\,\rho_m^{2/3}) \qquad (3.9)$$

The parameters V_o, a and γ have empirically been determined by adjusting them to the elastic scattering cross sections of 104 MeV alpha-particles from ^{40}Ca. It is interesting to note that the phenomenological value for γ obtained thereby is very close to 2 fm^2 as found in more fundamental investigations[30]. In Fig. 12 the Gaussian folding model description of 104 MeV alpha-particles with and without (γ = 0) the additional term (3.9) are compared clearly indicating the importance of this term for the cross sections at large scattering angles. The final N-α-interaction is displayed in Fig. 13a for a free nucleon ($r_N = \infty$) and for nucleons imbedded in a ^{40}Ca nucleus at different radii.

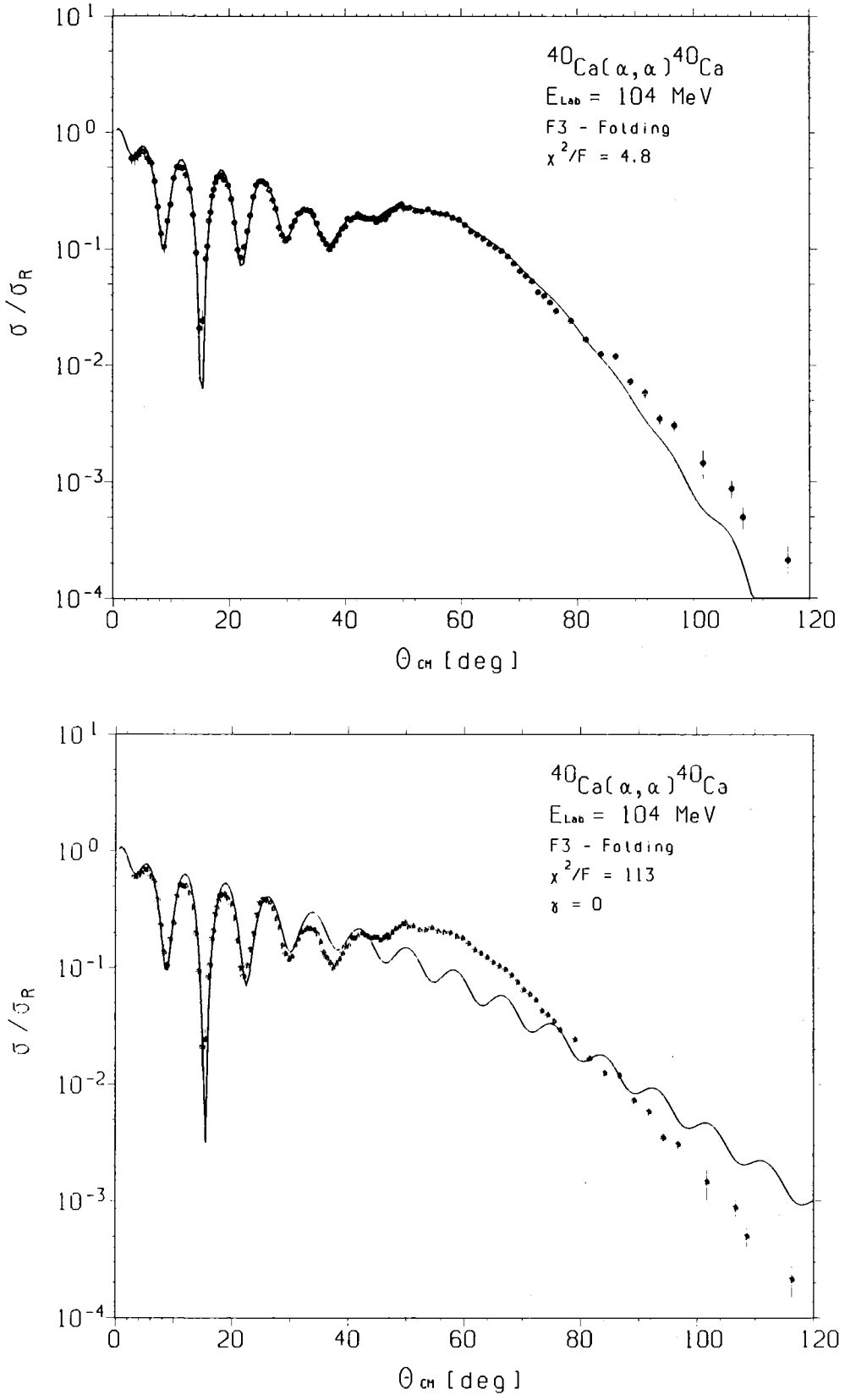

Fig. 12: Folding model description of 104 MeV alpha-particle scattering from ^{40}Ca without (γ = 0) and with the saturation term (eq. 3.9).

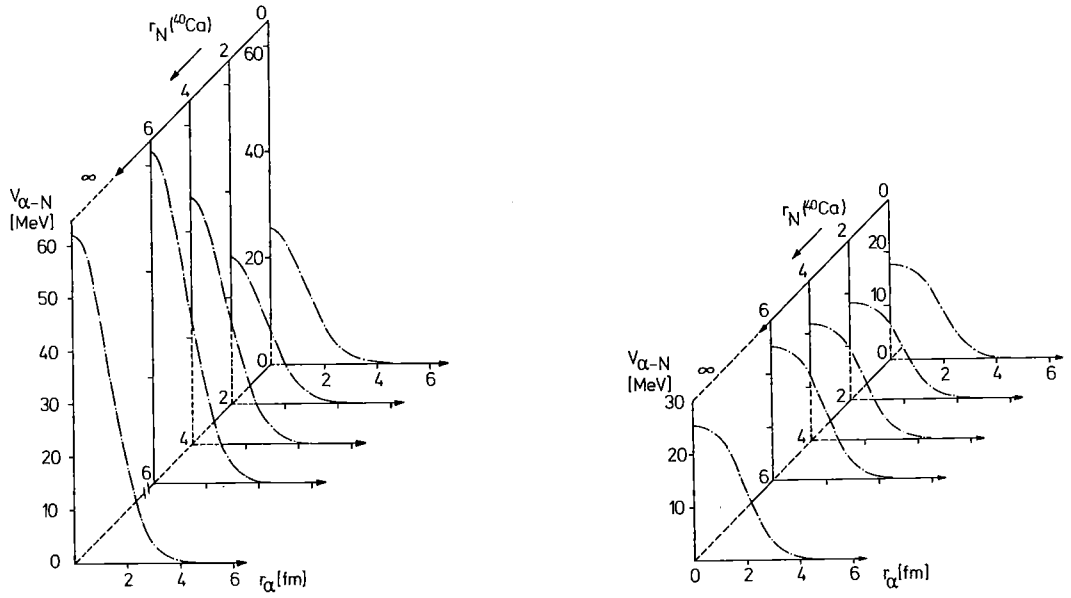

Fig. 13: a) Effective phenomenological N-α-interaction respecting saturation effects due to the target nucleus density for scattering of 104 MeV alpha-particles from ^{40}Ca.
b) Microscopic interaction from Majka (1978) Ref. 31.

The phenomenological Gaussian N-α-interaction can be compared with a microscopic interaction generated from Grenn's density dependent effective nucleon-nucleon interaction including anti-symmetrization effects[31] as shown in Fig. 13b). Only the strength and the saturation factor γ have been adjusted to the ^{40}Ca (α,α) cross sections in Fig. 13b). A good agreement of both interactions is observed for $r_\alpha > 2$ fm and $r_N > 2$ fm. The description of the elastic alpha-particle scattering cross sections by the microscopic interaction is only slightly worse when compared to the phenomenological Gaussian interaction.

A further step in the direction of a full microscopic description of alpha-particle scattering recently was performed by Majka et al.[32]. Alternatively to the folding over the target density ("target folding") by eq. (3.5) they started

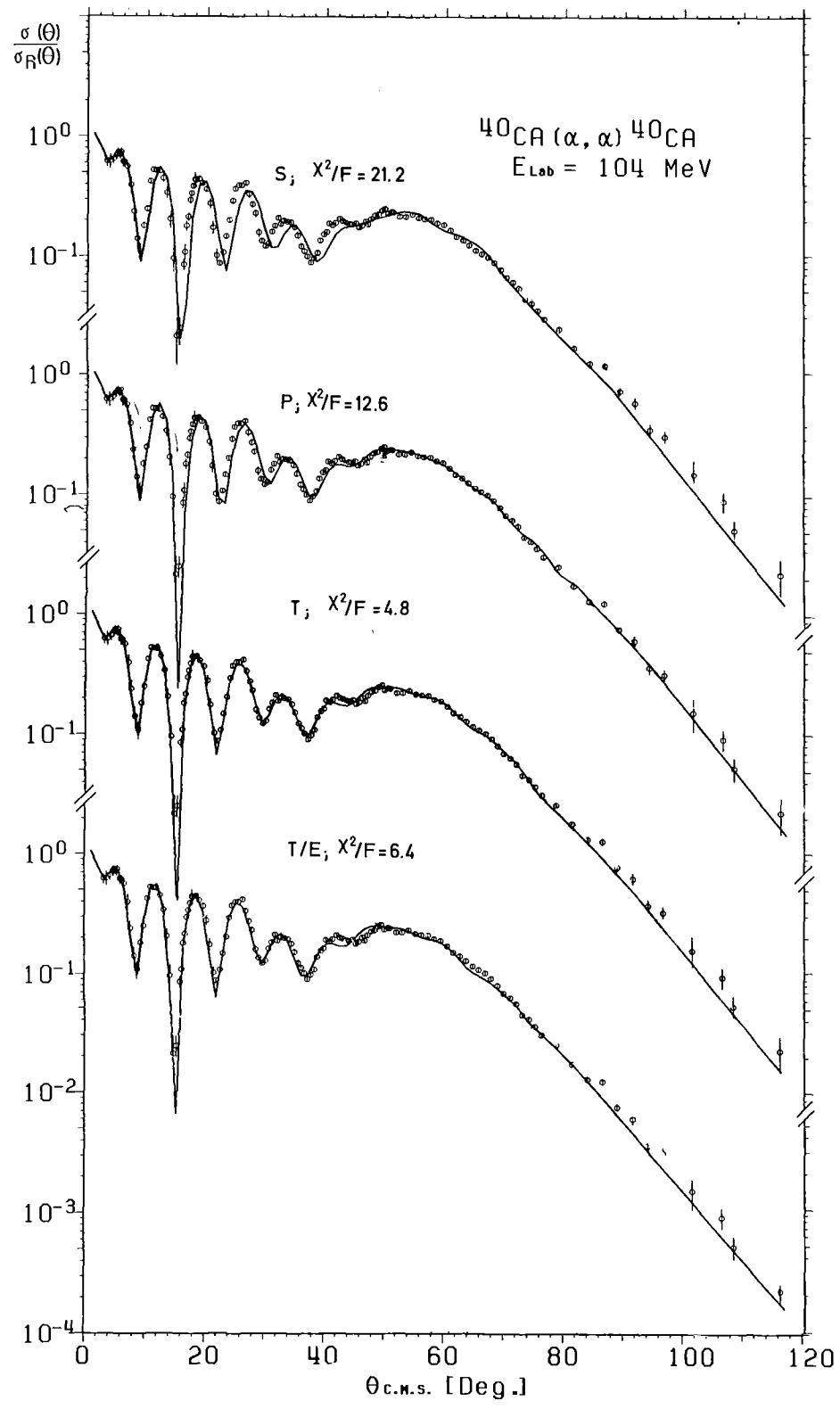

Fig. 14: Microscopic descriptions of $^{40}Ca(\alpha,\alpha)$ ^{40}Ca elastic cross sections using various approaches (see text)

with an adequate nucleon-target nucleus interaction V_{T-N} then constructing the real part of the projectile-target interaction by integrating over the complex projectile density

$$U_{PT}^{(T)}(r) = \int d\vec{Z}_P \; \rho_P(\vec{Z}_P) \; V_{T-N_P}(\vec{R}_T) \qquad (3.10)$$

In the nucleon-target interaction $V_{T-NP}(R_T)$ density dependence and exchange effects have been included similarly to the mentioned procedure generating the N-α-interaction[31]. Results for the procedures S (eq. 3.6), P (eq. 3.5) and T(eq. 3.10) are displayed in Fig. 14. In each case only the normalization factor of the potential λ_R and the imaginary part of the optical potential have been adjusted to the experimental data. The lowest curve shows the result of procedure T without respecting exchange effects which gives only a slightly worse reproduction of the cross sections indicating the minor importance of this effect.

A remaining considerable criticism of the presented folding model and also of other respective approaches[33] is the need of an empirical renormalization of the microscopically calculated potentials (by a factor $\lambda_R < 1$) indicating an insufficient understanding of important contributions. In order to overcome this deficiency an intermediate approximation has been introduced using eq. (3.6) with a density dependent NN-interaction $t_\rho(r_{NN}, \rho)$ and neglecting antisymmetrization effects (justified by the results of Fig. 14). In a local density approximation the density ρ appearing in t_ρ thereby is given by

$$\rho = m \cdot \rho_P(\vec{Z}_P + r_{NN}/2) + \rho_T(\vec{Z}_T + r_{NN}/2) \qquad (3.11)$$

The inner integral of eq. (3.6) which for m = 0 (the "adiabatic" approximation) is just the free nucleon-target potential V_{T-N_P} is now dependent on the density ρ_P of the imbedded projectile

nucleons. The factor m ($0 \leq m < 1$) accounts for the degree of the compressibility of the nuclear matter in the overlap region of the colliding nuclei. With the reasonable value m = 1/2 one obtains a satisfactory description of experimental (α,α) cross sections without any readjustment of the real potential ($\lambda_R = 1$) as shown in Fig. 15.

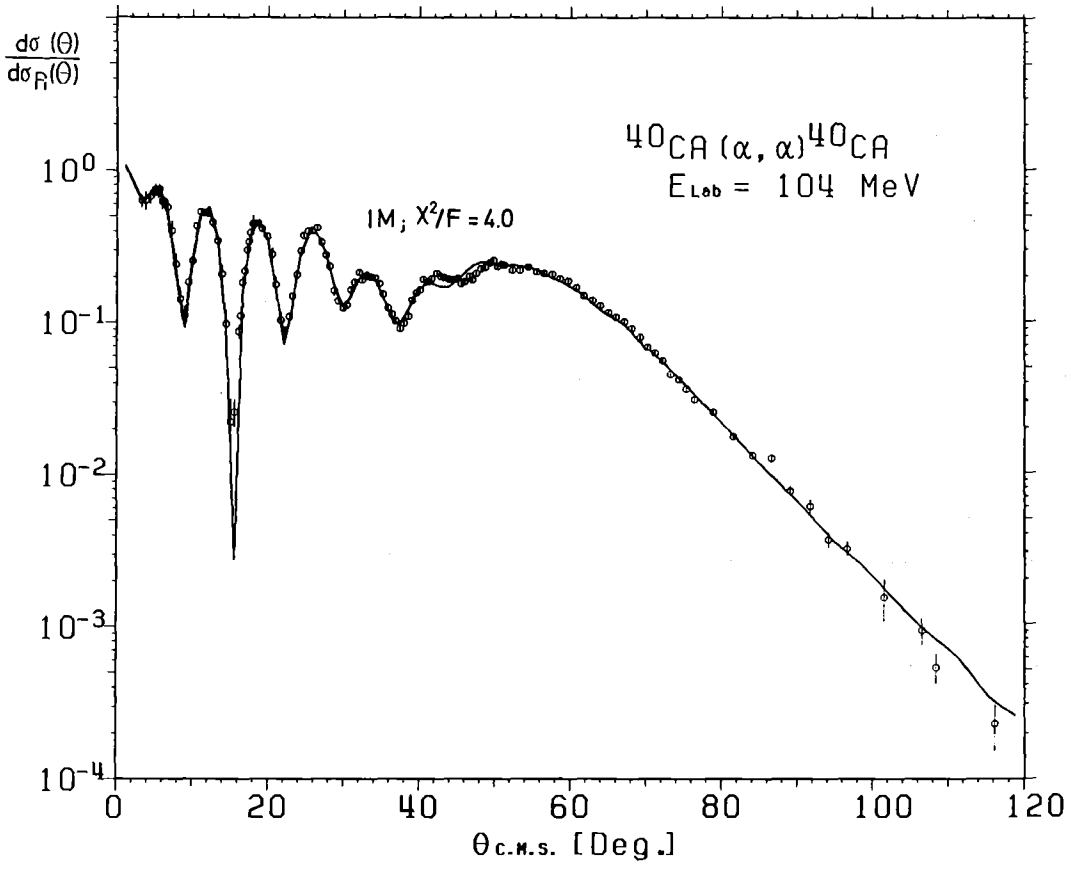

Fig. 15: "Intermediate approximation" describing $^{40}Ca(\alpha,\alpha)^{40}Ca$ cross sections without any parameter adjustment of the real potential.

Thereby the characteristica of the folded optical potential as rms-radius, volume integral and skin thickness are in reasonable agreement with the phenomenological potential obtained e.g. by the FB-method. *Thus we conclude that the refined folding models including density dependence are a*

useful, well-understood, and reliable description of elastic alpha-particle scattering at medium energies.

4. ELASTIC SCATTERING OF 104 MeV ALPHA-PARTICLES FROM $^{40,42,44,48}Ca$

4.1 Experiment

The particular experiment and analyses we now want to discuss more in detail is the elastic scattering of 104 MeV alpha-particles from $^{40,42,44,48}Ca$ performed at the Karlsruhe Isochronous Cyclotron. Part of the experimental results have been already presented in the previous general discussion.

The targets used for this experiment were self-supporting metal foils of natural Ca (96.9 % ^{40}Ca) and highly enriched $^{42,44,48}Ca$ (enrichment 94-99 %), respectively. The target thicknesses ranged from 1 to 5 mg/cm². The scattering chamber used had a diameter of 130 cm enabling to obtain a small acceptance of 0.15° of the slits in front of the 4 mm thick surface barrier detectors used for the detection of the scattered alpha-particles. The overall energy resolution was 150-180 keV sufficient to separate inelastic and contaminant peaks (C,O) at almost all scattering angles. Particle identification was not necessary because the maximum energy loss of protons, deuterons and tritons was less than 43 MeV far outside the interesting energy region of elastically scattered alpha-particles. ^{3}He-particles did not interfere with the spectra, because of the distinctly different Q-values (about 15 MeV) compared to alpha-particles. Great efforts were focussed to the determination of the absolute zero point of the scattering angles by measuring on both sides of the beam (left-right measurement) and by additionally observing the kinematical behavior of the carbon and oxygene target contamination peaks. The absolute total uncertainty of the scattering angles was

determined to within ± 0.05°.The targets were measured in turn at each scattering angle in order to avoid angular errors by new settings. The elastic scattering cross sections were measured from θ_{CM} = 3 up to θ_{CM} = 110° in steps of 0.5° in the diffraction region ($\theta_{CM} \lesssim 60°$) and in steps of 1.5° beyond. The beam current was measured on a Faraday cup behind the scattering chamber and additionally monitored by a fixed angle detector. The statistical errors were 1-2 % at most of the forward angles (<50°). The uncertainty of the absolute scattering angle was converted into cross section errors by taking into account the slope of the angular distributions. Since the uncertainties of target thickness, integrated beam current and detector acceptance determined the absolute scale of the cross sections only within 10 % accuracy the data were finally normalized at forward angles to optical model predictions. The experimental results covering nine orders of magnitude are displayed in Fig. 16. With increasing mass number the behavior of the cross sections in the transition region between diffraction and refraction and also the decrease at large angles are very similar for $^{40,42,44}Ca$, whereas the transition structure and the slope of the refractive decrease in the case of ^{48}Ca differ obviously from those of the other isotopes.

4.2 Analyses and Results

Concerning the determination of the optical potentials the experimental data have been analyzed by several approaches including a realistic Coulomb potential by double folding of the charge densities of projectile and target, using SW and SW^2 imaginary potentials, and FB-series for the real potentials with SW and SW^2-forms as "first guess". The final results of the various approaches are very similar at least when looking at the differences between the isotopes under investigation. As a representative result for a conventional optical potential

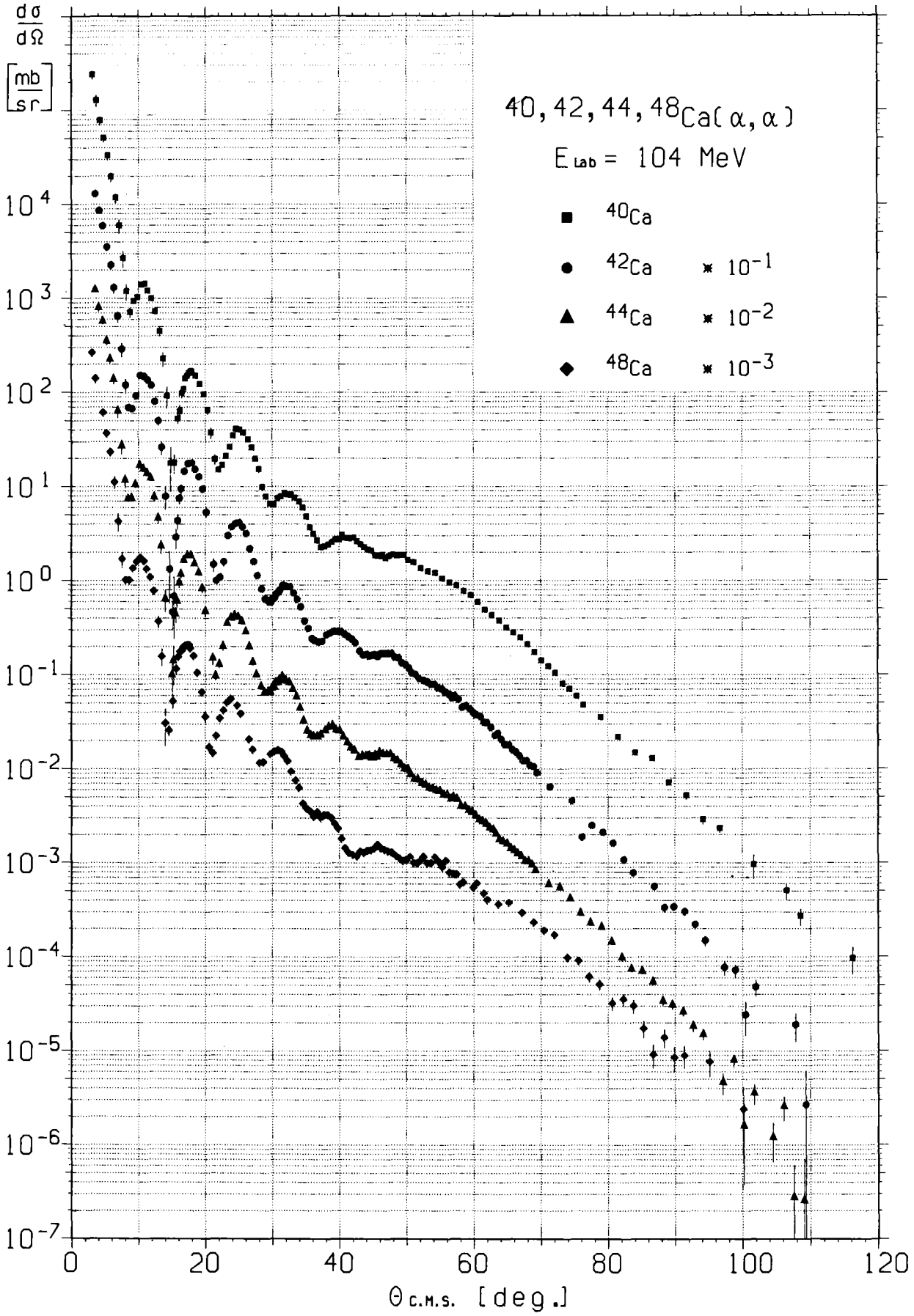

Fig. 16: Differential cross-sections of elastic 104 MeV alpha-particle scattering from $^{40,42,44,48}Ca$. The error bars include a contribution from the angular uncertainty ($\pm$ 0.05°) which has been converted into cross section errors.

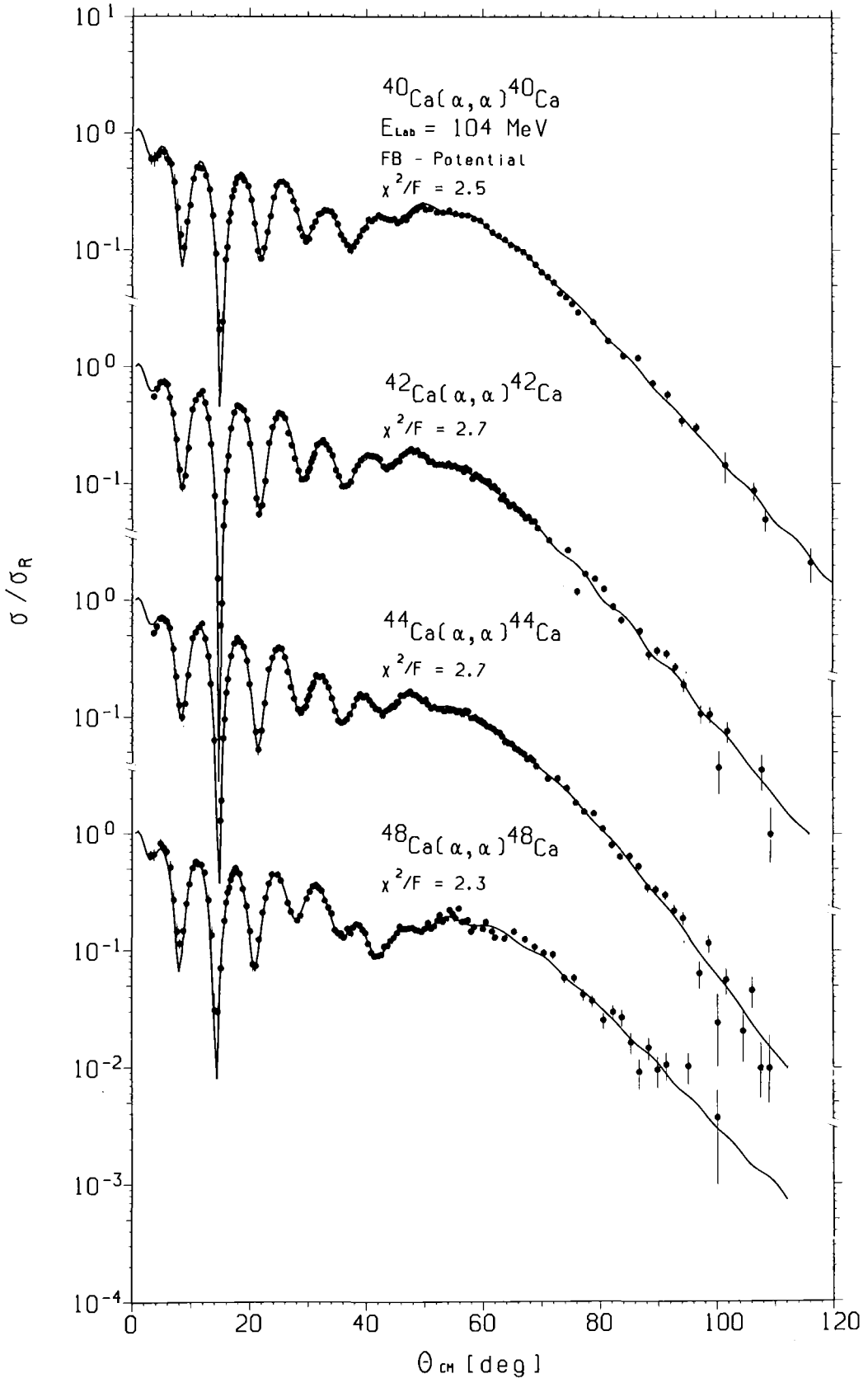

Fig. 17: Differential elastic scattering cross sections of $^{40,42,44,48}Ca$ (α,α) normalized to the Rutherford cross sections and FB-potential analyses (solid lines).

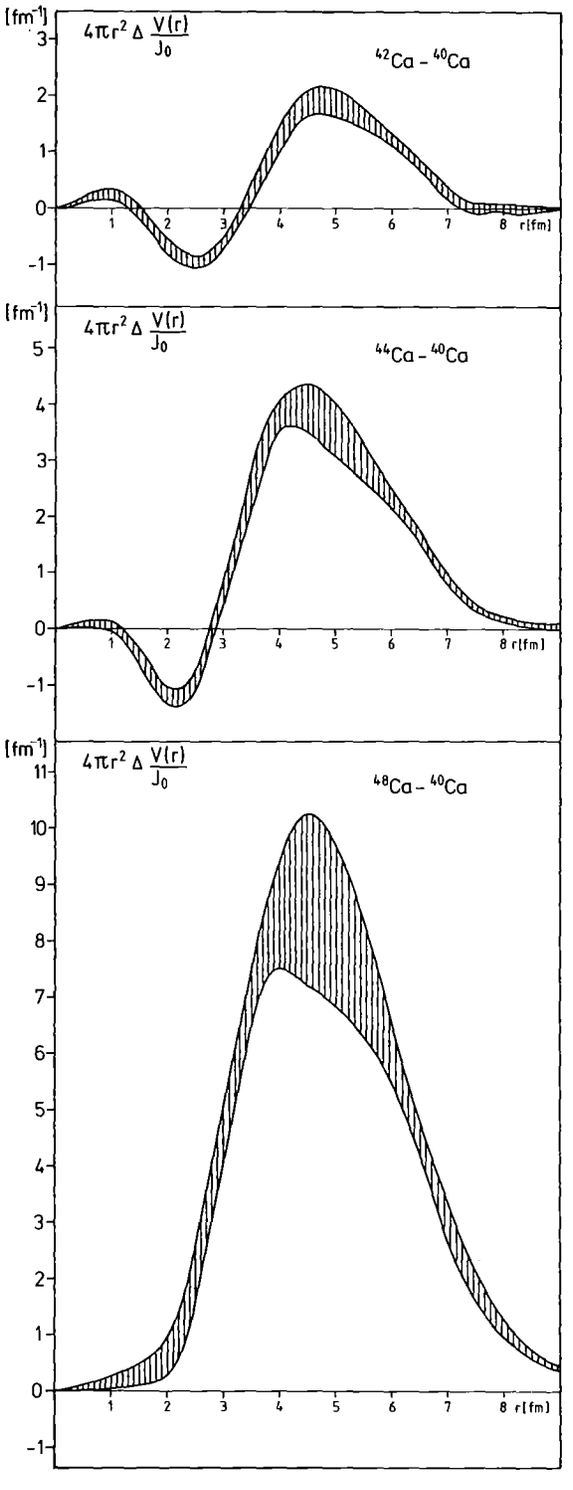

Fig. 18: Differences of the real optical potentials per volume integral $\frac{V(r)}{J_o/4A}$ between Ca-nuclei with mass number A and ^{40}Ca multiplied by $4\pi r^2$.

analysis Fig. 17 shows the results of the FB-analyses of the optical potential. The corresponding differences of the real potentials per volume integral

$$4\,\pi\,r^2\,\{\frac{V_A(r)}{J_o(A)/4A} - \frac{V_{40}(r)}{J_o(40)/4\cdot 40}\}$$

between the isotopes ^{42,44,48}Ca and ^{40}Ca including the corresponding error bands obtained from the FB-method are displayed in Fig. 18. The curves directly reflect the excess potential strength per nucleon in a spherical shell of 1 fm thickness.

For all three isotopes one observes a distinct potential excess at the nuclear surface while in the cases of ^{42,44}Ca additionally a more or less small depression is indicated inside the nuclei. *This result, though it tells us up to now nothing directly about rms-radii or any other features of the matter densities is the most reliable and least model dependent result which can be extracted from the present experiment.*

For a more direct interpretation of the experimental results in terms of the nucleon densities we have chosen the folding model using the Gaussian effective interaction including the saturation term (eq. 3.9). The more refined methods (eqs. 3.10 and 3.11) are too laborious to vary the assumed densities in a fit procedure. Adopting the usefulness and reliability of this interaction corroberated by many systematical studies we focussed our attention to the problem of the model dependence of the parametrized nucleon densities. Similar as in the case of the optical potentials the coupling of different radial regions of the densities given by widely used functional forms as e.g. the 3-parameter Fermi form (F3)

$$\rho(r) = \rho_o\,[1 + w\,\frac{r^2}{c^2}]\,[1 + \exp\frac{r-c}{a}]^{-1} \qquad (4.1)$$

may introduce undesirable model effects in the analyses as also observed in electron scattering analyses.

Therefore, we describe the nuclear matter distributions by

$$\rho_m(r) = \rho_o(r) + \sum_{n'=1}^{N'} \beta_{n'} j_o\left(\frac{n'\pi r}{R_c}\right) \qquad (4.2)$$

following the FB-method for the optical potential. In order to keep the volume integral of ρ_m constant only $\beta_2 \ldots \beta_{N'}$ were varied parameters and β_1 was determined from

$$\beta_1 = \sum_{n'=2}^{N'} \frac{(-1)^{n'} \beta_{n'}}{n'^2} \qquad (4.3)$$

For the "first guess" density $\rho_o(r)$ we studied different cases, each parametrized by the F3-form

A: $\rho_o(r) = \frac{A}{Z} \rho_p(r)$

with $\rho_p(r)$ derived from experimental charge distributions as described in sect. 3.

B: $\rho_o(r)$ = result of a fit procedure varying the parameters of F3 in order to reproduce best the cross sections under investigation.

In addition to these "first guess" densities we also chose different strengths V_o for the effective interaction:

I : V_o adjusted by means of the ^{40}Ca cross sections.

II: V_o slightly changed (via grid calculations) in order to give the best description in an F3-fit for each nucleus. The changes were less than 5 % compared to case I requiring weaker interactions for ^{42,44}Ca and stronger for ^{48}Ca.

For the FB series cut-off radii between 6 fm and 7.5 fm have been chosen and the number of terms (N') was between 6 and 9. The theoretical reproduction of the angular distributions obtained by these approaches were very similar. A typical example is shown in Fig. 19. The resulting matter densities averaging the single calculations are displayed in Fig. 20.

The corresponding rms-radii are compiled in Table I, together with radii of the corresponding proton distributions (from Ref. 34).

The differences of the matter densities including the respective error bands obtained from the FB-analysis are displayed in Fig. 21. For comparison corresponding charge density differences are plotted on the right-hand side. In all cases one observes a nucleon or charge excess at the nuclear surface when compared to the ^{40}Ca-core, indicating that a local increase of the neutron density (due to a filling of an additional shell) also leads to an increase of the proton density in the corresponding radial region. This effect generated by the dominating n-p force seems to be responsible for the surprising behavior of the nuclear charge radii, in particular for the small value of ^{48}Ca which is due to the fact that protons from the outermost surface are pulled into the region at $r \sim 3.8$ fm by the additional neutrons. When comparing finally the matter and charge differences for each nucleus one recognizes for ^{48}Ca a long positive tail for the matter and a negative bump for the charge difference which has to be interpreted as a distinct "neutron skin" of ^{48}Ca.

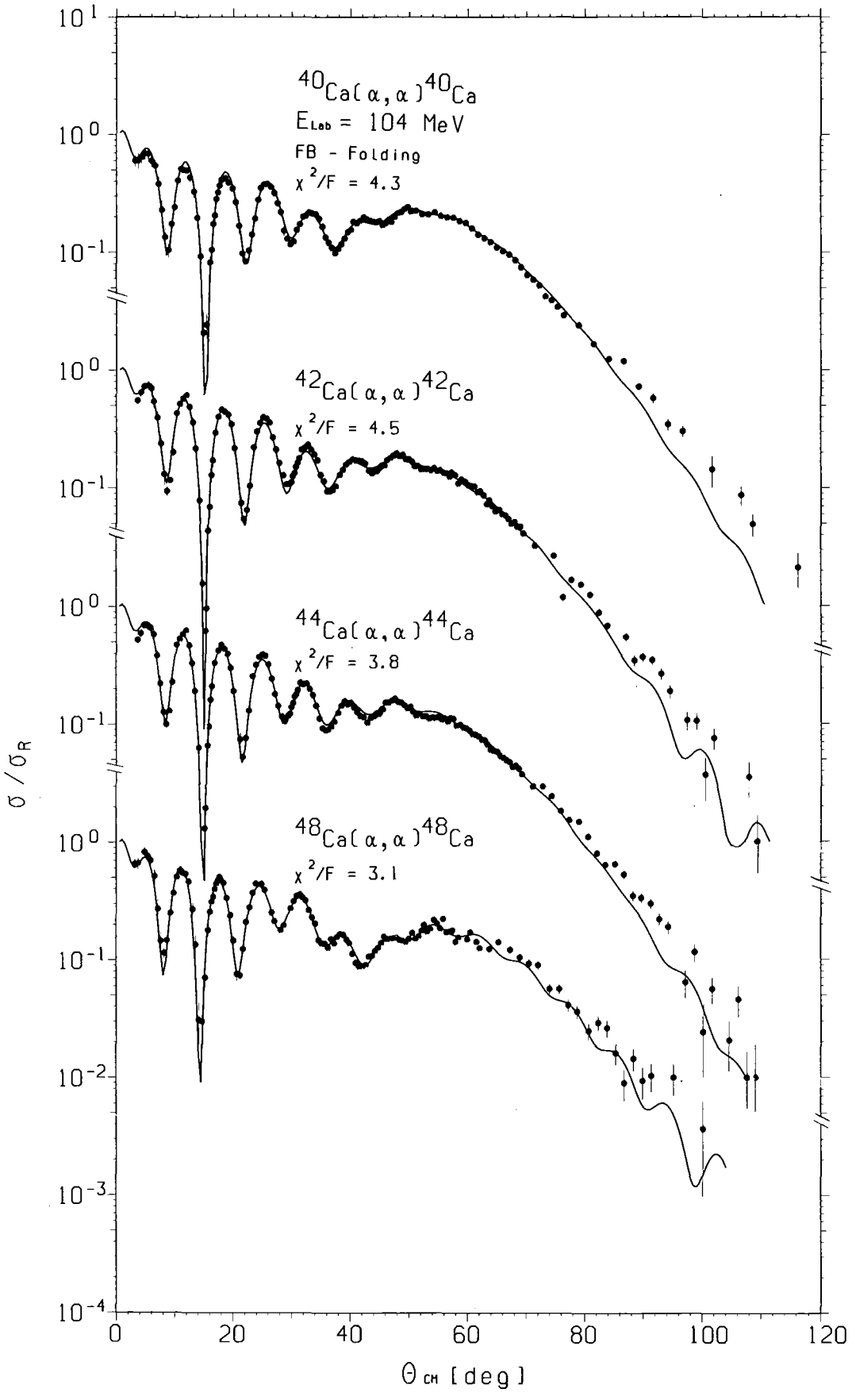

Fig. 19: Density dependent folding model descriptions of elastic alpha-particle scattering from $^{40,42,44,48}Ca$ using Fourier-Bessel densities.

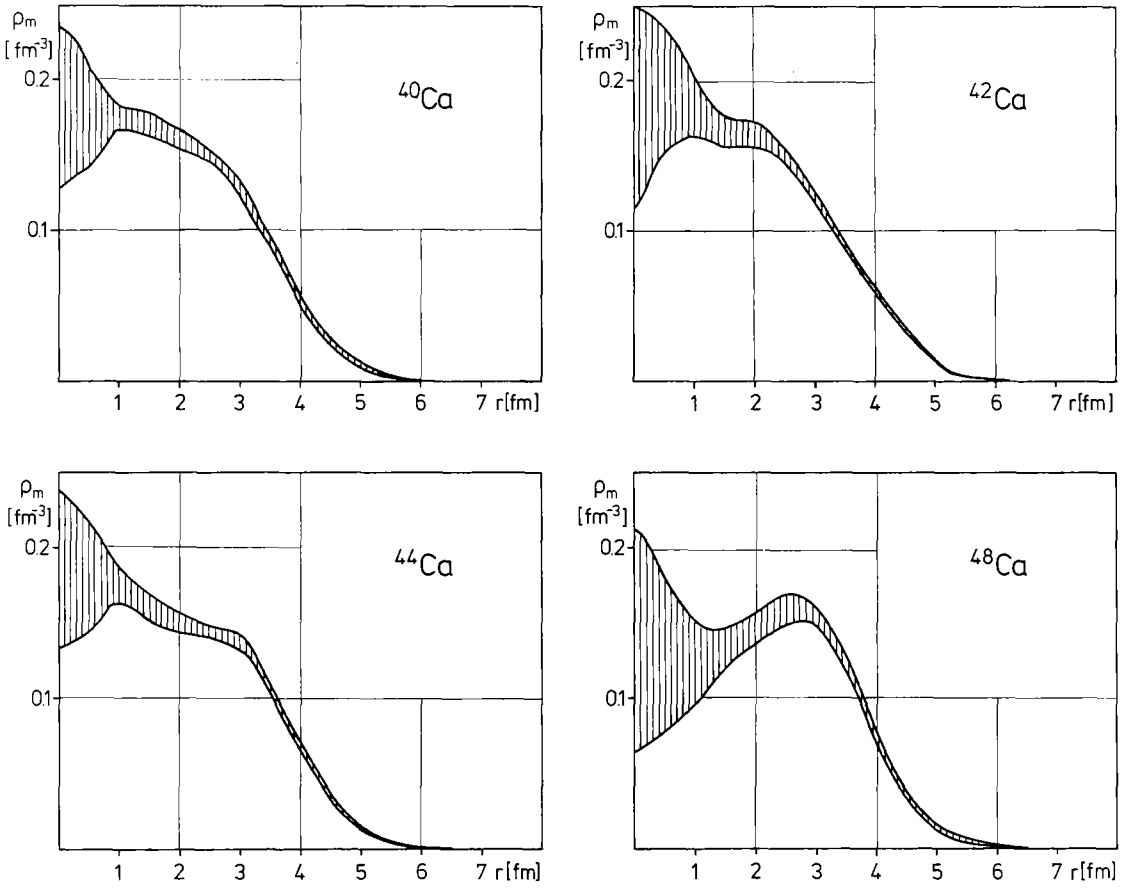

Fig. 20: Nuclear matter densities of ^{40,42,44,48}Ca obtained from folding model analyses of elastic alpha-particle scattering using Fourier-Bessel densities.

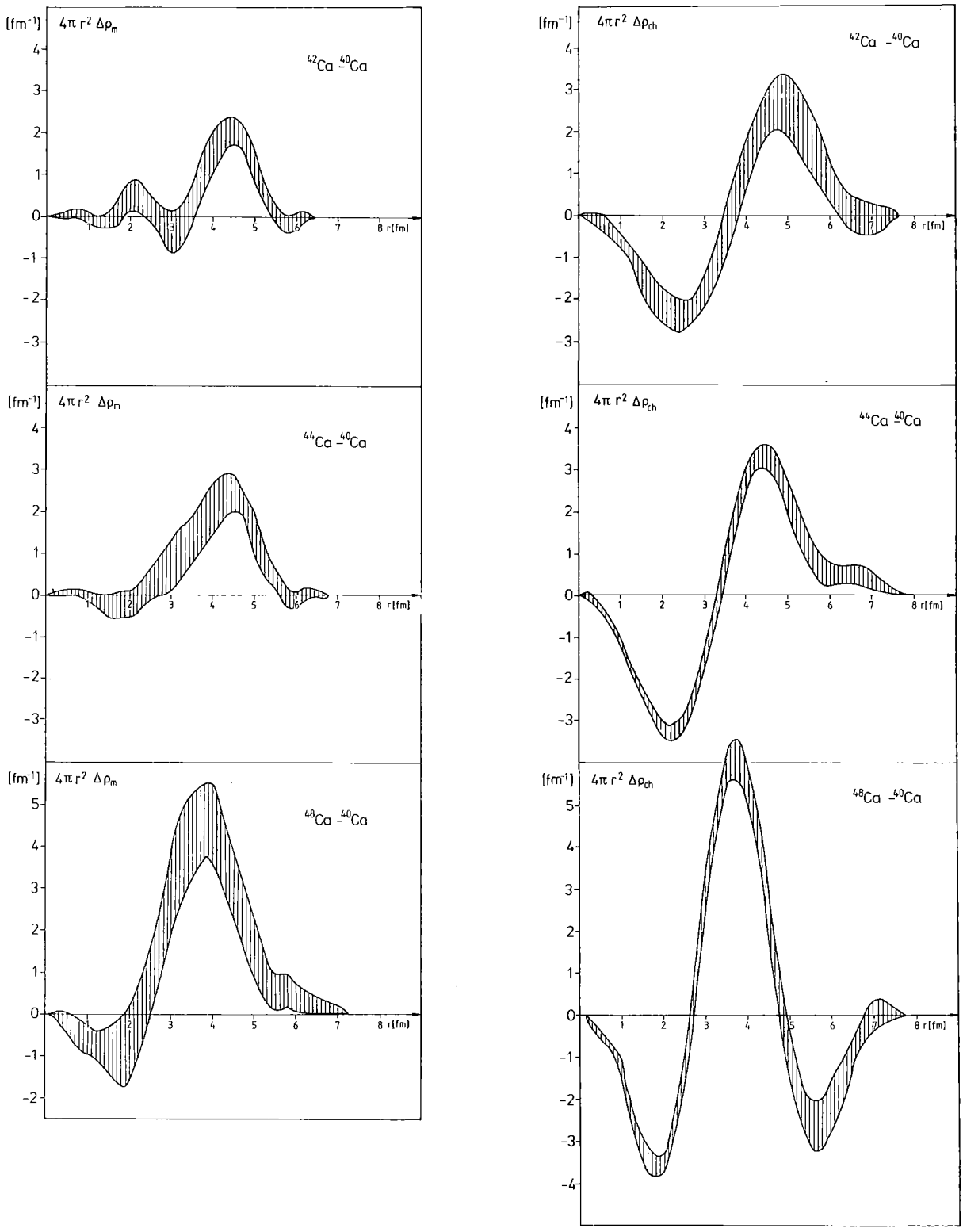

Fig. 21: Differences of nuclear matter densities ρ_m and nuclear charge densities ρ_{ch} of Ca-isotopes. ($\Delta\rho_{ch}$ from H.D. Wohlfahrt, private communication)

$\langle R^2_P \rangle^{1/2} = R_P$: RMS-RADII OF PROTONS

FROM H.D. WOHLFAHRT ET AL., PHYS. LETT. 73B (1978) 131

$\langle R^2_M \rangle^{1/2} = R_M$: RMS-RADII OF TOTAL MATTER

FROM (α,α) PRESENT WORK

$\langle R^2_N \rangle^{1/2} = \left[1/N\ (A \langle R^2_M \rangle - Z \langle R^2_P \rangle)\right]^{1/2} = R_N$: RMS-RADII OF NEUTRONS

RMS-RADII (FM)

A	R_P	ΔR_P (A-40)	R_N	ΔR_N (A-40)	R_M	ΔR_M (A-40)	$\Delta R_{N-P}(A)$
40	3.386		3.335		3.361		-0.051
42	3.422	0.036	3.420	0.085	3.421	0.060	-0.002
44	3.439	0.053	3.476	0.141	3.459	0.098	+0.037
48	3.407	0.021	3.633	0.298	3.541	0.180	+0.226

Table I : Root-Mean-Square-Radii
of Ca-Isotopes

5. COMPARISON WITH OTHER METHODS

The elastic scattering of protons[35-37], alpha-particles[24,25,38] and pions[39,40] as well as the total cross section for protons[41] and pions[42] and observations of pionic atoms[43] have been used for studies of the nuclear density distributions of calcium isotopes. Table II summarizes values of $\langle r^2_n \rangle^{1/2} - \langle r^2_p \rangle^{1/2}$, the differences between the neutron and proton rms radii, obtained by the various methods where in most cases the values for ^{40}Ca given in Table I have been used as "calibration". When comparing at first the present results with those obtained from other experiments of elastic scattering of alpha-particles we note that the flexible (model independent) FB-method had not been applied before for Ca-isotopes others than ^{40}Ca. Thus most of the previous analyses could have lead to results which depend on the assumptions made about the form of the distributions. In particular, no information is obtained on the nuclear interior if only the diffraction region is included and thus results depend on the arbitrary extrapolation due to the chosen functions. All previous experiments using alpha-particle scattering at about 100 MeV were confined to the diffraction region of the angular distribution. Indeed, if we analyze only the diffraction part of our data we find values for $\langle r^2_m \rangle^{1/2}$ quite different from those quoted for the full angular range strongly depending on the approach used for the density. Furthermore, the estimated errors (e.g. from the FB-procedure, if convergence is achieved at all) increase by factors of 2-3 (see Fig. 8).

The analysis of 1 GeV proton scattering[35-37] is a promising method thanks to the plausibility of using the free p-nucleon interaction. Procedures like the FB-method have already been used for the analysis of proton scattering[37].

METHOD	REFERENCE	$\langle R_N^2 \rangle^{1/2} - \langle R_P^2 \rangle^{1/2}$ [FM]			
		40	42	44	48
α-SCATTERING 79 MEV(DIFFRACT.)	LERNER ET AL. P.R. C12 (1975) 778	-0.02*			0.03 ± 0.08
104 MEV	PRESENT EXPERIMENT	(-0.05±0.03)	0.0±0.03	0.04±0.03	0.23 ± 0.04
166 MEV	BRISSAUD ET AL. N.P.A191 (1972) 145	-0.03±0.12		0.07±0.16	0.30 ± 0.12
1.37 GEV	ALKHAZOV ET AL. N.P.A280 (1977) 365	-0.02±0.03	0.03±0.03	0.07±0.03	0.18 ± 0.03
P-SCATTERING 1.04 GEV	CHAUMEAUX ET AL. P.L. 72B (1977) 33	-0.03	0.04±0.03	0.03±0.03	0.16 ± 0.03
REANALYSIS	SHLOMO AND SCHAEFFER PREPRINT 1979	-0.04*	0.0 ±0.03	0.0 ±0.03	0.10 ± 0.03
800 MEV	IGO ET AL. P.L. 81B (1979) 151	0.01±0.08	0.08±0.08	0.10±0.08	0.18 ± 0.08
π TOTAL CROSS SECTIONS	JAKOBSON ET AL. P.R.L. 38 (1977) 1201			0.01±0.05	0.12 ± 0.05
π ATOMS	BATTY ET AL. P.L. 81B (1979) 165			-0.05±0.05	
P TOTAL CROSS SECTIONS 700 MEV	ANDERSON ET AL. P.R. C19 (1979) 905			-0.05±0.09	0.52 ± 0.09
		*ASSUMED			

Table II: Differences between neutron and proton density rms-radii of Ca-isotopes

However, the models are unable to reproduce the data at angles beyond the third diffraction minimum and analyses have, therefore, been confined to very forward angles. This presumably leads to consequences regarding the nuclear interior similar to those discussed before. In contrast, in the folding model for alpha-particle scattering the density dependence was introduced in the present work in order to be able to include into the analysis the full range of angles that could be measured.

The elastic scattering of pions was analyzed[39,40] using a simplified model (of a black disc) and the results obtained could strongly depend on those assumptions. Total cross sections[41,42] and observation of pionic atoms[43] provide only one or two experimental numbers (cross section or level shift and width) and therefore the analysis must rely on the choice of functions for the density distributions. It is, therefore,not clear whether or not the results of these experiments can be presented by rms-radii, particularly when looking for small isotopic differences. In view of the above arguments one should also ask the question whether all the other experiments (if any) really determine the rms radii. Some of the conflicts between different results as observed in Table II may be resolved if a combined analysis of several experiments is performed, all of which probe different radial regions of the nucleus. For example, it may turn out that moments of the density distributions different from the second (i.e. the rms-radius) are better determined[37] and analyses of different moments may prove useful.

6. CONCLUSIONS

The experiments presented in section 4 fulfill the preconditions to reveal the whole slope of the optical potentials and nuclear matter densities of the calcium isotopes with good accuracy. The methods of analyses include refined

techniques as e.g. density dependence and the flexible Fourier-Bessel description which (i) are completely able to reproduce the experimental results over the whole angular range, which (ii) distinctly reduce the model dependence of the extracted quantities, and which (iii) have never been used before for alpha-particle scattering. Thus we claim the quoted results to be most reliable at least when regarding the differences of the shape of the potentials and matter density distributions.

Nevertheless, some deficiencies remain, namely

1. the unsatisfactory treatment of the imaginary potential, even though an important influence could not be observed when using different approaches[10].
2. nuclear structure influences not explicitly taken into account, but obvious from the different level schemes of the spherical nuclei ^{40,48}Ca and the softly deformed nuclei ^{42,44}Ca.

Both points are to some order connected with each other due to the fact that the imaginary part absorbs all inelastic and reaction channels which depend on the structure of the particular nucleus. An important step to improve this deficiency could be to consider at least the strongest inelastic channels directly in a coupled channel calculation. This is presently under investgation. Moreover, systematic studies are necessary to answer the question which experimental information provide an unambiguous determination of the imaginary potential and how the model dependence of the imaginary potential shape can be reduced. A microscopically evaluated imaginary potential should be the final aim of these efforts.

ACKNOWLEDGEMENTS

It is a pleasure for me to thank Professor Dr. E. Friedman, Professor Dr. H. Rebel, and Dr. Z. Majka for important contributions to the refined treatment of elastic alpha-particle scattering, for many valuable discussions and comments and fruitful cooperation. The encouraging interest and continuous support of Professor Dr. P. Brix and Professor Dr. G. Schatz is gratefully acknowledged. The Karlsruhe experiment was performed together with Mrs. G. Bechtold, J. Buschmann, H. Klewe-Nebenius, B. Neumann, R. Pesl, H. Rebel and S. Zagromski whose great efforts during the beam-periods and in data evaluation and analysis were the necessary and important prior condition for the presented results. I would like to thank Mrs. E. Maaß for the careful and patient preparation of the manuscript.

REFERENCES

1. H. Rebel, in: Radial Shape of Nuclei, eds. A. Budzanowski and A. Kapuscik (Cracow, 1976) p. 164.
2. Th. Delbar, Gh. Grégoire, G. Paic, R. Ceuleneer, F. Michel, R. Vanderpoorten, A. Budzanowski, H. Dabrowski, L. Freindl, K. Grotowski, S. Micek, R. Planeta, A. Strzalkowski, and K.A. Eberhard, Phys. Rev. C18 (1978) 1237.
3. A.M. Bernstein, M. Duffy, and E.P. Lippincott, Phys. Lett. 30B (1969) 20.
4. B. Fernandez and J.S. Blair, Phys. Rev. C1 (1970) 523.
5. K.W. Ford and J.A. Wheeler, Ann. Phys. (N.Y.) 7 (1959) 259, 297.
6. T. Koelling and R.A. Malfliet, Phys. Rep. C4 (1972) 153.
7. J. Knoll and R. Schaeffer, Ann. Phys. (N.Y.) 97 (1976) 97.
8. D.A. Goldberg and S.M. Smith, Phys. Rev. Lett. 29 (1972) 500.
9. A. Budzanowski, K. Grotowski, M. Grzywacz, and A. Strzalkowski, Progress Report, Institute for Nuclear Physics, Cracow (Poland) 1972.
   D.A. Goldberg; Phys. Lett. 55B (1975) 59.
   Z. Majka and T. Srokowski, Acta Phys. Polonica B9 (1978)53.
10. H.J. Gils, E. Friedman, H. Rebel, J. Buschmann, S. Zagromski, G. Bechtold, H. Klewe-Nebenius, B. Neumann, R. Pesl, Report KfK 2838, Kernforschungszentrum Karlsruhe (1979).
    H.J. Gils, E. Friedman, Z. Majka, and H. Rebel; Report KfK 2839, Kernforschungszentrum Karlsruhe (1979)
11. N. Vinh Mau; Phys. Lett. 71B (1977) 5.0
12. E. Friedman and C.J. Batty, Phys. Rev. C17 (1978) 34.
13. B. Dreher, J. Friedrich, K. Merle, H. Rothhaas, and G. Lührs, Nucl. Phys. A235 (1974) 219.

14. D.F. Jackson and V.K. Kembhavi, Phys. Rev. 178 (1969) 1626.
C.J. Batty, E. Friedman, and D.F. Jackson, Nucl. Phys. A175 (1971) 1.
15. P.P. Singh, P. Schwandt, and G.C. Yang, Phys. Lett. 59B (1975) 113.
16. A. Budzanowski, A. Dudek, K. Grotowski, and A. Strzalkowski, Phys. Lett. 32B (1970) 431.
A. Budzanowski, A. Dudek, K. Grotowski, Z. Majka, and A. Strzalkowski, Particle and Nuclei 5 (1973) 97.
17. Z. Majka, A. Budzanowski, K. Grotowski, and A. Strzalkowski, Phys. Rev. C18 (1978) 114.
18. J.P. Vary and C.B. Dover, Phys. Rev. Lett. 31 (1973) 1510.
19. J.S. Lilley; Phys. Rev. C3 (1971) 2229.
P. Mailandt, J.S. Lilley, and G.W. Greenlees, Phys. Rev. C8 (1973) 2189.
20. A.M. Bernstein, Advances in Nucl. Phys., ed. by M. Baranger and E. Vogt (Plenum Press, New York, 1969).
21. B. Tatischeff, I. Brissaud, and L. Bimbot, Phys. Rev. C5 (1972) 234.
22. H. Rebel, R. Löhken, G.W. Schweimer, G. Schatz, and G. Hauser, Z. Physik 256 (1972) 258.
23. R. Schaeffer, Nucl. Phys. A 158 (1970) 321.
24. I. Brissaud, Y. Le Bornec, B. Tatischeff, L. Bimbot, M.K. Brussel, and G. Duhamel, Nucl. Phys. A 191 (1972) 145.
25. G.M. Lerner, J.C. Hiebert, L.L. Rutledge, Jr., and A.M. Bernstein, Phys. Rev. C6 (1972) 1254.
26. H.J. Gils and H. Rebel, Z. Physik A274 (1975) 259.
H. Rebel, Z. Physik A277 (1976) 35.
27. H. Faust, A. Hanser, H. Klewe-Nebenius, H. Rebel, J. Buschmann and H.J. Gils; J. Phys. G. (Nucl. Phys.) 4 (1978) 247.
28. G.M. Lerner, J.C. Hiebert, L.L. Rutledge, Jr., C. Papanicolas, and A.M. Bernstein, Phys. Rev. C12 (1975) 778.

29. E. Friedman, H.J. Gils, H. Rebel, and Z. Majka, Phys. Rev. Lett. 41 (1978) 1220.
30. J.P. Jeukenne, A. Lejeune, and C. Mahaux, Phys. Rev. C16 (1977) 80.
31. Z. Majka, Phys. Lett. 76B (1978) 161.
32. Z. Majka, H.J. Gils, and H. Rebel, Z. Physik A288 (1978) 139.
33. G.R. Satchler, Phys. Lett. 59B (1975) 121.
34. H.D. Wohlfahrt, E.B. Shera, M.V. Hoehn, Y. Yamazaki, G. Fricke, and R.M. Steffen, Phys. Lett. 73B (1978) 131.
35. S. Shlomo and R. Schaeffer, Phys.Lett. 83B (1979) 5.
36. G. Igo, G.S. Adams, T.S. Bauer, G. Pauletta, C.A. Whitten, Jr. A. Wreikat, G.W. Hofmann, G.S. Blanpied, W.R. Coker, C. Harvey, R.P. Liljestrand, L. Ray, J.E. Spencer, H.A. Thiessen, C. Glashausser, N.M. Hintz, M.A. Oothoudt, H. Nann, K.K. Seth, B.E. Wood, D.K. McDaniels, and M. Gazzaly, Phys. Lett. 81B (1979) 151.
37. I. Brissaud and X. Campi, Phys. Rev. C15 (1977) 452. Compare also Contr. to this Meeting.
38. G.D. Alkhazov, T. Bauer, R. Bertini, L. Bimbot, O. Bing, A. Boudard, G. Bruge, H. Catz, A. Chaumeaux, P. Couvert, J.M. Fontaine, F. Hibou, G.J. Igo, J.C. Lugol, and M. Matoba, Nucl. Phys. A280 (1977) 365.
39. J.-P. Egger, R. Corfu, P. Gretillat, C. Lunke, J. Piffaretti, E. Schwarz, C. Perrin, J. Jansen, and B.M. Preedom, Phys. Rev. Lett. 39, (1977) 1608.
40. M.B. Johnsson and H.A. Bethe; Comments Nucl. and Part. Phys. 8 (1978) 75.
41. B.D. Anderson, P.R. Bevington, F.H. Cverna, M.W. McNaughton, H.B. Willard, R.J. Barrett, N.S.P. King, and D.J. Ernst, Phys. Rev. C19 (1979) 905.
42. M.J. Jakobson, G.R. Burleson, J.R. Calarco, M.D. Cooper, D.C. Hagerman, I. Halpern, R.H. Jeppeson, K.F. Johnson, L.D. Knutson, R.E. Marrs, H.O. Meyer, and R.P. Redwine, Phys. Rev. Lett. 38 (1977) 1201.
43. C.J. Batty, S.F. Biagi, E. Friedman S.D. Hoath, J.D. Davies, G.J. Pyle, G.T.A. Squier, D.M. Asbury, and M. Leon, Phys. Lett. 81B (1979) 165.

COULOMB DISPLACEMENT ENERGIES AND NEUTRON DENSITY DISTRIBUTIONS

S. Shlomo
CEN Saclay,
France

COULOMB DISPLACEMENT ENERGIES AND NEUTRON DENSITY DISTRIBUTIONS

Shalom Shlomo
Service de Physique Théorique
C.E.A., CEN-Saclay, BP n°2, 91190 Gif-sur-Yvette, France

Abstract

We present a short review of the present status of the theory of Coulomb displacement energies, ΔE_c , discussing the Okamoto-Nolem-Schiffer anomaly and its solution. We emphasize, in particular, that contrary to previous hopes, ΔE_c does not determine r_{ex} , the root-mean square (rms) radius of the excess (valence) neutron density distribution. Instead, ΔE_c is very sensitive to the value of $\Delta r = r_n - r_p$, the difference between the rms radii of the density distributions of all neutrons and all protons. For neutron rich nuclei, such as ^{48}Ca and ^{208}Pb, a value of $\Delta r = 0.1$ fm is found to be consistent with ΔE_c . This value of Δr , which is considerably smaller than that (of 0.2 - 0.3 fm) predicted by some common Hartree-Fock calculations, seems to be confirmed by very recent experimental results.

Conférence de Kernforschungszentrum Karlsruhe
2-4 May 1979

DPh-T/79/34
Avril 1979

INTRODUCTION

The Coulomb displacement energy, ΔE_c, between analog states is the binding energy difference between a pair of nuclear states which belong to the same isobaric multiplet but whose values of the third component of the isospin differ by one unit. These states, referred to as the parent $|\pi>$, and the analog state $|A>$, are related by

$$|A> = N_1^{-1/2} T_- |\pi> \quad , \quad N_1 = <\pi|T_+ T_-|\pi>, \tag{1}$$

where T_+ and T_- are the usual raising and lowering isospin operators, respectively. Experimentally, ΔE_c is determined from the relation

$$\Delta E_c = M_{Z_>} - M_{Z_<} + \delta_{np}, \tag{2}$$

where $M_{Z_>}$ and $M_{Z_<}$ are the atomic masses (in MeV) of the members of the isobaric multiplet with the greater and the lesser charges, respectively, and $\delta_{np} = m_n - m_H = 0.782$ MeV. It is important to note that, at present[1], ΔE_c are determined with an experimental accuracy of better than 1%. In particular, for mirror states the values of ΔE_c are known to an accuracy of 0.2%. The values of ΔE_c increase from 0.764 MeV for the A = 3 system to 18.83 MeV for the analog of the ground state of ^{208}Pb.

Bethe[2] (1938) was the first to make use of ΔE_c for mirror nuclei to extract some information concerning the size of the atomic nucleus. With simplifying assumptions, such as a uniform charge density distributions of equal radii for the two mirror nuclei, ΔE_c is given classically by

$$\Delta E_c = \frac{6}{5} \frac{Ze^2}{R} \tag{3}$$

Using the experimentally known values of ΔE_c for mirror nuclei and assuming $R = r_0 A^{1/3}$, a value of $r_0 = 1.45$ fm is obtained from (3). This value for r_0 is considerably larger than that obtained from electron scattering and muonic X-ray data, which give $r_0 \sim 1.20$ fm for medium and heavy nuclei. This apparent discrepancy between the experimental data concerning ΔE_c and the charge density distribution in nuclei was explained by noticing that (3) should be corrected for the exchange Coulomb term[2,3]. Also, in the shell model picture, the analog state is obtained from the parent state by replacing a valence neutron by a proton and everything else remaining the same. Hence, expression

(3) should be replaced by

$$\Delta E_c^{dir} = \frac{e}{N-Z} \int U_c(\underline{r}) \rho_{ex}(\underline{r}) d^3r \quad , \tag{4}$$

where $U_c(\underline{r})$ is the Coulomb potential which is due to the other Z protons of the core having a density distribution $\rho_c(\underline{r})$ (which is more like a Fermi type distribution than a uniform distribution). $\rho_{ex}(\underline{r})$ in (4) is the density distribution of the N - Z valence neutrons (excess neutrons) which is generally more extended than $\rho_c(\underline{r})$. Consequently, the value of r_0 extracted from the shell model (using (4)), by reproducing the data for ΔE_c, is expected to be smaller than that obtained using (3) (in which ρ_c and ρ_{ex} are of the same shape).

About a decade ago, the existing models of nuclear structure were challenged by the increasing experimental accuracy (of better than 1%) in determining ΔE_c and r_c, the charge rms radius defined by

$$r_c^2 = \int r^2 \rho_c(\underline{r}) d^3r \quad . \tag{5}$$

Nolen and Schiffer[4] (1968) have used (4) (with $U_c(\underline{r})$ deduced from the experimentally determined $\rho_c(\underline{r})$) including the exchange term and the effect of the electromagnetic spin-orbit interaction to determine r_{ex}, the rms radius of $\rho_{ex}(\underline{r})$. They found that in order to reproduce the experimental values of ΔE_c, values of r_{ex} had to be significantly smaller (10 - 20%) than those obtained from any reasonable single particle calculation. Otherwise, the calculated ΔE_c would be smaller than the experimental ones by 5 - 10%, which is far beyond the experimental error of 1%. Figure. 1 shows the quantities necessary to evaluate (4) for the case of the ground states of the mirror nuclei ^{41}Sc - ^{41}Ca. The Coulomb potential $U_c(r)$ is deduced from the experimentally determined[5] $\rho_c(r)$, of ^{40}Ca with a corresponding rms radius $r_c = 3.487$ fm. The radial wave function of the $1f_{7/2}$ neutron orbit is obtained from

$$\left(\frac{p^2}{2m} + U(r)\right)\varphi_n = E_n \varphi_n \tag{6}$$

using a Woods-Saxon form (with $R_1 = 4.60$ fm, $a = 0.68$ fm and $U_0 = -51.2$ MeV) for U(r). This potential well is consistent with the experimental value of r_c and also reproduces the experimental value of -8.36 MeV for the $1f_{7/2}$ neutron separation energy (in ^{41}Ca). We note that the value obtained for r_{ex} of the $1f_{7/2}$ neutron orbit is 4.13fm. From (4) we find the value of 7.045 MeV for the direct Coulomb term of the interaction between the valence $1f_{7/2}$ particle

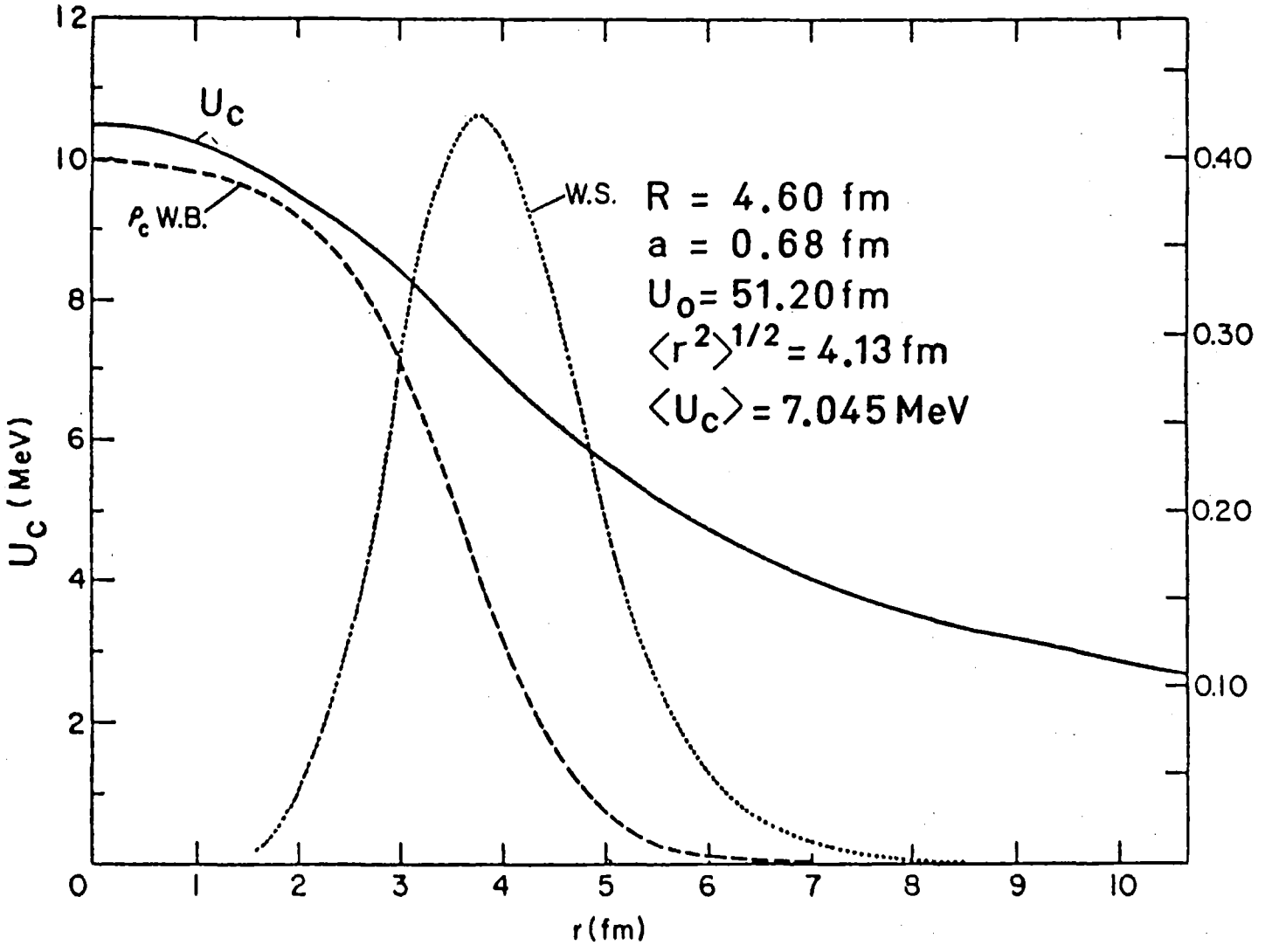

Fig. 1 Plot of the experimental charge density distribution, $\rho_c(r)$, of ^{40}Ca (wine bottle with c= 3.676 fm, a = 0.585 fm, w = -0.102 and rms radius of 3.487 fm, obtained by Frosch et al. (1968)), the corresponding Coulomb potential $U_c(r)$ of the protons in ^{40}Ca and a typical $1f_{7/2}$ radial density function $|R|^2$ with rms radius of 4.13 fm (which produces a direct Coulomb term of 7.045 MeV) obtained using a Woods-Saxon potential well. Note that the scale of the potential is on the left, that for the wave function is on the right.

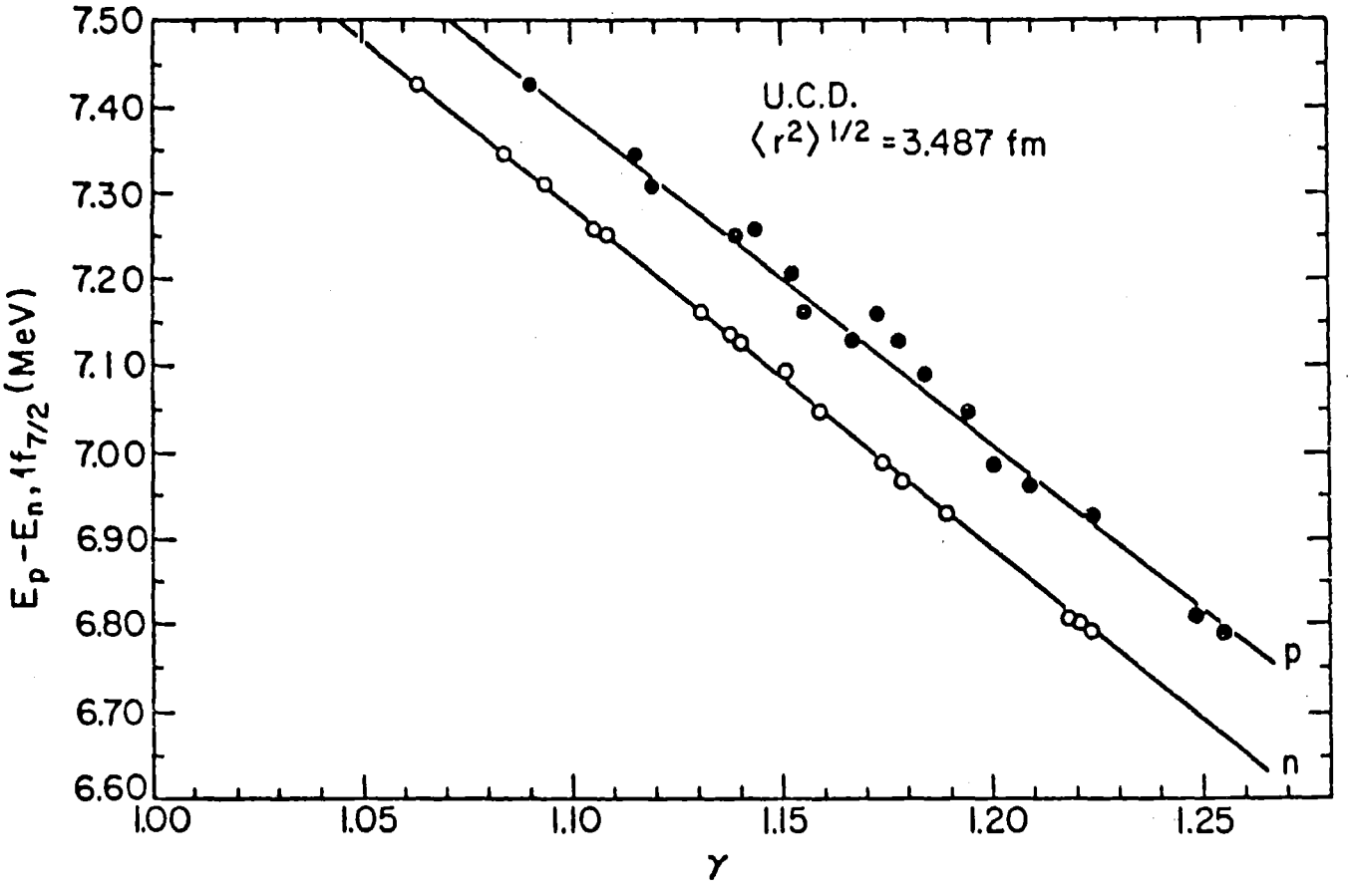

Fig. 2 Plot of $\Delta E_c(\text{dir}) = E_p - E_n$ for the $1f_{7/2}$ mirror states of ^{41}Sc - ^{41}Ca obtained with the help of eq. (8) and (6) as a function of the ratio γ between the rms radius of the $1f_{7/2}$ wave function and the rms radius of the charge distribution of ^{40}Ca. The upper line is for the proton wave function (γ_p) and the lower line is for the neutron wave function (γ_n).

with the Z = 20 protons of the core. Including the exchange Coulomb term, which is -3.7% of the direct term (-270 keV), and the contribution of the electromagnetic spin-orbit interaction (-100 keV), we find that the calculated value of ΔE_c is 6.675 MeV. This value is smaller than the experimental value of 7.28 MeV by 0.6 MeV (~9%).

Figure 2 demonstrates the fact that ΔE_c is practically determined by the rms radius of ρ_{ex}, for a fixed value of r_c. To take into account the Thomas-Ehrman effect, we redefine here the direct Coulomb term as

$$\Delta E_{dir} = E_p - E_n \quad , \tag{7}$$

where E_p is the proton single particle separation energy obtained from

$$\left(\frac{p^2}{2m} + U(r) + U_c(r)\right)\varphi_p = E_p \varphi_p \, , \tag{8}$$

and E_n is the corresponding one for the neutron, obtained from (6). In figure 2 we plot ΔE_{dir} as a function of

$$\gamma = r_{ex}(1f)/r_c \quad , \tag{9}$$

the ratio between the rms radius of the $1f_{7/2}$ neutron (or proton) orbit and the rms radius of the charge distribution of the core (^{40}Ca). The parameters of the Woods-Saxon potential U(r) were varied over a wide range, adjusting U_0 (the depth) to maintain the experimental value of E_n = -8.36 MeV. The Coulomb potential $U_c(r)$ of the core protons is that due to a uniform charge distribution with r_c = 3.49 fm. It is clear from figure 2 that ΔE_{dir} depends almost linearly on γ. Including the exchange Coulomb term and the effect of the electromagnetic spin-orbit interaction, we need a value of ΔE_{dir} = 7.60 MeV to account for the experimental value of 7.28 MeV. This is obtained, as shown in figure 2, for $\gamma \sim 1.05$ as compared to the value of $\gamma \sim 1.23$ which is obtained from reasonable shell model and Hartree-Fock calculations.

Table 1 demonstrates the fact that the problem exists for a wide range of nuclei and the discrepancy between theory and experiment increases with A. For the ground state analog of ^{208}Pb, the calculated ΔE_c is smaller than the experimental value by ~1 MeV. Okamoto has pointed out[6] that all published calculations of the ^3He - ^3H binding energy difference, in which the experimental charge density distributions were reproduced and in which the finite size of the proton charge distribution was taken into account, produce values which are

TABLE 1

Calculated Coulomb energy differences of mirror states with a finite potential well

Mirror States	Values in MeV				rms ratio[a]		
	ΔE_{dir}	Δ_{exc}	Δ_{exp}	Discrepancy	γ_p	γ_n	γ_p [b]
^{15}O - ^{15}N $1p_{1/2}^{-1}$	3.42	-0.21	3.54	0.33	1.05	1.04	0.87
^{17}F - ^{17}O $1d_{5/2}$	3.39	-0.19	3.54	0.34	1.38	1.33	1.15
^{17}F - ^{17}O $2s_{1/2}$	3.05	-0.15	3.17	0.27	1.65	1.55	1.45
^{39}Ca- ^{39}K $1d_{3/2}^{-1}$	7.05	-0.30	7.30	0.55	1.08	1.06	0.98
^{41}Sc- ^{41}Ca $1f_{7/2}$	6.85	-0.25	7.28	0.68	1.24	1.22	1.05
^{41}Sc- ^{41}Ca $2p_{3/2}$	6.55	-0.21	7.05	0.71	1.40	1.30	1.17

a) Ratio calculated using an appropriate Woods-Saxon potential.

b) Values which are in agreement with experimental Coulomb energy differences.

smaller by about 100 keV than the experimental value of 764 keV. On the experimental side, it has been shown more recently that reducing r_{ex} as a solution to the problem is highly improbable. The analysis of (i) electron scattering on isotones and neighbouring nuclei[7], (ii) magnetic scattering[8], and (iii) sub-Coulomb nuclear-transfer reactions[9] produce values for r_{ex} which are much larger than those needed to reproduce the experimental values of ΔE_c ($r_{ex} \sim 3.2$ and 4.0 fm for the $1d_{5/2}$ and $1f_{7/2}$ orbits, respectively).

This problem led to vigorous studies of previously neglected correction terms, charge dependence in the nuclear forces, the interplay between the Coulomb and the nuclear forces (second and higher order terms) and the relation between ΔE_c and the proton and the neutron densities (rms radii) in nuclei (see ref. 10 and references therein). In the following section we summarize these efforts in a systematic way, starting from a basic theory, we make a careful check of the assumptions made in the actual calculations of ΔE_c. In section 3, we present a solution to the problem and demonstrate the relation between ΔE_c and $r_n - r_p$. Section 4 is devoted to discussion and a conclusion.

2. BASIC THEORY OF ΔE_c

We start from the basic assumption that nuclei consist of interacting nucleons and obey the Schrödinger equation. Let us consider the Hamiltonians H_1 and H_2 which describe nuclei 1 and 2, respectively. Their energies are obtained by solving

$$H_1\psi_1 = E_1\psi_1 \quad \text{and} \quad H_2\psi_2 = E_2\psi_2 \ . \tag{10}$$

Here, we are interested in the energy difference

$$\Delta E_c = E_2 - E_1 \tag{11}$$

between isobaric analog states. It is not possible to obtain exact solution of (10), since the nuclear parts of H_1 and H_2 are not well known. Also the equations (10) are many particle equations. Consequently, we proceed by making the following simplifying assumptions :

Assumption 1 : Isospin T is a good quantum number and, hence, ψ_1 and ψ_2 are related by (1).

Assumption 2 : The nucleon-nucleon (NN) forces are charge independent, i.e., $[H^N, \underline{T}] = 0$.

From these assumptions it follows that

$$\Delta E_c = \langle\psi_2|H_2|\psi_2\rangle - \langle\psi_1|H_1|\psi_1\rangle = \langle\psi_2|H_2^{em}|\psi_2\rangle - \langle\psi_1|H_1^{em}|\psi_1\rangle \ . \qquad (12)$$

To carry out the calculation of (12) we assume that

Assumption 3 : The wave functions ψ_1 and ψ_2 can be well approximated by simple shell model wave-functions, which coincide with the independent-particle model (IPM) wave-functions for the simple cases of one particle or one hole outside closed shells. An underlying assumption of the simple shell model picture is that the core protons occupy exactly the same orbitals as the core neutrons and the analog state (ψ_2) is obtained from the parent state (ψ_1) by replacing a valence neutron in ψ_1 by a proton *without* perturbing the core, i.e., the cores of ψ_1 and ψ_2 are the *same*. Consenquently, ΔE_c is due to the electromagnetic interaction of the valence nucleon with those of the core, i.e. (12) is replaced by

$$\Delta E_c = \langle\psi_2|\Delta H^{em}|\psi_2\rangle \qquad (13)$$

where $\Delta H^{em} = H_2^{em} - H_1^{em}$. To simplify the calculation we also assume

Assumption 4 : The electromagnetic interaction among nucleons is well approximated by the Coulomb interaction between point protons, i.e.

$$\Delta H^{em} = \Delta H^{c} = \sum_{i<j} \frac{e^2}{r_{ij}} \ , \qquad (14)$$

and

Assumption 5 : The corresponding single-particle potential wells should be consistent with the experimental values of charge rms radii r_c of neighbouring closed-shell nuclei. To determine the size of the well we assume that

$$r_p = r_c \ , \qquad (15)$$

where r_p is the calculated shell-model rms radius of the corresponding density distribution of the protons.

Consider for example the case of $^{41}Sc - ^{41}Ca$. Within the shell-model picture, ΔE_c is due to the Coulomb interaction of the $1f_{7/2}$ proton with the $Z = 20$ protons of the core. Using the harmonic oscillator potential well, which is completely specified by the size parameter $\nu = m\omega/\hbar$, we obtain[10)]

$$\Delta E_c\,(^{41}Sc - ^{41}Ca) = (23.85 - 0.86)e^2\sqrt{\frac{\nu}{2\pi}} \qquad (16)$$

The first term in (16) is the direct Coulomb term (given by (4)) and the second term is the exchange term. We now determine the size parameter ν by making use

of (15). The experimental value of r_c for ^{40}Ca is 3.49 fm . Hence we have

$$\langle r^2 \rangle_{SM} = r_p^2 = \frac{3}{\nu} = (3.49)^2 \tag{17}$$

which gives $\nu^{-1/2} = 2.015$ fm. Substituting this value in (16) we find that $\Delta E_c(1f_{7/2}) = 6.55$ MeV, which is *smaller* than the experimental value of 7.28 MeV by about 10%. We note that within the harmonic oscillator model we have

$$\Delta E_c \propto \sqrt{\nu} \qquad \text{and} \qquad r_p \propto 1/\sqrt{\nu} \tag{18}$$

Consequently, using $\Delta E_c = 7.28$ MeV in (16) to determine ν, the calculated charge rms radius of ^{40}Ca becomes smaller than the experimental value by 10%. We emphasize that this discrepancy between theory and experiment is far beyond the experimental errors of 1% in the values of ΔE_c and r_c. A similar discrepancy is also found when using a Woods-Saxon potential or other potential wells and when applying wave functions obtained from Hartree-Fock calculations.

Therefore, looking for a solution to the problem, we consider now correction terms[10] to the simplifying assumptions made above. For simplicity we confine ourselves to several mirror nuclei with one particle or one hole outside closed shells in the A = 16 and 40 regions, and take into account correction terms which contribute more than 0.5% to ΔE_c (see ref. 10 for details). The results are summarized in Table 2. To correct for assumption 5, relation (15) is replaced by

$$\langle r^2 \rangle_{SM} + \langle r^2 \rangle_p + \langle r^2 \rangle_n - \frac{3}{2A\nu} = r_c^2 \quad , \tag{19}$$

where $\langle r^2 \rangle_p = 0.64$ and $\langle r^2 \rangle_n = -0.12$ fm^2 are, respectively the mean square radii of the proton and neutron charge density distribution and the last term in the l.h.s. of (19) is the correction due to the center of mass motion. Another effect of the finite size of the proton charge distribution is to modify the Coulomb interaction at short distance, so that e^2/r should be replaced by

$$V^{el} = \frac{e^2}{r}\,(1 + f(x)),\quad f(x) = -e^{-x}(48 + 33x + 9x^2 + x^3)/48, \quad x = \sqrt{12}\, r/0.8. \tag{20}$$

Thus, to correct for assumption 4 , we have replaced (14) by

$$\Delta H^{em} = \Delta H^{el} + \Delta H^{mag} + \Delta H^{vp} \tag{21}$$

where the magnetic interactions include the orbit-orbit, spin-orbit, spin-spin and the Darwin terms. For the case of a particle or a hole outside a LS closed shell, the contribution from the spin-orbit term dominates. ΔH^{vp} in (21) is

TABLE 2

Coulomb Energy Shift and Correction Terms (in MeV)

Contribution	$^{15}O - {}^{15}N$ $1p^{-1}_{1/2}$	$^{17}F - {}^{17}O$ $1d_{5/2}$	$2s_{1/2}$	$^{39}Ca - {}^{39}K$ $1d^{-1}_{3/2}$	$^{41}Sc - {}^{41}Ca$ $1f_{7/2}$	$2p_{3/2}$
1) Direct Coulomb	3.420	3.390	3.050	7.050	6.850	6.550
2) Exchange Coulomb	-0.210	-0.190	-0.150	-0.300	-0.250	-0.210
3) Coulomb perturbation[a]	(-0.025)	(-0.040)	(-0.070)	(-0.050)	(-0.060)	(-0.140)
4) Center of mass motion	-0.070	-0.070	-0.070	-0.040	-0.040	-0.040
5) Finite size of the proton	0.065	0.095	0.085	0.090	0.110	0.100
6) " " " " neutron	-0.035	-0.035	-0.035	-0.040	-0.040	-0.040
7) Magnetic interaction	0.100	-0.060	0.025	0.130	-0.090	-0.020
8) Vacuum polarization	0.020	0.020	0.020	0.040	0.040	0.040
9) p-n mass difference	0.025	0.035	0.035	0.025	0.035	0.035
10) Short range correlation	0.065	0.045	0.050	0.125	0.075	0.105
Total (calculated)	3.38	3.23	3.01	7.08	6.69	6.52
Experimental	3.54	3.54	3.17	7.30	7.28	7.05
Discrepancy[b]	0.16	0.31	0.16	0.22	0.59	0.53

(a) This contribution is included in the direct term.
(b) With uncertainties of 0.04 and 0.08 MeV for the A = 16 and 40 regions, respectively.

the correction due to vacuum polarization ($\sim 0.006\, e^2/r$).

Other correction terms[10] which were included in Table 2 are (i) the Coulomb perturbation effect which is known as the Thomas-Ehrman effect (most important for loosely bound orbits and orbits with small ℓ), (ii) the dynamic effect of the n - p mass difference, which takes into account the difference between the kinetic energies of a proton and a neutron in the same state, and (iii) the two-body short-range correlations which are calculated via the Bethe-Goldstone equation. We see from Table 2 that the contributions of the corrections terms are small (1-2%) and with alternating signs. Their sum does not resolve the Coulomb energy discrepancy. We note that by including the contribution of the Thomas-Ehrman effect we have improved upon assumption 1 (concerning isospin purity). The corrections describing deviation from the simple shell model prescription (assumption 3) are, in the language of perturbation theory, second and higher-order terms

$$\sum_m \frac{\langle 0|V_c|m\rangle\langle m|V_N|0\rangle}{\Delta E} + (\text{higher-order}) \quad , \tag{22}$$

which include the Coulomb, V_c, and the nuclear, V_N, interactions, each appearing (at least) once. These terms in (22) account for the interplay between the Coulomb and the nuclear forces. The short-range correlations are part of (22) and by including them in Table 2 we have only partially accounted for the assumption 3.

An important term in (22) is the effect of isospin mixing in the core suggested by Auerbach, Kahana and Weneser[11] (AKW) as a possible solution to the Coulomb energy problem. The Coulomb repulsion polarizes the N = Z core and leads to a non-vanishing proton-neutron density difference $\rho_1 = \rho_{pc} - \rho_{nc}$, which is positive at the surface region, for $r > r_1$, and negative for $r < r_1$. This induces a small symmetry potential through the isospin-dependent component of the NN interaction. In terms of perburtation theory, we are concerned with the mixing of the isovector monopole states (T = 1, J = 0) in the ground state of the N = Z system (V_c in (22) includes the core-core interactions and V_N includes the valence-core interaction). The contribution of this (AKW) effect to ΔE_c has been the subject of several investigations (see ref. 10 for details). Unfortunately, due to the lack of knowledge of the location of the isovector monopole states and the uncertainty in the isovector part of the nuclear interactions, the contribution of the AKW effect (which is about 2% of the direct Coulomb term)

is not quantitatively well established. The contribution depends strongly on the location of $\rho_{ex}(r)$ and consequently poses a significant state-dependent effect. A reasonable assessment[10] of the contributions to the ground states of the mirror nuclei with A = 15, 17, 39 and 41 produces the values of -0.15, 0.0, -0.25 and 0.1 MeV, respectively, when using the wave function applied in the calculations of Table 2. Hence, including the AKW effect we find that the discrepancies for neighbouring particle and hole states are about the same ; 0.30 ± 0.06 MeV and 0.50 ± 0.10 MeV for the A = 16 and 40 regions respectively.

There have been several calculations[10] of other certain selections of the terms (22), referred to as long-range and tensor correlations, core-polarization and configuration mixing. The calculations indicate that the contributions of these effects are not necessarily small (0-3%). However, the definitions of these effects in terms of (22) are overlapping and consequently lead to a double counting problem. The present results of these calculations (of (22)) do not seem to explain the discrepancies. Nevertheless, it should be emphasized that these calculations are rather incomplete and contain large theoretical uncertainties, due to the lack of knowledge of the response function of the nucleus and to uncertainties in the effective nuclear interaction. Consequently, it is quite likely that a reliable calculation of all the corrections (22) can resolve the Coulomb energy problem.

Let us consider now the possible contribution of charge dependent terms in the nuclear forces to ΔE_c and hence correct for the assumption 2 made above. Charge independence, which is represented by

$$[H^N, \underline{T}] = 0 \quad , \tag{23}$$

implies, assuming only two-body interactions, that $V_{nn} = V_{pp} = V_{np}$ in the T = 1 states. For a pair of mirror states, only the charge symmetry breaking (CSB) potential

$$V^{CSB} = V_{pp} - V_{nn}, \tag{24}$$

will contribute to ΔE_c, in first order, since the np interactions in both mirror states are equal. It has been suggested by Okamoto[6] that the discrepancy (of ~100 keV) for the ^{3}He - ^{3}H pair is due to CSB in the nuclear forces, and indeed this discrepancy seems to be strongest evidence for the occurence of a CSB potential. It was proposed by Negele[12] that the discrepancies in the higher mass regions are also due to a CSB potential. On the nucleon-nucleon level the

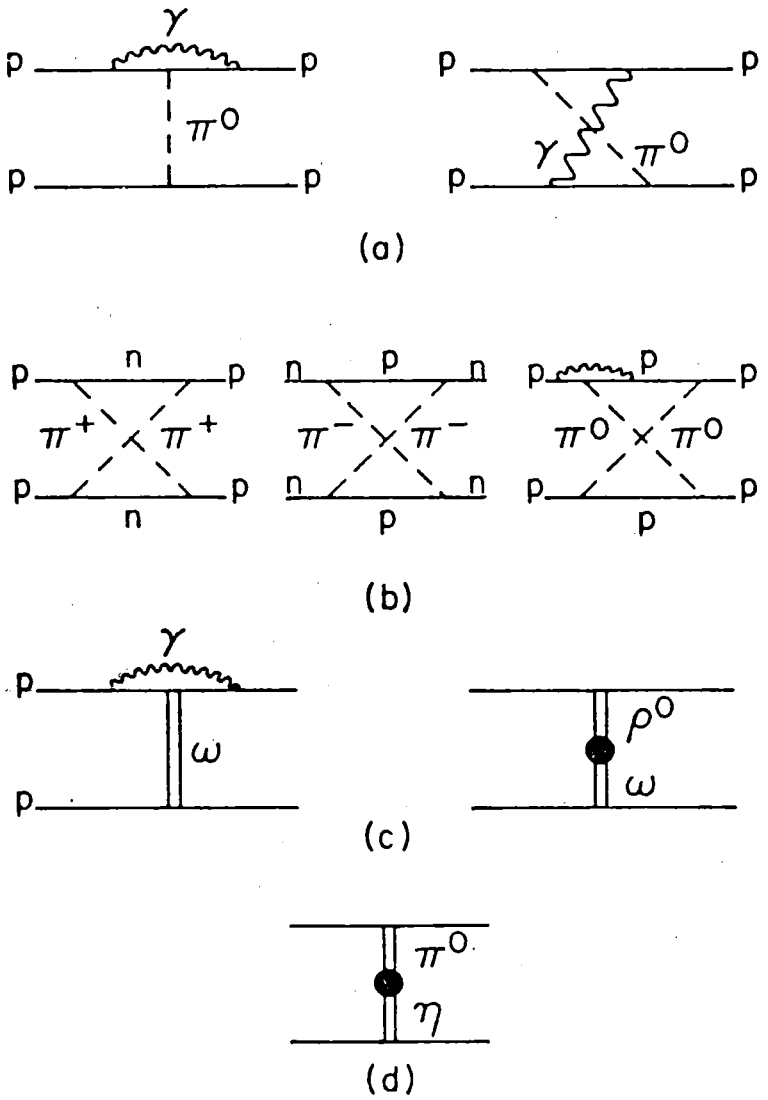

Fig. 3 Meson exchange mechanisms generating charge asymmetry in the nuclear force.

difference between the proton-proton and the neutron-neutron $^1S_0$ scattering length, $a_{pp} - a_{nn}$, was found experimentally[13] to be -0.9 ± 2.0 fm and is consistent (within the experimental error) with a CSB potential of the order of 1%. From theoretical considerations one expects[13] that indirect electromagnetic effects may induce a breaking of charge independence of the order of 1%. Figure 3 shows some meson exchange processes generating charge asymmetric in the nuclear force. The theoretical calculations of these processes are quite ambiguous due to the uncertainties in the signs and the magnitudes of the meson-nucleon coupling constants and of the isospin mixing coefficients. It is, however, of crucial importance to find out whether one can at all account for all the Coulomb energy discrepancies by a V^{CSB} which is compatible with the processes described in Figure 3.

Considering this question, Shlomo and Riska[10,14] made use of the fact that the range and the spin structure of the CSB potential, generated by an exchange mechanism, are determined by the masses and the quantum numbers of the particles exchanged in the process. Thus, one finds that the contributions of the processes of Figure 3 can be well approximated by

$$V^{CSB} = C_\pi V_\pi(r) + C_\sigma V_\sigma(r) + C_\omega V_\omega(r) \quad , \tag{25}$$

where the potentials V_π, V_σ and V_ω are due to the one π,σ and ω exchange potentials with the corresponding meson masses of 135, 550 and 783 MeV, respectively. The coefficients C, treated as free parameters, are expected to be of the order of 1%. It was concluded in this analysis[14] that it is not possible to obtain a V^{CSB} potential consistent with the requirements mentioned above. If one adjusts V^{CSB} in (25) to reproduce 100 keV for the A = 3 case, its contributions for the higher mass regions are too small to account for the discrepancies. Due to the present theoretical uncertainties in evaluating the processes of Figure 3, it is quite likely that the A = 3 problem is due to a CSB potential which is reasonably small and of short range. Its contribution to the A = 41 case is less than 200 keV (1/3 of the discrepancy). We thus conclude that contrary to previous conjecture, the Coulomb problem (for the higher mass regions) is not due to the assumption 2 made before and a closer look at assumption 3 (concerning wave functions) is called for.

3. A SOLUTION TO THE PROBLEM

We thus expect that the remaining discrepancy (more than half) between the experimental and calculated ΔE_c is due to deviations from the assumed wave functions (assumptions 1 and 3). Instead of evaluating all the correction terms (22) in a reliable and consistent way (almost an impossible task), we return to the starting equations (10) and consider the exact wave functions of the analog states. We look for the required properties, of the exact wave functions, needed to account for ΔE_c and for experimental evidence justifing these requirements.

Starting from (10) and using (1) we find that ΔE_c is given by

$$\Delta E_c = E_A - E_\pi = \frac{1}{N_1} \left(\langle\pi|T_+ H T_- |\pi\rangle - \langle\pi|T_+ T_- H|\pi\rangle\right)$$

$$= \frac{1}{N_1} \left(\langle\pi|[T_+,[H,T_-]]|\pi\rangle + \langle\pi|[H,T_-]T_+|\pi\rangle\right) \quad , \tag{26}$$

except for the Thomas-Ehrman correction[15]. The normalization constant is given by

$$N_1 = \langle\pi|T_+ T_-|\pi\rangle = 2T + (2T+2)\varepsilon^2, \tag{27}$$

where ε^2 is the amount of isospin mixing in $|\pi\rangle$, expected to be of the order of 1%, and $2T = N-Z$. Assuming pure isospin (assumption 1) we have that the last term in the r.h.s. of (26) vanishes ($T_+|\pi\rangle = 0$). If we now approximate the exact state $|\pi\rangle$ by a Slater determinant (of single particle orbits) consistent with ρ_p and ρ_n of $|\pi\rangle$, we have that the first term in the r.h.s. of (26) can be written as a sum of direct plus exchange terms, where the direct term is given by

$$\Delta E_c^{dir} = \frac{e}{N-Z} \int U_c(\underline{r})\, \Delta\rho(\underline{r})\, d^3r \quad , \tag{28}$$

with

$$\Delta\rho(r) = N\rho_n(\underline{r}) - Z\rho_p(\underline{r}) \quad , \tag{29}$$

i.e., $\Delta\rho(\underline{r})$ is the difference between the density distributions of *all* neutrons and *all* protons of the parent state. It is easily seen that (4) can be obtained from (28) by assuming $\rho_{ex}(\underline{r}) = \Delta\rho(\underline{r})$. This assumption holds in the simple shell model picture, since in this picture the core protons occupy exactly the same orbits as the core neutrons and the analog state is obtained from the parent state by replacing a valence neutron by a proton. In real nuclei, $\Delta\rho$ is expected to differ from the density distribution of the valence orbits (ρ_{ex}).

For a fixed value of r_p, the contribution of (28) is practically determined by the rms radius of $\Delta\rho$. Consequently, if $\Delta r = r_n - r_p$ is small enough (smaller than that obtained in the shell model prescription), the rms radius of $\Delta\rho$ will be smaller than r_{ex} and the value of ΔE_c^{dir} obtained from (28) will be larger than that obtained from (4). This enhancement in the calculated value of ΔE_c is obviously due to the difference between $\Delta\rho(\underline{r})$ and $\rho_{ex}(\underline{r})$.

To understand the origin of this enhancement in the calculated ΔE_c let us recall that it has been shown by Talmi and Shlomo[16] that if one *assumes* that the rms radii r_n and r_p are equal in the parent and also in the analog state,

$$r_n = r_p = r_m \quad , \tag{30}$$

then for a reasonable value of r_{ex}, in which $r_{ex} > r_p$, there is an additional term to the calculated ΔE_c which is due to the compression of the "core" Z protons in the analog state, *relative* to the parent state. In fact since the analog states are related by (1), the mass rms radius r_m of the analog state is equal to that of the parent state. Assuming (30) holds for both states, then r_p for the (Z + 1) protons in the analog state is equal to that of the parent state. Denoting by r_p' the rms radius of the density $\rho_p'(\underline{r})$ of the Z core protons in the analog state we have the relation

$$(Z+1)r_p^2 = Z\,r_p'^2 + r_{ex}^2 \tag{31}$$

Clearly, if $r_{ex} > r_p$, then $r_p > r_p'$, i.e. the core Z protons in the analog state are compressed relative to the core protons of the parent state by $\Delta r_c = r_p - r_p' > 0$. Since a shrunken core has a larger Coulomb interaction, this core-compression effect leads to an additional electrostatic term to ΔE_c. Using uniform charge distributions, this core-compression term can be approximated by

$$\Delta E_{cc} = \left(\frac{3}{5}\right)^{3/2} e^2 \frac{Z(Z-1)}{r_p} \left(\frac{\Delta r_c}{r_p}\right) \quad , \tag{32}$$

where the factor multiplying $\Delta r_c/r_p$ is the Coulomb self-energy of the core, which is of the order of ~100 MeV. Considering, for example, the case of $^{41}Sc - ^{41}Ca$, the assumption (30) implies that $r_p = 3.5$ fm is the same for both mirror nuclei. Putting the valence proton in Sc in the $1f_{7/2}$ orbit with $r_{ex} = 4.2$ fm (the shell model value), we find from (31) that the protons in the core of ^{41}Sc are compressed (relative to ^{41}Ca) by $\Delta r_c = 0.04$ fm. Using (32) we find that this corresponds to a correction of 0.8 MeV that should be added to that obtained from (4).

This core compression effect is large enough to explain the discrepancy of 0.6 MeV in the A = 41 case. The same situation was found to hold also for the other cases.

Clearly, the assumption of pure isospin which led to (28) and the assumption (30) concerning r_n and r_p are simplifying assumptions and are not expected to hold exactly. However, the main point is that these assumptions demonstrate the possible occurence of the core rearrangement effect. This means that, contrary to the shell model prescription, there is a difference between the cores of the analog states which contributes to the calculation of ΔE_c. In fact, if isospin is pure, then $\rho_n(\underline{r})$ and $\rho_p(\underline{r})$ are interchanged for a mirror pair when going from the parent to the analog state. This can be obtained using (26) and replacing H by the density operator. This result is equivalent in the simple shell model picture to the replacing of the valence neutron in the parent state by a proton to obtain the analog state. Since in this picture there is no difference between the densities of the neutrons and the protons of the core, i.e., $\rho_1(\underline{r}) = \rho_{pc}(\underline{r}) - \rho_{nc}(\underline{r}) \equiv 0$, no relative core compression occurs. In real nuclei $\rho_1(\underline{r})$ is not expected to be identically zero and if $\Delta r = r_n - r_p$ in both nuclei are smaller than the corresponding shell model values (and r_{ex} is large enough), the core-compression effect emerges. Under the assumption of pure isospin, $\rho_1(\underline{r})$ will reverse its sign going from the parent to the analog state. Of course, in a detailed calculation the isospin impurity should be taken into account.

Although the direct Coulomb term of (4) and ΔE_{cc} in (32) are quite sensitive to the value assumed for r_{ex}, their sum was found to be practically independent or r_{ex}. Thus, contrary to previous hopes, Coulomb displacement energy cannot be used to determine the value of r_{ex}, the rms radius of the valence neutrons density distribution. Instead, as it easily seen from (28), ΔE_c depends on the value assumed for $\Delta r = r_n - r_p$, and, of course, the value of r_p. This has been demonstrated recently by Friedman and Shlomo[17], applying the energy density formalism as a simple means to relate ΔE_c and Δr. The variational equations for the densities, derived by minimizing the symmetry plus the Coulomb energies, where solved for both ends of the isospin multiplet ($T_Z = \pm T$). The resulting neutron and proton densities were used to evaluate the direct Coulomb term, ΔE_d, the core compression term ΔE_{cc} and the difference between the symmetry energies of the analog states, ΔE_{sym}. Varying the parameters of the model, a rather unique relation is obtained between ΔE_c and Δr. This is demonstrated

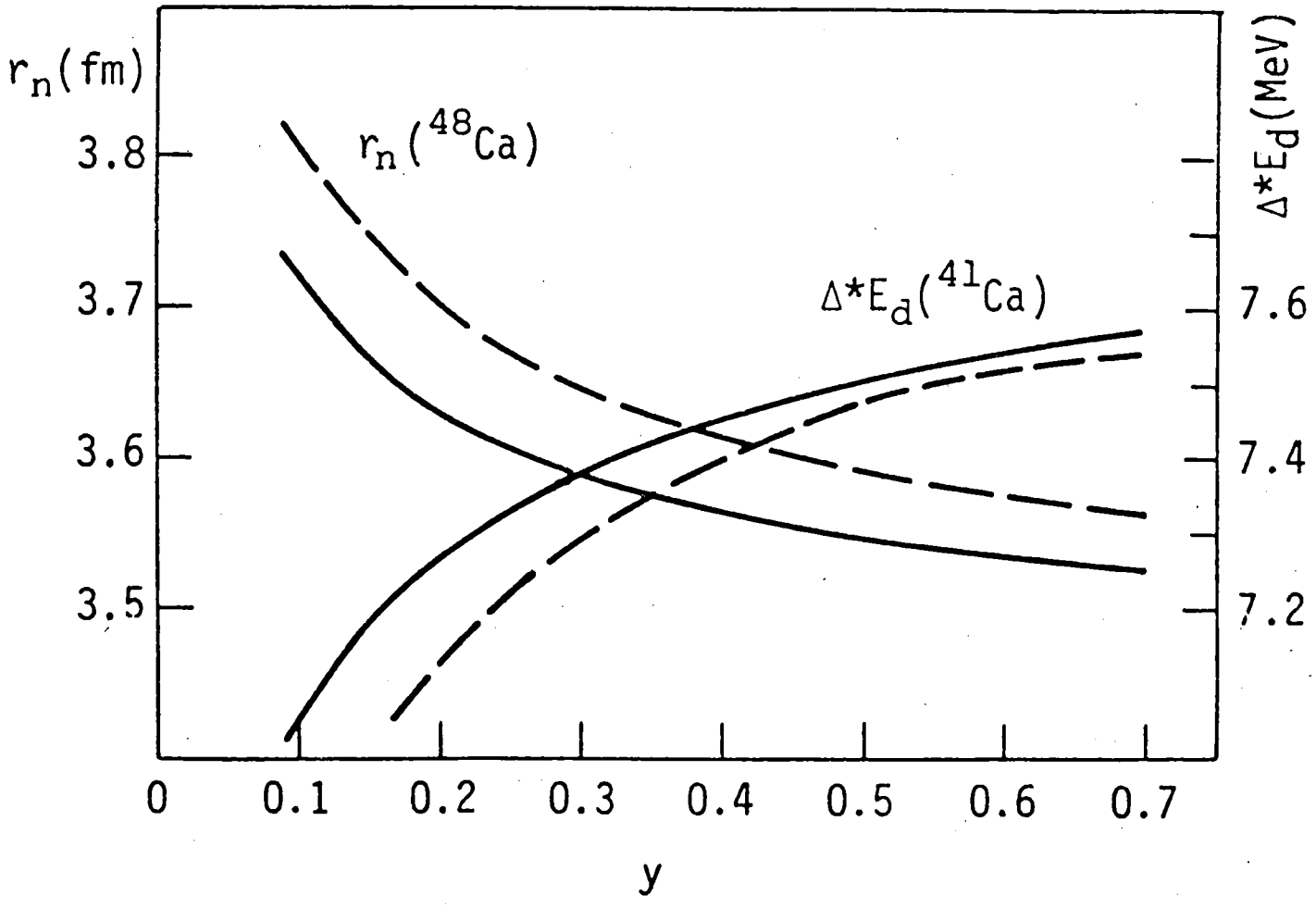

Fig. 4 Values of r_n in ^{48}Ca and the Coulomb displacement energy $\Delta^*E_d = \Delta E_d + \Delta E_{cc} + \Delta E_{sym}$ (direct Coulomb term + core compression term + change in symmetry energy) for ^{41}Ca calculated using the energy density formalism (Friedman and Shlomo 1977). y is the relative strength of the $1/\rho_m$ term in the symmetry interaction and the dashed and solid curves correspond to R_M = 5.2 fm and $R_M \to \infty$, respectively.

TABLE 3

Experimental and calculated results of nuclear radii, (in fm) and Coulomb displacement energies (in MeV) for ^{41}Ca, ^{48}Ca and ^{208}Pb analog states using the energy density formalism (Friedman and Shlomo 1977).

	^{41}Ca	^{48}Ca	^{208}Pb
Experimental			
r_p	3.508	3.487	5.487
$r_n - r_p$	-0.02±0.02	0.08±0.06	0±0.1
r_{ex}	4.0±0.1	4.0±0.1	6.15±0.1
ΔE_c	7.279±0.005	7.190±0.011	18.834±0.009
Calculated			
$r_n - r_p$	-0.002	0.082	0.040
Δr_c	0.013	0.010	0.005
ΔE_d	7.14	7.15	18.87
ΔE_{cc}	0.35	0.31	0.66
ΔE_{sym}	0.05	0.00	-0.05
ΔE correc[a)]	-0.27	-0.27	-0.40
ΔE_c[b)]	7.27±0.1	7.19±0.1	19.08±0.2

a) The corrections include: exchange Coulomb term, electromagnetic spin-orbit, vacuum polarization and dynamic effect of n-p mass difference.

b) The uncertainty results from the uncertainty in ΔE_{sym} and the correction terms (exchange Coulomb term). The uncertainties in the other quantities, such as $r_n - r_p$, were not taken into account.

in Figure 4. Table 3 shows some details of the calculation for the analog states of ^{41}Ca, ^{48}Ca and ^{208}Pb, adjusting the model to account for the experimental value of ΔE_c for ^{48}Ca. We see that the value of ΔE_c in ^{48}Ca is reproduced if $\Delta r = 0.08$ fm. This value of Δr is much smaller than that obtained by some common[18] Hartree-Fock calculations ($\Delta r \simeq 0.20$ fm) or the shell model prescription ($\Delta r = 0.30$ fm).

Very recently, some experimental data of hadron scattering seem to support this prediction that Δr in nuclei (particularly neutron rich nuclei) are significantly smaller than those predicted by the common Hartree-Fock calculations or shell model prescription (see ref. 19 and references therein). These data show that $\Delta r = r_n - r_p$ in ^{48}Ca and ^{208}Pb is about 0.10 fm, in good agreement with the prediction of ΔE_c as can be seen from Table 3. The very recent results of electron scattering at backward angles (magnetic scattering) which indicate[20] that r_{ex} in nuclei are somewhat smaller than the common Hartree-Fock prediction also support the present conclusion since a smaller r_{ex} indicates a smaller value for Δr. It should be emphasized that the amount of the core compression effect depends on the values taken for Δr and r_{ex}. It decreases with the increase of Δr and the decrease of r_{ex}. Considering the experimental values of $\Delta r = 0.08$ fm and $r_{ex} = 4.0$ fm for ^{48}Ca, shown in Table 3, we have a relative core compression of only 0.01 fm, as compared to 0.04 fm found if $\Delta r = 0$ and $r_{ex} = 4.2$ fm. Clearly, more accurate data concerning Δr, in particular, will help clear up the situation.

4. DISCUSSION AND CONCLUSION

We have discussed the theory of Coulomb displacement energies in nuclei considering, in particular, the solution to the long-standing Coulomb energy problem. Starting from a basic theory we have considered the simplifying assumptions which are usually adopted in the conventional calculation of ΔE_c. We found that it is most likely that the major part of the discrepancy between the calculated and experimental ΔE_c, in medium and heavy nuclei, is due to the assumption adopted for the wave-functions. More specifically, it is due to the assumption that the analog state is obtained from the parent state by replacing a valence neutron by a proton *without disturbing the core*. Considering mirror nuclei and assuming pure isospin, we have that $\rho_n(\underline{r})$ and $\rho_p(\underline{r})$ are interchanged when going from the parent to the analog state. Consequently, $\rho_1(\underline{r}) \simeq \rho_{pc}(\underline{r}) - \rho_{nc}(\underline{r})$ will change sign going from the parent to the analog state. Of course, the assumption of pure isospin is somewhat extreme. Still, it is reasonable to expect that the valence neutron affects the neutrons' core density differently that it affects

the protons' core density and vice versa for the valence proton. Hence the cores of the parent and the analog state differ, i.e., $\rho_1(\underline{r})$ in both states is not the same. This core rearrangement effect should be included in the calculation of ΔE_c. If the values of $\Delta r = r_n - r_p$ are small enough and r_{ex} is relatively large(larger than r_c), a compression of the core protons of the analog state *relative* to the parent core takes place, leading to an electrostatic correction to ΔE_c that helps resolve the anomaly.

We have emphasized in the last section that under the assumption of pure isospin, the direct Coulomb term is given by (28), in terms of $\Delta\rho = N\rho_n(\underline{r}) - Z\rho_p(\underline{r})$. The core rearrangement term is included in this formulation of (28), since we have used the relation (1). Thus, in a simplifying way, we can say that the origin of the Coulomb energy problem is due to the assumption $\rho_{ex}(\underline{r}) = \Delta\rho(\underline{r})$ which is adopted when (4) is used to evaluate the direct Coulomb term. The solution to the problem is simply given by the use of (28) with (most importantly) a relatively small value of Δr that leads to large enough value for the direct Coulomb term. Of course, in a more detailed calculation, correction terms, such as the exchange Coulomb term and the last term in the r.h.s. of (26), should be added to (28) for obtaining ΔE_c. It can be stated that it makes no difference whether (4) or (28) is used as a starting point for calculating ΔE_c as long as one takes into account all the corresponding corrections in a reliable and consistent way. However, using (28) is more preferable since. (i) It shows that ΔE_c depends on $\Delta r = r_n - r_p$ and not on r_{ex} and hence r_{ex} need not be small to account for ΔE_c. (ii) It takes into account the core rearrangement effect. (iii) It solves the problem in a simple way and gives a prediction for Δr in neutron rich nuclei, providing a check on various models for $\rho_n(\underline{r})$ (and $\rho_p(\underline{r})$). For the analog state of the ground state of ^{48}Ca (and ^{208}Pb) the value of $\Delta r \simeq 0.10$ fm is found to be consistent with ΔE_c. This value of Δr agrees with recent experimental results and is significantly smaller than that predicted by common Hartree-Fock calculations ($\Delta r \sim 0.20$ fm). Another problem with these calculations seems to be that the predicted values of r_{ex} are somewhat larger than the experimental results. These discrepancies in the values of ΔE_c, Δr and r_{ex} fit into a consistent picture indicating the missing of some effective neutron-proton attractions, if one *requires* that $\rho_n(\underline{r})$ and $\rho_p(\underline{r})$ of the exact wave-functions be reproduced by the Hartree-Fock wave-functions.

In conclusion, although the Coulomb energy anomaly for the ^3He - ^3H case

can be explained by CSB in the nuclear forces, this effect can explain less than half of the discrepancy in heavier nuclei. The remaining part of the discrepancy results from the approximations adopted for the wave functions. It can be corrected by the use of (28) instead of (4) with relatively small values of Δr. Clearly, more accurate experimental data concerning Δr (and r_{ex}) in neutron rich nuclei will help establish this (suggested) solution to the Coulomb energy problem.

ACKNOWLEDGEMENTS

The author would like to thank M. Anastasio for carefully reading of the manuscript.

REFERENCES

(1) W. J. Courtney and J. C. Fox, Atomic Data and Nucl. Data Tables 14 (1974) 479

(2) H. A. Bethe, Phys. Rev. 54 (1938) 436 ; H. A. Bethe and R. F. Bacher, Rev. Mod. Phys. 8 (1936) 82

(3) L. N. Cooper and E. M. Henley, Phys. Rev. 92 (1953) 801

(4) J. A. Nolen Jr. and J. P. Schiffer, Ann. Rev. Nucl. Sci. 19 (1969) 471

(5) R. F. Frosch et al., Phys. Rev. 174 (1968) 1380

(6) K. Okamoto, Phys. Lett. 11 (1964) 150 ; K. Okamoto and C. Pask, Ann. of Phys. 68 (1971) 18

(7) W. J. Gerace and G. C. Hamilton, Phys. Lett. 39B (1972) 381 ; J. Heisenberg et al., Phys. Rev. C6 (1972) 381 ; I. Sick et al., Phys. Lett. 39B (1972)443

(8) T. W. Donnelly and J. D. Walecka, Nucl. Phys. A201 (1973) 81 ; P. K. A. de Witt Huberts et al., Phys. Lett. 71B (1977) 317

(9) E. Friedman, Phys. Rev. C8 (1973) 996 ;
E. Friedman et al., Phys. Rev. C9 (1974) 2340 ;
H. J. Korner and J. P. Schiffer, Phys. Rev. Lett. 27 (1971) 1457 ;
G. D. Jones et al., Nucl. Phys. A230 (1974) 173 ;
J. L. Durrell et al., Nucl. Phys. A269 (1976) 443

(10) S. Shlomo, Rep. Prog. Phys. 41 (1978) 957

(11) E. H. Auerbach, S. Kakana and J. Weneser, Phys. Rev. Lett. 23 (1969) 1253

(12) J. W. Negele, Nucl. Phys. A165 (1971) 305 ; Invited talk, Int. Conf. on Nuclear Structure and Spectroscopy, Amsterdam 1974

(13) E. M. Henley, Isospin in Nuclear Physics, ed. D. H. Wilkinson (North-Holland, Amsterdam, 1969) ; E. M. Henley and D. H. Wilkinson, Few Particle Problems in the Nuclear Interaction, ed. I. Slaus (North-Holland, Amsterdam, 1972)

(14) S. Shlomo and D. O. Riska, Nucl. Phys. A254 (1975) 281

(15) N. Auerbach, J. Hüfner, A. K. Kerman and C. M. Shakin, Rev. Mod. Phys. 44 (1972) 48

(16) S. Shlomo, Ph D Thesis, Weizmann Institute 73/21 Ph

(17) E. Friedman and S. Shlomo, Z. Physik A283 (1977) 283

(18) J. W. Negele, Phys. Rev. C1 (1970) 1260 ;
D. Vatherin and D. Brink, Phys. Rev. C5 (1972) 626

(19) S. Shlomo and E. Friedman, Phys. Rev. Lett. 19 (1977) 1180 ;
S. Shlomo and R. Schaeffer, Phys. Lett. B to be published.

(20) I. Sick et al., Phys. Rev. Lett. 38 (1977) 1259 :
P. K. A. de Witt Huberts et al., Phys. Lett. 71B (1977) 317.

NEUTRON DENSITIES OF CALCIUM ISOTOPES

J. Brissaud and X. Campi
Institut de Physique Nucléaire,
Orsay, France

NEUTRON DENSITIES OF CALCIUM ISOTOPES

I. Brissaud and X. Campi*

Institut de Physique Nucléaire
B.P. 1, 91406 Orsay Cedex - France

The 600 MeV data of proton elastic scattering on ^{40}Ca [1] and the 1 GeV data of elastic scattering on $^{40\text{-}42\text{-}44\text{-}48}Ca$ [1,2] have been analyzed in the framework of the Glauber multiple scattering approximation in its optical limit. The effective pp and pn elementary scattering amplitudes we used were obtained from a fit of medium energy p-^{4}He scattering data using the same Glauber approximation [3]. The neutron densities are extracted from the data in an approximately model-independent form. Following the method developed in ref.[4] for charge densities in electron scattering, we divide the neutron density into two parts $\rho_n(r) = \rho_0(r) + \rho_1(r)$, where ρ_0 is arbitrary (it could be a Gaussian or a Fermi function) and ρ_1 is a correction which is expressed as a truncated Fourier series based on an interval $0 \leqslant r \leqslant R$:

$$\rho_1(r) = \sum_{m=1}^{L} \frac{2\beta_m}{rR} \sin\left(\frac{m\pi r}{R}\right) \qquad (1)$$

The outer radius R is chosen at the outer edge of the density, where ρ_0 is small and comparable with the uncertainties in its determination. The maximum number of coefficients L which can be determined is a function of the range of the momentum transfer in the analyzed data and the absorption of the projectile by the nuclear medium. The coefficients β_m are determined by minimizing the mean square error χ^2 between the experimental data and the

---

*Division de Physique Théorique, Laboratoire associé au CNRS

calculated differential cross sections. The procedure [5] is iterative, at the end of each iteration (i) the correction $\rho_1^{(i)}$ is added to $\rho_0^{(i)}$ to define a new "guess" density $\rho_0^{(i+1)}$. In that way the influence of the starting density $\rho_0^{(1)}$ on the final results is minimized. This method is much faster and systematic than the "trial and error" method used in ref.[6] . The procedure determines both the coefficients β_m and their mean square error, related to the purely statistical error of the experimental data. These errors are transformed into real space and provide a statistical error envelope for the fitted neutron density. The contribution of target protons to the scattering has been taken into account by using the proton densities deduced from electron scattering [8,9]. The effects of finite proton size, electromagnetic neutron form factor and electromagnetic spin-orbit coupling have been eliminated from the experimental charge densities. A more detailed description of the iterative method is given in ref.[5] . A similar technique was already used in the analysis of α-nucleus scattering [7] to determine the optimum real part of the phenomenological optical potential.

In the present analyses we have used at 600 MeV 94 data points for ^{40}Ca ($q_{max} \simeq 2.15$ fm^{-1}) and at 1 GeV 39 and 53 data points for ^{40}Ca ($q_{max} \simeq 2.1$ and 2.5 fm^{-1}), 55 for ^{42}Ca ($q_{max} \simeq 2.6$ fm^{-1}), 55 for ^{44}Ca ($q_{max} \simeq 2.6$ fm^{-1}) and 35 for ^{48}Ca ($q_{max} \simeq 2.10$ fm^{-1}). The results we have obtained for the neutron densities of ^{40,44,48}Ca are summarized in figures 1 and 2. The shaded areas (fig.1) or the areas covered by curves of the same type indicate the envelope of the different densities which give an agreement with the N experimental data points with $\chi^2/N \leqslant 1.3$. This upper bound of acceptable densities is somewhat arbitrary. It is fixed according to the best fit that can be obtained with conventional 3-parameters Fermi functions, i.e. give an idea of the range in

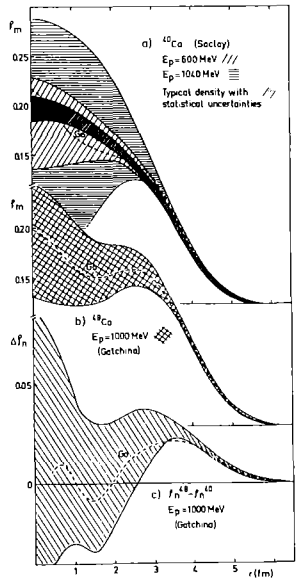

- Fig.1 -

which the densities are as good as the traditional specific functional forms. The upper and lower bounds of the densities are generated by changing R and L in the series of eq.1 within large bounds ($6 \leqslant R \leqslant 14$ fm and $5 \leqslant L \leqslant 10$). Our method of exploring the allowed regions of the densities is less restrictive than one used in ref.[10] in the analysis of 800 MeV proton elastic scattering data on $^{40,48}Ca$ which give optimistically small error envelopes.

The main results we have obtained in the present analyses are the following :

a) The neutron densities are not determined in the nuclear interior. This insensitivity is mainly due to the absorption of the projectile by the nuclear matter. These results are in agreement with the predictions of ref.[11]. b) Comparing the uncertainty envelope for ^{40}Ca at 600 MeV to that at 1 GeV (fig.1a) one sees that it follows the trend of the absorptive part of the elementary NN amplitude. From that point of view, the lowest energy compatible with the validity of the theory of scattering would provide the best determination of the densities. c) Eliminating in the analysis of ^{40}Ca the high momentum transfer data ($2 \leqslant q \leqslant 2.5$ fm^{-1}) (see figs. 1a and 2) the error envelopes increases by about 50 %. d) The indetermination arising from the purely statistical uncertainties in the experimental data is much smaller than the one produced by other sources of indetermination (shaded are in the middle of fig.1a). This is in marked contrast with the electron scattering analysis. e) The r.m.s. radii of neutron densities (point-like nucleons) follow approximately the low $r_n \simeq .98\ A^{1/3}$. We have used the point-like proton density radii deduced from the charge radii of ref.[13]. f) The surface thickness of the mass density ($\rho_n + \rho_p$) (see ref.[12] for the definition) is larger for the open shell nuclei $^{42-44}Ca$ than

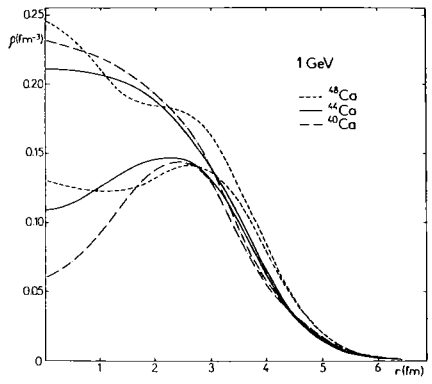

- Fig.2 -

for $^{40-48}Ca$.

A	r_n(fm)	a_M(fm)
40	3.38 ± 0.04	0.47 ± 0.02
42	3.42 ± 0.04	0.54 ± 0.02
44	3.49 ± 0.05	0.51 ± 0.02
48	3.58 ± 0.04	0.45 ± 0.02

[1] Report DPh-N-ME 78.1, edited by G. Bruge (Saclay) 1978 and to be published in Journal de Physique (France).

[2] G. Alklazov et al., Report 218 Gatchina, USSR (1976) and Phys. Lett. 57B (1975) 47.

[3] J.P. Auger and R. Lombard, to be published and Ann. of Phys. 115 (1978) 442.

[4] J.L. Friar and J.W. Negele, Nucl. Phys. A212 (1978) 93.

[5] I. Brissaud and X. Campi, submitted to publication and Report IPNO/TH 79-11 (Orsay) 1979.

[6] I. Brissaud and M.K. Brussel, Phys. Rev. C15 (1977) 452.

[7] E. Friedman and C.J. Batty, Phys. Rev. C17 (1978) 34, E. Friedman, H.J. Gils, H. Rebel and Z. Majka, Phys. Rev. Lett. 41 (1978) 1220.

[8] I. Sick, Phys. Lett. 53B (1974) 15.

[9] B. Frois et al., private communication.

[10] L. Ray, Preprint LA-UR-79.93 (1979).

[11] H.O. Meyer, Phys. Rev. C17 (1978) 1116.

[12] X. Campi, this conference.

[13] H.D. Wohlfahrt et al., Phys. Lett. 73B (1978) 131.

DETERMINATION OF MATTER RADII IN THE Ca REGION THROUGH LOW-ENERGY α-PARTICLE SCATTERING

F. Michel
University of Mons,
Belgium

DETERMINATION OF MATTER RADII IN THE Ca REGION THROUGH LOW-ENERGY α-PARTICLE SCATTERING

F. Michel★
Division de Physique Théorique☆
Institut de Physique Nucléaire
F-91406 ORSAY Cedex - France

Although low-energy α-particle scattering from medium weight nuclei has long been referred to as a strong absorption process, it is now known that, for some targets at least, the large angle cross sections are not only sensitive to the tail of the interaction potential, but also to its surface and interior regions[1,2] : notch tests[3] performed by Delbar et al[1] indicate that α-particle scattering from ^{40}Ca at E_α = 36.2 MeV is sensitive to modifications of the potential between 2 and 7 fm; Put[2] likewise showed scattering from ^{90}Zr at 40 MeV to be sensitive to the range 4-9 fm. This is illustrated for ^{40}Ca and ^{44}Ca in fig.1 where the effect of modifying the real part of an optical potential fitting the 29 MeV data on the whole angular range is displayed : this figure shows the ratio of χ^2 to the best fit χ^2_{min} as a function of the radius R of the distortion factor multiplying the real potential :

$$f(r;R) = (1 + f_o \exp(-((r-R)/a)^2)), \qquad (1)$$

where f_o=.1 and a=1 fm. Most of the effect is due to the large angle data, as can be seen for ^{44}Ca where the same modification was carried out with a data set truncated to θ= 90° (fig.1).

A convincing explanation of this sensitiveness has recently been put forward by Brink and Takigawa[4] who have shown in a

---

★ Permanent address : Faculté des Sciences, Université de l'Etat, B-7000 Mons, Belgium.

☆ Laboratoire associé au C.N.R.S.

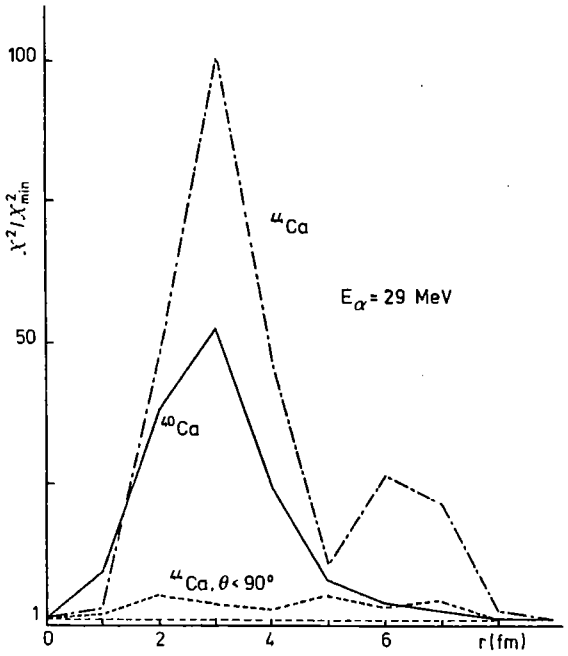

Fig.1.

semi-classical calculation of barrier penetration effects that the wave reflected at the most internal turning point of the effective potential can give an appreciable contribution to the elastic cross section at large angles when the absorption is moderate, this internal contribution being even responsible for the strong enhancement (commonly referred to as ALAS (see, e.g., ref.5)) observed in the backward hemisphere for ^{40}Ca and other nearby targets. An example of this semi-classical decomposition is displayed in fig.2. for ^{40}Ca (α,α) at 36.2 MeV[1] : σ_{SC} is the semi-classical cross section (which closely reproduces the results of a full quantal calculation), σ_B and σ_I denoting respectively the barrier cross section (which is seen to be dominant at small angles) and the internal cross section (which accounts for most of the full cross section beyond 120°). The corresponding amplitudes f_B and f_I are seen to interfere strongly at intermediate angles, making the full elastic cross section very sensitive to minor modifications of the potential, even at small distances. It thus appears that low-energy α-particle elastic cross sections are liable to provide information on the

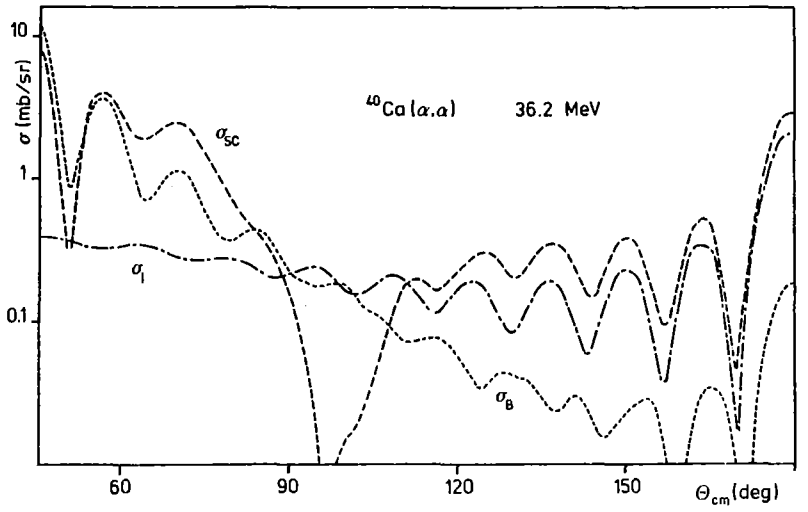

Fig.2.

interior region of the interaction potential if large angle data are considered and if the absorption is weak enough not to damp out completely the internal contribution σ_I (in that latter case, which is typical of scattering from heavy targets like ^{208}Pb, the cross section is completely insensitive to the interior and surface regions of the potential and the well-known "continuous ambiguities" set in).

These considerations have prompted us to undertake a detailed investigation of low-energy α-particle scattering from ^{36,40}Ar, ^{40,42,44,48}Ca on the whole angular range[6]; to avoid enforcing unphysical constraints on the interaction potential, we performed a "model-independent" analysis similar to those recently carried out at higher energy by Brissaud and Brussel[7], Friedman and Batty[8] and Friedman, Gils, Rebel and Majka[9], and also by Put and Paans[2] for ^{90}Zr between 40 and 141.7 MeV. The technique we used is essentially similar to that of ref.2, i.e. the real part of the potential was represented as a spline function[10] between 0 and 9 fm in 1 fm steps, the imaginary part of the potential being parametrized by means of a squared Woods-Saxon form factor. Elimination of the residual "discrete ambiguities" was obtained in the case of ^{40}Ca by requiring[2] a smooth connection between the low-energy potentials and the unique family fitting the high-energy data[11]. The main results of the analysis[6] are summarized here below :

- the low-energy ^{40}Ca potentials fitting the recent SIN data[12] display a smooth energy behaviour; their volume integrals per nucleon pair $J_v/4A$ and r.m.s. radii $\langle r^2 \rangle^{1/2}$ turn out to be well defined quantities, especially at low energies ($22 \leqslant E_\alpha \leqslant 34$ MeV) where typical fluctuations from energy to energy do not exceed 4 MeV. fm^3 and 0.02 fm respectively. The error band corresponding to an increase of χ^2 per degree of freedom of one unit is shown in fig.3; the real potential remains very poorly determined between 0 and 1.5 fm, as is also the case at higher energy[9].

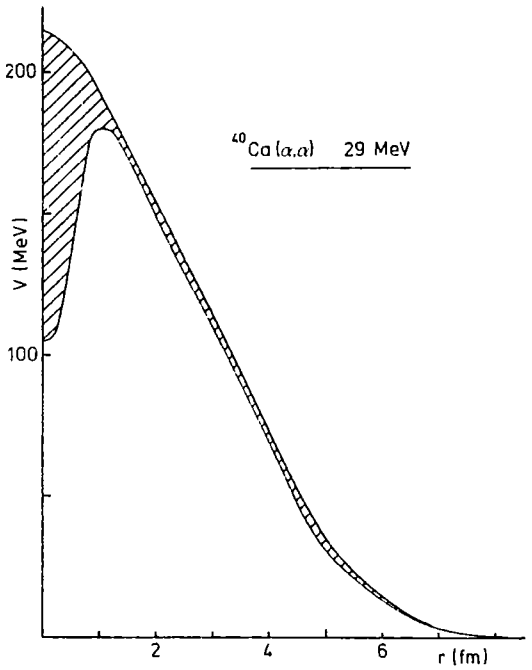

Fig.3.

- Although experiment shows spectacular changes in the backward hemisphere as a function of mass number for a fixed incident energy, an accurate description of the 29 MeV $^{36,40}Ar$, $^{42,44,48}Ca$ data[13] was achieved (fig.4), resulting in real potentials displaying a smooth A-dependence (fig.5); their volume integrals per nucleon pair do not vary by more than 3% with respect to the ^{40}Ca value, their r.m.s. radii increasing regularly with A.

It is tempting to try linking the changes seen in r.m.s. radii of the derived potentials, which seem to be determined with good accuracy, with changes in the r.m.s. radii of the corresponding matter distributions. It is well known[14] that, within the

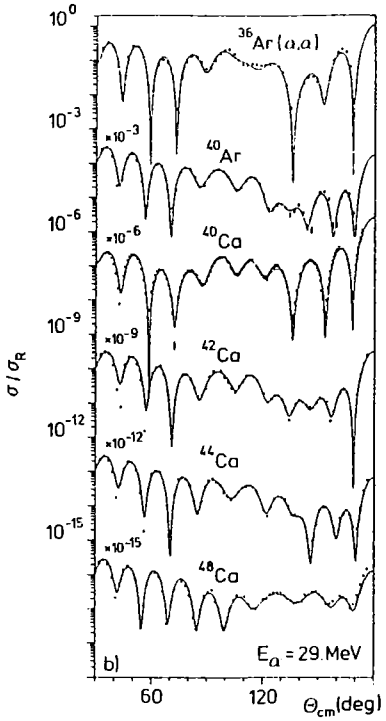

Fig.4.

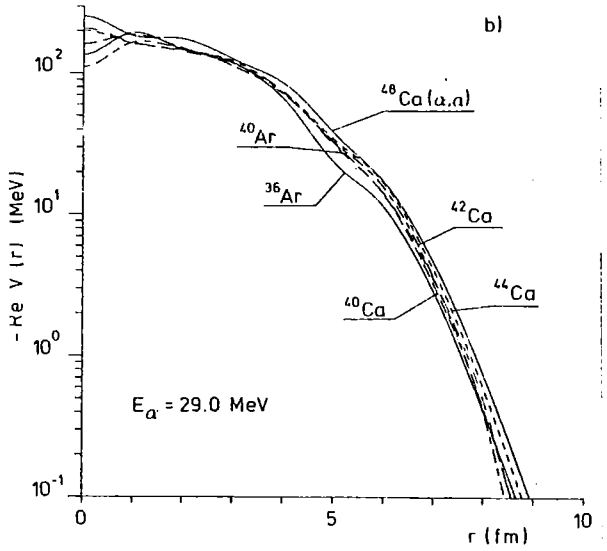

Fig.5.

frame of the usual folding model, the volume integral of the real potentials per pair of nucleons is independent of the target, and that its mean square radius is equal to the sum of the m.s. radius of the matter distribution and a constant (equal to the m.s. radius of the (density independent) effective nucleon-alpha interaction in the case of a single folding model description); differences between m.s. radii of the real potentials for two different targets are thus identical to the differences between the m.s. radii of the corresponding matter distributions[6,9]. It is interesting to inquire to what extent this result is affected when the potential is calculated within the frame of refined folding models including one nucleon exchange and/or density dependence of the effective interaction[15,16,17]. Fig.6 shows the m.s. radius of potentials calculated for nuclei between ^{28}Si and ^{64}Ni[17] within N. Vinh Mau's model[16] (which includes one nucleon exchange) as a function of the input m.s. matter radii, taking ^{40}Ca as a reference nucleus; the calculations were performed with Brink and Boeker's density independent interaction B1[18] and with the density dependent interaction G-o of Campi, Sprung and Banerjee[19] (within two different approximations[17]). All points are seen to

fall reasonably near to the bisector where they would be located in a usual folding model calculation, especially if we restrict to nuclei not too far from ^{40}Ca.

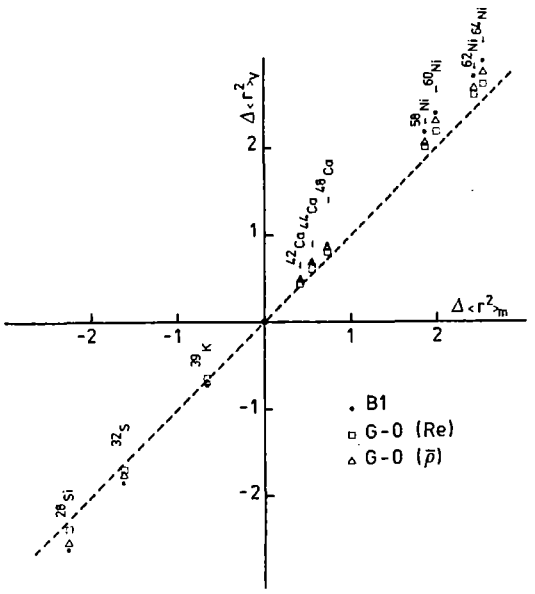

Fig.6.

We therefore calculated the matter radii of the targets considered in this study using the usual folding model prescription[6,9] taking ^{40}Ca as a reference nucleus; the neutron radius of ^{40}Ca was assumed to be equal to its experimentally determined proton radius of 3.39 fm[20]. This led us to the matter radii listed in table I; the radius found for ^{36}Ar (3.21±0.06 fm) is compatible with the proton radius recently determined by Finn et al[21] $\langle r^2\rangle_p^{1/2}$=3.23 fm. On the other hand, the difference between the ^{48}Ca and ^{40}Ca matter radii (+0.10±0.06 fm) is in good agreement with the difference found by Friedman et al. at higher energy[9] (+0.12±0.06 fm); it is also consistent with the recent determinations of the Saclay[22] and Gatchina[23] groups using 1 GeV (p,p) scattering. The corresponding r.m.s. neutron radii were also calculated from the relation $A\langle r^2\rangle_m = N\langle r^2\rangle_n + Z\langle r^2\rangle_p$, where $\langle r^2\rangle_p^{1/2}$ was taken from ref. 21 for ^{36,40}Ar, ref. 20 for ^{40}Ca and from the recent work of Wohlfahrt et al.[24] for ^{42,44,48}Ca; they can be found in table I, together with the differences Δ between the r.m.s. neutron and proton radii. The latter are found to be consistent with zero for ^{36}Ar and ^{42}Ca. Differences Δ of +0.20±0.09 fm and +0.14±0.09 fm were found for

Target	$\langle r^2 \rangle_v^{1/2}$	$\langle r^2 \rangle_m^{1/2}$	$\langle r^2 \rangle_m^{1/2} - \langle r^2 \rangle_{m,^{40}Ca}^{1/2}$	$\langle r^2 \rangle_p^{1/2}$	$\langle r^2 \rangle_n^{1/2}$	Δ
^{36}Ar	4.06	3.21	-0.17	3.23 [1]	3.18	-0.05
^{40}Ar	4.21	3.40	+0.01	3.30 [1]	3.50	+0.20
^{40}Ca	4.20	3.39	0	3.39 [2]	3.39	0
^{42}Ca	4.23	3.43	+0.04	3.42	3.43	+0.01
^{44}Ca	4.28	3.49	+0.11	3.44 [3]	3.53	+0.09
^{48}Ca	4.28	3.49	+0.10	3.41	3.55	+0.14
Est. Error	±0.03	±0.06	±0.06		±0.09	±0.09

1) J.M. Finn et al. - Nucl. Phys. A 274 (1976) 28

2) R.F. Frosch et al. - Phys. Rev. 174 (1968) 1380

3) H.D. Wohlfahrt et al. - Phys. Lett. 73B (1978) 131

Table I. (all lengths in fm)

^{40}Ar and ^{48}Ca respectively : this last estimate is again consistent with the high energy (α,α)[9] and (p,p) results[22,23], as well as with most of the recent HF calculations performed with density dependent interactions (see app. C of ref. 22); it would be interesting to have an independent determination of the neutron skin thickness for ^{40}Ar.

1) Th. Delbar et al- Phys. Rev. C18 (1978) 1237.

2) L.W. Put and A.M.J. Paans- Nucl. Phys. A 291 (1977); L.W. Put- Proc. Conf. on Microscopic Optical Potentials, Hamburg, Germany, September 25-27, 1978, ed. by H.V. von Geramb (Springer-Verlag, Berlin, 1979), p. 302.

3) P.J. Moffa et al.- Phys. Rev. C13 (1976) 147.

4) D.M. Brink and N. Takigawa- Nucl. Phys A279 (1977) 159.

5) Proc. Second Louvain-Cracow Seminar on the Alpha-Nucleus Interaction, Louvain-la-Neuve, Belgium, June 5-7, 1978, to be published.

6) F. Michel and R. Vanderpoorten- Phys. Lett. 82B (1979) 183.

7) I. Brissaud and M.K. Brussel- J. Phys. G3 (1977) 481.

8) E. Friedman and C.J. Batty- Phys. Rev. C17 (1978) 34.

9) E. Friedman et al.- Phys. Rev. Lett. 41 (1978) 1220.

10) J. Borysowicz and J.H. Hetherington- Phys. Rev. C7 (1973) 2293.

11) D.A. Goldberg- Phys. Lett. 55B (1975) 59.
12) H.P. Gubler et al.- Phys. Lett. 74B (1978) 202.
13) G. Gaul et al.- Nucl. Phys. A137 (1969) 177.
14) D.C. Weisser et al.- Phys. Rev. C2 (1970) 544.
15) B. Sinha- Phys. Rev. C11 (1975) 1546; Z. Majka et al.- Phys. Rev. C18 (1978) 114; Z. Majka et al.- Z. Phys. A288 (1978) 139.
16) N.Vinh Mau- Phys. Lett. 71B (1977) 5.
17) N. Vinh Mau, M. Lassaut, F. Duggan and F. Michel- to be published.
18) D.M. Brink and E. Boeker- Nucl. Phys. A91 (1967) 1.
19) D.W. Sprung and P.K. Banerjee- Nucl. Phys. A168 (1971) 273; X. Campi and D.W. Sprung- Nucl. Phys. A194 (1972) 401.
20) R.F. Frosch et al.- Phys. Rev. 174 (1968) 1380.
21) J.M. Finn et al.- Nucl. Phys. A274 (1976) 28.
22) A. Chaumeaux et al.- Ann. Phys. (N.Y.) 116 (1978) 247.
23) G.D. Alkhazov et al.- Phys. Rep. 42C (1978) 89.

"MODEL INDEPENDENT" POTENTIALS FOR ELASTIC α-^{40}Ca SCATTERING AND THE PROBLEM OF DEDUCING NUCLEAR MATTER DENSITIES

H.P. Gubler, G.R. Plattner, I. Sick
University of Basel,
Switzerland

"Model independent" potentials for elastic α - ^{40}Ca scattering and the problem of deducing nuclear matter densities

H.P. Gubler, G.R. Plattner, I. Sick
Department of Physics, University of Basel

This report describes an optical model analysis of α- ^{40}Ca elastic scattering. Initially, our work was undertaken to solve - at least partially - the puzzle of "anomalous large angle scattering" (ALAS) of α -particles, which is most prominent with ^{40}Ca. The feasibility of an optical model description of ALAS with little energy-dependence of the parameters was shown by several groups [1)-3)]. It was found that the imaginary part of the optical model has to be lowered compared to neighbouring nuclei, which do not show ALAS, and that the shape of the real part of the optical potential is different from a Woods-Saxon (WS) form factor. Woods-Saxon form factors raised to an exponential and folding-potentials were used in these investigations.

The phenomenological fact of reduced absorption in α -^{40}Ca scattering may lead to an increased sensitivity to the shape of the inner part of the optical potential, since in such a case the α-particle can penetrate deeper into the nucleus without being absorbed.

In fact, the scattering at intermediate angles and at ALAS-energies (i.e. from ~20 to ~50 MeV) is very sensitive to the detailed shape of the real part, since scattered waves from different parts of the effective potential interfere strongly. This interpretation is supported by semiclassical analyses [4)]. In order to investigate, whether this sensitivity can be used to accurately determine the effective α-nucleus potential in a "model independent" manner, we have tried to express the real

part of the potential by a sum of gaussians ("SOG") rather than by using a preconceived analytical form:

$$V(r) = \sum_{i=1}^{N} A_i \left\{ \exp\left[-(r-r_i)^2/\gamma^2\right] + \exp\left[-(r+r_i)^2/\gamma^2\right] \right\} \qquad (1)$$

The coefficients A_i are treated as free parameters. The position r_i and the widths γ of the gaussians are established a priori, but are changed in a random manner in different fits [5]. The values chosen for γ were in the range from 0.9 to 1.6 fm. The number N of gaussians can also be changed and is around 10 in our analysis.

The imaginary part is taken to have a WS-shape. Modified WS-potentials of the form

$$W(r) = W_0 \left\{ 1 + \exp\left[(r-R_I)/\nu_I\, a_I\right] \right\}^{-\nu_I} \qquad (2)$$

were also tried. No significant differences between the fits with different ν_I were found, so that there is no strong dependence on the form chosen for the imaginary part of the potential.

We find that the SOG-parametrization of the optical potential gives us enough flexibility to fit the data very well, with values of χ^2/degree of freedom between 1 to 7, depending on the angular distribution. The data cover the energy region from 18 to 166 MeV. It includes our own data measured at SIN between 26 and 47 MeV, as well as other sets from the literature [7)-11)]. With a few exceptions the angular distributions cover the full range from $\sim 30^\circ$ to $\sim 175^\circ$. We intentionally restricted our work to the potential family with a volume integral per nucleon pair of ~ 350 MeV fm^3. This family is required [6] if one wants to fit the data above ~ 100 MeV.

In Fig. 1 we show as an example a fit at 36 MeV with a SOG-potential.

At any one energy, we thus obtain the effective real potential and its uncertainty at different radii by taking the envelope of all the ($\sim$60) fitted potentials which fulfill the criterion

that $\chi^2_{min} < \chi^2 < \chi^2_{min} + 2$. Clearly, this choice is arbitrary, but we think it is justified in view of the fact that all of the "optically" good fits lie within this range. In Fig. 2 we show two potentials and their respective error bands, derived by the analysis described above. Clearly the shape of the effective two body potential describing the elastic scattering of α -particles from ^{40}Ca is dependent on the bombarding energy. This is not just an accident. In fact, taking a potential which describes the angular distribution at 36 MeV, and trying to fit another angular distribution at another energy by readjusting the strength and by freely fitting the imaginary part of the optical potential, we do not obtain acceptable fits. The discrepancies increase as the energy moves away from 36 MeV. Examples of the result of this procedure are shown in Figs. 3 and 4. This clearly shows that the shape of the effective real potential must be energy dependent. We can only speculate about the reasons. It is conceivable that we see here an effect of other channels coupling to the elastic scattering.

The volume-integral per nucleon pair J/4A reveals another interesting fact (see Fig. 5). Our analysis shows that the energy dependence is not linear over the full energy range, but is more complicated:

$$J(E) = J_o \cdot (1-a(E) \cdot E) \qquad (3)$$

Recently Fliessbach has derived an energy dependent strength of a folding potential by taking into account the Pauli-distortion of the incident α -particle [12]. We find that a(E) as calculated by Fliessbach follows roughly our empirical values as a function of energy. It is interesting to note that above E $\sim$ 60 Mev the energy dependence is approximately linear with a value for a of ~ 0.0016 MeV^{-1}. This corresponds closely to the theoretical predictions based on consideration of the inherent non-locality of the nuclear force.[13]

From our analysis we conclude that the derivation of nuclear matter distributions or of rms-radii of nuclear matter distributions by a simple folding procedure cannot be considered to be reliable in view of the following facts:

- Only the effective (local) two body potential for elastic scattering of α-particles can be derived directly from measurements of elastic α-scattering
- The shape (not just the strength) of the potential is found to be energy dependent
- The Pauli-principle has to be taken into account at least at energies below ~60 MeV
- At higher energies ($\gtrsim$100 MeV) the absorption becomes stronger, the nucleus less transparent, and consequently α-scattering probes only the outer nuclear region. In our analysis we observe a corresponding increase in the uncertainties (~5%) of the volume-integrals and the rms radii determined from the data.
- Even if only differences of rms-radii between various nuclei are considered, the required degree of cancellation of the systematical errors would have to be very large in order to achieve a meaningful accuracy. Unless this can be justified at least on theoretical grounds, such a procedure is unsound.

To state it simply and clearly:

The connection between the nuclear matter distribution and the effective α-nucleus two body potential is complicated. Effects which at present can not be included in a folding model will have to be investigated in detail before we can hope to extract precision information on nuclear matter distributions from the analysis of α-scattering.

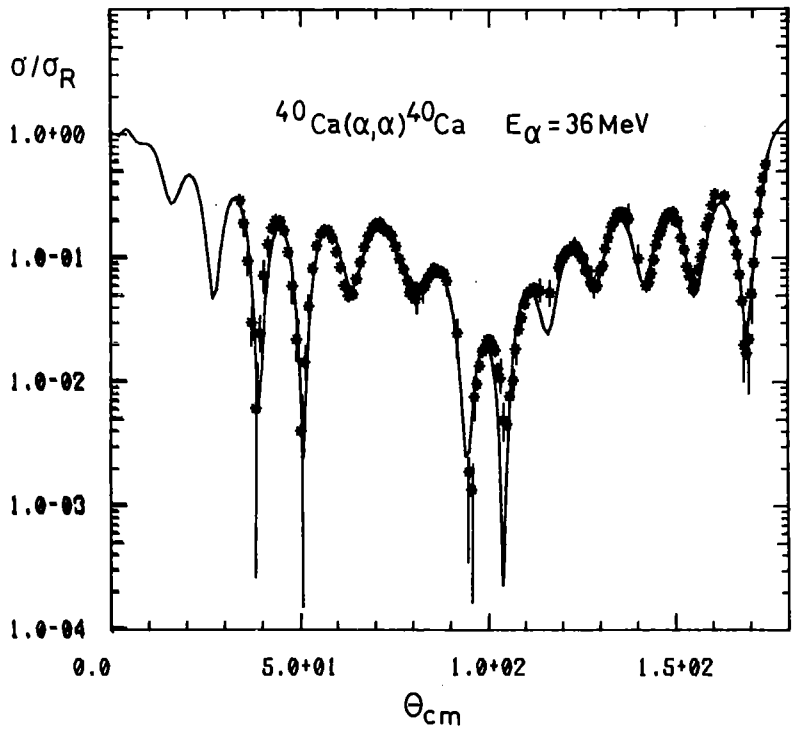

Fig. 1
Fit to the $^{40}Ca(\alpha,\alpha)^{40}Ca$ cross section at 36 MeV with a SOG-potential

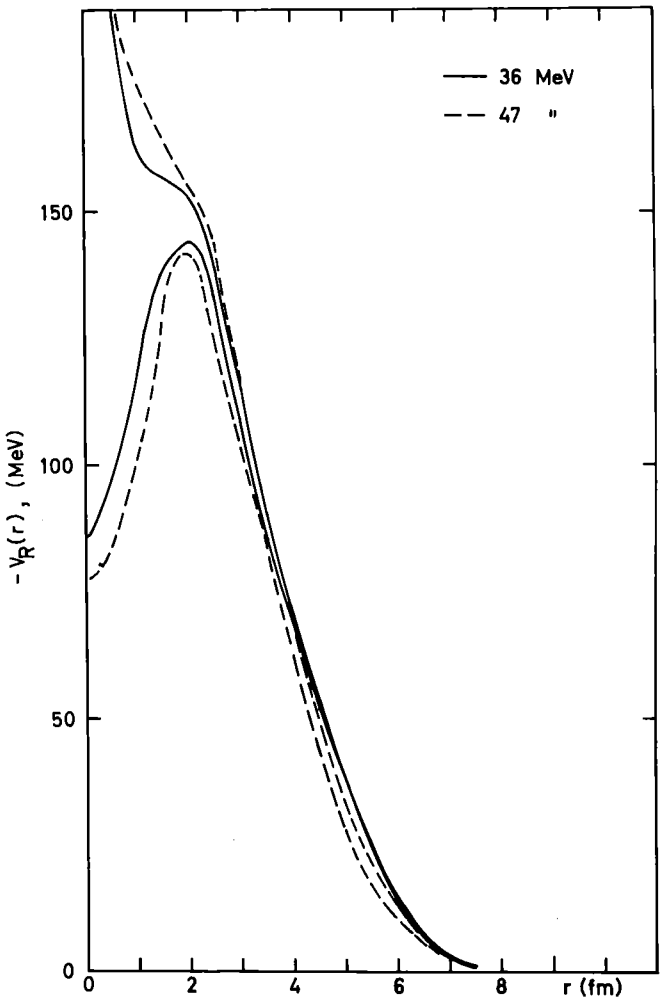

Fig. 2
Real part of the optical potential at 36 MeV (full lines) and at 47 MeV (dashed lines). Acceptable potentials lie within the corresponding curves

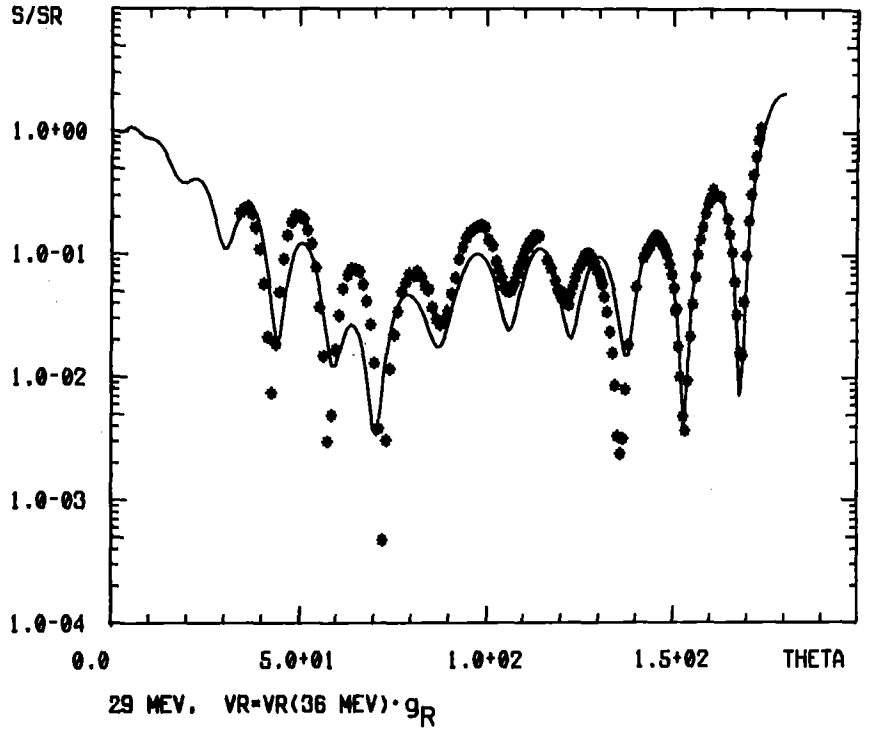

Fig. 3
Angular distribution at 29 MeV. Theoretical curve with the readjusted strength of the potential which fits the 36 MeV data (g_R = 0.995)

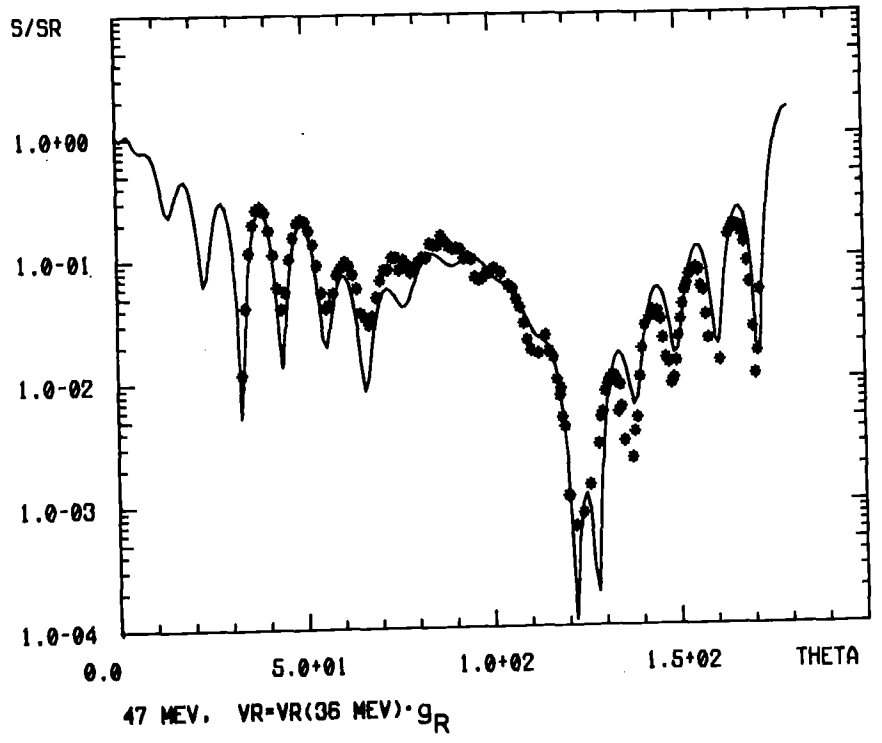

Fig. 4
Same as Fig. 3, but at 47 MeV (g_R = 0.976)

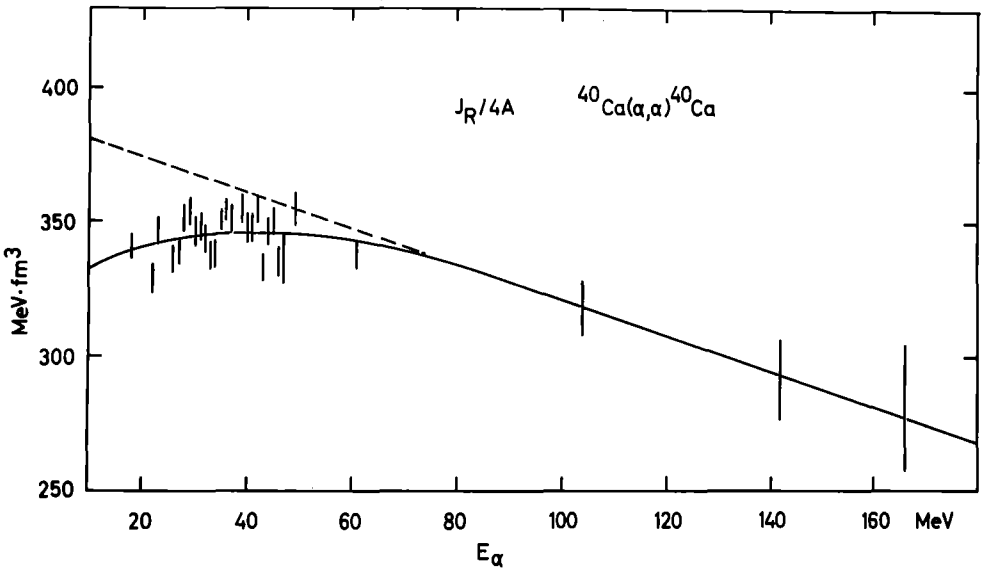

Fig. 5 Volume-integral per nucleon pair as a function of bombarding energy. The full curve is a polynomial fit to the data, the dashed line is an extrapolation of the "high energy" behaviour.

References

1) F. Michel, R. Vanderpoorten, Phys. Rev. C16 (1977), 142
2) Th. Delbar et al., Phys. Rev. C18 (1978), 1237
3) H.P. Gubler et al., Phys. Lett. 74B (1978), 202
4) N. Takigawa, S.Y. Lee, Nucl. Phys. A292 (1977), 173
5) I. Sick, Nucl. Phys. A218 (1974), 509
6) D.A. Goldberg et al., Phys. Rev. C10 (1974), 1362
7) G. Gaul et al., Nucl. Phys. A137 (1969), 177
8) H. Löhner et al., Z. Physik A286 (1978), 99
9) E. Friedmann et al., Phys. Rev. Lett. 41 (1978), 1220
10) D.A. Goldberg, Phys. Lett. 55B (1975), 59
11) I. Brissaud, M.K. Brussel, J. Phys. G3 (1977), 481
12) T. Fliessbach, Nucl. Phys. A315 (1979), 109
13) D.F. Jackson, R.C. Johnson, Phys. Lett. 49B (1974), 249

ALPHA OPTICAL POTENTIAL AND NUCLEAR RADII OF Ni ISOTOPES

A. Budzanowski, C. Alderliesten, J. Bojowald,
W. Oelert, and P. Turek
Kernforschungsanlage Jülich GmbH,
Federal Republic of Germany

and

H. Dabrowski and S. Wiktor
Institute of Nuclear Physics,
Krakow, Poland

Alpha Optical Potential and Nuclear Radii of Ni Isotopes

A. Budzanowski, C. Alderliesten, J. Bojowald, W. Oelert
and P. Turek
Institut für Kernphysik der Kernforschungsanlage Jülich,
D-517 Jülich, Germany

and

H. Dabrowski and S. Wiktor
Institute of Nuclear Physics, 31-342 Krakow, Poland

The elastic and inelastic scattering of alpha particles on ^{58,60,62,64}Ni isotopes was measured at E_α = 172.5 MeV using the α-particle beam from the Jülich isochronous cyclotron. The experiment has been performed in the 100 cm scattering chamber using two ΔE-E semiconductor telescopes. Each telescope consisted of a 1000 μm commercial silicone surface barrier ΔE transmission detector and a Ge(Li) E detector of the side entry type developed in the detector laboratory of the institute[1]. Cross sections were measured in the angular range from 45° - 70° (LAB) sufficiently broad to include the so called rainbow scattering. The energy resolution 250 keV (FWHM) allowed to resolve clearly peaks corresponding to the elastic scattering and inelastic scattering to the first 2^+, 4^+ and 3^- excited states in all four nuclides. The angular resolution was 0.2° and the uncertainty in the scattering angle was ±0.025°. The

angular step size was 0.5^{o} in the diffraction region (small angles) and 2^{o}-6^{o} in the nuclear rainbow region. The targets were 4-6 mg/cm^2 thick self-supporting foils, isotopically enriched to better then 99 %. The target thicknesses were determined by weighing and independently by alpha absorption methods. This last one allowed to test the target nonuniformities. Error analysis included contributions from statistics, angular uncertainties, peak fitting systematics and target nonuniformities.

Optical model analyses were performed using standard six-parameter potentials of the $(WS)^1(WS)^1$, $(WS)^2(WS)^2$ and $(WS)^2(WS)^1$ form for the real and imaginary part respectively. (WS) indicates as usual the Fermi function. The best-fit potential parameters together with χ^2 values per degree of freedom are shown in Table I. It can be seen that good fits of comparable quality are obtained for all investigated potentials. As an example the fits for the $(WS)^2(WS)^1$ combination are shown in Fig. 1.

The values of the root mean square radii and their differences for the real part of each of the obtained potentials are listed in Table II together with the corresponding values of r.m.s. radii of nuclear matter distribution obtained from the analysis of 1 GeV proton scattering[2], Hartree-Fock-Bogliubov type calculations[3] and microscopic analysis of 166 α-scattering data[4]. For comparison r.m.s. radii of the proton distribution[5] are given in the last column. We notice that the absolute values of r.m.s. radii of the real part of the optical potentials are model dependent being larger for $(WS)^1$ shape. The r.m.s. radii differences exhibit less model dependence and are pretty close to the corresponding values of

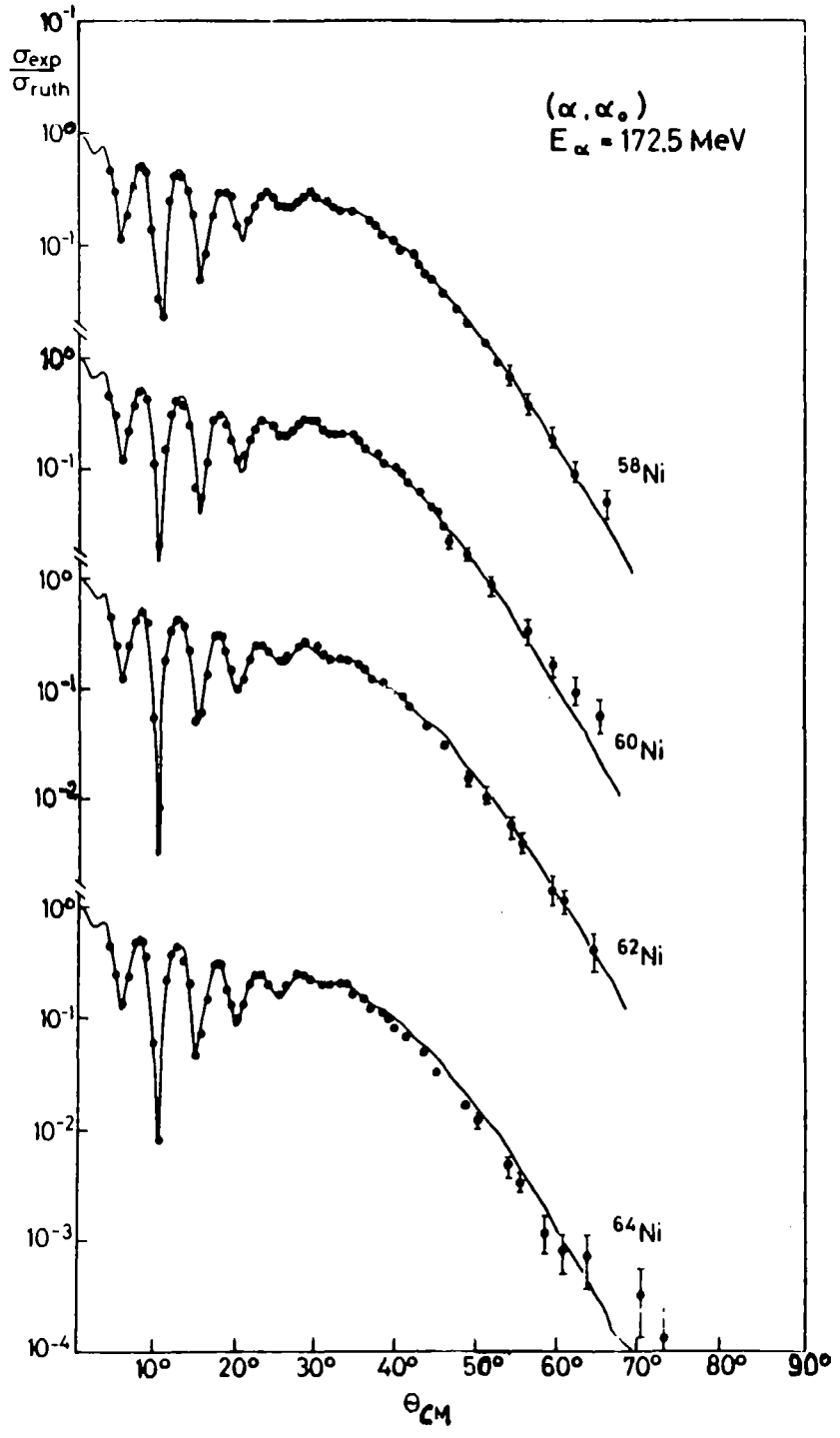

Fig. 1: Angular distributions of elastically scattered alpha-particles on Ni-isotopes fitted with the optical model potential of the $(WS)^2(WS)^1$ form.

the matter distribution predicted by the H.F.B. calculations. This feature of the optical model r.m.s. radii has been recently found by P.L. Robertson et al.[6] for the case of the 140 MeV α scattering from even titanium isotopes. Within the limits of ± 0.01 fm the r.m.s. radii of the real part of the optical model potentials obtained in the present work are proportional to $A^{1/3}$ (see fig. 2). This result agrees with the results of the microscopic analysis of the 166 MeV α scattering data obtained by Brissaud et al.[4] and with results of the optical model analysis of the 42 MeV α scattering by Fernandez and Blair[7]. These two last works were however confined to mass numbers 58-60-62 only. The r.m.s. radii of the matter distribution from 1 GeV proton scattering data of Alkhazov et al.[2] and Chaumeaux et al.[2] do not show a regular increase with $A^{1/3}$. We notice also that the r.m.s. radii of the proton distribution[5] increase with A though not as rapidly as $A^{1/3}$.

It has been argued for some time[8] that the real part of the α-nucleus optical model potential can be represented by the simple folding integral when antisymmetrization effects are neglected:

$$V_{\alpha-A}(\hat{r}) = \int \rho_A(\hat{r}')\, V_{n-\alpha}(|\hat{r}-\hat{r}'|)\, d\hat{r}' \quad \ldots \qquad (1)$$

where $V_{\alpha-A}$ and $V_{n-\alpha}$ indicate the real part of the α-nucleus and effective n-α potentials respectively, ρ_A being the matter point density distribution in the target nucleus of mass number A. According to Barret and Jackson[8] the following formula for the r.m.s. radii is then valid:

$$\langle r^2 \rangle_{\alpha-A} = \langle r^2 \rangle_{\rho_A} + \langle r^2 \rangle_{n-\alpha} \quad \ldots \qquad (2)$$

If we use for the analysis the optical potential of the shape given by the folding formula (1) then the differences between the m.s.r.

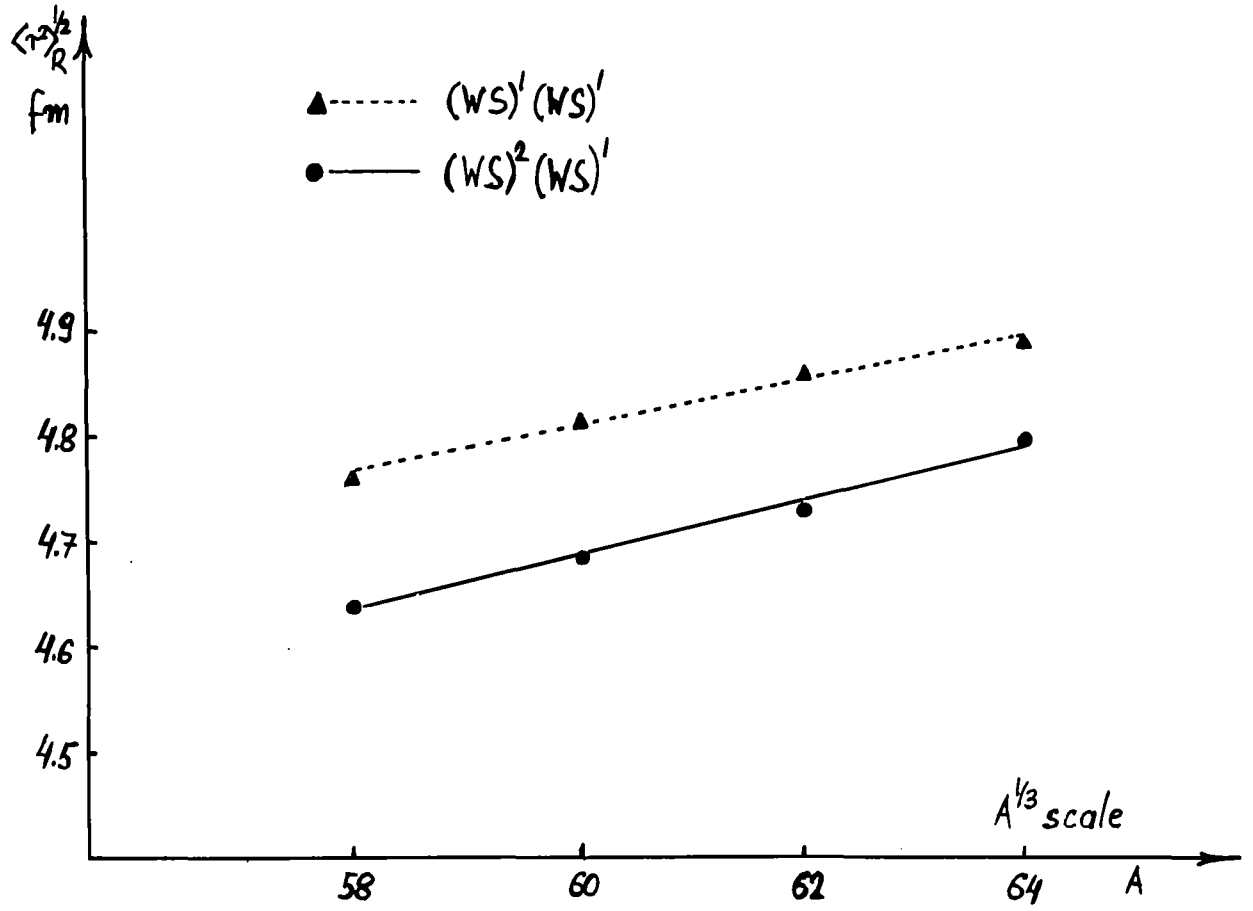

Fig. 2: Root mean square radii of the real part of the α-optical potentials for Ni isotopes. Straight lines are drawn to guide the eye.

of the potentials should be equal to the differences between the m.s.r. of the matter distribution for the corresponding isotopes providing that the effective α-nucleon interaction is constant.

It has been shown by Majka et al.[9] that the shape of the real part of the α optical potential for medium weight nuclei obtained from the folding model can be well approximated by the $(WS)^2$ form. The shape of the imaginary part of the α optical model potential calculated by Vinh Mau[10] in terms of the Feshbach formalism turned out to be close to the $(WS)^1$ form. Therefore further analysis in the present work is confined to the $(WS)^2(WS)^1$ potentials. In fig. 3 the r.m.s. radii of the matter distribution determined from the optical model analysis of the present α scattering data using formula (2) are plotted against $A^{1/3}$ for all four Ni isotopes. The triangles indicate r.m.s. matter radii calculated for $\langle r^2 \rangle^{1/2}_{\alpha-n} = 2.45$ fm. This value was used by Bernstein[11] and Vinh Mau[10] as describing the effective density independent α-nucleon interaction. The full circles indicate r.m.s. matter radii calculated for $\langle r^2 \rangle^{1/2}_{\alpha-n} = 2.89$ fm. This last value was obtained by requiring the equality between the r.m.s. matter radii obtained in the present work and those obtained from the 1 GeV proton scattering[2] for ^{58}Ni nuclei. The r.m.s. matter radii obtained by latest H.F.B. calculations[2,3] and from the 1 GeV proton scattering[2] are indicated by circles and crosses respectively. Examination of fig. 3 tells us that the matter radii obtained using formula (1) and (2) with non saturating free nucleon-alpha interaction are larger by about 0.3 fm from the real nuclear radii. Similar effect was also found by Majka et al.[9] in the anasysis of the α-scattering on ^{90}Zr using the double folding potentials. This discrepancy can be removed when using a density dependent α-nucleon potential. This potential has saturating properties and in

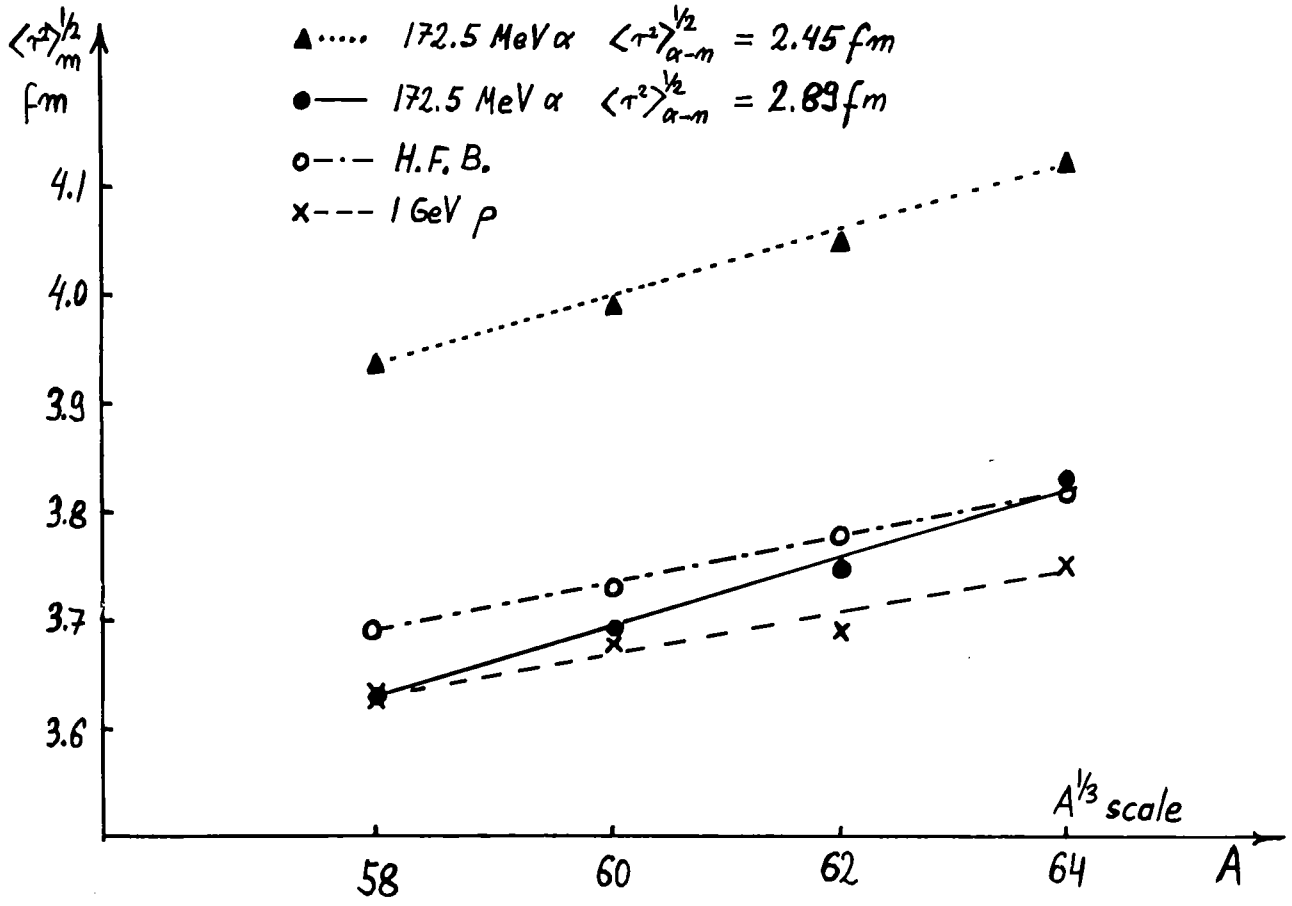

Fig. 3: Root mean square radii of the matter distribution for Ni isotopes obtained from 172.5 MeV α scattering data, H.F.B. calculations[2,3] and 1 GeV proton scattering analysis[2].

consequence suppress the interaction as the penetration into the nucleus becomes deeper what increases the r.m.s. radius of the potential. The importance of the density dependent interaction was recently shown by several authors[12,13,14]. In order to save the use of simple formula (2) a density independent α-nucleon interaction with larger r.m.s. radius has to be used what confirms the results obtained earlier by Friedman and Batty[14]. Using the value $\langle r^2 \rangle^{1/2}_{n-\alpha} = 2.89$ fm we can reduce the differences between the matter radii obtained from α-scattering, high energy proton scattering and H.F.B. calculations to within 0.07 fm. The slope of the increase of the r.m.s. radius value determined from alpha scattering is slightly larger than that obtained by other methods. This difference may be accounted for by the antisymmetrization effects. It has been shown by Majka et al.[9] that the inclusion of the one nucleon exchange terms increases the r.m.s. radius of the real part of the potential by about 0.02 fm. Since with increasing neutron number the importance of the exchange interaction will increase it is quite likely that some additional increase of the r.m.s. radius of the total potential will occur in comparison with the direct term given by formula (1). Finally we should comment on the possibility of the influence of the core polarization effects on the values of the r.m.s. radii of the optical potential. The dynamical deformation parameters α extracted from the inelastic scattering data by means of the DWBA analysis for the most strongly excited first 2^+ and 3^- states are collected in Table 3. As can be seen these values are very close to each other so that if any core polarization effects are present they should not influence the relative values of the r.m.s. radii obtained from the optical model analysis. On the other hand the coupled

channel analysis of the scattering of 104 MeV alpha particles by ^{58}Ni nuclei performed by A. Budzanowski et al.[15] have indicated that beside the 5 % decrease of W some slight modification of the real part of the optical model potential is also required in order to obtain a good fit to both elastic and inelastic scattering. However this modification leaves the mean square radius practically unchanged.

The elastic and inelastic scattering of alpha particles from Ni even isotopes was also studied at E_α = 104 MeV by H. Rebel et al.[16]. These last data did not extend far enough into the rainbow region so that the results concerning the r.m.s. matter radii can be only qualitatively compared with that obtained in the present investigation.

In conclusion we can say that the results of the present investigation confirm the necessity of using the model independent methods for the α-elastic scattering analysis as well as density dependent interactions. The extraction from such data informations about the r.m.s. radii of nuclear matter within the accuracy better than 0.07 fm would require better understanding of the exchange effects in the nucleus-nucleus collisions.

References

1) G. Riepe and D. Protić, Nucl. Instr. Meth. 101 (1972) 77; G. Riepe, D. Protić and J. Reich, Nucl. Instr. Meth. 124 (1975) 527; G. Riepe and D. Protić, IEEE Transactions Nucl. Science, NS-22 (1975) 1

2) A. Chaumeaux, V. Layly and R. Schaeffer, Ann. Phys. (N.Y.) 116 (1978) 247; G.D.Alkhazow, S.L. Belostotsky and A.A. Vorobyov, Phys. Reports C42 (1978) 89

3) J. Decharge, M. Girod and D. Gogny, Phys. Letters B55 (1975) 361

4) I. Brissaud and M.K. Brussel, Phys. Rev. C15 (1977) 452

5) E.B. Shera, E.T. Ritter, R.B. Perkins, G.A. Rinker, L.K. Wagner, H.D. Wohlfahrt, G. Fricke and R.M. Steffen, Phys. Rev. C14 (1976) 731

6) P.L. Roberson, D.A. Goldberg, N.S. Wall, L.W. Woo and H.L. Chen, Phys. Rev. Letters 42 (1979) 54

7) B. Fernandez and J.S. Blair, Phys. Rev. C1 (1970) 523

8) R.C. Barrett and D.F. Jackson, "Nuclear Sizes and Structure", Oxford University Press 1977, p. 6

9) Z. Majka, A. Budzanowski, K. Grotowski and A. Strzałkowski, Phys. Rev. C18 (1978) 114

10) N. Vinh Mau, Phys. Letters 71B (1977) 5

11) A.M. Bernstein and W.A. Seidler, Phys. Letters 34B (1971) 569

12) Z. Majka, H.J. Gils and H. Rebel, Microscopic Optical Potential" Proceedings of the Hamburg Topical Workshop on Nuclear Physics, September 25-27, 1978, Springer Verlag 1979, p. 293

13) B. Sinha, Phys. Rev. C5 (1975) 1546

14) E. Friedman and C.J. Batty, Phys. Rev. C17 (1977) 34

15) A. Budzanowski, H. Dabrowski, L. Freindl, K. Grotowski, S. Micek, R. Płaneta, A. Strzalkowski, M. Bosman, P. Leleux, P. Macq, J.P. Meulders and C. Pirart, Phys. Rev. C17 (1978) 951

16) H. Rebel, R. Löhken, G.W. Schweimer, G. Schatz and G. Hauser, Z. Physik 256 (1972) 258

Table I Optical model potential parameters

	V (MeV)	r_R (fm)	a_R (fm)	W (MeV)	r_I (fm)	a_I (fm)	$J^R/4A$ (MeV fm^3)	$\langle r^2\rangle_R^{1/2}$ (fm)	$J^I/4A$ (MeV fm^3)	$\langle r^2\rangle_I^{1/2}$ (fm)	χ^2/d.f.
					$(WS)^1$	$(WS)^1$					
^{58}Ni	111.47	1.248	0.792	22.73	1.564	0.580	287.1	4.761	99.3	5.161	2.8
^{60}Ni	111.29	1.245	0.804	21.68	1.577	0.603	285.3	4.815	97.4	5.281	2.3
^{62}Ni	108.84	1.256	0.797	22.20	1.572	0.623	283.1	4.858	99.3	5.347	3.2
^{64}Ni	112.54	1.240	0.818	21.22	1.586	0.608	285.0	4.900	96.7	5.409	2.4
					$(WS)^2$	$(WS)^2$					
^{58}Ni	149.76	1.340	1.336	25.55	1.671	1.123	270.8	4.639	90.5	5.189	2.8
^{60}Ni	142.79	1.354	1.319	24.35	1.696	1.143	265.7	4.682	90.3	5.318	1.6
^{62}Ni	140.84	1.361	1.316	26.42	1.672	1.197	265.9	4.728	93.4	5.352	2.4
^{64}Ni	154.02	1.316	1.423	20.14	1.756	1.024	265.1	4.794	84.7	5.478	3.2
					$(WS)^2$	$(WS)^1$					
^{58}Ni	140.34	1.379	1.266	25.14	1.458	0.766	275.0	4.639	96.5	5.217	3.1
^{60}Ni	131.98	1.402	1.229	23.90	1.493	0.754	275.5	4.685	97.0	5.326	1.4
^{62}Ni	132.72	1.400	1.242	25.00	1.478	0.777	272.0	4.731	99.2	5.373	2.4
^{64}Ni	146.53	1.354	1.359	19.08	1.583	0.686	273.0	4.798	98.0	5.527	4.6

Table II R.M.S. radii and their differences

	O.M. $(WS)^1(WS)^1$	O.M. $(WS)^2(WS)^2$	O.M. $(WS)^2(WS)^1$	matter 1 GeV proton[2]	matter H.F.B.[3]	matter 166 MeV alpha[4]	proton μ x-ray[5]
			R.M.S. radii (fm)				
^{58}Ni	4.761	4.639	4.639	3.63	3.69	3.66	3.781
^{60}Ni	4.815	4.682	4.685	3.68	3.73	3.71	3.818
^{62}Ni	4.858	4.728	4.731	3.69	3.78	3.76	3.847
^{64}Ni	4.900	4.794	4.798	3.75	3.82	--	3.866
			R.M.S. radii Differences (fm)				
$^{60}Ni-^{58}Ni$	0.054	0.043	0.046	0.05	0.04	0.05	0.037
$^{62}Ni-^{60}Ni$	0.043	0.046	0.046	0.01	0.05	0.05	0.029
$^{64}Ni-^{62}Ni$	0.042	0.066	0.067	0.06	0.04	--	0.019

Table III

Deformation parameters β for first 2^+ and 3^- excited states of even Ni isotopes

	E_α(MeV)	J^π	β
^{58}Ni	1.45	2^+	0.155
	4.47	3^-	0.122
^{60}Ni	1.33	2^+	0.167
	4.04	3^-	0.122
^{62}Ni	1.17	2^+	0.176
	3.75	3^-	0.126
^{64}Ni	1.35	2^+	0.152
	3.55	3^-	0.126

SATURATION EFFECT AND DETERMINATION OF NUCLEAR MATTER DENSITY DISTRIBUTION FROM OPTICAL POTENTIAL

Z. Majka
Jagellonian University, Cracow, Poland
H.J. Gils, H. Rebel
Kernforschungszentrum Karlsruhe GmbH,
Karlsruhe,
Federal Republic of Germany

Saturation Effect and Determination of Nuclear Matter Density Distribution from Optical Potential

Z. Majka
Institute of Physics, Jagellonian University, Cracow, Poland

H.J. Gils, H. Rebel
Kernforschungszentrum Karlsruhe GmbH, Institut für Angewandte Kernphysik, P.O.B. 3640, D7500 Karlsruhe
Federal Republic of Germany

Optical model fits (1) to the elastic scattering data of 104 MeV alpha particles from $^{48,40}Ca$ (2) using a Fourier Bessel description of the real potential show that the rms radius of the α-^{48}Ca potential is greater than the α-^{40}Ca one by an amount of $\langle r^2 \rangle^{1/2}_{Pot(48)} - \langle r^2 \rangle^{1/2}_{Pot(40)} = 0.13 \pm 0.04$ fm. Moreover, the volume integrals per nucleon pair for both potentials agree within the experimental error of $\pm$ 3 MeV.fm^3.

In the present note we are concerned with the question whether this difference reflects solely the density dependence of the nucleon-nucleon interaction or whether it uniquely implies a difference between the rms radii of the corresponding nuclear density distributions.

Recently, the double folding procedure has been refined so that in addition to an exchange term (3) the density dependence of the effective nucleon-nucleon interaction (4) has been included. The density dependence originates from the presence of the surrounding nucleons changing the intermediate processes

that might occur in the interaction of two nucleons. The importance of the saturation has been recently demonstrated for 104 MeV alpha-particle scattering (4) where a density dependent folding model was able to describe also the "rainbow" scattering resulting in reasonable values of the potential volume integral per nucleon pair. In that specific case exchange effects have been shown to be of minor importance.

The basis of our discussion is the refined double folding model described in detail in ref. (4) where

$$V_{\alpha\text{-}Ca}(r) = \int\int \rho_{\alpha}(\vec{Z}_{\alpha})\ \rho_{Ca}(\vec{Z}_{Ca})\ t(\vec{r},\vec{Z}_{\alpha},\vec{Z}_{Ca})\ d\vec{Z}_{\alpha}\ d\vec{Z}_{Ca} \qquad (1)$$

All quantities and the coordinates in eq. 1 are defined in ref. (4). The effective nucleon-nucleon interaction depends actually on the local density $\rho(\vec{r},\vec{Z}_{\alpha},\vec{Z}_{Ca})$ of the overlapping system. Due to the Pauli distortion this local density is assumed to be intermediate between the arithmetic sum of ρ_{α} and ρ_{Ca} (sudden approximation: maximum compression) and the adiabatic case $\rho = \rho_{Ca}$ (no compression). For simplicity we parametrized as follows $\rho(r, \vec{Z}_{\alpha}, \vec{Z}_{Ca}) = m\ \rho_{\alpha}(\vec{Z}_{\alpha}) + \rho_{Ca}(\vec{Z}_{Ca})$ with m ($0 \leq m \leq 1$) accounting for the compression of nuclear matter in the overlap region. The value* of the parameter m was fixed by requiring a fit to the $^{40}Ca(\alpha,\alpha)^{40}Ca$ data. To calculate the real part of the α-^{48}Ca potential using eq. 1 two extreme assumptions for the matter density distribution+ in the ^{48}Ca nucleus were examined.

---

*m = 0.5, see ref. (4).

+In eq. 1 for ρ_{Ca} we used the point matter density distribution deduced from matter density distribution ρ_m by unfolding the charge distribution of a single proton.

a. ρ_m (48) = $\frac{48}{20}$ ρ_p (48) where we use three parameter Fermi proton distribution ρ_p(48) derived from ref. 5.
This model provides a considerable increase of the central density in the ^{48}Ca nucleus as compared to the ^{40}Ca one leading to a modification of the density dependence of the nucleon-nucleon interaction.

b. Adopting the same value of the central density in ^{48}Ca as for the ^{40}Ca nucleus and adjusting the shape of ρ_m so that the rms radius was equal to that of the proton distribution used in case (a).

In Fig. 1 we compare the ^{40}Ca matter density distribution and that of ^{48}Ca obtained in (b). As one can see from table 1 the resulting rms radii of the folded potentials are equal for both

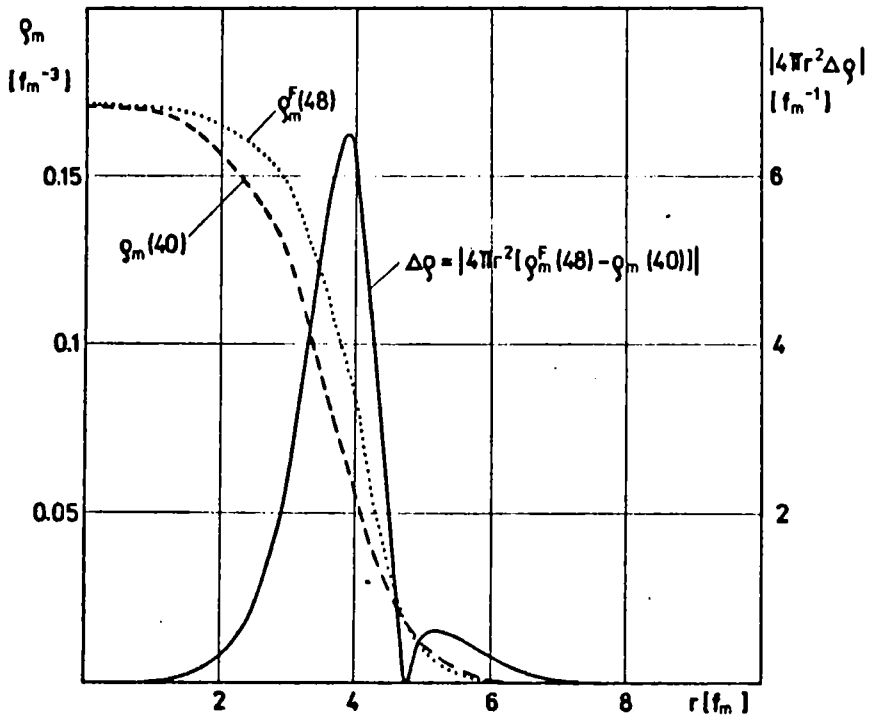

Fig. 1. Matter density distributions

Table 1. The rms radii and the volume integrals per nucleon pair of the calculated potentials.

Double folding potential	Matter density distribution in target nucleus^{+}	$\langle r^2 \rangle^{1/2}_{Pot}$ (fm)	J_N (MeV . fm^3)
$^{40}Ca(\alpha,\alpha)^{40}Ca$	$\rho_m(40) = \frac{A}{Z}\rho_p(40)$	4.22	298.0
$^{48}Ca(\alpha,\alpha)^{48}Ca$	$\rho_m(48) = \frac{A}{Z}\rho_p(48)$	4.23	280.3
$^{48}Ca(\alpha,\alpha)^{48}Ca$	$\langle r^2 \rangle^{1/2}_m(48) = \langle r^2 \rangle^{1/2}_p(48)$ $\rho_o(48) = \rho_o(40)$	4.21	283.6

means that the semimicroscopic double folding model with the saturation effect included is not able to reproduce the experimentally determined difference between rms radii of te potentials without additional assumption of increased size of the neutron distribution in the ^{48}Ca nucleus.

References

1. E. Friedman et al., Phys. Rev. Lett. 41 (1978) 1220.
2. H.J. Gils et al., to be published.
3. Z. Majka et al., Phys. Rev. C18 (1978) 114.
4. Z. Majka et al., Z. Physik, A288 (1978) 139.
5. J.B. Bellicard et al., Phys. Rev. Lett. 19 (1967) 527.

NUCLEAR SHAPES AND THE IMAGINARY PART OF THE LIGHT ION NUCLEAR OPTICAL POTENTIAL

F. Duggan
Institut de Physique Nucléaire,
Orsay, France

NUCLEAR SHAPES AND THE IMAGINARY PART OF THE LIGHT ION NUCLEAR OPTICAL POTENTIAL

F. DUGGAN
Division de Physique Théorique[x], Institut de Physique Nucléaire, B.P. 1, 91406 Orsay Cedex, France

ABSTRACT

The imaginary part of the light ion optical potential has some interesting features which may be usefully exploited. For the ^{3}He-nucleus system at medium energies it has been found that the elastic scattering cross-sections in the backward hemisphere are almost entirely determined by the imaginary part of the optical potential. The dynamics of this potential corresponds to energy conserving transitions in which (i) the ^{3}He excites the target collective states and (ii) the ^{3}He itself undergoes incoherent 1p 1h excitations using as intermediate states the single particle levels of the target nucleus. It has been found that the back angle elastic scattering data is very sensitive to the nature of the target collective states that enter into the calculation of the imaginary potential. Thus we have an additional way of studying nuclear shapes.

1. INTRODUCTION

Considerable effort[1] has been invested in understanding the light and heavy ion optical potentials. Most investigations have been addressed towards elucidating the nature of the real part of the nucleus-nucleus optical potential and also for determining an appropriate single particle model for it. However, several of the light ions[2,3] have their own special features and so require further investigation. Although the imaginary potential is strongly linked to the real part, the former has not received much attention as yet. Nevertheless the imaginary potential for the ^{3}He projectile has displayed some specific features which may be usefully exploited. In this paper we examine the coherent nature of the imaginary part of the ^{3}He optical potential and suggest an additional way of investigating nuclear shapes.

---

[x] Laboratoire Associé au C.N.R.S.

2. THE ^{3}HE-NUCLEUS INTERACTION POTENTIAL.

In this section a single particle model for the interaction is first considered in some detail because it is essential to understand exactly what dynamics is inherent in the model before including the coherent imaginary potential.

2.1 Single particle model.

Our starting point is the single particle folded model. In this model it is assumed that the interacting nuclei remain in their ground states throughout the collision. However for a weakly bound projectile like ^{3}He it is useful to extend[2] the folded model to include excitations of the nucleons in the ^{3}He but it is assumed that the target being relatively stable would remain in its ground state.

2.1.1 Formalism.

The ^{3}He-nucleus optical potential is conveniently expressed[2] in the Feshbach formalism to be

$$U^H_{opt} = \left\langle \phi_0(\xi_I)\phi_0(\xi_T) \middle| V + V Q_0 \frac{1}{E - Q_0 H Q_0 + i\epsilon} Q_0 V \middle| \phi_0(\xi_T)\phi_0(\xi_I) \right\rangle_A \qquad (1)$$

where the suffix A implies that the above matrix element is properly antisymmetrized. $\phi_0(\xi_T)$ and $\phi_0(\xi_I)$ are respectively the ground state internal wave functions of the target and projectile. H is the total Hamiltonian of the system and E is the c.m. energy of the projectile. Assuming that only two body interactions occur

$$V = \sum_{j=1}^{3} \sum_{i=1}^{A_T} v_{ij} \qquad (2)$$

where v_{ij} is a N-N interaction, A_T is the nucleon number of the target. The open channel projection operator P_0 projects the total wave function Ψ on to the ground state of the target plus projectile system as

$$P_0 \Psi = \mathcal{A} \phi_0(\xi_T)\phi_0(\xi_I) \qquad (3a)$$

where $\mathcal{A}$ is an antisymmetrization operator. Then the closed channel projection operator Q_0 is defined as

$$Q_0 = 1 - P_0 \qquad (3b)$$

and it projects off the ground state of the system. The first term of eq.(1) is the usual folded potential for the real part and the second term, containing a propogator, couples the elastic channel to a non-elastic one. The VQ_0 before the propagator couples the elastic channel to a non-elastic channel in Q_0 space and the Q_0V after the propagator decouples the same.

It is useful to transform eq.(1) in order to express the ^{3}He-nucleus optical potential as a function of the optical potentials of the constituent nucleons of the ^{3}He. This can be done by first summing over all the target nucleons in eq.(2), thus $V = \sum_{j=1}^{3} V_j$, where V_j is now the nucleon-nucleus optical potential for the j^{th} nucleon of the ^{3}He. Thus the ^{3}He-nucleus optical potential is

$$U^H_{opt} = \left\langle \phi_0(\xi_I) \left| \sum_{j=1}^{3} \left[V_j + V_j Q_0 \frac{1}{E - Q_0 H Q_0 + i\epsilon} Q_0 \sum_{j=1}^{3} V_j \right] \right| \phi_0(\xi_I) \right\rangle_A \qquad (4)$$

The propagator in eq.(4) contains the total Hamiltonian H. As before[2] we decompose the propagator to be a function of the Hamiltonian H_j for the j^{th} nucleon of the ^{3}He interacting with the target nucleus. Then only retaining terms second order in V_j we obtain

$$U^H_{opt} = \left\langle \phi_0(\xi_I) \left| \sum_{j=1}^{3} \left[V_j + V_j Q_j \frac{1}{E_{eff} + Q_j H_j Q_j + i\epsilon} Q_j \sum_{j=1}^{3} V_j + \cdots \right] \right| \phi_0(\xi_I) \right\rangle_A \qquad (5)$$

where Q_j is the analogeous operator to Q_0 of eq.(3b) for the nucleon-nucleus system and

$$E_{eff} = E - T_\ell - T_k \qquad (6)$$

where T_ℓ and T_k are the kinetic energy operators of the other two nucleons of the ^{3}He. Now calculating the potential at E_{eff} instead of E is equivalent to including the internal motion of the nucleons of the projectile. In eq.(5) there are 9 propagator terms. We distinguish between the protons (P_1,P_2) and neutron (n) of the ^{3}He and so j= P_1, P_2 or n.

2.1.2 Approximations.

We proceed as before[2]

(i) Choosing $\phi_0(\xi_I)$ to be symmetric with respect to exchange of the

positions of the nucleons of the ^{3}He allows us to put

$$V_{p_1} \equiv V_{p_2} \qquad \text{and} \qquad G_{p_1} \equiv G_{p_2} \tag{7a}$$

(ii) We make the additional approximation in second order only

$$V_n \sim V_p \tag{7b}$$

2.1.3 Meaning of propagator terms.

With the approximations of eqs.(7) the propagator terms refer to 1p 1h excitations of the nucleons of the ^{3}He. At low energies the intermediate states in the propagator are those of the ^{3}He-target compound nuclear system. At medium energies, in which we are interested here, the required intermediate states are the excited levels of the unperturbed system. Since the ^{3}He projectile has no excited levels[4] only the target excited states contribute. Thus the nucleons of the ^{3}He undergo 1p 1h excitations using as intermediate states the target excited levels. Therefore the presence of the propagator terms extends the folded model to include the excitations of the nucleons of the projectile. This amounts to simulating the effect of the break up of the ^{3}He projectile. Further in eq.(5) we have made a perturbation expansion, thus the propagator terms in our case will give an attractive potential.

2.1.4 Model representation of eq.(5).

The nucleon-nucleus optical potentials V_j have real and imaginary parts which are approximated as follows in the calculation of the ^{3}He optical potential.

(a) The real part is calculated in a folded model that takes into account exchange[5] scattering effects in the nucleon-nucleus optical potential. This exchange prescription has also been extensively[6,7] tested in α-nucleus scattering and found to be adequate[7] to represent single nucleon exchange effects. The effective interaction used is an extension of the Kuo[8] force where odd state forces and the energy dependence of the effective interaction have been included.[9,10]

(b) The imaginary part is calculated in a Fermi gas model where the potential is given by[9,11)]

$$W(r) = -\frac{1}{2}\hbar v_p \langle \sigma_T \rangle \left(1 + 0.6\nabla^2\right) \frac{U_R}{J_R} \qquad (8)$$

with v_p, the projectile velocity, $\langle \sigma_T \rangle$, the average nucleon-nucleon cross-section in nuclear matter, where the Pauli principle has been included. The term $(1 + 0.6\nabla^2)$ simulates[9,11)] the effect of non-forward N-N scattering amplitudes. The factor U_R/J_R gives the potential a finite range[9,11)] where U_R is the real potential as calculated above and J_R is its volume integral. Dynamically eq.(8) corresponds to an incoherent 1p 1h excitations mechanism.[12)]

(c) The ^{3}He-nucleus optical potential is calculated by folding the direct terms of the nucleon-nucleus optical potential with the local target density and the exchange terms with the equivalent local target density,[9)] so that eq.(5) is properly antisymmetrized. The classification of the terms of the potential is the same as before[2)] but suitably extended for the use of our effective N-N interaction.[9,10)] However unlike the previous[2)] calculation, the imaginary potential is split into its first and second order and energy dependent parts in an identical way to the real potential. This is possible since each component of the real potential yields an identical component for the imaginary potential as can be seen from eq.(8).

2.1.5 Physical content of the single particle model.

(1) The break up of the projectile ^{3}He has been simulated in a perturbation approximation as explained in subsection 2.1.3.

(2) Internal motion of the ^{3}He nucleons is included in the definition of E_{eff} in eq.(6).

(3) Single nucleon exchange has been included. This is likely to be the dominant exchange contribution since ^{3}He is a weakly bound projectile.

(4) Only single particle intermediate states have been included throughout.

2.2 Inclusion of coherent imaginary potential.

In subsection 2.1 the imaginary part of the nucleon-nucleus optical potential was calculated in a single particle approximation. However the imaginary potential is known to have a coherent[12] component which is difficult to include microscopically, so we resort to the phenomenological coupled channels approach[13] in the following manner. We preserve identically the single particle projection operators of eqs.(3), then we extend the open channel space by defining a new projection operator P to include both single particle and coherent components as

$$P\psi = P_o\psi + P_{in}\psi = \phi_o(\xi_T)\,\phi_o(\xi_I) + \sum_{i=1}^{n} \phi_i(\xi_T)\,\phi_o(\xi_I) \qquad (9)$$

where the projection operator P_{in} projects on to the inelastic collective states of the target and on to the ground state of the projectile. Then the projection operators for the closed channels are $Q_o = I_E - P_o$ and $Q_{in} = I_{in} - P_{in}$ with $I_E + I_{in} = 1$. Thus for all projections we have a separation of the single particle and coherent components. Therefore we can preserve intact the entire single particle potential calculated in subsection 2.1.

In the coupled channels method[13] the interaction potential has two components. The spherical part which describes the uncoupled single elastic channel and so is represented by the optical potential. The deformed part which couples the elastic channel with the target inelastic levels is represented by the coherent deformed optical potential. Therefore identifying the single particle potential of subsection 2.1 with the spherical component of the coupled channels potential leads automatically to the separation desired in eq.(9). However, in the conventional coupled channels approach[13] both the real and imaginary parts of the optical potentials are deformed, but in our calculations only the imaginary potential was deformed.

2.2.1 Dynamics of the imaginary potential.

Now the imaginary potential has contributions from (i) incoherent energy conserving 1p 1h excitations of the ^{3}He nucleons via

the single particle levels of the target and (ii) coherent energy conserving excitations to target collective levels. Also the dynamics described in subsection 2.1.5 are still inherent in the model.

3. RESULTS

Here we test the models of section 2 against elastic scattering cross-sections for ^{3}He scattering from ^{56}Fe between 30 - 85 Mev. It was hoped to test these models using the recently acquired[9] data at 53·53 Mev from ^{40}Ca, ^{44}Ca and ^{48}Ca, but the lengthy coupled channels analysis is as yet incomplete.

3.1 Single particle potentials.

The detailed results with this model are not of immediate importance to the aim of this paper, but it is a necessary step before we can discuss the results with the coherent imaginary potential. In Fig.1 the fits to the data are displayed for the present[9,10] extension of the Kuo interaction and also for the original[8] Kuo interaction.

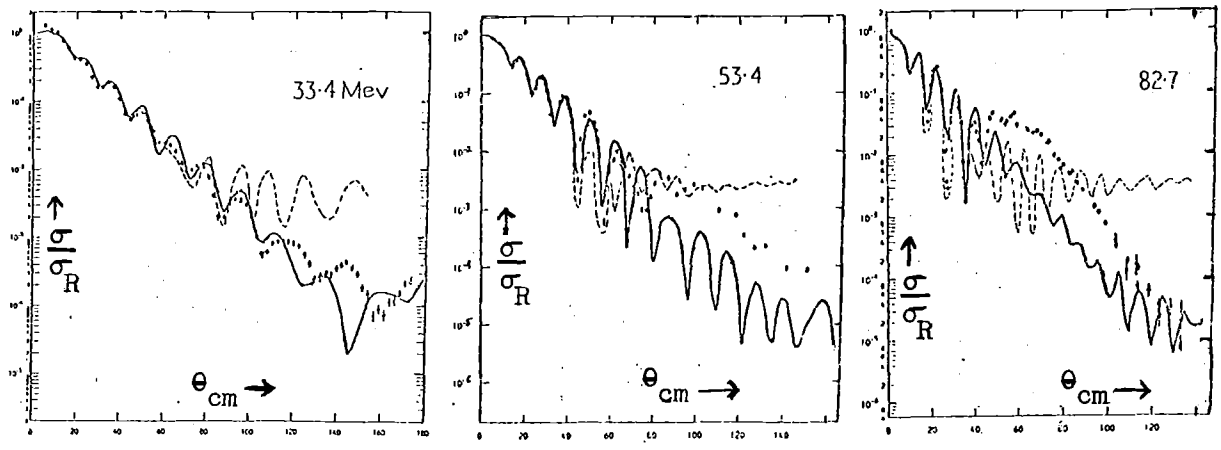

Fig. 1. - Fits to the ^{3}He - ^{56}Fe elastic cross-section data. The fit with the present interaction is the solid line and the fit with the Kuo interaction, taken from ref. 14, is the broken line.

From the data analysis the following points emerge:
(a) The analysis[14] with the Kuo force[8] using the potentials of ref. 2 for

the ^{3}He - ^{56}Fe system clearly shows that the model breaks down very severely for all but the forward angles.

(b) The situation is somewhat retrieved when we use the model of subsection 2.1.4 which includes[9,10] the energy dependence of the effective N-N interaction and odd state forces. Now the forward angle region is well fitted and the calculated cross-sections do fall off unlike the Kuo case. However, the renormalization parameters for the real and imaginary potentials are $S_R \sim 0{\cdot}5$ and $S_I \sim 1{\cdot}2$ respectively. For the real part we have not solved the renormalization problem, but it should be remembered that (i) in our model (subsection 2.1.3) the second order terms are a priori attractive; (ii) the closure approximation still persists in our interaction[9,10] and so the second order terms are probably overestimated; (iii) for the ^{3}He projectile, models[2,15,16] with a second order potential reproduce the data better. Thus both the perturbation expansion and the model representation of the second order terms require further investigations.

(c) In the present analysis an attempt was made to fit the data by introducing ad hoc renormalization parameters for the energy dependent and independent parts of both the real and imaginary potentials. At 53·4 and 82·7 Mev this procedure did not lead to any improvement, but the 33.4 Mev data could be fitted with unphysical renormalization parameters.

Therefore we conclude

(i) The ^{3}He-nucleus interaction for the 33·4 Mev data is different from the higher energy cases.

(ii) For the 53·4 and 82·7 Mev cases we have reached the limit of validity of the present single particle model.

(iii) Only the forward angle data can be fitted with our single particle model.

3.2. Inclusion of coherent imaginary potential.

From the above analysis it is clear that more physics should be included into the model for the ^{3}He-nucleus interaction.

3.2.1 Details of analysis.

We start by systematically considering the inclusion of collective levels for the 82·7 Mev case. The collective states were included so that the open channel space was gradually extended. The following models were considered:-

(i) The inclusion of the first 2^+ state at 0·8465 Mev as a one phonon vibration.

(ii) Mixture of a one phonon state 2^+ (0·8465) and two phonon states 4^+ (2·0851) and 2^+ (2.658). The figures in brackets are the energies of the states in Mev. In this case ^{56}Fe is treated as a typical vibrating nucleus.

(iii) Mixture of a quadrupole 2^+ (0·8465) and Octapole 3^- (3.27) one phonon states.

(iv) The inclusion of 2^+ (0·8465) and 4^+ (2·0951) levels as rotational states. Here ^{56}Fe is treated as a rotational nucleus.

In all the above cases the relevant coupling parameters were determined emperically by fitting the data. The renormalization parameters S_R and S_I respectively of the real and imaginary potentials were also optimised. None of the above models showed sufficient improvement to suggest that collective states contributed to the ^3He-nucleus interaction potential, but the rotational model was found to be the best. Therefore

(v) next we considered a deformed nucleus with a ground state rotational band 0^+ (0·0), 2^+ (0·8465), 4^+ (2·0851); a Beta band 0^+ (2·942); a Gamma band 2^+ (2·658) and an Octupole band 3^- (3·27). In order to determine the most important vibrations a careful search procedure had to be initiated.

(a) The initial values of the coupling parameters β_i for each of the abovementioned i bands was taken as in table 1. These β_i values were fixed and the renormalization parameters S_R and S_I were varied.

Table 1. Values of β_i obtained from previous analyses.

Band	β_i Value	Ref.
Ground state	$\beta_g = 0.19$	17
Beta	$\beta_\beta = 0.1$	18
Gamma	$\beta_\gamma = 0.11$	19
Octupole	$\beta_{oct} = 0.1$	20

(b) Then with the fixed new values of S_R and S_I, the coupling parameters for the vibrations were varied i.e. β_β, β_γ, β_{oct}. The ground state deformation parameter β_g was not varied as this caused random sign changes in other β_i parameters that were being varied simultaneously.
(c) Then S_R, S_I, β_β, β_γ and β_{oct} were all varied.
(d) The band structure was systematically changed at this stage using the criteria: As the coupling parameter for a given band tended towards zero, We removed the levels of that band and added levels of higher excitation energy to the bands with the largest values of the coupling parameter. Then sequence (c) was initiated again.
(e) Finally, having obtained a stable configuration by repeatedly performing sequences (c) and (d), we then allowed all the parameters to be varied including β_g. The value of β_{oct} was not well determined and was fixed in several of the search sequences.

Next the 53·4 Mev data was analysed starting with the converged β_i values and band structure obtained from the 82·7 Mev data analysis. Having followed the above search procedure it was found that the β_i values automatically converged very close to those for the 82·7 Mev. On exchanging the β_i values of the two cases we were able to get almost indistinguishable fits to the data in both cases. Therefore an average was taken of each β_i value obtained from the analysis of the data at 53·4 and 82·7 Mev. These values are presented in table 2 and the fits to the data are displayed in Fig. 2.

The 33·4 Mev data was similarly analysed using all five schemes described above but no evidence for collective effects was found. This result is in keeping with the observation in section 3.1 that

the 33·4 Mev data could be fitted by including various parameters into our single particle model.

Table 2. Parameters obtained from the analysis.

Energy	S_R	S_I	β_i Values
82·7 Mev	0·5	1·09	$\beta_\gamma = 0{\cdot}326$, $\beta_\beta = 0{\cdot}349$
53·4 Mev	0·48	1·02	$\beta_{ct} = 0{\cdot}15$

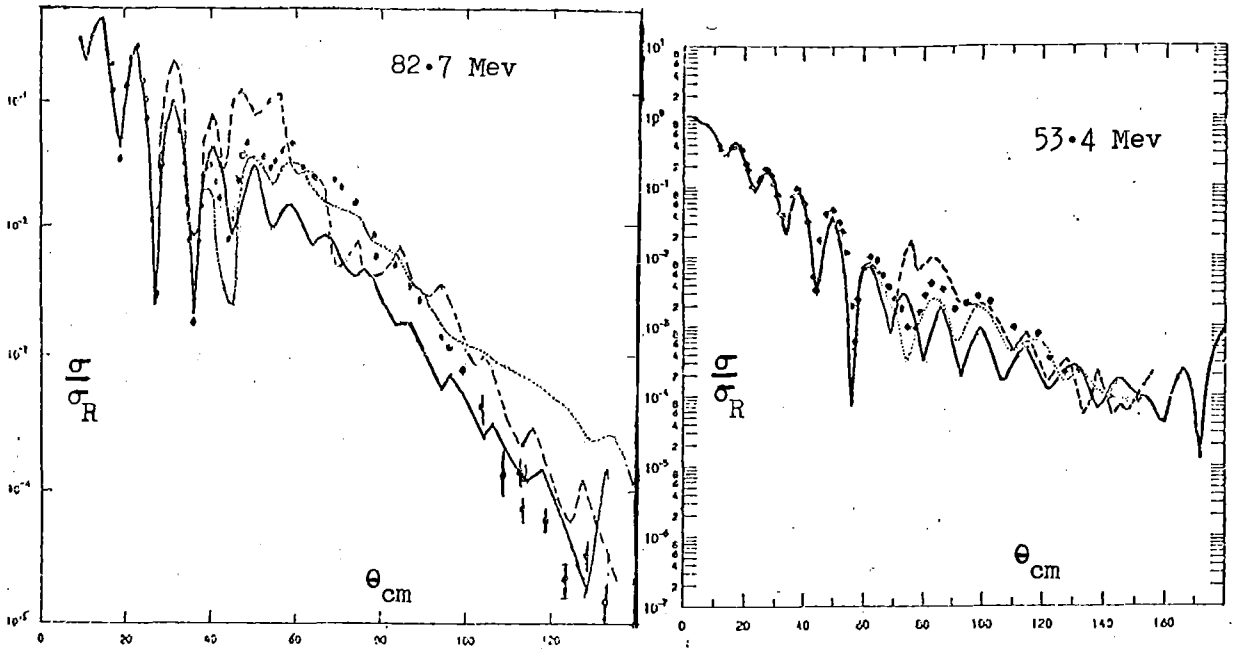

Fig. 2. - Best fits to the ^{3}He-^{56}Fe elastic cross-section data. The present model fits are the solid lines. The semi-microscopic (microscopic real and phenomenological imaginary) fits of ref. 16 are the broken lines. The phenomenological coupled channels fit of ref. 21 to the elastic channels are the dotted lines.

We conclude from this analysis that

(i) The magnitude and structure of the data is much better reproduced on including a coherent imaginary potential. Further improvement may be possible by coupling to more levels but this is beyond our scope at present. However, the essential features of the data are reproduced here.

(ii) The back angle elastic scattering data is almost completely determined by the imaginary part of the optical potential, while the forward angles are determined by the real potential.
(iii) The imaginary potential is very sensitive to the nature of the collective states that enter into its calculation. Thus this part of the potential is sensitive to the shape of the nucleus.

3.2.2 Comparison with other analyses.

In Fig. 2, along with the coherent imaginary fits, we show for comparison (i) the best fit taken from ref. 16, where the first and second order real potentials were calculated in a different single particle model, but the imaginary potential was phenomenologically fitted.
(ii) The best fit to the elastic channel taken from a phenomenological coupled channels analysis[21]. The following features appear from this comparison.
(a) In the backward hemisphere, where the data is almost entirely reproduced by the imaginary potential, we find that our prescription for the imaginary part is better, since the phenomenologically[16] fitted one produces rather erratic oscillations. Further the parameters introduced in our analysis (subsection 3.2.1) have a direct physical interpretation, unlike the phenomenological ones.
(b) Our fits are very similar to those obtained for the elastic channel in a phenomenological[21] coupled channels analysis. At 53·4 Mev our fits are only slightly inferior in reproducing the magnitude of the cross-section. At 82·7 Mev our model reproduces more closely the gradient of the fall off of the data, but cannot reproduce the magnitude of the last maxima at ~ 70. However, our analysis does clearly treat ^{56}Fe as a rotational nucleus while equivalent[21] fits were obtained phenomenologically using either a rotational or vibrational model.

3.2.3 Values of β_i.

The values of the β_i parameters of table 2 obtained from the present analysis are much larger than those of table 1 obtained from previous phenomenological analyses. Earlier[22] for α-nucleus inelastic

scattering exactly the same was observed. This feature may easily be explained. A phenomenological Woods-Saxon potential is on average proportional to the nuclear density ρ . However, a calculated microscopic potential is a complicated function of the density:

Direct density-independent part $\propto \rho$

Direct density-dependent part $\propto \rho \cdot \rho^{2/3}$

Exchange density-independent part $\propto \rho_M(r, r')$

Exchange density-dependent part $\propto \rho_M(r, r') \cdot \rho^{2/3}$

where the effective N-N interaction[9,10] has a $\rho^{2/3}$ dependence and $\rho_M(r,r')$ is the mixed density. It can be seen that only the first contribution is linearly proportional to the density. All other contributions are powers of the density, which give the calculated potential extra curvature i.e. diffuseness as compared to the phenomenological Woods-Saxon potential. Therefore larger values of β_i are required to achieve the same deformations as the phenomenological potential, although this feature is not quantitatively established yet. However, it has been pointed out[23] that values of β_i are not themselves comparable from one analysis to another, but the values of $\beta_i R$ are comparable, where R is the half value radius of the Woods-Saxon potential used in the analysis. This procedure is perfectly alright as long as we are comparing potentials that are parametric variations of a fixed form. In such a case the half value radius R simply becomes a reference point for comparison between two analyses. In a microscopic model the half value radius of the potential is determined by competition between physical effects such as energy dependence, odd state contributions, exchange scattering etc.. Therefore a single parameter like the half value radius is not sufficient to describe the surface region of the potential. Thus in the absence of a quantitative relation we suggest that larger values of β_i are obtained for microscopic potentials due to their larger diffuseness.

3.2.4 Suggested nuclear shape.

The present analysis clearly indicates that ^{56}Fe is a deformed nucleus. The phenomenological coupled channels analysis[21] is unable to distinguish between a rotational or vibrational model for ^{56}Fe even though the analysis included elastic and inelastic scattering data

between 30-83 Mev. The vibrational model yields[21] a value of $\beta_g = 0{\cdot}19$ and rotational $\beta_g = 0{\cdot}172$. The experimental[17] estimate of $\beta_g = 0{\cdot}19$, but the levels of the ground state band were fitted using a rotational model. We conclude that from our analysis that ^{56}Fe is a deformed nucleus, which is in agreement with experimental findings within the limitations mentioned in subsection 3.2.3.

4. CONCLUSIONS

(1) Forward angle elastic scattering cross-sections for the ^{3}He-nucleus system at medium energies are sensitive to the real part of the optical potential and the backward angles to the imaginary potential.

(2) Between about 50-80 Mev the imaginary potential is strongly coherent and the ^{3}He projectile excites target collective levels. It is found that the back angle data is sensitive to the nature of the target collective states that enters into the calculation of the imaginary potential. Thus this part of the potential is sensitive to the shape of the nucleus.

(3) The shape for ^{56}Fe determined from the present analysis is in agreement with experimental findings. However, a quantitative method of comparing deformations obtained from microscopic and phenomenological analyses still requires to be established.

(4) The dynamics of the imaginary part of the ^{3}He-nucleus optical potential is: (i) incoherent 1p 1h excitations of the nucleons of the ^{3}He using the excited single particle levels of the target as intermediate states
(ii) excitation of target collective states.

(5) The inclusion of the projectile excitations in a perturbation expansion requires to be examined.

(6) Experimentally and theoretically it is worth studying the ^{3}He-nucleus interaction because it is still possible to measure accurately cross-sections in the backward hemisphere, which gives a sufficient angular range to study the nature of target excited states if the excitations of the ^{3}He can be properly treated. Thus we have an additional way of suggesting the shape of a given nucleus.

ACKNOWLEDGEMENTS

I would like to thank N. M. Clarke for making available to me his version of T. Tamura's coupled channels code JUPITER and also for explaining its computational intricacies to me. I would like to thank E. W. Lees for useful discussions, R. J. Griffiths for his interest in this work and P. W. Tedder for computing assistance at an early stage of the work. Most of this work was done while the author was at Kings College and Imperial College, London. Finally I would like to warmly thank Professor R. Vinh Mau for his kind hospitality at Orsay and the C.N.R.S. for a research fellowship.

REFERENCES

1. H. V. von Geramb, Microscopic Optical Potentials, Springer-Verlag (1979).
2. B. Sinha, F. Duggan and R. J. Griffiths, Nucl. Phys., A241 (1975) 229.
3. G. R. Satchler and W. G. Love, Phys. Lett., 76B (1978) 23.
4. S. Fiarman and S. S. Hanna, Nucl. Phys., A251 (1975) 1.
5. G. L. Thomas, B. C. Sinha and F. Duggan, Nucl. Phys., A203 (1973) 305.
6. Z. Majka, A. Budzanowski, K. Grotowski, A. Strzalkowski, Phys. Rev., C18 (1978) 114.
   Z. Majka, H. J. Gils and H. Rebel, see Ref. 1.
7. Y. Eisen and B. Day, Phys. Lett., 59B (1976) 253.
8. T. T. S. Kuo, Nucl. Phys., A103 (1967) 71.
9. F. Duggan, Ph.D. thesis, London (1977), unpublished.
10. F. Duggan, Proceedings of Congrès de la Société Francaise de Physique, Toulouse 25-30 June 1979 - to be published in J. de Phys..
11. B. Sinha and F. Duggan, Phys. Lett., 47B (1973) 389.
    B. Sinha and F. Duggan, Nucl. Phys., A226 (1974) 31.
12. G. E. Brown, Comments Nucl. Part. Phys., 4 (1970) 75.
13. T. Tamura, Rev. Mod. Phys., 37 (1965) 679.
14. S. A. Weisrose, Ph.D. thesis, London (1973), unpublished.
15. S. K. Samaddar, R. K. Satpathy and S. Mukherjee, Nucl. Phys., A150 (1970) 653.
16. R. J. Griffiths, B. Sinha and N. M. Clarke, J. Phys., G2 (1976) 929.

17. P. M. S. Lesser, D. Cline, P. Goode and R. N. Horoshko, Nucl. Phys., A190 (1972) 597.
18. K. Matsuda, Nucl. Phys., 33 (1962) 536.
19. A. R. Mazumdar and H. M. Sen Gupta, Nucl. Phys., A118 (1968) 151.
20. G. R. Satchler, R. H. Bassel and R. M. Drisko, Phys. Lett., 5 (1963) 256.
21. N. M. Clarke, J. Phys., G1 (1975) 895.
22. R. S. Mackintosh, Nucl. Phys., A210 (1973) 245.
23. A. M. Bernstein, Advances in Nuclear Physics, Eds. M. Baranger and E. Vogt, 3 (1969) 325.

SCATTERING OF STRONGLY ABSORBED PARTICLES NEAR THE COULOMB BARRIER

B. Fernandez
CEN Saclay,
France

SCATTERING OF STRONGLY ABSORBED PARTICLES NEAR THE COULOMB BARRIER

B. Fernandez

DPh-N/BE, CEN Saclay, BP 2, 91190 Gif-sur-Yvette, France

Lecture presented at the International discussion meeting
"What do we know about radical shape of nuclei in the Ca region"?
Kernforschungszentrum Karlsruhe, 2-4 May, 1979

I. Introduction

What can we learn from the elastic scattering of strongly absorbed particles near the Coulomb barrier? If we define a strongly absorbed particle as a particle which is totally absorbed once it has surmounted the Coulomb barrier, we see immediately that we are going to learn something on the tail of the potential outside of the Coulomb barrier, which is in turn influenced by the tail of the density distributions of the colliding nuclei. In the present talk I will show in part II what can be deduced from α-scattering near the barrier on a large range of nuclei, *not including* calcium region, and in part III what can be deduced from ^{16}O scattering near the Coulomb barrier on some calcium isotopes.

II. Elastic scattering of α particles from medium and heavy nuclei

Figs. 1 and 2 show two examples of α-particle scattering near the Coulomb barrier on medium and heavy nuclei. Fig. 1 shows excitation functions which were measured near 180° at the Saclay tandem by Badawy et al. [1] from a range of nuclei from ^{110}Cd to ^{208}Pb. Fig. 2 shows an angular distribution measured at 22 MeV from ^{209}Bi by Barnett and Lilley [2]. Both types of data can be interpreted in the framework of a four-parameter optical model with strong absorption, and very good fits are obtained (the lines in Figs. 1 and 2 are optical model fits).

The signature of strong absorption is not as simple as it is at higher energies, where the reflection coefficients $|\eta_\ell|$ jump from zero to one in a few ℓ-values near the grazing angular momentum. Here, the angular momenta involved are small and their effective barriers are close to each other. As a result, η_ℓ varies smoothly from small values to one as a function of ℓ. Strong absorption is characterized by the fact that the calculated cross-sections are insensitive to the depth of the imaginary potential inside the Coulomb barrier, provided it has some minimum value which insures the total absorption of particles. This is apparent in Fig. 3, where the χ^2 is plotted as a function of W (all other parameters being kept fixed). Clearly any value between 10 and about 50 MeV will give almost the same fit to the data. Another indication is the agreement with incoming wave boundary (IWB) calculations which *assume* strong absorption from the beginning [3]. However, D.F. Jackson and M. Rhoades-Brown [4] have shown that strong absorption is not necessary to fit the data. Equally good fits are obtained with weakly absorbing potentials. The signature of weak absorption is here an odd-even staggering of $|\eta_\ell|$ as a function of ℓ, as compared to their smooth behaviour in the case of strong absorption. Fig. 4 from ref. [4], shows the reflection coefficients for different real potentials, and with a (weakly

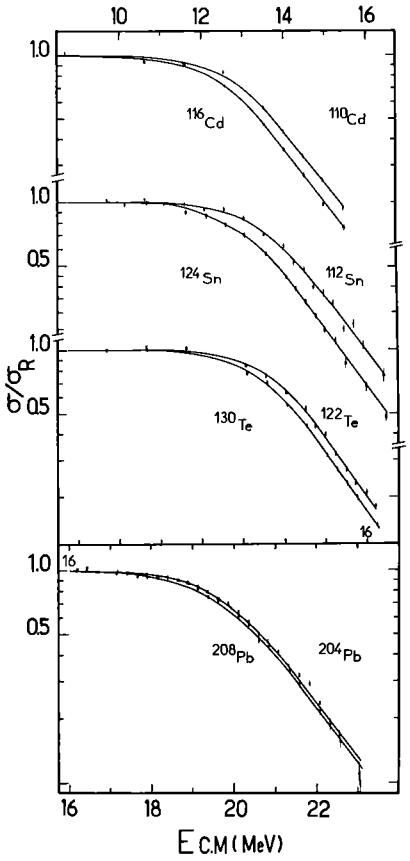

Figure 1

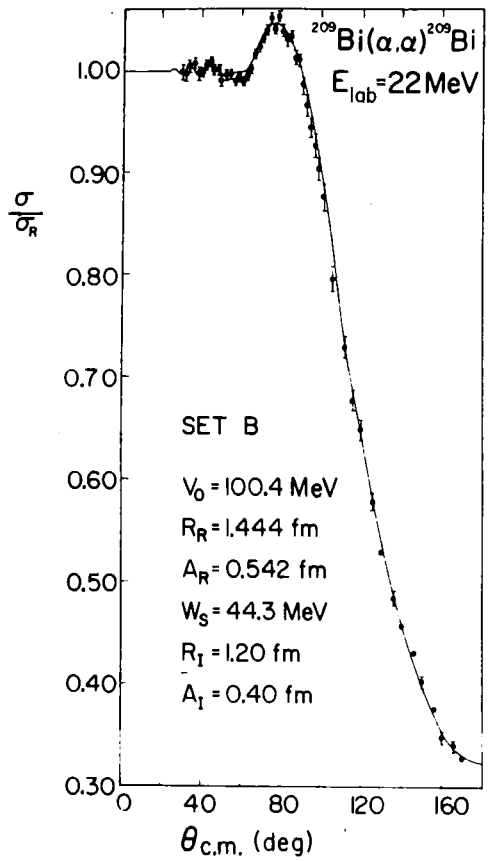

Figure 2

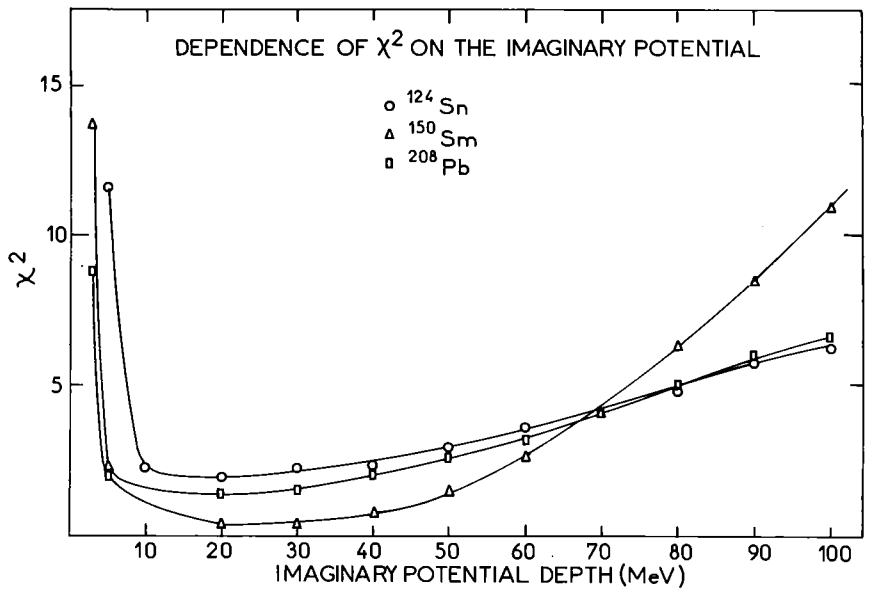

Figure 3

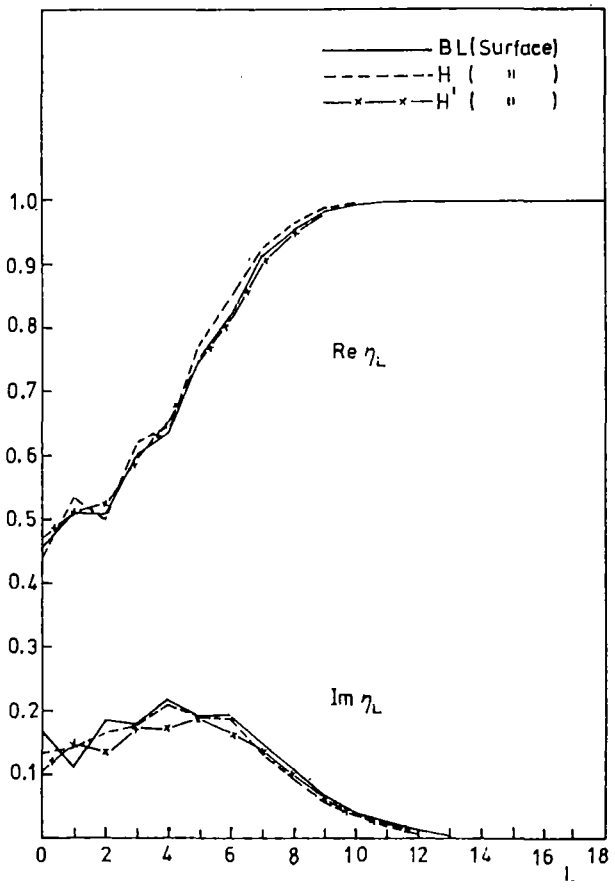

Figure 4

absorbing) surface imaginary potential which was ajusted to give the best fit to the Pb(α,α) data of Barnett and Lilley [2] at 22 MeV. Fig. 5 shows the η_ℓ^1s obtained by Barnett and Lilley for either volume (strong) absorption (full line) or surface (weak) absorption (dashed line). The calculated cross-sections are essentially identical except at small angles where the latter gives more interferences, but even there differences are on the 1 % level. In the absence of a small-angle, very precise experiment, it is largely a matter of taste to decide if there is weak or strong absorption. My personal prejudice is that an α particle which penetrates a ^{208}Pb nucleus has very little chances of not being absorbed and form ^{210}Po, which can certainly offer all possible phase space at 19 MeV excitation. That was in any case the attitude we adopted to analyse the Saclay data [1] and I will discuss now which conclusions can be arrived at if strong absorption is assumed.

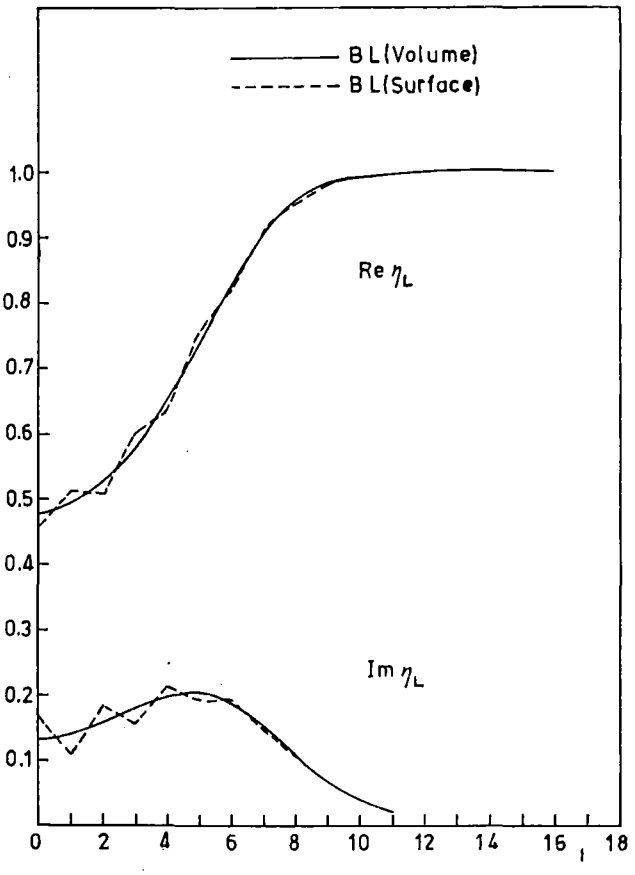

Figure 5

In a strong absorption situation, the data are only sensitive to the real potential outside of the Coulomb barrier. As a consequence, only two parameters at best can be determined namely the Igo constant V exp $\frac{R}{a}$ and the diffuseness parameter a. However, at energies close to the Coulomb barrier,

the data are very insensitive to the value of a and only one size parameter can be determined. Goldring et al.[5] have used the α-nucleus distance at the maximum of the Coulomb barrier, which they call the Rutherford radius r_R, while Tabor et al.[3] have used a "constant fraction" radius where the ratio of the nuclear and Coulomb potentials is 2 %. In the analysis of the Saclay data, we found that all potentials giving a good fit cross in a very narrow region, where their depth is about 0.2 MeV, see Fig. 6. Therefore the best choice for a size parameter is the α-nucleus distance $R_{0.2}$ such as $V(R_{0.2}) = -0.2$ MeV. In other words, all parameters V_o, R_{opt}, and a which give a good fit obey the relationship

$$V_o \exp\frac{R_{opt} - R_{0.2}}{a} = -0.2 \text{ MeV} \qquad (1)$$

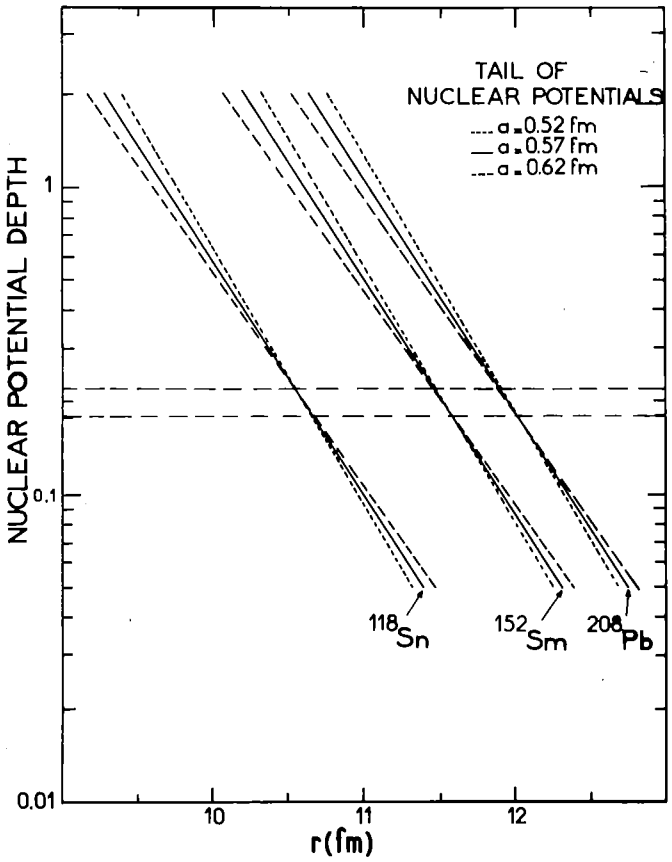

Figure 6

What does that imply on the density distribution of the target nucleus? Barnett and Lilley [2] have analysed their ^{209}Bi data by folding an effective force of Woods-Waxon type into various density distributions of Fermi shape and found that all densities which gave a good fit to the data crossed in a narrow region near 2×10^{-3} nucleon/fm^3. They used the effective α-nucleon interaction deduced from p-α and n-α free scattering at low energy by Mailandt et al.[6], namely at the barrier

$$V_{eff}(r) = 42.5 \left[1 + \exp\frac{r-2.27}{0.34}\right]^{-1}$$

(MeV, r in fm) (2)

The Saclay data were analysed using a variety of forces and density shapes, in order to determine which was the best determined density region and to which extend the result would depend on such choices. It was found that the choice of the shape of the distribution was not crucial. Either a simple Fermi shape

$$\rho(r) = \frac{\rho_o}{1 + \exp \frac{r - c_N}{a_N}} \qquad (F2)$$

or a "modified gaussian" shape [7]

$$\rho(r) = \rho_o \frac{1 + W \left(\frac{r}{c_N}\right)^2}{1 + \exp \frac{r^2 - c_N^2}{a_N^2}} \qquad (MG)$$

gave similar results.

In contrast, the results are more sensitive to the range of the effective force used. Four such forces have been used, either of gaussian shape

$$V_{eff}(r) = U_o \exp(- K^2 r^2)$$

or of Woods-Saxon shape

$$V_{eff}(r) = \frac{U_o}{1 + \exp \frac{r - R_{eff}}{a_{eff}}},$$

namely

(1) Gaussian, with $U_o = - 127$ MeV and $K = 0.6$ fm^{-1} (G1)
(2) Gaussian, with $U_o = - 42.5$ MeV and $K = 0.5$ fm^{-1} (G2)
(3) Gaussian, with $U_o = - 37$ MeV and $K = 0.5$ fm^{-1} (G3)
(4) Woods-Saxon, with $U_o = - 42.5$ MeV, $R_{eff} = 2.35$ fm and $a_{eff} = 0.34$ fm (WS)

The gaussian force G1 or, equivalently, the Woods-Saxon force WS, were found by Sumner [8] to give the best fit to his 42 MeV α scattering on ^{40}Ca, when he used for the ^{40}Ca density the Hartree-Fock calculation of Negele [9]. It is quite remarkable that this Woods-Saxon force WS is so close to the one deduced from quite different data by Mailandt et al. [6]. Batty et al. [10] have found that the range of gaussian forces should be between 0.5 and 0.6 fm^{-1}, and that U_o and K are then linked by the relationship

$$U_o K^{-6} \simeq 2600 \text{ MeV fm}^6. \qquad (2)$$

The gaussian force G1 and G2 have both

$$U_o K^{-6} = 2720 \text{ MeV fm}^6.$$

Finally, force G3 was derived by Bernstein [11] by folding a nucleon-nucleon force into a density distribution of the α particle. The calculated potentials with WS and G1 are equal within less than 1.5 keV outside of the Coulomb barrier, which makes these forces strictly equivalent.

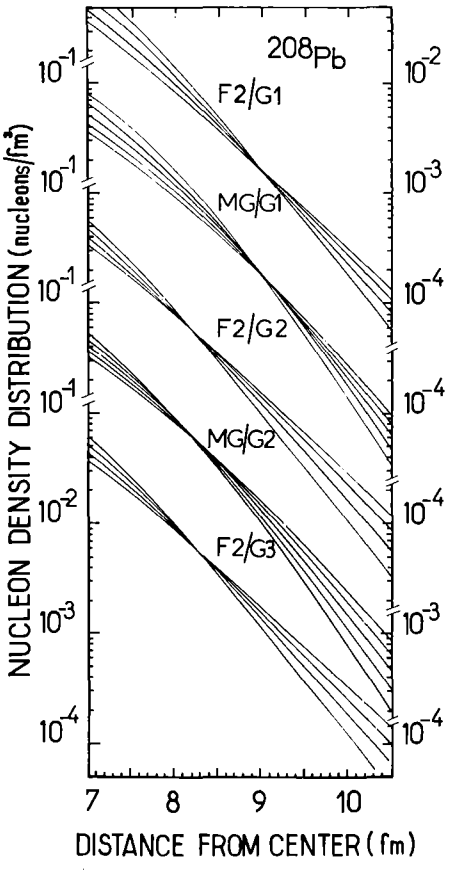

Figure 7

The different combinations of density shapes and effective forces which give a good fit to the $^{208}Pb(\alpha,\alpha)$ are represented on Fig. 7. Taking all such combinations into account leads to the determination of the radial distance $r_{0.002}$ where the density is 0.002 nucleon/fm^3 with a model-dependent uncertainty of ± 0.14 fm. From tin to lead, there exists a simple relationship between $r_{0.002}$ and the α-nucleus distance $R_{0.2}$ determined in the Woods-Saxon analysis :

$$r_{0.002} = R_{0.2} - (3.11 \pm 0.14)\text{fm}. \qquad (3)$$

If we restrict the values of the range of the force, the model-dependent uncertainty is much smaller. We feel that there are some good evidences in favor of G1 ($K = 0.6$ fm^{-1}) :

a) it is essentially identical to WS, which was deduced quite independently,

b) it also gives a good fit to the ^{208}Pb data both at 42 MeV and at the barrier when the best calculated densities are used (1).

If we therefore restrict ourselves to G1, we have

$$r_{0.002} = R_{0.2} - (3.06 \pm 0.03)\text{fm}. \qquad (4)$$

The values of $r_{0.002}$ were deduced that way for 23 nuclei from ^{110}Cd to ^{208}Pb. They are shown on Fig. 8.Spherical nuclei follow a line

$$r_{0.002} = 1.355\ A^{1/3} + 0.87\ \text{fm}. \qquad (5)$$

Now, what about the calcium region? Some time ago, we tried a measurement at Saclay on $^{40,42,44,48}Ca$, looking at the elastic scattering near 180° as a function of energy. The results are shown on Fig. 9. It is very clear from this figure that ALAS was also present at the barrier, and in fact on all four calcium isotopes, and consequently no simple optical model analysis could be done

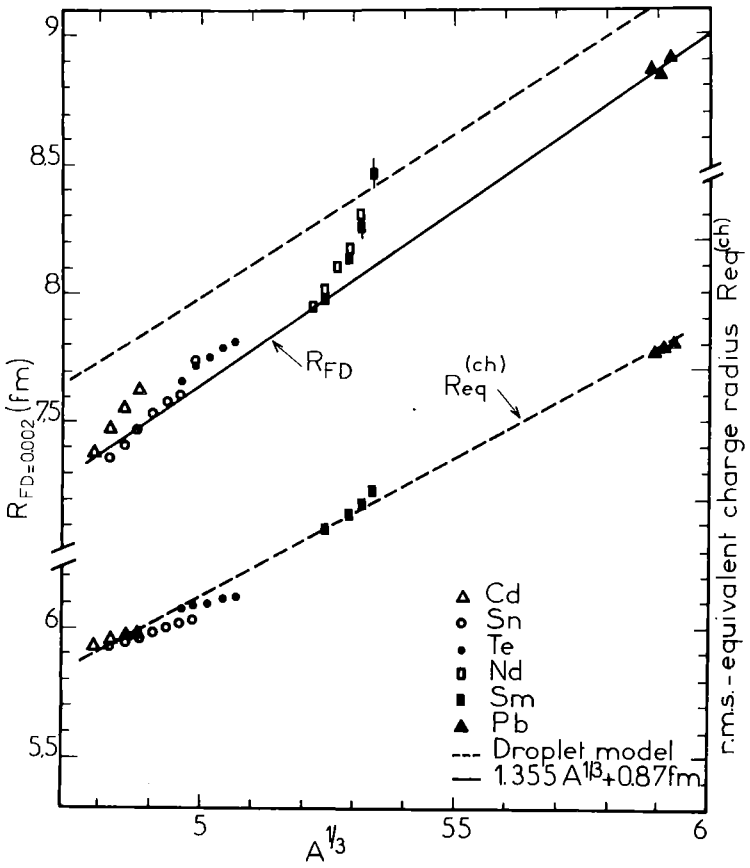

Figure 8

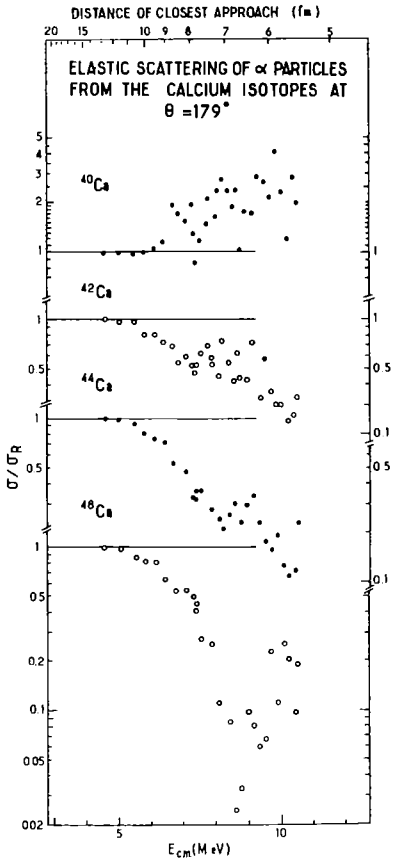

Figure 9

to learn something on the density distributions. I will therefore now turn to another projectile which *is* strongly absorbed in collisions with ^{40}Ca at the barrier, ^{16}O.

III. Elastic scattering of ^{16}O from calcium isotopes

The elastic scattering of ^{16}O near the Coulomb barrier was first used by Bertin et al.[12] in order to gain some information on the relative sizes of ^{40,44,48}Ca, after they observed that α scattering, as I said before, proved to be unsuitable for that purpose. They bombarded calcium targets by an oxygen beam between 20 and 42 MeV and observed the elastically scattered ions at lab.angles of 50°, 70°, 90°, 110° and 130°. The Coulomb barrier for ^{40}Ca is 23.5 MeV (c.m.) or 32.9 MeV (lab). The analysis of these data was made along the lines of ref. [5], in terms of the Rutherford radius deduced from a four-parameter optical model analysis. Fig. 10 shows their measurements for ^{48}Ca, with optical model fits to ^{48}Ca and ^{40,44}Ca as well.

A new measurement of elastic scattering of ^{16}O was made by Groeneveld et al. [13] on ^{40}Ca and ^{48}Ca, with another purpose in mind. They wanted to check a

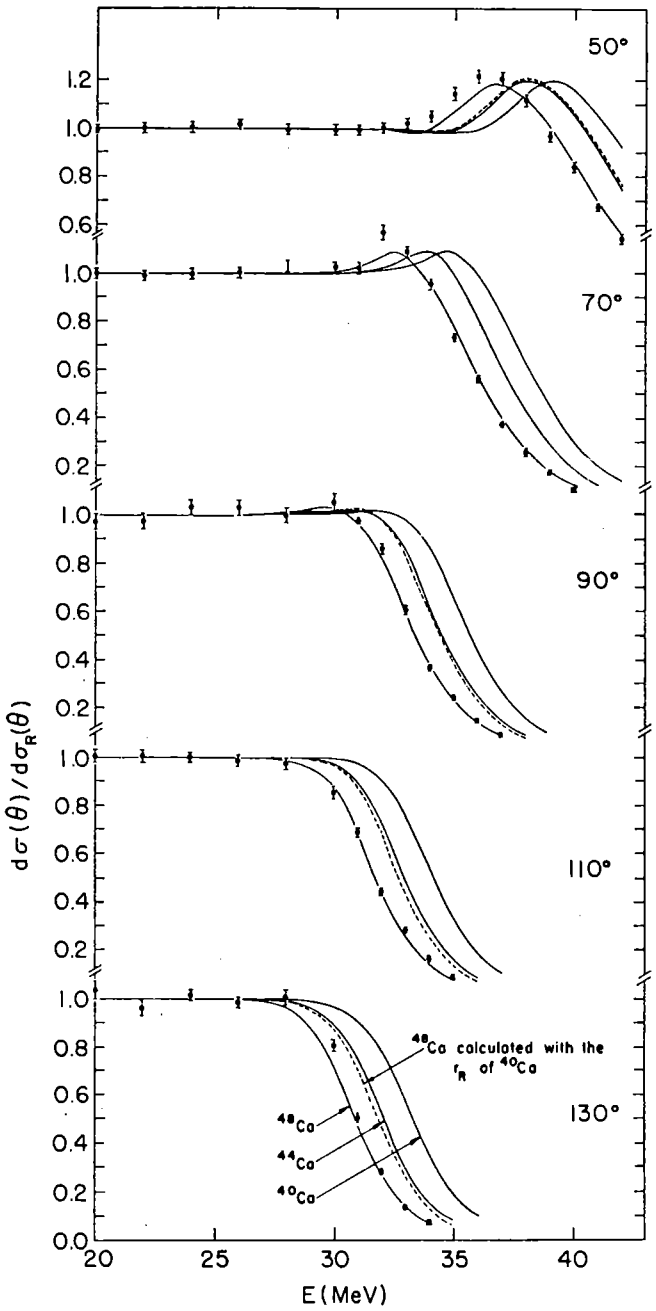

Figure 10

prediction made by Chatwin et al. [14] on the occurrence of resonances in the $^{16}O + ^{40}Ca$ elastic scattering, on the basis of the optical model with ℓ-dependent imaginary potential. Their data comprise excitation functions measured near 180° with an annular detector from 23 to 36 MeV, see Fig. 9, and angular distributions measured at 40 MeV(lab), see Fig. 11. The analysis of these data was made with a conventional four-parameter optical model (the lines in Figs. 11 and 12 are optical model fits) and the Rutherford radius was extracted. These data are very well suited to an analysis in terms of nuclear density distribution, which I have made recently and which I will now discuss.

A first investigation in terms of Woods-Saxon potential shows no sensitivity to the diffuseness parameter a, when it is allowed to vary from 0.5 to 0.7 fm. All potentials that give a good fit to the data lie within the hatched area of Fig. 13 (bottom part). It is clear that the nucleus-nucleus distance at which the potential is about 1 MeV deep is, to a large extent, independent of the choice of parameters V, R_{opt} and $\underline{a}$. We can for example determine for ^{40}Ca :

$$R_{1.0} = 9.50 \pm 0.03 \text{ fm}$$

or

$$R_{0.8} = 9.65 \pm 0.02 \text{ fm}.$$

The uncertainties quoted here are only the "model dependent" uncertainty.

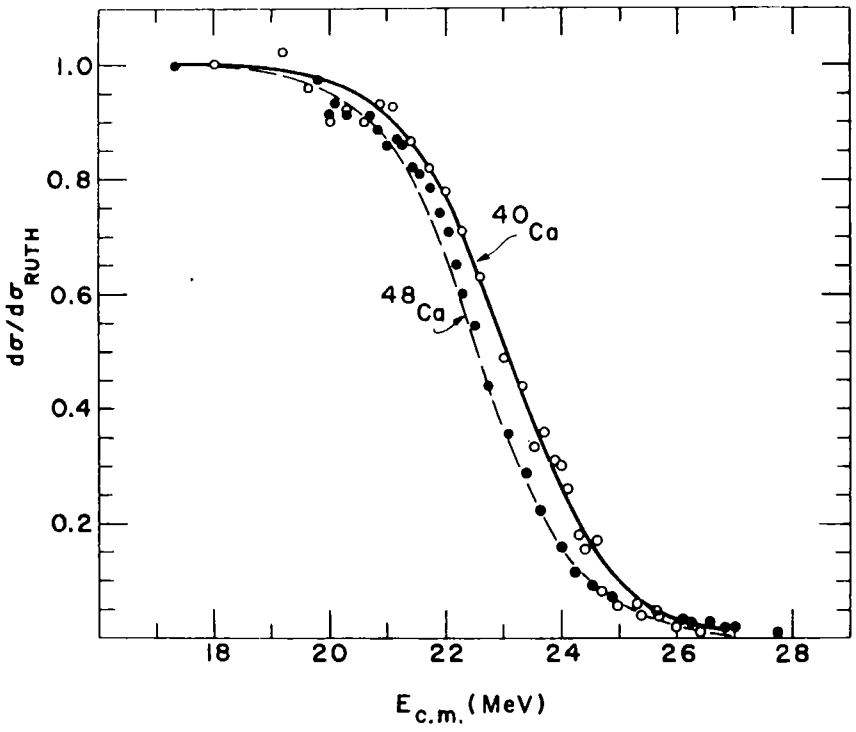

Figure 11

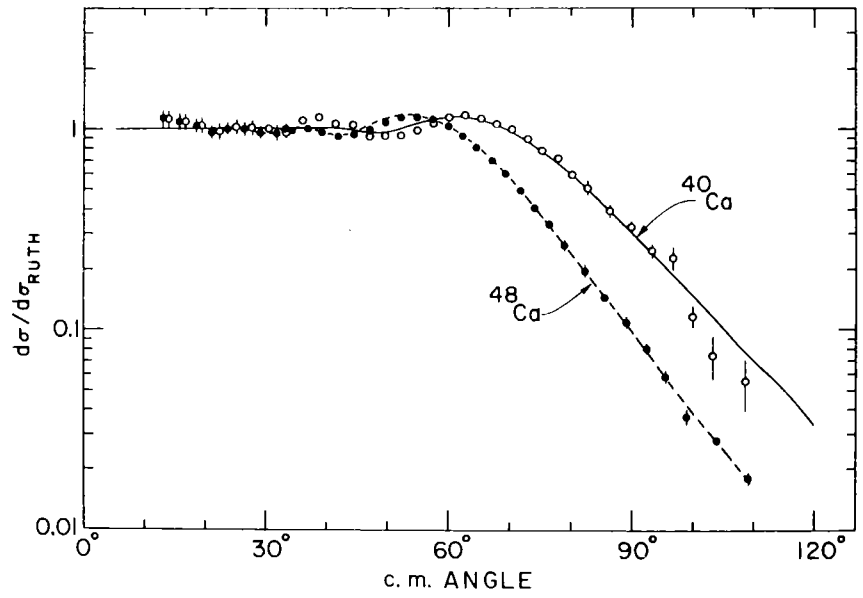

Figure 12

Let us now turn to a double folding model analysis. For that purpose I will take the view point that the best Hartree-Fock calculations available to-day for the doubly magic, N = Z, nuclei ^{16}O and ^{40}Ca give the neutron distribution as exactly as the proton distribution, to which they give very good fits. I have

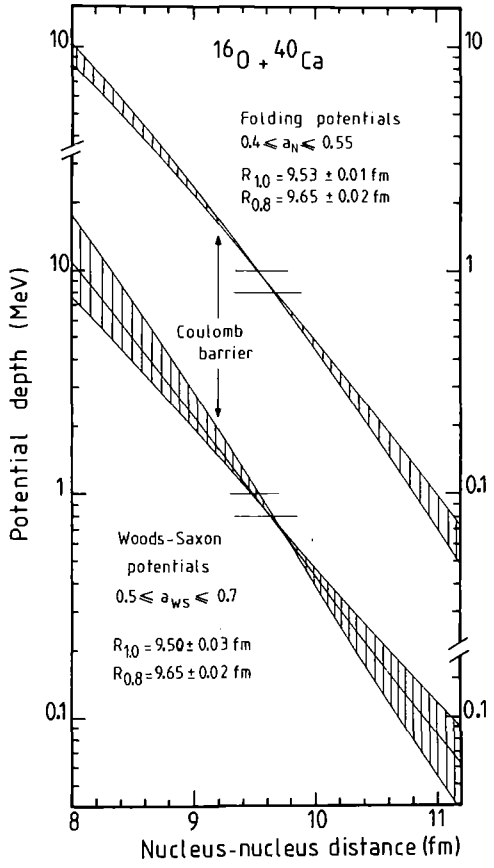

Figure 13

used the Hartree-Fock calculations of Campi [15]. It is now necessary to choose an effective nucleon-nucleon force which will generate by folding with these two densities a potential giving a good fit to the data. I have used the interaction of Satchler and Love [16], namely

$$V_{oo}(r) = U_1 \frac{\exp(-\mu_1 r)}{\mu_1 r} + U_2 \frac{\exp(-\mu_2 r)}{\mu_2 r} .$$

The parameters given by Satchler and Love, namely U_1 = 6315 MeV, μ_1 = 4 fm^{-1}, U_2 = - 1961 MeV and μ_2 = 2.5 fm^{-1} produce a potential which is, as noted by the authors, slightly too small in the tail. The best fit is obtained by varying slightly the strength U_2 of the second Yukawa potential from -1961 MeV to -2264 MeV or its range μ_2 from 2.5 fm^{-1} to 2.42 fm^{-1}. In both cases the fit to the data is exactly as good as with standard Woods-Saxon potential, such as shown in Figs. 11 and 12. This interaction, with μ_2 = 2.42 fm^{-1}, was then folded into the Hartree-Fock density of ^{16}O in order to produce a nucleon-^{16}O effective interaction with which we will now proceed to analyse (a) which region of the nucleon density of ^{40}Ca is most sensitive to the data and (b) other isotopes. This effective nucleon-^{16}O force is shown in Fig. 14 (full curve). On the same figure are plotted two approximations to it, which give in practice identical results, namely a Woods-Saxon form (dashed line, open circles)

$$\frac{22.45}{1 + \exp \frac{r-3.70}{0.51}} \quad \text{(MeV, r in fm)}$$

and a gaussian form (dotted line, open triangles)

$$137 \exp(-(0.42\, r)^2) \text{(MeV, r in fm)}.$$

Which is the radial region of the ^{40}Ca density which is most sensitive to ^{16}O scattering data near the Coulomb barrier? In order to answer this question let us first consider the following Fermi-2 parameter parameterization of the Hartree-Fock density of ^{40}Ca :

$$\rho(r) = \frac{0.1345}{1 + \exp \frac{r-3.88}{0.452}}.$$

This distribution differs from the Hartree-Fock one in the interior of the nucleus, but is within 1-2 % of it for r > 4 fm. It gives an equally good fit to the data. The diffuseness parameter of this distribution was varied from 0.400 to 0.575 fm in steps of 0.025 fm. In all cases an equally good fit could be obtained. All such densities fall in the hatched region of Fig. 15 where the Hartree-Fock density of Campi [15] is represented by a full line. It appears

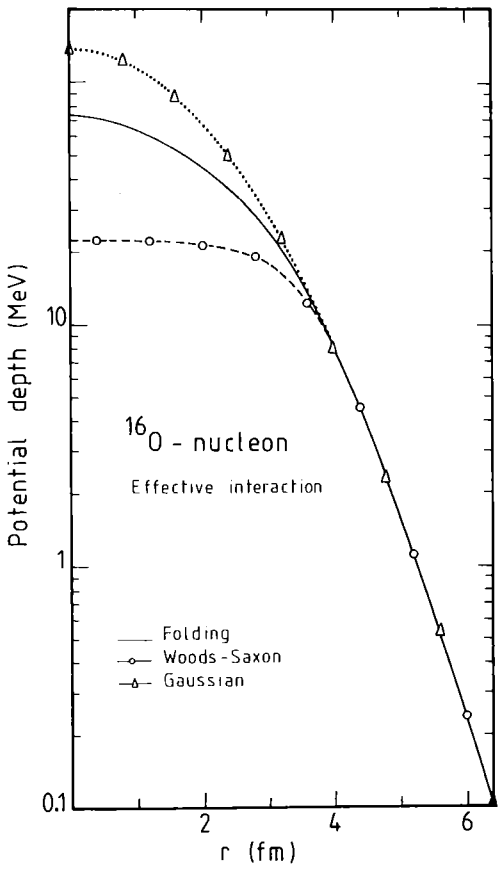

Figure 14

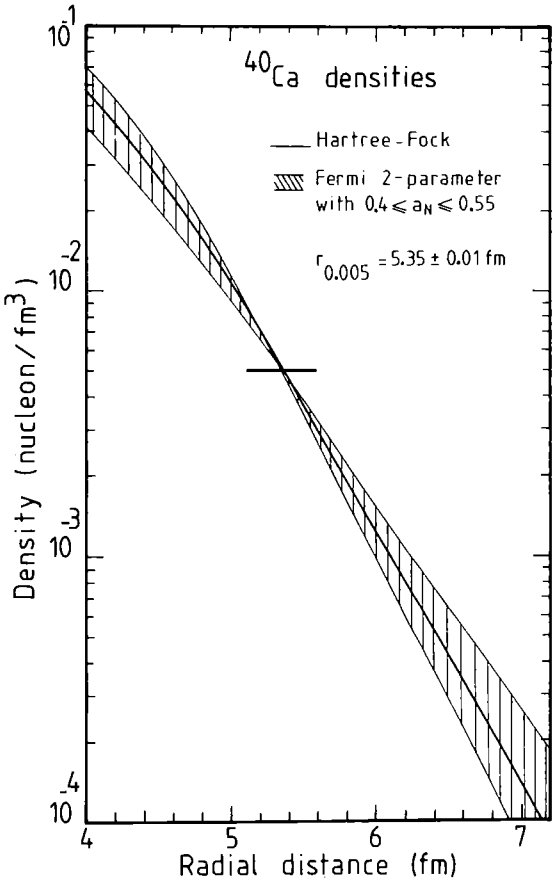

Figure 15

that all distributions cross in a radial region where the density is about 5×10^{-3} nucleon/fm^3, and in turn the elastic scattering of ^{16}O from ^{40}Ca is mainly influenced by a size parameter which can be taken as the radial distance $r_{0.005}$ where the ^{40}Ca density is 5×10^{-3} nucleon/fm^3. For ^{40}Ca, $r_{0.005} = 5.35$ fm.

The potentials generated by these density distributions are shown in the upper part of Fig. 13. They all cross for a depth of about 1 MeV, and give

$$R_{1.0} = 9.53 \pm 0.01 \text{ fm} \quad \text{or} \quad R_{0.8} = 9.65 \pm 0.02 \text{ fm}$$

in agreement with the value deduced from the Woods-Saxon analysis, but rather on the high side.

The same analysis was then performed on the ^{48}Ca data, using the same nucleon-^{16}O interaction. Very similar results are obtained, namely :

i) all potentials which give a good fit to the data cross in a region where they are about 1-MeV deep, and for ^{48}Ca, $R_{0.8} = 9.84 \pm 0.01$ fm,

ii) all densities (of Fermi shape) which give a good fit to the data give 5×10^{-3} nucleon/fm^3 at the same distance $r_{0.005} = 5.54 \pm 0.01$ fm.

From the ^{40}Ca and ^{48}Ca analyses, it is now possible to deduce the following simple relationship for this region :

$$r_{0.005} = R_{0.8}^{(WS)} - 4.30 \pm 0.02 \text{ fm}.$$

This relationship enables one to deduce $r_{0.005}$ from a simple Woods-Saxon analysis. Values of $r_{0.005}$ were in particular deduced that way from the results of ref.[12]. All results are summarized in table 1.

Table 1

Isotope	Ref.	$R_{0.8}$	$r_{0.005}$	
			exp.	theory [15]
^{40}Ca	13	9.65	5.35*	5.35*
^{40}Ca	12	9.58	5.28	
^{44}Ca	12	9.70	5.40	
^{48}Ca	13	9.84	5.54	5.58
^{48}Ca	12	9.88	5.58	

* taken as reference

There are some discrepancies between the data of refs.[12] and [13], which are not explained. The difference between $r_{0.005}$ values for ^{40}Ca - ^{48}Ca are 0.19 fm for ref.[13] and 0.30 fm for ref.[12] while the Hartree-Fock calculation gives 0.23 fm. It is hard to decide at present if such a discrepancy can be attributed to standard experimental uncertainties, or to some systematic difference in the data or in the analysis. Such a discrepancy was already apparent

in the analysis of Groeneveld et al.[13].

Summary

The elastic scattering of strongly absorbed particles near the Coulomb barrier is sensitive to one size parameter, which is the distance at which the real nuclear potential has some fixed value, 0.2 MeV for α-particle, 1 MeV for ^{16}O. This size parameter can be related in a simple way to the radial distance of the target nucleus where the density takes some given value, 2×10^{-3} nucleon/fm^3 for α-particle scattering and 5×10^{-3} nucleon/fm^3 for ^{16}O scattering.

References

[1] I. Badawy, B. Berthier, P. Charles, M. Dost, B. Fernandez, J. Gastebois and S.M. Lee, Phys. Rev. C17, 978 (1978).

[2] A.R. Barnett and J.S. Lilley, Phys. Rev. C9, 2010 (1974).

[3] S.L. Tabor, B.A. Watson and S.S. Hansen, Phys. Rev. C11, 198 (1975).

[4] D.F. Jackson and M. Rhoades-Brown, Nucl. Phys. A266, 61 (1976).

[5] G. Goldring, M. Samuel, B.A. Watson, M.C. Bertin and S.L. Tabor, Phys. Lett. 32B, 465 (1970).

[6] P. Mailandt, J.S. Lilley and G.W. Greenlees, Phys. Rev. Lett. 28, 1075 (1972) ; Phys. Rev. C8, 2189 (1973).

[7] J. Heisenberg, R. Hofstadter, J.S. McCarthy, I. Sick, B.C. Clark, R. Herman and D.G. Ravenhall, Phys. Rev. Lett. 23, 1402 (1969).

[8] W.Q. Sumner, Ph.D. Thesis, University of Washington, 1974 (unpublished) ; W.Q. Sumner and J.S. Blair, to be published.

[9] J.W. Negele, Phys. Rev. C1, 1270 (1970).

[10] C.J. Batty, E. Friedman and J.F. Jackson, Nucl. Phys. A175, 1 (1971).

[11] A.M. Bernstein, Advan. Nucl. Phys. 3, 325 (1969).

[12] M.C. Bertin, S.L. Tabor, B.A. Watson, Y. Eisen and G. Goldring, Nucl. Phys. A167, 216 (1971).

[13] K.O. Groeneveld, L. Meyer-Schützmeister, A. Richter and U. Strohbusch, Phys. Rev. C6, 805 (1972).

[14] R.A. Chatwin, J.S. Eck, A. Richter and D. Robson, in "Nuclear physics induced by heavy ions", edited by R. Bock and W. Hering (North Holland, Amsterdam, 1970) p. 76.

[15] X. Campi.and D.W. Sprung, Nucl. Phys. A194, 401 (1972).

[16] G.R. Satchler and W.G. Love, Phys. Lett. 65B, 415 (1976).

COMPARISON OF π^+ and π^- ELASTIC SCATTERING OFF Ca NUCLEI IN THE πN(3,3) RESONANCE REGION

J.-P. Egger
University of Neuchâtel,
Switzerland

COMPARISON OF π^+ AND π^- ELASTIC SCATTERING OFF Ca NUCLEI IN THE πN(3,3) RESONANCE REGION

J.-P. Egger
Institut de Physique, Université de Neuchâtel
CH - 2000 Neuchâtel (Switzerland)

ABSTRACT

Recent experiments on π^+ and π^- elastic scattering off calcium isotopes in the πN(3,3) resonance region are evaluated, and the merits of first theoretical attempts to extract information on neutron distributions with pions are discussed.

1. INTRODUCTION

The pion has long been considered as a powerful probe for the distribution of neutrons and protons in nuclei. That the pion has T = 1 leads to a specific isospin coupling of the pion-nucleon system. For instance at moderate energies (100 MeV $\lesssim T_\pi \lesssim$ 300 MeV) the pion nucleon interaction is dominated by the well known Δ_{33} resonance which acts in p-wave states with J = 3/2 and T = 3/2. The other partial waves are substantially smaller in this energy range. Around the resonance region the $\pi^-\to$n ($\pi^+\to$p) elastic scattering amplitude is approximately three times stronger than the corresponding $\pi^-\to$p ($\pi^+\to$n) amplitude since

$$\begin{aligned} f(\pi^+\to p) &= f_{el}(\pi^+ p) \\ f(\pi^-\to p) &= \tfrac{1}{3} f_{el}(\pi^- p) + \tfrac{2}{3} f_{ex}(\pi^0 n) \\ f(\pi^-\to n) &= f_{el}(\pi^- n) \\ f(\pi^+\to n) &= \tfrac{1}{3} f_{el}(\pi^+ n) + \tfrac{2}{3} f_{ex}(\pi^0 p) \end{aligned} \qquad (1)$$

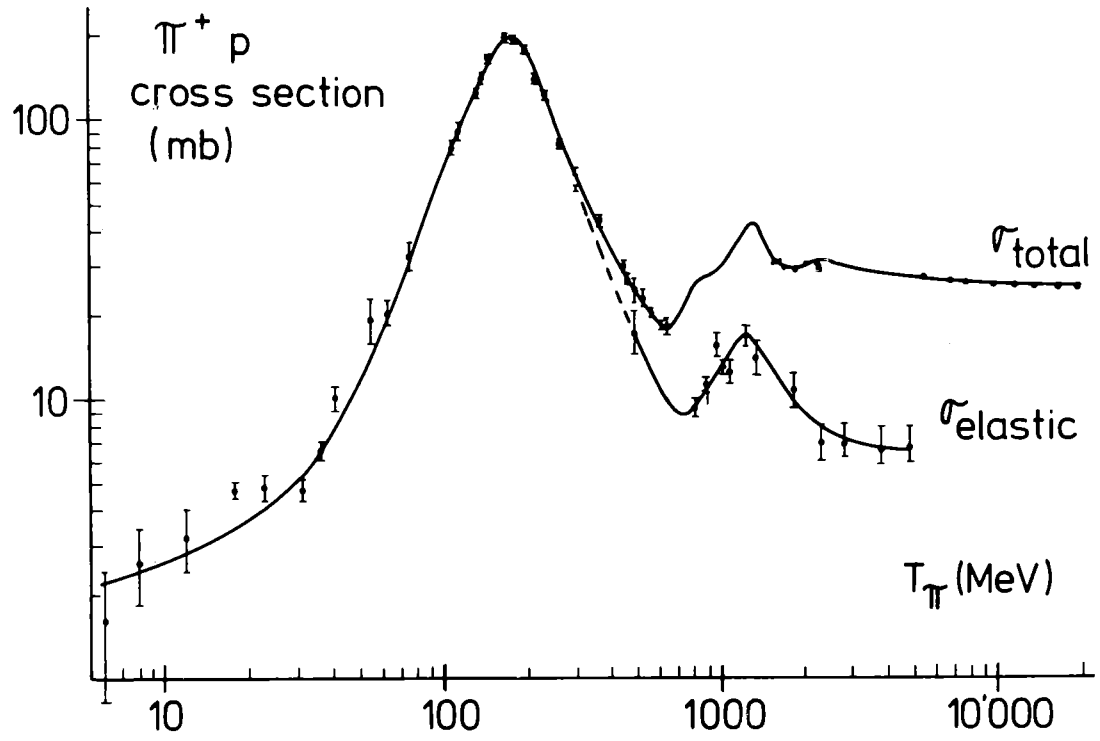

Fig. 1a Total and elastic cross sections for the scattering of positive pions by protons.

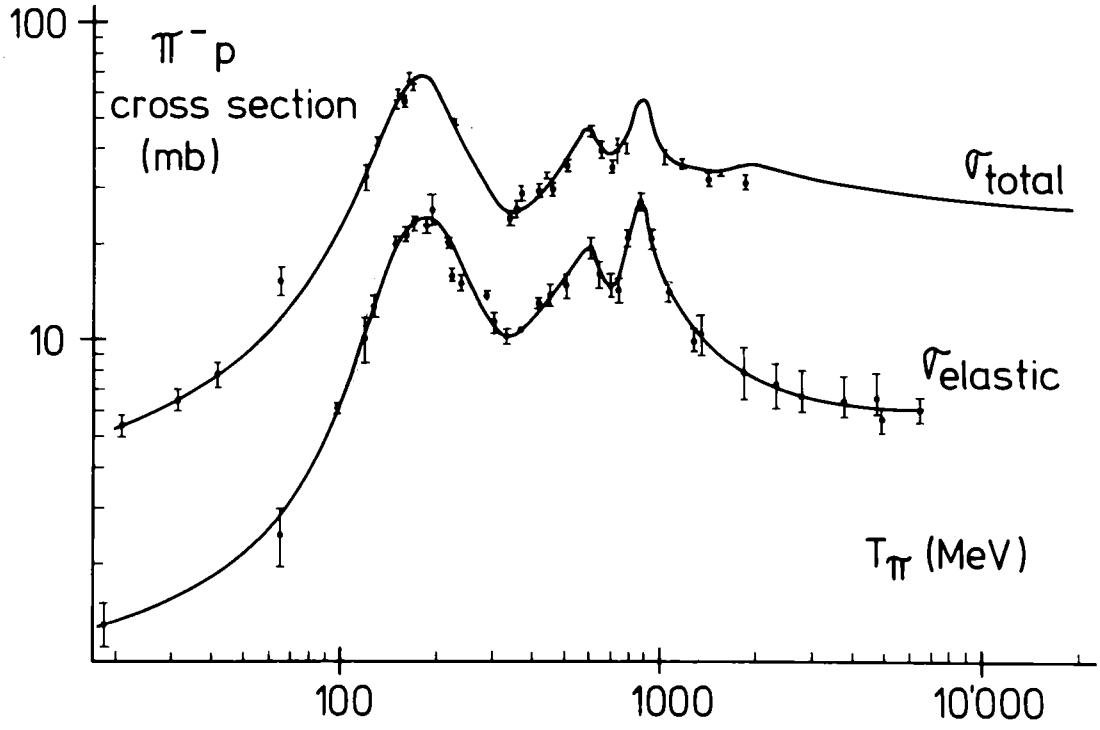

Fig. 1b Total and elastic cross sections for the scattering of negative pions by protons.

Therefore $\frac{d\sigma}{d\Omega} = |f|^2$ implies :

$$\frac{d\sigma}{d\Omega}(\pi^+p) = 9\,\frac{d\sigma}{d\Omega}(\pi^-p) \quad \text{and}$$
$$\frac{d\sigma}{d\Omega}(\pi^-n) = 9\,\frac{d\sigma}{d\Omega}(\pi^+n) \qquad (2)$$

Consequently the much stronger π^-n (π^+p) coupling should emphasize the effect of the neutron (proton) distribution of the nucleus. The total and elastic cross sections for the scattering of π^+ and π^- by protons are given in fig. 1a and 1b.

For the reasons stated above a comparative study of π^+ and π^- elastic scattering on the different Ca isotopes should lead to reliable information about the differences in the neutron distributions of these isotopes, provided the Coulomb distortion effects are well understood. In addition, both experimental and theoretical uncertainties are reduced significantly if isotopes are compared during the same experiment. However the blackness of the nucleus to pions in the πN(3,3) resonance energy region implies that experiments are sensitive to neutron distributions in the tail region of the nucleus rather than to a half density radius. This is illustrated in fig. 2.

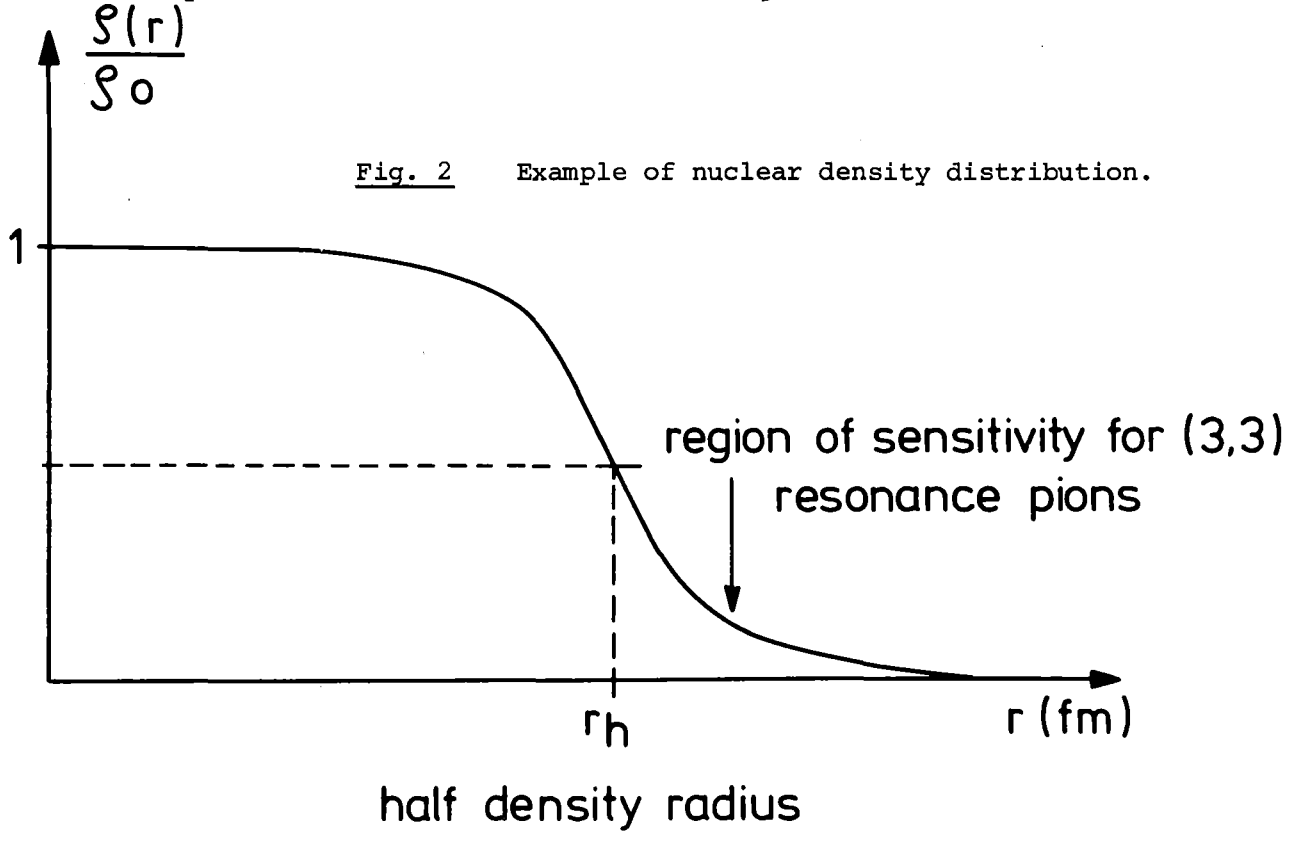

Fig. 2 Example of nuclear density distribution.

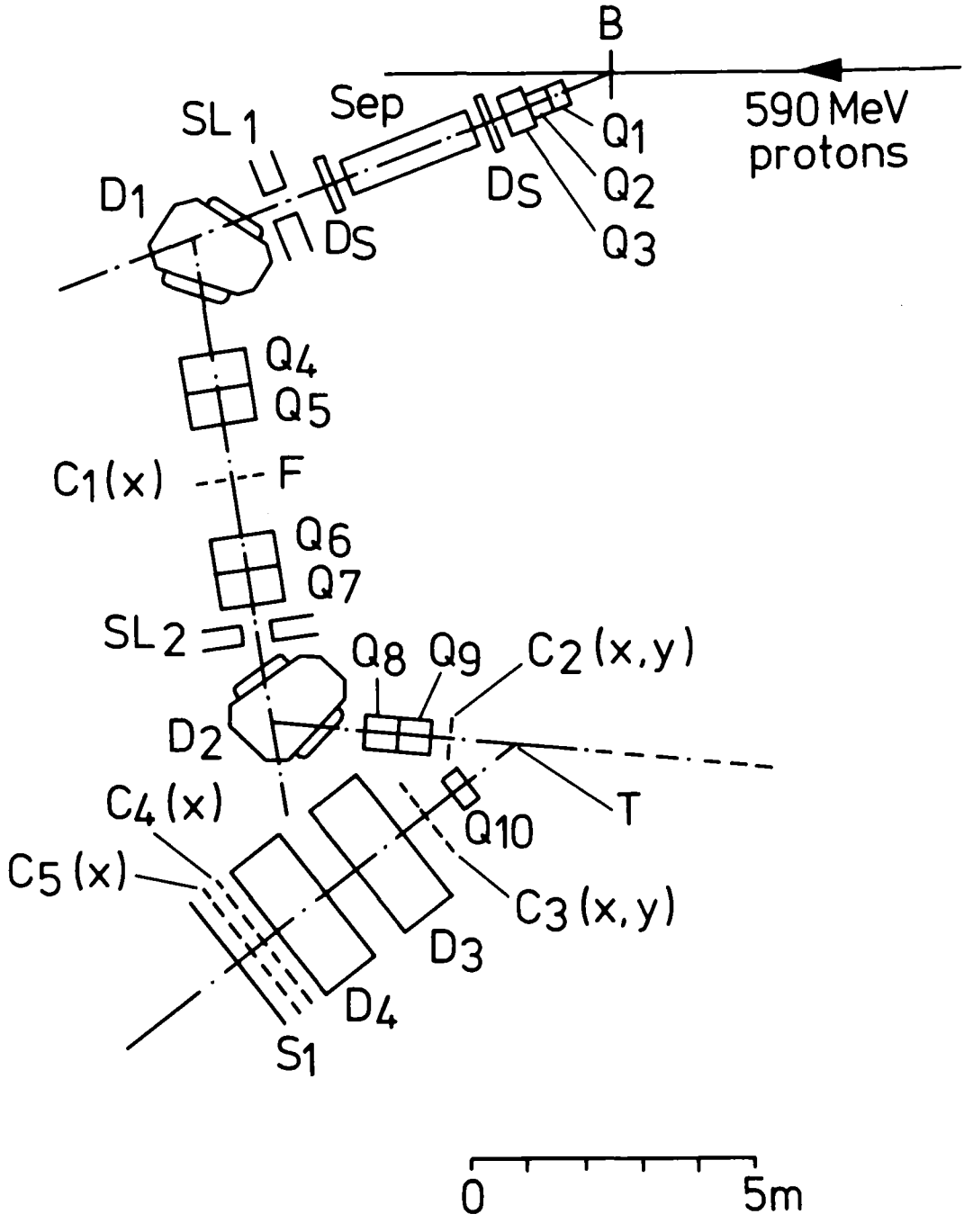

Fig. 3 Lay-out diagram of the SIN πM1 beam line and pion spectrometer. C = multi-wire proportional chamber, S = scintillator, T = scattering target, B = pion production target, D = dipole magnet, Q = quadrupole magnet, SEP = electrostatic separator, DS = separator magnet, SL = adjustable collimator, F = intermediate focal plane.

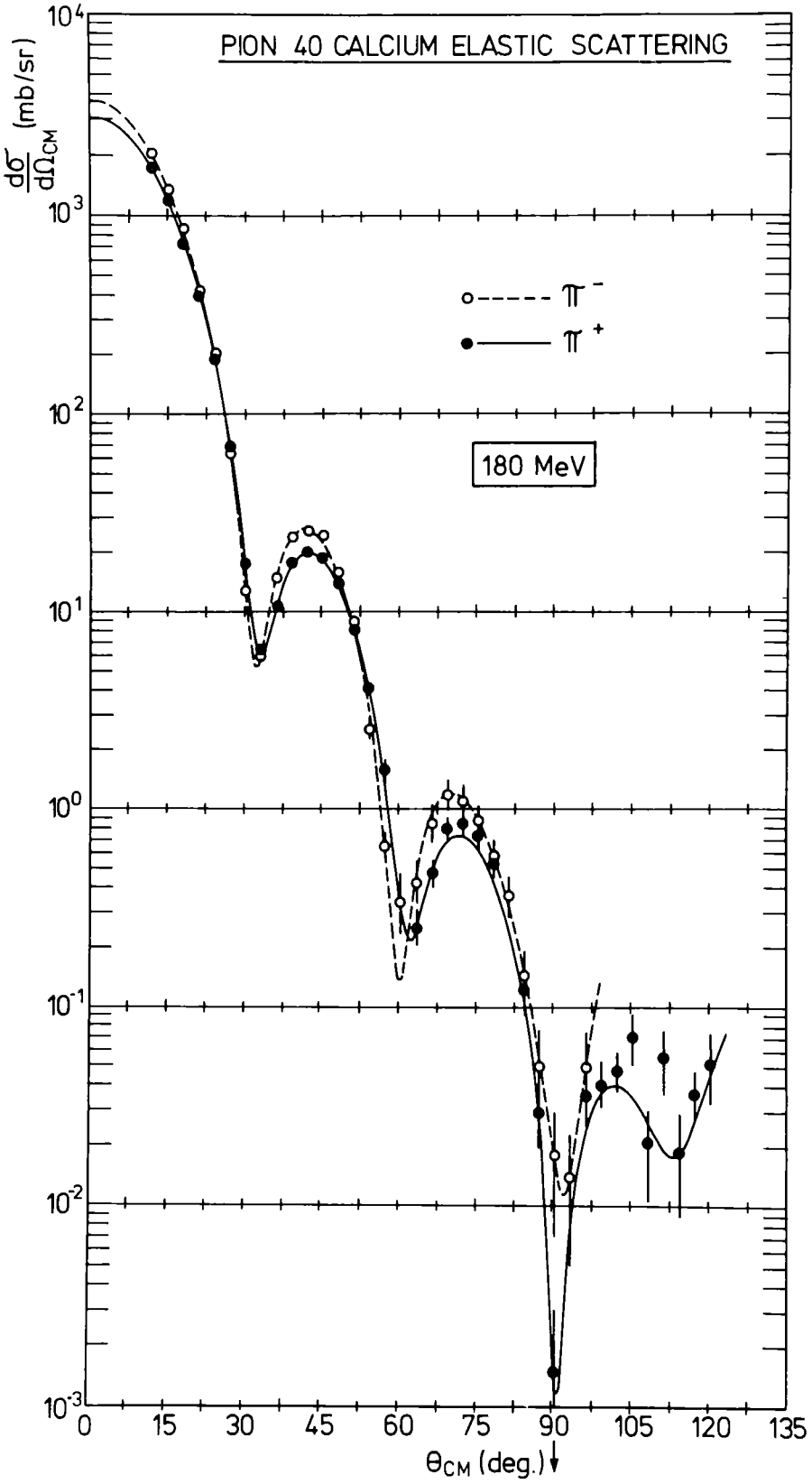

Fig. 4a Comparison of π^+ and π^- → ^{40}Ca CM elastic scattering differential cross sections at 180 MeV vs the pion scattering angle in the CM system. The curves result from a fit by a formula given in the text.

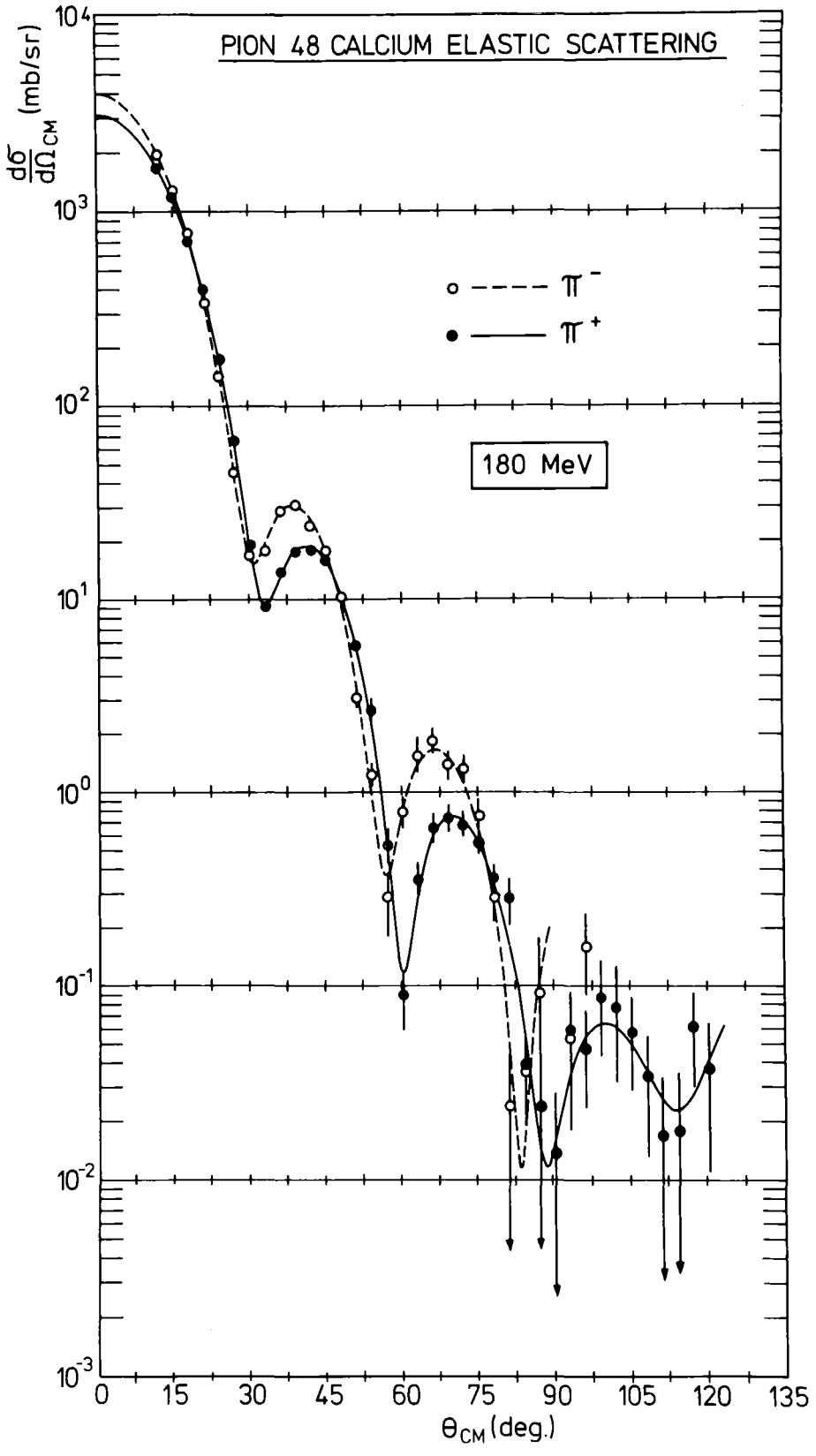

Fig. 4b Same as for fig. 4a but for ^{48}Ca.

In this paper we present some experimental procedures, the available data and some consistency checks. Then we discuss different interpretations of the data, in particular the black disk model, the detailed treatment of Coulomb effects by Germond and Wilkin[1], the improved black disk model by Johnson and Bethe[2] and an optical model analysis by Sternheim and Yoo[3]. Finally our conclusions and an outlook are presented.

2. EXPERIMENTAL PROCEDURE AND PRESENTATION OF THE DATA

With the advent of "Pion Factories" at LAMPF (Los Alamos), SIN (Zürich) and TRIUMF (Vancouver), good intensity and high resolution pion beams and spectrometers have become available making precise pion-nucleus scattering experiments possible.

As of now, elastic π^+ and π^- scattering data on calcium isotopes in the $\pi N(3,3)$ resonance region include :

- ^{40}Ca and ^{48}Ca comparison at 130[4], 180 and 230 MeV[5]
- ^{40}Ca measurements at 115, 163 and 241 MeV[6]
- $^{40,42,44,48}Ca$ comparison at 115, 180 and 291 MeV[7].

The $^{40,48}Ca$ comparison at 130, 180 and 230 MeV was carried out at SIN by a Neuchâtel - Grenoble - SIN - South Carolina (NGSS) collaboration with the SIN πM1 beam and pion spectrometer. The ^{40}Ca measurements were taken with the same equipment by a Karlsruhe - Grenoble - SIN (KGS) collaboration. Finally the $^{40,42,44,48}Ca$ comparison at 3 energies was measured at LAMPF with the EPICS system.

A detailed description of the SIN πM1 channel can be found in ref. 8 and a general layout of the NGSS experiment is shown in fig. 3.

As an example, elastic π^+ and π^- angular distributions are shown for ^{40}Ca and ^{48}Ca at 180 MeV[5] in fig. 4a and 4b. A clear shift in the position of the first minimum between π^+ and π^- data is seen for ^{48}Ca whereas this shift is much smaller for ^{40}Ca thus indicating the sensitivity of π^- to neutrons (π^+ to protons). The curves shown on these figures are a fit with a formula[9] for the scattering amplitude :

$$f(\theta) = f(0)\left[\prod_{i=1}^{4}\left(1 - \frac{q^2}{q_i^2}\right)\right] e^{-\alpha q^2/2} \qquad (3)$$

where f(0) is the forward scattering amplitude; q_i the complex zeros and α a slope parameter. Although there is no immediate physical meaning for these parameters, such a fit is extremely useful to determine the exact positions of the minima of the angular distributions. Moreover, it was used by Germond and Wilkin[1] to understand Coulomb effects in detail. Since ^{40}Ca data now exist at several energies, a consistency check was carried out. In fig. 5 we plotted the position of the first minimum (Re q_1^2) versus the pion kinetic energy. Square dots are for π^+ and circles for π^-. Black dots are KGS data and white dots NGSS data. Statistical errors are smaller than the dots. The lines drawn are a simple guide for the eye. The agreement between the different data points is unusually good except for the π^+ results at 163 MeV. In an analysis of all the data to extract some information on neutron distributions, the 163 MeV π^+ results should therefore be omitted. The LAMPF data are still preliminary. In general there is satisfactory agreement with the SIN data except on 2 points : There is a small systematic shift of the minima of the LAMPF results with respect to the SIN results. This may be due to a slight error in the energy calibration of the LAMPF or SIN pion beams. Furthermore at 180 MeV the SIN data have a shallower first minimum than the EPICS data, which probably results from EPICS superior angular resolution.

3. ANALYSIS

3.1. Black Disk Model

Although the black disk model is a very crude analysis, it can be justified by the fact that the nucleus in the region of the $\pi N(3,3)$ resonance is black. However since π-nucleus scattering in this energy region is a surface phenomenon, the black disk radii R obtained will be greater than the usual half-density radii. In the black disk framework the elastic scattering amplitude is given by

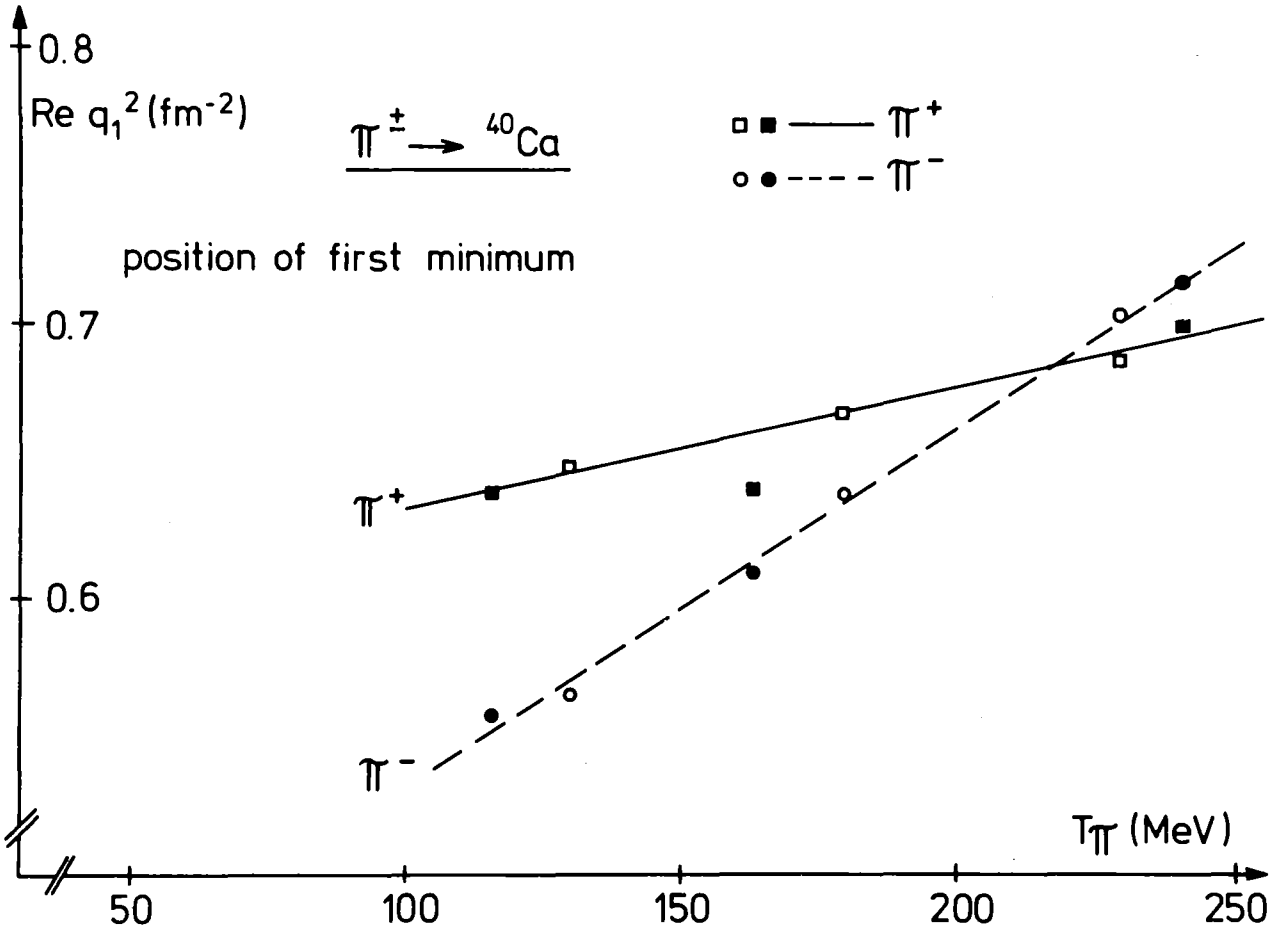

Fig. 5 Comparison of the position of the first minimum in pion - ^{40}Ca elastic scattering vs the incident lab pion energy. The position of the first minimum was obtained by fitting a formula given in the text. Statistical errors are smaller than the dots.

$$f(q) = ikR^2 \frac{J_1(qR)}{qR} \tag{4}$$

where $q = 2k \sin \frac{\theta}{2}$ = momentum transfer

θ = CM scattering angle

R = black disk radius

J_1 = Bessel function

k = pion wave number

The only experimental information that enters into this model is the position of the first minimum where $J_1(qR) = 0$ for $qR = 3.83$. The black disk radius R can also be given in function of the scattering amplitude parametrization (equation 3) :

$$R = 3.83 \cdot \sqrt{\mathrm{Re}\left(\frac{1}{q_1^2}\right)} \tag{5}$$

If the minimum is deep ($\mathrm{Im}\,(q_1^2) \ll \mathrm{Re}(q_1^2)$) one can write

$$R = 3.83 \,/\, \sqrt{\mathrm{Re}\,(q_1^2)} \tag{6}$$

The results of an analysis of the NGSS data in this framework are given in table 1 :

T_π (MeV)	^{40}Ca $\Delta R_{40} = R(\pi^-) - R(\pi^+)$ (fm)	^{48}Ca $\Delta R_{48} = R(\pi^-) - R(\pi^+)$ (fm)	$\Delta X = \Delta R_{48} - \Delta R_{40}$ (fm)
130	0.21	0.51	0.30
180	0.10	0.34	0.24
230	0.05	0.25	0.20

table 1

Black disk analysis of NGSS data at three energies.

In this crude model ΔR (^{40}Ca) is attributed to Coulomb effects and $\Delta X = \Delta R$ (^{48}Ca) - ΔR (^{40}Ca) is due to a larger neutron radius.

3.2. Germond and Wilkin Model[1)]

The Germond-Wilkin (GW) model is a tool for understanding the Coulomb effects in detail, the importance of which can be seen from the ^{40}Ca column in table 1. The Coulomb force modifies the elastic pion-nucleus scattering amplitude in impact parameter space in three distinct ways. There is an additive phase, a distortion of the trajectory of the pion and a shift in the effective energy of the pion-nucleus interaction. First GW fit separately π^+ and π^- elastic data with formula (3) and obtain parameter values in both cases. The average parameters give $f_N(\theta)$, the nuclear amplitude. They then introduce Coulomb effects in impact parameter representation and obtain an excellent agreement with the data as can be seen in fig. 6 (solid line). The success of this amplitude analysis suggests that Coulomb corrections are understood well enough so that neutron distributions may be meaningfully investigated with pions.

3.3. Johnson and Bethe Model[2)]

The Johnson and Bethe (JB) model is an improved black disk calculation. Their expression for the scattering amplitude is :

$$f(\theta) = \frac{ikR^2 J_1(qR)}{qR} + ikaRJ_0(qR)\left[C + \ln\ln 2 + \frac{1}{2}\ln(1+Y^2)\right] + kaR\,J_0(qR)\,\arctan Y \qquad (7)$$

where $Y = \dfrac{\mathrm{Re}\ K(\rho) - k}{\mathrm{Im}\ K(\rho)}$

$C = 0.577$ = Euler constant

J_0 and J_1 = Bessel functions

$K(\rho)$ = wave number of the pion in matter density $\rho(r)$

a = diffuseness parameter

The first term in equation (7) corresponds to the usual black disk model (equation 4). In addition the second term is important for energies away from

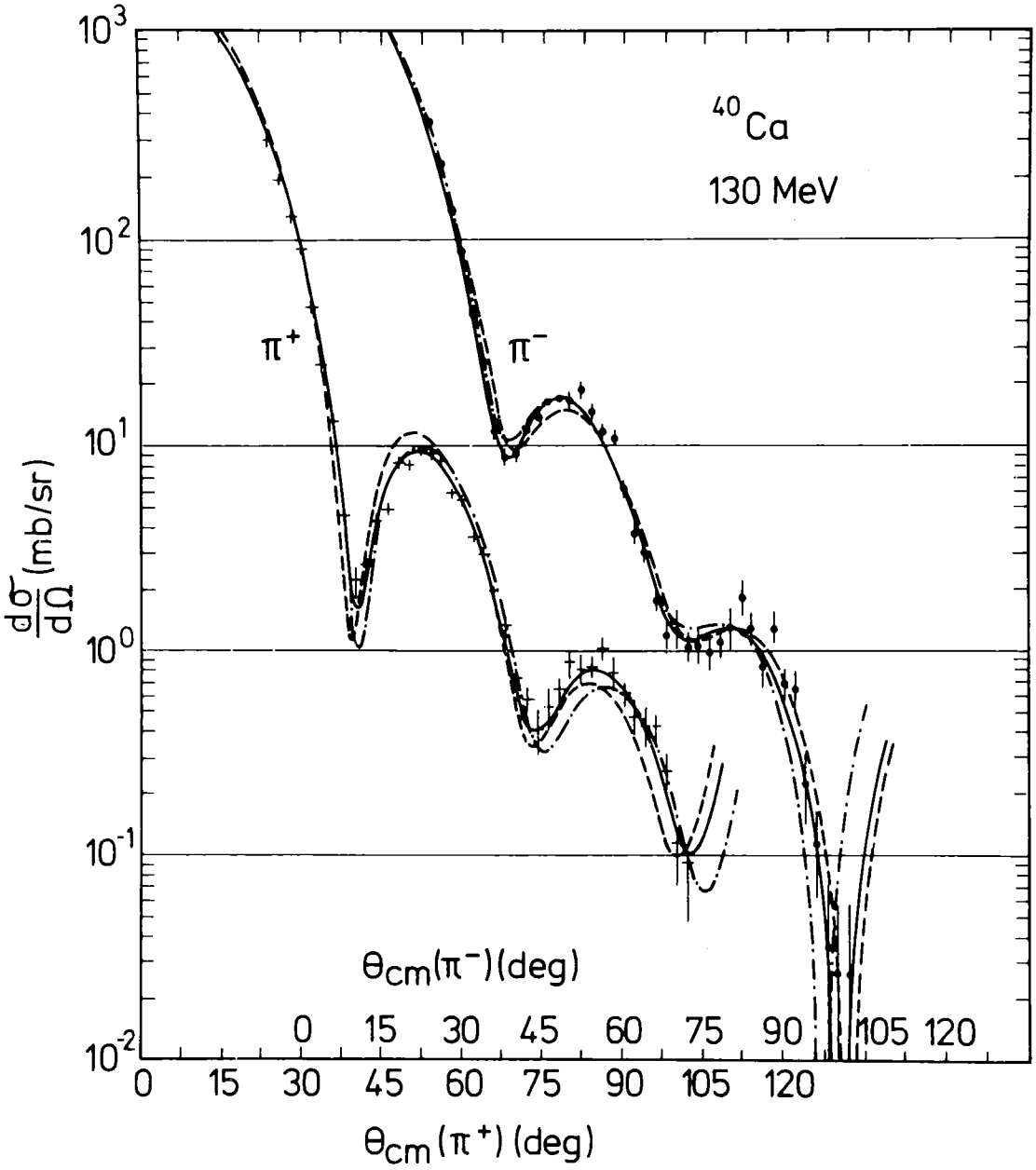

Fig. 6 Elastic π^+ and π^- scattering (NGSS data) from ^{40}Ca at 130 MeV. The effect of the Coulomb phase is shown as a dashed curve, with the trajectory distortion added as the dot-dashed and including also the energy shift as the solid curve.

the $\pi N(3,3)$ resonance since Y is small near T_π = 180 MeV. The third (real) term is neglected. The value of a is deduced from electron scattering and removal energies for the last-bound nucleon; it should be chosen so as to yield an accurate representation of the tail of the nucleus.

Furthermore JB calculate the density value $\rho(r)/\rho_0$ with density dependent Hartree Fock (DDHF) theory[10]. They find $\rho(R)/\rho_0$ values of 0.27 (T_π = 115 MeV), 0.20 (130 MeV) and 0.13 (163 MeV) for ^{40}Ca. These values are in good agreement with the fact that pions near the $\pi N(3,3)$ resonance are only sensitive to the tail of the nucleus.

JB conclude that from a comparison with 130 MeV data the tail of the neutron distribution in ^{48}Ca is shifted inwards by $\sim$ 0.1 fm with respect to DDHF theory which amounts to a neutron distribution of $\sim$ 0.15 fm larger than the proton distribution. However it would be quite useful to repeat the JB analysis at several pion energies and perform a GW type fit to yield a precise determination of the position of the first minimum.

3.4. Sternheim and Yoo Model[3]

Sternheim and Yoo (SY) compared the 130 MeV ^{40,48}Ca NGSS data with an optical model analysis. Contrary to the black disk type analysis they try to fit complete angular distributions by using a Kisslinger type potential with phenomenological parameters. The best χ^2 in fitting the ^{48}Ca data is obtained with $^{48}r_n - {}^{40}r_n$ (rms radius) $\approx$ 0.25 fm. However the change in χ^2 for different $^{48}r_n$ values is minimal and the fitted sets of optical-model parameters are not unique. If the SY analysis is applied to data at several energies it may be possible to determine unique parameter sets.

4. CONCLUSIONS

With pion elastic scattering results on the Ca isotopes now becoming available at several energies around the $\pi N(3,3)$ resonance it should be possible to test more elaborate optical model calculations with separate neutron and proton distributions. In addition the 291 MeV LAMPF data may be particularly interesting since at this energy the nucleus is not as black and therefore the

pion is more sensitive to a half-density type radius. Furthermore an experiment was proposed[11] at 600 MeV where π^+ are more sensitive to neutrons and π^- to protons (see fig. 1a and 1b) and the nucleus is not black. However it is not yet clear if reliable information on neutron distributions in calcium isotopes can be obtained from this type of experiment.

5. ACKNOWLEDGMENTS

I wish to thank all my friends in the NGSS group (1979 version); F. Goetz, P. Gretillat, J. Jansen, C. Lunke, R.E. Mischke, C. Perrin, B.M. Preedom and E. Schwarz for their support.

REFERENCES

1) J.-F. Germond and C. Wilkin, Ann. of Physics, to be published.

2) M.B. Johnson and H.A. Bethe, Comments Nucl. Part. Phys. 8 (1978) 75.

3) M.M. Sternheim and K.B. Yoo, Phys. Rev. Lett. 41 (1978) 1781.

4) J.-P. Egger et al., Phys. Rev. Lett. 39 (1977) 1608.

5) P. Gretillat et al., private communication.

6) C.H.Q. Ingram et al., Phys. Lett. 76B (1978) 173.

7) G.R. Burleson et al., private communication.

8) J.-P. Albanèse et al., Nucl. Inst. Meth. 158 (1979) 363;
R. Balsiger et al., Nucl. Inst. Meth. 157 (1978) 247.

9) J.-F. Germond and C. Wilkin, Nucl. Phys. A237 (1975) 477.

10) J.W. Negele, Phys. Rev. C1 (1969) 1260.

11) C. Perrin, private communication.

NUCLEAR RADII FROM PIONIC ATOMS

E. Friedman
The Hebrew University,
Jerusalem, Israel

NUCLEAR RADII FROM PIONIC ATOMS

E. Friedman
The Racah Institute of Physics
The Hebrew University, Jerusalem, Israel

1. Introduction

Pionic atoms offer another method for studying nuclear radii. The probe involved is a negative pion in an atomic orbit strongly interacting with the nucleus. As with any strongly interacting probe, there is the need for some "calibration" of the method and this is most naturally provided by ^{40}Ca, where one may safely assume that neutrons and protons have very similar density distributions. From the atomic point of view the Ca region is also the most suitable one for studies of nuclear radii using pionic atoms and, therefore, results of this method for calcium isotopes are interesting in connection with the comparison between different methods of investigating nuclear radii, which is the topic of the present conference. The analysis of pionic atom data is carried out with the help of an effective ("optical") pion-nucleus potential which is simply related to the nuclear densities. The potential is obviously a simplification of the true interaction and its parameters are obtained from fits to experimental results. However, the method is most likely quite reliable for the studies of differences between neighbouring nuclei or of isotopic effects.

The pionic atoms method consists essentially of the measurement of transition energies between the levels of a negative pion in atomic orbits. When the overlap between the atomic wave function and the nucleus becomes non-negligible, the binding energy deviates from that obtained for a point charge. The shift in the binding energy is due to the finite size of the charge distribution of the nucleus and due to the strong pion-nucleus interaction, which also causes a broadening of energy levels due to the absorption of pions, hence leading to a measured width of the transition (in addition to the electromagnetic width and, obviously, instrumental width). The measured shifts and widths are analysed with the help of a pion-nucleus potential, which is capable of supplying information on nuclear radii, within the framework of the simple models used.

The analysis to be presented here is based on the precision measurements of shifts and width of 2p states carried out recently by the team at the

Rutherford laboratory[1,2].

2. Outline of the Experiments and Results

The experiments were performed using the stopping meson beam from the 7 GeV proton synchrotron Nimrod. Stopping pions were detected and identified with a counter telescope system. The X-ray detectors used were a planar 5 cm^3 Ge(Li) and a coaxial 70 cm^3 Ge(Li) detector with 600 eV resolution at 122 keV and 1.68 keV resoltuion at 1.33 MeV, respectively. Figure 1 shows the general lay-out of the beam line. The X-ray signals in coincidence with identified stopped pions were analysed using an 8192 channel ADC and stored in an on-line computer system. Calibration spectra were recorded simultaneously with the data by forming random delayed coincidences between particles stopping in the target and events detected in the X-ray detector. The calibration spectrum was stored in the on-line computer separately from the data spectrum. The peaks in the calibration spectra were analysed using a least squares fitting procedure to obtain the energy calibration and detector response function. This experimentally determined response function was then folded with a Lorentzian and fitted to the strong interaction broadened peaks to obtain the energies and widths of the relevant X-ray lines.

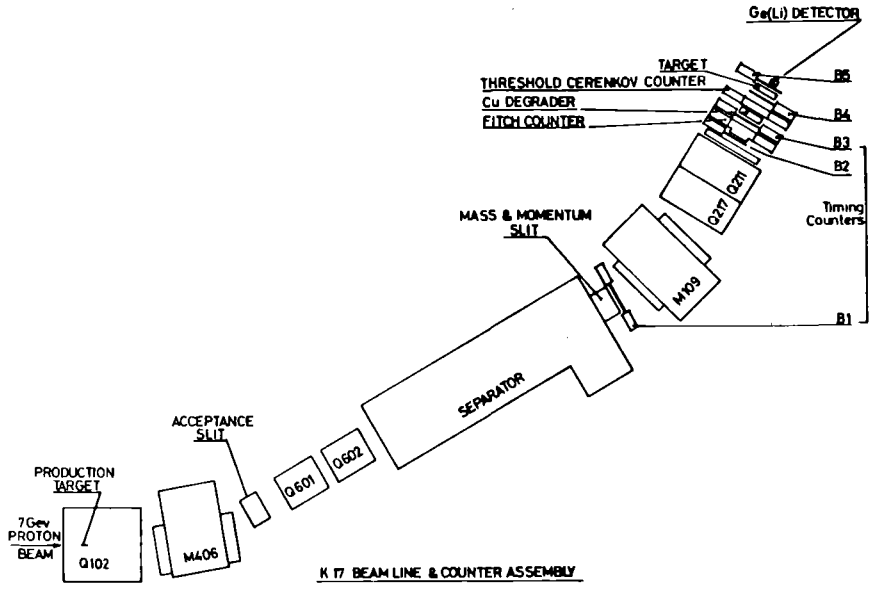

Fig. 1 Lay-out of the beam line

An example of a strong-interaction broadened peak is shown in fig. 2 together with an unbroadened gamma transition peak. Also shown are weak muonic transitions in the vicinity of the pionic peak and these were taken into account when the pionic peak was analysed.

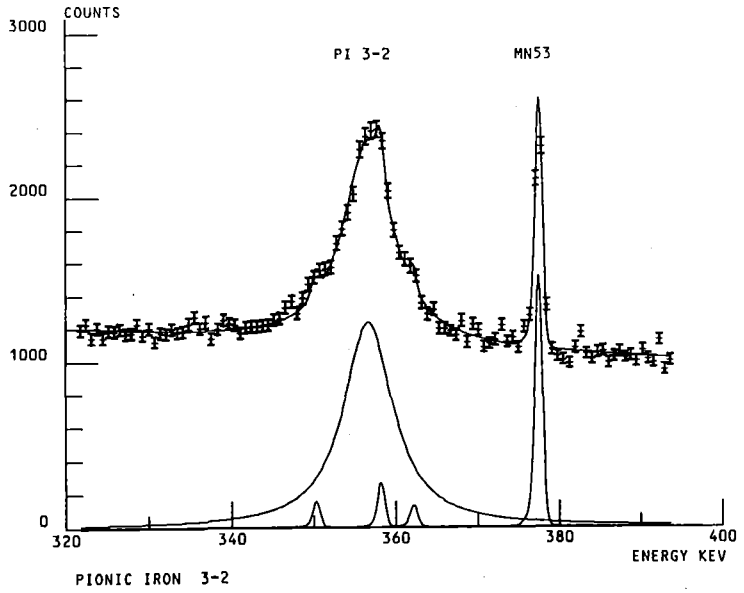

Fig. 2 An example for a strong interaction broadened peak and several background peaks.

Table I summarises the experimental results[1,2] for the 2p pionic states. Also given are previous results for the same targets and it is evident that in most cases the improvement in accuracy is by about an order of magnitude.

Table I Strong interaction shifts and widths

Element	Level	present work		previous work	
		shift (keV)	width (keV)	shift (keV)	width (keV)
Aℓ	2p	0.201 ± 0.009	0.120 ± 0.007	0.212 ± 0.023	
				0.12 ± 0.10	0.36 ± 0.15
Si	2p	0.308 ± 0.010	0.192 ± 0.009	0.29 ± 0.15	
S	2p	0.635 ± 0.016	0.422 ± 0.018	0.54 ± 0.10	0.79 ± 0.15
				0.7 ± 0.3	0.8 ± 0.4
				0.502 ± 0.035	0.50 ± 0.06
Ca	2p	1.929 ± 0.019	1.590 ± 0.023	1.97 ± 0.18	2.00 ± 0.25
				1.6 ± 0.3	2.1 ± 0.6
Fe	2p	4.368 ± 0.113	6.87 ± 0.21	4.0 ± 0.3	8.7 ± 0.6
				4.4 ± 1.0	6.0 ± 2.5
Cu	2p	6.67 ± 0.28	11.4 ± 0.8	7.0 ± 2.0	15.9 ± 4.0
Zn	2p	6.44 ± 0.38	12.4 ± 1.4	8.0 ± 3.0	16.8 ± 6.0

References to previous work can be found in Ref. 2.

Table II summarises the experimental results for the $^{44,40}Ca$ experiment[3] which was specifically designed to accurately measure small differences between isotopes. In order to reduce possible systematic errors the same chemical form ($CaCO_3$) was used in the two experiments in addition to the metallic Ca target studied before (^{44}Ca was available only as $^{44}CaCO_3$). This was important because in the initial stages of the atomic cascade there is a dependence of the intensities of various transitions on the chemical form of the target. It is seen that in this case of an isotopic difference the improvement in accuracy compared to the previous measurement[4] is also by about an order of magnitude.

Table II - Isotopic effects for $^{44,40}Ca$

	present experiment	previous experiment[a]
$\varepsilon(44) - \varepsilon(40)$ (keV)	-0.331 ± 0.027	-0.36 ± 0.17
$\Gamma(44) - \Gamma(40)$ (keV)	-0.040 ± 0.075	-0.22 ± 0.20

a) Ref. 4

3. The Pion-Nucleus Potential

The experimental results for the level shifts and widths have been analysed using a pion-nucleus effective potential. This momentum-dependent potential, which is used in the Klein-Gordon equation, has been shown[5] to yield good average fits to experimental results. The potential is written as

$$V(r) = \frac{1}{2\mu}\left[q(r) + \vec{\nabla}\,\alpha(r)\cdot\vec{\nabla}\right] \qquad (1)$$

where μ is the pion-nucleus reduced mass. The term $q(r)$ is parameterised in terms of the neutron (ρ_n) and proton (ρ_p) density distributions as follows

$$q = -4\pi(1+\tfrac{\mu}{m})\,[(b_o(\rho_n+\rho_p) + b_1(\rho_n-\rho_p)] - 4\pi(1+\tfrac{\mu}{2m})\,4\,B_o\rho_n\rho_p \qquad (2)$$

where m is the nucleon mass and b_o, b_1 and B_o are parameters determined from fits to the data. The parameter B_o is a complex number whose imaginary part represents the absorption of pions on pairs of nucleons.

The momentum-dependent part of the potential, α, is usually written as

$$\alpha = \frac{\alpha_o}{1 + \frac{1}{3}\,\xi\,\alpha_o} \qquad (3)$$

where $\xi (0 \leq \xi \lesssim 1)$ represents the Lorentz-Lorenz (LL) effect[5]. The term α_o is parameterised as follows

$$\alpha_o = 4\pi(1+\tfrac{\mu}{m})^{-1}\,[c_o(\rho_n+\rho_p) + c_1(\rho_n-\rho_p)] + 4\pi(1+\tfrac{\mu}{2m})^{-1}\,4\,C_o\rho_n\rho_p \qquad (4)$$

where again c_o, c_1 and C_o are parameters determined from fits to the data. The parameter C_o is a complex number in analogy with B_o. We have also analysed the data with a different form for the momentum-dependent component of the potential where the LL effect is included only in the term linear in the nuclear density. In this case α is written as

$$\alpha = \frac{\alpha_1}{1 + \frac{1}{3}\,\xi\,\alpha_1} + \alpha_2 \qquad (5)$$

where

$$\alpha_1 = 4\pi(1+\tfrac{\mu}{m})^{-1}\,[c_o(\rho_n + \rho_p) + c_1(\rho_n - \rho_p)] \qquad (6)$$

$$\alpha_2 = 4\pi(1+\tfrac{\mu}{2m})^{-1}\,4\,C_o\rho_n\rho_p. \qquad (7)$$

Strong interaction level shifts and widths were calculated by solving the Klein-Gordon equation with the pion-nucleus potential (1) and comparing the resulting complex binding energies with the real binding energies obtained by solving the same equation with only the electromagnetic interaction present. The Coulomb potential was that due to the charge distribution of the nucleus

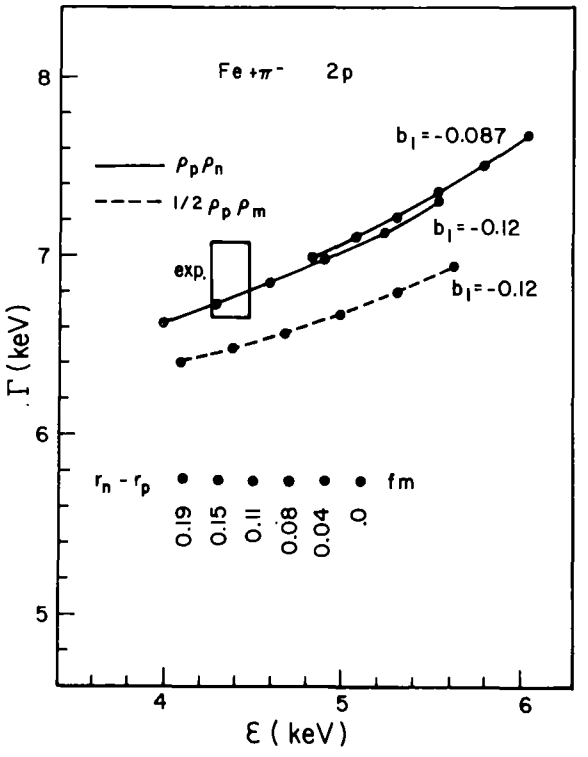

Fig. 3 An example for the coupling between b_1 and r_n-r_p for nuclei with an excess of neutrons.

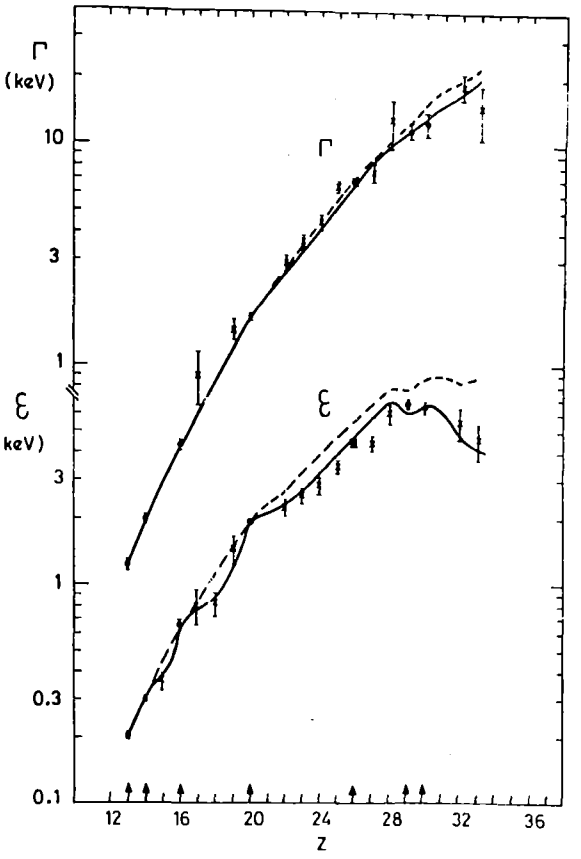

Fig. 4 Fits to all available data for 2p states.

Table III Parameters for effective pion-nucleus potential

The conventional units of m_π^{-1} = 1.4138fm are used

	(a)	(b)	(c)	(d)
b_o (m_π^{-1})	-0.017	-0.017	-0.017	-0.017
b_1 (m_π^{-1})	-0.12 ± 0.02	-0.12 ± 0.02	-0.12 ± 0.02	-0.13 ± 0.02
ImB_o (m_π^{-4})	0.0475	0.0475	0.0475	0.0475
ReB_o/ImB_o	-1.0	-1.0	-1.0	-1.0
c_o (m_π^{-3})	0.250 ± 0.003	0.21	0.21	0.21
c_1 (m_π^{-3})	0.17	0.17	0.17	0.17
ImC_o (m_π^{-6})	0.090 ± 0.005	0.080 ± 0.005	0.0425 ± 0.005	0.0425 ± 0.005
ReC_o/ImC_o	0.0	1.7 ± 0.1	1.95 ± 0.05	-0.80 ± 0.05

as determined from electron scattering and muonic atoms. The first order vacuum polarization potential was also included as it slightly affects the strong interaction shifts and widths.

Fits to the 2p data were made in two steps. First the parameters were adjusted to fit the Al, Si, S and Ca data. In the second step fits were made to the Fe, Cu and Zn data. The reason for this separation was that the neutron density distribution, ρ_n, which forms an essential ingredient of the pion-nucleus potential, is usually not as well known as the proton density distribution. Therefore, it was considered preferable to start with nuclei where one may safely assume that neutrons and protons have the same density distributions. Experience showed that any set of parameters which fitted the Ca data always gave very good agreement with the experimental results for Al, Si and S. Therefore, the first step was essentially a fit to the Ca data. As the data consists of just two numbers (level shift and width) we could only adjust two parameters in the first step of the fitting procedure. The choice was to vary two out of the three parameters c_o, ReC_o and ImC_o for the momentum-dependent potential, as these are the more relevant ones for the 2p state. Note that b_1 and c_1 are not effective for nuclei with equal numbers of neutrons and protons and have negligible effects in the case of Al. The parameters b_o and B_o of the local potential were taken from a fit[6] to 1s states.

Fits to the Ca data were made using four different sets of parameters: (a) c_o and ImC_o were adjusted, keeping $ReC_o = 0$. (b) c_o was held constant at its theoretical value[7] of 0.21 m_π^{-3} and the complex number C_o was adjusted. In both cases the conventional form of the LL effect was chosen, (Eq. (3)) with $\xi = 1$. (c) For the third parameter set the LL effect (with $\xi = 1$) was only included in the term which is linear in the density (Eq. (5)) and again C_o was adjusted whilst keeping c_o constant at 0.21 m_π^{-3}. Finally, parameter set (d) was obtained with $\xi = 0$ (i.e. no LL effect) and again adjusting C_o only. As mentioned above, excellent fits were obtained for Al, Si,S and Ca. Note that values for c_o obtained in previous fits, and also in parameter set (a), are quite close to the value expected for pions interacting with free nucleons.

In the second stage of the fitting procedure the data for Fe, Cu and Zn were used and only the coefficients of $(\rho_n-\rho_p)$ (i.e. b_1 and c_1) were

adjusted. This stage is the critical one when nuclear radii are concerned because for these nuclei, which have an excess of neutrons, the radial parameters of the neutron density distribution could no longer be considered as identical to those for the protons. Therefore, in each case the radius parameter of the neutron distribution was also allowed to vary. If the value of c_1 was held at its free-nucleon value (and this is reasonable because of the close connection between c_o and c_1) and if b_1 was also held constant at the value of $-0.087\ m_\pi^{-1}$ determined from fits to 1s states[6] then it was found that the rms radius of the neutron distribution, r_n, had to be about 0.3 fm larger than r_p, the rms radius of the proton distribution. This difference was also observed for nuclei as light as P and Ar which is clearly unreasonable. Alternatively, if the value of r_n-r_p was kept in the range 0.05 to 0.15 fm and the value of c_1 adjusted, it was necessary to reduce c_1 by some 200%, which is again unreasonable, particularly in view of the observation that c_o is found to be close to its free-nucleon value. However, if the absolute value of b_1 was increased by 40% very good fits to all available data for 2p levels were obtained. Figure 3 shows an example for the coupling between values of b_1 and values of r_n-r_p. Note that no fit is possible with the alternative form $\frac{1}{2}\rho_p\rho_m$ for the absorption terms. Figure 4 shows the good fits obtained for all available data on 2p states. It should be stressed that no precise values were assumed for r_n but only rather broad "reasonable" limits, hence the present potential parameters should enable to determine values of r_n within wide ranges although they, a priori, exclude large values of r_n-r_p such as 0.3 fm for P and Fe.

Table III summarises values of the parameters obtained for the four different forms of the potential.

The parameters listed in Table III were obtained by requiring a good fit to the experimental results for 2p states only. One can gain more confidence in the use of these parameters for determinations of nuclear radii if it is found that they have a wider range of validity, and indeed it was shown[2] that with these parameters good fits to the data are obtained for 1s states in light nuclei and for 3d and 4f states in heavy nuclei. In the latter case the neutron rms radii are not known and they can be determined from the fits to the data, or at least the values determined can be used as a check on the

overall consistency. Unlike the lighter nuclei, it was found that whilst the predictions for parameter sets (a), (b) and (c) were very similar to each other, the predictions for parameter set (d) differed by several standard deviations of recent experimental results. Consequently, whereas agreement with experiment was achieved for set (a), (b) and (c) using values of $r_n - r_p$ in the range of 0 to 0.1 fm, it was necessary to increase r_n by a further 0.15 to 0.2 fm in order to get agreement for parameter set (d).

Finally, we note that the 2p states, which form the basis of the present work, are most suitable for the determination of pion-nucleus potential parameters. In the case of 1s states there is a very small sensitivity to the momentum dependent component of the potential and for 3d and higher states the sensitivity to the strong interaction is reduced due to the smaller overlap with the nucleus.

4. Nuclear Radii in the Ca region

The careful measurements[3] of the differences between shifts and widths of 2p pionic levels in ^{44}Ca and ^{40}Ca, together with the potential parameters[2] presented above, serve as an interesting case for testing the capabilities of the pionic atom method for studies of nuclear radii. Figure 5 shows experimental and calculated values of $(\delta\varepsilon, \delta\Gamma)$, the differences between shifts and widths in ^{44}Ca and ^{40}Ca, where $r_n(44)$, the rms radius of the neutron distribution in ^{44}Ca is varied along the lines. Very good consistency is observed between the experimental results and the calculations. In the calculations we used $\rho_p(r)$ as known from muonic atoms and

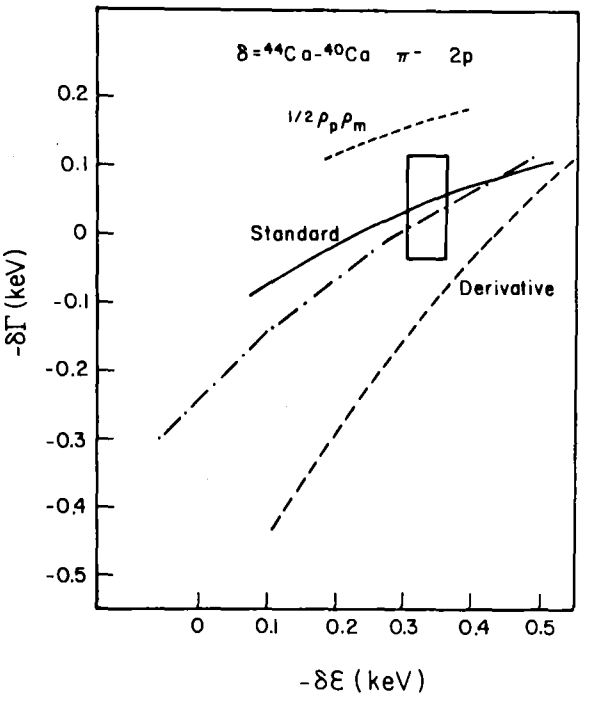

Fig. 5 Calculated and measured differences between shifts and widths in ^{44}Ca and ^{40}Ca.

electron scattering[8].

Having established the consistency between the experimental results and the predictions of all four potentials (a), (b), (c) and (d), we now proceed to determine nuclear radii. Figure 6 compares separately calculated values of $\delta\varepsilon$ and $\delta\Gamma$ vs. $r_n(44) - r_n(40)$ with the experimental results. As π^- pions interact predominantly with neutrons we chose $r_n(44)$ as the variable; if $r_m(44)$ is chosen then the scale of radii is simply compressed. The calculations displayed in Fig. 6 are based on the four parameters sets discussed

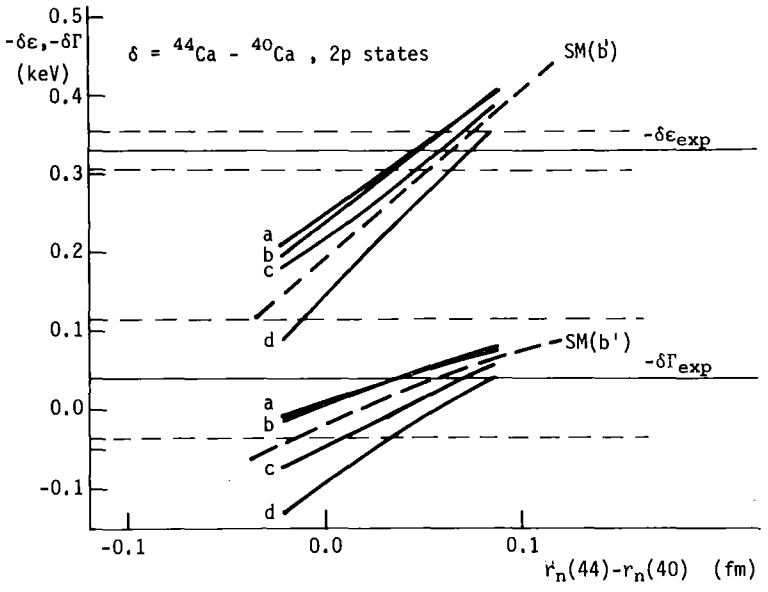

Fig. 6 Calculated and mesured differences between shifts and widths in ^{44}Ca and ^{40}Ca as functions of difference between neutron rms radii in the two isotopes.

above. Of a special interest are the dashed curves which are based on shell model density distributions for both ^{40}Ca and ^{44}Ca (contrary to all other cases where the Fermi form was used for the densities). The parameters used with these distributions are based on set (b) but very slightly modified to get a precise fit to ^{40}Ca, because for ^{40}Ca we used here $r_n - r_p = -0.04$ fm (and not 0), as obtained from many Hartree-Fock calculations. It is evident from the figure that the extracted value of $r_n(44) - r_n(40)$ depends little on the details of the analysis. In fact, the largest source of uncertainty is due to the parameter b_1. We stress again that b_1 was obtained essentially from fits to Fe,

Cu and Zn by requiring "reasonable" values for $r_n - r_p$; that amounts in the $^{44,40}Ca$ case to a "prejudice" that $r_n(44) - r_n(40) \leq 0.15$ fm. However, within this rather broad limit that difference is determined quite accurately.

One may choose the shell model density distributions as the most suitable ones for the present analysis, as they contain some additional information, i.e., that the four extra neutrons in ^{44}Ca are $1f_{7/2}$ ones. The results of the present experiment then becomes $r_n(44) - r_n(40) = 0.06 \pm 0.05$ fm, which is in good agreement with the results of other methods reported in this conference.

Figures 7 and 8 show predictions for $^{48-40}Ca$ for the four parameter sets (a) - (d) using Fermi density distributions and also for shell model distributions using a modified set (b). It is seen that in this case the various procedures give somewhat different results, although good experimental results should enable to determine $r_n(48) - r_n(40)$ to a reasonable accuracy.

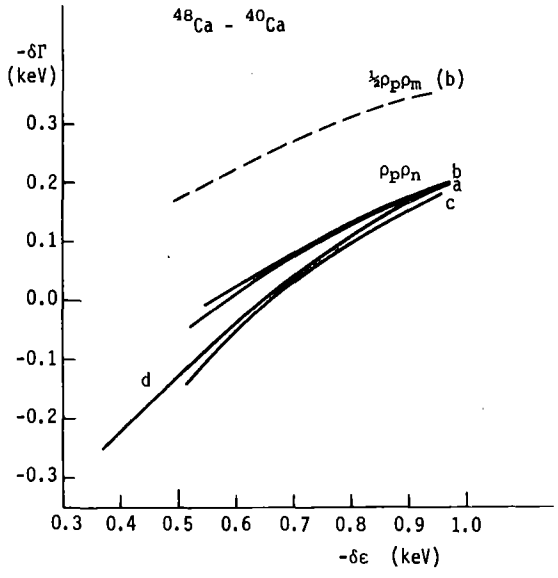

Fig. 7 Predictions for the ^{48}Ca-^{40}Ca differences.

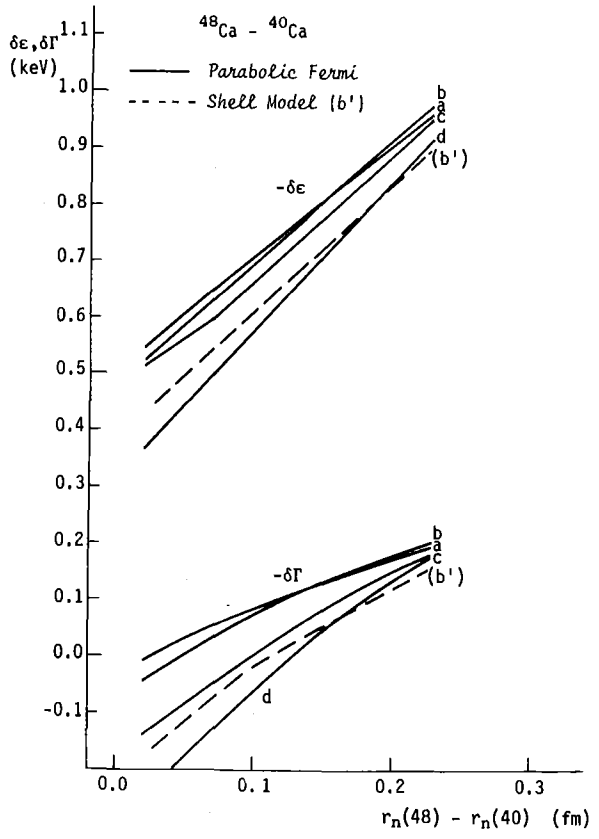

Fig. 8 Predictions for the ^{48}Ca-^{40}Ca differences.

5. Discussion

An effective pion-nucleus potential had been established which is based on precision measurements of strong interaction level shifts and widths for 2p levels and which had been shown to provide good fits to the data throughout the period table. The potential obtained is non-unique but nevertheless it predicts rather unique results for neutron radii when the neutron excess is not too large. The residual ambiguity concerning neutron radii can be considerably reduced if some additional information becomes available[9] relating e.g. to the value of the Lorentz-Lorenz parameter ξ or to the sign of ReC_0. (Parameter set (b) seems to be favoured).

The above potential is obviously an over-simplification of reality, particularly in its using zero-range forces. That could, in principle, have far reaching consequences, particularly with regard to the momentum-dependent term $\vec{\nabla} \alpha \vec{\nabla}$. It had recently been shown[10,11] that an infinity of strongly bound pionic states may exist for the potentials used here, if $Re\alpha > 1$ in the nuclear interior. However, if a finite range is introduced to the momentum-dependent interaction, only one or two of these states may survive[10,12,13]. It is, therefore, essential to analyse pionic atoms with a finite-range potential before full confidence can be established in its applicability to the problem of nuclear radii. This has yet to be done. However, the above mentioned phenomenon of strong binding results from a singularity in the wave equation and it can be shown[12], that under the conditions prevailing in pionic atoms the effects due to the singularity are negligibly small. Figure 9 shows calculated results for ^{40}Ca where a smooth transition through the critical value of $Re\alpha(0) = 1$ is observed, thus indicating that the introduction of finite range forces may have little effect (except, of course, changing values of the fit parameters). It is, therefore, suggested that at least for comparisons between different isotopes or between neighbouring nuclei pionic atoms provide a reliable means for studying nuclear radii.

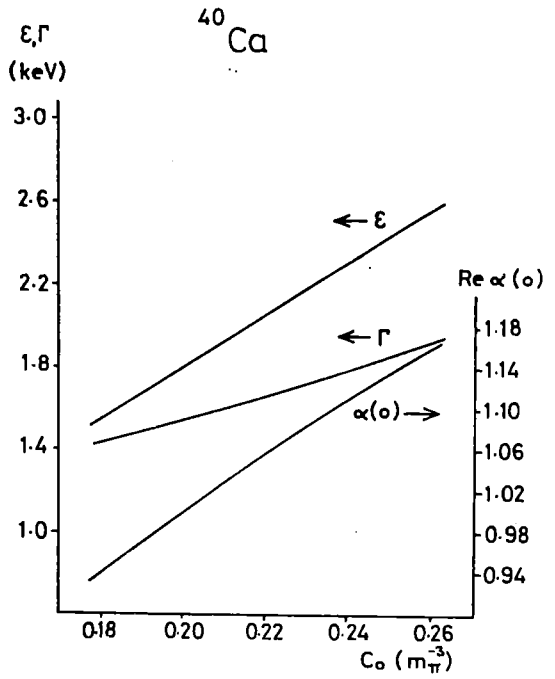

Fig. 9 The dependence of shifts and widths on Reα(0).

It is a pleasure to thank my colleagues at the Rutherford Laboratory and at the Racah Institute for many stimulating discussions.

REFERENCES

1. C.J. Batty, S.F. Biagi, E. Friedman, S.D. Hoath, J.D. Davies, G.J. Pyle and G.T.A. Squier, Phys. Rev. Lett. 40 (1978) 931.
2. C.J. Batty, S.F. Biagi, E. Friedman, S.D. Hoath, J.D. Davies, G.J. Pyle, G.T.A. Squier, D.M. Asbury and A. Guberman, Nucl. Phys. A (in press).
3. C.J. Batty, S.F. Biagi, E. Friedman, S.D. Hoath, J.D. Davies, G.J. Pyle, G.T.A. Squier, D.M. Asbury and M. Leon, Phys. Lett. 81B (1979) 165.
4. R. Kunselman and G.A. Grin, Phys. Rev. Lett. 24 (1970) 838.
5. M. Ericson and T.E.O. Ericson, Annals of Physics 36 (1966) 323; M. Krell and T.E.O. Ericson, Nucl. Phys. B11 (1969) 521.
6. L. Tauscher and W. Schneider, Z. Phys. 271 (1974) 409.
7. J. Hüfner, Phys. Rep. 21C (1975) 1.
8. C.W. de Jager, H. de Vries and C. de Vries, At. Data Nucl. Data 14 (1974) 479.
9. E. Oset, W. Weise and R. Brickman, preprint (1979).
10. T.E.O. Ericson and F. Myhrer, Phys. Lett. 74B (1978) 163.
11. E. Friedman, A. Gal and V.B. Mandelzweig, Phys. Rev. Lett. 41 (1978) 794.
12. V.B. Mandelzweig, A. Gal and E. Friedman, Ann. Phys. (submitted).
13. E. Friedman, Proc. Conf. on Meson-Nuclear Physics, Houston, March 1979 (in press).

TOTAL CROSS SECTIONS AND THE NUCLEAR MATTER DISTRIBUTION

H.O. Meyer
Indiana University,
Bloomington, U.S.A.

Total Cross Sections and the Nuclear Matter Distribution

H. O. Meyer, Indiana University, Bloomington, IN 47401, U.S.A.

"Truth is not always in a well. In fact, as regards the more important knowledge, I do believe that she is invariably superficial."

Edgar Allan Poe

Introduction

In fig. 1, π^+-π^- averaged total cross sections at the maximum of the (3,3) resonance are shown for a number of nuclei. In this case, as well as for total cross sections of other projectiles, one finds a striking dependence on the

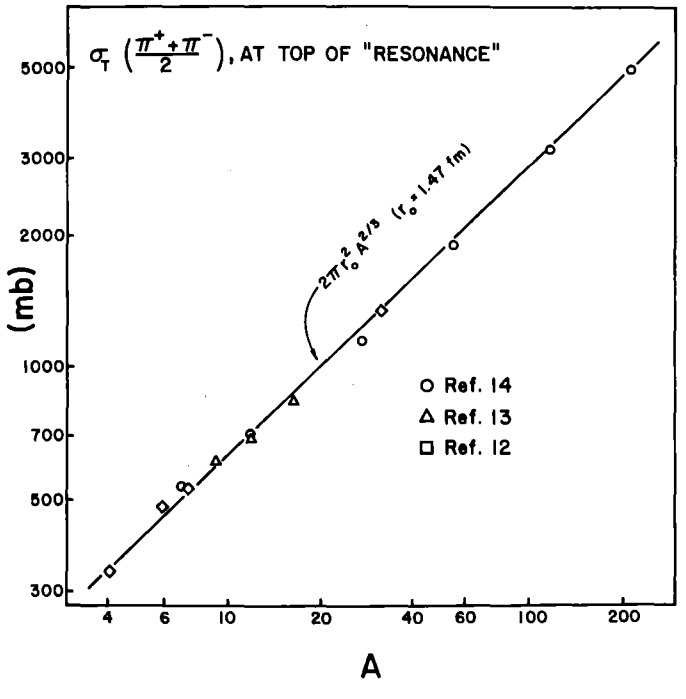

Fig. 1: Average π^+-π^- total cross sections at the pion energy which corresponds to the top of the (3,3) resonance peak. The solid line represents the geometrical cross section.

mass A of the target nucleus $\sigma_T = \text{const} \cdot A^{2/3}$ (solid line). This probably is the origin of the idea to connect total cross sections and reaction cross sections with aspects of the nucleon distribution $\rho(r)$ in the nucleus. Assuming

incompressibility of nuclear matter, any observable which scales with $A^{2/3}$ has to be connected to the lateral extent of the probed nucleus and thus, to its radius. If the nucleus was an object with a sharp surface we even would know exactly what is meant by its "radius." However, since the nucleus has a diffuse surface we need a definition of the radius R. There are "point-like" definitions (e.g. "R is the radius where the nuclear density $\rho(r)$ has fallen below a certain value") or integral definitions (e.g. the r.m.s. radius of $\rho(r)$). In any case, we need information on the shape of $\rho(r)$ to make such definitions meaningful. It is therefore incorrect to separate the search for R, using whatever definition, from the investigation of the shape of $\rho(r)$. In fact, it must be our goal to measure the nuclear nucleon distribution $\rho(r)$ to an extent and accuracy comparable with what has been achieved with respect to the proton distribution $\rho_p(r)$ by means of elastic electron scattering.

In view of the obstacles, this goal is ambitious, indeed. In order to be sensitive also to the neutrons in the nucleus we have to use strongly interacting probes. Not only do we have to understand their interaction with the nucleus as a whole, we also have to formulate this interaction in terms of "elementary" projectile-nucleon amplitudes, in order to be able to isolate the "observable" $\rho(r)$. Furthermore, we have to understand in detail the contribution of the electromagnetic force to the strong part of the interaction (e.g. ref. 1).

In this talk, I will address the following topics. Which features of the point-nucleon density $\rho(r)$ can be determined from a measurement of a hadron-nucleus total cross section σ_T or total reaction cross section σ_R? What are the problems in determining the r.m.s. radius? How does the elastic scattering differential cross section $d\sigma/d\Omega$ as a source of information compare to the observables σ_T and σ_R? With respect to the analysis of actual data I will emphasize the simultaneous analysis of σ_R for various projectiles and bombarding energies for one given target nucleus, the comparison of "neighboring" cases (e.g. isotopes) and the combined analysis of σ_T and $d\sigma/d\Omega$. Finally, I will conclude with some thoughts about possible future developments in the determination of $\rho(r)$.

The observables σ_T and σ_R have the advantage that their measurement requires only very low beam intensities ($<10^6$ particles per second). Data at many bombarding energies and for many targets can be obtained quickly. Also, the use of more exotic probes such as $K^{\pm}$ and $\bar{p}$ becomes practical. In the case of σ_T, a

disadvantage is the necessary correction for the contribution of the interfering Coulomb amplitude. At low energies and for high Z targets this contribution is sizeable. In its usual definition, σ_T becomes dependent on a model. Only recently has it been suggested[2] that σ_T could be defined in such a way that its determination is model independent.

Which features of $\rho(r)$ can be determined from σ_T or σ_R?

To discuss qualitatively to which features of the nucleon distribution $\rho(r)$ σ_T or σ_R are sensitive, one chooses a formally simple model, rather than the most realistic one. Therefore, recent investigations on this subject[3)-5)] all made use of the optical model in the impulse approximation with an eikonal propagator (meaning simply straight line trajectories). Such a model neglects higher order terms in the optical potential and corrections arising from the use of the free projectile-nucleon T-matrix.

In the following, I also neglect spin, isospin, and the real part of the elementary forward amplitude. The projectile (X) - nucleon (N) contribution is then represented by the elementary total cross section σ_{XN}. Let me define

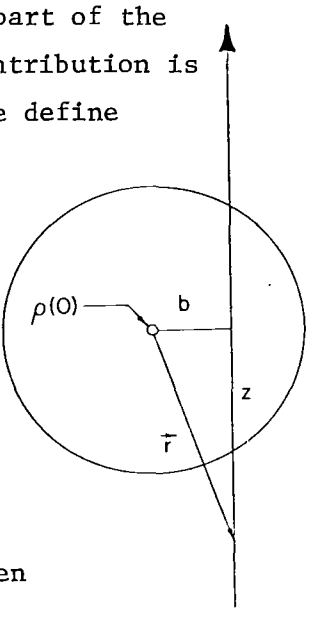

the profile function
$$S(b) \equiv \frac{1}{\rho(0)} \int_0^\infty \rho(z,b)dz \qquad (1)$$

which is the "thickness" of the target nucleus at impact parameter b and

the mean free path
$$\lambda \equiv (\rho(0)\cdot\sigma_{XN})^{-1} \qquad (2)$$

where $\rho(r)$ is the nucleon density. The total cross section can then be written

$$\sigma_T = 4\pi \int_0^\infty (1 - e^{-\frac{S(b)}{\lambda}})bdb \qquad (3)$$

In order to evaluate what features of the radial function $\rho(r)$ (contained in $S(b)$) are determined by a measurement of σ_T we calculate the cross section $\sigma_T' = \sigma_T + \Delta\sigma_T$ generated by a slightly different density $\rho'(r) = \rho(r) + \Delta\rho(r)$. Conserving the number of nucleons means that the change $\Delta\rho(r)$ is normalized to zero. Expanding $S'(b)$ and retaining only terms linear in $\Delta\rho(r)$ one obtains[3]

$$\Delta\sigma_T = \sigma_{XN} \cdot 4\pi \int_0^\infty r^2 A_o(r) \Delta\rho(r) dr \qquad (4)$$

where $A_o(r)$ is a "radial weight function" which can be written as

$$A_o(r) = \int_0^1 e^{-\frac{S(r\xi)}{\lambda}} \xi \, (1 - \xi^2)^{-1/2} \, d\xi \qquad (5)$$

As an example, consider a transparent nucleus, i.e. one for which $S(b) \ll \lambda$ for all b. In this case, $A_o(r) \simeq 1$ everywhere, and $\Delta\sigma_T$ (eq. 4) only depends on the volume integral of $\Delta\rho(r)$. This means that σ_T is sensitive only to changes in the number A of nucleons in the target. In this case, σ_T would thus be a trivial observable. We conclude that <u>only if there is substantial absorption of the projectile, can σ_T be sensitive to any aspect of the density distribution</u>!

On the other hand, if the nucleus is strongly absorptive inside some radius R this means that $S(b<R) \gg \lambda$ and $A_o(r) \sim 0$ for $r < R$. A calculation of $A_o(r)$ for some realistic cases has been carried out. The result is shown in fig. 2.

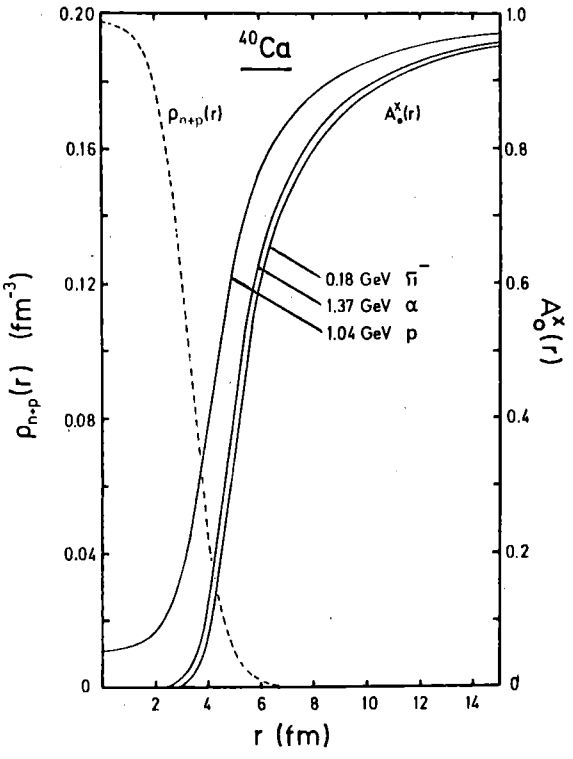

Fig. 2: Radial weight $A_o(r)$ for several projectiles bombarding ^{40}Ca. Also shown (dashed line) is the point nucleon density of ^{40}Ca used in the calculation of $A_o(r)$. The figure is from ref. 3.

As can be seen, $A_o(r)$ typically is small in the interior absorptive region and rises steeply outside this region. To a first approximation eq. 4 therefore becomes

$$\Delta\sigma_T = \sigma_{XN} \cdot 4\pi \int_R^\infty r^2 \, \Delta\rho(r) \, dr$$

This means that σ_T is sensitive to the number of nucleons outside a sphere of radius R, where R is loosely defined as the extent of the "black", i.e. strongly absorptive, region of the nucleus. For most cases, R lies in a region where $\rho(r)$ is exponentially decreasing. Relative changes of $\rho(r)$ in the region beyond R are thus most effective right at the radius R. We are thus led to the qualitative statement that σ_T is sensitive to the value of the density $\rho(r)$ in the neighborhood of a certain radius R which is located by the onset of $A_o(r)$ and the fall-off of $\rho(r)$. With minor modifications similar arguments can also be made with respect to the total reaction cross section σ_R. The radial weight functions found in this case[3] have the same general dependence on r as $A_o(r)$.

From the above arguments we must conclude that σ_T or σ_R never directly determines the r.m.s. radius $\langle r^2 \rangle^{1/2}$ of $\rho(r)$. In order to determine such an integral quantity we need to assume a continuation of $\rho(r)$ into the "black" region. Often a Woods-Saxon (WS) distribution is used to express $\rho(r)$ at all radii. Since the norm is fixed, there remain two free parameters: the radius parameter c and the diffuseness a. In fig. 3 the parameter space for a typical WS distribution is

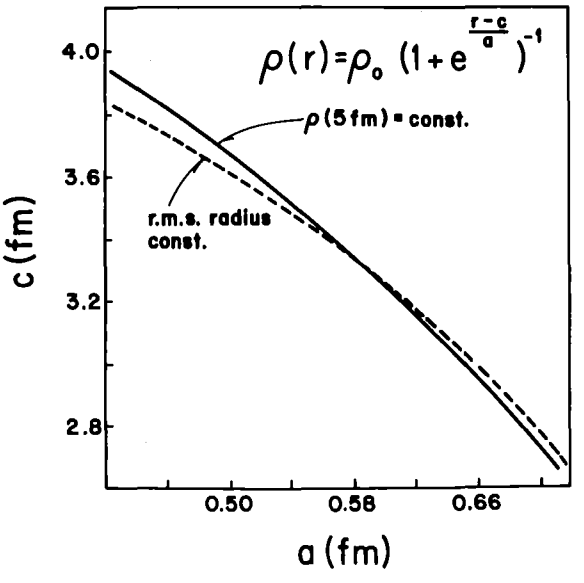

Fig. 3: Effect of restricting a WS distribution. Shown are the loci in (c,a) - parameter space for i) a constant r.m.s. radius (dashed curve) and ii) a constant density in the tail region, at r = 5 fm (solid line). The norm of $\rho(r)$ is kept constant at all times.

displayed. The measurement of an observable which depends on $\rho(r)$ puts a restriction on c and a, leading to a locus in fig. 3. The locus given by a constant r.m.s. radius (dashed line) is compared to the locus determined by a constant value $\rho(r_o)$ at a fixed r_o in the tail region (solid line). It can be seen that the two loci almost coincide. This means that a measurement of $\rho(r)$ in the tail region is equivalent with a determination of $\langle r^2 \rangle^{1/2}$. There is physical truth to this statement only if $\rho(r)$ in reality is identical to a WS distribution. This we should keep in mind whenever discussing $\langle r^2 \rangle^{1/2}$ derived from hadron-nucleus observables.

In so called model independent analyses[4),6)] one tries to avoid a rigid functional dependence on r, using a flexible, unbiased parametrization for $\rho(r)$ or the profile function S(b). The space of all test functions $\rho'(r)$ which lead to the same calculated σ_T is then evaluated. For a given $\rho'(r)$ often the so-called density moments M_k are evaluated:

$$M_k \equiv \left[\frac{4\pi}{A} \int_0^\infty \rho(r)\, r^{k+2}\, dr \right]^{1/k} \qquad (7)$$

The constrained space of all test functions $\rho(r)$ resulting in a constant σ_T then determines an "error" $\delta M_K / M_K$. For $\pi^\pm$ total cross sections in the resonance region with ^{40}Ca as a target it has been found[4)] that the moment determined best is between M_2 and M_4. The physics insight gained by such an analysis is questionable since in principle one obtains just an expansion of the radial weight function $A_o(r)$ into an orthogonal set of M_k. In addition it turns out that it is necessary to restrict the space of test functions by imposing upper and lower bounds for $\rho(r)$ and its derivatives and it is not clear how such restrictions affect conclusions about the sensitivity to specific moments.

Elastic scattering angular distributions $d\sigma(\theta)/d\Omega$

It is interesting to compare $d\sigma/d\Omega$ as a source of information on $\rho(r)$ to the observables σ_T and σ_R. Arguments similar to the ones mentioned in the preceeding section are also possible for the scattering amplitude F(q) in $d\sigma/d\Omega = |F(q)|^2$. The change $\Delta F(q)$ caused by changing the original $\rho(r)$ by an amount $\Delta\rho(r)$ is then found to be[3)]

$$\Delta F(q) = f_{XN}(q=0) \sum_{j=0}^{\infty} \left[q^{2j} \frac{(-1)^j}{(2j+1)!} \int_0^{\infty} r^{2j+2} A_j(r) \Delta\rho(r) dr \right] \qquad (8)$$

This relation is analogous to eq. 4. for the case of σ_T. Here also, the density change $\Delta\sigma(r)$ is folded with radial weight functions $A_j(r)$. The expression for $A_j(r)$ is given in ref. 3. In fig. 4. A_o-A_3 are shown for 1 GeV

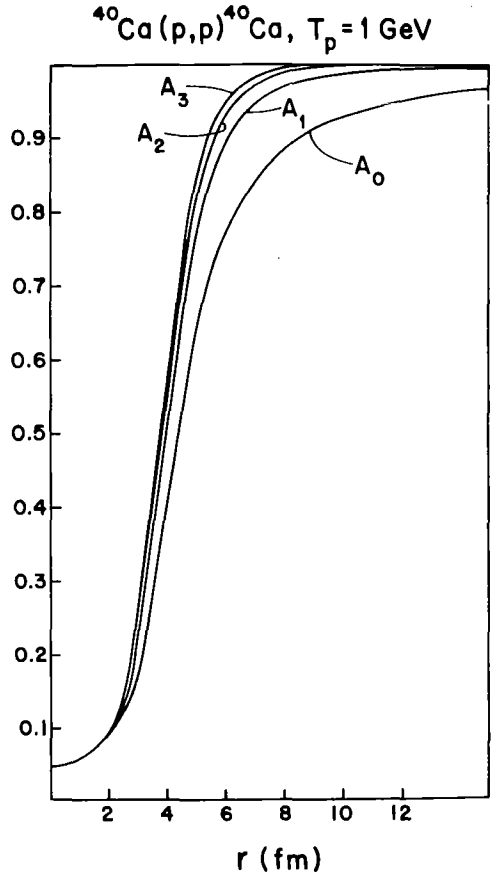

Fig. 4: Dependence of the radial weight function on momentum transfer. The $A_j(r)$ are defined in eq. 8. For details refer to the text.

proton scattering on ^{40}Ca. As can be seen, the $A_j(r)$ for all j look very similar to $A_o(r)$. It is true, that for larger momentum transfer q the higher moments of $\Delta\rho(r)$ become important but the masking by the radial weight function still occurs at approximately the same r. By the same argument as used above, we would expect $d\sigma/d\Omega$ <u>also</u> to be sensitive to the value of $\rho(r)$ in the neighborhood of a certain $r = R_{eff}$. This conclusion is in agreement with a recent analysis[7] of the angle at which diffraction minima occur in $\pi^{\pm}$ scattering from $^{48,40}Ca$ in the (3,3) resonance region. It is in fact shown

that the radius extracted from the zero of the Bessel function is directly related to the impact parameter at which the profile function assumes a given value.

In view of this, one tends to suspect that in the case of strongly absorbed projectiles the information on $\rho(r)$ gained from σ_R or σ_T is very similar to what one can learn from elastic scattering angular distributions.

Analysis of σ_R for various projectiles on the same target

The fact that σ_R is sensitive to the density near a certain radius (or in the language of the Glauber model, the profile function near a certain impact parameter) has also been pointed out in a recent analysis of hadron reaction cross sections[5] . Again using the impulse approximation with an eikonal propagator, the following remarkable result has been obtained. First, an effective radius based on the observed σ_R is defined

$$R_{eff} \equiv \sqrt{\sigma_R/\pi} \quad . \tag{9}$$

Making several simplifying assumptions and using an approximation for the integration over impact parameter, a relation is obtained between the profile function (eq. 1) and the mean free path (eq. 2):

$$2\, S(R_{eff}) \simeq \lambda \quad . \tag{10}$$

The striking aspect of such a relation is that if it would hold exactly, a measurement of σ_R would tell us at which impact parameter $b = R_{eff}$ the "thickness of the nucleus" $S(b)$ is equal to the mean free path. Since neither the nature of the projectile nor the bombarding energy is specified in eq. 10 one could change λ by varying the probe. Thus $S(b)$ could be mapped out over a range of impact parameters. From this knowledge the value of the density in some corresponding interval of r could be obtained free of a model assumption about the shape of $\rho(r)$.

The immediate question is, of course, to which degree the relation eq. 10 holds in reality. In order to investigate this, one may plot R_{eff} (defined by eq. 9 in terms of the experimental σ_R) versus the mean free path λ, derived from the free projectile-nucleon cross section. This is carried out in fig. 5 for σ_R on ^{12}C for a variety of projectiles, including π^+, π^-, p, $\bar{p}$, K^+ and K^- over a range of incident momenta from 0.29 GeV/c to 200 GeV/c. The data are from

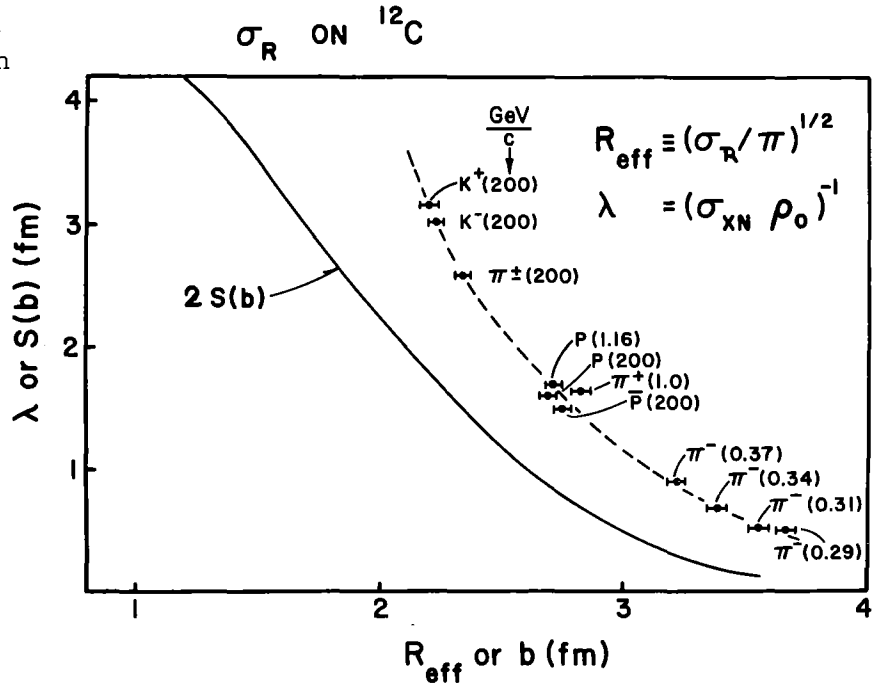

Fig. 5: The mean free path λ versus R_{eff} defined by the reaction cross section for many projectiles and bombarding energies. Also shown is the profile function to test the relation $\lambda \simeq S(R_{eff})$. The data are from refs. 8-11.

refs. 8 -11 . The dashed line is a guide to the eye. The solid line corresponds to 2S(b), where the profile function has been calculated from a single particle shell model density. If the relation eq. 10 would hold,the dashed and solid lines in fig. 5 are expected to coincide. That this is not the case is not surprising in view of the many assumptions made to derive eq. 10. However, what is truly remarkable is that the data for many different projectiles, spanning three orders of magnitude of incident momentum, indeed fall on a common locus which in addition seems to be related to S(b). This suggests that a relation like eq. 10 indeed exists and, if known, can be used to map out S(b) and thus $\rho(r)$ over a fair range of r. This teaches us that we probably learn more about $\rho(r)$ from simultaneously analyzing many different hadron-nucleus data as compared to concentrating our efforts on one projectile at a single energy. At the same time,we have to keep in mind that a relation like eq. 10 is approximate and we need to fill in the details.

That such details can be important is shown in the example of π^+ and π^- total cross sections across the (3,3) resonance of which there are now several systematic studies available[12)-14)] (see fig. 6). As is well known, the peak in σ_T, corresponding to the (3,3) resonance, broadens and shifts towards smaller pion energies if A is increased. Based on ref. 15, McVoy showed[16)] that this shift is due to a sign change of the nuclear potential at the energy of the (3,3) resonance. This means that at some level the real part of the elementary amplitude can not be neglected as has been done e.g. in the derivation of eq. 10.

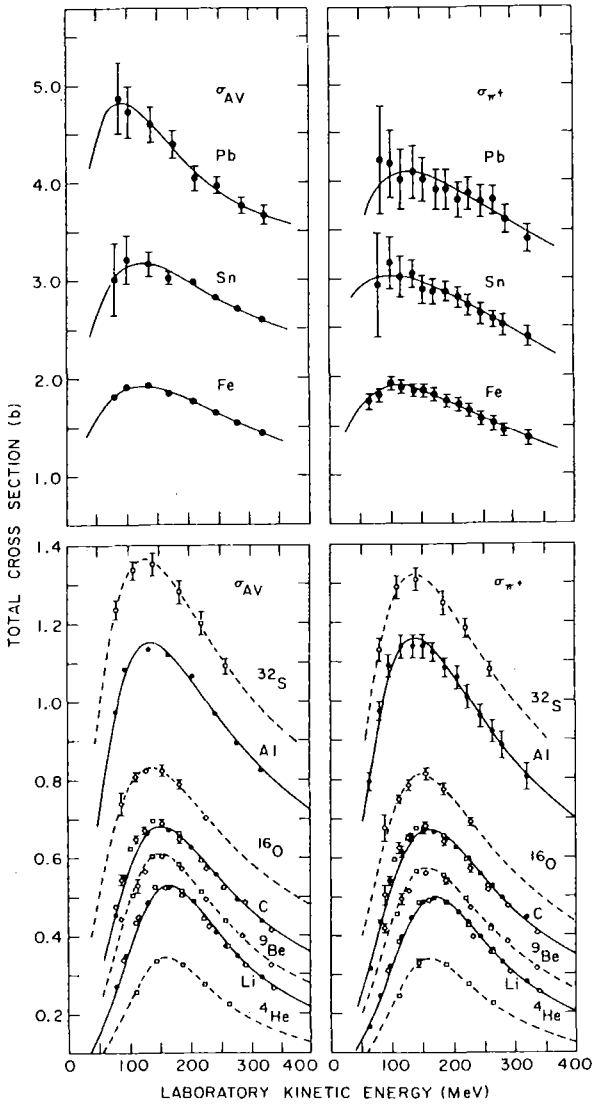

Fig. 6: Pion nucleus total cross sections in the (3,3) resonance region. The data are from refs. 12-14, the figure from ref. 14.

Ratios or differences of cross sections

It is reasonable to assume that an accurate description of the projectile-nucleus interaction is less important if one only attempts to compare cross section data, either for similar projectiles or for similar targets.

It is tempting to make use of the isospin dependence of the pion-nucleon interaction in order to learn about differences in the neutron and proton distributions. A comparison[11] of $\sigma_R(\pi^-)$ with $\sigma_R(\pi^+)$ in the 1 GeV/c region on C, Ca and Pb is an example. As it turns out, the measured ratios $\sigma_R(\pi^-)/\sigma_R(\pi^+)$ are close to 1. In addition the Coulomb distortion, computed following

a semiclassical treatment[17] accounts for most of the effect. The extraction of information on ρ_n/ρ_p therefore not only relies on very accurate measurements but also on a thorough understanding of the interplay between the strong and the Coulomb interaction.

A comparison of isotopic targets is less affected by difficulties due to the Coulomb interaction. An example is the measurement[18] of σ_T with 90-250 MeV π^+ and π^- for the isotopes ^{40,44,48}Ca. In fig. 7 the differences $\Delta\sigma_T(\pi^+)$ and $\Delta\sigma_T(\pi^-)$

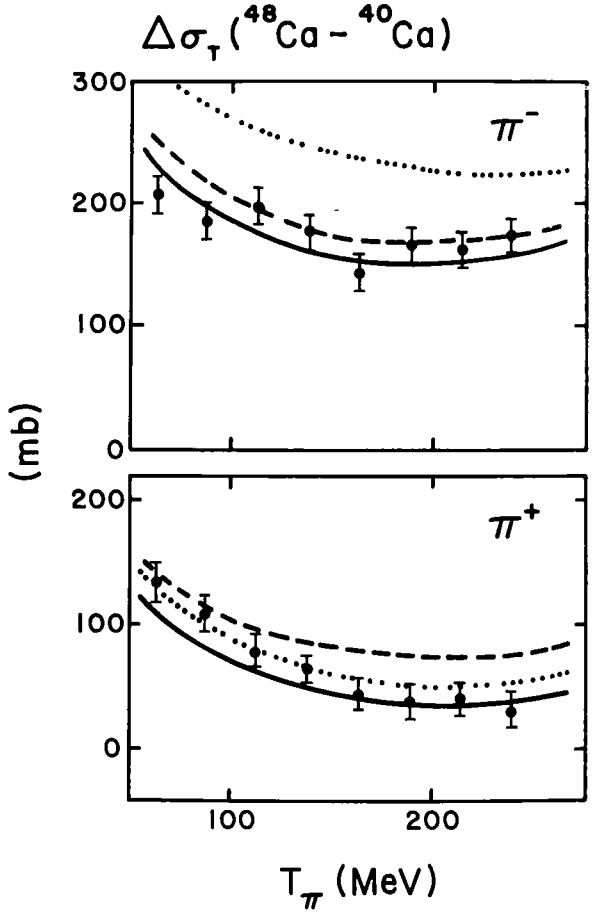

Fig. 7: Isotopic total cross section differences for π^- and π^+ in the (3,3) resonance region. The solid line represents the best fit. The dotted and dashed curves show the effect of increasing the r.m.s. radius of the neutron and proton distribution by 0.1 fm, respectively. The figure is from ref. 18.

for the pair ^{48}Ca, ^{40}Ca are shown vs. the bombarding energy. Nucleon distributions assumed to have a WS shape, were used to construct an optical potential. Since essentially two numbers ($\Delta\sigma_T(\pi^+)$, $\Delta\sigma_T(\pi^-)$) were measured, two free parameters could be determined. These were chosen to be the isotopic difference between the neutron and proton r.m.s. radii $\Delta\langle r_n^2\rangle^{1/2}$ and $\Delta\langle r_p^2\rangle^{1/2}$ for the two isotopes. The

advantage of this is the fact that $\Delta\langle r_p^2\rangle^{1/2}$ of course is well known from electron scattering which allows an overall consistency check of the procedure. For the isotope difference in neutron r.m.s. radius the result[18] is

$$\Delta\langle r_n^2\rangle^{1/2} = \begin{array}{ll} 0.09 \pm 0.05 \text{ fm} & (^{44}\text{Ca} - ^{40}\text{Ca}) \\ 0.14 \pm 0.05 \text{ fm} & (^{48}\text{Ca} - ^{40}\text{Ca}) \end{array}$$

(By the way, these numbers have been quoted incorrectly in at least two recent publications[5),19)].)

Recently, reaction cross sections σ_R of 700 MeV protons on the isotopes ^{48,44,40}Ca have been measured[20]. An analysis[5] leads to a result compatible with pion total cross sections[18] in the case of the pair ^{44,40}Ca but to a very large difference $\Delta\langle r_n^2\rangle^{1/2} = 0.62 \pm 0.15$ fm for ^{48,40}Ca.

Differences between the neutron distributions of the isotope pair ^{48}Ca, ^{40}Ca have indeed drawn much interest in the recent past. Invariably, the difference between r.m.s. radii is quoted. A glance at compilations (e.g. refs. 5, 19, 21) of this parameter as extracted from a variety of experiments reveals the puzzling fact that the range from 0 fm to 0.75 fm is essentially covered by $\Delta\langle r_n^2\rangle^{1/2}$ "data points" often with error bars as small as 0.05 fm. Theoretical predictions of the ^{48}Ca - ^{40}Ca neutron radius difference (ranging from 0.06 fm to 0.42 fm) are compiled in ref. 19 . Here, one has to remember that the primary quantity determined from a hadron-nucleus experiment is inherently coupled to a narrow region in impact parameter space. It is thus likely that different projectiles on the same target (or target combination) test disjunct features of $\rho(r)$ (or $\Delta\rho(r)$). The discrepancies between r.m.s. radii extracted from different experiments may well be explained by the model dependence of the continuation of $\rho(r)$ into regions of r to which the observables are not sensitive. However, in order to really decide this issue, we have to be able to exclude discrepancies introduced by the interaction model.

For completeness sake, I would like to mention another recent investigation[22] of the ^{44}Ca, ^{40}Ca r.m.s. radius difference using data on the shift and width of pionic X-ray transitions (a "total cross section" in some sense, too). This approach leads to a result which is also in agreement with pion total cross sections[18].

σ_R or σ_T versus $d\sigma/d\Omega$ as a source of information on $\rho(r)$

The question whether to use σ_T (or σ_R) to extract information on $\rho(r)$ rather than some other observable such as the elastic scattering angular distribution $d\sigma/d\Omega$ is irrelevant. Either the two sources contain equivalent information (as we suspect to be approximately the case with very opaque nuclei) or, if they do not, we have to require the results from both to be consistent. In this sense, one observable may be viewed as a constraint in the analysis of the other, hopefully leading to a reduction of ambiguities (rather than a contradiction).

As an example, I mention a recent unified analysis[23] of σ_T and $d\sigma/d\Omega$ for 130 MeV π^+ and π^- on ^{48}Ca and ^{40}Ca. In this analysis, the first step was to search for a microscopic optical potential (Kisslinger model) reproducing the elastic scattering angular distributions by varying the nucleon distributions and the π-nucleon related parameters in the potential. It was found that a number of such potentials exist which give equivalent fits to $d\sigma/d\Omega$. In fig. 8 the ^{48}Ca - ^{40}Ca total cross section difference $\Delta\sigma_T$ predicted by these potentials is plotted vs. the corresponding $\Delta\langle r_n^2\rangle^{1/2}$ calculated from the nucleon distributions used in the analysis. The solid and the dashed curve represent the correlation between $\Delta\langle r_n^2\rangle^{1/2}$ and $\Delta\sigma_T$ which is generated by the interaction model. However, only

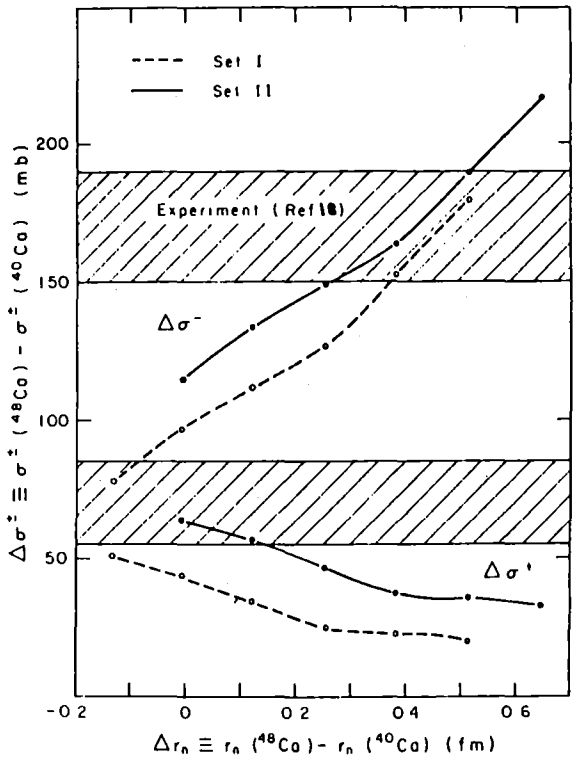

Fig. 8: Total cross section difference versus neutron r.m.s. radius difference from an optical model analysis of the differential cross section of π elastic scattering from ^{48}Ca, ^{40}Ca (solid and dashed curves). The shaded region indicates the experimental values for $\Delta\sigma_T$ from ref. 18. The figure is from ref. 23.

these potentials are acceptable which agree with the experimentally determined[18] $\Delta\sigma_T$ (shaded region in fig. 8, refer also to fig. 7). This is done for π^- as well as for π^+ (upper and lower part of fig. 8). As can be seen, there is no $\Delta\langle r_n^2\rangle^{1/2}$ which is consistent with all the experimental information introduced into the analysis. This proves the presence of deficiencies in the used interaction model, not withstanding the fact that the elastic angular distributions are fitted very well. This analysis also teaches us that elastic scattering angular distributions by themselves cannot always be used as a source of information on $\rho(r)$. In contrast to the above example, elastic scattering of 800 MeV protons on ^{40}Ca (ref. 19) seems to be a case where only little can be gained by a knowledge of σ_T. A recent analysis[24] in terms of the KMT microscopic optical model reveals almost no dependence of the calculated σ_R on variations of the parameters of the model, if the fit to $d\sigma/d\Omega$ is restored by readjusting all other parameters. In addition, the value for σ_R predicted on the basis of the elastic scattering data agrees well with a subsequent measurement of σ_R with 700 MeV protons[20].

Conclusions

We have seen that strong absorption of hadrons by nuclei is at the same time making possible and inhibiting the use of total cross section in learning about nuclear density distributions. While without the absorptivity σ_R or σ_T would be trivial observables, it is the same absorptivity which limits probing to a region outside the "black" nuclear interior. In fact, roughly speaking, hadron-nucleus experiments are sensitive to $\rho(r)$ within a narrow radial region most often located in the tail of the nuclear density. It is for this reason that integral aspects of $\rho(r)$ such as the r.m.s. radius are difficult to extract from hadron-nucleus data, including elastic scattering differential cross sections.

We are confident that the goal to accurately determine nuclear matter distributions, and thus the neutron density distribution $\rho_n(r)$, will be gradually approached in the near future. It is obvious that what is needed is a more detailed knowledge of the hadron-nucleus interaction in all its aspects. At present there is a trend to accept model deficiencies and to just make them less important by e.g. comparing isotopes. Eventually, we have to get away from this and aim at absolute information for a given single nucleus.

It seems important to point out that it is unlikely that a single type of experiment will emerge as the prime source of information on matter distributions. The credibility of experimentally determined $\rho(r)$ (or aspects of $\rho(r)$) will be born out by the consistency of results obtained with many different projectiles over a wide range of bombarding energies, analyzing σ_T, σ_R, $d\sigma/d\Omega$ (elastic) and possibly reaction channels. In addition, the use of projectiles with different mean free paths in nuclear matter will provide us with the radial sensitivity (see fig. 5) which is lacking if only one measurement is considered. Pions on resonance probably will be useful to investigate the far tail of $\rho(r)$. In this case, elastic scattering angular distributions are not expected to yield much more information than σ_R or σ_T. Nevertheless, $d\sigma/d\Omega$ data will serve their purpose as a more sensitive test of the interaction model used.

On the other hand, we also need strongly interacting probes which are only weakly absorbed by the nucleus, in order to map out S(b) to smaller impact parameters. In this case, the variation of the momentum transfer and thus elastic scattering data will be the prime source of information while σ_T or σ_R become less important with increasing transparency of the nucleus. A candidate for such a weakly absorbed but strongly interacting probe is the K^+. Beam intensities for K^+ of $\sim 10^5$ sec^{-1} are currently available (AGS,1976), but kaon factories may become a reality in the future. The average K^+_p, K^+_n cross section at low energies is ~9 mb as compared to 200 mb for π^+_p at the (3,3) resonance. The mean free path of K^+ in nuclear matter thus becomes $\lambda \sim 7$ fm, i.e. larger than the radius of all known nuclei. In addition, the K^+-nucleon interaction exhibits a number of features which greatly simplify K^+-nucleus interaction models[25]. The main disadvantage of kaons as nuclear probes currently lies in the insufficient knowledge of the elementary amplitudes but this should be no obstacle once intense K^+ beams are available.

Another weakly absorbed hadron is the low energy pion ($T_\pi < 50$ MeV). Besides experimental difficulties there are also considerable theoretical uncertainties which at present prohibit the extraction of reliable information on $\rho(r)$. It is mandatory that very low energy pion scattering and pionic atoms are understood in the same framework, a task which is currently receiving attention[26].

Acknowledgements

I greatly appreciated a number of helpful discussions with my colleagues, A.D. Bacher, J.T. Londergan, R.E. Pollock, and P.P. Singh.

References

1. H. Leśniak and L. Leśniak, Nucl. Phys. B38, 221 (1971).
2. M.D. Cooper and M.B. Johnson, Nucl. Phys. A260, 352 (1975).
3. H.O. Meyer, Phys. Rev. C17, 1116 (1978).
4. J.P. Auger and R.J. Lombard, Phys. Lett. 77B, 165 (1978).
5. D.J. Ernst, Phys. Rev. C19, 896 (1979).
6. R.J. Lombard and C. Wilkin, Lett. Nuovo Cimento 13, 463 (1975).
7. M.B. Johnson and H.A. Bethe, Comments Nucl. Part. Phys. 8, 75 (1978).
8. F. Binon, P. Duteil, J.P. Garron, J. Gorres, L. Hugon, J.P. Peigneux, C. Schmit, M. Spighel and J.P. Stroot, Nucl. Phys. B17, 168 (1970).
9. P.U. Renberg, D.F. Measday, M. Pepin, P. Schwaller, B. Favier, and C. Richard-Serre, Nucl. Phys. A183, 81 (1972).
10. A.S. Carroll, I.H. Chiang, T.F. Kycia, K.K. Li, M.D. Marx, D.C. Rahm, W.F. Baker, D.P. Earty, G. Giacomelli, A.M. Jonckheere, P.F.M. Koehler, P.O. Mazur, R. Rubinstein, and O. Fackler, Phys. Lett. 80B, 319 (1979).
11. B.W. Allardyce, C.J. Batty, D.J. Baugh, E. Friedman, G. Heymann, M.E. Cage, G.J. Pyle, G.T.A. Squier, A.S. Clough, D.F. Jackson, S. Murugesu and V. Rajaratnam, Nucl. Phys. A209, 1 (1973).
12. C. Wilkin, C.R. Cox, J.J. Domingo, K. Gabathuler, E. Pedroni, J. Rohlin, P. Schwaller, and N.W. Tanner, Nucl. Phys. B62, 61 (1973).
13. A.S. Clough, G.K. Turner, B.W. Allardyce, C.J. Batty, D.J. Baugh, W.J. McDonald, R.A.J. Riddle, L.H. Watson, M.E. Cage, G.J. Pyle and G.T.A. Squier, Nucl. Phys. B76, 15 (1974).
14. A.S. Carroll, I.H. Chiang, C.B. Dover, T.F. Kycia, K.K. Li, P.O. Mazur, D.N. Michael, P.M. Mockett, D.C. Rahm and R. Rubinstein, Phys. Rev. C14, 635 (1976).
15. T.E.O. Ericson and J. Hüfner, Phys. Lett. 33B, 601 (1970).
16. K.W. McVoy, Nucl. Phys. A276, 491 (1977).
17. G. Fäldt and H. Pilkuhn, Phys. Lett. 46B, 337 (1973).
18. M.J. Jakobson, G.R. Burleson, J.R. Calarco, M.D. Cooper, D.C. Hagerman, I. Halpern, R.H. Jeppeson, K.F. Johnson, L.D. Knutson, R.E. Marrs, H.O. Meyer, and R.P. Redwine, Phys. Rev. Lett. 21, 1201 (1977).
19. G. Igo, G.S. Adams, T.S. Bauer, G. Pauletta, C.A. Whitten, A. Wreikat, G.W. Hoffmann, G.S. Blanpied, W.R. Coker, C. Harvey, R.P. Licjestrand, L. Ray, J.E. Spencer, H.A. Thiessen, C. Glashausser, N.M. Hintz, M.A. Oothoudt, H. Nann, K.K. Seth, B.E. Wood, D.K. McDaniels, and M. Gazzaly, Phys. Lett. 81B, 151 (1979).

20. B.D. Anderson, P.R. Bevington, F.H. Cverna, M.W. McNaughton, H.B. Willard, R.J. Barrett, N.S.P. King and D.J. Ernst, Phys. Rev. C19, 905 (1979).
21. S. Shlomo and E. Friedman, Phys. Rev. Lett. 39, 1180 (1977).
22. C.J. Batty, S.F. Biagi, E. Friedman, S.D. Hoath, J.D. Davies, G.J. Pyle, G.T.A. Squier, D.M. Asbury, and M. Leon, Phys. Lett. 81B, 165 (1979).
23. M.M. Sternheim and Kwang-Bock Yoo, Phys. Rev. Lett. 26, 1781 (1978).
24. L. Ray, Los Alamos Scientific Lab, private communication.
25. C.B. Dover and P.J. Moffa, Phys. Rev. C16, 1087 (1977).
26. K. Stricker, H. McManus and J.A. Carr, Phys. Rev. C19, 929 (1979).

RADIAL DISTRIBUTION OF SINGLE PARTICLES IN NUCLEI FROM TRANSFER DATA

A. Moalem
Ben Gurion University,
Beer Sheva, Israel

Radial Distributions of Single Particles in Nuclei from Transfer Data

A. Moalem

Department of Physics, Ben Gurion University,
Beer-Sheva, Israel.

1. Introduction

Single nucleon transfer reactions as well as electron and hadron scattering, pion absorption, pion and ρ meson photoproduction, k^- and $\bar{p}$ captures etc., depend strongly on nuclear density near and outside the nuclear surface. However the removal and addition of a nucleon with specific angular momenta l and j provide a unique information which concerns the radial distribution of a single particle orbit. It is the purpose of the present contribution to demonstrate that the enormous amount of transfer data that has been accumulated in the literature can serve to extract root mean square (rms) radii of single particle orbits with accuracy, at least in certain cases, comparable to that achieved in large angle electron scattering.

In the distorted wave Born approximation (DWBA) analyses of single nucleon transfer reactions the differential cross-section factorizes as follows:

$$\sigma_{exp}(\theta) = N\, G^2_{lj}\, \sigma_{DWBA}(\theta) \qquad \ldots\ (1)$$

where the reaction normalization N, and the transition strength G^2_{lj} are essentially two overlap integrals; the first involving the projectile and ejectile wave functions and the latter involving the target and residual nuclei. The transition strength G^2_{lj} contains most of the spectroscopic information while all aspects of the reaction dynamics are included in $\sigma_{DWBA}(\theta)$. A major problem in using the DWBA to calculate σ_{DWBA} concerns the radial distribution of the transferred nucleon. Particularly σ_{DWBA} depends strongly on the usually unknown rms radius, $\langle r^2\rangle^{\frac{1}{2}}$, of the transferred nucleon wave function. On the other hand, the quantity σ_{DWBA} is correlated almost uniquely with $\langle r^2\rangle^{\frac{1}{2}}$. Such a correlation confirms that $\langle r^2\rangle^{\frac{1}{2}}$ is a physical quantity which can be extracted by comparing experimental cross-sections with those calculated in DWBA techniques. Obviously N and G^2_{lj} must be reliably known in order to enable a meaningful interpretation of measured cross-sections. Absolute values of G^2_{lj} as obtained from standard DWBA analyses are not reliable. As demonstrated in Sec. 2 a change of 1% in $\langle r^2\rangle^{\frac{1}{2}}$ induces a change of 10% in values of G^2_{lj}. However a simultaneous analysis of stripping and pickup data on the same nucleus leads to absolute G^2_{lj} values

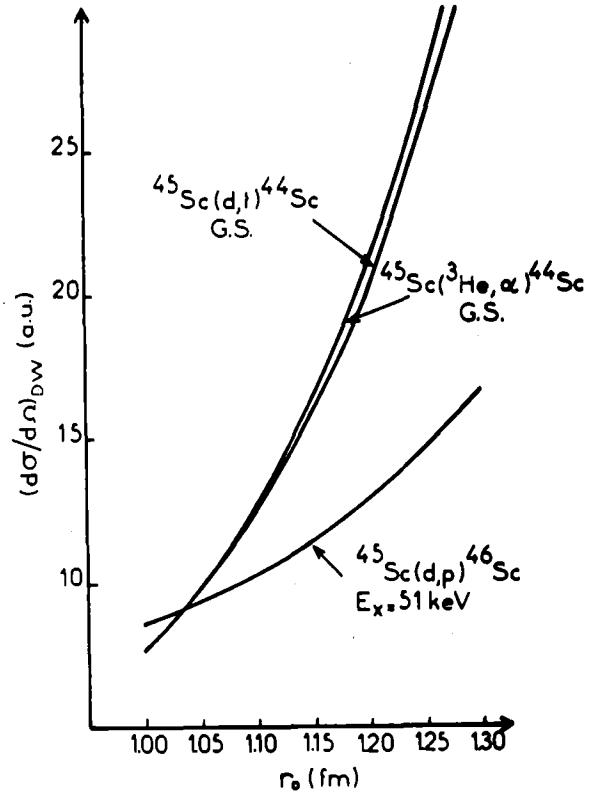

Fig.1. Dependence of ℓ = 3 $f_{7/2}$ neutron transfer cross sections on the radius parameter r_0. The single-particle potentials include a real volume term whose depth was adjusted to reproduce the experimental binding energy and a common spin-orbit term λ = 25 *and diffusness parameter* a = 0.65 *fm. (Ref.3)*

which are free from systematic errors in N and σ_{DWBA} [1] (see Sec.3). Further the normalization constants from various sources seem to fit into a most consistent pattern[2,3] and typical errors in N for reactions with light (A $\lesssim$ 4) projectiles are estimated to be about 10%. We note that the normalization for (p,d) and (d,p) is among the better known quanities in nuclear physics what makes these two processes particularly interesting in studying neutron distributions.

2. Anatomy of DWBA Analyses

A major problem in calculating σ_{DWBA} concerns the radial form factor, i.e., the wave function of the transferred nucleon. It is a standard procedure to calculate the radial form factors in a Woods-Saxon (WS) well. A radius parameter r_0 ~ 1.2 fm, diffuseness a = 0.65 fm and a spin-orbit term λ = 25 are often used. The depth of the well is adjusted to reproduce the experimental values of binding energies, i.e., the nuclear separation energies. Since the geometrical

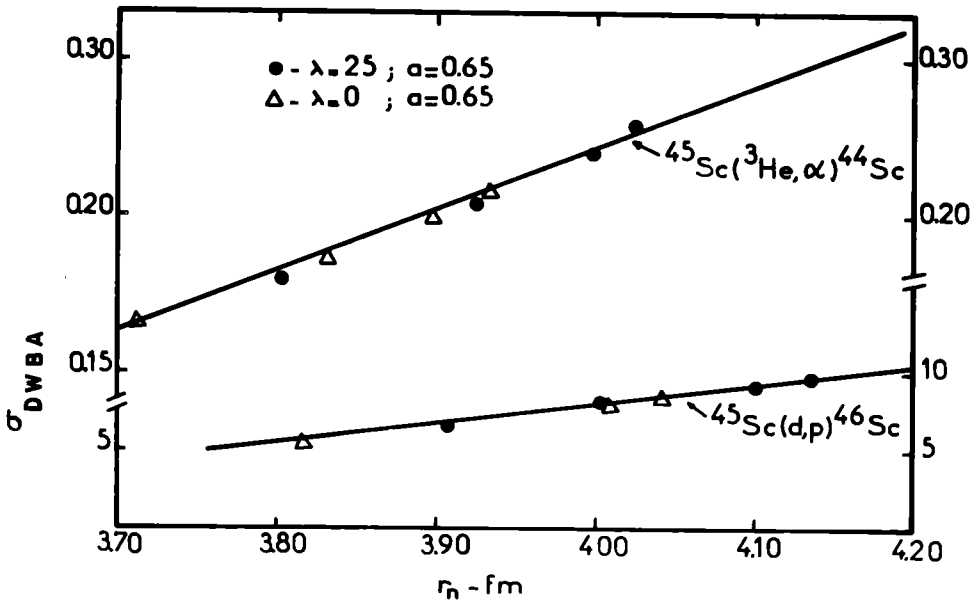

Fig. 2. Dependence of $\ell = 3$ $f_{7/2}$ neutron transfer cross sections on $\langle r^2 \rangle^{\frac{1}{2}}$. The depth of the single particle potential was adjusted to reproduce the experimental binding energies.

parameters of the WS well are not uniquely determined the calculated cross sections are not reliable. In particular the calculated cross sections (and hence the transition strength $G^2_{\ell j}$) are quite sensitive to values of r_0 [5]; a 4% change in r_0 leads to 30-40% change in the cross sections (see fig.1). On the other hand, the cross sections are better correlated with the rms radius, $\langle r^2 \rangle^{\frac{1}{2}}$, than with the radial parameter or the form of the single particle potential (see fig.2). Subject to the condition that the radial parameter r_0 is chosen to reproduce a specific value of $\langle r^2 \rangle^{\frac{1}{2}}$ the cross section becomes insensitive to values of λ or non-locality corrections. Also a change of 1% in the diffuseness parameter a induces only a 0.5 - 0.8% change in σ_{DWBA}.

Clearly the WS shape is not necessarily the correct one, but the results should not be very different for other similar shapes which reproduce the binding energy correctly. While the shape of the form factor in the nuclear interior is open to some question, the exponential fall-off in the nuclear exterior is rather well defined by the separation energy. By forcing the radial form factor to reproduce a specific value of rms radius we determine in fact, the normalization of the radial form factor near the surface and outside nucleus.

The DWBA results depend also on the optical potentials for the entrance

and exit channels. There is internal evidence from different transfer reactions and different methods of analysis that uncertainties due to optical potentials can be reduced down to 5 - 10% (see ref.4). We also note that at energies below the Coulomb barrier the results are less ambigous[2].

3. SDSR Analyses

3.1 Spin Dependent Sum Rules

Partial and total spin dependent sum rules are assesed via the following expressions :

$$S^{+}_{J_\beta} + S_{c_{J_\beta}} + (2J_\beta + 1)(-1)^{2J_r+1} \sum_{J_\alpha} \begin{Bmatrix} J_\beta & j & J_r \\ J_\alpha & j & J_r \end{Bmatrix} S^{-}_{J_\alpha} = \frac{(2J_\beta + 1)}{(2J_\alpha + 1)} (1 - \Delta) \qquad \ldots\ (2)$$

$$\sum_{J_\beta} (S^{+}_{J_\beta} + S_{c_{J_\beta}}) + \sum_{J_\alpha} S^{-}_{J_\alpha} = (2j + 1)(1 - \Delta) \qquad \ldots\ (3)$$

where J_r denotes the target spin, J_α and J_β spin of final states populated in pickup and stripping, and Δ represents a constant correction due to center of mass. $S^{+}_{J_\beta}$ and $S^{-}_{J_\alpha}$ are related to the conventional C^2S values deduced from experiment:

$$S^{+}_{J_\beta} = \frac{(2J_\beta + 1)}{(2J_r + 1)} \sum_{\beta, J_\beta \text{fixed}} C^2_\beta \, S_\beta(n\ell j t_3) = \sum_{\beta, J_\beta \text{fixed}} G^2_{\ell j}\ (\beta) \qquad \ldots\ (4)$$

$$S^{-}_{J_\alpha} = \sum_{\alpha, J_\alpha \text{fixed}} C^2_\alpha \, S_\alpha(n\ell j t_3) = \sum_{\alpha, J_\alpha \text{fixed}} G^2_{\ell j}\ (\alpha) \qquad \ldots\ (5)$$

Here t_3 is the charge of the transferred nucleon. The contribution from the continuum is denoted by $S_{c_{J_\beta}}$ but is neglected at first.

As indicated in the previous section, because of the large sensitivity of σ_{DWBA} on $\langle r^2 \rangle^{\frac{1}{2}}$, the absolute values of $G^2_{\ell j}$ extracted using the standard DWBA techniques are not reliable. However, detailed calculations show that relative values of $G^2_{\ell j}$ are almost independent on the rms radius of the transferred nucleon wave function, and any reasonable choice of $\langle r^2 \rangle^{\frac{1}{2}}$ can serve to determine a set of relative values of $G^2_{\ell j}$. To account for overall systematic errors in N and σ_{DWBA} the sum rules are written as follows

$$Q_{J_\beta} = (n^{+} S^{+}_{J_\beta}) + (2J_\beta + 1) \left| \sum_{J_\beta} \begin{Bmatrix} J_\beta & j & J_r \\ J_\alpha & j & J_r \end{Bmatrix} \left(n^{-} S^{-}_{J_\alpha} \right) - (1 - \Delta) \right| \qquad \ldots\ (6)$$

$$\sum_{J_\beta} (n^+ S^+_{J_\beta}) + \sum_{J_\alpha} (n^- S^-_{J_\alpha}) = (2J + 1)(1 - \Delta) \quad \ldots\ (7)$$

where the normalized experimental spectroscopic factors $(n^+ S^+_{J_\beta})$ and $(n^- S^-_{J_\alpha})$ can have only random uncorrelated errors. The present analysis is essentially a fitting procedure of the partial sum rules to data by varying n^+ and n^-. The following criteria are used to evaluate the quality of a fit:

(a) The overall relative error

$$\sigma = \sum_{J_\beta} \frac{\mathrm{Var}(Q_{J_\beta})}{(2J_\beta + 1)} \Big/ \Big| \sum_{J_\beta} \frac{(n^+ S^+_{J_\beta})^2}{(2J_\beta + 1)} + \sum_{J_\alpha} \frac{(n^- S^-_{J_\alpha})^2}{2J_\alpha + 1} \Big| \quad \ldots\ (8)$$

(b) the number of partial sum rules N for which $Q^2_{J_\beta} > \mathrm{Var}(Q_{J_\beta})$; where the variance $\mathrm{Var}(Q_{J_\beta})$ is calculated assuming a relative error $\sigma_e = 10\%$ in the individual spectroscopic factors S_β and S_α.

(c) The sum $S = \sum_{J_\beta} Q_{J_\beta}$ must vanish when data are perfectly fitted. We can use this criterion when n^- and n^+ are varied independently.

The results from fitting sum rules to neutron transfers on ^{45}Sc are shown in fig.3 (see ref.3). Comparable overall errors are obtained for $1.10 < n^- < 1.35$ and $0.95 < n^+ < 1.15$, but using the criterion c we find

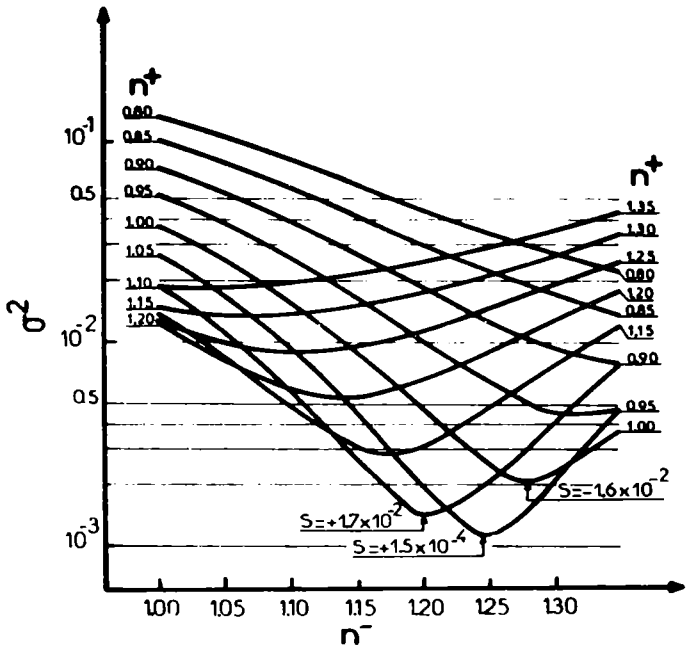

Fig.3. The overall error versus the normalizations n^+ and n^-. The figures indicated by S represent the sum of Q_{J_β}. The curves are reproduced with neutron transfers on ^{45}Sc (ref.3).

$$n^{+} = 1.05 \pm 0.05$$

$$n^{-} = 1.25 \pm 0.05$$

with $\sigma = 3.3\%$. Using curves similar to those of fig.2 we associate these values of n^{+} and n^{-} with specific rms radii $\langle r_{-}^2 \rangle^{\frac{1}{2}} = 3.83$ fm, $\langle r_{+}^2 \rangle^{\frac{1}{2}} = 4.03$ fm for 1 $f_{7/2}$ neutron in ^{45}Sc and ^{46}Sc.

Table 1

Spectroscopic factors S' for the $\ell = 3$ $f_{7/2}$ proton pickup in the $^{51}V(d,^{3}He)^{50}Ti$ reaction (ref.7-9).

E_x (MeV)	J^{π}	S'_{ZRL} a)	S'_{ZRL} b)	S'_{FRNL} a)	S'_{FRNL} b)
0.00	0^{+}	0.73 ± 0.04	0.80 ± .06	0.64 ± 0.01	0.82 ± .06
1.56	2^{+}	0.35 ± 0.03	0.40 ± .03	0.30 ± 0.02	0.38 ± .03
2.68	4^{+}	0.65 ± 0.06	0.72 ± .05	0.55 ± 0.02	0.70 ± .05
3.20	6^{+}	1.00 ± 0.09	1.10 ± .07	0.86 ± 0.05	1.10 ± .07

a) DWBA analysis with $\langle r_{-} \rangle^{\frac{1}{2}} = 3.99$ fm. ZRL calculations with $D^2 = 1.9 \times 10^4$ MeV^2 fm^3; FRNL calculations with $D_0^2 = 1.6 \times 10^4$ MeV^2 fm^3 and $\beta = 1.42$ fm^{-1}. The errors are the spread of various independent determination from the quoted average values.

b) Values obtained from partial sum rule fit to data S'_{ZRL} (b) = 1.10 S'_{ZRL} (a). The errors represent the overall error σ of eq.8.

3.2 Radii of 1 $f_{7/2}$ protons in ^{51}V and ^{52}Cr.

We present some details of SDSR analyses of 1 $f_{7/2}$ proton transfers on ^{51}V. In this case the rms radius of 1 $f_{7/2}$ proton has been determined via large angle electron scattering[6] and hence provides a very good case for illustrating the reliability of our results. Tables 1-2 summarize the spectroscopic factors $\frac{1}{8}(2J_{\beta} + 1)S'_{\beta}$ and S'_{α} obtained from zero range local (ZRL) and finite range non-local (FRNL) DWBA analyses along with J^{π}_{β} and J^{π}_{α}, the spins and parities of the corresponding final states. For proton pickup we have three sets of data from the $^{51}V(d,^{3}He)^{50}Ti$ reaction[7-9]. For proton stripping we included two sets of data from the $^{51}V(^{3}He,d)$ reactions[10,11] and one from the $^{51}V(\alpha,t)^{52}Cr$ reaction[12]. Two sets of spectroscopic factors are given in each of tables 1-2. Sets (a) are the nominal values obtained from our DWBA analyses with a rms radius $\langle r^2 \rangle^{\frac{1}{2}} = 3.99$ fm. Sets (b) are the normalized

Table 2

Spectroscopic factors $\frac{1}{8}(2J_\beta+1)S'$ for $\ell = 3$ $f_{7/2}$ transitions in the $^{51}V(^3He,d)^{52}Cr$ (refs. 10,11) and $^{51}V(\alpha,t)^{52}Cr$ (ref. 12) reactions

E_x (MeV)	J^π	$\frac{1}{8}(2J_\beta+1)S'_{ZRL}$ a)	$\frac{1}{8}(2J_\beta+1)S'_{ZRL}$ b)	$\frac{1}{8}(2J_\beta+1)S'_{FRNL}$ a)	$\frac{1}{8}(2J_\beta+1)S'_{FRNL}$ b)
0.00	0^+	0.50 ± 0.03	0.48 ± .03	0.46 ± 0.05	0.48 ± .03
1.43	2^+	0.79 ± 0.03	0.75 ± .05	0.76 ± 0.06	0.80 ± .05
2.36	4^+	0.68 ± 0.04	0.65 ± .05	0.65 ± 0.08	0.68 ± .05
2.77	4^+	1.23 ± 0.05	1.17 ± .08	1.12 ± 0.10	1.18 ± .08
3.11	6^+	2.51 ± 0.09	2.39 ± .17	2.31 ± 0.15	2.43 ± .17

a) DWBA analysis with $\langle r_+^2\rangle^{1/2}$=3.99 fm; ZRL calculations with D^2 = 2.8, 20.5 × 10^4 MeV^2 fm^3 for (^{3}He,d) and (α,t) FRNL calculations with D^2 = 2.4, 9.8 × 10^4 MeV^2 fm^3 and β = 1.42, 1.23 fm^{-1} for (^{3}He,d) and (α,t). The errors are the spread of various independent determinations from the quoted average values.

b) Values obtained from partial sum rule fit to data; $S'_{ZRL}(b) = 0.95 \times S'_{ZRL}(a)$ and $S'_{FRNL}(b) = 1.05 \times S'_{FRNL}(a)$
The errors represent the overall error σ of eq.8.

Table 3

Normalization constants n^+, n^-, partial sums and best fit overall error from sum rule fit to data

DWBA analysis	n^+	n^-	$\Sigma_{J_\beta}(n^+S^+_{J_\beta})$	$\Sigma_{J_\alpha}(n^-S^-_{J_\alpha})$	σ % c)
ZRL a)	0.95	1.12	5.43	3.04	7.0
ZRL b)	1.05	1.07	5.34	3.13	7.6
FRNL a)	1.05	1.24	5.56	2.91	6.5
FRNL b)	1.10	1.28	5.26	3.29	8.5

a) with $\langle r^2\rangle^{1/2}$ = 3.99 fm

b) with r_0 = 1.241, 1.219 fm for stripping and pickup

c) the overall fit σ of eq.8.

($n^+ S_\beta^+$) and ($n^- S_\alpha^-$) spectroscopic factors obtained from SDSR analysis. The errors quoted for sets (a) represent the spread of various independent determinations of spectroscopic factors from average values. Although the absolute values of the spectroscopic factors S'_{ZRL} and S'_{FRNL} are somewhat different, we obtain the same normalized spectroscopic factors. The normalizations $n^\pm$ from various analyses are given in table 3. Since it is not clear if the rms radius is the same to all final states we have included results obtained with a common radial parameter r_0 for all $\ell = 3$ transitions. It should be noted however that similar analyses[13] of analogue states indicate that reproducing the same rms radius is more correct. From table 3 we obtain the following average values:

$$n^+ = 1.18 \pm 0.10$$

$$n^- = 1.04 \pm 0.07$$

These values correspond to $\langle r^2_+ \rangle^{\frac{1}{2}} = (3.97 \pm 0.04)$fm and $\langle r^2_- \rangle^{\frac{1}{2}} = (3.92 \pm 0.06)$fm for 1 $f_{7/2}$ proton in ^{52}Cr and ^{51}V.

3.3 RMS radii of 1 $g_{9/2}$ nucleon in Sr isotopes

Partial and total strength for $\ell = 4$, 1 $g_{9/2}$ nucleon transfers on Sr isotopes are summarized in table 4 (see ref.14 for details). For even A targets only total strength can be analyzed. The results of table 4 were obtained with $\langle r^2 \rangle^{\frac{1}{2}} = 4.66$ fm as determined by Sick et al.[15]. The total neutron transfer strength are ~ 10% smaller than the upper limit of 10.67 (Eq.3). This result is significant because it is obtained independently for all four isotopes. A 1% decrease in $\langle r^2 \rangle^{\frac{1}{2}}$ could, of course, lead to a better agreement between calculations and experiment but it would be more natural to attribute the 'missing' strengths to weakly excited or continuum states which are not identified

Table 4

Partial and total strengths for $\ell = 4$, 1 $g_{9/2}$ nucleon transfers on Sr isotopes. The partial and total sums are defined as in Ref.1, i.e., $S_i^+ = \Sigma_{J_\beta} S_{i,J_\beta}^+$, $S_i^- = \Sigma_{J_\alpha} S_{i,J_\alpha}^-$, and $S_i = S_i^+ + S_i^-$, with i = p,n (ref.14).

Target Nucleus	Neutron Transfer S_n^+	S_n^-	S_n	Proton Transfer S_p^+	S_p^-	S_p
^{88}Sr	0	9.94±1.3	9.94±1.3	11.7±1.7	0.0	11.7±1.7
^{87}Sr	1.24±0.2	6.48±0.7	7.72±0.7	Not reported	0.0	
^{86}Sr	2.0±0.2	7.3±0.7	9.3±0.7	10.0±1.0	0.97±0.1	11.0±1.0
^{84}Sr	4.0±0.3	4.5±0.4	9.5±0.5	Not resolved	Not reported	

experimentally. On the other hand the total proton sums slightly exceed the sum rule value, thus indicating that the rms radius of 1 $g_{9/2}$ may be slightly larger than that of the 1 $g_{9/2}$ neutrons.

4. Concluding Remarks

The deviations of $n^{\pm}$ from unity originates from three main sources: (1) Improper values of $\langle r^2 \rangle^{\frac{1}{2}}$ (2) Inaccuracies in the DWBA calculations, such as systematic errors in N, finite range parameter, optical potentials for the entrance and exit channels or experimental cross sections. (3) Not all strength is included in the analyses. The radii quoted in sec.3 are based on the assumption that the deviations of $n^{\pm}$ are due to slightly incorrect values of $\langle r^2 \rangle^{\frac{1}{2}}$. There is internal evidence in our results that contributions from the various sources of items 2-3 are not significant. Data from various reactions and different analyses lead to $n^{\pm}$ values with a scatter of 5-10% from average values. Further, stripping strength into the continuum plays a minor role only. In the case of ^{51}V the inclusion of 5% strength due to the continuum, all evenly distributed among the final states J_β deteriorates the fit and gives a violation of one partial sum rule. Finally the dependence of the cross section on the diffuseness parameter a is another source of uncertainty which is not compiled in the errors quoted for $n^{\pm}$. Following the discussion of sec.2 a 10% change in a may induce 5-10% change in σ_{DWBA}. For the particular case of ^{51}V it is more realistic that errors in n^+ and n^- are ~ 20%, which in turn correspond to errors of about 2% in the rms radii.

References

1. C.F. Clement and S.M. Perez, Nucl.Phys. A 213 (1973) 510; and references mentioned therein.
2. E. Friedman, A. Moalem, D. Suraqui and S. Mordechai, Phys.Rev. C 14 (1976) 2082; ibid Phys.Rev. C 15 (1977) 1604.
3. A. Moalem, Nucl.Phys. A 289 (1977) 45.
4. A. Moalem and Z. Vardi to be published.
5. H.J. Körner and J.P. Schiffer, Phys.Rev.Lett. 27 (1971) 1457; J.P. Schiffer and H.J. Körner, Phys.Rev. C 8 (1973) 841.
6. P.K.A. de Witt Huberts, L. Lapikas, H. de Vries, J.B. Bellicard, J.M. Cavedon, B. Frois, M. Huet, Ph. Leconte, A. Nakada, Phon Xuan Ho, S.K. Platchkov and I. Sick, to be published.
7. E. Newman and J.C. Hiebert, Nucl.Phys. A 110 (1968) 366.
8. F. Hinterberger, G. Mairle, I. Schmidt-Rohr, P. Turek and G.J. Wagner, Zeit. für Phys. 202 (1967) 236.
9. J.N. Craig, N.S. Wall and R.H. Bassel, Phys.Rev.Lett.36 (1976) 656.

10. F. Pellegrini, I. Filosofo, M.I. El Zaiki and J. Gabrielli, Phys.Rev. C 8 (1973) 1547.

11. D.D. Armstrong and A.G. Blair, Phys. Rev. 140 (1965) B 1226.

12. Masaru Matoba, Nucl.Phys. A 118 (1968) 207.

13. A. Moalem, J.F.A. van Hienen and E. Kashy, Nucl.Phys. A 307 (1978) 277.

14. A. Moalem and E. Friedman, Phys.Rev.Lett. 40 (1978) 1064.

15. I Sick et al. Phys.Rev.Lett. 38 (1977) 1259.

THE MEASUREMENT OF NUCLEON ORBIT SIZES IN THE Ca REGION BY SUB-COULOMB TRANSFER REACTIONS

J.L. Durell
University of Manchester,
England

THE MEASUREMENT OF NUCLEON ORBIT SIZES IN THE Ca REGION BY SUB-COULOMB TRANSFER REACTIONS

J. L. Durell

The Schuster Laboratory,
The University of Manchester,
U.K.

1. Introduction

Sub-Coulomb transfer reactions have proved to be a powerful means of determining the size in the asymptotic region of the wavefunction of the single-particle component of a nuclear state. Within the framework of the DWBA the cross-section for a heavy-ion sub-Coulomb transfer reaction (HITR) A(a,b)B may be written schematically [1] as

$$d\sigma(\theta) \propto S_{bn}\, S_{An}\, N^2_{bn}\, N^2_{An} \qquad \ldots(1)$$

where $S_{bn}\, N^2_{bn}$ refers to the spectroscopic factor and size of the tail of the wavefunction of the nucleon n bound to core b, and $S_{An}\, N^2_{bn}$ similarly refers to the nucleon n bound to the core A. In exact finite range codes now available [2] the dependence on the bound-state wavefunctions does not appear explicitly, but the sensitivity of the cross-section to these wavefunctions is still essentially as expressed above in eq. (1)

For light-ion transfer reactions (LITR) such as A(t,d)B the differential cross-section in the Sub-Coulomb regime may be written [3] as:-

$$d\sigma(\theta) = \frac{3}{2} D^2\, S_{An}\, d\sigma_{zR}(\theta) \qquad \ldots(2)$$

where D^2 is a normalization factor dependent upon the $\langle t|dn\rangle$ vertex function, S_{An} is the spectroscopic factor of state populated in nucleus B, and $d\sigma_{zR}(\theta)$ is the zero-range DWBA prediction that depends implicitly on the wavefunction of the neutron bound to nucleus A.

From equations (1) and (2) we see an important feature of all transfer reactions - that no information on the $\langle An|B\rangle$ overlap can be obtained without knowing the properties of the projectile-ejectile system. A series of HITR experiments has been performed [4] which has calibrated many of the useful

projectile-ejectile systems for sub-Coulomb neutron transfer. These experiments have also provided an indirect calibration of the (t,d) reactions by comparison with the data of ref [5]. As yet no such project has been completed for heavy-ion proton transfers. However, a series of experiments has just been completed[6] to calibrate the sub-Coulomb (t,α) reaction by comparison with recent magnetic electron scattering results. We are now in a position therefore to remove the ambiguity inherent in eq.(1) and (2) and obtain a value for the $\langle An|B\rangle$ overlap by comparing experimentally measured cross-sections with theoretical predictions calculated using the calibration information.

In order to determine the tail size of the single-particle wavefunction component of the nuclear state in nucleus B it is necessary to disentangle the contribution of the spectroscopic factor. The value of the spectroscopic factor can be found in general by carrying out a sum-rule analysis of all available single-nucleon stripping and pick-up data on the target nucleus involved. Such an analysis removes the dependence of the spectroscopic factor on an arbitrary choice of bound-state well geometry (see ref [7]) for an example of the application of a sum-rule analysis). The uncertainties that remain in S_{An} are those due to possible missing stripping and pick-up strength at high excitation in the residual nuclei, and the use of the approximation that the same bound-state well geometry applies to all states in a nucleus.

Knowing the spectroscopic factor leads therefore to a determination of the tail size. By postulating a form for the bound-state potential it is then possible to deduce from this tail size the rms radius of the single-particle wavefunction. There is, of course, a degree of model dependence in the transformation of a tail size into an rms orbit radius. The uncertainty in $\langle r^2\rangle^{\frac{1}{2}}$ due to this model dependence is however small if one accepts that a Woods-Saxon functional form is a reasonable representation of the average nucleon-nucleus bound-state potential. In the Woods-Saxon potential there are two parameters (r_o,a) that fix the geometry. The depth is determined by requiring that the potential reproduces the nucleon separation energy. It is found that there is an infinite number of combinations of r_o and a that produce the same tail size, and each of these combinations gives a slightly different value for the rms radius of the nucleon orbit. The model dependence

of $\langle r^2 \rangle^{\frac{1}{2}}$ derived from a tail size in this way needs to be determined for each separate case, but in general the uncertainty introduced into $\langle r^2 \rangle^{\frac{1}{2}}$ is small and is of the order of ± 0.05 fm. A further model dependence is introduced by the specification of the spin-orbit component of the bound-state potential. This will be somewhat (nlj) dependent. The derived rms radius of a nucleon orbit does not depend very sensitively on the spectroscopic factor, a 10% change in S leading in general to approximately 0.05 fm change in $\langle r^2 \rangle^{\frac{1}{2}}$ (i.e. $\sim$ 1%).

One further feature of sub-Coulomb transfer reactions needs to be discussed. This is the sensitivity of predicted cross-sections to nuclear interactions between the core nuclei. HITR have a particularly nice feature that the small de Broglie wavelength of heavy-ions ensures good localization of the incident projectile. This means that it is always possible to choose a bombarding energy at which the effect of including an optical potential is negligible. This makes heavy ions the most accurate means, in principle, of determing orbit radii. This semi-classical characteristic of HITR does lead to an associated disadvantage. This is the need to match the Rutherford-like orbits in the exit and entrance channels. Whether a HITR is matched or not depends upon the Q-value. Any significant departure from a well-matched Q-value leads to a large reduction in the cross-section. For example, in a neutron transfer reaction, where the products of charges in the entrance and exit channels are equal, the Q-value should be close to zero. This condition requires one to choose a suitable projectile-ejectile system to study a given nucleus.

The large de Broglie wavelength of low-energy light ions implies that the converse situation applies in reactions such as sub-Coulomb (d,p) or (t,d). Even at energies well below the nominal Coulomb barrier there is some nuclear interaction between the colliding particles. The degree of sensitivity of predicted cross-sections to different choices of optical model potentials that fit entrance and exit channel elastic scattering is still however rather small, there being an optical model dependence of the predicted cross-section of the order of 10-15%. This leads to errors in rms radii of about 0.05 fm. The (t,d) reaction is less specific from the kinematic point of view in the final

states populated compared to HITR, because of the reasonable overlap of the entrance and exit channel "orbits" even in cases where the Q-value is far from zero. The sub-Coulomb LITR are therefore extremely useful in making systematic studies of nucleon orbit sizes over, say, an isotopic or isotonic sequence of nuclei.

2. The $^{40}Ca(^{13}C, ^{12}C)^{41}Ca$ Reaction

We have recently measured [8] the angular distribution of the $^{40}Ca(^{13}C, ^{12}C)^{41}Ca$ reaction at 18.5 and 19.0 MeV. The work was carried out at the University of Oxford EN tandem accelerator. The $1f_{7/2}$ ground state and $J^{\pi} = 3/2^-$ first and third excited states of ^{41}Ca were populated. The $1f_{7/2}$ data were fitted using a spectroscopic factor of 0.90 ± 0.05 and the $(^{13}C, ^{12}C)$ calibration of ref [4]. The size of the tail of the $1f_{7/2}$ neutron wavefunction was the free parameter. The rms radius of the $1f_{7/2}$ neutron orbit in ^{41}Ca was found to be 3.89 ± 0.12 fm. This value corresponds to a choice of diffuseness parameter of the bound-state well of a = 0.60 ± 0.10 fm. The range of uncertainty in a contributes ± 0.05 fm to the error in $\langle r^2 \rangle^{\frac{1}{2}}$. A further ± 0.02 fm comes from the dependence of the predicted cross-section on the optical model parameters in the exit channel. The large positive Q-value of this reaction makes the cross-section more optical model dependent than is usual for better matched reactions. The remaining contribution to the error (± 0.05 fm) comes from experimental statistics, the uncertainty in the spectroscopic factor, and the error on the $(^{13}C, ^{12}C)$ calibration.

Two previous determinations [9, 10] of this orbit size have been made using the (t,d) reaction. Comparison with the published values of $\langle r^2 \rangle^{\frac{1}{2}}$ is not meaningful since these authors used different values for the spectroscopic factor, bound-state well diffuseness and values of the (t,d) normalization factor different from the value consistent with the presently used $(^{13}C, ^{12}C)$ calibration (see Franey et al., ref [4]). In order to make a meaningful comparison, table 1 presents the results of the three experiments, analysed in a consistent way. The spectroscopic factor was taken as 0.90, the diffuseness parameter as 0.65 fm and D^2 (t,d) = 3.26 10^4 MeV^2 fm^3.

Table 1

^{41}Ca ground state orbit size.

Experiment	$\langle r^2 \rangle^{\frac{1}{2}}$ (fm)
Present	3.86
ref. [9]	3.91
ref. [10]	3.96 (3.84)

The errors on each of these measurements is approximately ± 0.07 fm (this error does not now include any contribution from uncertainties in choice of diffuseness parameter). One problem with this comparison is that the Strasbourg data reanalysed in ref [10] is approximately 28% higher in magnitude than the data of ref. [9]. If the Strasbourg data is renormalized downwards then the rms radius given in brackets is obtained. The difference in the rms radii of ref [9] and ref [10], using the same cross-sections, presumably arises from the different optical model parameters used in the analyses. This highlights one of the difficulties with light ion experiments. However within the quoted errors the agreement is good, and the present heavy-ion result lies between the two light-ion values.

The experimentally determined rms radius for the ground-state of ^{41}Ca can be compared with values deduced from analyses of the Coulomb energy difference (CED) between ^{41}Ca and ^{41}Sc, and with HF calculations. It is found that the observed value of the neutron excess radius is 0.4 ± 0.1 fm larger than that deduced from the CED. This anomaly has been the subject of much discussion [11] and suggestions have been made that C.E.D. may not in fact be as directly sensitive to neutron excess radii as was originally supposed. The radius determined in the present work is also somewhat smaller than that predicted in HF calculations. Part of the discrepancy is caused by the failure of HF calculations to reproduce the correct separation energy for the $f_{7/2}$ neutron in ^{41}Ca. However, the discrepancy remains when this effect is taken into account. One point of importance that this comparison reveals is that HF calculations that reproduce charge radii of nuclei do not lead to mean field potentials that correctly reproduce individual neutron orbits.

1) P. J. A. Buttle and L. J. B. Goldfarb, Nucl. Phys. A176(1971)299 and references therein.

2) P. J. A. Buttle, Comp. Phys. Comm. 14(1978)133

3) L. J. B. Goldfarb and E. Parry, Nucl. Phys. A116(1968) 289

4) J. L. Durell et al., Nucl. Phys. A269(1976) 443

M. Franey, J. S. Lilley and W. R. Phillips, to be published

5) H. J. Körner and J. P. Schiffer, Phys. Rev. Lett. 27(1971) 1457

6) A. I. Warwick et al., University of Manchester, to be published

7) R. Chapman, J. N. Mo, J. L. Durell and N. H. Merrill, J. Phys. G2 (1976) 951

8) C. Harter, J. L. Durell, J. N. Mo and W. R. Phillips, to be published

9) L. J. B. Goldfarb, J. A. Gonzalez, M. Posner and K. W. Jones, Nucl. Phys.A185(1972) 337

10) E. Friedman, A. Moalem, D. Suraqui and S. Mordechai, Phys. Rev. C14 (1976) 2082

11) S. Shlomo, Contribution to this workshop

NEUTRON RADIAL DISTRIBUTIONS FROM ELECTRON SCATTERING

I. Sick
University of Basel,
Switzerland

NEUTRON RADIAL DISTRIBUTIONS FROM ELECTRON SCATTERING

I. Sick

Department of Physics
University of Basel
Basel, Switzerland

The density distribution of protons, as everybody knows, is obtained mainly from electron scattering and μ-X-ray experiments. The reasons for this are familiar. Rms-radii can be determined to 1%, and the density can be obtained to 1%, provided data up to momentum transfers of $q \simeq 3.5 fm^{-1}$ are available. Moreover, reasonably model-independent densities, i.e. densities $\rho(r)$ accompanied by a realistic uncertainty estimate $\delta\rho(r)$, can be obtained. As an example let us consider a density (fig.1) that has received much attention in the past, the one of ^{40}Ca. This new density[1] results from an experiment done initially at Stanford, and recently extended to higher q at Saclay, to $q_{max} = 3.5 fm^{-1}$. Once one goes to that high q, and once one can measure $d\sigma/d\Omega$ down to $10^{-12} mb/sr$, one can obtain $\rho(r)$ to better than 1%, without any ambiguity. In which case one can measure the amount of shell structure, i.e. the property where different Hartree-Fock calculations (solid D.Gogny, dashed J.Negele, dash-dot X.Campi, dotted M.Pearson) differ most.

These achievements of electron scattering are such that nowadays no other type of experiment even tries to determine proton densities. For neutrons, however, the situation is very different. Many types of experiments are exploited to determine properties of $\rho_n(r)$, and many of them are discussed at this meeting. If I try to paraphrase the results - and when doing so I necessarily oversimplify things - then I would have to say that :

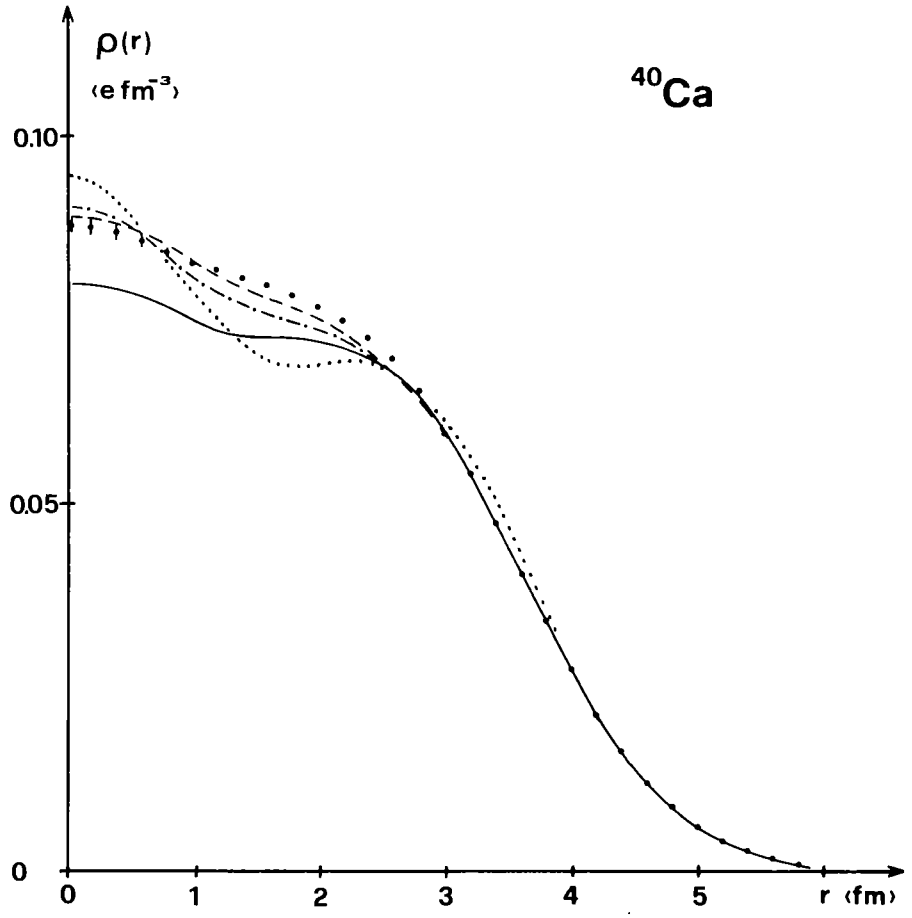

Fig. 1

1) there is no method that allows to measure $\rho_n(r)$ the way electron scattering measures $\rho_p(r)$ point by point. Either $\rho_n(r)$ at large radii, or the large-r properties of a valence shell is sampled. And 2) that in many cases there are still considerable uncertainties concerning the reaction mechanism.

In this talk, I would like to discuss the measurement of neutron radial distributions by electron scattering[2]. This new method will not deal with the limitation 1); only valence neutron radial wave functions can be determined, not $\rho_n(r)$. However, this can be done with good sensitivity to all radii, and with very little ambiguity due to the reaction mechanism.

What I will deal with concerns elastic electron scattering from the components of the nuclear magnetization density of large mul-

tipolarity λ . In this context, I have to explain two things : how to extract these components from electron scattering experiments, and how to interpret them in terms of the radial wave function R(r) of the valence nucleons. In order to cope with the first point, the following equation displays (in PWBA, which is good enough for the qualitative discussion given here) the different contributions to the elastic cross section

$$\frac{d\sigma}{d\Omega}(\theta,E) = \sigma_{Mott}\cdot\left[Z^2F_{C0}^2(q) + \sum_{\lambda=2}^{\Lambda} F_{C\lambda}^2(q) + \left(\tfrac{1}{2}+tg^2\tfrac{\theta}{2}\right)\sum_{\lambda=1}^{\Lambda} F_{M\lambda}^2(q)\right] \qquad (1)$$

Here, σ_{Mott} is the cross section for scattering from a pointlike charge, q is the momentum transfer $\sim 2E\sin\theta/2$, F are the form factors for scattering due to the charge (C) and magnetic (M) multipole distributions. The sums run up to a maximum multipolarity $\Lambda = 2j$, where j is the spin of the nuclear ground state. By doing experiments at variable scattering angle θ but constant q, the magnetic and charge contributions can be separated. This is feasible in particular at large q, where F_M drops off less quickly than F_C. (See Fig. 2 where F_{CD} is given for $\theta = 155^o$). The individual multipoles cannot be separated in general, unless polarization measurements are done. However, the multipole of the highest allowed order, $\Lambda = 2j$, dominates F_M over a large q-range and therefore can be isolated de facto (see fig. 2). Can this form factor be interpreted unambiguously in terms of R(r) ? To answer this question, let us consider a particularly simple case, the one where the j of the valence shell is the highest one of all occupied states. Given the fact that multipolarity $\Lambda = 2j$ corresponds to a complete j-flip, and given the fact that (in the impulse approximation) the electron interacts with one nucleon at a time only, no other but shell j can contribute to multipolarity Λ . In which case F_M depends on R(r) of this shell exclusively. Via the relationship

$$F_{M\Lambda}(q) = \text{const}\cdot q\cdot\int R^2(r)\, j_{\Lambda-1}(qr)\, r^2 dr \qquad (2)$$

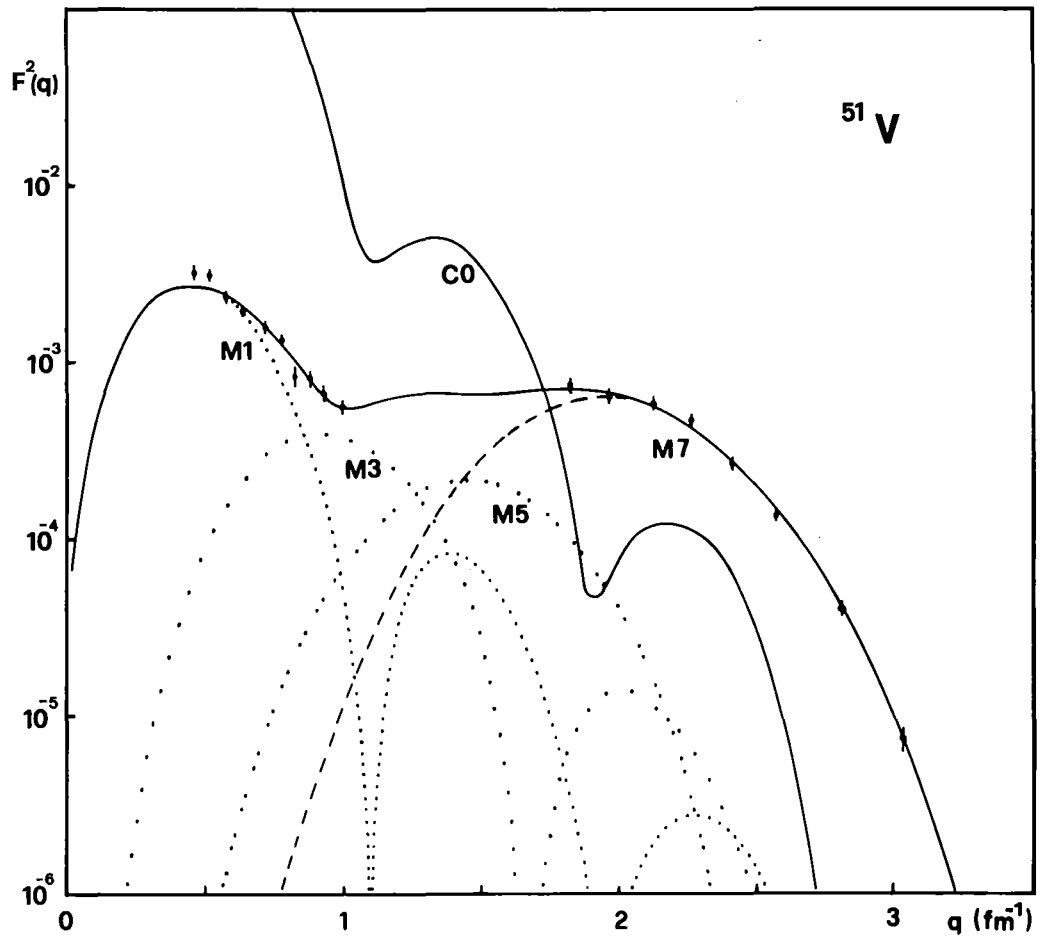

Fig.2

R(r) can be extracted.

When deriving this equation I have made two simplifying assumptions, the ones concerning the absence of configuration mixing and meson exchange currents. Configuration mixing in the ground state leads to pronounced changes of $F_{M\lambda}$ for $\lambda < \Lambda$. For the highest multipole the shape of $F_{M\Lambda}$ is not changed significantly, just its overall magnitude (i.e. the occupation of shell j) is reduced. Only if strong 2p2h-excitations involving shells with $j' > j$ occur, will the shape of $F_{M\Lambda}(q)$ be changed. Such contributions have been calculated by Arita et al[4]. For the nuclei to be discussed here, the change in $F_{M\Lambda}(q)$ found leads to a change of the rms-radius of the R(r) extracted that is less than 0.3%.

This leaves us with meson exchange currents (MEC) as the only potentially appreciable correction to eq.2. Contrary to charge scattering, MEC can contribute in first order already to magnetic scattering. Fortunately, for the highest multipole the MEC process also includes at least one nucleon of shell j. Consequently, ΔF_{MEC} has a shape quite similar to the one of $F_{M\Lambda}$. A number of calculations[5] for the contribution of MEC, by Suzuki and Dubach, have been carried out. From the calculations that do include the πNN-vertex form factors we deduce that their effect on the rms-radius of the R(r) extracted is 1.1 ± 0.5% (for ^{51}V) i.e. quite small.

This means that magnetic scattering from the highest allowed multipole distribution, $\Lambda = 2j$, can be interpreted unambiguously in terms of R(r). And moreover, as I will show now, it also can be measured !

Fig. 2 already showed that for a nucleus with an unpaired $1f_{7/2}$ proton, ^{51}V, this could be done[3]. The emphasis in this talk mainly concerns neutrons, so let us look at an example of an unpaired neutron. Fig. 3 shows the data[6] the Saclay group obtained for ^{49}Ti, a nucleus that has a $1f_{7/2}$ neutron-hole configuration. You note that data have been taken between 1.8 and 3.3 fm^{-1}. At lower q we run, at a maximum scattering angle of $\theta = 155^{o}$, into troubles with charge scattering, at higher q the cross sections become smaller than 10^{-10}mb/sr. In the region where F_M can be measured, it is due to the M7 component mainly. The $\lambda \leq 5$ components are less than 10%, and I will skip them in the qualitative discusssion given here.

In order to compare to theory, Fig.3 shows a prediction from a DDHFB calculation of Gogny[7], a calculation that does extremely well for proton-densities. The too large form factor in the M7 maximum is expected, since the $f_{7/2}$ depopulation due to configuration mixing is not included. More important,

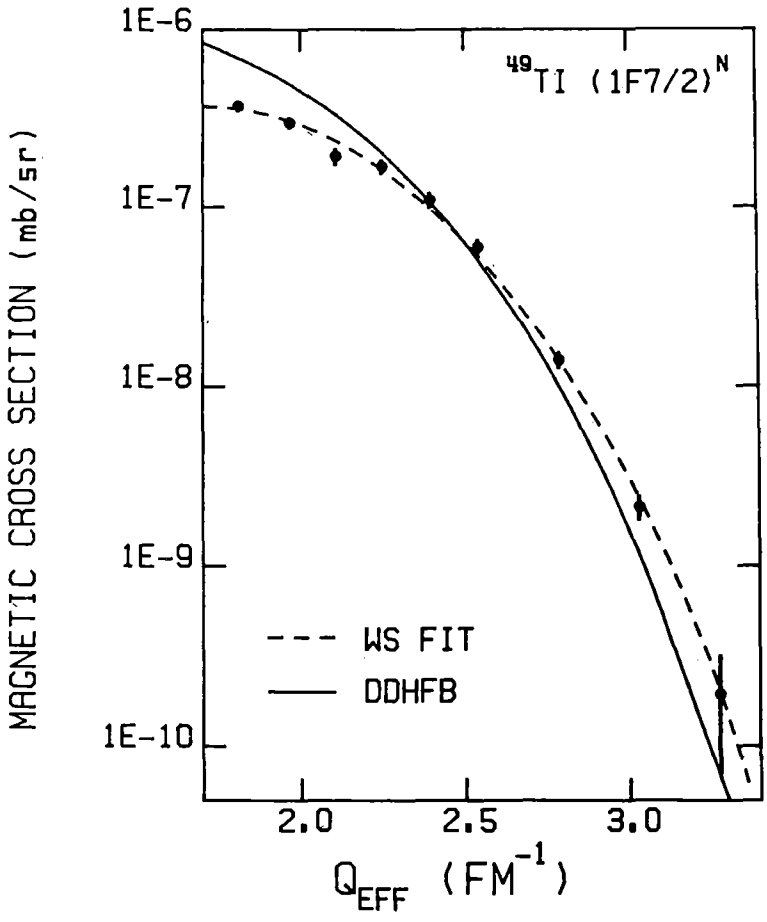

Fig. 3

however, the DDHF form factor falls off too quickly at large q. This shows that the radial extension of R_{DDHF} is too large, i.e. that the maximum of the DDHF radial wave function occurs at too large a radius.

A quantitative estimate for this difference can be obtained by fitting the M7-data using a radial wave function R(r) calculated in a WS-potential. The radius of this potential is fit to the M7-data, while the depth is determined by the neutron separation energy. The skin thickness of the potential (which from HF-calculations is known to be very similar for all shells) is obtained by fitting the charge scattering cross sections with a charge density calculated from a WS potential.

The resulting fit is shown in Fig.3. The rms-radius of the $1f_{7/2}$ neutron orbit turns out to be 4.011 ± 0.04 fm, while DDHFB yields 4.159 fm. The difference of 3.7% is quite surprising since in HF-calculations protons and neutrons are strongly coupled, the protons being responsible for ~70% of the effective potential seen by the neutrons, and vice versa. A calculation doing very well for the protons would have been expected to do as well for the neutrons.

Often it is of particular interest to determine the relative size of neutron and proton orbits rather than to determine absolute p- and n-radii separately. This is particularly desirable if you consider that in most cases neutron radii are obtained (implicitly at least) from a difference of the measured matter-radius, and the known proton radius. The obligation to take this difference increases the effect of systematical errors by a factor of 2.

From electron scattering, we actually can get the relative size of p- and n-orbits directly[2]. Consider neighbouring nuclei having an unpaired proton or unpaired neutron respectively. From HF-calculations we know that the shape of the radial wave functions of p and n are very similar, the main difference being a small change in the radial scale. It therefore seems reasonable to try the ansatz

$$R_p(r) = R_n(\beta r) \cdot \beta^{-3/2} \qquad (3)$$

where β is a factor close to one describing the squeezing of the radial scale. If this is reasonable an assumption, then we can derive immediately that

$$F^p_{M\Lambda}(q) = F^n_{M\Lambda}(q/\beta) \cdot \frac{\mu_p \alpha_p}{\mu_n \alpha_n} \qquad (4)$$

A comparison of the MΛ-form factors then will give β directly. We never have to talk about the R(r) actually used, and we can make a n-p comparison of an unusual model independence.

Fig. 4 shows the M7 data for ^{51}V (unpaired $1f_{7/2}$ proton) compared to the data for ^{49}Ti (unpaired $1f_{7/2}$ neutron) plotted on a compressed q-scale. The data clearly define a unique M7-curve, thus showing that eq. 3 is sensible. From the compression factor β (plus a $\sim$1% correction accounting for the different tails of R(r) at large r as imposed by different separation energies[2]) we obtain directly $rms_n(Ti) - rms_p(V) = -0.4 \pm 0.8\%$. This value has the great merit of being insensitive to systematical experimental errors, model assumptions on R(r), or MEC corrections. The theoretical value for this difference, + 1.3%, again indicates that DDHF predicts neutron orbits with radii 2% too large. For heavier nuclei[2] ($A \simeq 90$) this tendency is amplified.

How do these electron scattering results compare to other information ? Concerning the comparison with transfer reactions, I do not have to go into details after A. Moalem's talk. If transfer reactions are analyzed using the R(r) provided by electron scattering, one can determine absolute spectroscopic factors. This allows for the first time to determine to which degree occupation number sum rules are exhausted. For the Sr-isotopes Moalem[8] finds that about 10% of the strength has not yet been observed, the missing strength amounting to 25% for ^{87}Sr. For ^{51}V, where I have carried out a similar analysis, one finds a deficit of 18%. Which is quite reasonable given the fact that transfer reactions have observed states in the residual nucleus up to 6 MeV only. A comparison with subcoulomb transfer reactions will be most fruitful once the asymptotic normalizations of R(r) discussed by J.Durell are available.

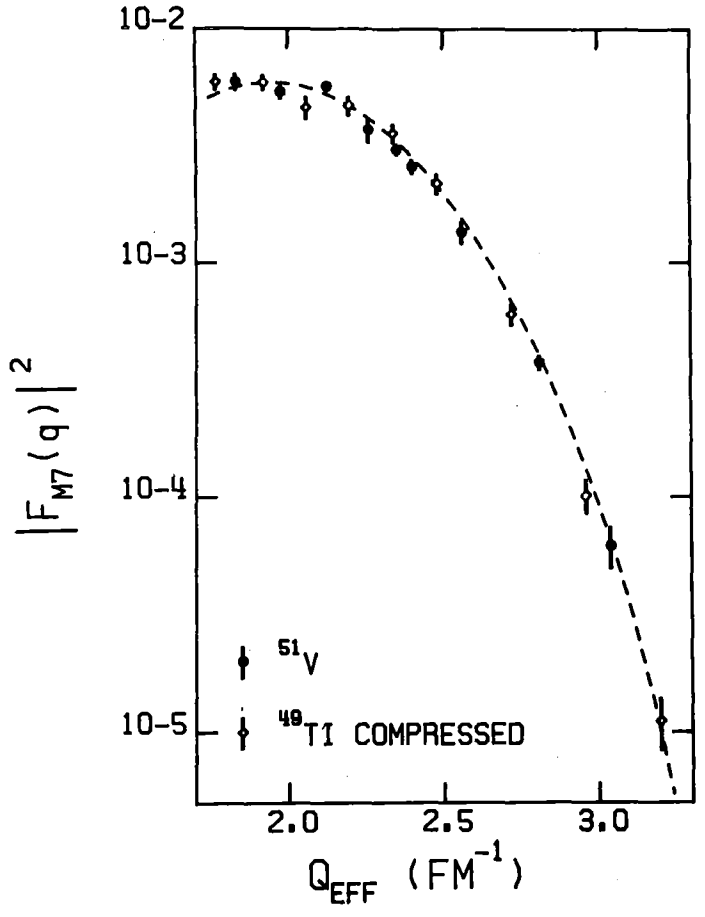

Fig. 4

Concerning (pp), ((α,α)) the comparison is not quite straightforward if one thinks that these experiments determine $\rho_n(r)$, while (e,e) determines the density of a valence nucleon orbit only. Still, a direct comparison should be possible : protons (alpha particles) are strongly absorbed in the nuclear interior. Therefore, they only provide information on $\rho_n(r)$ at large radii, where ρ_n is smaller than about 30% (10%) of the central density. At these radii $\rho_n(r)$ is dominated by the valence nucleons due to the surface-peaked nature of large-ℓ radial wave functions, (leading, incidentally, to the fact that in ^{49}Ti the $1f_{7/2}$ neutrons account for ~37% of the contribution to the total rms_n!)

In order to make such a comparison, we can consider the nuclei ^{48}Ca and ^{49}Ti (neglecting differences in $R(r)_{7/2}$). For the former one there are a number of (p,p) and (α,α), for the latter one an (e,e)-experiment. Starting from a Woods-Saxon or Hartree-Fock calculation, one can deduce the ratio of the contribution of the filled $1f_{7/2}$ neutron shell to the total neutron density. In the region where this ratio is close to one, one can combine it with the neutron-density determined[9] by (p,p), or (α,α), and derive the "experimental" contribution of the $1f_{7/2}$ neutron shell. This density then can be compared to the one obtained from electron scattering. The result of this comparison shows a non-negligible difference : At 5 fm, where (p,p) and (α,α) are very sensitive to $\rho_n(r)$ and where the $f_{7/2}$ neutrons dominate $\rho_n(r)$, one finds a radial displacement of 0.1-0.15 fm. If we can trust the subtraction of the core-part, this would indicate that (p,p), (α,α) give rms-radii too large. This finding would be compatible with the fact that rms_n-rms_p as determined by hadron scattering is in quite good agreement with HF-calculations, while electron scattering places the neutrons 1 - 2% further inside the nucleus. These differences may be connected to the fact that (p,p) and (α,α) at large r yield too slow a fall-off of R(r). The comparison of these results with other experimental information is very interesting and will have to be carried out in more detail. The hope is to use the few cases where electron scattering is applicable as test cases for the analyses of experiments using strongly interacting probes.

References

1) I.Sick et al, to be published

2) I.Sick et al, PRL 38 (77) 1259

3) P.deWitt-Huberts et al, P.L. 71B (77) 317

4) A.Arita et al, priv.com.

5) J.Dubach, PL 81B (69) 124, T.Suzuki, priv.com. and PRL 40 (78) 1001.

6) S.Platchkov et al, to be published

7) D.Gogny et al, priv.com.

8) A.Moalem, E.Friedman, PRL 40 (78) 1064

9) A.Chaumeaux et al, Ann.Phys. 116 (78) 247
G.Lerner et al, PR C12 (75) 778
G.Alkhazov et al, NP A280 (77) 365

BACKWARD-ANGLE ELASTIC ELECTRON SCATTERING FROM ^{39}K

C.W. de Jager, P. Keizer, L. Lapikás,
and H. de Vries
IKO Amsterdam,
The Netherlands

and

S. Kowalski
M.I.T. Cambridge

BACKWARD-ANGLE ELASTIC ELECTRON SCATTERING FROM ^{39}K

C.W. de Jager, P. Keizer, L. Lapikás and H. de Vries (I.K.O., Amsterdam) and S. Kowalski (M.I.T., Cambridge)

In a simple-minded shell model picture the nucleus ^{39}K can be regarded as a $1d_{3/2}$ proton hole coupled to ^{40}Ca. Elastic electron scattering from the ^{39}K magnetization distribution was studied in an attempt to map out the radial behaviour of this valence nucleon.

The cross section for elastic electron scattering from a spin J nucleus can be written in PWBA as

$$\frac{d\sigma}{d\Omega} = \sigma_{Mott} \{F_L^2(q) + (\tfrac{1}{2} + \tan^2 \tfrac{\theta}{2}) F_T^2(q)\}$$

In the single-particle model the transverse form factor is given by

$$F_T^2(q) = \sum_{\substack{\lambda=1 \\ \text{odd}}}^{2J} N_\lambda^{lj} \{ \langle j_{\lambda-1} \rangle^{nl} + A_\lambda^{lj} \langle j_{\lambda+1} \rangle^{nl} \}^2$$

involving the radial integrals

$$\langle j_\lambda \rangle^{nl} = \int R_{nl}^2 \, j_\lambda(qr) r^2 dr$$

The PWBA is quite accurate in practice if one uses the effective-momentum-transfer representation

$$q_{eff} = q(1 + \frac{4}{3} \frac{Z\alpha\hbar c}{RE})$$

Data were taken at energies between 60 and 90 MeV with the 180^0 facility of IKO (Amsterdam) [1] and at energies up to 255 MeV at scattering angles of 160^0 and 180^0 [2] at the MIT-Bates facility. Metallic targets of natural isotopic abundancy were used. The cross sections were measured relative to that of the proton [3]. The contribution from charge scattering to be subtracted from the measured cross section was calculated with the charge-distribution parameters determined by Sinha et al [4]. The magnetic form factor data thus obtained are shown in the figure. Good agreement between the different data sets is apparent.

The experimental data clearly deviate from the simple single-particle prediction, indicated by the dotted curve. Several

generalizations of the SP model were attempted in order to fit the data where the experimental value for the magnetic dipole moment was always used as a constraint. The only successful parametrization found was

$$F_T^2 = \{(\alpha_1 \langle j_0 \rangle + \beta_1 \langle j_2 \rangle)^2 + (\alpha_3 \langle j_2 \rangle + \beta_3 \langle j_4 \rangle)^2\} F_{CM}^2(q) f_p^2(q)$$

where F_{CM} and f_p denote the centre-of-mass and the proton form factors, respectively. This amounts to allowing different effective g-factors for the M1 and M3 form factors. The radial wave function R(r) for a $1d_{3/2}$ proton was calculated either in a HO or in a WS well. For the WS well the separation energy was taken to be the experimental proton separation energy (6.38 MeV), the spin-orbit term conforming to a spin-orbit splitting of 5.75 MeV and the diffuseness parameters 0.65 fm. Both the HO and WS wave functions yielded equally acceptable fits:

	HO	WS	
b or r	1.89 ± 0.02	4.26 ± 0.05	(fm)
$\langle r^2 \rangle^{\frac{1}{2}}$	3.54 ± 0.03	3.59 ± 0.03	(fm)
Ω	6.8 ± 0.9	6.6 ± 0.9	($\mu_N$fm^2)

Here only the statistical errors have been quoted. The value of the octupole moment Ω obtained is approximately seven times larger than the single-particle prediction — the dipole moment is enhanced by a factor of three —. For the WS fit effective g-factors are found of $g_s = 4.64 \pm 0.11$ and $g_l = 0.99 \pm 0.02$ for the M1 and $g_s = 5.5 \pm 0.5$ and $g_l = -1.60 \pm 0.14$ for the M3 form factor. At present adequate theoretical predictions of the effects due to configuration mixing and core polarization are lacking.

References

1. G.J.C. van Niftrik et al., Nucl. Instr. 93(1971)301
2. G.A. Peterson et al., Nucl. Instr. 160(1979)375
3. F. Borkowski et al., Z. Phys. A275(1975)29
4. B.B.P. Sinha et al., Phys. Rev. C7(1973)1930

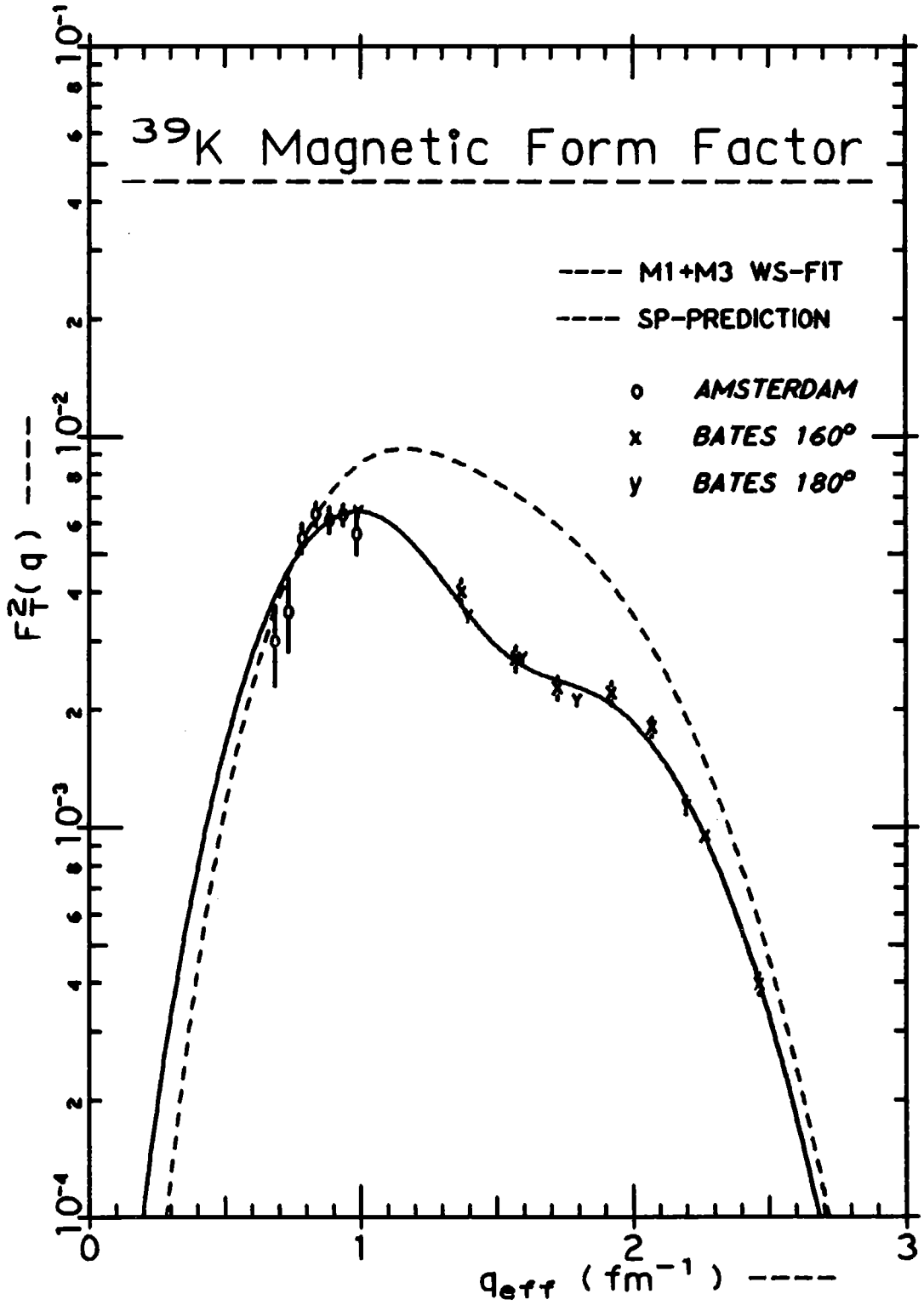

Form factor for elastic electron scattering from the ground state magnetization distribution of ^{39}K versus the effective momentum transfer q_{eff}.

EFFECT OF THE FREQUENCY DEPENDENCE OF THE NUCLEAR MEAN FIELD ON THE RADIUS OF A VALENCE ORBIT

A. Lejeune and C. Mahaux
Université de Liège,
Belgium

EFFECT OF THE FREQUENCY DEPENDENCE OF THE NUCLEAR MEAN FIELD ON THE RADIUS OF A VALENCE ORBIT

A. Lejeune† and C. Mahaux,
Institut de Physique, Université de Liège,
B4000 Liège 1, Belgium

Abstract. The mean field felt by nucleons is not only non-local, but also energy (or frequency) dependent. The latter dependence arises partly from core polarization and becomes particularly large for valence orbits. It is neglected in the Hartree-Fock approximation and is only roughly included in previous Brueckner-Hartree-Fock or in standard density-dependent Hartree-Fock calculations. We investigated the influence of this energy dependence on the single-particle energies and on the shape of the valence orbit, for several nuclei. The resulting single-particle spectrum is compressed near the Fermi surface, in keeping with experimental evidence. The root mean square radius of the valence orbit is squeezed by about one per cent. This reduction is about four times smaller than the one measured by recent magnetic scattering data. This may be an indication of the importance of current exchange corrections.

Contribution to the Discussion Meeting on "What do we know about radial shapes of nuclei in the Ca region", Karlsruhe May 2-4, 1979

† presented by A. Lejeune

EFFECT OF THE FREQUENCY DEPENDENCE OF THE NUCLEAR MEAN FIELD ON THE RADIUS OF A VALENCE ORBIT

A. Lejeune and C. Mahaux,
Institut de Physique, Université de Liège,
B4000 Liège 1, Belgium

1. *INTRODUCTION*

In the independent-particle model, each nucleon is assumed to move in an average mean field created by the other nucleons. This model has proved quite successful in reproducing the spatial distribution of protons and of neutrons [1] as well as several other single-particle properties, e.g. the single-particle energies. Nevertheless, this simple model cannot hopefully be exact, and corrections must be considered if one wants to achieve detailed agreement with experimental data. In the present contribution, we try to consider some of these corrections while remaining in the framework of a mean field theory. Our purpose is not to fit any particular experimental quantity, but rather to exhibit semi-quantitatively the nature, the effect and the magnitude of these corrections.

2. *MEAN FIELD APPROXIMATIONS*

In increasing order of sophistication, the various mean-field theories can be grouped into the following three main categories.

2A. *Local Mean Field*

In early calculations, the mean field was assumed to be local and independent of energy. Its depth was given a simple parametric form, for instance a Woods-Saxon radial shape :

$$M^{(WS)}(r) = \frac{V^{(WS)}(o)}{1 + \exp[(r-R)/a]} \quad . \qquad (1)$$

It is now well-established that this simple assumption cannot reproduce simultaneously the density distributions and the single-particle energies.

2B. *Non-Local Static Mean Field*

More elaborate approaches are based on a non-local field, usually computed in the framework of the Hartree-Fock approximation. Let us use the simple example of infinite nuclear matter with uniform density $\rho = 2(3\pi^2)^{-1} k_F^3$. Here, k_F is the Fermi momentum. The Hartree-Fock field felt by a nucleon with momentum k is given by

$$M_\rho^{(HF)}(k) = \sum_{j<k_F} \langle \vec{k}, \vec{j} | v | \vec{k}, \vec{j}-\vec{j}, \vec{k} \rangle$$

where $\vec{j}$ denotes a plane wave and where v is the nucleon-nucleon interaction. This approximation is represented by graph (a) in Fig. 1, where the horizontal dashes represent v . In coordinate space, the Fourier transform of $M_\rho^{(HF)}(k)$ yields the non-local Hartree-Fock field $M_\rho^{(HF)}(|\vec{r}-\vec{r}'|)$. The single-particle energies are given by

$$e_\rho^{(HF)}(k) = \frac{\hbar^2}{2m} k^2 + M_\rho^{(HF)}(k) . \quad (2)$$

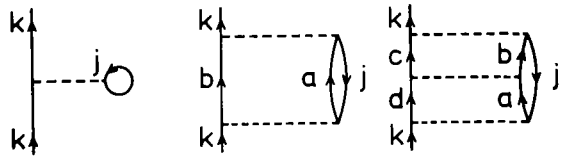

Fig. 1

We note that equation (2) yields a relation $k(e)$ which can be used to replace the dependence upon k (non-locality) by a dependence upon energy :

$$M_\rho^{(HF)}(k) \to M_\rho^{(HF)}(k(e)) = M_\rho^{(HF)}(e) \quad . \quad (3)$$

The energy dependence of the resulting local-equivalent (energy-dependent) Hartree-Fock mean field is characterized by the effective mass m^* :

$$m_\rho^{(HF)*}(e) = 1 - \frac{d}{de} M_\rho^{HF}(e) \quad . \quad (4)$$

In order to obtain a crude estimate of the Hartree-Fock field $M^{(HF)}(r,e)$ in a finite nucleus, one could use the simple local density approximation [2]

$$M^{(HF)}(r,e) = M^{(HF)}_{\rho(r)}(e) \quad , \tag{5}$$

where $\rho(r)$ is some input density distribution, e.g. the one given by eq. (2.29) of ref. [3]. In order to compare the "Hartree-Fock" approximation for the mean field with the simple Woods-Saxon parametrization (1), we shall rather adopt the following (equally crude) prescription :

$$M^{(HF)}(r,e) = \frac{V^{(HF)}(r,e)}{1 + \exp[(r-R)/a]} \quad , \tag{6}$$

where

$$V^{(HF)}(r,e) = V^{(HF)}_{\rho(r)}(e) = C^{(HF)} + \int_{e_F}^{e} [1 - m^{(HF)\star}_{\rho}(E)/m]dE \; . \tag{7}$$

Below, we choose the integration constant C^{HF} in such a way that the two mean fields $M^{(WS)}(r)$ and $M^{(HF)}(r,e_F)$ both have a bound state at the experimental value e_F of the Fermi energy (binding energy of the last closed shell).

The strength of the free nucleon-nucleon interaction is too strong to justify the use of first-order perturbation theory, i.e. of the Hartree-Fock approximation. In practice, one therefore replaces v by a weak "effective" nucleon-nucleon interaction. The latter may for instance be a purely phenomenological one, fitted to some nuclear properties [4]. It can alternatively be estimated from standard nuclear matter calculations based on a realistic nucleon-nucleon force [3]. In all these cases, this effective interaction v is such that the effective mass $m^{(HF)\star}_{\rho}$ defined in eq. (4) is essentially independent of the energy e . As indicated, the effective mass may in some approaches depend on the density. This is the case when one uses a density-dependent Skyrme force [5].Then, $m^{(HF)\star}_{\rho}(e)$ approaches m when $\rho \to 0$, as required on rather general grounds.

G.E. Brown et al. [6] pointed out long ago that empirical data on single-particle energies contradict the assumption that $m^{\star}_{\rho}$ is

independent of e . These authors showed that one should have $m^*_\rho(e_F) \simeq m$, while $m^*(e) \simeq 0.7\ m$ for $|e-e_F| > 20$ MeV . This "enhancement" of the effective mass near the Fermi energy e_F was interpreted by Bertsch and Kuo [7] as originating partly from the process represented by the diagram (b) in Fig. 1. In the standard Bethe-Brueckner approach to nuclear matter calculations, the contribution of this diagram to the mean field is strongly suppressed by requiring that the energy difference $e(a) + e(b) - e(k) - e(j)$ be larger than about 100 MeV . In other words, the standard approach disregards the possibility of exciting low-lying core states by letting the valence nucleon k interact with the core nucleon j .

2C. Non-Local, Frequency-Dependent Mean Field

Together with J.P. Jeukenne [8], we had investigated a new version of the Bethe-Brueckner theory of nuclear matter, in which the difference $e(a) + e(b) - e(k) - e(j)$ is allowed to be very small. In the Brueckner-Hartree-Fock approximation, the corresponding mean field (sum of diagrams (a),(b),(c),... in Fig. 1) is both non-local and frequency- (or energy-) dependent :

$$M_\rho^{(BHF)}(k,e) = \sum_{j<k_F} \langle \vec{k},\vec{j}\,|\,g(e)\,|\,\vec{k},\vec{j}-\vec{j},\vec{k}\rangle \quad , \tag{8}$$

where $g(e)$ is the energy-dependent Brueckner reaction matrix. The single-particle energies are now given by

$$e_\rho^{(BHF)}(k) = \frac{\hbar^2}{2m} k^2 + M_\rho^{(BHF)}(k, e_\rho^{(BHF)}(k)) \quad . \tag{9}$$

This equation gives a relation $k(e)$ which can be used to replace the dependence upon k (non-locality) by a dependence upon energy:

$$M_\rho^{(BHF)}(k,e) \to M_\rho^{(BHF)}(k(e),e) = M_\rho^{(BHF)}(e) \quad . \tag{10}$$

The energy dependence of the corresponding local equivalent Brueckner-Hartree-Fock field is characterized by the effective mass (see eq. (4))

$$m_\rho^{(BHF)*}(e) = 1 - \frac{d}{de} M_\rho^{(BHF)}(e) \quad . \tag{11}$$

In Fig. 2 (from [8]), we show the quantity (11) as calculated from Reid's hard core interaction (long dashes, left-hand scale). We note that the effective mass now displays the required enhancement near the Fermi energy $e(k_F) = e_F$.

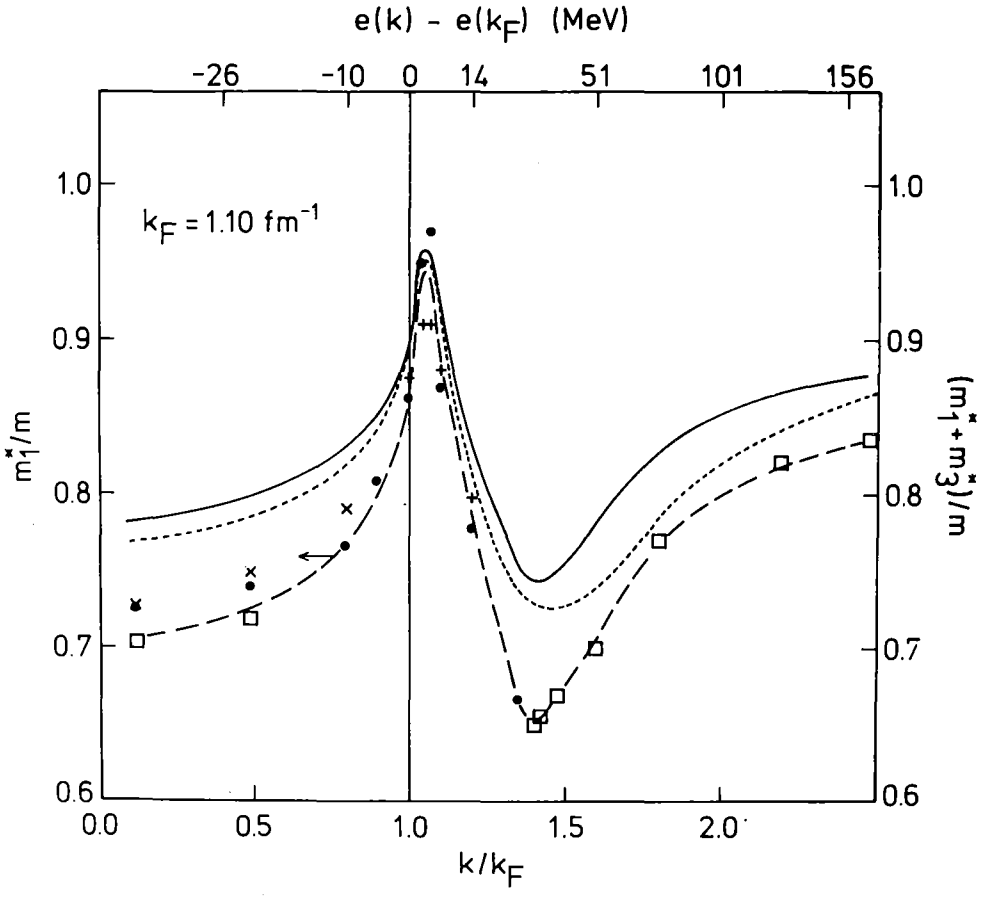

Fig. 2

In order to compare this approach with approximations (1) and (6), we used the parametrization

$$M^{(BHF)}(r,e) = \frac{V^{(BHF)}(r,e)}{1 + \exp[(r-R)/a]} \quad , \tag{12}$$

where

$$V^{(BHF)}(r,e) = V^{(BHF)}_{\rho(r)}(e) = C^{(BHF)} + \int_{e_F}^{e} [1 - m_\rho^{(BHF)*}(E)/m]dE \quad . \tag{13}$$

Below, we choose the integration constant $C^{(BHF)}$ in such a way that the mean field $M^{(BHF)}(r,e_F)$ has a bound state at the experimental value e_F of the Fermi energy, thus sharing this property with $M^{(WS)}(r)$ and $M^{(HF)}(r,e_F)$.

3. *NUMERICAL RESULTS*

We compared the single-particle energies, total densities and single-particle wave functions obtained from the potentials $M^{(WS)}(r)$, $M^{(HF)}(r,e)$ and $M^{(BHF)}(r,e)$, respectively. In the case of the "Hartree-Fock" field, we used for $m_\rho^{(HF)}(e)$ the value obtained from interpolating $m_\rho^{(BHF)}(e)$ by a straight line between the values calculated at $e-e_F = -50$ MeV and $e-e_F = 150$ MeV . We arbitrarily chose typical values $a = 0.62$ fm and $R = 1.230\ A^{1/3}$ fm for the geometrical parameters in eqs. (1),(6),(12).

For illustration, we give some results in the case of the nucleus ^{41}Sc . We took $e_F = -8.365$ MeV (binding energy of the $1d_{3/2}$ level). The binding energy $e(1s_{1/2})$ of the deepest single-particle state, that of the $1f_{7/2}$ valence orbit and its root mean square radius $\langle r^2_{f_{7/2}}\rangle^{1/2}$, and the root mean square radius $\langle r^2_c\rangle^{1/2}$ of the total charge distribution are collected in the table. As expected [6], the gap $e(1d_{3/2}) - e(1f_{7/2})$ is smallest in the case of $M^{(WS)}(r)$ and largest in the case of $M^{(HF)}(r,e)$.

^{41}Sc

	$e(1s_{1/2})$ (MeV)	$e(1d_{3/2})$ (MeV)	$e(1f_{7/2})$ (MeV)	$\langle r^2_{f_{7/2}}\rangle^{\frac{1}{2}}$ (fm)	$\langle r^2_c\rangle^{\frac{1}{2}}$ (fm)
$M^{(WS)}$	- 33.14	- 8.365	- 1.727	4.034	3.283
$M^{(BHF)}$	- 42.16	- 8.365	- 1.420	4.076	3.245
$M^{(HF)}$	- 41.64	- 8.365	- 0.801	4.106	3.245

The root-mean square radius of the valence $1f_{7/2}$ orbit is squeezed by about one per cent in the case of $M^{(BHF)}(r,e)$ as compared to $M^{(HF)}(r,e)$. This goes in the right direction to account for part of the difference between recent experimental measurements [9,10] and Hartree-Fock calculations.

There exists an intimate physical relationship between the effect investigated above and the recent work by Castel and Goeke [11]. These authors adopted, in a density-dependent Hartree-Fock

calculation, a Skyrme-2 effective nucleon-nucleon interaction ($m^*/m = 0.58$) for all core orbits (up to ^{40}Ca) and a Skyrme-6 interaction ($m^*/m = 0.95$) for the valence $f_{7/2}$ orbit. This mocks up the frequency dependence of the effective interaction, or equivalently the frequency dependence of the mean field. The value (0.37 m) assumed by Castel and Goeke [11] for the difference $m^*(f_{7/2}) - m^*(d_{3/2})$ is much larger than the one ($\simeq 0.04$) that we have calculated. Hence, it is not surprizing that they found a much larger squeeze ($\simeq 4.5$ %) for the radius of the valence orbit.

The possible importance, in the present context, of the enhancement of the effective mass near the Fermi energy was pointed out by Zamick [12]. The physical interpretation is that the enhancement of $m^{(BHF)*}(e)$ somewhat above $e=e_F$ renders $M^{(BHF)}(e)$ deeper than $M^{(HF)}(e)$, for $e-e_F \simeq$ several MeV .

According to Bertsch [private communication, 1979] the excitation of low-lying vibrations could reduce the size of the squeeze of the radius of the valence orbit. Bertsch argues that these vivrations will render the enhancement of $m^*_\rho(e)$ particularly large at the nuclear surface. However, we have seen that the enhancement already exists in uniform nuclear matter. We note that our expression for $m^*_\rho(e)$ has been chosen in such a was that $m^*_\rho(e_F) \to 1.22$ m for $\rho \to 0$, in order to account qualitatively for the role of surface vibrations.

Brown et al. [private communication, 1979] have investigated the effect on an orbit of the fact that $m^*_\rho(e)$ is larger at the nuclear surface than in the nuclear interior. Inasmuch as we are informed of their work, it seems that these authors compared the $(1f_{7/2})$ wave functions in two potential wells, one which is non-local and one which is local. Both are chosen in such a way that they yield the same binding energy $e(1f_{7/2})$. They find that the orbit in the non-local well is dilated with respect to that in the local well. Thus, the non-locality of the mean field cannot account for the squeeze of the valence orbits. We emphasize that nuclear matter calculations show that the non-locality is approximately the same for all orbits [8]. This is why in our model the squeeze of the valence orbit originates from the energy dependence of the mean field, and not from its non-locality.

In conclusion, we believe that the frequency dependence of the mean field leads to a squeeze of the valence orbits with respect to the bulk of the nucleus. However, this effect appears to be too small to explain the empirical observations. It has recently been suggested by Dubach [13] that meson exchange current corrections may play an important role in the analysis of the data.

We are grateful to G. Bertsch, G.E. Brown, B. Castel, K. Goeke and L. Zamick for stimulating discussions and correspondence.

References

[1] J.W. Negele, L. Zamick and G.K. Varma, Comments in Nuclear and Particle Physics, in press

[2] J.P. Jeukenne, A. Lejeune and C. Mahaux, Phys.Rev. C16(1977)80

[3] J.W. Negele, Phys.Rev. C1 (1970) 1260

[4] P. Quentin and H. Flocard, Ann.Rev.Nucl.Sci. 28 (1978), in press

[5] D. Vautherin and D.M. Brink, Phys.Rev. C5 (1972) 626

[6] G.E. Brown, J.H. Gunn and P. Gould, Nucl.Phys. 46 (1963) 598

[7] G.F. Bertsch and T.T.S. Kuo, Nucl.Phys. A112 (1968) 204

[8] J.P. Jeukenne, A. Lejeune and C. Mahaux, Phys.Reports 25C (1976) 83

[9] P.K.A. De Witth Huberts et al., Phys.Letters 71B §1977) 317

[10] I.Sick et al., Phys.Rev.Letters 38 (1977) 1259

[11] B. Castel and K. Goeke, Phys.Letters 82B (1979) 160

[12] L. Zamick, Proceedings of the Summer Institute in Nuclear Theory, Banff, Aug. 21-Sept. 1, 1978 (to be published by Plenum Press)

[13] J. Dubach, Phys. Letters 81B (1979) 124.

SELFCONSISTENT CALCULATIONS OF NUCLEAR DENSITIES OF NUCLEI IN THE Ca REGION

X. Campi
Institut de Physique Nucléaire,
Orsay, France

SELFCONSISTENT CALCULATIONS OF NUCLEAR DENSITIES OF NUCLEI OF THE Ca REGION

X. Campi
Division de Physique Théorique*
Institut de Physique Nucléaire
B.P. 1, 91406 Orsay Cedex - France

In recent years, a number of powerful methods have been developed for deriving the gross properties of finite nuclei from the two-nucleon force. Among these properties the nuclear densities appears to be the richest source of information by which the validity of these methods can be studied. The aim of this talk is first briefly overview the status of theoretical efforts to evaluate nuclear densities and secondly examine how well the calculated densities of nuclei of the Ca region agree with experiment.

THE NUCLEAR MEAN FIELD APPROXIMATIONS

The reaction G matrix

Most of the microscopic calculations of the ground state of nuclei in the medium mass region are more or less based on (or supported by) the Brueckner theory. The basic element of this theory is a microscopically derived effective interaction $G(\omega) = V + VQ(\omega - H_0(1) - H_0(2))^{-1}QG(\omega)$ which accounts for the scattering of two nucleons in the nuclear medium up to all orders in the free-nucleon potential V. 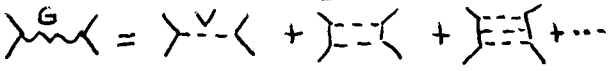 Thus are built into the wave function the short-range correlations resulting from the repulsive core of the nuclear interaction. The parameter ω is the energy available for the two interacting nucleons. The reaction matrix $G(\omega)$ depends on the Pauli operator Q

*Laboratoire associé au C.N.R.S.

and on the single-particle hamiltonian $H_0 = K + U$, where K is the kinetic energy and U the average single-nucleon potential in the nucleus. A second form of resummation of the perturbation series involves the definition of this one-body potential. It has been explicitely shown that the three classes of diagrams

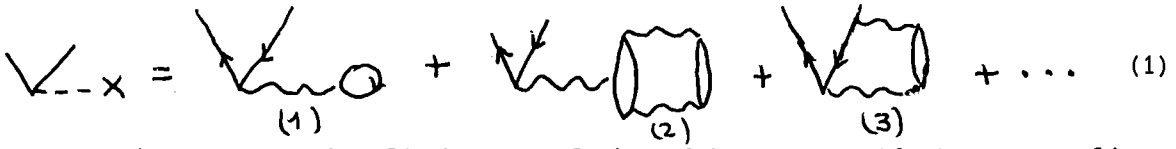

(1)

are very important in finite nuclei. This means that every diagram which contains the one-body potential $--X$ exactly cancels an important class of similar diagrams in which $--X$ is replaced by the terms shown on the right. Diagram (1) corresponds to the standard definition of the Hartree-Fock potential. It's the only one retained in the calculations denominated Brueckner-Hartree-Fock (BHF) [1]. Diagrams (1) and (2) (single particle spectra rearrangement) are included in the Renormalized-Brueckner-Hartree-Fock calculations (RBHF) [2]. The three insertions (1) + (2) + (3) (Pauli rearrangement) are needed in order to make the two-body cluster energy stationary. This is realized in the calculations called Density-Dependent-Hartree-Fock [3,4].

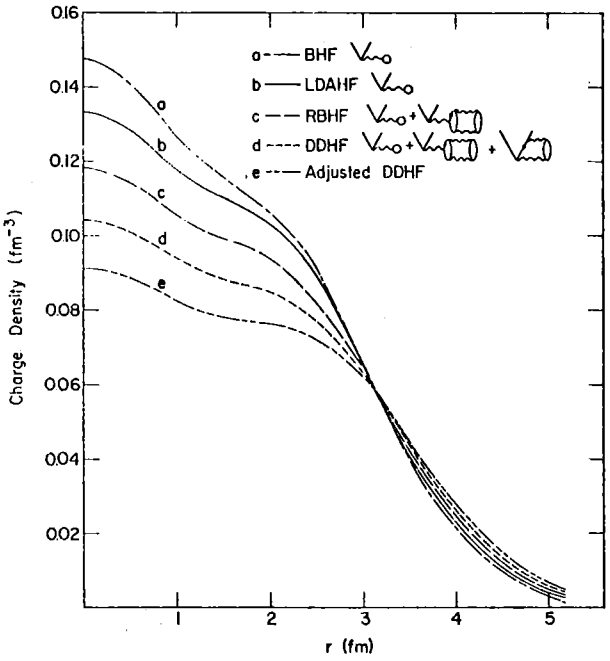

- Fig. 1 -

The necessity of including the important diagrams in the one-body potential becomes apparent when one calculates the one-body density. As an example, comparing curves a,c and d in Fig.1, taken from Ref.[5], one sees the crucial role of the rearrangement diagrams (2) and (3) in obtaining the proper saturation for the charge density of ^{40}Ca. (The experimental density is practically indistinguishable from curve e). However the crucial

point in these Brueckner calculations appears to be the convergence of the series. Because of the numerical complexity, present calculations of medium mass nuclei do not go beyond this mean field approximation including diagrams (1), (2) and (3). However, recent calculation in infinite nuclear matter [6] including higher order diagrams, seems to indicate a convergence in the binding energy and in the saturation density.

The perfect agreement with experiment it is not for the moment the main objective of these calculations based on "first principles". We know from the three-body problem (where the Schrödinger equation may be solved nearly exactly with realistic two-body forces) and also from the calculations of light nuclei based on the formalism of Coester, Kümmel and Zabolitzki [7] (which is equivalent to summing G-matrix ladder diagrams, three-body Faddeev diagrams and RPA ring diagrams) that an agreement between theory and experience it is never achieved for the one-body densities. This is probably due to the shortcomings of the used two-body force (the Reid soft-core potential in most cases), but also for neglecting three-body forces and relativistic effects.

Because of the inadequacy of our present understanding of nuclear forces and relativistic corrections and given the difficulty to calculate higher order diagrams in the mean field expansion, in some approaches it has been introduced a phenomenological adjustment of the calculated G-matrix to account for the deficiencies in the saturation properties [3,4]. A single choice of a two-parameter correction to the short range part of the G-matrix yields systematic agreement with experiment throughout the periodic table. (For double-magic nuclei maximum deviations between theory and experience are of the order of 2 % for the binding energies and less than 1 % for the r.m.s. radii of charge densities [4]). The effect of this adjustment on the charge density of ^{40}Ca is represented by the difference between curves d and e in Fig.1 [5]. These gratifying results give some confidence on the validity of the mean field approximation and encourage the hope that in a near future, using better nucleon-nucleon forces [8] and more efficient techniques for evaluating diagrams, a more complete understanding of the properties of the nuclear ground state will

be achieved.

Phenomenological effective interactions

In parallel with the development of the theories we have overviewed, many other calculations with simple phenomenological interactions have been performed. The goal with these phenomenological interactions is to fit, rather than derive, the principle characteristics of the nuclear ground state. The great advantage with these interactions is that they reduce drastically the computational complexity of the calculations. The price we pay for this is that there is no way to theoretically improve the method because one never deals with the free nucleon-nucleon interaction. The functional structure of these simple effective forces is substantiated by a density matrix expansion of the exchange terms in the HF equations (case of the Skyrme [9,10] , Moszkowski [11] and Beiner-Lombard [12] forces, including zero range, gradients and polynomials in the density terms) or by a schematic parametrization in r-space of the general behaviour of G-matrices (case of forces B of Brink and Boeker [13] and force D1 of Gogny [14]). The values of the different parameters (six free parameters in the Skyrme forces, fourteen in the Gogny force) have been adjusted to achieve the best possible description of a given set of experimental data. At this point it is interesting to notice that the fit of solely binding energies and r.m.s. radii do not suffices to define the optimal incompressibility of the nuclear matter and the non-locality of the mean field, quantities which play an important role in determining the properties of the nuclear densities.

Corrections to the HF densities

Before to be compared with experiment the calculated point-like proton densities have to be corrected for the well established electromagnetic corrections : proton and neutron form factors and spin-orbit coupling. Both proton and neutron densities have to be transformed to the center of mass frame. This

transformation is not unique and the resulting uncertainties are not negligeable in light nuclei.

Another significant question concerns higher order contributions to the perturbation expansion of the ground state expectation value of the one-body density operator. The lowest order contributions may be written

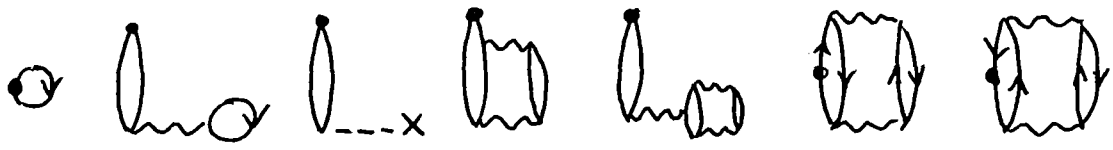

(the dot denotes the density operator and -- X the one-body potential). The first term is the Hartree-Fock or single particle density. By taking into account in the definition of the potential the terms of equation (1), the next four graphs cancel. The only second order correction is the sum of the last two diagrams, which describes the change in the one-body density due to two-body correlations. Numerical evaluations of these diagrams [3,15] in ^{40}Ca yields very small corrections. Low lying excitations, however, which give rise to long range correlations, are not properly handled in these calculations.

An alternative approach is to evaluate the ground state correlations in the framework of the RPA [16] . Recently using a phenomenological effective interaction the corrections to the densities of ^{40}Ca and ^{48}Ca have been calculated [17] . The results are shown in figure 2. We see that these corrections are very large, in apparent contradiction with the perturbation results. It is interesting to remark that in this calculation 80 % of the correction to the central density of ^{40}Ca (and 56 % in ^{48}Ca) arise from the coupling with the 3^- state, which is very collective in the RPA. Obviously more work in this direction is needful.

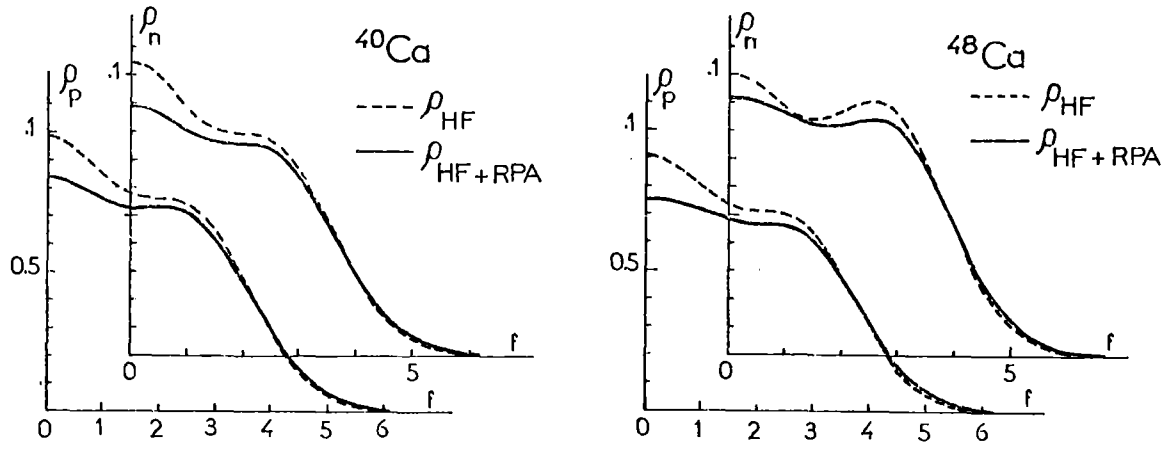

- Fig. 2 -

COMPARISON OF THEORETICAL DENSITIES WITH EXPERIMENT

The best test of the quality of the theoretical densities is the direct comparison with experiment of the calculated elastic scattering cross sections of various projectiles (e^- for charge densities, p, ^{4}He.. for neutron densities). At the same time, it should be pointed out that in this direct comparison it is difficult to recognize the origin of particular disagreements or even accidental agreements between experiment and theory.

To understand the origin of the shortcomings of the various methods it is more instructive to discuss the behaviour of $\rho(\vec{r})$ in real space. The big advantage is that one can use more physical intuition in attempting to recognize the origin of certain salient features of the densities, such as the r.m.s. radii, the surface thickness or the quantum oscillations.

Principle characteristics of nuclear densities : Radial moments, surface thickness and quantum oscillations

The radial moments $\langle r^k \rangle = \int \rho(\vec{r}) r^k d\vec{r} \Big/ \int \rho(\vec{r}) d\vec{r}$ are among the few characteristics of the density which are objectively well defined. The r.m.s. radii $r_c = \langle r^2 \rangle^{1/2}$ of charge densities can be measured and calculated with great accurancy. However the comparison of theory with experiment for a single nucleus like ^{40}Ca is of few interest, because as we already mentioned, most of the calculations have been adjusted to reproduce the observed r.m.s. radii of double magic nuclei. Although the absolute value of r_c for a given nucleus is not well defined by the theory, its variation with the mass number should be. This is because the variation of the radius depends critically on a balance between the incompressibility of nuclear matter and shell effects. It is this balance which one hopes to have correctly reproduced. Also the neutrons radii r_n and the differences between protons and neutrons $r_n - r_p$, which have not been adjusted in the theories, are of great interest in many problems of nuclear physics. In table 1 we compare to experiment the results of a DDHF calculation [4] (which contains a phenomenological adjustment consisting in a single choice of two parameters chosen to improve on average E/A and k_F in nuclear matter and the binding energies and r_c radii of double magic nuclei). It is quite remarkable the agreement for the neutron radii, in absolute value and for the differences between neighbouring nuclei. For the series of isotopes, the variation of the r_n radius is the consequence of the increasing number of particles in an external orbit ($f_{7/2}$), which is a first order effect and follows approximately the low $A^{1/3}$. This effect is partly compensated by a second order effect, the core polarization of the core neutrons by the extra neutrons in the external shell (see Fig.1c of Ref.[19]). For Ca isotopes one observes that $r_n \simeq .98\ A^{1/3}$.

As was shown by Bertozzi et al. [18] the famous anomaly between the charge radii of ^{48}Ca-^{40}Ca can be nearly resolved by taking into account the effective charge densities generated by the neutrons form factor and the e.m. spin-orbit interaction. Some remaining disagreement can be attributed to a shell closure

	Experiment			G-0 force[e]		
	r_c	r_n^{*a}	$r_n - r_p^*$	r_c	r_n^*	$r_n - r_p^*$
^{40}Ca	3.479 [b]	3.38±.04	-.02±.04	3.46	3.36	-.04
^{42}Ca	3.509 [g]	3.42±.04	-.02±.04	3.46	3.44	.02
^{44}Ca	3.507 [g]	3.49±.05	.04±.04	3.46	3.50	.08
^{48}Ca	3.467±.007 [d]	3.58±.04	.17±.04	3.46	3.59	.18
^{39}K	3.429±.018 [d]	-	-	3.42	3.35	-.01
^{48}Ti	3.57 [f]	-	-	3.54	3.56	.06

All lengths in fm

(*) Point -like nucleons ; (a) Ref.[19] ; (b) Ref.[20] ;
(c) From isotope shifts $^{40-42}Ca$ and $^{40-44}Ca$ Ref.[21] ;
(d) Ref.[22]; (e) Calculated with the formalism of Ref.[4] ;
(f) From the ^{48}Ti-^{40}Ca isotone shift Ref.[21] .
(g) From Ref.[27].

- Table 1 -

effect, which is known to be more marked for ^{48}Ca than for ^{40}Ca(*). In the RPA calculations of Gogny [17] this correction is even too large. It has to be emphasized that one obtains these sensible results only if one uses a theory which reproduces the binding energy difference between ^{40}Ca and ^{48}Ca and which places the $f_{7/2}$ neutron orbital correctly. This is because the isotope shift of charge densities is a polarization effect of the proton core by the extra neutrons. The magnitude of the effect depends critically

(*) Presumably the observed large isotope shifts for ^{40}Ca-^{42}Ca and ^{40}Ca-^{44}Ca, not reproduced by the present DDHF calculation, are also due to the effect of the neutron open shell.

on relative radial positions of the proton core density and the density of the polarizing neutrons. As an example, by shifting (changing the spin-orbit force) the neutrons $1f_{7/2}$ energy by 4 MeV (many HF calculations give larger errors for the ^{40}Ca-^{48}Ca binding energies difference) causes a change in the charge radius of ^{48}Ca of .006 fm. This is of the same order as the experimental difference between the charge radii of ^{40}Ca and ^{48}Ca. The energy of the $1f_{7/2}$ neutron orbit is also strongly correlated with the $r_n - r_p$ differences. We see in table 1 that these differences for the Ca isotopes are understood in the framework of a DDHF calculation.

The surface thickness is a second characteristic quantity for the densities which can be defined without great ambiguity. One definition [23] which gives an average over the entire surface region is given by the slope of the radial moments : $a_k = [6\ R_k\ R'_k]^{1/2}\ /\pi$ where $R_k = \left[\frac{k+3}{3} <r^k>\right]^{1/k}$ and $R'_k = \frac{dR_k}{dk}$. For a well-behaved density, a_k is practically independent of k ($1 \lesssim k \lesssim 5$). For a Fermi distribution with parameters R,a this definition gives $a_k \approx a$, to terms of the order $(a/R)^4$. The surface thickness of the calculated densities is governed essentially by the non-locality of the nuclear mean field and by the incompressibility of the nuclear matter(+) [25,23].

In table 2 we compare the surface thickness of the charge densities calculated with various interactions. We see that forces with small incompressibility and large non-locality (Brink-Boeker force B1) yield larger thickness than forces like Skyrme III (large K and reduced non-locality). From the comparison with experiment we remark that all calculations account for the decreasing in the thickness between ^{40}Ca and ^{48}Ca.

(+) A semi-quantitative relation between the surface thickness and the incompressibility of the nuclear matter and the non-locality of the potential has been derived for semi-infinite systems [26] .

Effective interaction	Surface Thickness (fm) ^{40}Ca	^{48}Ca
Skyrme III	0.50	0.47
Skyrme V	0.52	0.50
Beiner-Lombard	0.53	0.49
Brink-Boeker B1	0.54	0.50
DDHF - G0	0.52	0.48
Experiment (calculated from data of Ref.[20,22]	0.53±.01	0.49±.01

- Table 2 -

The surface thickness of the experimental mass distributions ($\rho_n + \rho_p$) deduced in the analysis of Ref.[19] are compared to the results of the calculation DDHF-G0 in table 3.

a_{Mass} (fm)	^{40}Ca	^{42}Ca	^{44}Ca	^{48}Ca
Exp(±.02)	.47	.54	.51	.45
DDHF-G0	.49	.48	.48	.47

- Table 3 -

Presumably the observed large values for ^{42}Ca and ^{44}Ca are also due to long-range correlations in the open shell $f_{7/2}$, not taken into account by the DDHF calculation.

The situation for the quantum density fluctuations in the interior of the charge densities is summarized in fig. 3 where we have compared to experiment [20] the densities calculated with two Skyrme interactions SIII and SV [10] and with the G-0 force. We see that the purely phenomenological interactions give about the right amplitude of the oscillations whereas the semi-phenomenological long range force G-0 gives too large oscillations. This particular behaviour is common to all forces based in a short range

expansion (Skyrme [12] , Moszkowski [11] , Beiner-Lombard [13]) on one side and to long range forces (Negele [3] , G0 [4] , Gogny [14]) on the other side. Notice that the situation is the opposite for ^{208}Pb (Skyrme-like forces give larger oscillations). To explain this particular effect Friar and Negele [25] used an argument based on the relation between the density and the one-body potential. However the reason why the sophisticated semi-phenomenological approaches give too much oscillations is still an open question. Probably the corrections due to the two-body correlations must help in solving this problem.

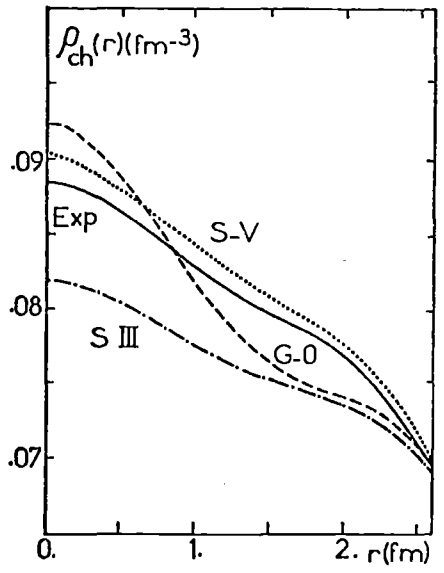

- Fig. 3 -

Density differences between neighbouring nuclei

The density differences between neighbouring nuclei (isotones/isotopes) provide an intuitive picture on how the nucleons distribute in valence orbits and/or how the core is polarized by these valence particles. In figure 4, taken from Ref.[24] is shown the charge density difference between the isotones ^{40}Ca-^{39}K. The proton $1d_{3/2}$ single particle radial wave function and a small proton core dilatation are clearly seen. Figure 5 shows the charge density difference ^{48}Ca-^{40}Ca taken from Refs.[20,22], i.e. the polarization of the Z = 20 protons by

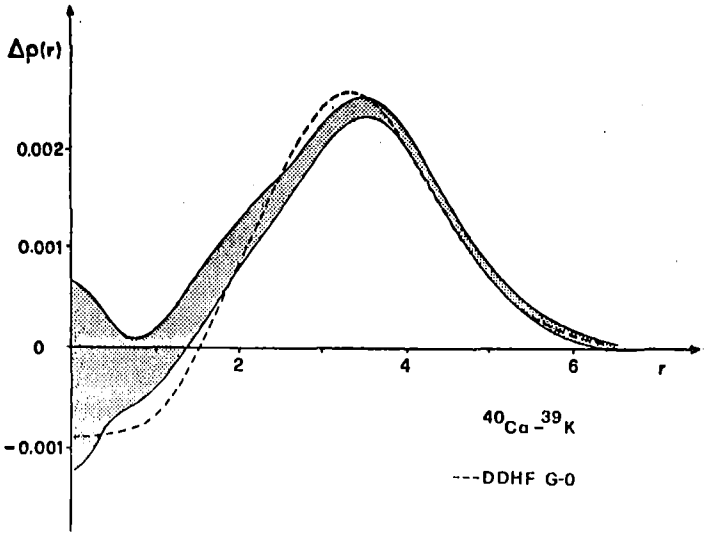

- Fig. 4 -

the 8 extra neutrons in the orbit $f_{7/2}$. We see in both examples that a DDHF calculations accounts semi-quantitatively for the experimental results. An example of neutrons density difference (^{48}Ca-^{40}Ca) is shown in Fig. 1c of Ref.[19].

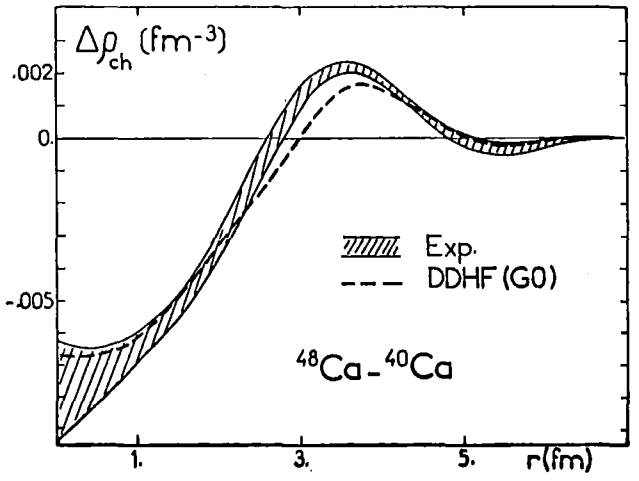

- Fig. 5 -

CONCLUSIONS

We have briefly overviewed the present status of theoretical efforts to derive the radial shape of nuclear densities in the framework of the mean field approximations. Some emphasis has been putted in clarifying the various approaches according to their degree of phenomenology : Calculations in which the mean nuclear field is derived from the bare two-nucleon interaction (RBH and unadjusted DDHF), with one or two free parameters improving the saturation properties (adjusted DDHF), and purely phenomenological. For nuclei in the Ca region not far from the closed shells to which the mean field approximation is applicable the last two approaches yield reasonable agreement with experiment for most of the salient features of density distributions (r.m.s. radii of charge and neutron densities, surface thickness, isotope and isotone shifts). On the other hand the problem of the amplitude of the quantum oscillations in the interior of the densities is in our opinion not well understood. Another completely open question is the importance of the long-range correlations and the related question of the significance of the ground state RPA correlations.

The author is very indebted to his colleagues of the Division de Physique Théorique for many useful discussions and to B. Frois and I. Sick for making experimental data available prior to publication.

[1] K.T.R. Davies, R.J. Mc Carthy and P.U. Sauer, Phys. Rev. C6 (1972) 1461.

[2] K.T.R Davies, R.J. Mc Carthy and P.U. Sauer, Phys. Rev. C7 (1973) 943.

[3] J.W. Negele, Phys. Rev. C1 (1970) 1260.

[4] X. Campi and D.W.L. Sprung, Nucl. Phys. A194 (1972) 401.

[5] K.T.R. Davies et al., Phys. Rev. C10 (1974) 2607.

[6] B.D. Day, Rev. Mod. Phys. 50 (1978) 495.

[7] H. Kummel, K.H. Luhrmann and J.G. Zabolitzky, Phys. Rev. 36 (1978) 1.

[8] M. Lacombe, B. Loiseau, J.M. Richard and R. Vinh Mau, P. Pirès and R. de Tourreil, Phys. Rev. D12 (1975) 1495 ; and Preprint IPNO/TH 78-46.

[9] D. Vautherin and D.M. Brink, Phys. Rev. C5 (1975) 1.

[10] M. Beiner, H. Flocard, Nguyen Van Giai and Ph. Quentin, Nucl. Phys. A238 (1975) 29.

[11] J.W. Ehlers and S.A. Moszkowski, Phys. Rev. C6 (1972) 217.

[12] M. Beiner and R. Lombard, Ann. of Phys. 86 (1974) 262.

[13] D.M. Brink and E. Boeker, Nucl. Phys. A91 (1967) 1.

[14] D. Gogny, Proc. Int. Conf. Nucl. Phys. ed. De Boer H.J. Mang, Vol. 1, p.48 North-Holland (1973).

[15] M.R. Strayer, W.H. Bassichis and A.K. Kerman, Phys. Rev. C8 (1973) 1269.

[16] D. Agassi, V. Gillet and A. Lumbroso, Nucl. Phys. A130 (1969) 129 ;
A. Bouyssy and N. Vinh Mau, Nucl. Phys. A229 (1974) 1 ;
A. Faessler et al., Z. Physik A276 (1976) 95.

[17] D. Gogny, 5è Session d'Etudes Biennale de Physique Nucléaire, I.P.N. Lyon, Lycen 7902.

[18] W. Bertozzi et al., Phys. Lett., 41B (1972) 408.

[19] I. Brissaud and X. Campi, Contribution to this conference.

[20] B. Frois, private communication.

[21] Atomic Data and Nucl. Data Tab. 14 (1974)

[22] I. Sick, Phys. Lett. 53B (1974) 14 and private communication.

[23] X. Campi in Nucl. Self. Fields, G. Ripka editor North-Holland (1975).

[24] I. Sick, Proc. of the 6th Int. Conf. on High Energy Physics and Nucl. Struct. Santa Fe (1975).

[25] J. Friar and J.W. Negele, Advances in Nucl. Phys. 8 (1975) Plenum Press.

[26] X. Campi and S. Stringari, to be published.

[27] H.D. Wohlfahrt et al., Phys. Lett. 73B (1978) 131.

THE NEUTRON AND PROTON DISTRIBUTIONS OF THE CALCIUM ISOTOPES

B.A. Brown, S.E. Massen,
and P.E. Hodgson
Nuclear Physics Laboratory,
Oxford, England

THE NEUTRON AND PROTON DISTRIBUTIONS OF THE CALCIUM ISOTOPES

B.A.Brown, S.E.Massen and P.E.Hodgson

Nuclear Physics Laboratory,

Oxford

The calcium isotopes are worthy of special study because they are the first long chain of experimentally-accessible isotopes in the periodic table and they are bounded by two nuclei, ^{40}Ca and ^{48}Ca, with closed-shell configurations that are suitable for Hartree-Fock calculations. As shown in Table 2, their RMS charge radii are very irregular compared with the global $A^{1/3}$ variation. It is thus an important test of nuclear theories to see whether this microscopic structure can be understood.

Ideally, it would be desirable to carry out Hartree-Fock calculations for all the calcium isotopes, constraining the occupations of orbitals near the Fermi surface by the results of ancillary shell model calculations and by experimental data. Since this is very difficult, we use a simpler approach in which it is assumed that all nucleons feel the same average potential whose parameters are adjusted to reproduce experimental single-particle centroid energies and RMS radii. It is also assumed that all orbitals except those near the Fermi

surface are completely filled. This method is in a sense complementary to the Hartree-Fock calculation.

In our model, the roles of the isoscalar core density, the isovector core density and the valence density are distinguished, the interaction between the core and valence particles is included and the Coulomb and isovector potentials are treated self-consistently. These calculations are first made for the core nucleus ^{40}Ca, and are then extended through the isotopic sequence by the addition of a valence potential.

Our calculations proceed in two stages: we first obtain semi-self-consistent distributions for the core nucleus and then extend the calculations to include the valence nucleons.

We use a potential of the standard form

$$V_{p,n}(r) = V_{Coul}(r) + V_{p,n}f(r) + V_{so}(r) \tag{1}$$

where $V_{Coul}(r)$ is the Coulomb potential that is present only for protons, $V_{p,n}f(r)$ the central potential, $V_{so}(r)$ the spin-orbit potential and $f(r)=[1+\exp\{(r-R)/a\}]^{-1}$.

Instead of the usual expression

$$V_{p,n} = V_o \pm \frac{N-Z}{A} V_1 \tag{2}$$

we use

$$V_{p,n} = V_o \pm \frac{\rho_1(r)}{\rho_o(r)} V_1 \tag{3}$$

where

$$\rho_o = \rho_n(r) + \rho_p(r) \tag{4}$$

and

$$\rho_1 = \rho_n(r) - \rho_p(r)$$

where $\rho_n(r)$ and $\rho_p(r)$ are the neutron and proton distributions respectively. Unlike (2) the form (3) has an isovector potential which is non-zero for N=Z nuclei, and so enables the difference between the neutron and proton distributions for these nuclei to be calculated self consistently.

We begin by adjusting the parameters V_o and R to give the rms charge radius of a closed-shell (core) nucleus, and the experimental proton single-particle centroid energies. The neutron and proton distributions are defined by expressions of the form

$$\rho(r) = \frac{1}{4\pi} \Sigma\, n(nlj) \mid \frac{1}{r} U_{nlj}(r) \mid^2 \tag{5}$$

where the n(nlj) are occupation probabilities, $U_{nlj}(r)$ the radial wavefunctions and the sum runs over all occupied orbits. The symmetry potential V_1=-30 MeV and the other parameters have standard values V_{so}=7 MeV, a=0.65fm.

After the first calculation, the proton and neutron distributions are inserted in (3) and the whole calculation iterated to self-consistency in the proton and neutron distributions.

To extend the calculation to nuclei with valence nucleons, the central potential is written in the form

$$V_{p,n}f(r) = \{V_o\ \rho_o(r) \pm V_1\ \rho_1(r)\}\ F(r) \qquad (6)$$

where $F(r)=f(r)/\rho_o^c(r)$, and $\rho_o^c(r)$ refers to the core nucleus. This expression is identical to (3) for the core nucleus but for nuclei with valence nucleons, it has additional terms that include the effects of the interaction between the core and valence nucleons.

Using this potential, the calculation can then be repeated for the nuclei in an isotopic sequence without any additional parameters. Throughout the calculation the potentials are constrained to fit the single-particle centroid energies and the orbit occupation probabilities are taken from analyses of nucleon transfer reactions, from shell-model calculations, or as parameters adjusted to reproduce the isotopic changes in charge radii.

The experimental charge density of ^{40}Ca is shown in Fig.1. The two experimental curves arise from a discrete ambiguity in the analysis of the charge form factor which results from a phase ambiguity in the data around $q \approx 3.2$fm (Sick 1974a). Recent experiments at high q transfer have shown that the smoother density (curve I in Fig.1) is correct (Frois 1978).

The charge density has been calculated assuming a closed shell configuration (labelled IIA in Fig.1) and a non-closed shell configuration (labelled IIB in Fig.1); the parameter R is 4.614fm and 4.562fm, respectively. It is amusing that the calculated shape corresponds closely to the "incorrect" experimental distribution (II). Hartree-Fock calculations give a shape of the charge distribution nearly identical to the present calculation but with an interior magnitude which is quite sensitive to the interaction (Negele 1970, Campi and

Sprung 1972). In all of the calculations the interior bump is due to the filled s orbits.

Thus all calculations for ^{40}Ca show much more interior structure than is found experimentally; this may mean that the effective many-body interaction is more complicated than the ones which have been inferred from the "surface" properties of nuclei.

Numerous calculations for the Ca isotopes have been carried out using the standard Woods-Saxon approach (Gibson and Van Oostrum 1967, Elton 1967, Elton and Webb 1970, Malaguti et al 1979). Relative to the present calculation the fault of these calculations is that there are too many parameters. Hartree-Fock calculations have been carried out for ^{40}Ca and ^{48}Ca but they do not give very good agreement with experiment (Negele 1970, Bertozzi et al 1972). As will be shown below the probable fault in the conventional Hartree-Fock approach is that non-closed shell configurations are ignored.

The most accurate experimental data on the rms radii is provided by the muonic atom experiments. The Barrett radii are given in Table 1 and these are converted into equivalent RMS radii using the scaling relation

$$(r_{ch})_{\mu}^{IIB} = \left[\frac{\langle r^k e^{-\alpha r} \rangle_{exp}}{\langle r^k e^{-\alpha r} \rangle_{th}^{IIB}} \right]^{0.52} (r_{ch})_{th}^{IIB}$$

and the results are given in Table 2. The comparison of the RMS radii using a Fermi shape in the muonic atom analysis $[(r_{ch})_{\mu}^{F}]$ is quite close to the values we infer from the Barrett radii $[(r_{ch})_{\mu}^{IIB}]$. $((r_{ch})_{\mu}^{IIB} = (r_{ch})_{\mu}^{IIA}$ to within ± 0.002fm).

The experimental density difference between ^{48}Ca and ^{40}Ca is shown in Fig.2. The broken lines are the model-independent analyses of Sick (1974a, 1978), the two corresponding to the discrete ambiguity of ^{40}Ca of which (I) is correct (Frois 1978). The solid line is the model-dependent analysis of Frosch et al (1968) for which a modified Fermi distribution was assumed. The various densities agree relatively well. The model dependent densities of Frosch et al for ^{42}Ca and ^{44}Ca relative to ^{40}Ca are shown by the solid lines in Figs.3 and 4, respectively; a model independent analysis is not available in these cases. It is interesting to note that the magnitudes of the density change relative to ^{40}Ca as shown by the solid lines in Figs.2, 3 and 4 become progressively larger in going from ^{42}Ca to ^{48}Ca whereas the RMS charge radii of ^{40}Ca and ^{48}Ca are nearly equal.

In our calculation we first consider the situation for a closed sd shell and valence neutrons in the fp shell. We use simplified but realistic (McGrory et al 1970) fp shell occupation probabilities of 90% $1f_{7/2}$ particles plus 10% $2p_{3/2}$ particles. The isotopic dependence of the RMS radii is small and smooth in disagreement with experiment (Table 2). However, the density changes as shown by the dot-dashed (labelled IIA) curves in Figs.3, 4 and 5 are large and in rough qualitative agreement with experiment.

Hartree-Fock calculations (Negele 1970) have been made with this assumption of a closed sd shell. If we further restrict the neutron configuration in ^{48}Ca to be 100% $f_{7/2}$ then our calculated proton charge density difference $\Delta\rho(r)^{p}_{ch}$ is similar to the Hartree-Fock results as shown in Fig.6.

Now we consider the amount of excitation of protons from the sd shell to the fp shell which is needed to reproduce the Ca RMS radii. In order to limit the number of parameters we first notice that the density change in the region r=0-1fm is extremely sensitive to the change in occupation of the $2s_{1/2}$ orbit. The small dip in the centre of the experimental (Sick I) ^{48}Ca-^{40}Ca density difference shown in Fig.2 can be explained by a change of only 0.04 particles in the $2s_{1/2}$ orbit between ^{40}Ca and ^{48}Ca. The flat interior density differences for ^{42}Ca and ^{44}Ca obtained by Frosch et al shown in Figs.3 and 4 indicates that there is no change in the $2s_{1/2}$ occupation probability between ^{40}Ca, ^{42}Ca and ^{44}Ca; however, this is probably due to the restricted Fermi shape used in the experimental analysis and a model independent analysis of higher q data would probably reveal interesting interior structure for ^{42}Ca and ^{44}Ca. For the present, it is be adequate to assume that the $2s_{1/2}$ orbit is full for all the Ca isotopes.

The Ca isotopes have been studied with the following one-parameter wave functions, for $n \geq 2$

$$|^{40+n}Ca\rangle = \alpha|(\nu f_{7/2}\, p_{3/2})^n\rangle$$
$$+\beta|(\pi d_{3/2})^{-2}\,(\pi f_{7/2}\, p_{3/2})^2\,(\nu f_{7/2}\, p_{3/2})^n\rangle \qquad (7)$$

and for ^{40}Ca

$$|^{40}Ca\rangle = \alpha|0\rangle$$
$$+\beta|(\pi d_{3/2})^{-1}\,(\pi f_{7/2}\, p_{3/2})\,(\nu d_{3/2})^{-1}\,(\nu f_{7/2}\, p_{3/2})^1\rangle \qquad (8)$$

where $|0\rangle$ is the closed shell configuration. We use this wave function schematically to obtain the number of proton holes in the $d_{3/2}$ orbit relative to ^{40}Ca which is given by

$$\Delta(n) = 2\beta^2(^{40+n}Ca) - \beta^2(^{40}Ca). \qquad (9)$$

As above, it is assumed that the $f_{7/2}\ p_{3/2}$ configuration is 90% $f_{7/2}$ and 10% $p_{3/2}$.

At first $\Delta(n)$ is chosen to reproduce the experimental RMS radii and then the density difference is compared with experiment to test our assumptions. For $\Delta(n)$ we find $\Delta(2)=1.0$, $\Delta(4)=1.1$, $\Delta(6)=0.35$ and $\Delta(8)=-0.4$. The negative number for $^{48}Ca-^{40}Ca$ is not surprising; it means that there is more core excitation in ^{40}Ca than in ^{48}Ca. The wave functions we have used correspond to values of $\beta^2=0.7$, 0.85, 0.9, 0.525, and 0.15 for ^{40}Ca to ^{48}Ca, respectively. It should be emphasized that these wave functions have little meaning in themselves because they do not explicitly contain the more complex four-hole configurations, whereas the values of Δ obviously depend on the total number of proton holes coming from all configurations .

In Fig.5 the calculated difference for the $^{48}Ca-^{40}Ca$ charge density is shown for the various approximations which have been used; for a closed sd shell plus eight $f_{7/2}$ neutrons, for a closed sd shell plus an (fp) neutron configuration (IIA) and finally for the $\Delta(8)=-0.4$ configuration (IIB). As pointed out by Bertozzi et al (1972) the contributions from the neutron finite size and spin-orbit corrections are important in this case. These corrections have been included in all our calculations. In Fig.7 the spin-orbit correction for the $(1f_{7/2})^8$ configuration is shown and compared with the more realistic $(fp)^8$ neutron configuration which has 10% $p_{3/2}$. The calculation with $\Delta(8)=-0.4$ is compared with experiment in Fig.8 (Sick I from Fig.2); the agreement is excellent.

A comparison of the calculated and experimental charge density differences for ^{42}Ca-^{40}Ca and ^{44}Ca-^{40}Ca is shown in Figs.3 and 4, respectively. In both cases but especially for ^{42}Ca the calculations which include core excitation (IIB) are much improved compared with the closed shell calculations (IIA) especially in the important surface region. In these figures we give a third calculation (IIC) in which the amount of $2p_{3/2}$ admixture has been increased to 20% to show the sensitivity to this parameter. A more detailed comparison in these cases must await a better experimental determination of the density change and theoretical calculations of the form factors F(q). For completeness the calculated density change for ^{46}Ca-^{40}Ca is shown in Fig.9.

Now it is very interesting to compare our values of Δ with other experimental and theoretical determinations of this quantity. One-proton transfer spectroscopic factors should be a sensitive measure of the number of proton holes and the literature concerning these reactions for the Ca isotopes is extensive. For example, the stripping reaction on ^{42}Ca leading to positive parity states in ^{43}Sc is a direct measure of the number of proton holes in the sd shell H(sd) in ^{42}Ca, and the pickup reaction on ^{42}Ca leading to negative parity states in ^{41}K is a direct measure of the number of proton particles in the fp shell, P(fp). Values of H(sd) and P(fp) extracted from a sum-rule analysis are given in Table 3. If everything has been carried out properly for a given nucleus we should have $\Delta+\delta=P(fp)=H(sd)$ where δ is chosen to give the absolute number of proton holes in ^{40}Ca and we have rather arbitrary chosen $\delta=0.7$. It is seen in Table 3 that in fact none of these three quantities agree very well. For the stripping and pickup reactions this

is a serious problem which has been pointed out previously (Dehnhard and Cage 1974, Doll et al 1976). We feel that the main difficulty is that in order to make use of a sum-rule analysis one must be careful to include all the high-lying levels and to take into account the well-known anomalies that result from comparing levels with very different binding energies (Moalem et al 1978). The parameter Δ should be the most direct measure of the number of proton holes in the Ca isotopes.

Shell model calculations for the Ca isotopes which include excitations from the sd shell have been progressively improved but still seem far from explaining the entire experimental situation. Many calculations have used a $(d_{3/2}, f_{7/2})$ basis. Three different types of calculations have been made for ^{40}Ca within this basis; Gerace and Green (1967, 1969) have considered configurations up to 8p-8h but in which the $f_{7/2}$ particles are restricted to couple to isospin T=0, Federman and Pittel (1969) and more recently Seth et al (1974) have considered configurations up to 4p-4h but allowing all values of T for the $f_{7/2}$ particles, and finally Sakakura et al (1976) have used a complete basis (up to 8p-8h with all values of T). The values obtained for the number of proton holes in the $d_{3/2}$ orbit in ^{40}Ca in these three calculations are δ=0.19, δ=0.53 and δ=0.76, respectively. Only the least two are in agreement with the experimental values given in Table 3.

It is interesting to compare our value of $\Delta(2)$=1.0 with the values obtained from these shell model calculations. Gerace and Green obtain $\Delta(2)$=0.24 and Seth et al obtain $\Delta(2)$=0.37; both are in poor agreement with the experimental value. The full-basis calculations such as

Sakakura carried out for ^{40}Ca apparently fail completely when they are extended to ^{48}Ca (Graf et al 1978) and the results of these calculations have thus not been reported. It seems, however, that full-basis calculations of this type will be needed in order to understand ^{42}Ca. Flowers and Skouras (1969) considered an extended basis of ($s_{1/2}$, $d_{3/2}$, $f_{7/2}$, $p_{3/2}$) for ^{42}Ca with 2p and 4p-2h components. In two approximations, A and B, they obtain wave functions which give $\Delta(2)+\delta=0.20$ and 0.41, respectively; these are in very poor agreement with the present value of $\Delta(2)+\delta=1.7$.

In addition to these fully microscopic calculations, simple schematic wave functions with two or three components have been constructed in order to understand transition matrix elements and alpha transfer for the Ca isotopes (de Voight et al 1974, Towsley et al 1973, Fortune and Cobern 1978, and Graf et al, 1978). The two-component wave function which Towsley et al use to explain E2 transitions in ^{42}Ca gives $\Delta(2)=0.52$ and the three-component wave function which Fortune and Cobern use to explain alpha-transfer to ^{42}Ca gives $\Delta(2)=0.47$, neither of which is in agreement with the present value of $\Delta(2)=1.0$ obtained from the ground state charge radii. However, one must consider whether or not the transition rate and alpha-transfer data could be equally well explained by using wave functions with more components with more core excitation. Graf et al have considered two-component wave functions to explain the excitation energies and the E0 transition matrix elements to the excited 0^+ states for all of the even-even Ca isotopes. With their wave functions they find $\Delta(2)=1.09$, $\Delta(4)=0.81$, $\Delta(6)=0.24$ and $\Delta(8)=-0.08$ (see Table 5 in Graf et al 1978), which are in rather good agreement with the present results of 1.0, 1.1, 0.35 and -0.4, respectively.

However, the value of δ=0.21 which they obtain for ^{40}Ca seems too small. Thus at present it seems that we need different models to explain different data for the Ca isotopes and clearly the only unified approach to this problem is a careful calculation of all quantities in a large shell model basis such as has been used by Sakakura et al (1976) for ^{40}Ca.

We want to emphasize the differences between the occupation numbers imposed by the electron scattering data and the occupation numbers obtained from one-proton transfer experiments. In Table 4 we list the "experimental" occupation probabilities obtained by Malaguti et al (1979) from a combination of the stripping and pick-up strengths summarized by Doll et al (1976). These occupations have been used to calculate the charge densities, and the differences are plotted in Fig.10. First we note that the calculated differences in the RMS charge radii of 0.006fm and 0.019fm for ^{42}Ca-^{40}Ca and ^{44}Ca-^{40}Ca, respectively are not in agreement with the experimental values of 0.031fm and 0.039fm, respectively. Secondly the density changes shown in Fig.10 are not in good agreement with experiment. In particular, in ^{44}Ca-^{40}Ca the large central peak in the calculated density is due to the large number of holes in the $2s_{1/2}$ orbit in ^{44}Ca. However, it should be remembered that the electron scattering has been analyzed with a restricted form for the density. New, less model-dependent, analyses and new experiments of higher q on ^{42}Ca and ^{44}Ca may reveal interesting interior density changes due to the $2s_{1/2}$ orbit.

An important feature of the present calculation is the self-consistency between the Coulomb potential and the symmetry potential. Once the proton and neutron occupation probabilities and the potential

for the protons are fixed, the neutron single-particle energies and densities are determined with the assumption that the nuclear force is charge symmetric, i.e. that the pp and nn nuclear interactions are equal. It is well known that the neutron single-particle energies calculated in this way for mirror nuclei deviate from the experimental values by about 10% (Nolen and Schiffer 1969). This is also the case in the present calculations and a detailed report of the results for Coulomb energies and the displacement energies of mirror nuclei will be presented elsewhere (Brown et al 1979). The results for the neutron densities will be discussed and compared with experiment to see if any related anomalies appear.

It is fortunate that for most nuclei considered here the neutron occupations are theoretically well-determined relative to the proton occupations. For example in an N=Z nucleus it is a good assumption that $n_n=n_p$ for each orbit. And in Eq.(7) the neutron occupations are independent of β^2 due to the structure of the wave functions.

It is important to emphasise that the neutron distribution alone cannot be measured and that one must consider carefully what assumptions have been made when an "experimental" neutron radius is quoted from an analysis of hadron scattering. Alpha scattering and high energy proton scattering experiments determine most directly the matter radius r_m defined by $Ar_m^2=Zr_p^2+Nr_n^2$.

There are many sources of uncertainty in the extraction of r_m (Ray et al 1978b) but many of them are probably not so important for the change in the mass radius $\Delta r_m=r_m(A)-r_m(^{40}Ca)$; we will concentrate here on these numbers Δr_m. The theoretical and experimental values for Δr_m

are given in Table 5. We have not included results of analysis of low energy proton and alpha scattering since there is great uncertainty in the optical model which leads to results to which one must assign a large errors. For example, a value of $\Delta r_m = 0.12 \pm 0.06$fm was obtained from a careful analysis of 104 MeV α scattering (Friedman et al 1978) but larger values are obtained from the more simplified folding model analysis of the same data, $\Delta r_m = 0.17$fm, and other data, $\Delta r_m = 0.38$ (Brissaud et al 1972).

As seen in Table 5 different analyses of four different sets of experimental data yield quite consistent values for Δr_m and this leads us to choose "adopted" values with errors of ±0.02fm.

Now we consider the theoretically interesting quantity $r_{np} = r_n - r_p$, the difference between the neutron and proton RMS radii. An experimental value for this quantity can be found by combining the results for the charge and matter radii. We will define a quantity r_e by the relation $r_{ch} \equiv r_p + r_e$, where r_p is the point proton radius and r_e is the correction due to the proton and neutron finite charge distribution and to relativistic effects (Bertozzi et al 1972, and Chandra and Sauer 1976). We first concentrate on $r_{np}(^{40}Ca) \approx 2(r_m - r_{ch} + r_e)$. We could take $r_m^{exp} = 3.39(3)$fm from Table 5, $r_{ch}^{exp} = 3.479$fm from Table 2, and the calculated value of $r_e = 0.10$fm and we obtain

$$r_{np}^{exp}(^{40}Ca) = 0.02 \pm 0.06 \text{ fm}$$

It is unfortunate that there is such a large error in the experimental $r_n - r_p$ value in ^{40}Ca. The values of $r_n - r_p$ in N=Z nuclei are relatively well determined theoretically since the difference is only due to Coulomb effects (the known charge-asymmetric force is much

smaller than the Coulomb effect). Since the radial dependence of the Coulomb force in nuclei is dominated by a one-body term proportional to r^2, in an harmonic-oscillator basis its effect is simply a scale change in the potential; i.e. $\hbar\omega_p = \alpha\hbar\omega_n$ (Soper 1968). In addition the dominance of the r^2 term leads to a very simple form for the isovector density difference (Auerbach 1974),

$$\rho_1(r) = C\left[3\rho_o(r) + r\frac{d\rho_o(r)}{dr}\right] \tag{8}$$

where

$$\int \rho_1(r)\,d\tau = 0 \tag{9}$$

and

$$\frac{\int \rho_1(r) r^2 dr}{\int \rho_o(r) r^2 dr} = -2C \tag{10}$$

and thus

$$C = -\frac{1}{2}(r_n^2 - r_p^2)/(r_n^2 + r_p^2) \approx -\frac{1}{2}(r_n - r_p)/r_p \tag{11}$$

This simplicity suggests the following procedure for the analysis of hadron scatering on N=Z nuclei. First one can obtain the proton point density from electron scattering experiments (i.e. by correcting for the proton and neutron finite charge distribution). Then for the neutron point density one can use:

$$\rho_n(r) = \rho_p(r) + 2C\left[3\rho_p(r) + r\,\frac{d\rho_p(r)}{dr}\right] \tag{12}$$

where C is a parameter. In particular, if good fits cannot be obtained from this one-parameter model, this strongly suggests that the reaction

theory analysis rather than the nuclear density distribution is at fault. In the present calculation for ^{40}Ca we have C=0.0077, but other models may give slightly different values.

We now consider the values of r_{np} for the other calcium isotopes. To obtain a simple relationship between r_{np} and the well determined experimental quantities Δr_m and Δr_{ch} we use $r_m \simeq r_p + N r_{np}/A$, then

$$r_{np}^{exp}(A) = \frac{A}{N}\left[\Delta r_m^{exp} - \Delta r_{ch}^{exp} + \Delta r_e + \frac{1}{2} r_{np}\ (^{40}Ca)\right] \qquad (13)$$

and we will assume that $r_{np}(^{40}Ca)$ is accurately given by the theoretical value of -0.056fm. The values of Δr_{ch}^{exp} are taken from Table 2 and Δr_e is the calculated correction due to the neutron charge distribution and valence spin-orbit corrections. The adopted values of Δr_m^{exp} from Table 5 are used to obtain the value of r_{np}^{exp} given in Table 6.

It is interesting to notice that the value of

$$r_{np}^{exp}\ (^{48}Ca) = 0.11 \pm 0.04 \text{ fm}$$

which we have arrived at is smaller than any value quoted previously (Igo et al 1979); we have tried to combine the most accurately measured quantities with what we believe are well determined theoretical corrections and this has not previously been done.

The interaction of pions with nuclei gives new information; however, the optical model analyses are yet at a primitive stage and theere are large uncertainties in the densities extracted from these experiments (Sternheim and Yoo 1978). However, analyses have been attempted and values for the change in neutron radius Δr_n are given in

Table 7. Also we give the result obtained from a combination of the experimental quantities Δr_m and Δr_{ch} with the relation

$$\Delta r_n^{exp} = 2\Delta r_m^{exp} - \Delta r_{ch}^{exp} + \Delta r_e - \frac{(N-Z)}{A} r_{np} \quad (^{48}Ca) \qquad (14)$$

and using the theoretical value of $r_{np}(^{48}Ca)=0.168$fm (note that this last term is a small quantity).

There is a final category of experiments with which it is interesting to compare our calculations, namely those which are sensitive to the density of a particular orbit. The cross sections for one-nucleon transfer are very sensitive to the RMS radius of the orbit of a particular nlj from which the transfer takes place. If one has an independent estimate of the spectroscopic factors involved one can extract relative RMS radii such as those between different nuclei in the $1f_{7/2}$ shell or those between $T_<$ and $T_>$ states of a given nucleus. Sub-Coulomb heavy-ion transfer experiments are particularly useful since the trajectories can be accurately calculated. In particular, the one-neutron transfer reactions (^{13}C,^{12}C) and (^{17}O,^{16}O) have been used to obtain absolute RMS radii of valence orbits. (Jones et al 1974, Durell et al 1976 1977, Franey et al 1979). Finally the electron scattering experiments have determined magnetic form factors of odd-even nuclei from which the highest multipole component has been used to extract radii for the odd particle (de Witt Huberts et al 1977 and de Witt Huberts 1978).

Results from the experimental analyses are given in Table 8. We should remark on some of the uncertainties in these analyses which are not included in the errors. The sub-Coulomb (^{17}O, ^{16}O) and (^{13}C, ^{12}C)

reactions must be "calibrated", that is the amplitudes of the $^{17}O+^{16}O+n$ and $^{13}C+^{12}C+n$ parts of the reaction must be known if one wants to extract information on the target. Due to a change in this calibration (Franey et al 1979) the values for the $1d_{5/2}$ and $2s_{1/2}$ radii quoted by Durell et al (1977) have been increased by about 10% (Durell 1978) and the new values are quoted in Table 8.

For the magnetic electron scattering, corrections for core-polarization and mesonic exchange effects must be taken into account. Since the RMS radii are determined primarily from the shape and not the magnitude of the high-q form factor data, any correction which is equivalent to a q-independent (but perhaps λ-dependent) renormalization will not be important for the extracted radii. The core-polarization calculations which have been carried out thus far (Arima et al 1978, Arita 1977) give relatively large (up to about 30%) but q-independent quenchings (for a given λ) and hence the effect on the extracted radii is small (less than 1%) (deWitt Huberts 1978). Calculations of the mesonic exchange effects on the other hand give a more q-dependent renormalization (Arima et al 1978, Dubach 1978). In the simple cases of A=17 ($d_{5/2}$) and A=41 ($f_{7/2}$) it was found that for neutrons (protons) the extracted RMS radii were about 2.5% (1.5%) larger when mesonic exchange is included than they were when mesonic exchange is not included (deWitt Huberts 1978). The electron scattering RMS radii given in Table 8 do not include the core-polarization and mesonic-exchange corrections.

The comparison between experiment and theory is in general good but there is a systematic tendency for the experimental radii to be a few percent smaller than those calculated. For the radii obtained from

magnetic electron scattering the estimates quoted above for the mesonic exchange correction would bring all experimental results within about 2% of the theoretical calculations. To be certain that this is not due to a calibration problem in the one-nucleon transfer experiments it would be interesting to measure the radius of a hole orbit, for example by a $^{40}Ca+^{39}Ca$ reaction. The RMS radius of the $d_{3/2}$ orbit in ^{40}Ca should be closer to the average RMS radius and hence there is less theoretical uncertainty. The calculated value is $r_n(d_{3/2})=3.649$fm and $r_n(d_{3/2})/r_n=1.098$ (in the harmonic oscillater limit $r_n(d)/r_n=1.080$).

The largest anomaly in Table 8 is in the comparison of the change in the $1f_{7/2}$ neutron radius between ^{48}Ca and ^{40}Ca from the (d,t) and (t,d) reactions (Friedman et al 1977) which gives 0.17±0.03fm compared with the calculated value of -0.026fm.

It should be mentioned here that a 2-6% change in the valence radius would have little effect on the calculated Coulomb energy differences between mirror nuclei. The dependence of the direct term in the Coulomb energy on the RMS radii is approximately given by (Brown et al 1979)

$$\Delta E_c = \frac{6}{5}\frac{e^2 Z}{R}\left\{1 - \frac{1}{4}\left[\frac{r_v^2}{r_{ch}^2} - 1\right]\right\} \qquad (15)$$

where $R= (5/3)^{1/2} r_{ch}$ and r_v is the rms charge radius of the valence orbit. From this equation it is easy to see that in order to explain a 10% anomaly in ΔE_c one needs to change r_v by at least 20% as concluded by Nolen and Schiffer. In addition the core polarization contribution tends to reduce the dependence of ΔE_c on r_v (Auerbach 1974) and in the

limit of $r_n=r_p$ (Friedman and Schlomo 1977, Schlomo and Friedman 1977) $\Delta E_c \to 6e^2Z/5R$ which is the classical liquid drop limit and does not depend at all on r_v.

The model for calculating nuclear densities presented in this paper is in several respects complementary to the Hartree-Fock method. The present model takes full account of the complex configuration mixing found in light nuclei but is only semi-selfconsistent because we only allow the potential to vary linearly with the density. In Hartree-Fock the density is fully self-consistent but the configuration is restricted to a single Slater-determinanent with the particles in the lowest spherical or deformed configuration. For most of the nuclei we have considered the results using the linear density approximation are in good agreement with the Hartree-Fock method when we confine ourselves to the closed shell configurations assumed in Hartree-Fock. However, the experimental density differences are not well reproduced by these closed-shell calculations and we have found much better agreement by allowing excitations out of the closed shells.

The charge densities are mainly sensitive to the proton occupations and these can also be obtained from one-proton transfer reactions. For the Ca isotopes the proton occupations determined from the charge densities are consistent with the one-proton transfer data. However it is not possible to calculate accurate charge densities based on the one-proton transfer data because of the inconsistency between occupations obtained from stripping and pickup reactions which exists at present. We plan to investigate this problem further in order to understand whether this inconsistency is due to problems with the form factor or problems with the sum rule analysis.

To illustrate the present status of our knowledge about neutron densities it is interesting to summarize all results for ^{40}Ca and ^{48}Ca including the RMS radii of the $1f_{7/2}$ valence neutrons. In table 9, typical experimental results are compared with the present calculation as well as with Hartree-Fock calculations (Lane et al 1978). Our results are very similar to the Skryme IV Hartree-Fock calculation. The Skryme III calculation gives some interesting differences which are in slightly better agreement with experiment. The only theoretical value given in Table 9 which is very sensitive to the ^{40}Ca core excitations is the quantity Δr_n. If we regard the present calculations as a correction to the Hartree-Fock results then the best theoretical estimate is $\Delta r_n(\text{SkIII})+[\Delta r_n(\text{IIB})-\Delta r_n(\text{IIA})]=0.21\text{fm}$ which is in better agreement with the experimental determination.

TABLE 1

Experimental and calculated Barrett radii for calcium isotopes

	Exp[a]				Th(IIA)	Th(IIB)
	α	k	R_k	$\langle r^k e^{-\alpha r}\rangle$	$\langle r^k e^{-\alpha r}\rangle$	$\langle r^k e^{-\alpha r}\rangle$
^{40}Ca	0.065	2.114	4.4609(12)	10.871(6)	10.897	10.851
^{42}Ca	0.065	2.114	4.4998(13)	11.049(6)	10.949	11.052
^{44}Ca	0.065	2.114	4.5126(13)	11.108(6)	10.995	11.091
^{46}Ca	0.065	2.114	4.4881(45)	10.996(21)	11.037	10.972
^{48}Ca	0.065	2.114	4.4621(12)	10.877(6)	11.074	10.865

a) Wohlfahrt et al (1978a)

TABLE 2

RMS charge radii for calcium isotopes

	Exp			Th(IIA)	Th(IIB)
	(e,e)	μ atom	μ atom		
	r_{ch}	$(r_{ch})_{\mu}^{F}$ a)	$(r_{ch})_{\mu}^{IIB}$ b)	r_{ch}	r_{ch}
^{40}Ca	3.474(3) c	3.480	3.479	3.483	3.476
^{42}Ca	3.504 d	3.510	3.510	3.490	3.510
^{44}Ca	3.502 d	3.520	3.518	3.497	3.515
^{46}Ca		3.501	3.497	3.503	3.493
^{48}Ca	3.465(5) c	3.481	3.475	3.509	3.473

a) From the analysis in the references given in footnote (a) in Table 1 based on a Fermi (F) distribution shape.

b) Obtained from Table 1 using the present density shapes given by IIB.

c) Sick (1978).

d) Values normalized to ^{40}Ca from Frosch et al (1968).

TABLE 3

Comparison of the number of proton holes in the sd shell obtained from electron scattering ($\Delta+\delta$), pickup reactions [P(fp)], and stripping reactions [H(sd)].

	$\Delta+\delta$	H(sd)[a]	H(sd)[b]	P(fp)[c]	P(fp)[d]
^{40}Ca	0.7	0.4	0.27	0.73	0.3
^{42}Ca	1.7	0.9	1.12	1.03	0.4
^{44}Ca	1.8	1.9	1.98	1.01	0.6
^{46}Ca	1.05	0.4			0.2
^{48}Ca	0.3	0.15	0.44	0	0

a) (^{3}He,d), quoted by v.d.Decken et al (1972)

b) (^{3}He,d), quoted by Doll et al (1976)

c) (d,^{3}He), Doll et al (1976)

d) (t,α), quoted by Dehnhard and Cage (1974)

TABLE 4

Experimental occupation probabilities for ^{40}Ca, ^{42}Ca and ^{44}Ca used for Fig.10. The proton occupation probabilities are from Malaguti et al (1979) and are based on the one-proton transfer data summarized by Doll et al (1976). Simple neutron configurations are assumed.

		n_p	n_n
^{40}Ca	$p_{3/2}$	0.15	0.15
	$f_{7/2}$	0.56	0.56
	$d_{3/2}$	3.59	3.59
	$s_{1/2}$	1.70	1.70
^{42}Ca	$p_{3/2}$	0.15	0.20
	$f_{7/2}$	0.92	1.80
	$d_{3/2}$	3.37	4.00
	$s_{1/2}$	1.56	2.00
^{44}Ca	$p_{3/2}$	0.16	0.40
	$f_{7/2}$	0.83	3.60
	$d_{3/2}$	3.57	4.00
	$s_{1/2}$	1.44	2.00

TABLE 5

RMS matter radius of ^{40}Ca and relative matter radii, $\Delta r_m = r_m(A) - r_m(^{40}Ca)$

	Theory	Experiment					
		(a)	(b)	(c)	(d)	(e)	adopted
^{40}Ca	3.369	3.40(3)	3.39(4)	3.40	3.39	3.38(3)	3.39(3)
^{42}Ca	0.055	0.06			0.08	0.06	0.06(2)
^{44}Ca	0.099	0.08			0.08	0.09	0.08(2)
^{46}Ca	0.123						
^{48}Ca	0.143	0.10	0.12	0.10	0.09	0.12	0.11(2)

(a) 1.05 Gev p; Chaumeaux et al (1978), Table X.

(b) 1.05 GeV p; Brissaud and Campi (1979)

(c) 1 GeV p; Alkhazov et al (1978), Table 6.1.

(d) 0.8 GeV p; Igo et al (1979)

(e) 1.37 GeV α; Alkhazov et al (1977)

TABLE 6

Differences between neutron and proton RMS radii, $r_{np}=r_n-r_p$.

	Δr_{ch}[a]	Theory		Experiment[c]
	μ atom	Δr_e[b]	r_{np}	r_{np}
^{40}Ca			-0.056	≡-0.056
^{42}Ca	0.031	0.001	-0.010	0.00(4)
^{44}Ca	0.039	-0.004	0.053	0.02(4)
^{46}Ca	0.018	-0.011	0.116	
^{48}Ca	-0.004	-0.019	0.168	0.11(4)

(a) From column 4 of Table 2

(b) $r_{ch}\equiv r_p+r_e$

(c) Based on the adopted values in Table 5

TABLE 7

Relative RMS neutron radii $\Delta r_n = r_n(A) - r_n(^{40}Ca)$

	Theory	Experiment		
		(a)	(b)	(c)
^{42}Ca	0.079	0.12(4)		
^{44}Ca	0.152	0.09(4)	0.09(5)	0.05(5)
^{46}Ca	0.201			
^{48}Ca	0.240	0.18(4)	0.14(5)	

(a) Based on the adopted values in Table 5.

(b) $\pi^{\pm}$ total cross sections; Jakobson et al (1977)

(c) π^{-} pionic X rays; Batty et al (1979)

TABLE 8

Point RMS radii of valence orbits

	Nucleus	nlj	Theory[a] r (fm)	Exp r (fm)	Exp/Th	Reaction	Reference
Neutrons	^{41}Ca	$1f_{7/2}$	4.096	4.00(9)	0.976(22)	^{40}Ca(^{13}C,^{12}C)	Durell et al (1978)
		$2p_{3/2}$	4.350	4.24(6)[b]	0.975(14)	^{40}Ca(^{13}C,^{12}C)	Durell et al (1978)
	^{49}Ti	$1f_{7/2}$	4.070	4.01(4)	0.985(10)	^{49}Ti(e,e)	deWitt Huberts (1978)
	^{44}Ca-^{40}Ca	$1f_{7/2}$	0.005	-0.02(8)		Ca(^{17}O,^{16}O)	Jones et al (1974)
	^{48}Ca-^{40}Ca	$1f_{7/2}$	-0.026	0.17(3)		Ca(d,t),(t,d)	Friedman et al (1977)
	^{48}Ca-^{40}Ca	$2p_{3/2}$	-0.069	0.06(7)		Ca(^{17}O,^{16}O)	Jones et al (1974)
Protons	^{48}Ca-^{40}Ca	$1f_{7/2}$	-0.113	-0.10(5)		Ca(^{3}He,d)	Friedman et al (1977)
	^{51}V	$1f_{7/2}$	4.093	4.01(4)	0.980(10)	^{51}V(e,e)	deWitt Huberts (1978)

a) Occupation set IIB

b) This is for the 1.94 MeV $3/2^-$ level in ^{41}Ca.

TABLE 9

Comparison of neutron RMS radii in ^{40}Ca and ^{48}Ca

	$r_n(1f_{7/2})$			$r_n - r_p$		r_n
	^{40}Ca	^{48}Ca	^{48}Ca–^{40}Ca	^{40}Ca	^{48}Ca	^{48}Ca–^{40}Ca
Exp	4.00(9)[a]	4.01(4)[b]	0.01(10)		0.11(4)[d]	0.18(4)[e]
			0.17(3)[c]			
Th Present	4.096	4.070	-0.026	-0.056	0.163	0.240
HF SkIII[f]	4.001	4.096	0.095	-0.044	0.138	0.237
HF SkIV	4.153	4.159	0.006	-0.046	0.172	0.254

a) ^{40}Ca(^{13}C,^{12}C) Durell et al (1978)

b) ^{49}Ti(e,e) deWitt Huberts (1978)

c) Ca(d,t) and (t,d) Friedman et al (1977)

d) Table 6

e) Table 7

f) The Hartee-Fock calculations are from Lane et al (1978)

References

Alkhazov G D Bauer T, Bertini R, Bimbot L, Bing O, Boudard A, Bruge G, Catz H, Chaumeaux A, Couvert P, Fontaine J M, Hibou F, Igo G J, Lugol J C and Matoba M 1977 Nucl.Phys. A280, 365

Alkhazov G D, Belostotsky S L and Vorobyov A A 1978 Physics Reports 42C, 89

Arima A, Horikawa Y, Hyuga H and Suzuki T 1978 Phys.Rev.Lett. 40, 1001

Arita K 1977 Proceedings of the International Conference on Nuclear Structure, Tokyo - Contributed Papers p.252

Auerbach N 1974 Nucl.Phys. A229, 447

Batty C J, Biagi S F, Friedman E, Hoath S D, Davies J D, Pyle G J, Squier G T A, Asbury D M and Lem M 1979, Phys.Lett. 81B, 165

Barrett R C and Jackson D F 1977 Nuclear Sizes and Structure Clarendon Press Oxford

Bertozzi W, Friar J, Heisenberg J and Negele J W 1972 Phys.Lett. 41B, 408

Brissaud I, Le Bornec Y, Tatischeff B, Bimbot L, Brussel M K and Duhamel G 1972, Nucl.Phys. A191, 145

Brissaud I and Campi X 1979 preprint

Brown B A, Massen S E and Hodgson P E 1979 unpublished

Campi X and Sprung D W 1972 Nucl.Phys. A194, 401

Chandra H and Sauer G 1976 Phys.Rev. C13, 245

v.d. Decken A, Dehnhard D, Goldschmidt M, Reiter W, Rieck D, Saathoff W and Wiedner C A 1972 Phys.Lett. 41B, 477

Dehnhard D and Cage M E 1974 Nucl.Phys. A230, 393

deWitt Huberts P K A, Lapikas H, De Vries H, Bellicard J B, Cavedon J M, Frois B, Huer M, Leconte Ph, Nakada A, Phan Xuan Ho, Platchkovsk and Sick I 1977 Phys.Lett. 71B, 317

deWitt Huberts P K A 1978 Proceedings of the Conference on Modern Trends in Elastic Electron Scattering, Amsterdam, p.21

Doll P, Wagner G J, Knöpfle K T and Mairle G 1976 Nucl.Phys. A263, 210

Dubach J 1978 preprint

Durell J L, Buttle P J A, Goldfarb L J B, Phillips W R, Jones G D, Hooton B W and Ivanovich M 1976 Nucl.Phys. A269, 443

Durell J L, Harter C and Phillips W R 1977 Phys.Lett. 70B, 405

Durell J L 1978 private communication

Elton L R B 1967 Phys.Rev. 158, 970

Elton L R B and Webb S J 1970 Phys.Rev.Lett. 24, 145

Federman P and Pittel S 1969 Phys.Rev. 186, 1106

Flowers B H and Skouras L D 1969 Nucl.Phys. A136, 353

Fortune H T and Cobern M E 1978 Phys.Lett. 77B, 21

Franey M, Lilley J S and Phillips W R 1979 to be published

Friedman E and Shlomo S 1977 Z.Phys. A283, 67

Friedman E, Gils H J, Rebel H and Majka Z 1978 Phys.Rev.Lett. 41, 1220

Frois B 1978 Proceedings of the Conference on Modern Trends in Elastic Electron Scattering Amsterdam, p.1

Frosch R F, Hofstadter R, McCarthy J S, Nöldeke G K, van Oostrum K J, Yearian M R, Clark B C, Herman R and Ravenhall D G 1968 Phys.Rev. 174, 1380

Gerace W J and Green A M 1967 Nucl.Phys. A93, 110; 1969 Nucl.Phys. A123, 241

Gibson B F and Van Oostrum K J 1967 Nucl.Phys. A90, 159

Gräf H D, Feldmeier H, Manakos P, Richter A, Spamer E and Strottman D 1978 Nucl.Phys. A295, 319

Igo G, Adams G S, Baur T S, Pauletta G, Whitten C A, Wreikat A, Hoffmann G W, Blanpied G S, Coker W R, Harvey C, Liljestrand R P, Ray L, Spencer J E, Thiessen H A, Glashausser C, Hintz N M, Oothoudt M A, Nam H, Seth K K, Wood B E, McDaniels D K and Gazzaly M 1979 Phys.Lett. 81B, 151

Jakobsen M J, Burleson G R, Calarco J R, Cooper M D, Hagerman D C, Halpern I, Jeppeson R H, Johnson K F, Knutson L D, Marrs R E, Meyer H O and Redwine R P 1977 Phys.Rev.Lett. 38, 1201

Jones G D, Durell J L, Lilley J S and Phillips W R 1974 Nucl.Phys. A230, 173

Lane A M, Martorell J, Zamick L 1978 unpublished

Malaguti F, Uguzzoni A, Verondini E and Hodgson P E 1978 Nucl.Phys. A297, 287; 1979 to be published

McGrory J B, Wildenthal B H and Halbert E C 1970 Phys.Rev. C2, 186

Moalem A, van Hienen J F A and Kashy E 1978 Nucl.Phys. A 307 (1978) 277

Negele J W 1970 Phys.Rev. C1, 1260

Nolen J A and Schiffer J P 1969 Ann.Rev.Nucl.Sci. 19, 471

Ray L, Rory Coker W and Hoffman G W 1978b Phys.Rev. C18, 2641

Sakakura M, Arima A and Sebe T 1976, Phys.lett. 61B, 335

Seth K K, Saha A, Benenson W, Lanford W A, Nann H and Wildenthal B H 1974 Phys.Rev.Lett. 33, 233

Sick I 1974a Phys.Lett. 53B, 15; 1974b Nucl.Phys. A218, 509; 1978 private communication

Shlomo S and Friedman 1977 Phys.Rev.Lett. 39, 1180

Soper J M 1968 Isospin in Nuclear Physics edited by D.H.Wilkinson (North Holland) p.229.

Sternheim M M and Yoo K-B 1978 Phys.Rev.Lett. 41, 1781

Towsley C W, Cline D and Horoshko R N 1973 Nucl.Phys. A204, 574

de Voight M J A, Cline D and Horoshko R N, 1974 Phys.Rev. C10, 1798

Wohlfahrt H D, Shera E B, Hoehn M V, Yamazaki Y, Fricke G and Steffen R M 1978a Phys.Lett. 73B, 131; 1978b private communication

Figure Captions

1) Experimental and theoretical charge densities of ^{40}Ca. The two experimental curves correspond to the form factor ambiguity discussed by Sick (1974a, 1978). IIA and IIB refer to the calculations with closed shell and non-closed shell configurations, respectively.

2) Experimental charge density difference between ^{48}Ca and ^{40}Ca obtained by electron scattering. The solid curve is from the model-dependent fit to the data by Frosch et al (1968) and the two dashed curves are from the model-independent fits of Sick (1974a, 1978) corresponding to the ambiguity in the ^{40}Ca data shown in Fig.1.

3) Experimental and theoretical charge density differences between ^{42}Ca and ^{40}Ca. The experimental curve is from the model-dependent fit to the electron scattering data by Frosch et al (1968). The three theoretical curves correspond (1) to a closed sd shell configuration, (2) to a non-closed sd shell configuration with 10% $2p_{3/2}$ and (3) to a non-closed sd shell configuration with 20% $2p_{3/2}$.

4) Experimental and theoretical charge density differences between ^{44}Ca and ^{40}Ca (see caption to Fig.3).

5) Theoretical charge density differences between ^{48}Ca and ^{40}Ca. For curves (1) and (2) a closed sd shell for both ^{48}Ca and ^{40}Ca is assumed and for curve (3) sd shell core excitations are allowed for. For (1) the valence neutrons are in a pure $(1f_{7/2})^8$

configuration and for (2) a configuration with 90% $1f_{7/2}$ and 10% $2p_{3/2}$ has been used.

6) Comparison between the present calculation and the Hartree-Fock calculation of Negele (1970). The same assumption for the shell model configuration, namely $(1f_{7/2})^8$ for the valence neutrons, has been made in both calculations.

7) Spin-orbit correction to the charge density difference between ^{48}Ca and ^{40}Ca. Curve (1) was obtained using a pure $(1f_{7/2})^8$ configuration and curve (2) was obtained using a configuration with 90% $1f_{7/2}$ and 10% $2p_{3/2}$.

8) Experimental and theoretical charge density difference between ^{48}Ca and ^{40}Ca. Curve (1) is from Fig.2, and curve (2) is from Fig.5.

9) Theoretical charge density difference between ^{46}Ca and ^{40}Ca.

10) Theoretical charge density differences between ^{44}Ca and ^{40}Ca and between ^{42}Ca and ^{40}Ca as calculated using the experimental occupation probabilities given in Table 4 and discussed in the text.

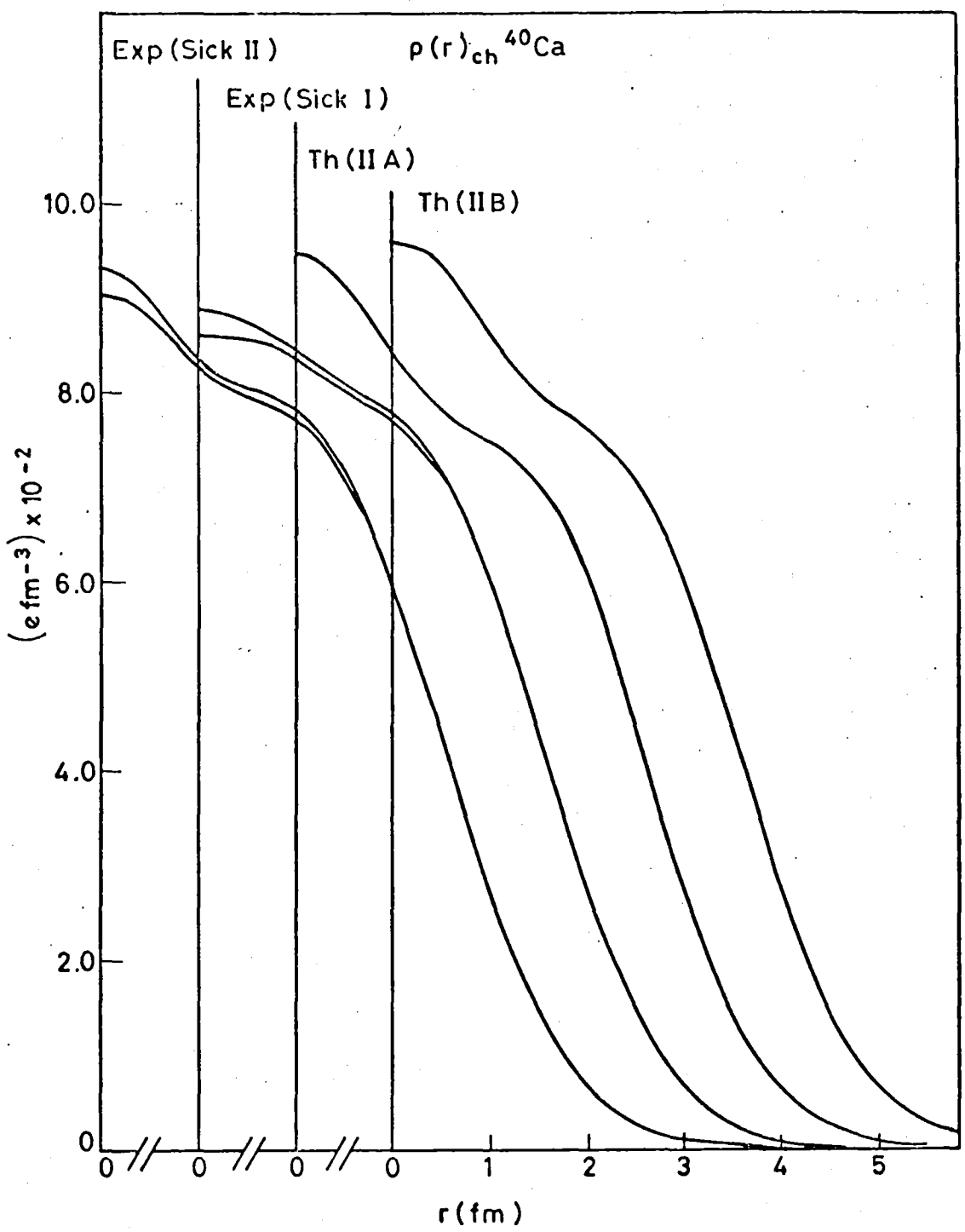
Exp (Sick II)
ρ(r)ch 40Ca
Exp (Sick I)
Th (II A)
Th (II B)
10.0
8.0
6.0
4.0
2.0
0
(e fm-3) x 10-2
0
0
0
0
1
2
3
4
5
r (fm)

Figure 1

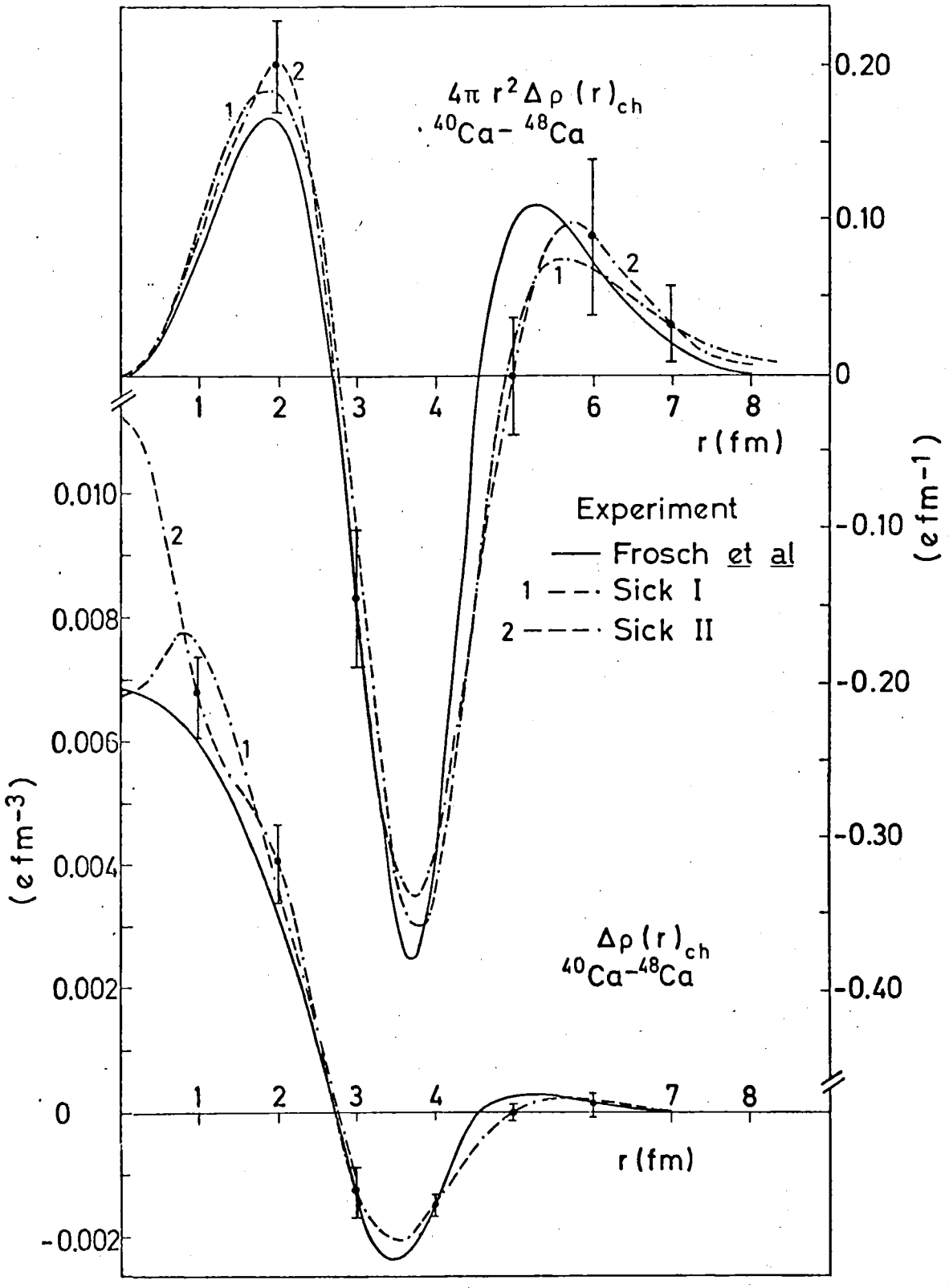
$4\pi r^2 \Delta\rho(r)_{ch}$
$^{40}Ca - ^{48}Ca$
0.20
0.10
0
1
2
3
4
6
7
8
r (fm)
Experiment
Frosch et al
1 Sick I
2 Sick II
0.010
0.008
0.006
0.004
0.002
0
-0.002
(e fm^{-3})
-0.10
-0.20
-0.30
-0.40
(e fm^{-1})
$\Delta\rho(r)_{ch}$
$^{40}Ca - ^{48}Ca$
r (fm)

Figure 2

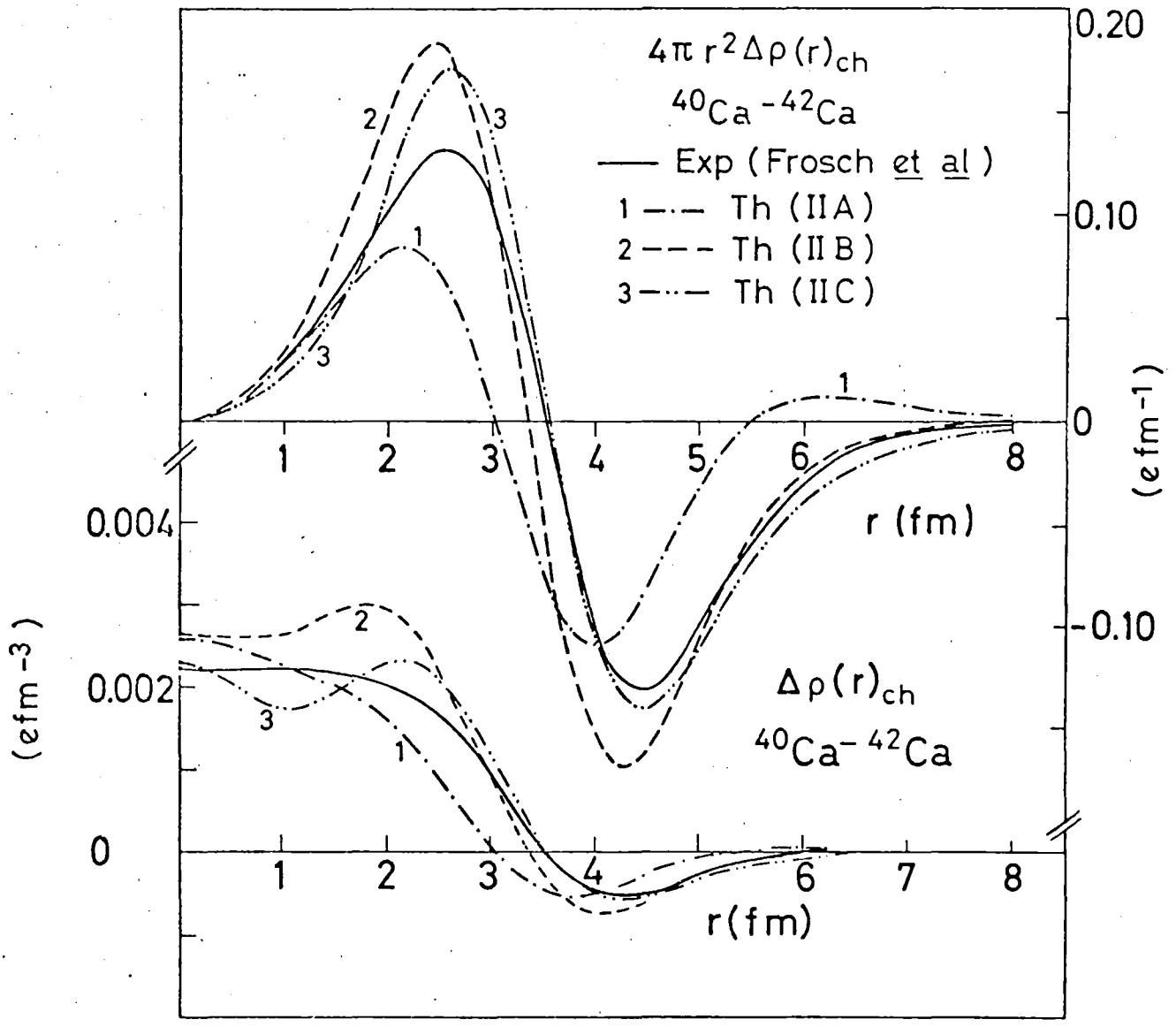
$4\pi r^2 \Delta\rho(r)_{ch}$
$^{40}Ca - ^{42}Ca$
Exp (Frosch et al)
1 Th (IIA)
2 Th (IIB)
3 Th (IIC)
0.20
0.10
0
-0.10
(efm^{-1})
r (fm)
0.004
0.002
0
(efm^{-3})
$\Delta\rho(r)_{ch}$
$^{40}Ca - ^{42}Ca$
r(fm)

Figure 3

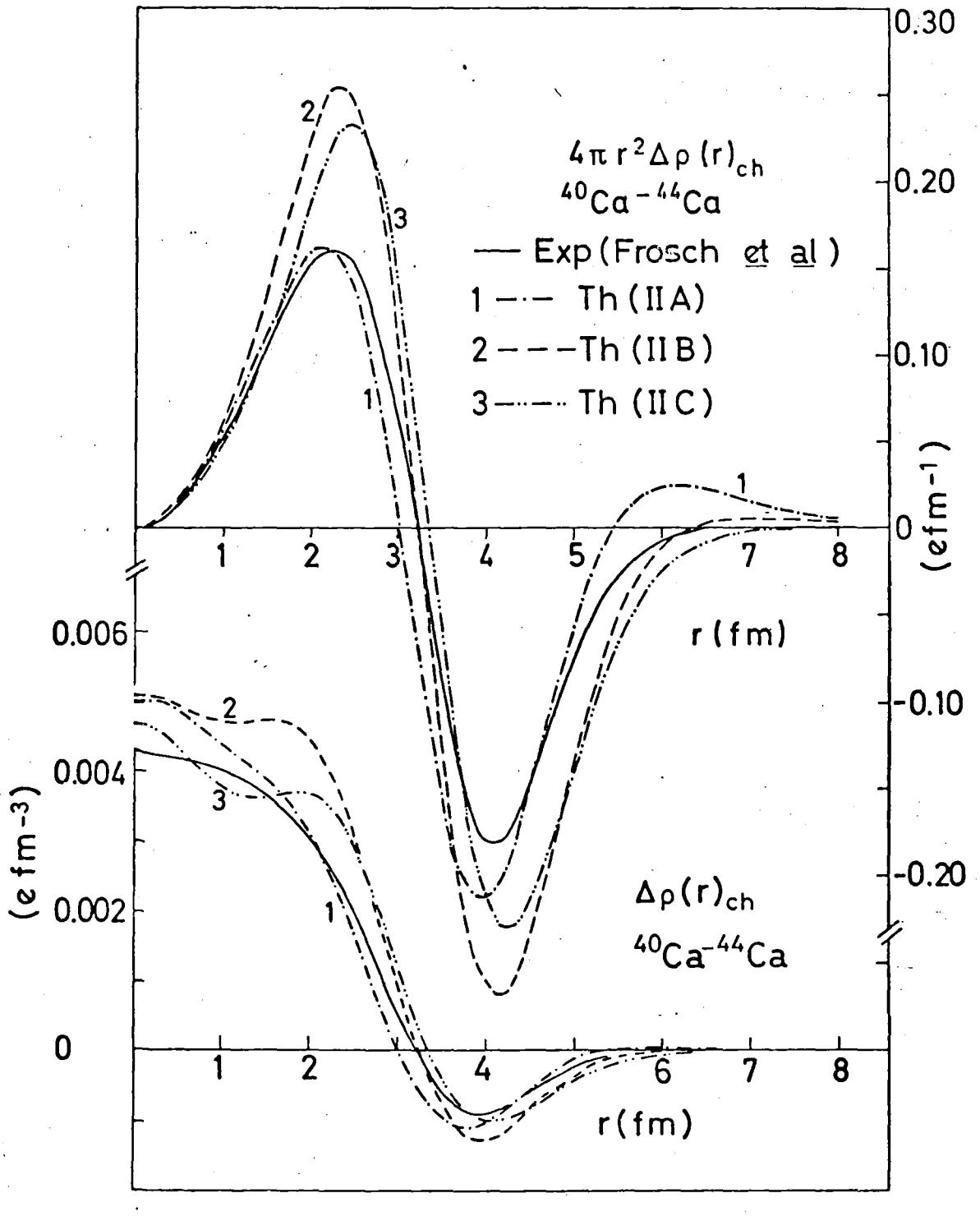
$4\pi r^2 \Delta\rho(r)_{ch}$
$^{40}Ca - ^{44}Ca$
Exp (Frosch et al)
1 Th (IIA)
2 Th (IIB)
3 Th (IIC)
r (fm)
$(e\,fm^{-1})$
$\Delta\rho(r)_{ch}$
$^{40}Ca - ^{44}Ca$
r (fm)
$(e\,fm^{-3})$

Figure 4

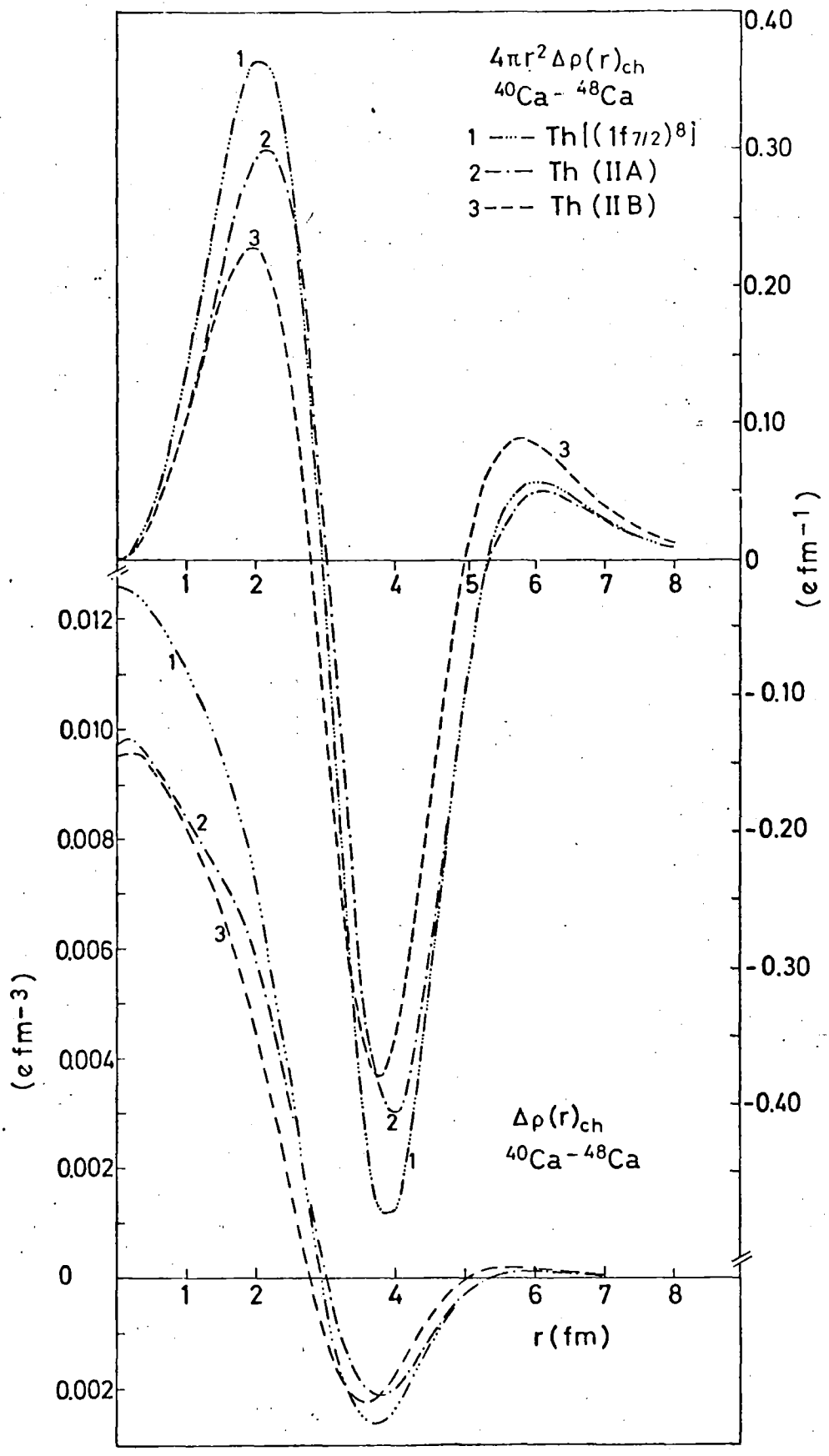
$4\pi r^2 \Delta\rho(r)_{ch}$
$^{40}Ca - ^{48}Ca$
1 —·— Th[$(1f_{7/2})^8$]
2 —·— Th (IIA)
3 --- Th (IIB)
$\Delta\rho(r)_{ch}$
$^{40}Ca - ^{48}Ca$
(e fm^{-3})
(e fm^{-1})
r (fm)
0.012
0.010
0.008
0.006
0.004
0.002
0
0.40
0.30
0.20
0.10
-0.10
-0.20
-0.30
-0.40
1
2
3
4
5
6
7
8

Figure 5

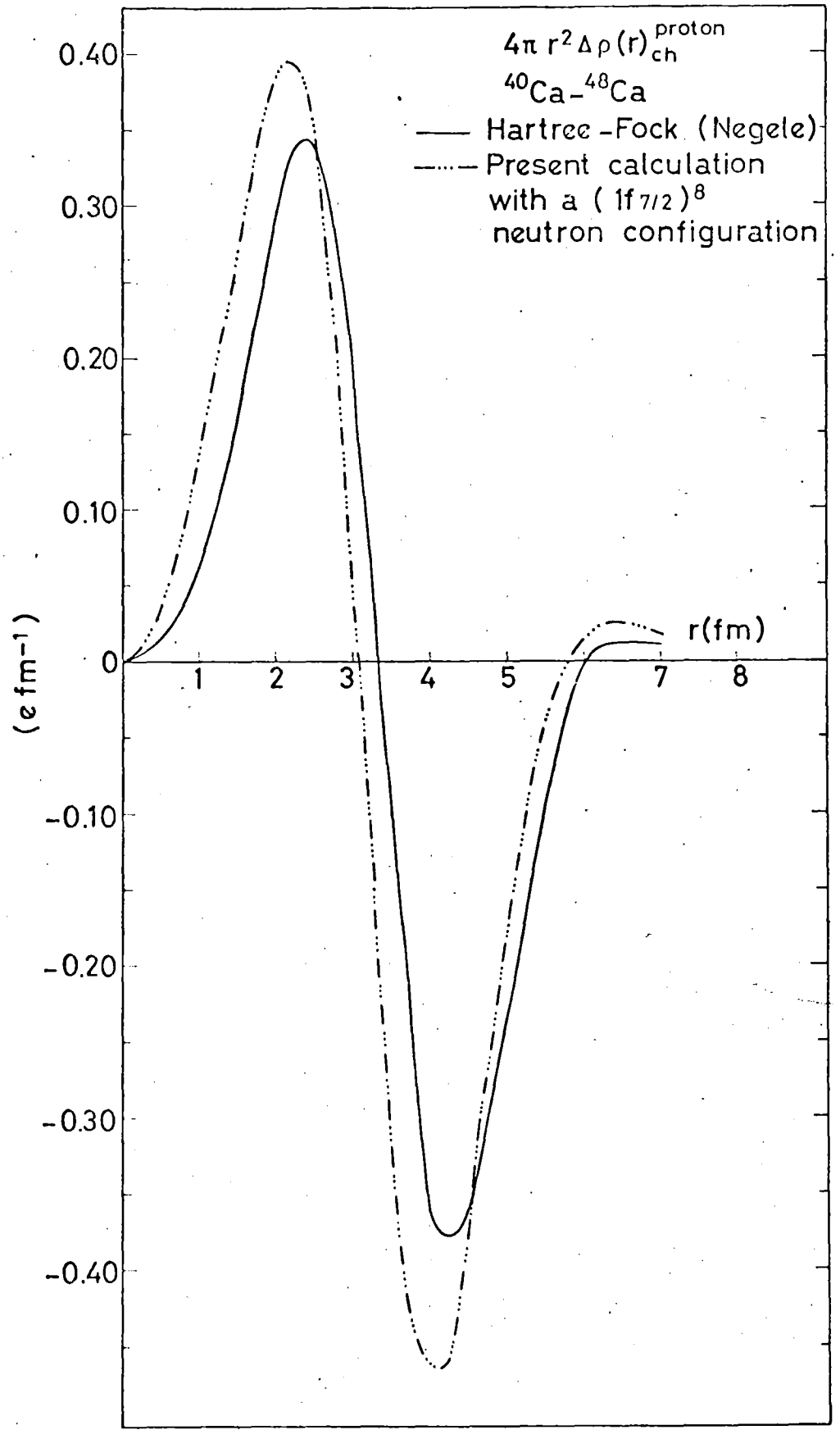
$4\pi\, r^2 \Delta\rho(r)^{proton}_{ch}$
$^{40}Ca - ^{48}Ca$
Hartree-Fock (Negele)
Present calculation with a $(1f_{7/2})^8$ neutron configuration
0.40
0.30
0.20
0.10
0
-0.10
-0.20
-0.30
-0.40
(e fm^{-1})
r(fm)
1
2
3
4
5
7
8

Figure 6

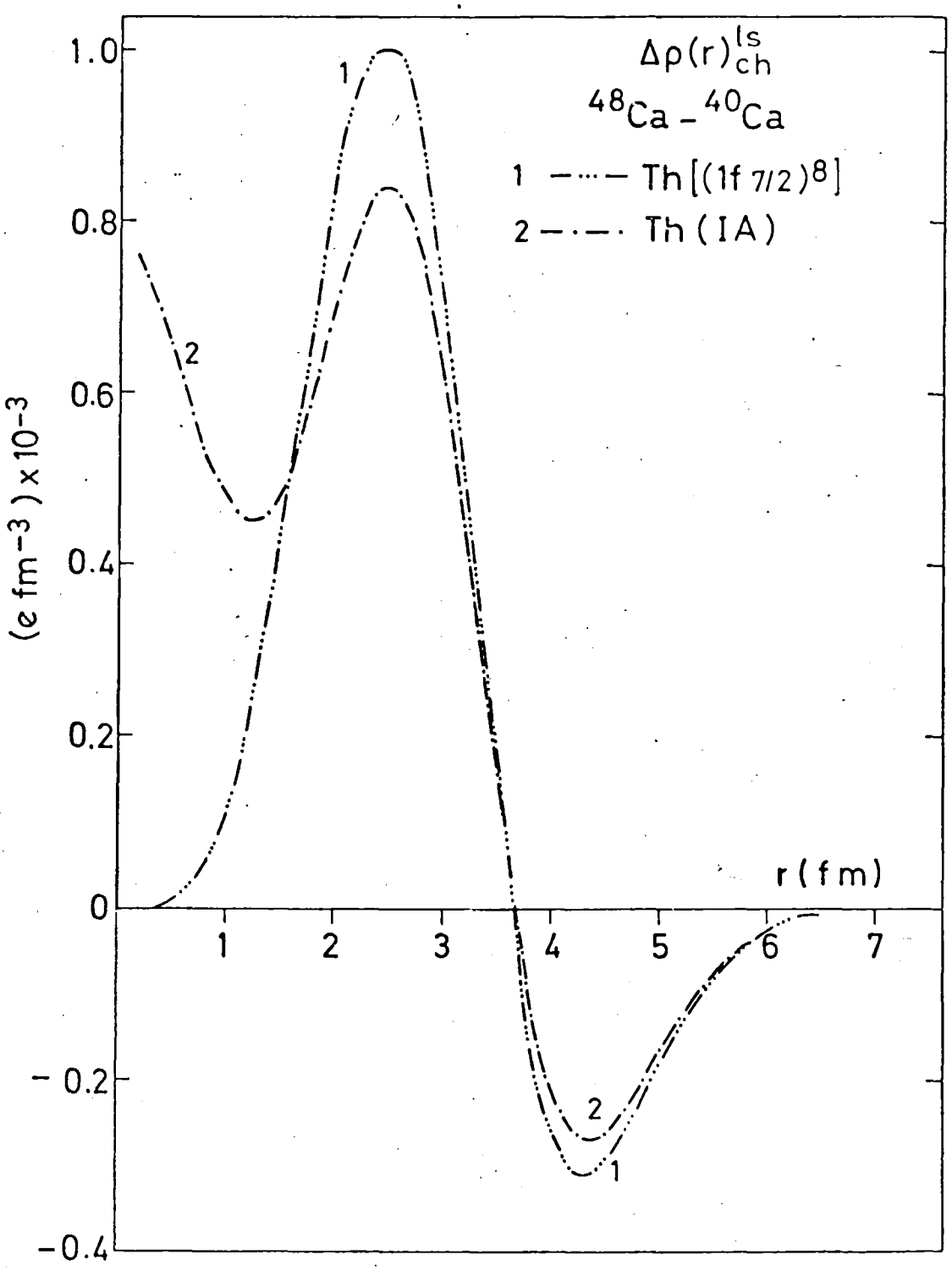
$\Delta\rho(r)^{ls}_{ch}$
$^{48}Ca - ^{40}Ca$
1 — Th [(1f 7/2)^8]
2 — Th (IA)
$(e\,fm^{-3}) \times 10^{-3}$
r (fm)
1.0
0.8
0.6
0.4
0.2
0
- 0.2
-0.4
1
2
3
4
5
6
7

Figure 7

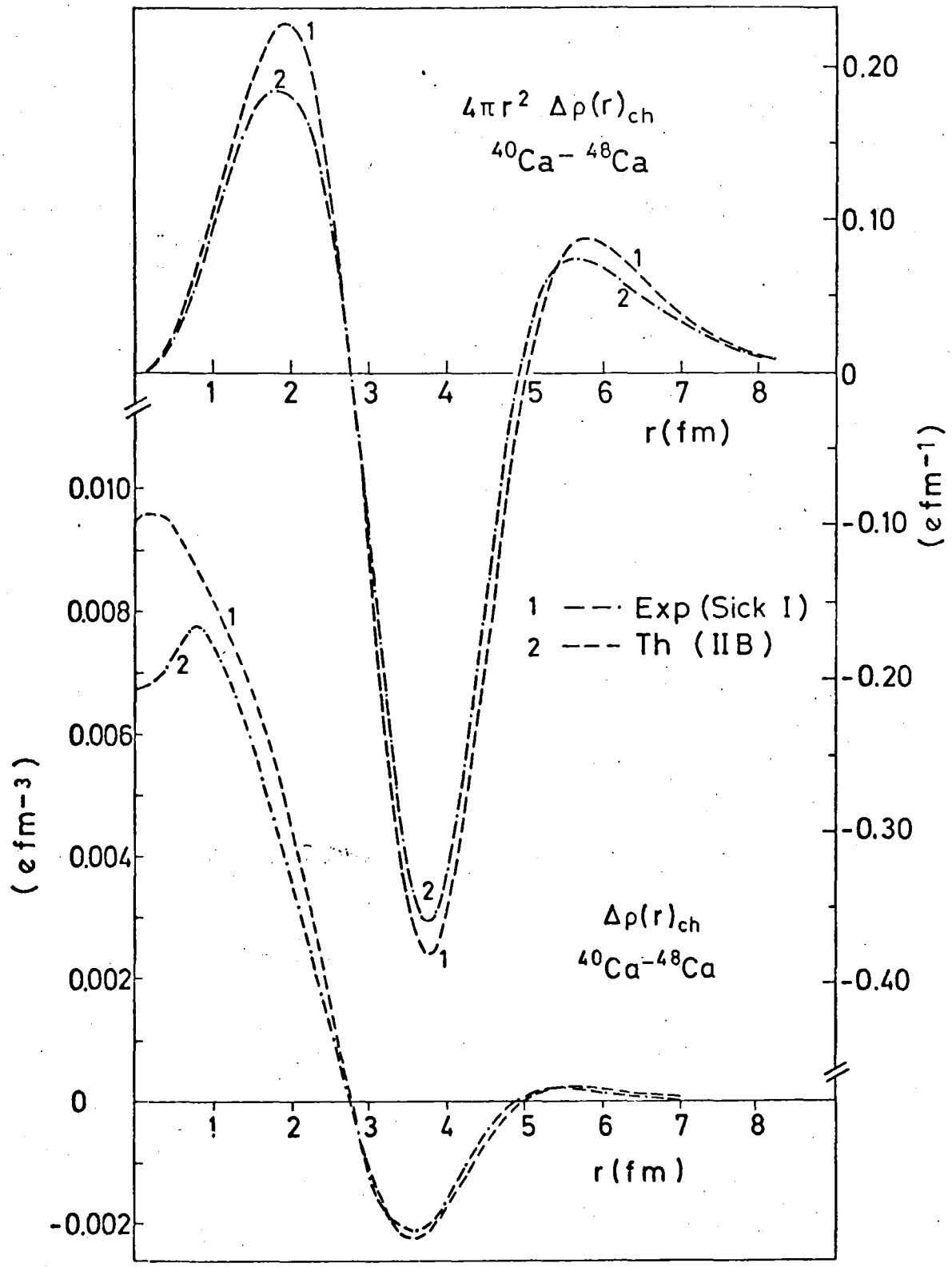
$4\pi r^2 \Delta\rho(r)_{ch}$
$^{40}Ca - ^{48}Ca$
r(fm)
1 —·— Exp (Sick I)
2 --- Th (IIB)
$\Delta\rho(r)_{ch}$
$^{40}Ca - ^{48}Ca$
(e fm^{-3})
(e fm^{-1})
0.010
0.008
0.006
0.004
0.002
0
-0.002
0.20
0.10
-0.10
-0.20
-0.30
-0.40
1 2 3 4 5 6 7 8

Figure 8

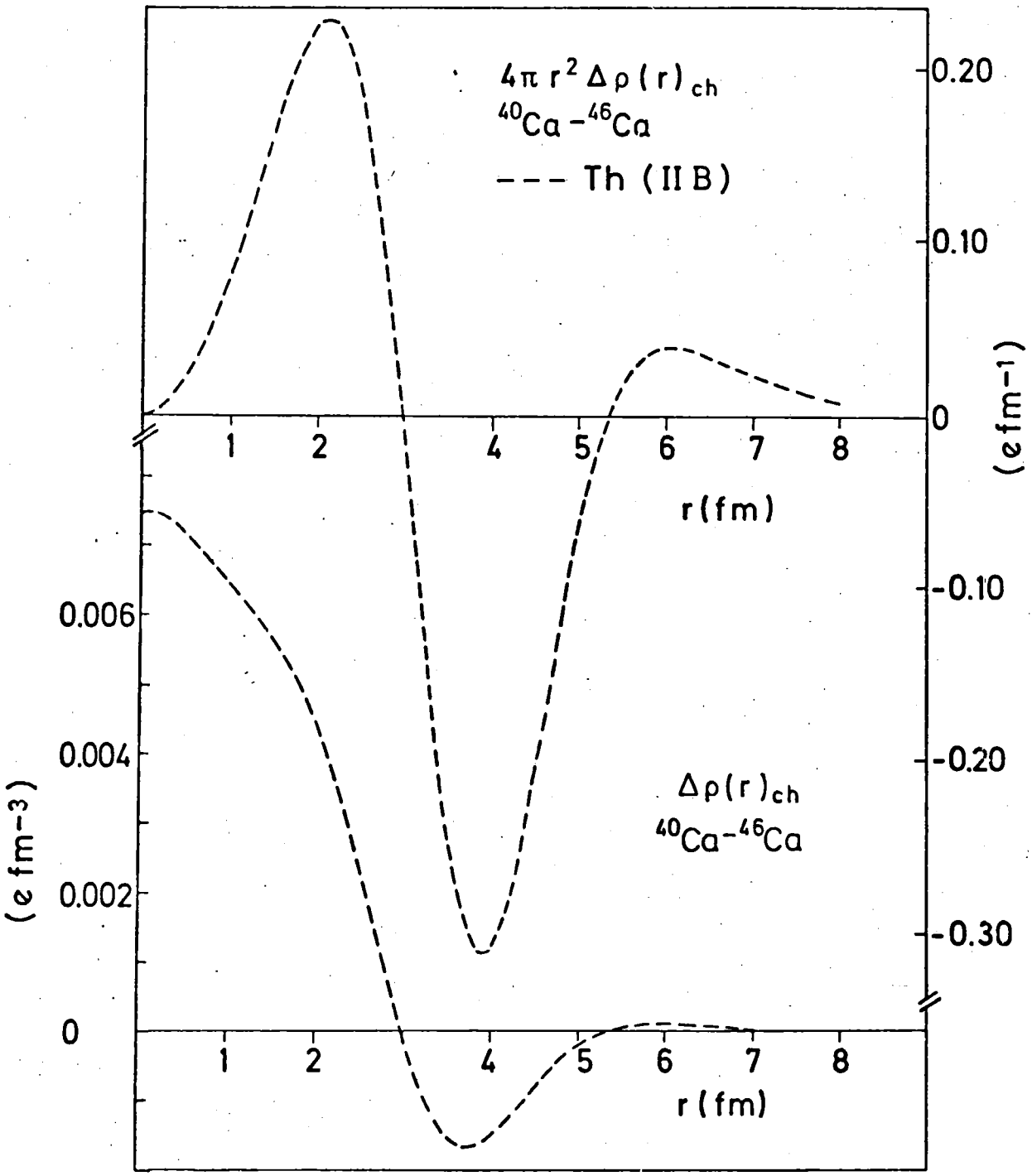
$4\pi r^2 \Delta\rho(r)_{ch}$
$^{40}Ca - ^{46}Ca$
--- Th (II B)
0.20
0.10
0
(e fm^{-1})
1
2
4
5
6
7
8
r(fm)
0.006
0.004
0.002
0
(e fm^{-3})
$\Delta\rho(r)_{ch}$
$^{40}Ca - ^{46}Ca$
-0.10
-0.20
-0.30
1
2
4
5
6
7
8
r(fm)

Figure 9

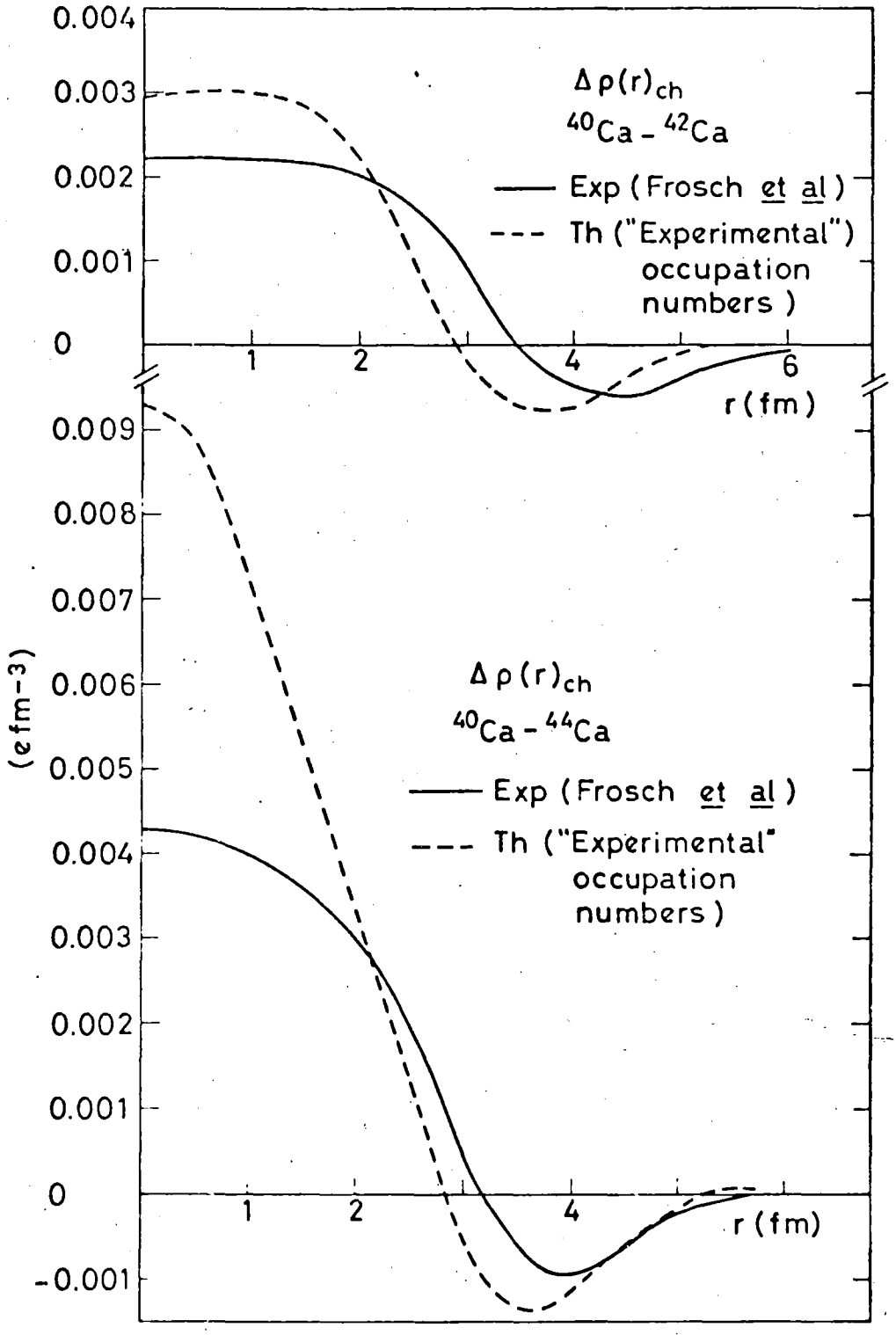
0.004
0.003
0.002
0.001
0
Δρ(r)ch
40Ca - 42Ca
Exp (Frosch et al)
Th ("Experimental" occupation numbers)
1
2
4
6
r (fm)
0.009
0.008
0.007
0.006
0.005
0.004
0.003
0.002
0.001
0
-0.001
(e fm-3)
Δρ(r)ch
40Ca - 44Ca
Exp (Frosch et al)
Th ("Experimental" occupation numbers)
1
2
4
r (fm)

Figure 10

REVIEW OF THEORETICAL RESULTS

R.C. Barrett
University of Surrey,
Guildford, England

REVIEW OF THEORETICAL RESULTS

R.C. Barrett
University of Surrey
Guildford, U.K.

1. Introduction

I realized with some surprise recently that about 10 years have already elapsed since I gave a talk on "Shapes of Nuclei" at the Montreal conference on Properties of Nuclear States (Barrett 1969). A casual glance at the situation pertaining then showed quite a few similarities with the present state of affairs: purely theoretical calculations could be carried out to produce proton and neutron densities which would fit the electron scattering, hadron scattering and other experimental results. These "successful" calculations were done using the single particle shell model (SPSM), and the few Hartree-Fock (HF) or Mean Field Approximation (MFA) calculations which were being displayed gave poor fits to electron scattering. Since that time there have been many revolutions in theory and experiment and, particularly, in the analysis of experiments to deduce charge distributions. We have heard about some of the most sophisticated of these as applied to nuclei of the Ca- region discussed during the last three days. The general techniques of obtaining both theoretical and "experimental" charge distributions have been reviewed and updated regularly during the last few years (e.g. Negele 1976, 1977, 1978; Frois 1978, Barrett 1974; Barrett and Jackson, 1977). Nowadays the "experimental" charge densities are produced with convincing error estimates due to the innovations of workers such as Lenz (1969), Friar and Negele (1973, 1975) and Sick (1973). In addition the accuracy of experiments such as those described by Wohlfahrt (1979) means that root mean square radii are known to an accuracy of a few hundredths of a fermi (and the model-independent radii to about 0.001 fm!). This kind of accuracy means that the theorists are left far behind. It is not possible to obtain densities to anything like this accuracy using the HF approximation. It is very much to be hoped however that it will be possible to use the A-particle non-relativistic Hartree-Fock calculation as starting point and obtain corrections due to correlations, relativistic effects and exchange currents as small perturbations. We shall discuss these corrections in the next sections.

When we consider matter densities or neutron densities the picture is completely different. The task of deducing ρ_m (r) from hadron experiments is very much more difficult and there have been hardly any attempts to obtain model- independent densities or radii except fairly recently in the case of proton and α-scattering experiments. This is a pity because it is possible to state what properties of the density are being measured by π-scattering for example, by carrying out a model-independent analysis. If the resulting error bars are 100% or greater this does not mean that they should not be published.

We now consider the developments in probing individual orbits by magnetic scattering. Dramatic developments in this subject have been reported by de Witt Huberts (1978), Lapikas (1978) and Sick (1979). Although it is not possible to obtain densities of valence neutrons and protons with anything like the accuracy of total charge densities, (certainly not in a model-independent way) we do obtain a very interesting test of the HF wave functions obtained using effective forces, and are able to probe neutron wave functions directly.

In §2 we discuss the single particle shell model, in §3 the Hartree-Fock or mean field approximation, in §4 corrections to the mean field approximation and in §5 some examples and conclusions.

2. The Single Particle Shell Model

The earliest attempts to fit electron scattering with anything other than a simple "model density" or parametrized shape met with a fair measure of success (Elton and Swift, 1967). A Woods-Saxon potential was constrained to fit separation energies but its parameters were otherwise allowed to vary freely so that the densities fitted electron scattering. This was easy to do at first when the experimental range of momentum transfer q was not too large but became increasingly difficult as higher energy experiments were done. Eventually new parameters had to be introduced, namely the occupation numbers of the single-particle orbits (Elton and Webb, 1970). It is reasonable to vary these because of the 2p-2h (two-particle: two-hole) and 4p-4h correlations. The main objection of this approach is the large number of parameters which have to be adjusted and the fact that they do not vary smoothly with N or Z.

Some interesting new calculations have been carried out by Brown et al. (1979). They use a single-particle "self-consistent local potential based on the optical model". The depth of the real part of the optical model can be fitted globally over a range of targets by the formula (Becchetti and Greenlees 1969)

$$U = 54 + 24.0\ (N-Z)/A + 0.4/A^{1/3} - 0.32\ E.$$

The second term is from the isospin dependence and would have the opposite sign for neutron scattering. Brown et al. consider the first two terms for their SPSM calculation but replace the isospin term by a term proportional to the local difference $(\rho_p(r) - \rho_n(r)$ in neutron and proton densities. Their proton and neutron potentials are given by the equations

$$V_p = \left[V_o + V_1 \frac{\rho_n - \rho_p}{\rho_n + \rho_p}\right] f(r) + V_c$$

$$V_n = \left[V_o - V_1 \frac{\rho_n - \rho_p}{\rho_n + \rho_p}\right] f(r)$$

where the function f(r) is the Woods-Saxon shape and V_c is the coulomb potential. In order to extend this from a nucleus with proton and neutron densities ρ_p^c and ρ_n^c to a neighbouring nucleus with densities differing by $\Delta\rho_p$ and $\Delta\rho_n$ they change the quantity inside the square brackets by

$$V_o\left(\frac{\Delta\rho_n + \Delta\rho_p}{\rho_n^c + \rho_p^c}\right) \pm V_1\left(\frac{\Delta\rho_n - \Delta\rho_p}{\rho_n^c + \rho_n^c}\right)$$

where the +(-) sign is for protons (neutrons). Thus no additional parameters are needed. In this way the added particle or particles produce a core polarization. For ^{40}Ca the neutron-proton rms radius difference which they obtain is -0.056 fm with the isospin (V_1) term and -0.092 fm without it. (Experiment gives -0.04). The corresponding differences in charge density are shown in Fig 1 together with the isospin part of the potential.

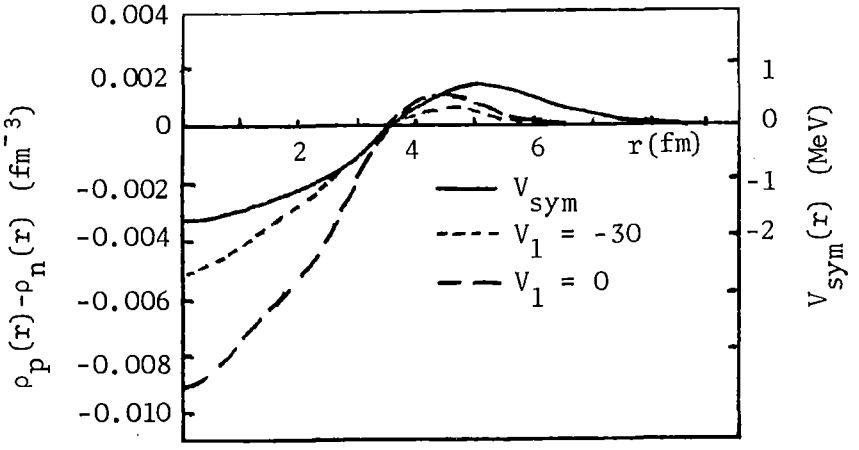

Fig. 1

The charge density which they obtain for ^{40}Ca is shown by the points (marked +) in Fig. 2 together with the experimental density and the results of some self-consistent field calculations (Frois, 1978). The curve GO was calculated with incorrect parameters and should be deleted. The method clearly needs some refinement in order to compete with the Hartree-Fock type calculations. Improving these calculations may turn out to be too complicated but one possibility which could easily be tried is to include the 0.4 $Z/A^{1/3}$ term in the proton potential in order to simulate the non-locality.

In some of their calculations Brown et al. used non-integer occupation numbers of the neutron orbits obtained from calculations of 2p-2h admixtures and they also varied the occupation numbers of the proton orbits, promoting them from the $d_{3/2}$ to the $f_{7/2}$ orbit in order to reproduce experimental charge

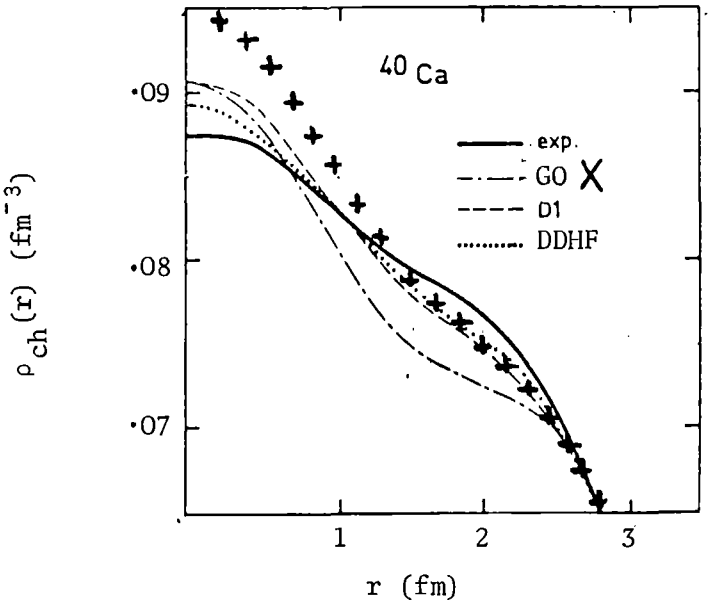

Fig. 2

radius differences. Fig. 3 shows the result of such a calculation for the ^{48}Ca-^{40}Ca density difference, together with the range of experimental densities determined by Sick.

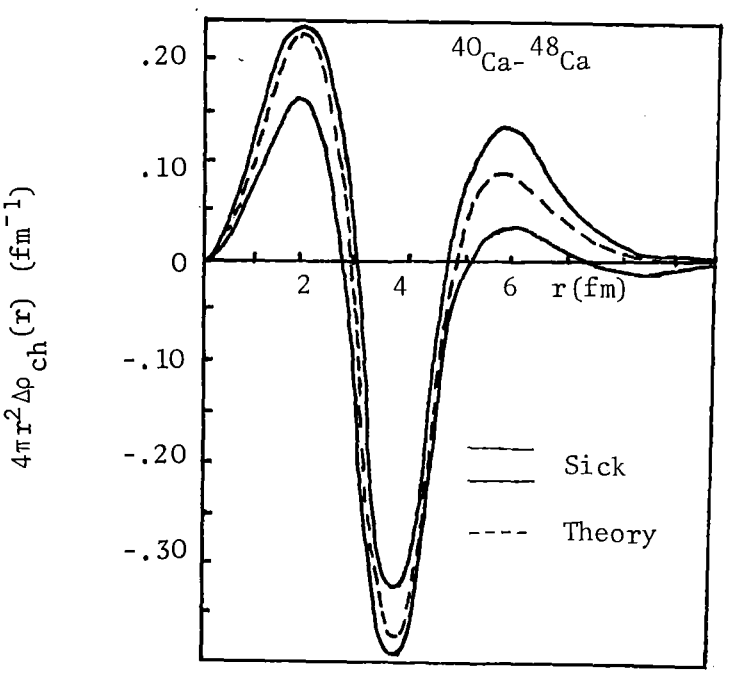

Fig. 3

Here the agreement is impressive and could no doubt be improved by altering the 2S occupation number.

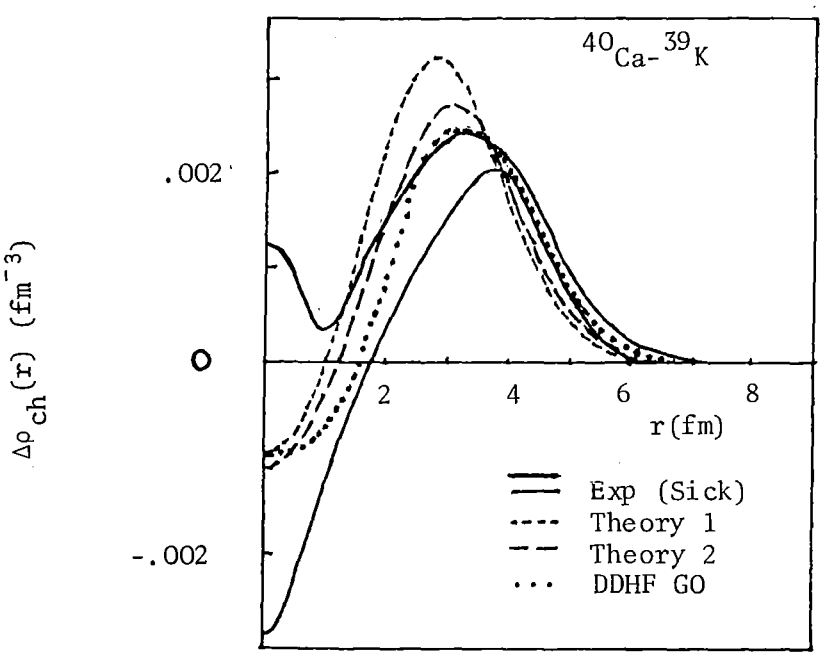

Fig. 4

We now consider much larger density changes, namely isotone shifts. Fig. 4 shows the familiar experimental results analyzed by Sick (1975) together with theoretical curves by Brown et al. The core polarization is clearly in evidence but the agreement is not as good as with Hartree-Fock.

This single particle method provides a very simple way of including some self-consistency and may turn out to be very useful.

3. The Mean Field Approximation

I am trying to follow the recommended terminology and avoid the use of the term "Hartree-Fock" because it is sometimes used to refer to a particular sort of self-consistent calculation in terms of free two-body forces. Strictly speaking the terms "Brueckner-Hartree Fock", "Local-Density-Approximation-Hartree-Fock", "Renormalized-Brueckner-Hartree-Fock" and "Density-Dependent-Hartree-Fock" refer to calculations which include quite different diagrams and produce dramatically different densities as shown in Fig. 5 (Negele 1974).

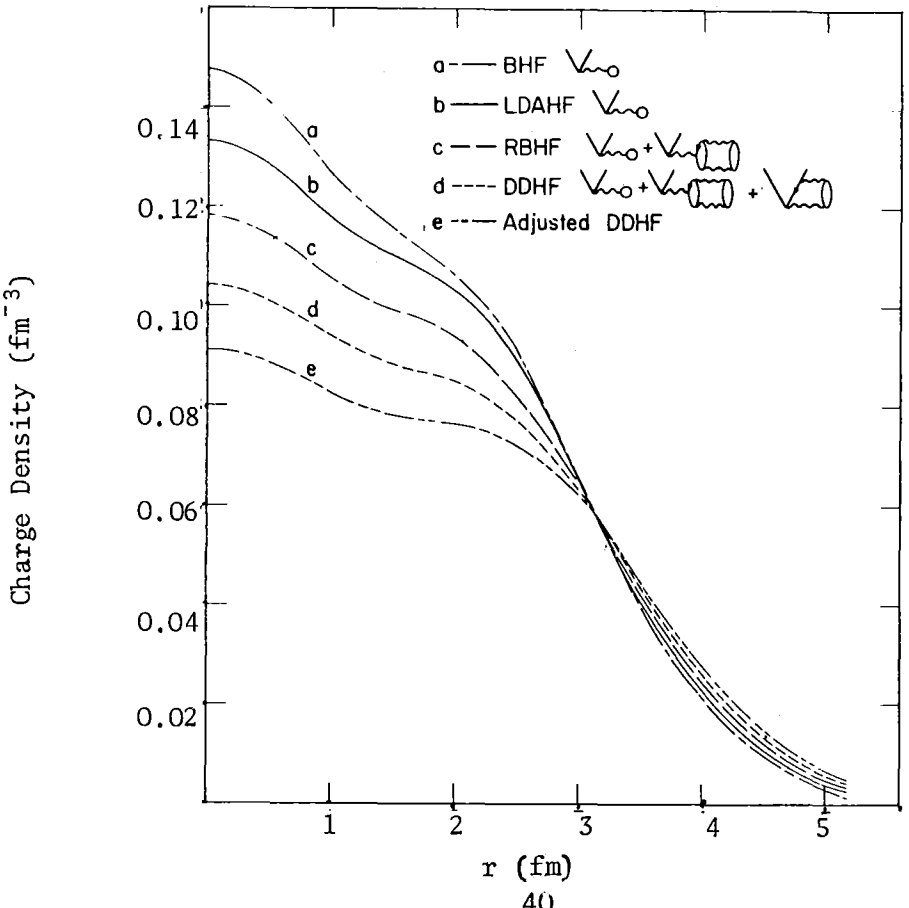

Fig. 5: Charge density distributions for ^{40}Ca. Results b-d include the indicated diagrams in the single particle potential, a and b correspond to oscillator space and LDA calculations respectively (and should give the same result but differ for technical reasons), and curve e indicates the effect of the phenomenological adjustment to obtain observed radii and binding energies.

In comparisons with experiment these self-consistent field calculations have achieved some impressive results. The central density is still a problem for many nuclei: for ^{208}Pb it is now measured with about 1% accuracy and the calculations give results about 15% too high. Some of the ways of improving or correcting such calculations are discussed in the next section.

4. Corrections to the Non-Relativistic Mean-Field Approximation

In order to apply the HF method a single determinant wave function must be a good approximation. One of the requirements for this is that the binding energy should have a deep minimum as a function of deformation. Fig. 6 shows that this condition is reasonably met for ^{40}Ca and ^{48}Ca. The curves suggest that ^{40}Ca is a better closed shell nucleus than ^{48}Ca but the latter is probably more stable against octupole deformations. A linear combination of determinants

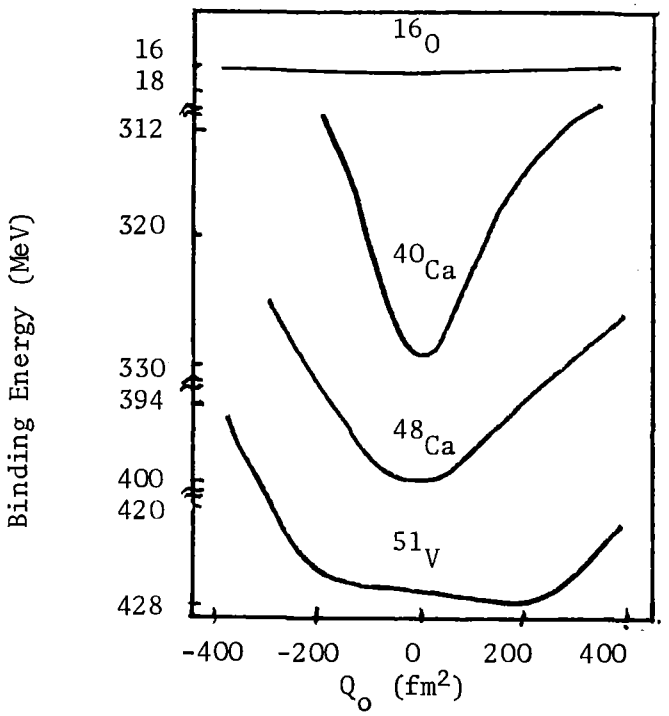

Fig. 6

represents the addition of 2p-2h and 4p-4h states and the usual effect of this is to lower the central density by removing s-state protons. This also damps the fluctuations which always seems to be bigger in HF-type calculations. The results of a RPA calculation of this depletion in ^{40}Ca are shown in Fig. 7.

The effect of neutron charge densities is now well-known, especially in the case of ^{48}Ca (Bertozzi et al., 1972) and the results of applying it to the ^{40}Ca-^{48}Ca charge difference is shown in Fig. 8 (Negele 1976).

Of course these curves refer to calculations in which the binding energy and charge radius are different from each other and from experiment and it remains necessary to insert one or two parameters into the theory in order to obtain these experimental quantities. (It should be stressed, however, that these parameters are adjusted just once to fit all closed shell nuclei).

A different point of view is to abandon any attempt to use free two-body forces and do all the adjustment in the parameters of the effective two-body force, as has been done by Vautherin and Brink (1972) and many other workers. This method is easier since the forces are chosen for convenience and calculations may be carried out for a much larger range of nuclei including non-closed shell and deformed nuclei (the reason for this is not one of principle but it is because the DDHF calculations are too difficult to carry out in practice except for closed-shell nuclei). Since they are effective forces any shortcomings in the theory due to the inadequacy of the mean-field approximation can be masked by the parameters.

Negele (1976) has considered differences between adjusted DDHF calculations and effective force calculations, especially those with zero range. He has looked at the predictions for the two types of calculations of a) central density, b) average interior slope, c) surface diffuseness, d) oscillations or fluctuations. He found that for a) and b) there is little to choose between the calculations. In the case of diffuseness, however, although this is mainly determined by the single particle binding energies, there is a difference in that the larger range and non-locality of DDHF tend to increase the diffuseness. In the case of fluctuations a δ-function term tends to enhance the oscillations and a $\nabla^2\rho$ modification to suppress them so that it is a matter of chance which of these effects dominates.

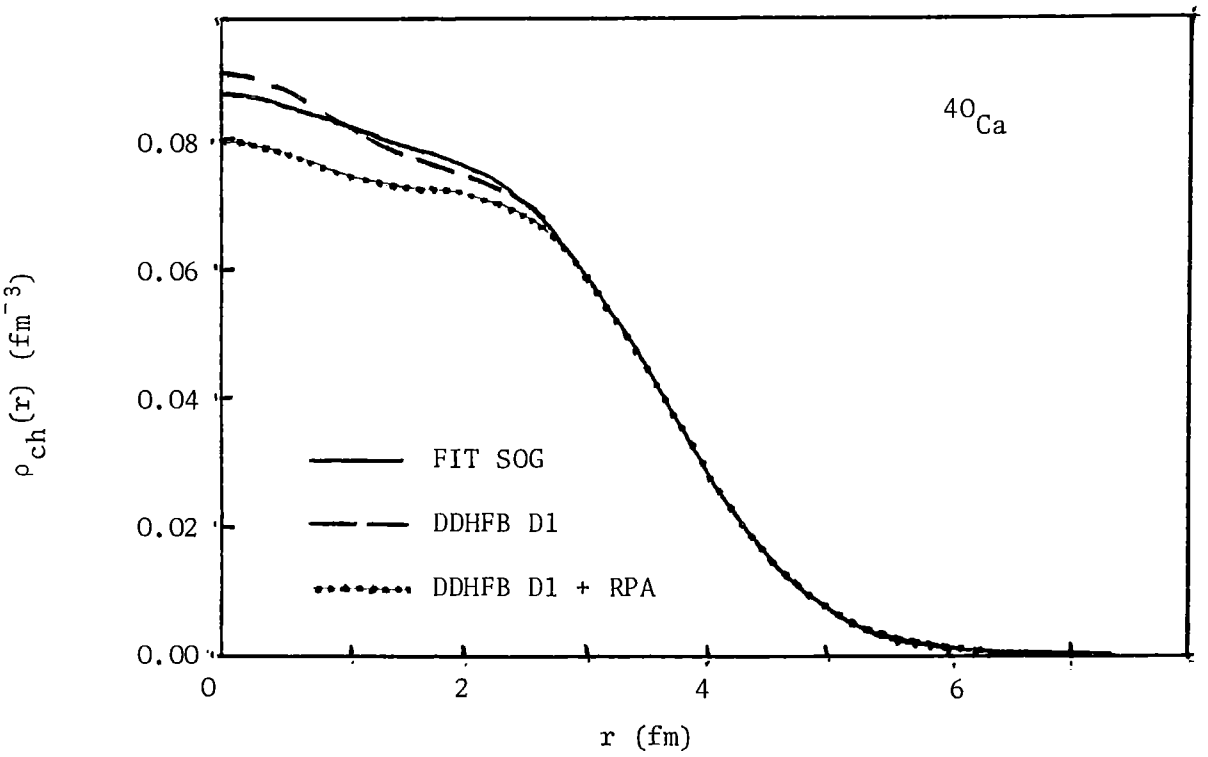

Fig. 7

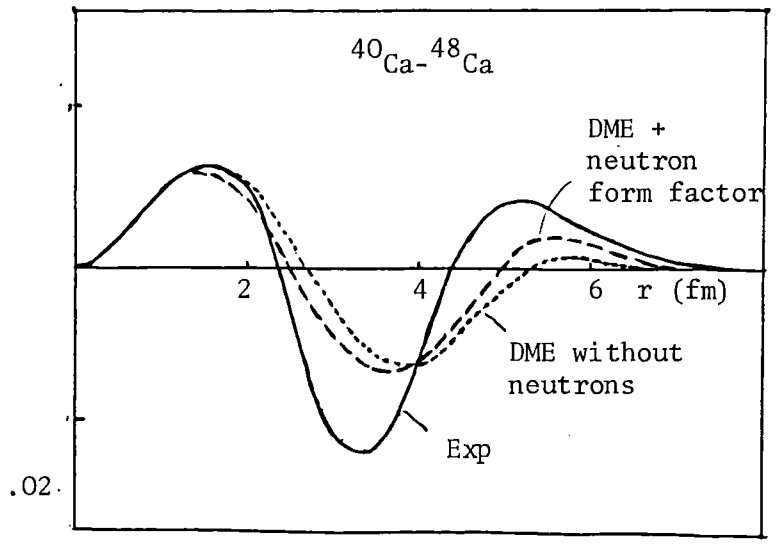

Fig. 8

Another effect studied by Chandra and Sauer (1976) is the departure of the proton form factor from that due to a single gaussian. They tried a sum

of three gaussians but in fact the single dipole form factor (as used by Bertozzi et al. 1972) is about as good. Perhaps we should be more accurate than this and use the exact Mainz form factor for the proton (Borkowski et al., 1975, Walther, 1978).

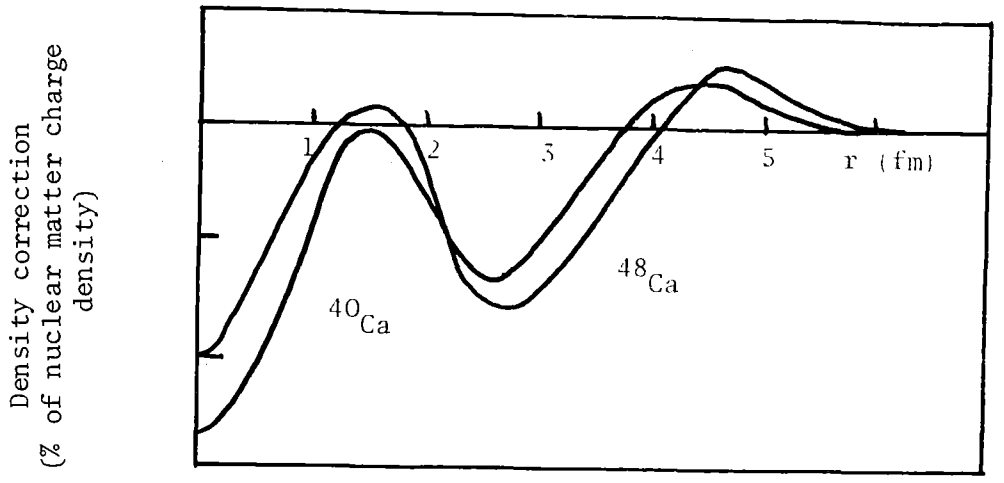

Fig. 9

Corrections due to the meson exchange current (MEC) are significant and have been calculated for a range of nuclear by Negele and Riska (1978). The resulting density corrections are shown in Fig. 9. The effect of including these in calculating magnetic form factors is quite dramatic, as shown in Figs. 10 and 11 (Negele 1978) although Sick (1979) finds that the inclusion of the π-nucleon form factor reduces the effect at high momentum transfer by up to a factor of two.

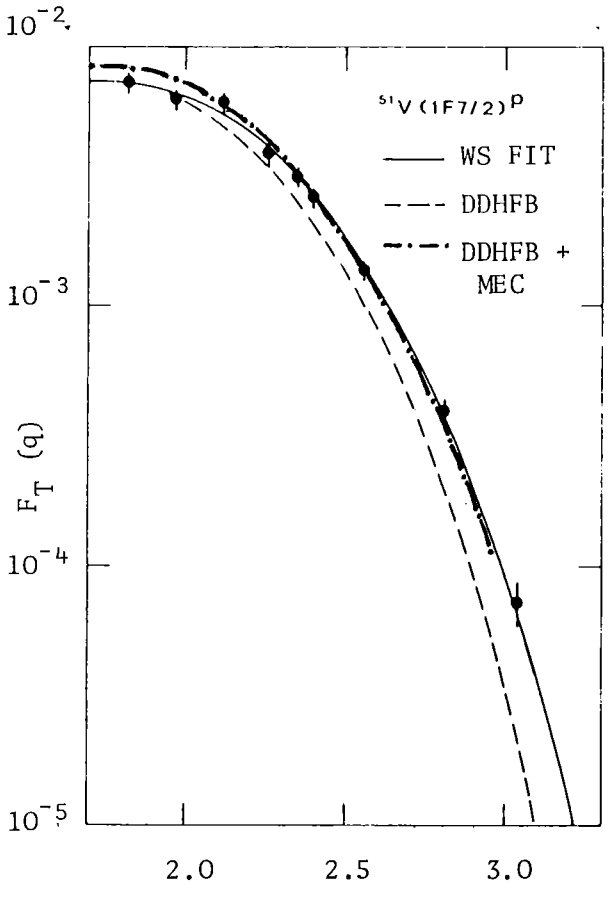

Fig. 10

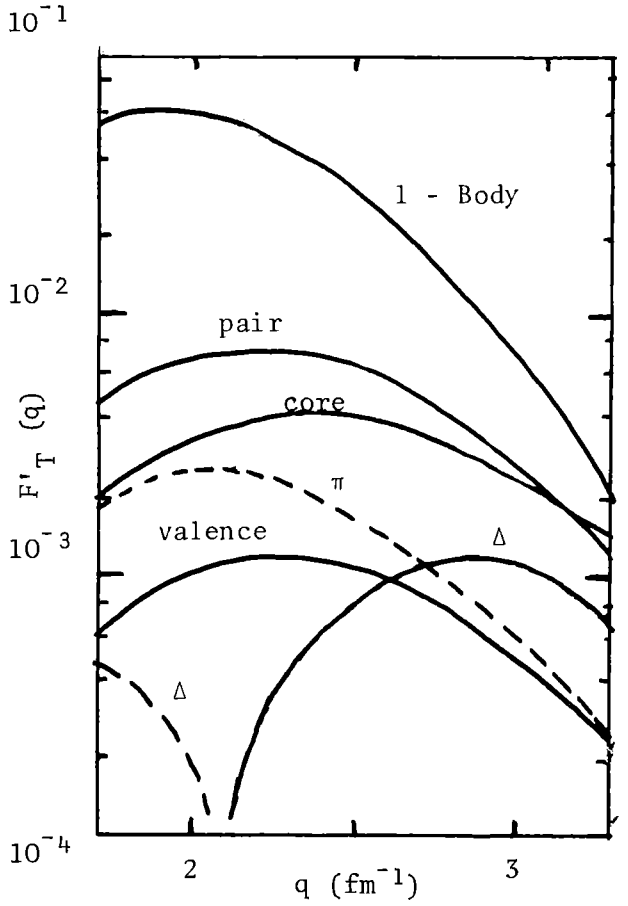

Fig. 11: Individual M7 contributions to the ^{51}V form factor (negative contributions shown as dashed curves)

Conclusions

It seems to me that the situation regarding charge densities of closed shell nuclei is almost satisfactory. There is still some work to be done in putting in the RPA corrections and renormalizing the ADDHF calculations to take account of this. The charge density test of calculations is a very severe one and the theory is now to be trusted in most respects. The tests of individual orbits come from isotone shifts, and magnetic scattering. The latter can be fitted very well by scaling the proton wave functions in the case of ^{93}Nb, ^{87}Sr by a factor of 0.954(6) which after corrections implies a radius ratio of 0.962 compared with MFA prediction of ∿1.00 (Negele, 1978). In the case of ^{51}V and ^{49}Ti the ratio is 0.996(8) compared with a prediction of 1.014 from a HFB calculation.(Sick 1979).

All this suggests to me that the HF type calculations are just as likely to give correct neutron distrubutions as hadron experiments. This does not mean that the latter should be stopped because HF calculations are cheaper! Perhaps we are on the verge of finding a disagreement but I am not too worried about the present figure of 100 millifermis (or attometers). Perhaps more attention should be paid to the surface thickness parameter which has been defined (in terms of the equivalent uniform k^{th} moment radius R_k) by Campi (1974) as

$$a = \frac{1}{\pi} \left[6R_k \frac{dR_k}{dk}\right]^{\frac{1}{2}}$$

Although I don't think rms radii are the best quantities to compare, in the absence of something more model-independant I have collected together a few of the numbers which you have been seeing regularly in Table I and Campi's surface thickness parameter in Table II.

Table I = Proton neutron and charge rms radii for Ca isotope

		40	42	44	46	48
r_{ch}		3.480	3.510	3.520	3.501	3.481
r_ρ	Exp	3.40	3.46	3.46		3.41
r_n		3.38(4)	3.44(4)	3.52(5)		3.58(4)
$r_n - r_\rho$		-.02(4)	-.02(4)	.06(4)		.17(4)
GO	$r_n - r_p$	3.46	3.46	3.46	3.46	3.46
GO		-.04	.02	.08		.18
Lane		-.04				.14
Brown	$r_n - r_p$	-.06				.163
Negele		-.04				.19

Table II Surface Thickness of ^{40}Ca and ^{48}Ca (Campi 1979)

		40	48
a_{ch}	Skyrme	0.50	0.47
	Skyrme	0.52	0.50
	Go	0.52	0.48
	Exp	0.53(1)	0.49(1)
a_{mass}	Go	0.49	0.47
	Exp	0.47(2)	0.45(2)

It seems that a fair amount of work remains to be done. We will soon be cut off by the law of diminishing returns but before then I should think the numbers will change a bit, perhaps in both theory and experiment, and quite possibly in the direction which brings them into agreement.

I am indebted to R.C. Johnson, X. Campi, I. Sick and D.F. Jackson for discussions and comments.

References

Barrett R C 1969 Proc. Int. Conf. on Properties of Nuclear States ed. M Harvey, J Y Cusson, J S Geiger and J M Pearson (Montreal: Universite de Montreal) 109-23.

———— 1974 Rep. Prog. Phys. 37 1-54

Barrett R C and Jackson D F 1977 Nuclear Sizes and Structure (Oxford: Clarendon Press)

Becchetti F G and Greenless 1969 Phys. Rev. 182 1190

Bertozzi W, Friar, J L, Heisenberg J and Negele J W 1972 Phys. Lett. 41B 408-14

Borkowski F, Simon G G, Walther V H and Wendling R D 1975 Nucl. Phys. B93 461

Brown B A, Massen S E and Hodgson P E 1979 preprint

Campi X 1974 Proc. Int. Conf. on Nuclear Self-Consistent Fields ed. G Ripker and M Porneuf (Amsterdam: North-Holland) 271-294

———— 1979 contribution to this conf.

De Witt Huberts P K A 1978 Proc. Conf. on Modern Trends in Electron Scattering (Amsterdam: IKO) 21-48

Elton L R B and Swift A 1967 Nucl. Phys. A94 52-72

Elton L R B and Webb S J 1970 Phys. Rev. Lett. 24 145

Friar J L and Negele J W 1973 Nucl. Phys. A 212 93

———— 1975 Adv. Nucl. Phys. 8 214

Lapikas L 1978 Proc. Conf. on Modern Trends in Electron Scattering (Amsterdam: IKO) 49-72

Lens F 1969 Z. Phys. 222 491-503

Lane A M, Martorell J and Zamick L 1978 preprint

Negele J W 1970 Phys. Rev. C1 1260-1320

———— 1974 Proc. Int. Conf. on Nuclear Self-Consistent Fields ed. G Ripker and M Porneuf (Amsterdam: North-Holland) 113-143

———— 1976 Proc. EPS Conf. on Radial Shapes of Nuclei, Cracow ed. A. Budzanowski and A Kapuscik (Cracow: Jagellonian University) 79-102

———— 1977 Proc. VII Int. Conf. on High Energy Physics and Nuclear Structure, ed. M P Locher (Basel: Birkhauser Verlag) 17-34

———— 1978 Proc. Conf. on Modern Trends in Electron Scattering (Amsterdam: IKO) 73-102

Negele J W and Riska D O 1978 Phys. Rev. Lett. 40 1005

Riska D O 1978 Proc. Conf. on Modern Trends in Electron Scattering (Amsterdam: IKO) 119-132

Sick I 1973 Nucl. Phys. A 208 557

———— 1975 Proc. Santa Fe Conference AIP Conf. Proc. 26 388

———— 1979 Invited talk at this conference

Walther V H 1978 Proc. Conf. on Modern Trends in Electron Scattering (Amsterdam: IKO) 103-118

Wohlfahrt H D 1978 Phys. Lett. 73B 131

SUMMARY TALK

P. Brix
Max-Planck-Institute,
Heidelberg,
Federal Republic of Germany

What do we know about the radial shape of calcium nuclei?

Closing remarks instead of a summary lecture

Peter Brix

Max-Planck-Institut für Kernphysik
Postfach 103980, D-6900 Heidelberg 1

There are well established traditions for summary lectures at international conferences. One extreme is that the speaker takes intensive notes at every lecture, adds a couple of jokes - possibly new ones - as well as his own modest personal opinion, and presents a thorough mixture of all this, trying to do justice to every main speaker. The other extreme possibility is to give that uninvited lecture which the speaker wanted to present, without much reference to previous talks.

Fortunately this was not an international conference but a discussing meeting. The facts and figures are still in everybody's memory,and there is no need to repeat them. In addition, Dr. Barrett has just given not only an excellent review of the theoretical results but also of the experimental situation and the historical background. Let me therefore try to formulate a summary not for the experts but for nuclear and non-nuclear physicists who may be interested in a short answer to the question which brought us together.

As nuclear physicists we are occasionally asked whether times have not passed when nuclear physics was an exciting science, and whether exciting new developments have not shifted to other fields inside or outside of physics. My answer is that I can make up a list of, say, twelve fascinating "news about atomic nuclei" which are the results of very recent research and discovery. By "recent" I mean the last few years. The first three items on my list are the following:

1. The size of the atomic nucleus, that fuzzy ball, has now been measured in quite a few cases with an accuracy of 1% as far as the spatial distribution of the charge density, with an accuracy of 0.1% as far as a well defined radial extension is concerned. The measurement of length has recently reached the attometer (10^{-18}m) region.

The small irregular changes of the nuclear charge distribution which occur when neutrons or protons are added have been studied precisely for selected regions of the isotopic chart.

2. For several nuclei, the spatial distribution of the magnetization and of the intrinsic charge deformation have been measured. We begin to "see in space" what happens when nuclei are excited.

3. From theoretical arguments there has never been much doubt that the neutrons have about the same spatial distribution as the protons. However, it has only been recently possible to measure reliably where the neutrons are. For ^{48}Ca it has now been established that neutrons and protons are not uniformly mixed: ^{48}Ca has a "neutron skin".

I do not want to bother you with my nine other "news from the world of nuclei". Please make up your own personal list.

A useful, but imaginary Physics Journal contains frequently updated short articles, always with the same titles, devoted to important basic subjects. One of my favorite titles would be "What do we know about the radial shape of nuclei in the Ca-region?"

Dr. Träger has pointed out in his contribution why the Ca-region is an ideal playground which nature has given us for

studying nuclear radii: ^{40}Ca is the heaviest stable closed shell nucleus with equal numbers of protons and neutrons; the addition of 8 neutrons leads to an even better closed shell nucleus, ^{48}Ca, with sufficient abundance to make isotopically pure targets; there are four more stable Ca-isotopes; finally there exist five stable isotones for Z=20 as well as 28. This is the reason why it pays to concentrate present efforts of measuring proton- and neutron distributions on these nuclides. However, as indicated by the title, I shall confine the following remarks to the calcium isotopes.

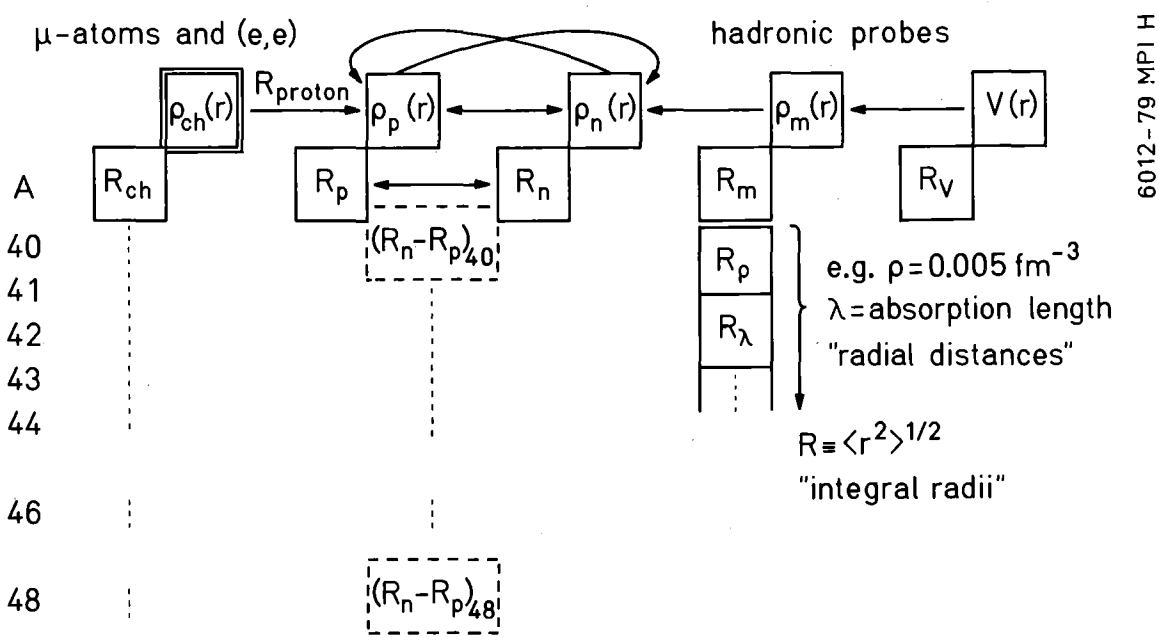

Fig. 1: The radial shapes and the many different nuclear radii of calcium isotopes: a survey

Fig 1 can serve as a guide for our survey. We are mainly interested in the ground state proton and neutron distributions $\rho_p(r)$ and $\rho_n(r)$. Neither of them is determined directly from experiment. Apart from other corrections, the finite size of the proton and the neutron form factor lead to a difference between $\rho_p(r)$ and the charge distribution $\rho_{ch}(r)$ measured by

electron scattering and muonic atoms. An iterative procedure is, therefore, necessary in deriving $\rho_p(r)$ and $\rho_n(r)$ from a measured matter distribution $\rho_m(r)$, and $\rho_{ch}(r)$. This is indicated by the curved arrows in Fig. 1 (see also, e.g., Ray 79). Another problem is the connection between $\rho_m(r)$ and the real potential V(r) for hadronic probes.

Let us start with ρ_{ch} for ^{40}Ca. This quantity is the corner-stone in our network. So far it was not available. If one wanted to draw a diagram of the charge distributions of closed shell nuclei (see, e.g., Bri 77), one could not include ^{40}Ca because an ambiguity in the analysis resulted in two different charge distributions for the central region which were compatible with previous data. It is great news from this meeting that Dr. Frois has shown us the new Saclay results. The momentum transfer has been extended to 3.6 fm^{-1}, and cross sections down to 10^{-38} cm^2 have been measured. We have heard that this means recording two counts per day with a beam power of 10 MW! One could imagine a bell being rung at Saclay whenever another scattered electron gave news about the very interior of the ^{40}Ca nucleus! For this important nuclide the experiment has reached a precision where the errors of the experiment are of the same order of magnitude as the various uncertainties of the analysis. The charge density of ^{40}Ca, including that in the center of the nucleus, is now known with a precision of at least $\pm$ 1%.

As we know, the analysis of $\rho_{ch}(r)$ from electron scattering needs the precise radius parameter R_k obtainable from muonic 2p-1s x-rays. One the other hand, R_{ch} can be evaluated from the Barret radius R_k if $\rho_{ch}(r)$ is known.

This leads us to the "many different nuclear radii" of Fig. 1. By writing this I want to stress that there are several isotopes (mass number A); that one has to state whether the charge-,

proton-, neutron-, matter-distribution or the potential is meant; and - above all - that there are many different definitions of the radius itself. Finally, in addition to the data referring to all protons or neutrons, there may be specific information on single nucleon orbits. The distribution for a valence nucleon as measured by magnetic electron scattering is an impressive example.

The rms radius R may be called an "integral radius". On the other hand, hadronic probes usually probe the nucleus predominantly at some characteristic radial distance. Dr. Meyer spoke of "point like" radii. The symbol R_λ reminds of his talk, the symbol R_ρ of what Dr. Fernandez has told us. One cannot be careful enough in always stating precisely which radius is meant. On the other hand it has become evident at this meeting that important information will be obtained by combining the results from various experiments, using a consistent set of input data.

At this point it should be mentioned that this manuscript was written after the oral presentation at the end of the Karlsruhe meeting. In writing it, I felt that I could now happily omit those figures and data of some of the exciting brand new results which I showed at that time. Nothing could be gained by repeating here what the authors themselves had formulated best. The information is easily accessible by turning back the leaves of these proceedings. Let me arbitrarily select two "news" which I personally would include in a report on this meeting.

1. The revival of optical isotope shifts as a tool for nuclear physics is impressive, and its applicability to nuclei as light as Ca quite surprising for someone who worked in this field earlier. Since the charge density of the atomic s-electrons is constant over the nuclear volume, differences of rms radii

R_{ch} are the relevant measurable quantities. Fortunately, the charge radii of Ca-isotopes do not change in a regular way with neutron number. Only this fact gives the optical spectroscopist a handle to separate the mass dependent effects which lead to regular changes of the isotopic frequences from the irregular contributions of the nuclear volume effect. (By the way: why not forget the unnecessary separation of "normal" and "specific" mass effect, at least when talking to non-specialists?). A news at this meeting was the radius of ^{41}Ca measured at Heidelberg (KowT 79). We have learnt that it agrees exactly with that of ^{40}Ca within ± 0.006 fm. We also heard that the accuracy of the optical measurements can possibly be improved by a factor of 10, and that the charge radius of ^{45}Ca (163 days half-life) is within reach. - It is remarkable that isotopic and isotonic rms-charge radii differences for even-even nuclei in the Ca-region derived from precise energies of muonic K_α-rays show almost the same trend as function of neutron or proton number, including the sudden increase at Z or N equal 28.

2. As far as neutron radii are concerned, the quantity most reliably determined experimentally seems to be (Fig. 1):

$$\Delta = (R_n - R_p)_{48} - (R_n - R_p)_{40}. \quad (1)$$

New values for Δ were presented at this meeting (see also the table in Dr. Gils' contribution), and a recent compilation may be found in (IgoA 79). The value $\Delta = 0.13(4)$ fm from a recent analysis (Ray 79) of 0.8 GeV polarized proton elastic scattering at Los Alamos may be added to the list. I think that one now may tell everybody that Δ is without doubt different from zero and positive. This is clear experimental evidence of differences in neutron and proton distributions. I shall refrain from writing down a number because that needs a careful discussion. Karlsruhe has done much to emphasize the importance of such a discussion.

One may look at (1) in two ways: For theorists, $(R_n-R_p)_{40}$ is small and calculable, and Δ thus a measure of the "neutron skin" of ^{48}Ca. The experimentalist may start from the experimental fact that R_p is pratically the same for ^{40}Ca and ^{48}Ca. Δ then reliably indicates different neutron distributions in both isotopes.

In closing, let me repeat two remarks which I shall remember: the surprizing statement made by Edgar Allan Poe on V(r) as quoted by Dr. Meyer: "Truth is not always in a well. In fact, as regards the more important knowledge, I do believe that she is invariably superficial", and Dr.Hüfner's comment: "The point you want to omit may be the only one that contains a lot of physics".

Incidentally, this meeting took place 70 years after Geiger and Marsden discovered the back scattered alpha rays which started the discovery of the atomic nucleus. It managed to get together scientists working in many different fields but having the same scientific interest (For many conferences it is the other way round). As the last speaker, I have the pleasure and privilege to thank the Kernforschungszentrum Karlsruhe, and especially Prof. Klose, in the name of all participants for making this useful meeting possible, and for their generous hospitality. We are very grateful to our colleagues Gils, Rebel, and Schatz from Karlsruhe for their initiative and for all the work that was the result.

References:

Bri 77: P. Brix: Naturwiss. 64, 293 (1977)

IgoA 79: G. Igo et al.: Phys. Lett. 81B, 151 (1979)

KowT 79: J. Kowalski, F. Träger, S. Weißhaar, H.-B. Wiegemann and G. zu Putlitz: Z. Physik 290, 345 (1979)

Ray 79: L. Ray: Preprint LA-UR 79-93; submitted to Phys. Rev. C

The papers presented at the Karlsruhe discussion meeting have not been listed.